Physics of the Solid State, Vol. 43, No. 10, 2001, pp. 1801–1806. Translated from Fizika Tverdogo Tela, Vol. 43, No. 10, 2001, pp. 1729–1734.

METALS AND SUPERCONDUCTORS

Analysis of Dispersion of Long-Wavelength Optical Phonons in Zinc with the Help of Light Scattering

G. A. Bolotin*, Yu. I. Kuz'min*, Yu. V. Knyazev*, Yu. S. Ponosov*, and C. Thomsen**

** Institute of Metal Physics, Ural Division, Russian Academy of Sciences, ul. S. Kovalevskoĭ 18, Yekaterinburg, 620219 Russia*

*** Institute of Solid State Physics, Technical University, Berlin, 10623 Germany*

e-mail: ponosov@imp.uran.ru

Received November 13, 2000; in final form, February 7, 2001

Abstract—The temperature dependences (5–300 K) of the Raman spectra of E_{2g} phonons and optical constants in zinc single crystals are measured in the excitation energy range 1.4–2.54 eV. It is found that phonon damping decreases upon an increase in the wavelength of exciting radiation. The obtained results are compared with the dependence of the phonon width on the excitation energy (the probed wave vector of the excitations under investigation), which are presented for the first time for the transition metal osmium, as well as with the calculated electron–phonon renormalization of damping, taking into account the actual distribution of wave vectors.

1. INTRODUCTION

The exceptionally strong dispersion of self-energies (anomalous frequency dispersion and threshold damping of optical phonons) in a range of small wave vectors ($q \sim 10^6$ cm^{-1}) recently observed during an analysis of Raman spectra of transition metals [1] raised a question as to the origin of electron excitations that determine nonadiabatic effects in electron–phonon interaction.

The effects of nonadiabatic renormalization of the long-wavelength optical-phonon spectrum (anomalous dispersion and the Landau damping threshold) [2–4] in the region of $q \sim \omega_0/v_F$ (ω_0 is the phonon frequency and v_F is the Fermi velocity for electrons) are based on the intraband mechanism and, hence, must exist in transition (*d*) as well as in simple (*s*, *p*) metals. Such effects were sought for the latter metals (Zn [5–7], Cd [5], Bi, Sb [5, 7], Be [8]) while studying the temperature dependences of the phonon frequencies and width by using the method of inelastic light scattering. The experiments with these metals revealed an increase in energies and a narrowing of phonon lines during cooling and made it possible to estimate the contributions of anharmonism and of the electron–phonon interaction to the frequency shifts and to the damping of phonons at low temperatures. However, early measurements were made in a narrow excitation energy range (2.41–2.54 eV), which did not permit study of the dependences of the phonon self-energies on their wave vector. An estimate of the threshold value of the wave vector $q_0 \sim \omega_0/v_F$ (near which the renormalization effects must increase) obtained from the available data on the average electron velocity at the Fermi surface gives the value $\sim 1.6 \times 10^5$ cm^{-1} for zinc, while the effective value of the momentum probed in such experiments was an order of magnitude larger: $\sim 16 \times 10^5$ cm^{-1}. In the present work, the range of excitation energies is considerably extended in the course of investigating the temperature dependences of the phonon frequencies and widths for the *p*-metal Zn with a view to obtaining information on the change in phonon parameters in the accessible range of wave vectors being probed, and the obtained results are compared with theoretical predictions and observed anomalies in transition *d* metals.

2. EXPERIMENT

The measurements were made on a zinc crystal with a resistivity ratio $\rho_{300\,\mathrm{K}}/\rho_{4.2\,\mathrm{K}} = 560$. This ensures conservation of the wave vector so that $ql \gg 1$, where l is the electron mean free path. Previous investigations were either carried out on polycrystals [5, 6] or contained no information on the purity of the single crystals under investigation [7]. The surfaces used for measurements were prepared by cleaving the crystal at right angles to its hexagonal axis. Since we studied backward scattering in our experiments, the obtained results correspond to the phonon wave vector directed along the **c** axis. The excitation was carried out through krypton and titanium–sapphire laser radiation (1.4–2.6 eV), which allowed us to study a fairly wide range of phonon momenta, $(7–16) \times 10^5$ cm^{-1} for $T = 5$ K. The spectral resolution in our measurements was <1 cm^{-1}. The magnitude of the momentum being probed and its uncertainty as a result of absorption in the surface layer of the metal were estimated on the basis of ellipsometric measurements of the optical constants on the crystal under investigation at temperatures of 80 and 300 K in the energy range 0.5–3 eV, as well as on the basis of earlier

optical measurements at 4.2 K [9]. The optical parameters were measured on a sample placed in a ultrahigh-vacuum chamber with a residual gas pressure of 10^{-8} Pa. Before measurements, the sample surface was cleaned again by bombarding it with argon ions (accelerating voltage 300 V, ion current 1 μA, cleaning time 10 min). The obtained optical constants were also used for determining the efficiency of light scattering for various excitation energies and for simulating the observed resonance dependence of the scattering cross section. The temperature of the samples placed in an Oxford cryostat varied from 5 to 300 K. The light scattering spectra were analyzed using a Dilor XY (with a cooled multichannel detector) or a DFS-24 (single-channel detection on the basis of a cooled photomultiplier) spectrometer.

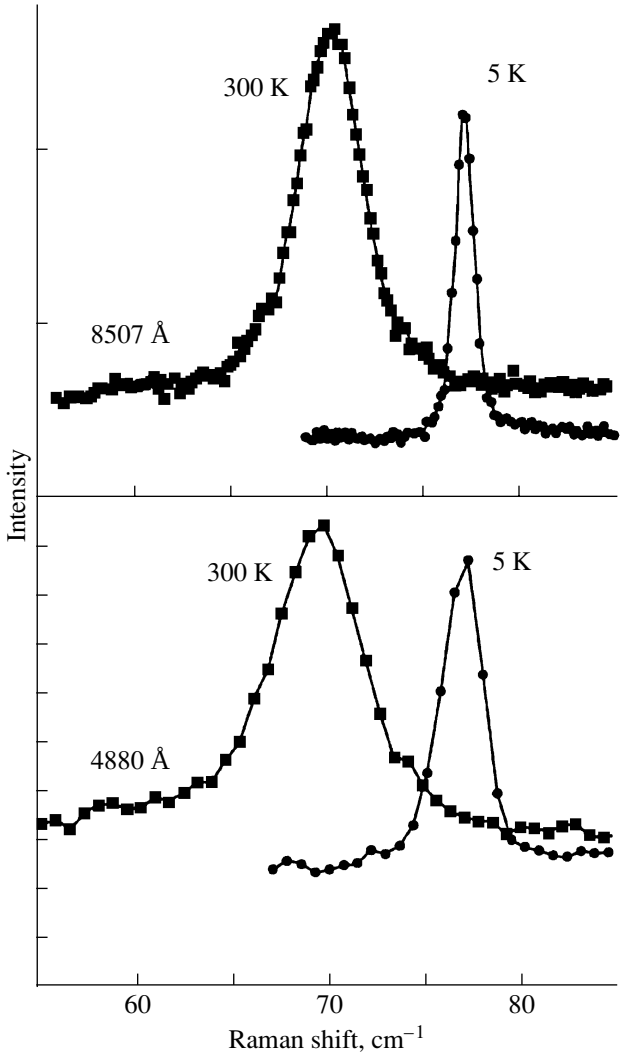

Fig. 1. Raman spectra of E_{2g} phonons in Zn measured at various temperatures for the two extreme laser lines in the range of excitation energies used.

3. DISCUSSION OF RESULTS

The Raman spectra of zinc measured at various temperatures and wavelengths λ_L of laser light are shown in Fig. 1. As was also reported in earlier publications, a decrease in temperature leads to an increase in frequency of the single Raman-active E_{2g} mode in a crystal with a hexagonal close-packed structure (space group D^4_{6h}) and narrows the spectral lines. The experimental profiles of the phonon lines were approximated by Voigt profiles, which are a convolution of a Gaussian (instrumental contour) and a Lorentzian (phonon line). The phonon energy and width obtained as a result of this analysis are shown in Figs. 2 and 3 for the two extreme points of the excitation energy range.

The frequencies of optical phonons measured with the two wavelengths of incident radiation coincide at high temperatures (to within experimental error). At the lowest temperatures, the phonon energy measured for laser radiation of the larger wavelength is found to be 0.5 cm^{-1} higher (Fig. 2). Much larger differences are observed for the widths of the phonon lines at low temperatures; the width is less by half for the case of λ_L = 8507 Å (Fig. 3). The change in the phonon energy is within the experimental error, while the difference in the line width is undeniable. The low-temperature width ~1.7 cm^{-1} measured by us at λ_L = 4880 Å turned out to be slightly larger than the value determined earlier [5, 6] (in those experiments, the measurements were made on polycrystals with an unknown purity and with an insufficient spectral resolution), while the width measured for the first time at λ_L = 8507 Å is as small as ~0.8 cm^{-1}. Figure 3 also shows the temperature dependences of the phonon line width in the transition metal osmium for two values of the wave vector **q** || **c** (probed using incident radiation with wavelengths 4880 and 6764 Å) in the range of considerable dispersion of the phonon branch.

It was in osmium [1] that we observed (in the spectra of light scattering by electrons) electron excitations with energies close to the phonon frequency, which determine the renormalization of vibrational excitations and depend not only on the magnitude but also on the direction of the wave vector. The fact that the difference between the phonon widths measured at different wavelengths of laser radiation (i.e., for phonons with different values of momenta) increases upon cooling in both metals suggests that the effects observed both in zinc and in osmium are determined by interactions with electron excitations. It can be seen from Fig. 3 that the difference between the two metals lies in that the difference between the low-temperature widths is larger in the transition metal osmium, which demonstrates an anomalous temperature dependence of the linewidth in contrast to conventional anharmonic behavior in the case of zinc. This indicates that the electron–phonon interaction in the case of osmium makes a dominant contribution to the line width even at high tempera-

tures; this is in contrast to zinc, in which anharmonic processes of phonon decay predominate upon an increase in temperature.

The temperature variation of the phonon frequencies and widths in zinc was considered in [5–7] taking into account the contributions of anharmonic three- and four-phonon processes. As a result of processing the experimental temperature dependences, anharmonic coefficients were determined and the contribution of the electron–phonon interaction was estimated. Since the low-temperature data [5, 6] obtained for excitation at the 4880 and 5145 Å lines are close to our results for the same values of excitation energy, we believe that the results of the analysis carried out in those publications can be used for estimating the anharmonic contributions to the phonon parameters at low temperatures. It follows from [5, 6] that the contributions from anharmonism to the residual width at low temperatures amount to ~0.15–0.4 cm^{-1}. It should be noted that the similar analysis contained in [5–7] presuming the presence of constant electron contributions to the phonon energy and damping is not quite correct, because it leads only to order-of-magnitude estimates of low-temperature contributions to the phonon parameters. This also follows from the results presented by us here and earlier [1, 10], indicating that the temperature variation of the phonon line widths and energies in metals depends on the frequency of the exciting radiation used, that is, on the magnitude and direction of the momenta of the phonons involved.

Returning to the observed changes in the low-temperature phonon damping in zinc, we note that apart from the electron–phonon interaction, there are other possible contributions to the phonon line width that depend on the excitation energy (phonon momentum). One of such contributions, which was considered in [5], is associated with dispersion of the optical branch near the center of the Brillouin zone as a result of short-range ion–ion interactions. The estimate of this contribution for the phonon wave vectors and their uncertainties in question was based on the neutron diffraction data for phonon dispersion and led to an insignificant value equal to ~0.1 cm^{-1}. Another possible reason behind the dependence of the line width on the excitation energy might be the presence of stresses or disorder in the surface layer of the crystal. However, such an explanation appears vague since the damping mainly changes in the energy range 2–2.54 eV, where the skin depth remains practically unchanged (or even increases slightly).

The width Γ of a phonon line associated with one-particle electron excitations (Landau damping) is usually estimated by replacing the wave vector q in the dependence

$$\Gamma(q) = \frac{\Gamma_0 q_0}{q} \qquad (1)$$

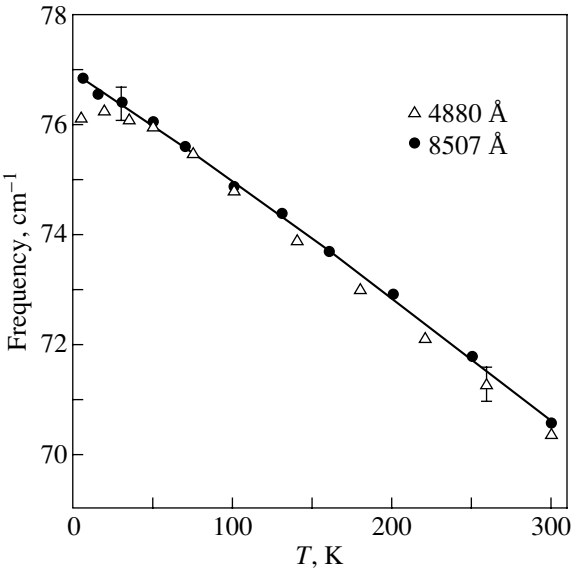

Fig. 2. Temperature dependence of the E_{2g} phonon frequency in Zn.

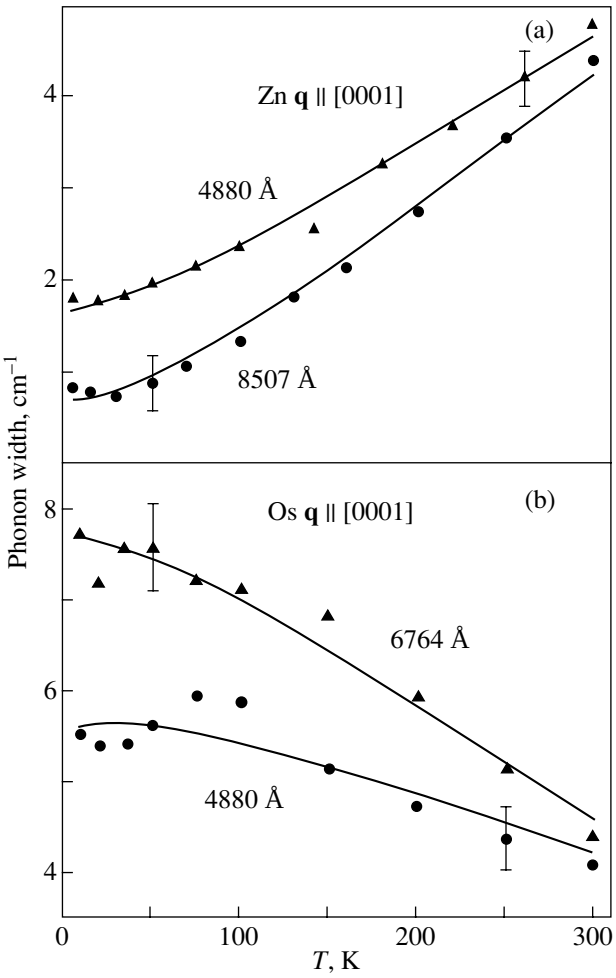

Fig. 3. Temperature dependences of phonon damping in (a) Zn and (b) Os measured at different excitation energies.

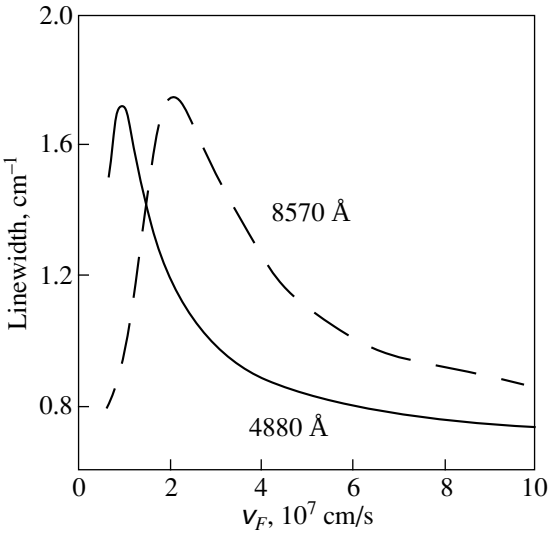

Fig. 4. Dependence of the phonon line width in Zn on the electron velocity calculated from Eq. (5) for the two extreme laser wavelengths of incident radiation.

with the effective value q_{eff}. Here, $\Gamma_0 = \pi\omega_0\lambda$ is the jump in damping at the threshold wave vector q_0 and λ is the electron–phonon interaction constant averaged over the Fermi surface. While estimating $\Gamma(q_{\text{eff}})$ qualitatively, it is often assumed that $q_{\text{eff}} \sim 1/\delta \sim 10^6$ cm^{-1}, where δ is the skin depth for the corresponding laser radiation frequency. Consequently, the line width is proportional to the skin depth [5, 6].

In the case of Zn, the skin depth varies insignificantly almost in the entire excitation energy range used by us, exhibiting a considerable (almost threefold) increase only over the region below 1.6 eV. According to the above estimate, this must lead to an increase in the linewidth for the lowest values of excitation energy. However, the linewidth for $\lambda_L = 4880$ Å was found to be twice as large as that for $\lambda_L = 8507$ Å. The reason behind this discrepancy is probably an inaccurate estimate of q_{eff}. The effective value of q emerging as a result of an uncertainty in the wave vector of probing radiation in the absorbing medium (metal) must be determined taking into account the distribution $W(q)$ of the light field in the metal over the wave vectors:

$$\Gamma(q_{\text{eff}}) = \frac{1}{\pi\delta}\int_0^\infty \Gamma(q)W(q)dq. \qquad (2)$$

For example, for the distribution used in [11] and taking into account the specular reflection of phonons at the metal–vacuum interface, the line width $\Gamma(q)$ depending on q is blurred with a weight

$$W(q) = \frac{4q^2}{\left|q^2 - q_M^2\right|^2}, \qquad (3)$$

where the doubled complex wave vector q_M of a light wave propagating in the metal is given by $q_M = \zeta_1 - i\zeta_2 = (4\pi/\lambda_L)(n - ik)$. As a result of blurring, we obtain

$$\frac{1}{q_{\text{eff}}} = \frac{1}{\pi\zeta_2}\left(\arctan\frac{\zeta_1 - q_0}{\zeta_2} + \arctan\frac{\zeta_1 + q_0}{\zeta_2}\right). \qquad (4)$$

Thus, the value of q_{eff} depends not only on the imaginary part of the complex refractive index $n - ik$ of the metal but also on its real part and, which is important, on the magnitude of the threshold wave vector q_0 at which the Landau damping appears. For small threshold vectors $q_0 \leq \zeta_1 \ll \zeta_{22}$, we have $\Gamma(q_{\text{eff}}) \sim \omega_0\delta/v_F$; however, for $q_0 \gg \zeta_1, \zeta_2$ (small electron velocities), the inverse dependence on the skin depth holds: $\Gamma(q_{\text{eff}}) \sim v_F/\omega_0\delta$. The difference in optical constants for the laser lines 8507 and 4880 Å leads to the effect where the relation between the phonon line widths for different values of the excitation energy can change depending on the value of v_F on account of the dependence of q_{eff} on the characteristic velocity of electrons. An additional factor determining the shape and width of the phonon line is the dispersion of the phonon branch near the Landau damping threshold. The electronic parameters for the possible scenario of electron–phonon interaction were estimated on the basis of numerical calculations of the spectral profile of phonon lines, with the polarization operator calculated in the model of free electrons [3, 4] and integrated over the wave vector distribution in Eq. (3):

$$I(\omega) = \frac{1}{\pi}\int_0^\infty \frac{4\omega_0^2\Gamma_{\text{ph}}(q,\omega)W(q)dq}{\left[\omega^2 - \omega_0^2 - 2\omega_0^2\Sigma'(q,\omega)\right]^2 + 4\omega_0^2\Gamma_{\text{ph}}(q,\omega)^2}. \qquad (5)$$

Here, $\Gamma_{\text{ph}} = \Gamma_{\text{an}} + \Sigma''(q,\omega)$ and $\Sigma'(q,\omega)$ and $\Sigma''(q,\omega)$ are the real and imaginary parts of the polarization operator, respectively [3, 4]:

$$\Sigma(q,\omega) = \frac{4}{\omega_0}\int\frac{g^2 q v}{\mathbf{qv} - (\omega + i\gamma)}\frac{ds}{v}, \qquad (6)$$

where ds is the area element of the Fermi surface, which was assumed to be spherical, and g is the matrix element of the electron–phonon interaction. The bare line width Γ_{an}, including the contribution of anharmonism and other temperature-independent contributions, was assumed to be 0.6 cm^{-1}; the electron-scattering frequency, $\gamma = 1$ cm^{-1}. The matrix element g of the electron–phonon interaction was varied for fitting of the calculated widths to experimental data. The results are presented in Fig. 4 in the form of the dependence of the line width on the Fermi velocity of electrons for the two extreme excitation energies. It can be seen that the phonon line width corresponding to the shorter wavelength excitation is almost twice as large if phonons interact with electrons with low velocities ~10^7 cm/s. At the same time, phonons excited at $\lambda_L = 8507$ Å and hav-

ing a smaller wave vector must give broader lines as a result of interaction with faster electrons ($v_F \sim 10^8$ cm/s). These facts may indicate that even if the electron mechanism of anomalous dispersion of phonons is of purely intraband origin, it is associated with sheets of the Fermi surface corresponding to very low velocities and, hence, with local regions of the phase space. The multisheet nature of the Fermi surface of Zn permits several spikes in the Landau damping due to charge carriers belonging to different sheets of the Fermi surface. These groups of carriers might differ considerably in their values of characteristic velocity and in the electron–phonon coupling parameter involved. The relation between the phonon line widths for excitation at 8507 and 4880 Å observed for Zn can be attributed to the Landau damping due to a group of charge carriers with anomalously low velocities, which, however, interact intensely with E_{2g} phonons.

In addition, the degeneracy of bands in the AL direction of the Brillouin zone for hexagonal metals and the small band gaps in the vicinity of this direction, which are due to spin–orbit interaction, could be responsible for another mechanism of formation of the electron continuum that interacts with phonons. Interband transitions may also lead to dispersion of phonon frequencies and to Landau damping characterized by specific values of parameters (such as q_0) which are not related to the values of the electron velocity and the electron–phonon coupling constant averaged over the Fermi surface. The complete pattern of the phonon spectrum renormalization in the region of small wave vectors can be obtained taking into account the actual band structure of the metal.

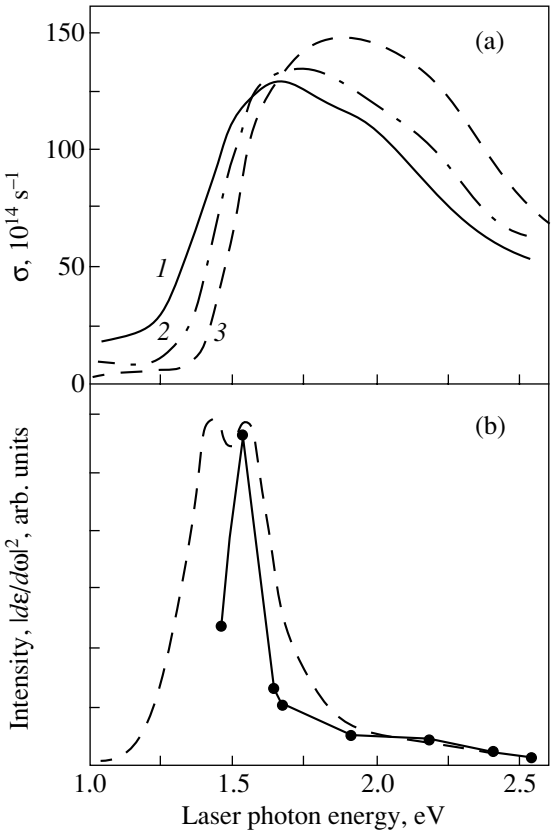

Fig. 5. (a) Optical conductivity in Zn at various temperatures *T*, K: (*1*) 300, (*2*) 80, and (*3*) 4.2 [9]; and (b) corrected dependences of the intensity of scattering by E_{2g} phonons (dark circles and solid curve) and the derivative $|d\varepsilon/d\omega|^2$ calculated from optical data (dashed curve) for 80 K.

4. RESONANCE EFFECTS

The energies corresponding to the spectral lines of pumping laser radiation at which our measurements were made lie in the region of high-intensity interband absorption with a peak shifting upon cooling from 1.7 eV (300 K) to 1.9 eV (4.2 K) and are located within the band half-width interval (Fig. 5). According to the interpretation based on the pseudopotential model [12], this absorption band corresponds to transitions between almost parallel bands that are formed in the free electron spectrum in the presence of the Fourier transform $V_{1\bar{1}0,1}$ of the pseudopotential; the positions of the peaks of the absorption band correspond to a doubled value of $[V_{1\bar{1}0,1}]$. The doubly degenerate (1, 2) and (3, 4) bands in the AHL plane are almost parallel in the LH direction, and high-intensity transitions are realized in the vicinity of the bottom of the Brillouin zone, bounded by empty states of bands 1 and 2 at H on one side and by electron packets of bands 3 and 4 at L on the other. Since the band degeneracy is removed outside of the AHL plane, and (due to the spin–orbit interaction), in this plane also (except the AL direction), the absorption band associated with the pseudopotential component $V_{1\bar{1}0,1}$ is formed by many types of transitions $1 \longrightarrow 2$, $1 \longrightarrow 3$, $1 \longrightarrow 4$, $2 \longrightarrow 3$, $2 \longrightarrow 4$, $3 \longrightarrow 4$.

The excitation of Raman spectra in the region of this absorption band leads to considerable resonance effects and makes it possible to make measurements down to excitation energies of ~1.4 eV. In order to obtain a correct dependence of the scattering cross section on the energy of incident (scattered) radiation, the measured intensities were corrected to take into account the transmission coefficients at the air–sample interface, the change in the solid angle in the sample, and the skin depth, and were calibrated by comparing them with the intensities of scattering for a standard CaF_2 sample measured under the same conditions. The obtained resonance behavior is illustrated in Fig. 5 together with the energy dependence of the function $|d\varepsilon/d\omega|^2$ (calculated from the measured optical constants), which is normally used for describing the contribution from two-band terms in an analysis of resonances in semiconductors [13]. This derivative was calculated using only the interband component of the permittivity. The obtained

resonance enhancement band in the scattering cross section is in satisfactory agreement with the behavior of $|d\varepsilon/d\omega|^2$ in the energy range under investigation; the observed difference in the form of the resonance may be due to the difference in the deformation potentials for the above-mentioned multitude of transitions forming the absorption band.

ACKNOWLEDGMENTS

One of the authors (Yu. S. P.) expresses his gratitude to S. Reich and A. Gony for their help in carrying out the experiments.

This work was supported by the Russian Foundation for Basic Research, project no. 99-02-17390.

REFERENCES

1. Yu. S. Ponosov, G. A. Bolotin, C. Thomsen, and M. Cardona, Phys. Status Solidi B **208** (2), 257 (1998).
2. I. P. Ipatova, M. I. Kaganov, and A. V. Subashiev, Zh. Éksp. Teor. Fiz. **84**, 1830 (1983) [Sov. Phys. JETP **57**, 1066 (1983)].
3. S. Engelsberg and J. R. Schrieffer, Phys. Rev. **131** (3), 993 (1963).
4. I. P. Ipatova and A. V. Subashiev, Zh. Éksp. Teor. Fiz. **66** (2), 722 (1974) [Sov. Phys. JETP **39**, 349 (1974)].
5. W. B. Grant, H. Schultz, S. Hufner, and J. Pelzl, Phys. Status Solidi B **60** (1), 331 (1973).
6. H. Schultz and S. Hufner, Solid State Commun. **20**, 827 (1976).
7. V. V. Baptizmanskiĭ, I. I. Novak, and A. F. Naĭdenov, Fiz. Tverd. Tela (Leningrad) **21** (9), 2584 (1979) [Sov. Phys. Solid State **21**, 1488 (1979)].
8. Yu. S. Ponosov and G. A. Bolotin, Fiz. Tverd. Tela (Leningrad) **27** (9), 2636 (1985) [Sov. Phys. Solid State **27**, 1581 (1985)].
9. J. H. Weaver, D. W. Lynch, and R. Rosei, Phys. Rev. B **5** (8), 2829 (1972).
10. Yu. S. Ponosov, C. Thomsen, and M. Cardona, Physica C (Amsterdam) **235–240**, 1153 (1994).
11. A. Dervisch and R. Loudon, J. Phys. C **9**, L869 (1976).
12. G. P. Motulevich and A. A. Shubin, Zh. Éksp. Teor. Fiz. **56** (1), 45 (1969) [Sov. Phys. JETP **29** (1), 24 (1969)].
13. M. Cardona, in *Light Scattering in Solids*, Ed. by M. Cardona and G. Güntherodt (Springer-Verlag, Berlin, 1982; Mir, Moscow, 1984), Vol. II, p. 12.

Translated by N. Wadhwa

Physics of the Solid State, Vol. 43, No. 10, 2001, pp. 1807–1810. Translated from Fizika Tverdogo Tela, Vol. 43, No. 10, 2001, pp. 1735–1738.

METALS AND SUPERCONDUCTORS

A High-Modulus Metastable Phase in Mg–Ni–Y Alloys

N. P. Kobelev, Ya. M. Soifer, G. E. Abrosimova, I. G. Brodova*, and A. N. Manukhin*

Institute of Solid State Physics, Russian Academy of Sciences, Chernogolovka, Moscow region, 142432 Russia
e-mail: kobelev@issp.ac.ru

** Institute of Physics of Metals, Russian Academy of Sciences, Yekaterinburg, 620219 Russia*

Received March 7, 2001

Abstract—The evolution of the elastic properties and the character of the structural changes occurring during the crystallization of amorphous Mg–Ni–Y alloys are investigated. The process of crystallization is shown to proceed in two stages with formation of an intermediate metastable phase at the first stage. This phase has higher elastic characteristics than those of the stable crystalline phases of this system. © *2001 MAIK "Nauka/Interperiodica".*

1. INTRODUCTION

Recently, noticeable attention has been paid to the investigation of materials whose new physical properties are determined by the formation of nonequilibrium amorphous, quasicrystalline, or nanocrystalline phases. First and foremost, this occurs in the case of light alloys based on magnesium or aluminum. As was shown in our previous works [1, 2], the evolution of the amorphous-nanocrystalline structure of $Mg_{84}Ni_{12.5}Y_{3.5}$ alloy during its thermal treatment substantially affects its final elastic and dissipation characteristics. The crystallization of this alloy from an amorphous state was found to be a multistage process (proceeding through the formation of a metastable phase named the $Mg_xNi_yY_z$ phase). The appearance of the metastable phase was accompanied by an anomalous increase in Young's modulus of the alloy. This phase was assumed to possess higher elastic characteristics than those of the stable phases of this system. The obtained diffraction patterns of the metastable phase were analyzed and compared with the diffraction patterns of the known structures of magnesium, nickel, yttrium, and their compounds. However, we failed to identify the metastable phase because of the absence of data on phases with characteristics corresponding to this particular phase. The appearance of metastable phases during the crystallization of magnesium–nickel alloys close in chemical composition was later detected in works [3, 4], wherein the effect of the structure on the hydrogenation of these alloys was studied. In this work, we tried to clarify whether the discovered anomaly in the behavior of the elastic characteristics is typical of ternary Mg–Ni–Y alloys solely or if it is more general and can be observed in binary alloys of the Mg–Ni type as well.

2. EXPERIMENTAL

As the main subject of investigation, an $Mg_{87}Ni_{13}$ alloy of eutectic composition was chosen. For comparison, alloys containing up to 4% Y were also used. The alloys were obtained as bands approximately 0.03 mm thick and 1 to 3 mm wide as a result of fast quenching (at a cooling rate of 5×10^6 K/s) from a temperature of 510°C on a copper wheel in a vacuum. Young's modulus of specimens was measured with the use of the technique of flexural vibrations ("tongue") at frequencies around 250 Hz in a temperature range from 20 to 330°C in a vacuum of 10^{-3} torr. This technique is described in detail in [5]. The rate of temperature changes used in heating–cooling cycles was approximately 1.5 K/min.

Specimens for structural study were prepared by annealing in vacuumed ampoules at a constant rate (1.5 K/min) of heating up to a chosen temperature with subsequent quenching in water. The structures were investigated [6] at room temperature with the use of the x-ray diffraction technique on a SIEMENS D-500 diffractometer with CuK_α radiation. The diffractometrical measurements were carried out at the reflection orientation; the specimens were fastened to a monocrystal silicon plate positioned in such a manner that the plate did not affect the diffraction pattern.

3. RESULTS AND DISCUSSION

Upon being obtained, the specimens were amorphous. No sign of crystalline phases could be noticed in the x-ray patterns.

The behavior of Young's modulus of specimens with various yttrium contents undergoing heat treatment was qualitatively the same and similar to that of the $Mg_{84}Ni_{12.5}Y_{3.5}$ alloy studied earlier [1, 2]. Figure 1 shows the temperature dependence of the relative change in Young's modulus of the $Mg_{87}Ni_{13}$ alloy exhibited during two heating–cooling cycles of the specimen. Up to approximately 140°C, Young's modulus E linearly decreases with an increase in temperature. This change is practically completely reversible and corresponds to the temperature dependence of E.

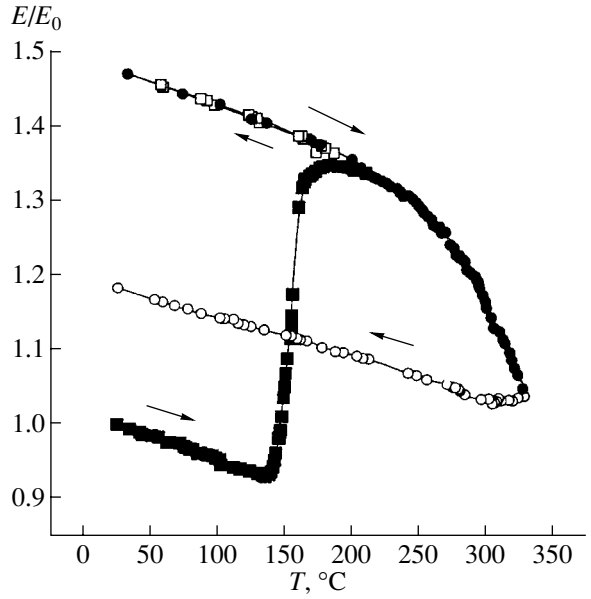

Fig. 1. The relative change in Young's modulus E of the $Mg_{87}Ni_{13}$ alloy that occurs during two heating–cooling cycles. In the first cycle, the specimen is heated to 200°C (filled squares) and cooled to room temperature (open squares). In the second cycle, it is heated to 330°C (filled circles) and cooled to room temperature (open circles). The rate of temperature change is 1.5 K/min.

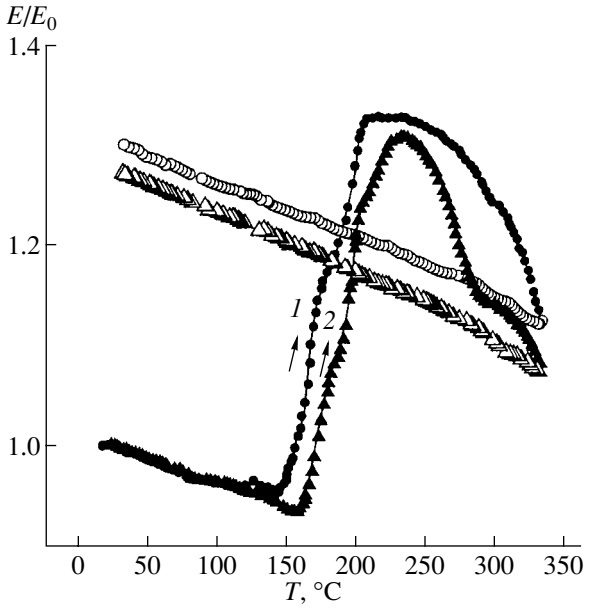

Fig. 2. The relative change in Young's modulus of (*1*) $Mg_{85}Ni_{13}Y_2$ and (*2*) $Mg_{81}Ni_{13}Y_4$ alloys during a cycle of heating to 330°C (filled symbols) and cooling to room temperature (open symbols). The rate of temperature change is 1.5 K/min.

Above 140°C, Young's modulus sharply increases (by nearly 50% with respect to the amorphous state). This change is irreversible, which is indicated by the character of the temperature dependence of E during cooling from a temperature of 200°C (Fig. 1). As the specimen is further heated (or during repeated heating, as in Fig. 1) to a temperature of approximately 230°C, E slightly decreases linearly with temperature, which satisfactorily corresponds to its temperature dependence. During the subsequent increase in temperature, Young's modulus begins to irreversibly decrease, so that upon cooling of the specimen from 330°C, its value at room temperature is only 20% higher than that in the amorphous state (and, accordingly, approximately 30% lower than the maximum value recorded after annealing at a temperature of 220 to 230°C). A similar temperature change in Young's modulus (with slight differences in the values of characteristic temperature points) is observed also for alloys containing yttrium (Fig. 2). This behavior, which was earlier discovered in the case of the $Mg_{84}Ni_{12.5}Y_{3.5}$ alloy [1, 2], was explained on the basis of a hypothesis concerning two-stage crystallization from the amorphous state through the formation of a metastable crystalline phase with a high Young's modulus.

This idea is confirmed by the data of structural investigations carried out in this work. Figure 3 shows diffraction patterns of a $Mg_{87}Ni_{13}$ specimen after annealing at various temperatures. Upon heating above 140°C (curve *a*), there appear maxima in the diffraction pattern corresponding to the reflections of magnesium and an unknown phase. Upon heating from 200 to 230°C (curve *b*), the intensities of these lines substantially increase and small traces of the Mg_2Ni can be noticed in a number of cases. At the same time, no reflections related to certain other known phases of Mg–Ni system are present. Upon further increase in the temperature of annealing (curve *c*), the intensities of lines attributed to the unknown phase decrease, but the reflections related to the Mg_2Ni phase become well pronounced (the maxima are marked with triangles). Heating to 360°C (curve *d*) results in a diffraction pattern in which only those lines that represent Mg and Mg_2Ni crystalline phases remain, and the whole diffraction pattern corresponds to the equilibrium of this system. Thus, the x-ray data confirm the two-stage character of the crystallization of the alloy from the amorphous state and the appearance of an intermediate metastable phase at the first stage.

A similar metastable phase is observed in alloys containing yttrium as well. Figure 4 shows comparative diffraction patterns for alloys with and without yttrium after annealing at close temperatures corresponding to the maxima of the temperature dependences of Young's modulus (Figs. 1, 2). Curve *a* in Fig. 4 represents an $Mg_{87}Ni_{13}$ alloy upon annealing at 200°C, while curve *b* corresponds to an alloy containing 4 at. % yttrium ($Mg_{83}Ni_{13}Y_4$) annealed at 230°C. As can be seen, both spectra have the same set of lines, which indicates the

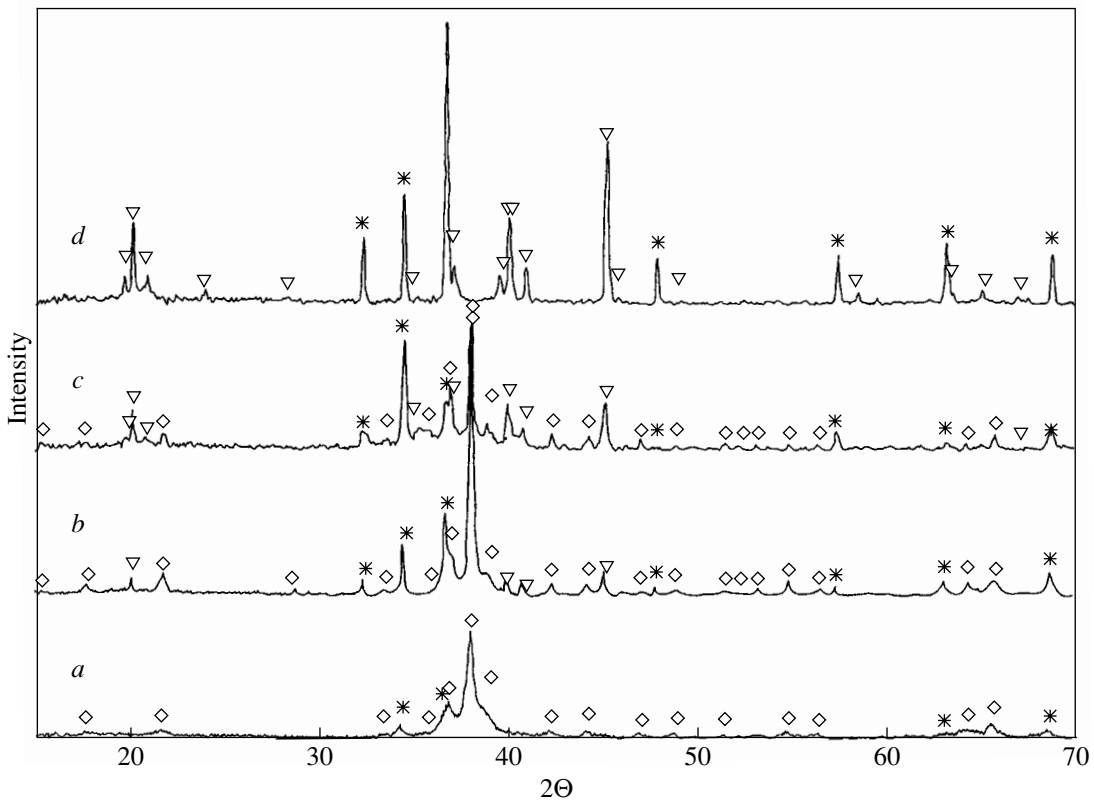

Fig. 3. The diffraction patterns of $Mg_{87}Ni_{13}$ specimens after annealing at temperatures (°C) (*a*) 180, (*b*) 210, (*c*) 290, and (*d*) 360. Asterisks, triangles, and diamonds mark the lines of Mg, Mg_2Ni, and the metastable phase, respectively.

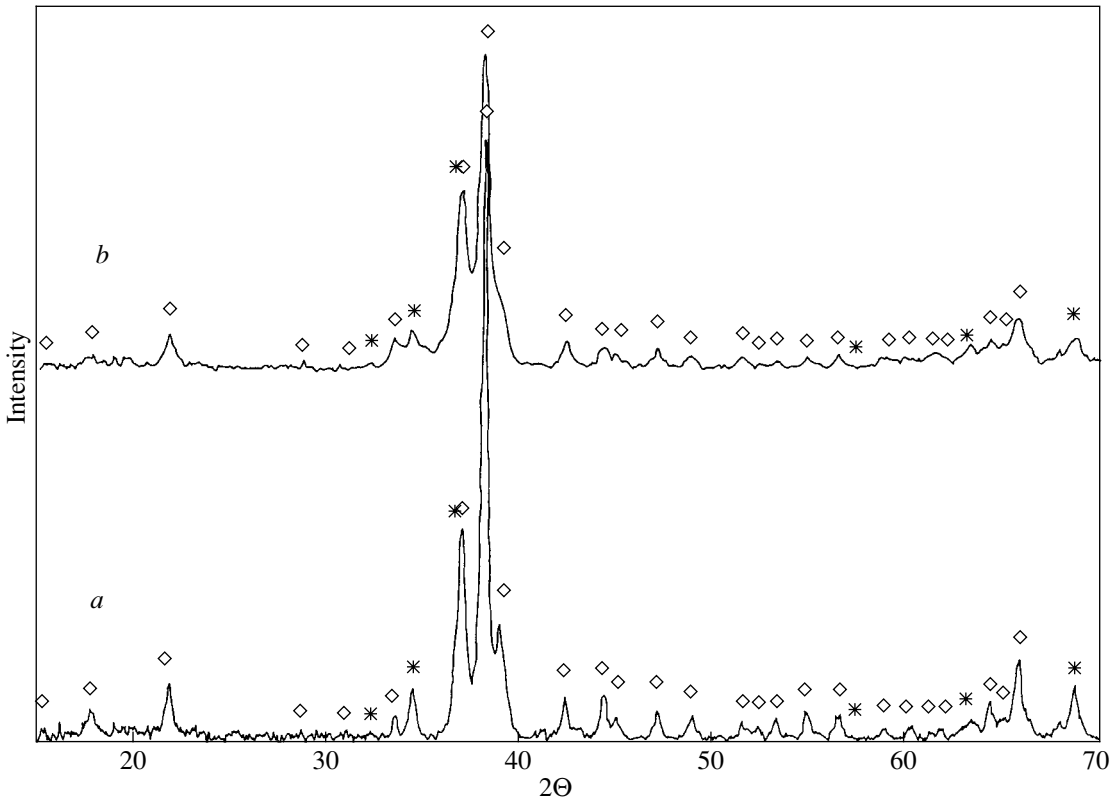

Fig. 4. The diffraction patterns of (*a*) $Mg_{87}Ni_{13}$ (annealed at 200°C) and (*b*) $Mg_{83}Ni_{13}Y_4$ (annealed at 230°C). Asterisks and diamonds mark the lines corresponding to magnesium and the metastable phase, respectively.

formation of the same metastable phase in both alloys. The differences in the half-widths of the diffraction lines are related to the difference in the grain size of the nanocrystal structure formed in the alloys, and the small deviations in the relative intensities correlate with the unequal parts of magnesium and the metastable phase caused by the dependence of the crystallization temperature on the chemical composition of the alloy. Note also that in the case of compositions containing yttrium, Mg lines are slightly shifted toward smaller diffraction angles, which means that yttrium is at least partly dissolved in the Mg lattice.

A similar phase with the same set of characteristic lines was found in the $Mg_{87}Ni_{12}Y_1$ alloy in [3]. The authors of that work supposed that this metastable phase had an Mg_6Ni_i composition and a face-centered cubic lattice with an a parameter of about 2.01 nm. On the other hand, the author of [6] concludes that the same set of lines of the metastable phase is better reproduced by a simple cubic lattice with $a \approx 1.004$ nm, because some of the strong lines typical of fcc structures proposed in [3] are absent in the experimental spectrum, and suggests Mg_3Ni as a possible chemical composition of the phase. At present, x-ray diffraction measurements do not allow one to unambiguously determine the chemical composition of the intermediate phase. However, we can already state that intermetallides with a heightened elasticity can form in magnesium–nickel alloys under certain conditions. A simple calculation supports this idea. On the basis of the variants of chemical composition proposed in [3, 6] and the analysis of x-ray patterns recorded after annealing the alloys at various temperatures, we can conclude that the part of the metastable phase does not exceed 70% at the maximum values of Young's modulus, while its own Young modulus is higher than that of compositions of the stable phases (Mg and Mg_2Ni) by at least 40%.

This work was financially supported by the Russian Foundation for Basic Research, project no. 99-02-17477.

REFERENCES

1. N. P. Kobelev, Ya. M. Soifer, I. G. Brodova, and A. N. Manukhin, Fiz. Tverd. Tela (St. Petersburg) **41** (4), 561 (1999) [Phys. Solid State **41**, 501 (1999)].
2. Y. M. Soifer, N. P. Kobelev, I. G. Brodova, *et al.*, Mater. Res. Soc. Symp. Proc. **554**, 293 (1999).
3. T. Spassov and U. Köster, J. Alloys Compd. **287**, 243 (1999).
4. G. Fridlmeier, M. Arakawa, T. Hirai, and E. Akiba, J. Alloys Compd. **292**, 107 (1999).
5. N. P. Kobelev, Ya. M. Soifer, V. G. Shteinberg, and Yu. B. Levin, Phys. Status Solidi A **102** (2), 773 (1987).
6. G. E. Abrosimova, Fiz. Tverd. Tela (St. Petersburg) **43**, (2001) (in press) [Phys. Solid State **43** (2001) (in press)].

Translated by Yu. Novakovskaya

Physics of the Solid State, Vol. 43, No. 10, 2001, pp. 1811–1815. Translated from Fizika Tverdogo Tela, Vol. 43, No. 10, 2001, pp. 1739–1743.

METALS AND SUPERCONDUCTORS

Thermal Conductivity of the "Light" Heavy-Fermion Compound $YbIn_{0.7}Ag_{0.3}Cu_4$

A. V. Golubkov*, L. S. Parfen'eva*, I. A. Smirnov*, H. Misiorek, J. Mucha**, and A. Jezowski****

**Ioffe Physicotechnical Institute, Russian Academy of Sciences, ul. Politekhnicheskaya 26, St. Petersburg, 194021 Russia*
e-mail: Igor.Smirnov@pop.ioffe.rssi.ru

*** Institute of Low-Temperature and Structural Research, Polish Academy of Sciences, Wroclaw, 53-529 Poland*

Received March 12, 2001

Abstract—This paper reports on the electrical resistivity and thermal conductivity of polycrystalline $YbIn_{0.7}Ag_{0.3}Cu_4$ at temperatures from 4.2 to 300 K, which exhibits, at T_v, a continuous isostructural first-order phase transition from a Curie–Weiss paramagnet with localized magnetic moments (for $T > T_v$) to a Pauli paramagnet in a nonmagnetic Fermi liquid state with the Yb ion in a mixed valence state (for $T < T_v$). It is shown that for $T < T_v$, the Lorenz number behaves in accordance with the theoretical model developed for heavy-fermion materials, while for $T > T_v$, it acquires the value typical of standard metals. © *2001 MAIK "Nauka/Interperiodica".*

During the last decade, the world's leading laboratories (particularly in the USA, Japan, and Germany) have been paying particular attention to the investigation of the $YbInCu_4$ and $YbAgCu_4$ intermetallic compounds and their intermediate compositions, $YbIn_{1-x}Ag_xCu_4$.[1]

These compounds crystallize in the $AuBe_5$-type fcc lattice [C15b structure, $F\bar{4}3m(T_d^2)$ space group] and possess very unusual physical properties.

At $T_v \sim 40$–80 K under atmospheric pressure, $YbInCu_4$ undergoes an isostructural phase transition from a Curie–Weiss paramagnet with localized magnetic moments (for $T > T_v$) to a Pauli paramagnet in a nonmagnetic Fermi liquid state with the Yb ion in a mixed valence state (for $T < T_v$).

It is generally agreed that at the phase transition, the Yb valence changes from 3 in the high-temperature phase to 2.9 in the low-temperature phase. At the same time, studies of the L_3 x-ray absorption spectra [5, 6] and x-ray *K*-line shifts [7] suggest that the Yb valence for $T > T_v$ is ~2.9 [5–7] and for $T < T_v$ is ~2.8 [5, 6]. The high- and low-temperature phases are a semimetal and a metal, respectively, with weak and strong hybridization of the Yb 4*f* electrons with the conduction electrons, accordingly. For $T < T_v$, $YbInCu_4$ has a high density of states at the Fermi level, a feature characteristic of heavy-fermion and mixed-valence rare-earth systems. The parameter γ (the coefficient of the term linear in temperature in the electronic thermal conductivity) of the $YbInCu_4$ low-temperature phase is ~50 mJ/mol K^2 [6, 8, 9], which indicates a fairly large effective carrier mass.

The $YbInCu_4$ system is classed among the light heavy-fermion systems [5].

$YbAgCu_4$ is a heavy-fermion compound. It undergoes a transition from the single-impurity Kondo regime at high temperatures ($T > T_K$; T_K is the Kondo temperature) to a coherent Kondo lattice (the heavy-fermion regime) that persists at low temperatures ($T < T_K$). The value of T_K derived from analyzing various physical effects varied from 40 to 130 K [10–16]. The effective carrier mass in $YbAgCu_4$ for $T < T_K$ is ~$60m_0$ (m_0 is the electronic mass) [13, 17], and the Yb ion valence at temperatures both below and above T_K is close to 3. The parameter γ for $T < T_K$ is ~200–250 mJ/mol K^2 [1, 6, 9, 17–19], which permits one to assign $YbAgCu_4$ to moderately heavy-fermion systems [19], because for classical heavy-fermion systems, $\gamma > 400$ mJ/mol K^2.

$YbIn_{1-x}Ag_xCu_4$ features a continuous transition from the properties characteristic of $YbInCu_4$ to those typical of $YbAgCu_4$. The limiting critical concentration x_{cr} up to which, in the effects studied, a distinct enough phase transition at a certain T_v is still observed (similar to that occurring in $YbInCu_4$) was found to be ~0.2–0.25 [6, 9, 19–22]. Within the interval $x = (0.2$–$0.25)$–0.5, there is a continuous phase transition from a Pauli paramagnet in a nonmagnetic Fermi liquid state with a mixed Yb ion valence (~2.8) at low temperatures to a Curie–Weiss paramagnet with localized magnetic moments (and a Yb ion valence of ~2.91) at high temperatures [6, 9, 19–21]. At the same time, no sharp changes are observed to occur in the temperature dependences of the magnetic

[1] References to numerous studies on the physical properties of $YbInCu_4$ and $YbAgCu_4$ can be found in [1–3].

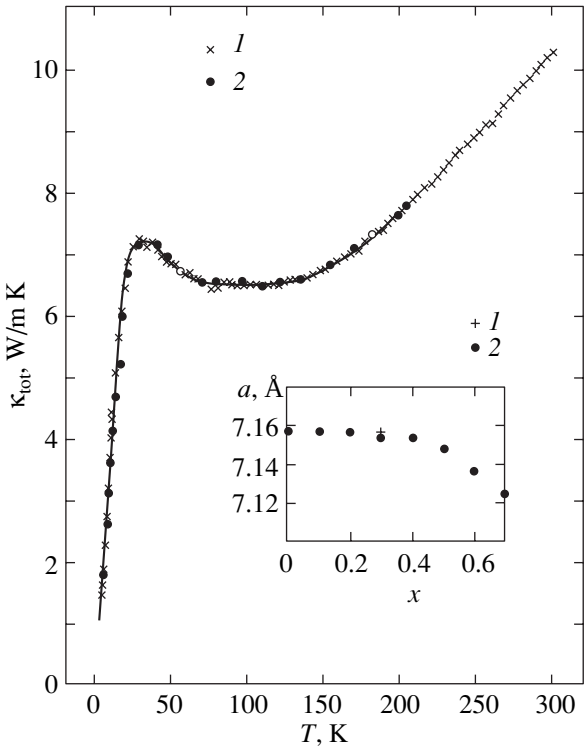

Fig. 1. Temperature dependence of κ_{tot} for an $YbIn_{0.7}Ag_{0.3}Cu_4$ sample; (*1*) measurements from 300 to 4.2 K and (*2*) reverse run (4.2 to 200 K). The inset is the dependence of the lattice constant of $YbIn_{0.7}Ag_{0.3}Cu_4$ on x; (*1*) our data and (*2*) data from [19].

susceptibility [19–22], electrical resistivity [9, 21], heat capacity [6, 9], Hall coefficient [6], and volume expansion coefficient [6]. An increase in x in the $YbIn_{1-x}Ag_xCu_4$ system entails an increase in T_v. The value of γ remains constant and approximately equal to 50 mJ/mol K^2 within the interval $x = 0$–0.5 [6, 9]. Thus, it can be maintained that, within this interval of x, the corresponding compositions in the $YbIn_{1-x}Ag_xCu_4$ system (similar to $YbInCu_4$) should likewise be classed among the light heavy-fermion systems. Calculations [6] show that, with increasing x in this interval, the Kondo temperature T_K^+ for the high-temperature state increases, while T_K^- for the low-temperature state first grows (up to $x = 0.2$) then falls off. For instance, for the $YbIn_{0.7}Ag_{0.3}Cu_4$ composition, $T_K^+ \sim 150$ K and $T_K^- \sim 580$ K (whereas for $YbInCu_4$, $T_K^+ \sim 25$ K and $T_K^- \sim 500$ K) [6].

For $x > 0.5$, $YbIn_{1-x}Ag_xCu_4$ undergoes a fairly fast transition to properties characteristic of the heavy-fermion compound $YbAgCu_4$.

To make the picture complete, we list other physical parameters of $YbIn_{1-x}Ag_xCu_4$ that have been studied in various laboratories of the world in recent years. The lattice constant [19, 21], ^{115}In NMR [20], magnetic phase diagram [23], neutron scattering [24], and ultrasound propagation [22] have been measured.

The thermal conductivity of $YbInCu_4$ and $YbAgCu_4$ was measured in [2, 3, 25, 26]. Unfortunately, we have not been able to locate information on measurements of the thermal conductivity in the $YbIn_{1-x}Ag_xCu_4$ system.

We chose $YbIn_{1-x}Ag_xCu_4$ with $x = 0.3$ as the subject for our study. The main reasons which account for our selection were that (i) the physical parameters of this compound do not undergo sharp changes at the phase transition[2] and that (ii) this composition belongs to the light heavy-fermion systems.

This choice also makes the goal of our study clear. It was of interest to see whether the electronic thermal conductivity of a light heavy-fermion system would reveal features of the behavior of the Lorenz number that are inherent to classical heavy-fermion systems [27, 28].

We carried out measurements of the thermal conductivity κ and of the electrical resistivity ρ of a cast polycrystalline $YbIn_{0.7}Ag_{0.3}Cu_4$ sample in the temperature 4.2–300 K.

The sample was prepared according to the technique described in [7]. $YbIn_{0.7}Ag_{0.3}Cu_4$ was synthesized from $YbInCu_4$ and $YbAgCu_4$ obtained from stoichiometric mixtures of pure metals. We used doubly sublimated Yb that was recast in a tantalum crucible (to remove the oxide), Ag and In of 99.99% purity, and Cu of 99.998% purity. $YbIn_{0.7}Ag_{0.3}Cu_4$ was melted in a tantalum crucible in an induction furnace in a vacuum of $\sim 10^{-4}$ mm Hg with subsequent annealing at $T \sim 700$°C. The sample was characterized on a DRON-2 x-ray diffractometer in CuK_α radiation. It was found to be single phase and to have an $AuBe_5$-type structure (C15b) with a lattice constant of 7.159 Å at 300 K, which is in good agreement with literature data [19, 21] (see inset to Fig. 1).

The thermal conductivity κ and electrical resistivity ρ were measured on a setup similar to that used in [29]. Figure 1 presents the experimental data obtained for the total thermal conductivity $\kappa_{tot}(T)$; Fig. 2, for the electrical resistivity $\rho(T)$. The forward (300 $\longrightarrow$ 4.2 K) and reverse (4.2 $\longrightarrow$ 200 K) runs of the $\kappa_{tot}(T)$ measurements were found to coincide.

The insets in Fig. 2 are a comparison of the data on $\rho(T)$ obtained by us for $YbIn_{0.7}Ag_{0.3}Cu_4$ with those quoted in [21]. Our data and that found in the literature are seen to coincide quite well. Significantly, the $x = 0.3$ composition studied by us exhibits a continuous rather than stepwise phase transition (the upper inset in Fig. 2).

According to the available data on the Hall effect [6], throughout the temperature range covered (before and after the completion of the phase transition), our

[2] As follows from studies of the thermal conductivity of YbInCu4 [2], interpretation of experimental results obtained at sharp phase transitions presents certain difficulties.

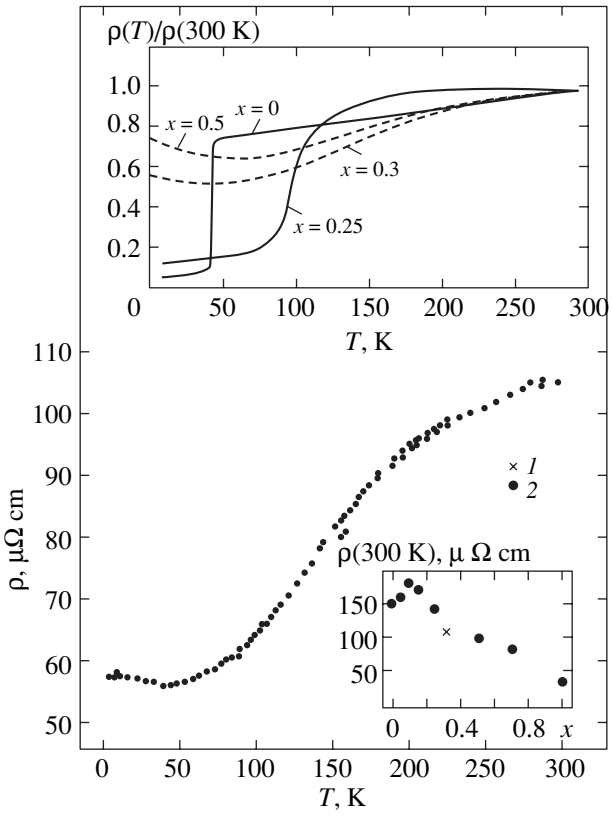

Fig. 2. Temperature dependence of ρ for an $YbIn_{0.7}Ag_{0.3}Cu_4$ sample; bottom inset is the dependence of ρ(300 K) on x for the $YbIn_{1-x}Ag_xCu_4$ system; (*1*) our data on an $YbIn_{0.7}Ag_{0.3}Cu_4$ sample and (*2*) data from [21]. The top inset is the temperature dependence of $\rho(T)/\rho(300\ K)$ for the $YbIn_{1-x}Ag_xCu_4$ system; the data for $x = 0.3$ relate to our sample, and those for the samples with $x = 0$, 0.25, and 0.5 were taken from [21].

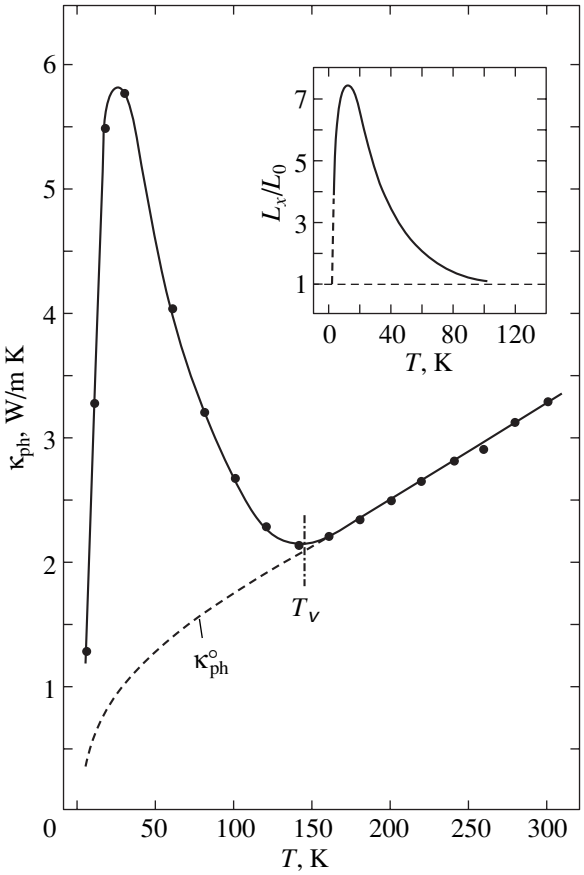

Fig. 3. Temperature dependence of κ_{ph} for $YbIn_{0.7}Ag_{0.3}Cu_4$. The solid curve is the calculation of κ_{ph} using Eqs. (1) and (2) with $L = L_0$. The points were obtained through calculations from the averaged values of κ_{tot} and ρ presented in Figs. 1 and 2 using Eqs. (1) and (2). The dashed line (κ^0_{ph}) plots the lattice thermal conductivity obtained by extrapolation of the experimental data for κ_{ph} from the high-temperature region. The inset is the temperature dependence of L_x/L_0 for our $YbIn_{0.7}Ag_{0.3}Cu_4$ sample.

composition with $x = 0.3$ can be classed among those metals whose κ_{tot} can be presented as a sum of the lattice (κ_{ph}) and electronic (κ_e) components of thermal conductivity [30]:

$$\kappa_{tot} = \kappa_{ph} + \kappa_e; \quad (1)$$

κ_e obeys the Wiedemann–Franz law and can be written as

$$\kappa_e = LT/\rho, \quad (2)$$

where L is the Lorenz number. For $T \gtrsim \Theta/3$ (Θ is the Debye temperature) and at very low temperatures for "pure" metals, as well as for low and high temperatures in "dirty" metals, $L = L_0$ [30], where L_0 is the Sommerfeld value of the Lorenz number ($L_0 = 2.45 \times 10^{-8}$ WΩ/K^2). The $YbIn_{0.7}Ag_{0.3}Cu_4$ sample studied by us can in no way be classed as a very pure metal; therefore, throughout the temperature region covered here, one can accept $L = L_0$ in a first approximation.

Figure 3 plots $\kappa_{ph}(T)$ as calculated from Eqs. (1) and (2) under the assumption of $L = L_0$. Within the 140–300 K region, κ_{ph} is seen to follow a power law ($\kappa_{ph} \sim T^{0.6}$), while at ~140 K, it deviates strongly from this law. Thermal conductivity κ_{ph} increases with decreasing temperature, passes through a maximum, and decreases subsequently to the values of κ^0_{ph} obtained by extrapolating κ_{ph} from the high- to the low-temperature region. How can one explain this behavior of κ_{ph}? A power-law growth of $\kappa_{ph}(T)$ at temperatures from 60 to 300 K and for $T > T_v$, which is characteristic of amorphous materials, was observed in $YbAgCu_4$ [3] and $YbInCu_4$ [2], respectively, and was assigned to their having strong site disorder. For instance, strong site disorder in $YbInCu_4$ can appear both for $T > T_v$ and for $T < T_v$ as a result of indium substituting for Yb [31] or

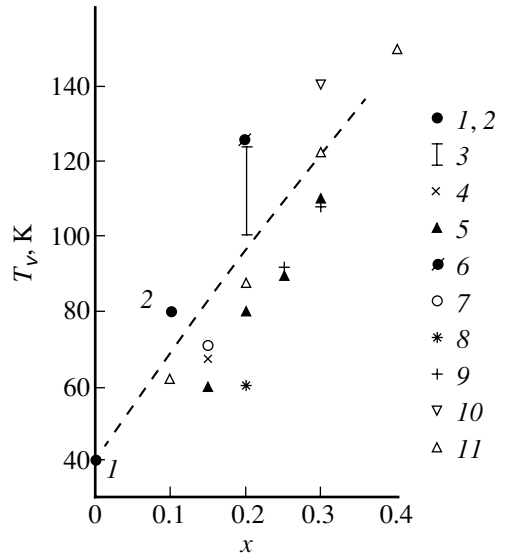

Fig. 4. Dependence of T_V for x for the $YbIn_{1-x}Ag_xCu_4$ system derived from literature data for the temperature dependences of the magnetic susceptibility, electrical resistivity, heat capacity, volume expansion coefficient, and elastic constants and from our present data on the lattice thermal conductivity; (*1*) data from [6, 9, 20–22], (*2*) [9, 20, 22], (*3*) [20], (*4*) [19], (*5*) [6], (*6*) [9], (*7*) [33], (*8*) [21], (*9*) [22], (*10*) our data obtained from the behavior of $\kappa_{ph}(T)$ (Fig. 3), and (*11*) [34].

of In being replaced by copper [32]. The presence of strong site disorder can also account for the behavior of κ_{ph} in $YbIn_{0.7}Ag_{0.3}Cu_4$ within the 140–300 K region.

The behavior of κ_{ph} of $YbIn_{0.7}Ag_{0.3}Cu_4$ at temperatures $T < 140$ K comes as a surprise. What could produce the sharp rise of κ_{ph} at $T \sim 140$ K? As already mentioned, no sharp changes in the temperature dependences of the magnetic susceptibility, electrical resistivity, heat capacity, and volume expansion coefficient were reported to occur at this temperature. Therefore, there are no grounds for the jumplike growth of the lattice thermal conductivity at $T \sim 140$ K. This anomaly is most probably the result of our having wrongly taken into account the contribution of κ_e to κ_{ph} [more specifically, of having wrongly taken into account the Lorenz number in Eq. (2)]. As mentioned above, at low temperatures, the $YbIn_{0.7}Ag_{0.3}Cu_4$ composition transfers to a state corresponding to a light heavy-fermion system. The point $T = 140$ K (Fig. 3) could correspond to the temperature of this phase transition T_V (Fig. 4).[3] The behavior of the Lorenz number in a classical heavy-fermion system differs considerably both in magnitude and in temperature dependence from that characteristic of both pure and dirty metals. In a classical system, L/L_0 increases from 1 (at $T = 0$), then passes through a maximum and falls off down to 0.648, and grows again to reach unity at $T \gtrsim T_K$ [27, 28]. Let us accept the explanation that the anomaly we observed in the behavior of $\kappa_{ph}(T)$ for $T < 140$ K is due to our having wrongly taken into account the Lorenz number in deriving $\kappa_{ph}(T)$ from the experimental values of $\kappa_{tot}(T)$. We shall assume that κ_{ph} scales as $\kappa_{ph} \sim T^{0.6}$ throughout the temperature range covered by us (as is the case for $T > 140$ K, $T > T_V$). We extrapolate $\kappa_{ph}(T)$ from the 140–300 K region to low temperatures (κ_{ph}^0) and determine $L_x/L_0(T)$ for the 4–140 K interval from the relation $\kappa_{ph} - \kappa_{ph}^0 = L_x T/\rho$. The results of this calculation are plotted in the inset to Fig. 3, which shows that $L_x/L_0(T)$ behaves in accordance with the above theoretical pattern for the Lorenz number behavior in a heavy-fermion system [27]. One can thus conclude that the features observed in the behavior of the Lorenz number in a classical and in a light heavy-fermion system are similar.

[3] The data on T_V for $YbIn_{1-x}Ag_xCu_4$ presented by points *1–9* in Fig. 4 refer to samples synthesized by a technology which permits preparation of $YbInCu_4$ with $T_V = 40$ K. The technique used to prepare our composition with $x = 0.3$ yields ~80 K for the T_V of $YbInCu_4$ [2].

ACKNOWLEDGMENTS

The authors are indebted to N.F. Kartenko and N.V. Sharenkova for the x-ray diffraction measurements.

This work was conducted within a bilateral agreement between the Russian and Polish Academies of Science and was supported by the Russian Foundation for Basic Research (project no. 99-02-18078) and by the Polish Academy of Sciences (project no. 2 ROZV 129-19).

REFERENCES

1. J. L. Sarrao, C. D. Immer, Z. Fisk, *et al.*, Phys. Rev. B **59** (10), 6855 (1999).
2. I. A. Smirnov, L. S. Parfen'eva, A. Jezowski, *et al.*, Fiz. Tverd. Tela (St. Petersburg) **41** (9), 1548 (1999) [Phys. Solid State **41**, 1418 (1999)].
3. A. V. Golubkov, L. S. Parfen'eva, I. A. Smirnov, *et al.*, Fiz. Tverd. Tela (St. Petersburg) **43** (2), 210 (2001) [Phys. Solid State **43**, 218 (2001)].
4. R. Kojima, Y. Nakai, T. Susuki, *et al.*, J. Phys. Soc. Jpn. **59** (3), 792 (1990).
5. I. Felner, I. Nowik, D. Vakin, *et al.*, Phys. Rev. B **35** (13), 6956 (1987).
6. A. L. Cornelius, J. M. Lawrence, J. L. Sarrao, *et al.*, Phys. Rev. B **56** (13), 7993 (1997).
7. V. A. Shaburov, A. E. Sovestnov, Yu. P. Smirnov, *et al.*, Fiz. Tverd. Tela (St. Petersburg) **42** (7), 1164 (2000) [Phys. Solid State **42**, 1199 (2000)].
8. J. L. Sarrao, A. P. Ramírez, T. W. Darling, *et al.*, Phys. Rev. B **58** (1), 409 (1998).
9. N. Pillmayr, E. Bauer, and K. Yoshimura, J. Magn. Magn. Mater. **104–107**, 639 (1992).

10. P. Waibel, M. Grioni, D. Malterre, *et al.*, Z. Phys. B **91**, 337 (1993).
11. P. Schlottman, J. Appl. Phys. **73**, 5412 (1993).
12. T. Graf, J. M. Lawrence, M. F. Hundley, *et al.*, Phys. Rev. B **51** (21), 15053 (1995).
13. J. S. Kang, J. W. Allen, C. Rossel, *et al.*, Phys. Rev. B **41** (7), 4078 (1990).
14. J. M. Lawrence, G. H. Kwei, P. C. Canfield, *et al.*, Phys. Rev. B **49** (3), 1627 (1994).
15. G. Polatsek and P. Bonville, Z. Phys. B **88**, 189 (1992).
16. H. Nakamura, K. Nakajima, Y. K. Kitaoka, *et al.*, Physica B (Amsterdam) **171**, 238 (1991).
17. C. Rossel, K. N. Yang, M. B. Maple, *et al.*, Phys. Rev. B **35** (4), 1914 (1987).
18. N. Tsujii, J. He, K. Yoshimura, *et al.*, Phys. Rev. B **55** (2), 1032 (1997).
19. J. L. Sarrao, C. L. Benton, Z. Fisk, *et al.*, Physica B (Amsterdam) **223/224**, 366 (1996).
20. K. Yoshimura, T. Nitta, T. Shimuzu, *et al.*, J. Magn. Magn. Mater. **90/91**, 466 (1990).
21. J. L. Sarrao, C. D. Immer, C. L. Benton, *et al.*, Phys. Rev. B **54** (17), 12207 (1996).
22. S. Zherlitsyn, B. Lüthi, B. Wolf, *et al.*, Phys. Rev. B **60** (6), 3148 (1999).
23. H. Aruga Katori, T. Goto, and K. Yoshimura, J. Magn. Magn. Mater. **140–144**, 1245 (1995).
24. J. M. Lawrence, R. Osborn, J. L. Sarrao, and Z. Fisk, Phys. Rev. B **59** (2), 1134 (1999).
25. E. Bauer, E. Gratz, G. Hutflesz, *et al.*, Physica B (Amsterdam) **186/188**, 494 (1993).
26. E. Bauer, in *Transport and Thermal Properties of f-Electron Systems*, Ed. by G. Oomi, H. Fujii, and T. Fujita (Plenum, New York, 1993), p. 133.
27. V. I. Belitsky and A. V. Goltsev, Physica B (Amsterdam) **172**, 459 (1991).
28. I. A. Smirnov and V. S. Oskotskii, in *Handbook on the Physics and Chemistry of Rare Earth*, Ed. by K. A. Gschneidner, Jr. and L. Eyring (Elsevier, Amsterdam, 1993), Vol. 16, p. 107.
29. A. Jezowski, J. Mucha, and G. Pompe, J. Phys. D **20**, 1500 (1987).
30. I. A. Smirnov and V. I. Tamarchenko, *Electron Heat Conductivity in Metals and Semiconductors* (Nauka, Leningrad, 1977).
31. J. M. Lawrence, G. H. Kwei, J. L. Sarrao, *et al.*, Phys. Rev. B **54** (9), 6011 (1996).
32. A. Loffert, M. L. Aigner, F. Ritter, and W. Assmus, Cryst. Res. Technol. **34**, 267 (1999).
33. C. D. Immer, J. L. Sarrao, Z. Fisk, *et al.*, Phys. Rev. B **56** (1), 71 (1997).
34. K. Yoshimura, N. Tsujii, K. Sorada, *et al.*, Physica B (Amsterdam) **281/282**, 141 (2000).

Translated by G. Skrebtsov

Physics of the Solid State, Vol. 43, No. 10, 2001, pp. 1816–1822. Translated from Fizika Tverdogo Tela, Vol. 43, No. 10, 2001, pp. 1744–1750.

METALS AND SUPERCONDUCTORS

An Exact Solution to the Problem of Current Transport through the Grain Boundary in a Metal

A. V. Latyshev and A. A. Yushkanov

Moscow Pedagogical University, ul. Radio 10a, Moscow, 107005 Russia

Received March 20, 2001

Abstract—The problem of electrical resistance of a planar boundary between two crystalline grains of a polycrystalline metal is solved analytically. The solution is derived using the Case method. The electric field and the electron distribution function are represented in the form of an eigenfunction expansion of the corresponding characteristic equation. It is demonstrated that the electric field at the interface increases drastically when the Debye frequency substantially exceeds the frequency of electron collisions in the bulk of the metal. It is found that the resistance of the grain boundary does not depend on the frequency of electron collisions in the bulk, i.e., on their mean free path. *© 2001 MAIK "Nauka/Interperiodica".*

1. INTRODUCTION

The majority of the metals used in practice have a polycrystalline structure. For these materials, the estimate of the contribution from the crystal boundaries to the total electrical resistance is of great practical importance. However, the calculation of the electrical resistance due to planar defects presents considerable mathematical difficulties.

In this work, we considered the problem of the electrical resistance of a planar boundary between two crystalline grains in the case when the direction of the electric current is perpendicular to the interface. This problem has already been treated in our earlier work [1]. However, in the present work, the solution of the problem was worked out up to a numerical value and the electric field and the electron distribution function at the interface were determined in an explicit form. For this purpose, we used the expansion of the solution to the boundary value problem in the regular and singular eigenfunctions of the corresponding characteristic equation. This method was proposed by Case for solving problems of the neutron transport theory (see, for example, [2]). The Case method is particularly appropriate for analyzing boundary value problems of the transport theory, because it allows one to describe all the physically significant modes of the solution in an explicit form and allows one to calculate the distribution function and its integral characteristics at the boundary. For example, a similar calculation within the framework of the Wiener–Hopf method involves special procedures [3, 4]. The Case method, as applied to solid-state plasma, was elaborated in our recent work [5]. Mention should be made of the work by Landauer [6], who treated the problem only qualitatively and, for the most part, restricted his consideration to the case of one-dimensional systems; in particular, the behavior of the electric field in the vicinity of the boundary was not analyzed.

2. THEORETICAL BACKGROUND

Let us assume that the Fermi surface for a metal has a spherical form. The interface is taken to be perpendicular to the direction of the electric field **E**. It is also assumed that the electric field is small enough for the linear approximation [7] to be applicable. In this case, we can seek the electron distribution function in the form

$$f = f_0 - \psi\frac{\partial}{\partial\varepsilon}f_0.$$

Here, f_0 is the Fermi distribution function and ε is the kinetic energy of electrons. In all the cases under consideration, the temperature can be taken equal to zero. Hence, we have

$$\frac{\partial}{\partial\varepsilon}f_0 = -\delta(\varepsilon - \varepsilon_F),$$

where ε_F is the Fermi energy and $\delta(x)$ is the δ-function.

We assume that the x axis is aligned with the electric field and the origin of coordinates on the x axis is placed at the interface. In this case, the $\psi(x, \mathbf{v})$ function satisfies the following equation [8, 9]:

$$v_x\frac{\partial}{\partial x}\psi(x, \mathbf{v}) = e_0 v_x E - \nu(\psi - \bar{\psi}). \qquad (1)$$

Here, e_0 is the electron charge, ν is the collision frequency, and $\bar{\psi}$ is the excess electron density,

$$\bar{\psi} = 2\int(2\pi\hbar)^{-3}(f - f_0)d^3p.$$

The field $E(x)$ obeys the equation

$$E'(x) = 4\pi e_0\bar{\psi}. \qquad (2)$$

1063-7834/01/4310-1816$21.00 © 2001 MAIK "Nauka/Interperiodica"

Since $v_x = v_F\cos\theta$, it is appropriate to introduce the variable $\mu = \cos\theta$. In addition, we introduce the following dimensionless coordinate, function, and parameter:

$$x' \equiv x\nu/v_F, \quad e(x) \equiv E(x)/E_0, \quad k^2 \equiv 3(\omega_p/\nu)^2,$$

where ω_p is the frequency of plasma oscillations and E_0 is the field far away from the interface. Let us introduce the function $\varphi \equiv \nu(e_0E_0v_F)^{-1}\psi$. Consequently, the set of equations (1) and (2) for the φ and e functions can be written as

$$\mu\frac{\partial}{\partial x}\varphi(x,\mu) + \varphi(x,\mu) = \mu e(x) + \bar{\varphi}(x), \tag{3}$$

$$e'(x) = k^2\bar{\varphi}(x), \tag{4}$$

where

$$\bar{\varphi}(x) = \frac{1}{2}\int_{-1}^{1}\varphi(x,\mu)d\mu.$$

In view of the symmetry of the problem, we will restrict our consideration to the case of a half-space $x > 0$. The condition for $e(x)$ at infinity follows from its definition and has the form

$$e(\infty) = 1. \tag{5}$$

It is assumed that electrons undergo diffuse scattering by the surface. The probability of the forward scattering of an electron is equal to α ($0 \le \alpha \le 1$ for electron scattering by the surface). Because of the diffuse scattering of electrons by the interface, the condition imposed on the distribution function at $x = 0$ has the form

$$\varphi(0,\mu) = a, \quad 0 < \mu < 1. \tag{6}$$

The value of a is determined from the condition

$$a = -2(1-2\alpha)\int_{-1}^{0}\mu\varphi(0,\mu)d\mu. \tag{7}$$

In the case of isotropic scattering ($\alpha = 1/2$), we have $a = 0$.

Away from the surface, the distribution function is transformed into its asymptotic form

$$\varphi(x,\mu) = \mu + o(1), \quad x \longrightarrow +\infty, \quad -1 < \mu < 0. \tag{8}$$

The boundary sets up an additional electrical resistance to the current. This resistance can be determined from the condition

$$R = j^{-1}\int_{-\infty}^{\infty}[E(x) - E_0]dx. \tag{9}$$

Here, j is the current density and R is normalized to the unit area of the interface. By virtue of the symmetry of the problem, relationship (9) can be written in the form

$$R = 2j^{-1}\int_{0}^{\infty}[E(x) - E_0]dx.$$

Now, we change over to the dimensionless variables and obtain

$$R = \left[b\int_0^\infty (e(x)-1)dx\right]\left[\int_{-1}^{1}\mu\varphi(0,\mu)d\mu\right]^{-1}, \tag{10}$$

where $b = 4mv_F/(3ne_0^2) = 4v_F/(3\sigma\nu)$ and σ is the electrical conductivity of the metal.

3. EIGENVALUES AND EIGENFUNCTIONS

We seek the solution to Eqs. (3) and (4) in the following form:

$$\varphi_\eta(x,\mu) = \Psi(\eta,\mu)\exp(-x/\eta),$$
$$e_\eta(x) = E(\eta)\exp(-x/\eta).$$

As a result, we obtain the characteristic system

$$(\eta-\mu)\Psi(\eta,\mu) = \frac{1}{2}\eta n(\eta) + \mu\eta E(\eta),$$

$$E(\eta) = -k^2\frac{1}{2}\eta n(\eta),$$

where

$$n(\eta) = \int_{-1}^{1}\Psi(\eta,\mu)d\mu.$$

Let us adopt the normalizing condition

$$\frac{1}{2}\eta n(\eta) = 1. \tag{11}$$

Under this condition, the characteristic system can be rewritten in the form

$$(\eta-\mu)\Psi(\eta,\mu) = 1 - k^2\mu\eta, \quad E(\eta) = -k^2.$$

From the first equation of this system and condition (11), we determine (see [10]) the generalized eigenfunctions of the continuous spectrum, that is,

$$\Psi(\eta,\mu) = -k^2\mu + (1-k^2\mu^2)P\frac{1}{\eta-\mu} + 2\frac{\lambda(\eta)}{\eta}\delta(\eta-\mu), \quad -1 < \eta < 1. \tag{12}$$

Here, P is the symbol of the principal integral value and $\lambda(z)$ is the dispersion function,

$$\lambda(z) = (1-k^2z^2)\lambda_0(z),$$

where $\lambda_0(z)$ is the Case dispersion function [2],

$$\lambda_0(z) = 1 + \frac{1}{2}z\int_{-1}^{1}\frac{d\tau}{\tau - z}.$$

By definition, the discrete spectrum consists of the zeroes of the dispersion equation $\lambda(z)/z = 0$. In this case, there are three zeroes: $\eta_0 = \infty$ and $\eta_{\pm 1} = \pm 1/k$ ($k > 0$). They correspond to the following eigenfunctions:

$$\Psi(\eta_0, \mu) = -k^2\mu, \quad E(\eta_0) = -k^2,$$

$$\Psi(\pm\eta_1, \mu) = \frac{1 \mp k^2\eta_1\mu}{\pm\eta_1 - \mu} = \pm k, \quad E(\pm\eta_1) = -k^2.$$

Now, we write the corresponding characteristic (particular) solutions of the initial system that satisfy condition (8); that is,

$$\varphi_{\eta_0} = -k^2\mu, \quad e_{\eta_0} = -k^2;$$

$$\varphi_{\eta_1} = k\exp(-kx), \; e_{\eta_1} = -k^2\exp(-kx)$$

(the Debye mode). The first mode φ_{η_0} describes the electrical conductivity of the metal; the second mode φ_{η_1} corresponds to the Debye screening of the electric field (the Debye screening radius is $r_D \sim 1/k$).

4. EIGENFUNCTION EXPANSION OF THE SOLUTION

Let us now demonstrate that the solution of the boundary value problem (3)–(6) can be represented in the form of the eigenfunction expansion

$$\varphi(x, \mu) = \mu + A_1\exp(-kx) + \int_0^1 \exp(-x/\eta)\Psi(\eta, \mu)A(\eta)d\eta, \tag{13}$$

$$e(x) = 1 - A_1 k\exp(-kx) - k^2\int_0^1 \exp(-x/\eta)A(\eta)d\eta. \tag{14}$$

Here, A_1 and $A(\eta)$ are the coefficients of the discrete and continuous spectra, respectively. Note that expansions (13) and (14) satisfy the boundary condition (5).

Substituting relationship (12) into expansion (13) and using the boundary condition (6), we obtain a singular integral equation with the Cauchy kernel [11]:

$$-a + \mu + A_1 - k^2\mu\int_0^1 A(\eta)d\eta + (1 - k^2\mu^2)\int_0^1 \frac{A(\eta)d\eta}{\eta - \mu} + 2\frac{\lambda(\mu)}{\mu}A(\mu) = 0, \quad 0 < \mu < 1. \tag{15}$$

We introduce the auxiliary function

$$N(z) = \int_0^1 \frac{A(\eta)d\eta}{\eta - z}. \tag{16}$$

This function is analytical in the complex plane with the dimension along segment [0, 1], for which the boundary values from above and below within the cut are related through Sokhotsky formulas:

$$N^+(\mu) - N^-(\mu) = 2\pi i A(\mu), \quad 0 < \mu < 1,$$
$$\frac{1}{2}[N^+(\mu) + N^-(\mu)] \equiv N(\mu), \tag{17}$$

where

$$N(\mu) = \int_0^1 \frac{A(\eta)d\eta}{\eta - \mu}, \quad 0 < \mu < 1.$$

The Sokhotsky formulas for the $\lambda(z)$ function are as follows:

$$\lambda^+(\mu) - \lambda^-(\mu) = \pi i\mu(1 - k^2\mu^2), \quad -1 < \mu < 1,$$
$$\frac{1}{2}[\lambda^+(\mu) + \lambda^-(\mu)] = \lambda(\mu),$$

where

$$\lambda(\mu) = (1 - k^2\mu^2)\left(1 + \frac{\mu}{2}\ln\frac{1 - \mu}{1 + \mu}\right), \quad -1 < \mu < 1.$$

Now, we solve Eq. (15) using the Carleman–Vekua method [11] under the assumption that the regular part $\int_0^1 A(\eta)d\eta$ of this equation is known. By designating

$$\psi(\mu) = a - \mu - A_1 + k^2\mu\int_0^1 A(\eta)d\eta$$

and using the boundary values of $N(z)$ and $\lambda(z)$, we change over from Eq. (15) to the Riemann boundary value problem [11]

$$\lambda_0^+(\mu)[N^+(\mu) - \psi(\mu)/(1 - k^2\mu^2)] - \lambda_0^-(\mu) \times [N^-(\mu) - \psi(\mu)]/(1 - k^2\mu^2) \equiv 0, \quad 0 < \mu < 1. \tag{18}$$

As a solution to the appropriate homogeneous problem

$$\frac{X^+(\mu)}{X^-(\mu)} = \frac{\lambda_0^+(\mu)}{\lambda_0^-(\mu)}, \quad 0 < \mu < 1,$$

we take the following solution bounded at zero:

$$X(z) = \frac{1}{z}\exp V(z), \quad V(z) = \frac{1}{\pi}\int_0^1 \frac{\zeta(\tau)}{\tau - z}d\tau.$$

Here, $\zeta(\tau) = \theta(\tau) - \pi$ and $\theta(\tau) = \arg\lambda_0^+(\tau)$ is the regular branch of the argument of the $\lambda_0^+(\tau)$ function, which is specified at zero by the condition $\theta(0) = 0$. It is easy to see that

$$\zeta(\tau) = \arctan\frac{\pi\tau}{2\lambda_0(\tau)} - \pi\theta_+(\tau_0 - \tau),$$

where $\tau_0 = 0.8335565596\ldots$ is the zero of the $\lambda_0(\tau)$ function, $\theta_+(\tau)$ is the Heaviside function, $\theta_+(\tau) = 1$, $\tau \geq 0$, $\theta_+(\tau) = 0$, and $\tau < 0$. Using the homogeneous problem, we transform the inhomogeneous problem (18) into the boundary value problem for determining the analytical function from its zero jump, that is,

$$X^+(\mu)[N^+(\mu) - \psi(\mu)/(1-k^2\mu^2)]$$
$$- X^-(\mu)[N^-(\mu) - \psi(\mu)/(1-k^2\mu^2)] = 0, \quad 0 < \mu < 1.$$

Its general solution has the form

$$N(z) = \frac{\psi(z)}{1-k^2z^2} + \frac{C}{(1-k^2z^2)X(z)}, \tag{19}$$

where C is an arbitrary constant. In order for the general solution (19) to be taken as the auxiliary function (16), it is necessary to eliminate the singularities (poles) of the general solution. Since the pole $z = -1/k$ does not lie in the cut, it can be eliminated under the condition

$$\psi(-1/k) + C/X(-1/k) = 0. \tag{20}$$

At $k > 1$, the pole $z = 1/k$ lies in the cut ($0 < 1/k < 1$), and when $0 < k < 1$, it does not. If this pole does not lie in the cut, it can be eliminated under a similar condition,

$$\psi(1/k) + C/X(1/k) = 0. \tag{21}$$

We now assume that this pole lies in the cut. In this case, the general solution takes the form

$$N(\mu) = \frac{\psi(\mu)}{1-k^2\mu^2} + \frac{C}{1-k^2\mu^2}\frac{1}{2}\left[\frac{1}{X^+(\mu)} - \frac{1}{X^-(\mu)}\right]$$

or

$$N(\mu) = \frac{\psi(\mu)}{1-k^2\mu^2} + \frac{C}{1-k^2\mu^2}\frac{\cos\zeta(\mu)}{X(\mu)}.$$

It is clear that the pole under consideration can be eliminated under the condition

$$\psi(1/k) + C\cos\zeta(1/k)/X(1/k) = 0. \tag{22}$$

Therefore, in order to determine unknown constants A_1 and C of the general solution, it is necessary to solve Eqs. (20) and (21) when $0 < k < 1$ or Eqs. (20) and (22) when $k > 1$. However, a certain subtlety should be recognized. The value of the integral $\int_0^1 A(\eta)d\eta$ involved in $\psi(z)$ depends on whether or not the pole $1/k$ lies in the cut. From expression (19), we determine the coefficient of the continuous spectrum:

$$A(\eta) = \frac{C}{2\pi i(1-k^2\eta^2)}\left[\frac{1}{X^+(\eta)} - \frac{1}{X^-(\eta)}\right]. \tag{23}$$

Consequently,

$$k\int_0^1 A(\eta)d\eta = -C\frac{1}{2}[J(1/k) - J(-1/k)],$$

where

$$J(z) = \frac{1}{2\pi i}\int_0^1\left[\frac{1}{X^+(\eta)} - \frac{1}{X^-(\eta)}\right]\frac{d\tau}{\tau - z}. \tag{24}$$

According to [5], in the case when $z \in (0, 1)$, we obtain

$$J(z) = \frac{1}{X(z)} - z + V_1, \tag{25}$$

where

$$V_1 = -\frac{1}{\pi}\int_0^1 \zeta(\tau)d\tau = 0.71045,$$

and when $z \in (0, 1)$, we have

$$J(\mu) = \frac{1}{2}[J^+(\mu) + J^-(\mu)] = \frac{\cos\zeta(\mu)}{X(\mu)} - \mu + V_1. \tag{26}$$

Hence,

$$k\int_0^1 A(\eta)d\eta = C\left[\frac{1}{k} - \frac{\theta_+(k-1)\cos\zeta(1/k) + \theta_+(1-k)}{2X(1/k)} + \frac{1}{2X(-1/k)}\right].$$

In both cases ($0 < k < 1$ or $k > 1$), we obtain from Eqs. (20), (21) or (20), (22) that $C = 1$ and the formulas for A_1 can be combined into the formula

$$A_1 = a + \frac{\theta_+(k-1)\cos\zeta(1/k) + \theta_+(1-k)}{2X(1/k)} + \frac{1}{2X(-1/k)}. \tag{27}$$

Thus, we determined the coefficients A_1 and $A(\eta)$ of expansions (13) and (14). However, the A_1 coefficient is expressed in terms of an unknown constant a. In order to determine the a constant, we substitute expansion (13) into condition (7). Taking into account the property of the eigenfunctions,

$$\int_{-1}^1 \mu\Psi(\eta, \mu)d\mu \equiv 0, \quad 0 < \eta < 1,$$

we obtain

$$\int_{-1}^1 \mu\varphi(0, \mu)d\mu = \frac{2}{3}. \tag{28}$$

Consequently, according to condition (7), we can write

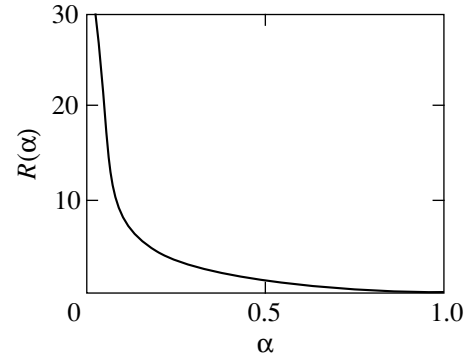

Fig. 1. Dependence of the electrical resistance on the probability of electron forward scattering.

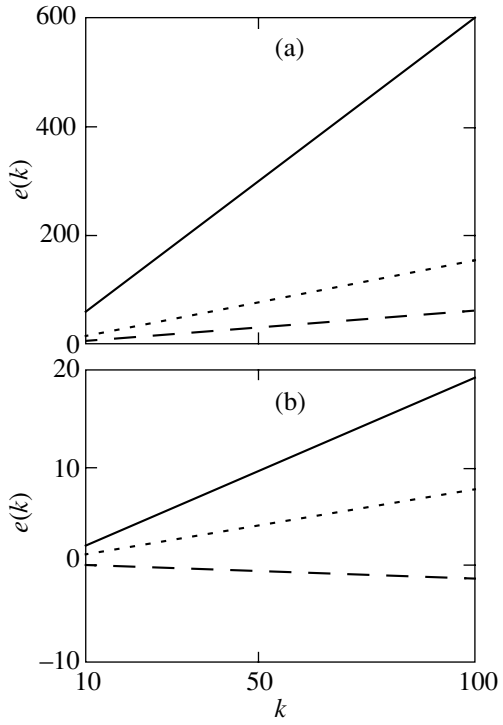

Fig. 2. Dependences of the electric field at the grain boundary on the quantity k ($0 < k < 100$): (a) $\alpha = 0.1$ (solid line), 0.3 (dotted line), and 0.5 (dashed line) and (b) $\alpha = 0.7$ (solid line), 0.8 (dotted line), and 0.9 (dashed line).

the relationship

$$a = (4\alpha - 2)\left[\int_{-1}^{1} \mu\varphi(0, \mu)d\mu - \int_{-1}^{1} \mu\varphi(0, \mu)d\mu\right] = (4\alpha - 2)\left(\frac{2}{3} - \frac{1}{2}a\right).$$

Hence, it follows that $a = (4\alpha - 2)/(3\alpha)$.

5. THE ELECTRICAL RESISTANCE, FIELD, AND DISTRIBUTION FUNCTION

Substituting the value of the current density (28) and expansion (14) into expression (10), we obtain

$$R = -\frac{3}{2}b\left[A_1 + k^2\int_0^1 \eta A(\eta)d\eta\right]. \quad (29)$$

According to expression (23),

$$k^2\int_0^1 \eta A(\eta)d\eta = -\frac{1}{2}[J(1/k) + J(-1/k)],$$

where $J(z)$ [see Eq. (24)] is determined by expression (25) when $0 < k < 1$ or by formula (26) at $k > 1$. According to formula (29), in both cases, the electrical resistance is expressed through the same formula (Fig. 1),

$$R = b\left[\frac{3}{2}V_1 - 2 + \frac{1}{\alpha}\right]. \quad (30)$$

Hence, it can be seen that, in the case of purely isotropic reflection of electrons from the interface ($\alpha = 1/2$), we have $R = 1.5bV_1 = 1.06568(4V_F m)/(3ne_0)$.

Thus, we obtain the exact solution (30) of the problem of electrical resistance of a planar boundary between two crystalline grains. The results of this work can be used in determining the electrical resistance of a polycrystalline metal.

It follows from formula (30) that the resistance R does not depend on the electron collision frequency in the bulk of the metal. It is also evident from formula (30) that, when $\alpha \longrightarrow 0$, the resistance increases indefinitely, which corresponds to the impenetrability of the crystalline grain boundary with respect to electrons.

Let us now determine the electron distribution function and the electric field at the boundary between two crystalline grains. From expansions (13) and (14), we have

$$\varphi(0, \mu) = \mu + A_1 - k^2\mu\int_0^1 A(\eta)d\eta + (1 - k^2\mu^2) \times \int_0^1 \frac{A(\eta)d\eta}{\eta - \mu}, \quad -1 < \mu < 0, \quad (31)$$

$$e(0) = 1 - k^2A_1 - k\int_0^1 A(\eta)d\eta. \quad (32)$$

Using relationships (16), (17), (19), and (21), we recast expression (31) into the form

$$\varphi(0, \mu) = \frac{4\alpha - 2}{3\alpha} + \frac{1}{X(\mu)}.$$

If we substitute the above coefficients into formula (32), in both cases, we obtain the same formula for the electric field at the grain boundary (the plots of the dimensionless field are depicted in Figs. 2 and 3), that is,

$$e(0) = -k\left[\frac{1}{X(-1/k)} + \frac{4}{3\alpha}\left(\alpha - \frac{1}{2}\right)\right]. \quad (33)$$

The electric field profile in the half-space ($x > 0$) is determined using the formulas derived for coefficients A_1 and $A(\eta)$. As a consequence, for the cases of $k > 1$ and $0 < k < 1$, we obtain two expressions which are then combined into the formula

$$e(x) = 1 - k\exp(-kx) \times\left[a + \frac{\theta_+(k-1)\cos\zeta(1/k) + \theta_+(1-k)}{2X(1/k)} + \frac{1}{X(-1/k)}\right] - \frac{1}{\pi}\int_0^1 \exp\left(-\frac{x}{\eta}\right)\frac{\sin\zeta(\eta)d\eta}{(\eta^2 - k^{-2})X(\eta)}.$$

The profiles of the electric (dimensionless) field on each side of the boundary between two crystalline grains ($x = 0$) are shown in Fig. 4. Figure 5 displays the profiles of the electron (charge) density on both sides of the interface, which is determined by the formula

$$e'(x) = k^2\exp(-kx) \times\left[a + \frac{\theta_+(k-1)\cos\zeta(1/k) + \theta_+(1-k)}{2X(1/k)} + \frac{1}{2X(-1/k)}\right] - \frac{1}{\pi}\int_0^1 \exp\left(-\frac{x}{\eta}\right)\frac{\sin\zeta(\eta)}{(\eta^2 - k^{-2})X(\eta)}\frac{d\eta}{\eta}.$$

Now, we consider the case when the frequency of plasma oscillations ω_p is considerably higher than the electron collision frequency $\nu(\omega_p \gg \nu)$. This is true for the majority of the metals under normal conditions. In this case, $X(-1/k) \approx X(-0) = -\sqrt{3}$. Hence, the electric field [see expression (33)] is given by

$$e(0) = k\left[\frac{1}{\sqrt{3}} - \frac{4}{3\alpha}\left(\alpha - \frac{1}{2}\right)\right]. \quad (34)$$

It is evident from formula (34) that, in the case under consideration, the electric field $e(0)$ at the grain boundary substantially exceeds the field that is far from the interface (in our designations, $e(0) \equiv 1$). This phenomenon (an abrupt increase in the electric field at the grain boundary) is explained by the fact that, as the electron collision frequency ν decreases (and k increases with the proviso that $\omega_p = \text{const}$), the bulk conductivity of the metal increases and, consequently, the electric current in a fixed field increases. The interface has a constant electrical resistance. In this case, the potential difference should increase; in turn, an increase in the potential difference is accompanied by an increase in the electric field.

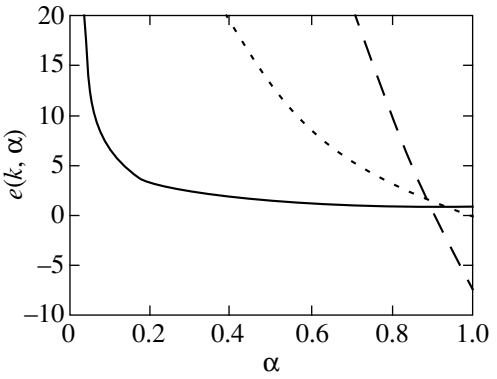

Fig. 3. Dependences of the electric field at the grain boundary on the probability of electron forward scattering: $k = 1$ (solid line), 20 (dotted line), and 100 (dashed line).

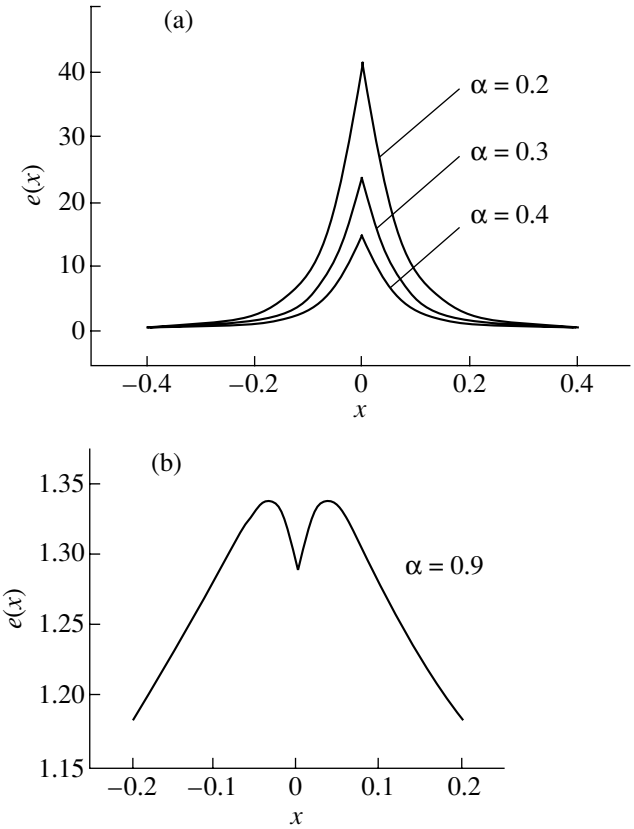

Fig. 4. Profiles of the electric field on both sides of the grain boundary at $k = 16$.

Let us consider the Debye mode for the electric field at the interface [see formula (27)]. It follows from expression (27) at $k \gg 1$ that

$$A_1 = a - \frac{1}{2X(+0)} + \frac{1}{2X(-0)} = a - \frac{1}{\sqrt{3}} = \frac{4}{3\alpha}\left(\alpha - \frac{1}{2}\right) - \frac{1}{\sqrt{3}}. \quad (35)$$

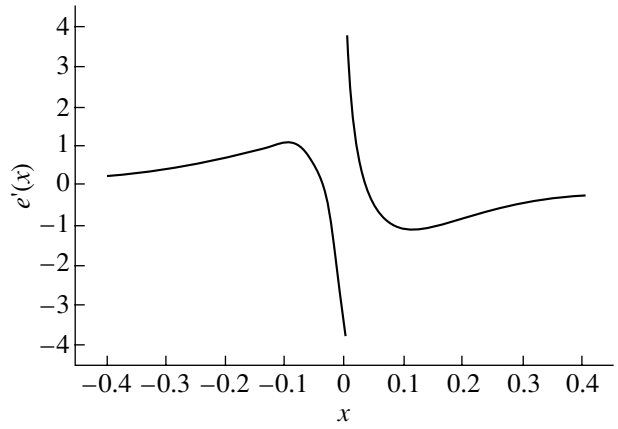

Fig. 5. Profiles of the electron density on both sides of the grain boundary ($\alpha = 0.9$, $k = 16$).

A comparison of the Debye mode (35) with the electric field $e(0)$ [see expression (33)] demonstrates that the field at the interface in the limit $k \longrightarrow \infty$ is determined by the Debye mode: $e(0) \equiv e_D$, where $e_D = -kA_1$. Since the Debye mode is damped out at distances of the Debye radius, the deviation of the electric field from its value determined away from the interface is predominantly concentrated at distances of the order of the Debye radius from the boundary between the crystalline grains.

It can be seen from Fig. 4 that, when α is close to unity, the dependence of the electric field on the distance to the grain boundary exhibits a nonmonotonic behavior. The case of $\alpha > 1/2$ corresponds to the situation when electrons at the interface undergo essentially forward scattering. The mean velocity of electrons decreases as the result of scattering. By virtue of the electron conservation law, a decrease in the velocity leads to an increase in the electron density, which, in turn, gives rise to a space charge (the configuration of this charge can be seen in Fig. 5). At $\alpha < 1/2$, this effect is leveled out due to the predominant backscattering of electrons.

At large distances from the interface, a dominant role is played by the effects of decrease in the effective conductivity of the metal (due to the scattering by electrons on the interface). This brings about an increase in the electric field. This effect becomes progressively pronounced with an increase in the k quantity (proportional to the plasma oscillation frequency ratio) and corresponds to the decrease in frequency of electron collisions in the bulk of the metal. Consequently, the effect of electron scattering on the interface on the conductivity increases.

ACKNOWLEDGMENTS

This work was supported in part by the Russian Foundation for Basic Research, project no. 99-01-00336.

REFERENCES

1. A. V. Latyshev and A. A. Yushkanov, Zh. Vychisl. Mat. Mat. Fiz. **33** (4), 600 (1993).
2. K. M. Case and P. F. Zweifel, *Linear Transport Theory* (Addison-Wesley, Reading, 1967; Mir, Moscow, 1972).
3. I. F. Voloshin, V. G. Skobov, L. M. Fisher, and A. S. Chernov, Zh. Éksp. Teor. Fiz. **80** (1), 183 (1981) [Sov. Phys. JETP **53**, 92 (1981)].
4. V. M. Gokhfel'd, M. A. Gulyanskiĭ, M. I. Kaganov, and A. G. Plyavenek, Zh. Éksp. Teor. Fiz. **89** (3), 985 (1985) [Sov. Phys. JETP **62**, 566 (1985)].
5. A. V. Latyshev and A. A. Yushkanov, Zh. Tekh. Fiz. **70** (8), 1 (2000) [Tech. Phys. **45**, 955 (2000)].
6. R. Landauer, Z. Phys. B **21** (2), 217 (1975).
7. A. A. Abrikosov, *An Introduction to the Theory of Normal Metals* (Nauka, Moscow, 1972).
8. J. M. Ziman, *Electrons and Phonons* (Clarendon, Oxford, 1960; Inostrannaya Literatura, Moscow, 1962).
9. E. M. Lifshitz and L. P. Pitaevskiĭ, *Physical Kinetics* (Nauka, Moscow, 1979; Pergamon, Oxford, 1981).
10. V. S. Vladimirov, *Generalized Functions in Mathematical Physics* (Nauka, Moscow, 1976).
11. F. D. Gakhov, *Boundary Value Problems* (Nauka, Moscow, 1977, 3rd ed.; Addison-Wesley, Reading, 1966).

Translated by O. Moskalev

Physics of the Solid State, Vol. 43, No. 10, 2001, pp. 1823–1826. Translated from Fizika Tverdogo Tela, Vol. 43, No. 10, 2001, pp. 1751–1753.

METALS AND SUPERCONDUCTORS

Structure of the Abrikosov Vortex Lattice in a Thin Superconducting Film in a Parallel Magnetic Field

D. A. Luzhbin

Institute of Metal Physics, National Academy of Sciences of Ukraine, pr. Vernadskogo 36, Kiev, 03680 Ukraine
e-mail: luzhbin@d24.imp.kiev.ua

Received January 10, 2001

Abstract—The structure of a vortex lattice in thin ($d < \lambda$, where d is the film thickness and λ is the London penetration depth) superconducting films is investigated in a magnetic field parallel to the film surface. It is shown that the stable configuration has the form of discrete vortex rows whose number changes discretely with an increase in the applied magnetic field. The entry fields $H_{c1}^{(N)}(d)$ for vortex rows are calculated for $N = 1, 2$. It is shown that the structural transition in the vortex ensemble is a second-order phase transition. A simpler method (as compared to the Monte Carlo technique) is proposed for calculating the vortex lattice parameters.

1. The structure of the vortex lattice in a thin film of a type II superconductor in a constant magnetic field parallel to the film surface differs considerably from the vortex lattice structure in an infinite crystal, in which vortices (in an isotropic sample) are known to be ordered in the absence of pinning to form a 2D regular triangular lattice [1]. It was proved for the first time by Abrikosov [2, 3] that the field $H_{c1}^{(1)}(d)$ at which the formation of vortices becomes energetically favorable in a film placed in a parallel field is much stronger than the field H_{c1}^{bulk} for a bulk sample and is given by

$$H_{c1}^{(1)}(d) = \frac{H_{c1}^{\text{bulk}} - \dfrac{\Phi_0}{2\pi\lambda^2}\displaystyle\sum_{n=1}^{\infty}(-1)^n K_0(nd/\lambda)}{1 - 1/\cosh(d/2\lambda)}. \quad (1)$$

This formula leads to asymptotic expressions $H_{c1}^{(1)}(d) \approx H_{c1}^{\text{bulk}}(1 + 2\exp(-d/2\lambda))$ for $d > \lambda$ and $H_{c1}^{(1)}(d) \approx (2\Phi_0/\pi d^2)\ln(\gamma d/\pi\xi) \sim (\lambda/d)^2 H_{c1}^{\text{bulk}}$ for $d \ll \lambda$. Here, ξ is the coherence length and $\gamma = e^c = 1.78$.

In a field $H \geq H_{c1}^{(1)}(d)$, the vortex structure is a row of vortices arranged at the center of the film. As the external field H increases, the only parameter that is dependent on the field is the separation $a(H)$ between vortices (Fig. 1a). As the field increases further to $H_{c1}^{(N)}(d)$, the vortex lattice structure changes so that the number of vortex rows in the film increases by unity. This effect was studied in [4, 5] for isotropic films (through the summation of modified Bessel's functions) and in [6, 7] for anisotropic samples (by using the Monte Carlo method), where it was proved that the structural transition is virtually jumpwise at a small number ($N = 1, 2, 3, 4$) of vortex rows. In other words, the transition interval $\Delta H \ll H_{c1}^{(N+1)} - H_{c1}^{(N)}$. This discreteness was observed experimentally in [7–9] in the form of peaks in the curve of the reversible magnetic moment of the film and in the magnetic field dependence of the critical current [10]. The experiments based on the vibrating-reed magnetometer method [9, 11] revealed a nonmonotonic dependence of the measured quantities on the external magnetic field; consequently, the discreteness in the variation of the number of vortex rows in a film can be regarded as an experimentally confirmed fact.

In this work, the structure of a vortex ensemble at $N = 1, 2$ was analyzed in detail and the transition between these states was studied in an increasing external dc magnetic field. The proposed method made it possible to calculate numerically the vortex lattice parameters without resorting to the Monte Carlo procedure or to the summation of modified Bessel's functions. The change in the Gibbs free energy upon a structural transition from one row to two rows allowed us to treat the structural transition in the vortex system as a second-order phase transition.

2. For a type II superconductor with $\kappa \gg 1$, the distribution of the field H_V of a vortex ensemble is described by the equation [12]

$$H_V + \lambda^2 \operatorname{curl}\operatorname{curl} H_V = \Phi_0 \sum_{n,m} \delta(r - R_{n,m}) \quad (2)$$

with the boundary conditions

$$H_V\big|_{z=-d/2} = H_V\big|_{z=d/2} = 0, \quad (3)$$

which are equivalent to the physical condition of zero current transport through the surface. Here, $R_{n,m}$ is a 2D

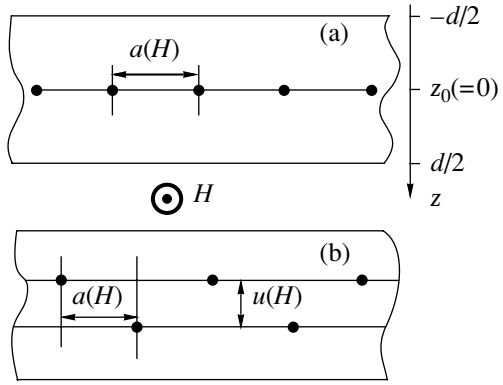

Fig. 1. Structure of the vortex lattice in a film in a parallel magnetic field H: (a) one row of vortices exists at the center of the film in a field $H_{c1}^{(1)}(d) < H \le H_{c1}^{(2)}(d)$ and (b) the structure splits into two vortex rows in a field $H_{c1}^{(2)}(d) < H \le H_{c1}^{(3)}(d)$. Dark points depict vortices. The external field is perpendicular to the plane of the figure.

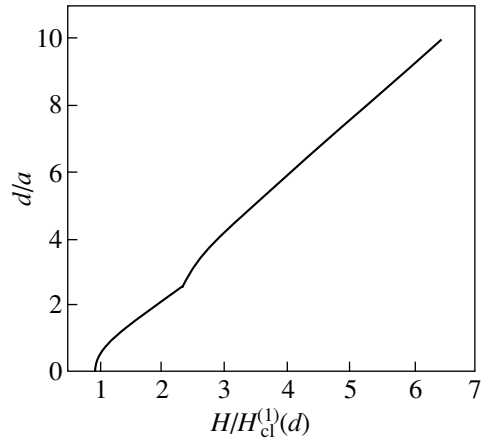

Fig. 2. Separation $a(H)$ between neighboring vortices as a function of the external field H.

radius vector with coordinates $(x_{n,m}, z_{n,m})$. This condition can be satisfied by introducing an infinite alternating series of images symmetric relative to the film surfaces [4, 12] and by solving Eq. (1) for an infinite superconductor with alternating series of vortices. Naturally, the solution has a physical meaning only in the range $-d/2 \le z \le d/2$. The solution is an alternating sum of modified Bessel's functions K_0. However, it is inconvenient to operate with this sum and we will seek another representation of the solution to Eq. (2).

An equivalent solution to Eqs. (2) and (3) in the case of a single vortex row ($x_{n,m} = ma$, $z_{n,m} = z_0$, $m = 0, \pm1, \pm2\ldots$) can be presented in the form [12]

$$H_V(x,z) = \frac{\Phi_0}{d\lambda^2}\sum_{n=1}^{\infty}\sum_{m=-\infty}^{\infty}\int_{-\infty}^{\infty}\frac{dk}{2\pi}\exp(ik(x-ma)) \times \frac{\cos\frac{n\pi}{d}(z-z_0) - \cos\frac{n\pi}{d}(d+z+z_0)}{k^2 + \frac{1}{\lambda^2} + \left(\frac{n\pi}{d}\right)^2}, \quad (4)$$

where z_0 is the coordinate of the row relative to the film center and $a = a(H)$ is the distance between neighboring vortices (Fig. 1a).

Using the equality $\sum_n \exp(inp) = 2\pi\sum_n \delta(p - 2\pi n)$ and the relationship [13]

$$\sum_n \frac{\exp(i\gamma n)}{n^2 + a^2} = \frac{\pi}{a}\frac{\cosh((\pi - |\gamma|)a)}{\sinh(\pi a)},$$

we can write solution (4) in the form

$$H_V(x,z) = \frac{\Phi_0}{2d\lambda}\sum_{n=1}^{\infty}\frac{\cos\frac{n\pi}{d}(z-z_0) - \cos\frac{n\pi}{d}(d+z+z_0)}{\nu_n} \times \frac{\cosh\left(\nu_n\frac{a-2x}{2\lambda}\right)}{\sinh\left(\nu_n\frac{a}{2\lambda}\right)}, \quad (5)$$

which is valid for $-d/2 \le z, z_0 \le d/2$, and $0 \le x \le a$, where $\nu_n = \sqrt{1 + (n\pi\lambda/d)^2}$. If the film contains several vortex rows, the total field is equal to the sum of fields (5).

The structure of the vortex ensemble in a film for a given field H is determined by the condition of the minimum of the Gibbs energy. It was proved in [14] that the free energy G of the vortex ensemble is defined by the formula

$$G = \sum_n \frac{H_n(0)\Phi_0}{8\pi} - \frac{H\Phi_n(0)}{4\pi}, \quad (6)$$

where summation is carried out over all vortices, $H_n(0)$ is the field at the center of the nth vortex created by the vortex system alone, and $\Phi_n(0)$ is the flux of the nth vortex. According to [2, 3], the equilibrium structure at $N = 1$ is a single row of vortices at the center of the film. At $N = 2$, the equilibrium structure (away from the transition field $H_{c1}^{(2)}(d)$) has the form of two rows of vortices separated by a distance $2u_{\max}$ from each other, where $a = a(H)$ and $2u_{\max} = d/3$ is independent of H [7, 8]. It is reasonable to assume that in the immediate vicinity of the transition, i.e., for $H \cong H_{c1}^{(2)}(d)$, both $a = a(H)$ and $u = u(H)$ are functions of the field H and the

transition corresponds to a change in the value of u from 0 to u_{max} (Fig. 1b).

In this case, the free energy (6) (per unit area) has the form

$$G = \frac{1}{a}\left(\frac{H_V(0)\Phi_0}{8\pi} - \frac{H\Phi_0}{4\pi}\left[1 - \frac{\cosh(u/\lambda)}{\cosh(d/2\lambda)}\right]\right), \quad (7)$$

where $H_V(0)$, in accordance with Eq. (5), has the form

$$H_V(0) = \frac{\Phi_0}{2d\lambda}\sum_{n=1}^{\infty}\frac{\left(1-(-1)^n\cos\frac{2\pi nu}{d}\right)\cosh\left(\nu_n\frac{a-\xi}{\lambda}\right)+\left(\cos\frac{2\pi nu}{d}-(-1)^n\right)\cosh\left(\nu_n\frac{\xi}{\lambda}\right)}{\nu_n\sinh\left(\nu_n\frac{a}{\lambda}\right)} \quad (8)$$

(in order to avoid divergence in the intrinsic energy of the vortex, we used the standard truncation at a distance ξ from the vortex axis). Obviously, the case of $u = 0$ corresponds to a structure with $N = 1$.

In order to find the equilibrium parameters of the vortex lattice, we will use the system of equations (following from the condition of the minimum free energy)

$$\left(\frac{\partial G}{\partial u}\right)_a = \left(\frac{\partial G}{\partial a}\right)_u = 0, \quad (9)$$

which enables us to calculate numerically the equilibrium parameters $u(H)$ and $a(H)$ for a given value of H.

3. For our calculations, we used a sample with parameters $d = 0.5\lambda$, $\kappa = 100$, and $\lambda = 10^{-5}$ cm, which correspond to the characteristic parameters of HTSC materials.

The results of numerical solution of system (9) are presented in the figures. Figure 2 shows the magnetic field dependence of the separation between vortices (in the form d/a); the singularity at point $H = H_{c1}^{(2)}(d)$ is associated with the transition at which one plane $z_0 = 0$ in the vortex structure splits into two planes $z_0 = \pm u$ at a constant density of vortex rows (Fig. 1). Figure 3 presents the dependence of the distance $u(H)$ between vortex rows (in $d/2$ units) on the external field H. The value of $u(H)$ varies continuously from 0 to $u_{max} \cong d/6$ (according to [7, 8]). Therefore, the field $H_{c1}^{(2)}(d)$ of the transition can be determined as a solution to the system

$$\left(\frac{\partial^2 G(u=0)}{\partial u^2}\right)_a = \left(\frac{\partial G}{\partial a}\right)_{u=0} = 0. \quad (10)$$

For the specified parameters, we have $H_{c1}^{(2)}(d) \approx 2.35 H_{c1}^{(1)}(d)$.

It can be proved that for small values of $u \ll u_{max}$, Eq. (7) satisfies the Landau expansion

$$G(H) \cong G(0) + G_1 u^2 + G_2 u^4, \quad (11)$$

where $G_2 \cong \text{const}_{(H)}$ and $G_1 \cong (H_{c1}^{(2)}(d) - H)\text{const}_{(H)}$. The field dependences of the free energy (7) and its second derivative are depicted in Fig. 4. The behavior of the free energy with an increase in the field (continuity of the function in the vicinity of $H_{c1}^{(2)}(d)$ and discontinuity of the second derivative in the same region), as well as the possibility of expanding Eq. (10), in which the coefficient of u^2 changes sign at the transition point $H =$

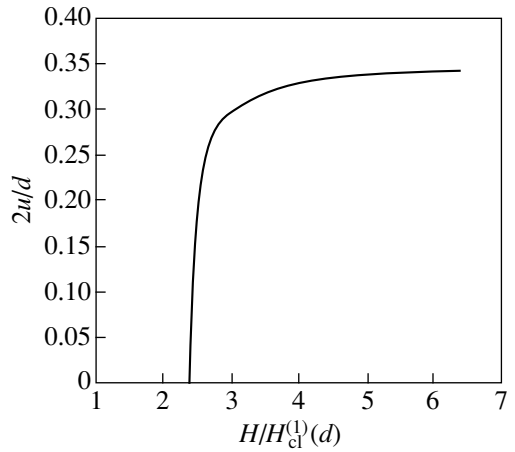

Fig. 3. Dependence of the distance $u(H)$ between vortex rows on the external field H.

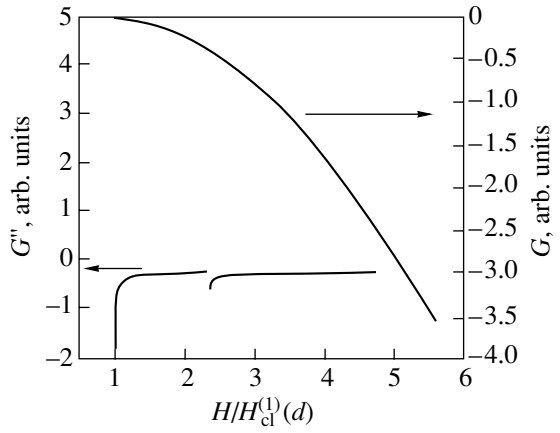

Fig. 4. Field dependences of the free energy of the film and of its second derivative with respect to the field.

$H_{c1}^{(2)}(d)$, leads to the conclusion that the structural transition from one to two vortex rows is, at the same time, a second-order phase transition. It should be noted that the algorithm of the solution itself presumed a second-order phase transition (since we assumed that the quantity $u(H)$, which can serve as the order parameter, varies continuously from 0 to u_{max}; hence, we can differentiate system (9) with respect to u). If this assumption were incorrect, system (9) would not have a solution for small values of u.

Thus, using the approach proposed above, we can calculate the equilibrium parameters of the vortex lattice in the entire range of fields $H \le H_{c1}^{(3)}(d)$ and state that the structural rearrangement of the vortex lattice in a parallel field, which corresponds to a discrete variation in the number of vortex rows [4–7], is a second-order phase transition.

ACKNOWLEDGMENTS

The author is grateful to A.L. Kasatkin and I.M. Dubrovsky for discussing the results.

REFERENCES

1. E. H. Brandt, Rep. Prog. Phys. **58** (11), 1465 (1995).
2. A. A. Abrikosov, Zh. Éksp. Teor. Fiz. **46** (4), 1464 (1964) [Sov. Phys. JETP **19**, 988 (1964)].
3. A. A. Abrikosov, *Fundamentals of the Theory of Metals* (Nauka, Moscow, 1987; North-Holland, Amsterdam, 1988).
4. C. Carter, Can. J. Phys. **47** (14), 1447 (1969).
5. S. Takács, Czech. J. Phys. B **28** (11), 1260 (1978).
6. G. Garneiro, Phys. Rev. B **57** (10), 6077 (1998).
7. S. H. Brongersma, Ph.D. Dissertation (Vrije Univ., Amsterdam, 1996).
8. S. H. Brongersma, E. Verweij, N. J. Koeman, *et al.*, Phys. Rev. Lett. **71** (14), 2319 (1993).
9. A. Pan, M. Ziese, R. Höhne, *et al.*, Physica C (Amsterdam) **301**, 72 (1998).
10. Y. Mawatari and K. Yamafuji, Physica C (Amsterdam) **228**, 336 (1994).
11. M. Ziese, P. Esquinazi, P. Wagner, *et al.*, Phys. Rev. B **53** (13), 8658 (1996).
12. V. V. Shmidt and G. S. Mkrtchyan, Usp. Fiz. Nauk **112** (3), 459 (1974) [Sov. Phys. Usp. **17**, 170 (1974)].
13. I. S. Gradshteyn and I. M. Ryzhik, *Table of Integrals, Series, and Products* (GITTL, Moscow, 1951; Academic, New York, 1980).
14. V. V. Shmidt, Zh. Éksp. Teor. Fiz. **61** (7), 398 (1971) [Sov. Phys. JETP **34**, 211 (1971)].

Translated by N. Wadhwa

Physics of the Solid State, Vol. 43, No. 10, 2001, pp. 1827–1833. Translated from Fizika Tverdogo Tela, Vol. 43, No. 10, 2001, pp. 1754–1760.

METALS AND SUPERCONDUCTORS

Pinning of Vortices by the Domain Structure in a Two-Layered Type II Superconductor–Ferromagnet System

Yu. I. Bespyatykh*, W. Wasilevski, M. Gajdek**, I. P. Nikitin*, and S. A. Nikitov***

** Institute of Radio Engineering and Electronics, Russian Academy of Sciences (Fryazino Branch), pl. Vvedenskogo 1, Fryazino, Moscow oblast, 141120 Russia*

e-mail: svg318@ire216.msk.ru

*** Technical University, Radom, Poland*

Received January 12, 2001

Abstract—The effectiveness of magnetic pinning of vortices in a layered system formed by a uniaxial ferromagnet and type II superconductor is considered. It is shown that, irrespective of the saturation magnetization of the ferromagnet, the energy of pinning at the domain structure does not exceed, in order of magnitude, the energy of artificial pinning at a column-type defect. The limitation of pinning energy is caused by the interaction of external vortices with a spontaneous vortex lattice formed in the superconducting film when the magnetization of the ferromagnetic film exceeds the critical value. *© 2001 MAIK "Nauka/Interperiodica".*

1. INTRODUCTION

Static and dynamic properties of type II superconductors are determined to a considerable extent by the vortex structure and pinning of vortices. It is well known [1, 2] that the most effective pinning of vortices at defects occurs when the characteristic size of the defects is of the order of the vortex core diameter, i.e., the correlation length ξ or the diameter of the field component of a vortex, i.e., the London penetration depth λ. In many superconducting materials (including high-temperature superconductors), pinning is quite weak and, hence, the critical current is small, which considerably narrows the range of their practical application. In order to increase the critical current, various methods of artificial pinning of vortices have been used. These methods include the introduction of ferromagnetic impurities [3] and the decoration of the superconducting-film surface [4] (even by producing a system of holes of micrometer size in it [5]). In recent years, the pinning of vortices at column-type defects obtained by bombarding a superconductor with heavy ions [6–8], as well as the pinning at ferromagnetic particles [9–11] and magnetic dots [12–16] on the surface of a superconducting film, has been studied intensely.

The physical mechanisms leading to vortex pinning in superconducting films with ferromagnetic impurities and particles on the surface are not completely clear. Although Alden and Livingston [3] assume that the electromagnetic interaction of impurity spins with conduction electrons in the superconductor is responsible for pinning, the proximity effect cannot be ruled out. The latter effect leads to the suppression of the superconducting order parameter and is apparently more effective. In experiments with superconducting films with ferromagnetic particles or magnetic dots deposited on their surface, the presence of a buffer layer between the superconducting and ferromagnetic materials cannot be controlled either. According to Marty *et al.* [17], in a weak external magnetic field normal to the film surface, magnetic dots have a multidomain structure, the magnetization in each domain being parallel to the plane of the superconducting film. For such a magnetization distribution, the magnetic coupling of perpendicular vortices with the magnetization must be very weak and the strong pinning is, in all probability, due to the suppression of the superconducting order parameter by the proximity effect.

The above-mentioned methods of artificial pinning of vortices require the use of labor-consuming technology. Moreover, magnetic impurities, surface decoration, holes, and bombardment with heavy ions damage the structure of the superconducting film and considerably deteriorate its transport properties. In the present work, we will estimate the effectiveness of vortex pinning by the field of magnetic domains in a layered system formed by a uniaxial ferromagnet and a type II superconductor. The indisputable advantage of such a system is the simplicity of its preparation and the possibility of easily controlling the presence and thickness of the insulating layer between the magnetic and superconducting materials. The system can be monolithic or compound. In the latter case, the electromagnetic interaction between the magnetic and superconducting subsystems can be controlled by varying the distance between the ferromagnetic and superconducting layers.

2. FORMULATION OF THE PROBLEM. THE ENERGY OF THE SYSTEM

Depending on the thickness and physical parameters of ferro- and ferrimagnetic films, the size of domains in them can change from fractions of a micrometer to tens

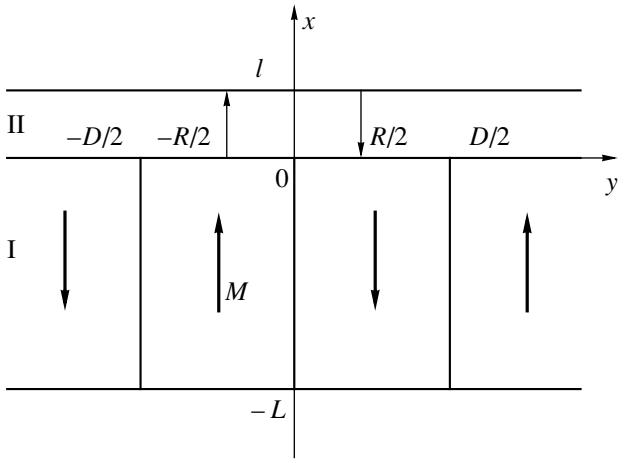

Fig. 1. Layered structure formed by (I) a ferromagnet with a domain band structure and (II) a type II superconductor with a vortex–antivortex pair; the directions of magnetization in domains are denoted by bold arrows and the positions and directions of vortices are indicated by thin arrows.

of micrometers [18–20]. However, the domain structure period in a magnet with a considerably large anisotropy and coercive extends from a few micrometers to tens of micrometers, which considerably exceeds the correlation length and the London penetration depth. In the case of magnets with weak anisotropy, the size of domains can be small, but the stray field of the domain structure and, hence, the electromagnetic coupling between vortices and magnetization are weak because of the presence of closure domains. For this reason, we cannot expect a strong force of vortex pinning in the two-layered system under investigation. For the same reason, the size effects observed in superconducting films with artificial periodic defects [5, 11, 15, 16, 21–23] will be manifested weakly. Nevertheless, the energy of vortex pinning in the case of magnets with a domain structure of the open type can be high since the interaction between the layers is quite strong.

Let us calculate the pinning force and energy for vortices in a superconducting film under the action of the field of the domain structure of a uniaxial ferromagnetic film. We assume that the superconducting and ferromagnetic materials are insulated from each other by a buffer layer of thickness δ ($\xi \ll \delta \ll \lambda$) and that the interaction between the spin subsystem of the magnet and the conduction electrons in the superconductor is purely electromagnetic. Let the ferromagnet possess magnetic anisotropy of the easy-axis type and the direction of the anisotropy axis $\mathbf{n}_a$ be perpendicular to the developed surface of the system. Since most high-T_c superconductors are typical type II superconductors, we confine our subsequent analysis to superconducting materials characterized by a large Ginzburg–Landau parameter $\kappa = \lambda/\xi \gg 1$. In addition, we can disregard the vortex pinning at intrinsic defects of the superconductor. The system geometry is presented in Fig. 1.

The energy U of the system in a zero external magnetic field has the form

$$U = \frac{1}{8\pi}\int_V dv H^2 + \int_{V_f} dv\left(\frac{\alpha}{2}\frac{\partial \mathbf{M}}{\partial x_i}\frac{\partial \mathbf{M}}{\partial x_i} - \frac{\beta}{2}M_y^2\right) + \frac{\lambda^2}{8\pi}\int_{V_s} dv(\nabla \times \mathbf{H})^2, \quad (1)$$

where $\mathbf{H}$ is the magnetic field; $\mathbf{M}$ is the magnetization; V is the total volume of the system; V_f and V_s are the volumes of the ferromagnetic and superconducting layers, respectively; α is the nonuniform exchange constant; and $\beta > 0$ is the anisotropy constant. The first term in Eq. (1) is the magnetic field energy, the second is the sum of the exchange and anisotropy energies, and the third is the kinetic energy of paired electrons.

The spatial distributions of magnetization $\mathbf{M}$ and magnetic field $\mathbf{H}$ in the ferromagnet in vacuum are described by the magnetostatics equations

$$\nabla \times \mathbf{H} = 0, \quad \nabla \cdot \mathbf{B} = 0 \quad (2)$$

and by the equation of state

$$[\mathbf{M} \times \mathbf{H}_{\text{eff}}] = 0, \quad (3)$$

while the distribution of the magnetic field $\mathbf{H}$ in the superconductor is described by the London equation

$$\mathbf{H} + \lambda^2[\nabla \times [\nabla \times \mathbf{H}]] = \Phi_0 \sum_\nu \int d\mathbf{r}_\nu \delta(\mathbf{r} - \mathbf{r}_\nu), \quad (4)$$

where $\mathbf{B} = \mathbf{H} + 4\pi\mathbf{M}$ is the magnetic induction, $\mathbf{H}_{\text{eff}}$ is the effective magnetic field

$$\mathbf{H}_{\text{eff}} = \mathbf{H} + \beta M_y \mathbf{n}_y - \alpha\nabla^2\mathbf{M}, \quad (5)$$

and $\mathbf{r}_\nu$ is the distance from the origin to an infinitely small element $d\mathbf{r}_\nu$ of the νth vortex; summation in Eq. (4) is carried out over all vortices and integration extends over the total length of each vortex. At the interface between the media, the standard electrodynamic continuity conditions for the tangential components of the magnetic field $\mathbf{H}$ and the normal component of the magnetic induction $\mathbf{B}$ must be satisfied. Moreover, the normal component of the superconducting current density $\mathbf{j}_s$ must vanish at the superconductor surface.

The magnetic field $\mathbf{H}$ in the system is the sum of the vortex field $\mathbf{H}_{\text{vort}}$ of the superconductor and the field $\mathbf{H}_M$ created by the magnetization of the ferromagnet:

$$\mathbf{H} = \mathbf{H}_{\text{vort}} + \mathbf{H}_M. \quad (6)$$

The latter field includes the dipole field $\mathbf{H}_D$ of an isolated ferromagnet and the field $\mathbf{H}_{\text{Meis}}$ of Meissner currents in the absence of vortices. Accordingly, the energy U of the system can be presented in the form

$$U = U_M + U_{\text{vort}} + U_{\text{int}}, \quad (7)$$

where U_M is the energy of the magnetic subsystem together with the energy of the Meissner currents in the absence of vortices, U_{vort} is the energy of the vortex subsystem, and U_{int} is the energy of interaction of vortices with the magnetization:

$$U_M = \frac{1}{8\pi}\int_V dv H_M^2 + \frac{1}{2}\int_{V_f} dv\left(\alpha\frac{\partial \mathbf{M}}{\partial x_i}\frac{\partial \mathbf{M}}{\partial x_i} - \beta M_y^2\right) + \frac{\lambda^2}{8\pi}\int_{V_s} dv[\nabla\times\mathbf{H}_M]^2, \quad (8)$$

$$U_{\text{vort}} = \frac{1}{8\pi}\int_V dv\{H_{\text{vort}}^2 + \lambda^2[\nabla\times\mathbf{H}_{\text{vort}}]^2\}, \quad (9)$$

$$U_{\text{int}} = \frac{1}{8\pi}\int_V dv\{\mathbf{H}_M\cdot\mathbf{H}_{\text{vort}} + \lambda^2[\nabla\times\mathbf{H}_M]\cdot[\nabla\times\mathbf{H}_{\text{vort}}]\}. \quad (10)$$

The energy U_M as a function of the spatial distribution of magnetization $\mathbf{M}$, London penetration depth λ, and the thicknesses of the superconducting and ferromagnetic layers is presented in [24–26]. In the present work, this energy is of no interest to us for the following reasons. If the thickness of a layer of a magnetically soft material is sufficiently large, the magnet is divided into domains whose size depends only weakly on the state of the superconductor [24]. On the other hand, the domain structure of a magnetically hard material does not change upon an increase in the external magnetic field up to the coercive field and the effect of the superconductor on the domain structure can be disregarded. We will confine the subsequent analysis to ferromagnetic films with a high coercivity and assume that the magnetization distribution in them is preset and the potential U_M is constant.

Following Brandt [27], we represent the vortex field $\mathbf{H}_{\text{vort}}$ in the form

$$\mathrm{H}_{\text{vort}} = \mathbf{H}_{\text{v}} + \mathbf{H}_{\text{stray}}, \quad (11)$$

where $\mathbf{H}_{\text{v}}$ is the sum of the field $\mathbf{H}_{\text{vr}}$ of real vortices and the field $\mathbf{H}_{\text{vi}}$ of image vortices,

$$\mathbf{H}_{\text{v}} = \mathbf{H}_{\text{vr}} + \mathbf{H}_{\text{vi}}, \quad (12)$$

and $\mathbf{H}_{\text{stray}}$ is the stray field. Then, the energy U_{vort} of the vortices can be presented as the sum of two terms:

$$U_{\text{vort}} = U_{\text{v}} + U_{\text{stray}}, \quad (13)$$

where

$$U_{\text{v}} = \frac{1}{8\pi}\int_V dv\{H_{\text{v}}^2 + \lambda^2[\nabla\times\mathbf{H}_{\text{v}}]^2\}, \quad (14)$$

$$U_{\text{stray}} = \frac{1}{8\pi}\int_V dv\{H_{\text{stray}}^2 + \lambda^2[\nabla\times\mathbf{H}_{\text{stray}}]^2\}. \quad (15)$$

It will be shown in the Appendix that the interaction energy U_{int} between the magnetic and vortex subsystems is equal to the Zeeman energy of a ferromagnet in an external field equal to the stray field of the vortices:

$$U_{\text{int}} = -\int_{V_f} dv\mathbf{M}\cdot\mathbf{H}_{\text{vort}} = -\int_{V_f} dv\mathbf{M}\cdot\mathbf{H}_{\text{syray}}. \quad (16)$$

The thickness l of the superconducting film is usually smaller than the period D of the domain structure. Consequently, the tilt of vortices can be neglected and it is sufficient to consider a superconducting film with a system of vortices perpendicular to its surface. The general expressions for energies U_{v} and U_{stray} have the form [28]

$$U_{\text{v}} \cong [\Phi_0^2 l/(4\pi^2\lambda^2)] \times\sum_{\mu,\nu}\eta_\mu\eta_\nu K_0(\lambda^{-1}\sqrt{|\boldsymbol{\rho}_\mu - \boldsymbol{\rho}_\nu|^2 + \xi^2}), \quad (17)$$

$$U_{\text{stray}} = \frac{1}{4\pi}\int\frac{dq}{4\pi^2}\Phi_{\mathbf{q}}P_{-\mathbf{q}}, \quad (18)$$

where $K_0(x)$ is the zero-order Macdonald function; $\boldsymbol{\rho}_\mu = \{x_\mu, 0, z_\mu\}$ is the radius vector that connects the origin with the axis of the μth vortex and lies in the plane of the film; $\eta_\mu = 1$ if the μth vortex is parallel to the y axis and $\eta_\mu = -1$ if it is antiparallel to the y axis; $\mathbf{q} = \{q_x, 0, q_z\}$; $\Phi_{\mathbf{q}}$ is the Fourier transform of the potential of the stray field $\mathbf{H}_{\text{stray}}$ of vortices;

$$\Phi_{\mathbf{q}} = TP_{\mathbf{q}}/[q(T + q\coth Tl/2)]; \quad (19)$$

and $P_{\mathbf{q}}$ is the Fourier transform of the field component H_{vy} at the lower surface of the film:

$$P_{\mathbf{q}} = H_{vy\mathbf{q}}(0) = \frac{\Phi_0}{\lambda^2 T^2}\sum_\mu\eta_\mu\exp(-i\mathbf{q}\boldsymbol{\mu}), \quad (20)$$

where $T^2 = q^2 + \lambda^{-2}$.

We assume that domain walls in the ferromagnetic film are infinitely thin and that the magnetization in the domains is parallel or antiparallel to the y axis. In this case,

$$U_{\text{int}} = -\int\frac{dq}{4\pi^2}\Phi_{\mathbf{q}}M_{-\mathbf{q}}[1 - \exp(-qL)] \quad (21)$$

(here and below, the subscript y on the magnetization component M_y is omitted).

3. MAGNETIC VORTEX PINNING ENERGY

Let us suppose that the axis of a solitary vortex passes through the point $\boldsymbol{\rho}_0 = \{x_0, 0\}$ on the xz plane and is parallel to the y axis. We calculate the interaction potential between the vortex and the field of a stripe domain structure with period D (Fig. 1). In this case, the

Fourier transform of the normal magnetization component has the form

$$M_{\mathbf{q}} = 8\pi i M_0 \sum_{n=-\infty}^{+\infty} \frac{\sin^2 \pi n/2}{n} \delta(q_x - k_n)\delta(q_z), \quad k_n = 2\pi n/D \tag{22}$$

and the interaction energy between the vortex and magnetization is given by

$$U_{\text{int}} = -\frac{2\Phi_0 M_0 D}{\pi^2} \sum_{n=1}^{\infty} \frac{\sin^2(\pi n/2)\sin(k_n x_0)}{n^2\lambda^2\tau_n[\tau_n + k_n \coth(\tau_n l/2)]} \times [1 - \exp(-k_n L)], \quad \tau_n^2 = k_n^2 + \lambda^{-2}. \tag{23}$$

If the layer thicknesses are large enough ($l \gg \lambda$, $L \gg D \gg l$), then the periodic potential (23) has minima at the centers of domains in which the magnetization is parallel to the direction of the vortex and maxima at the centers of domains with the opposite direction of magnetization. The absolute value of the interaction energy at the maxima and minima is the same. The vortex pinning energy U_{pin}, which is equal to the difference in the values of U_{int} at the maxima and minima, is found to be

$$U_{\text{pin}} \cong (4/\pi^2)\Phi_0 M_0 D. \tag{24}$$

In this case, we have

$$U_v \cong \Phi_0^2 l/(8\pi^2\lambda^2)\ln\kappa, \quad U_{\text{stray}} \cong \frac{(\pi-2)}{16\pi^2}\frac{\Phi_0^2}{\lambda} \ll U_v. \tag{25}$$

The interaction energy of antivortices with the magnetization is opposite in sign to that in Eq. (23); consequently, the potential maxima and minima change places relative to those for vortices. When the magnetization of the ferromagnet exceeds the critical value M_c [28],

$$M_c \cong [\Phi_0 l/(16\lambda^2 D)]\ln\kappa, \tag{26}$$

the total energies of a vortex at the potential minima and of an antivortex at the potential maxima become negative and the superconducting film acquires a spontaneous lattice of vortices and antivortices. Otherwise, the equilibrium state of the superconductor is the Meissner phase.

If the system is in a weak external magnetic field $\mathbf{H}_0 \parallel \mathbf{n}_y$, the concentration of external vortices is low and the interaction between them can be disregarded. When the ferromagnetic film magnetization $M_0 < M_c$, spontaneous vortices and antivortices are absent; however, the presence of the periodic potential (23) hampers the motion of external vortices in a direction perpendicular to domain walls. In other words, the interaction with the stray field of the domain structure can lead to magnetic pinning of the vortices. The pinning energy U_{pin} for a system of thick layers with $l \gg \lambda$, $L \gg D \gg l$ is defined by formula (24), and the maximum pinning force $f_{p\max} = \max(\partial U_{\text{int}}/\partial x_0)$ is given by

$$f_{p\max} \cong (2/\pi)\Phi_0 M_0 \ln(D/l) \propto U_{\text{pin}}/D. \tag{27}$$

The logarithm appearing in this formula is associated with the divergence of the derivative of the series in Eq. (23) and with its truncation at $n \propto D/l$. In the general case, the series in Eq. (23) must be truncated at $n \propto \min(D/l, D/\lambda, D/\Delta, D/\delta)$, where Δ is the domain wall width and δ is the thickness of the buffer layer.

In order to estimate the pinning energy U_{pin} numerically, we consider a $YBa_2Cu_3O_7$ superconducting film with Curie temperature $T_c \cong 90$ K, $\lambda = 3 \times 10^{-5}$ cm, $l = 10^{-4}$ cm, and $\ln\kappa \propto 1$. Let the saturation magnetization of the ferromagnet be M_c and the domain structure period $D = 5 \times 10^{-4}$ cm. In this case, $4\pi M_0 \cong 20$ G and

$$U_{\text{pin}} \cong \Phi_0^2 l/(4\pi^2\lambda^2)\ln\kappa, \tag{28}$$

so that $U_{\text{pin}} \propto 10^{-10}$ erg and $f_{p\max} \propto 10^{-7}$ g cm s^2. It should be noted for comparison that the pinning energy for a vortex at a column-type defect of diameter ξ is given by

$$U_{\text{pin}} \propto \Phi_0^2 l/(64\pi^2\lambda^2); \tag{29}$$

i.e., it is of the same order of magnitude as the energy given by Eq. (28). However, the pinning force at a defect of the column type is several orders of magnitude larger than the magnetic pinning force in Eq. (27).

The saturation magnetization of ferro- and ferrimagnets can exceed 10^3 G, but an increase in magnetization does not lead to an increase in the pinning energy and force for external vortices, because they interact with the spontaneous lattice of vortices and antivortices. For example, the stray field of domains at the surface of the ferromagnet for $4\pi M_0 \propto 10^3$ G is of the order of $2\pi M_0 \propto 10^3$ G and the concentration of spontaneous vortices and antivortices in this case is $n \propto 4\pi M_0/\Phi_0 \propto 10^{10}$ cm^{-2}. The field components of neighboring vortices and antivortices strongly overlap in this case, and the energy of their interaction is high. An external vortex created by a bias field interacts not only with the magnetization but also with the spontaneous structure of vortices and antivortices. As a result, the effective potential of this vortex is strongly renormalized. The equilibrium spontaneous structure of vortices and antivortices exhibits a minimum in free energy; consequently, the emergence of an external vortex in the presence of spontaneous vortices, as well as in the presence of spontaneous antivortices, increases the total energy of the system. The dependence of the potential created by an external vortex on coordinate x_0 is qualitatively the same as that in the case when $M_0 < M_c$. This means that its effective pinning energy does not exceed, in order of magnitude, the pinning energy of an external vortex for $M_0 = M_c$.

The critical current in this case can be even smaller than that for $M_0 = M_c$, since the spontaneous vortex–

antivortex structure can be set in motion by the Lorentz force induced by the transport current, which is accompanied by annihilation and production of vortex–antivortex pairs [28]. If the effect of the spontaneous lattice of vortices and antivortices is disregarded, the estimate obtained for the pinning effectiveness for vortices in the field of a domain structure is exaggerated [29].

If the saturation magnetization of the ferromagnetic film is equal to the critical value, but its thickness is small and the inequality $L \gg D$ is not satisfied, the pinning energy U_{pin} is approximately equal to double the vortex energy (25) and coincides with (28). It follows, hence, that the maximum value of U_{pin} in a system of thick films is proportional to the superconductor film thickness and depends only weakly on the thickness of the ferromagnetic film.

With decreasing thickness of the ferromagnetic film, the pinning energy decreases, while the critical magnetization M_c increases, which allows us to compensate for the decrease in the pinning energy by using ferromagnets with a higher saturation magnetization.

Let us now calculate the interaction potential between a vortex and the magnetization in the case of a regular lattice of cylindrical magnetic domains of radius R and distance a between the centers of neighboring domains (Fig. 2). Magnetization $\mathbf{M}$ is parallel to the y axis in the domains and antiparallel to this axis outside the domains. The position vectors $\boldsymbol{\rho}_{mn}$ of the domain axes in the plane of the ferromagnetic film are given by

$$\boldsymbol{\rho}_{mn} = m\mathbf{b}_1 + n\mathbf{b}_2, \quad m, n = 0, \pm 1, \pm 2, \ldots,$$
$$\mathbf{b}_1 = a\mathbf{n}_x, \quad \mathbf{b}_2 = (a/2)(\mathbf{n}_x + \mathbf{n}_z\sqrt{3}). \tag{30}$$

The magnetization distribution in the ferromagnetic film has the form

$$M_{x,z} = 0, \quad M_y = M_0\left[-1 + 2\sum_{m,n}\theta(R - |\boldsymbol{\rho} - \boldsymbol{\rho}_{mn}|)\right], \tag{31}$$
$$\theta(x) = \begin{cases} 1, & x > 0 \\ 0, & x < 0, \end{cases}$$

and the Fourier transform $M_{y\mathbf{q}}$ is given by

$$M_{y\mathbf{q}} = -\frac{6\pi^2 M_0}{R}\sum_{m,n}{}'\frac{J_1(qR)}{q}\delta(\mathbf{q} - \mathbf{G}_{mn}), \tag{32}$$

where $\mathbf{G}_{mn}$ are the reciprocal lattice vectors,

$$\mathbf{G}_{mn} = \frac{2\pi}{a}\left[m\mathbf{n}_x + \frac{(2n-m)}{\sqrt{3}}\mathbf{n}_z\right], \tag{33}$$
$$m, n = 0, \pm 1, \pm 2, \ldots;$$

$J_1(x)$ is the first-order Bessel function; and the prime on the sum symbol in formula (32) indicates the absence of the term with $m = n = 0$. Substituting Eqs. (32) and (19) into Eq. (21), we obtain the interaction energy U_{int} as a function of the position vector $\boldsymbol{\rho}_0$ of the vortex axis in the xz plane:

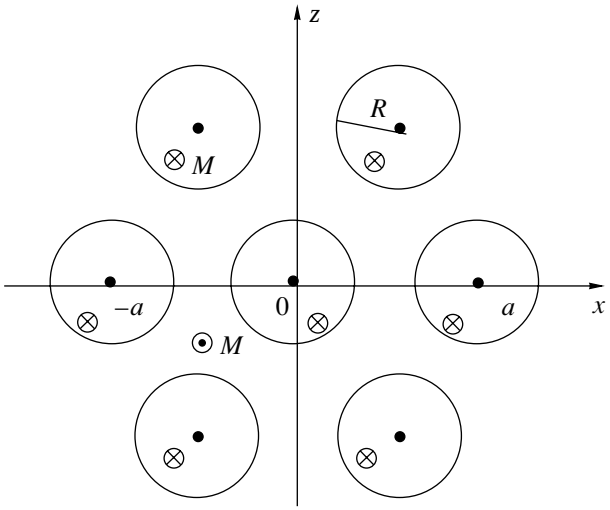

Fig. 2. Triangular lattice of cylindrical magnetic domains.

$$U_{\text{int}} = -\frac{8\pi}{\sqrt{3}}\frac{\Phi_0 M_0 R}{a^2\lambda^2}$$
$$\times\sum_{m,n}{}'\frac{J_1(G_{mn}R)\cos(\mathbf{G}_{mn}\cdot\boldsymbol{\rho}_0)}{T_{mn}G_{mn}^2[T_{mn} + G_{mn}\coth(T_{mn}l/2)]} \tag{34}$$
$$\times[1 - \exp(-G_{mn}L)].$$

The distance a between the centers of the nearest cylindrical magnetic domains and the ratio R/a depend on the thickness L, saturation magnetization M_0, exchange constant α, and anisotropy constant β of the ferromagnetic layer. We will not dwell on the details of calculating the domain lattice parameters and will assume, in the subsequent analysis, that a and R are connected through the relation

$$R^2 = (\sqrt{3}/4\pi)a^2. \tag{35}$$

Condition (35) follows from the equality to zero of the total magnetic charge on each surface of the ferromagnetic plane. It holds to a high degree of accuracy for thick films with $L \gg a$.

The potential of the external vortex (34) has minima at the points at which the vortex axis coincides with the center of one of the cylindrical domains and maxima at the points where the vortex axis coincides with the center of a regular triangle, with its apexes coinciding with the centers of the three nearest domains (Fig. 2). In contrast to Eq. (23), the absolute values of the interaction energy (34) at minima and maxima are generally different. Nevertheless, only vortex–antivortex pairs can be formed spontaneously in a system with a lattice of cylindrical magnetic domains, as well as in a system

with a stripe domain structure. This is due to an abrupt increase in the magnetic field energy upon violation of the equality between the concentrations of vortices and antivortices in a layered system with a large transverse dimension. When the minimum values of the reciprocal periods coincide ($a = D/\sqrt{3}$), the absolute values of the maxima and minima of the interaction potential of an external vortex with the magnetization for a lattice of cylindrical magnetic domains are slightly smaller than in the case of a stripe domain structure.

4. DISCUSSION OF RESULTS AND CONCLUSIONS

Thus, we have proved that the energy of vortex pinning by a domain structure for $D \gg l \gg \lambda$ cannot exceed, in order of magnitude, the vortex pinning energy at defects which are formed as a result of bombardment of the superconductor by heavy ions. The limitation of the pinning energy is due to the formation of a spontaneous vortex–antivortex lattice, when the magnetization of the ferromagnet exceeds its critical value, and to the interaction between an external vortex and the spontaneous vortex structure. The pinning energy can be increased by increasing the superconducting-film thickness. The critical magnetization increases in this case, but the pinning energy per unit vortex length remains virtually unchanged. The pinning force for vortices in such a system is relatively small.

Instead of monocrystalline ferro- and ferrimagnetic films, one can use polycrystalline films, provided their surface quality is high enough; otherwise, the nonuniform interaction potential between the magnetic and superconducting layers will be low. The crystallite size in polycrystalline magnets varies from a few micrometers to hundredths of a micrometer. In a substance with large uniaxial magnetic anisotropy, the domain size is of the order of the crystallite size. Using such materials, it is possible to attain not only a high pinning energy but also a considerable pinning force, since the nonuniformity scale of the interaction potential is comparable with the London penetration depth. Unfortunately, our results are inapplicable in this case and can only be used for obtaining rough estimates.

The effect of interaction between vortices and the domain structure on pinning was analyzed by Gaĭvoron *et al.* [30]. They used a compound system formed by a polycrystalline film of the high-temperature superconductor $YBa_2Cu_2O_7$ and a monocrystalline Fe–Y garnet film. Instead of the expected growth of the critical current, its slight decrease was observed. The Curie temperature of the transition to the superconducting state was also lower than in the absence of the magnet. The results obtained in that publication were not explained. Taking into account the estimates given above and the results obtained in [28], we can state that one of the most probable reasons behind the decrease in the critical current observed in [30] is the motion of the spontaneous vortex lattice.

ACKNOWLEDGMENTS

This study was supported by the Polish Committee on Scientific Research.

APPENDIX

In order to reduce expression (10) for U_{int} to the form of Eq. (16), we transform the integrals appearing in Eq. (10). Using the formulas of vector analysis

$$\begin{aligned}&[\nabla \times \mathbf{A}][\nabla \times \mathbf{B}]\\ &= \nabla[\mathbf{B} \times [\nabla \times \mathbf{A}]] + \mathbf{B}[\nabla \times [\nabla \times \mathbf{A}]]\end{aligned} \tag{A1}$$

and the equation for the magnetic field $\mathbf{H}_M$ in the superconductor,

$$\mathbf{H}_M + \lambda^2[\nabla \times [\nabla \times \mathbf{H}_M]] = 0, \tag{A2}$$

we obtain

$$\begin{aligned}&\frac{1}{4\pi}\int_{V_s} dV(\mathbf{H}_M\mathbf{H}_v + \lambda^2[\nabla \times \mathbf{H}_M][\nabla \times \mathbf{H}_v])\\ &= \frac{\lambda^2}{4\pi}\int_{V_s} dV\nabla[\mathbf{H}_v \times [\nabla \times \mathbf{H}_M]]\\ &= \frac{\lambda^2}{4\pi}\int_{S_s} d\mathbf{s}[\mathbf{H}_v \times [\nabla \times \mathbf{H}_M]].\end{aligned} \tag{A3}$$

The integral over the volume outside the superconductor is given by

$$\begin{aligned}&\frac{1}{4\pi}\int_{V-V_s} dV\mathbf{H}_M\mathbf{H}_v\\ &= \frac{1}{4\pi}\int_{V-V_s} dV\mathbf{B}_M\mathbf{H}_v - \int_{V-V_s} dV\mathbf{M}\mathbf{H}_v,\end{aligned} \tag{A4}$$

where $\mathbf{B}_M = \mathbf{H}_M + 4\pi\mathbf{M}$ is the magnetic induction in the absence of vortices. Taking into account the potential nature of the magnetic field of vortices $\mathbf{H}_v = \nabla\Phi$ outside the superconductor, the vortex nature of the magnetic induction $\mathbf{B}_M$ ($\nabla\mathbf{B}_M = 0$), and the identity

$$\mathbf{A}(\nabla\Psi) = \nabla(\Psi\mathbf{A}) - \Psi(\nabla\mathbf{A}), \tag{A5}$$

we can reduce the first integral on the right-hand side of Eq. (10) to the integral over the surface S_s of the superconductor:

$$\frac{1}{4\pi}\int_{V-V_s} dV\mathbf{B}_M\mathbf{H}_v = -\frac{1}{4\pi}\int_{S_s} d\mathbf{s}(\Phi\mathbf{B}_M). \tag{A6}$$

This transformation is valid if the product $\Phi\mathbf{B}_M$ rapidly tends to zero for $y \longrightarrow \pm\infty$. The stray field of the domain structure with period D (for $y \gg D$ or $|y + L| \gg D$) decreases exponentially with increasing distance to the magnetic film, while the potential Φ either decreases

exponentially or exhibits a power-low dependence on the coordinate *y*. The normal component of the induction $\mathbf{B}_M$ is continuous at the interfaces; consequently, we can substitute $\mathbf{H}_M = -\lambda^2[\nabla \times [\nabla \times \mathbf{H}_M]]$ for $\mathbf{B}_M$ in the superconductor on the right-hand side of (A6). Since

$$\Psi[\nabla \times \mathbf{A}] = [\nabla \times (\Psi \mathbf{A})] + [\mathbf{A} \times (\nabla \Psi)], \quad \text{(A7)}$$

the following equality holds:

$$\frac{1}{4\pi}\int\limits_{V-V_s} dv \mathbf{B}_M \mathbf{H}_v = -\frac{\lambda^2}{4\pi}\int\limits_{S_s} d\mathbf{s}\{[\nabla \times (\Phi[\nabla \times \mathbf{H}_M])] + [[\nabla \times \mathbf{H}_M] \times \mathbf{H}_v]\}. \quad \text{(A8)}$$

In order to calculate the surface integral in the last formula, we must know only the values of Φ and its derivatives with respect to coordinates *x* and *z* on the superconductor surface. However, the transition from the surface integral in (A8) to the volume integral cannot be made since the function Φ is not defined in the superconductor.

Using formulas (A3), (A4), (A6), and (A8), we obtain the following expression for U_{int}:

$$U_{\text{int}} = -\int\limits_{V_f} dv \mathbf{M}\mathbf{H}_v + \frac{\lambda^2}{4\pi}\int\limits_{S_s} d\mathbf{s}[\nabla \times (\Phi[\nabla \times \mathbf{H}_M])]. \quad \text{(A9)}$$

If the edge effects are insignificant, the surface integral in this formula can be omitted and expression (A9) is transformed into Eq. (16).

REFERENCES

1. A. M. Campbell and J. E. Evetts, *Critical Currents in Superconductors* (Taylor and Francis, London, 1972; Mir, Moscow, 1975).
2. R. P. Huebener, *Magnetic Flux Structures in Superconductors* (Springer-Verlag, Berlin, 1979; Mashinostroenie, Moscow, 1984).
3. T. H. Alden and J. D. Livingston, J. Appl. Phys. **37** (9), 3551 (1966).
4. O. Daldini, P. Martinoli, J. L. Olsen, and G. Berner, Phys. Rev. Lett. **32**, 218 (1974).
5. M. Baert, V. V. Metlushko, R. Jonckheere, *et al.*, Phys. Rev. Lett. **74**, 3269 (1995).
6. L. Civale, A. D. Marvick, T. K. Wortington, *et al.*, Phys. Rev. Lett. **67**, 648 (1991).
7. D. R. Nelson and V. M. Vinokur, Phys. Rev. Lett. **68**, 2398 (1992).
8. D. R. Nelson and V. M. Vinokur, Phys. Rev. B **48**, 13060 (1993).
9. Y. Otani, B. Pannetier, J. P. Nozieres, and D. Givord, J. Magn. Magn. Mater. **126**, 622 (1993).
10. D. J. Morgan and J. B. Ketterson, Phys. Rev. Lett. **80**, 3614 (1998).
11. I. K. Marmorkos, A. Matulis, and F. M. Peeters, Phys. Rev. B **53**, 2677 (1996).
12. J. I. Martin, M. Velez, J. Nogues, and I. K. Schuller, Phys. Rev. Lett. **79**, 1929 (1997).
13. Y. Jaccard, J. I. Martin, M.-C. Cyrylle, *et al.*, Phys. Rev. B **58**, 8232 (1998).
14. J. I. Martin, M. Velez, J. Nogues, *et al.*, J. Appl. Phys. **84**, 411 (1998).
15. J. I. Martin, M. Velez, J. Nogues, *et al.*, J. Magn. Magn. Mater. **177**, 915 (1998).
16. J. I. Martin, M. Velez, A. Hoffmann, *et al.*, Phys. Rev. Lett. **83**, 1022 (1999).
17. F. Marty, A. Vaterlau, U. Majer, and D. Pescia, J. Appl. Phys. **87**, 5099 (2000).
18. F. Hellman, A. L. Shapiro, E. N. Abarra, *et al.*, Phys. Rev. B **59**, 11408 (1999).
19. F. Hellman, M. Messer, and E. N. Abarra, J. Appl. Phys. **86**, 1047 (1999).
20. N. D. Rizzo, T. J. Silva, and A. B. Kos, Phys. Rev. Lett. **83**, 4876 (1999).
21. C. Reinchhard, J. Groth, C. J. Olson, *et al.*, Phys. Rev. B **54**, 16108 (1996).
22. W. Schindler, B. Roas, G. Saemann-Ischenko, *et al.*, Physica C (Amsterdam) **169**, 117 (1990).
23. F. M. Sauerzopf, H. P. Wiesinger, W. Kritscha, *et al.*, Phys. Rev. B **43**, 3091 (1991).
24. Yu. I. Bespyatykh, W. Wasilevski, M. Gajdek, *et al.*, Fiz. Tverd. Tela (St. Petersburg) **36**, 586 (1994) [Phys. Solid State **36**, 323 (1994)].
25. A. Stankiewicz, S. Robinson, G. F. Gering, and V. V. Tarasenko, J. Phys.: Condens. Matter **9**, 1019 (1997).
26. Yu. I. Bespyatykh, W. Wasilevski, É. G. Lokk, and V. D. Kharitonov, Fiz. Tverd. Tela (St. Petersburg) **40** (6), 1068 (1998) [Phys. Solid State **40**, 975 (1998)].
27. E. H. Brandt, J. Low Temp. Phys. **44** (1/2), 59 (1981).
28. Yu. I. Bespyatykh and W. Wasilevski, Fiz. Tverd. Tela (St. Petersburg) **43** (2), 215 (2001) [Phys. Solid State **43**, 224 (2001)].
29. L. N. Bulaevskii, E. M. Chudnovsky, and M. P. Maley, Appl. Phys. Lett. **76**, 2594 (2000).
30. V. G. Gaĭvoron, Yu. F. Ogrin, N. I. Polzikova, and V. V. Tarasenko, in *Proceedings of the V All-Union School on Spin Microwave Electronics, Zvenigorod, 1991*, p. 45.

Translated by N. Wadhwa

Physics of the Solid State, Vol. 43, No. 10, 2001, pp. 1834–1844. Translated from Fizika Tverdogo Tela, Vol. 43, No. 10, 2001, pp. 1761–1771.

METALS AND SUPERCONDUCTORS

The Nernst–Ettingshausen Coefficient in Conductors with a Narrow Conduction Band: Analysis and Application of Its Results to HTSC Materials

N. V. Ageev and V. É. Gasumyants

St. Petersburg State Technical University, ul. Politekhnicheskaya 29, St. Petersburg, 195251 Russia

e-mail: VGAS@twonet.stu.neva.ru

Received October 6, 2000; in final form, March 1, 2001

Abstract—A theoretical analysis is made of the Nernst–Ettingshausen coefficient Q for the case of a narrow conduction band present in the band spectrum of a material. It is shown that the presence of such a band results in a qualitative change in the mechanism responsible for the Nernst–Ettingshausen effect as compared to the classical case of a broad conduction band and that the behavior of this coefficient reveals a number of specific features that are different from the case of the classical theory of transport coefficients in semiconductors and metals. It is demonstrated that the pattern of the $Q(T)$ relation in the case of a narrow band is drastically affected by the asymmetry of the dispersion curve, whereas the other features of the band spectrum and of the properties of the carrier system, including the character of the energy dependence of the relaxation time, are less significant and, in a first approximation, can be disregarded. The calculated $Q(T)$ curves are in qualitative agreement with the experimental relationships obtained for doped HTSCs of the $YBa_2Cu_3O_y$ system. The possibility of using this approach for a complex analysis of the experimental temperature dependences of the four transport coefficients in the normal phase of HTSC materials is demonstrated. © *2001 MAIK "Nauka/Interperiodica".*

1. INTRODUCTION

The band structure and, more generally, the nature of the normal state in HTSC materials has been a subject of intense interest since the moment of discovery of this class of compounds. Among the bright manifestations of the unusual properties of the normal state, which are directly related to the band spectrum structure of these compounds, one can class the experimental results obtained in studies of the electronic transport phenomena. A wealth of experimental data on the temperature dependences of the transport coefficients (the electrical resistivity ρ, the Seebeck coefficient S, and the Hall constant R_H) in high-temperature superconductors of various kinds, as well as on the character of their transformation for various deviations from stoichiometry, has been accumulated (see [1–3]). These dependences were found to exhibit a number of nontrivial characteristics that discriminate HTSC compounds from traditional subjects of investigation in solid state physics, namely, metals and semiconductors.

In contrast to the copious experimental information on the behavior of the three transport coefficients mentioned above, data on the temperature dependences of the Nernst–Ettingshausen (NE) coefficient Q in the normal state are presently scarce. Attempts at analyzing the experimental $Q(T)$ relations [4–6] are limited to a qualitative discussion of one $Q(T)$ curve obtained for a specific sample and are based on assumptions which are insufficiently validated and require serious additional examination. An approach drawing on a comparative analysis of a large volume of experimental data, including information on the character of transformation of the $Q(T)$ relations caused by a purposeful variation of the sample composition, could become truly useful and of value to the theory. It also appears important to consider the behavior of the NE coefficient not separately but rather combined with the results obtained for the other coefficients. This approach would permit one to explain, within a common framework, the totality of data on the electronic transport phenomena in the normal phase. This would offer the possibility, first, to obtain more complete information on the specific features of electronic transport in the normal phase of the HTSC compounds and, second, to extract more useful and objective information from the $Q(T)$ relations.

We chose, as a basis for such an analysis, the narrow band model first proposed in [7] and described in considerable detail in [8]. This model draws on the assumption of the existence of a narrow density-of-states peak in the HTSC band spectrum. Note that a number of both experimental [9–21] and theoretical [22–28] studies have also come to the conclusion that the HTSC spectrum has a narrow conduction band or a narrow density-of-states peak in which the Fermi level is located. We see the narrow-band model as more advantageous in that it is based on a small number of parameters having a clear physical meaning, permits one to describe the behavior of three rather than one transport coefficient (the electrical resistivity and the Seebeck and Hall coef-

1063-7834/01/4310-1834$21.00

ficients), and offers the possibility of deriving the parameters of the band spectrum and of the carrier system in the normal phase from a quantitative analysis of experimental data for samples of different composition. It appears important to include data on the NE coefficient in analyzing the electronic transport phenomena made in terms of the narrow-band model. Because no analysis of the NE effect in narrow-band conductors has been carried out systematically thus far (with the exclusion of [29], a paper briefly discussing the dependence of Q on the filling of a narrow band by electrons in a metal for the case of an energy-independent relaxation time), realization of this approach requires preliminary, comprehensive, theoretical consideration, which is a point of independent significance.

This has stimulated the present theoretical analysis of the NE coefficient for the case of a narrow density-of-states peak located in the band spectrum of a material, as well as a consideration of the specific features in the application of the results of this analysis to treating experimental temperature dependences of the NE coefficient in high-temperature superconductors of the $YBa_2Cu_3O_y$ system in the normal state.

2. SPECIFIC FEATURES OF THE NERNST–ETTINGSHAUSEN EFFECT IN THE CASE OF A NARROW CONDUCTION BAND

The NE effect is essentially as follows. Let a sample be placed in a magnetic field H, whose vector is directed perpendicular to the temperature gradient ∇T applied to the sample. An electric field E_N, perpendicular to the magnetic field and to the temperature gradient and proportional to their magnitude, $E_N = QH\nabla T$, will be created. It is the coefficient of proportionality Q in this expression that is the NE coefficient. In the classical case, its magnitude and sign are determined by the character of the energy dependence of the carrier relaxation time τ. If τ increases with increasing energy, the coefficient Q is positive; if it decreases, Q is negative; and in the case of the relaxation time being independent of energy, $Q = 0$. Thus, by analyzing the data obtained for the NE coefficient, one can draw a conclusion concerning the mechanism of carrier scattering in the materials under study.

This is valid, however, only in the classical case of a wide conduction band and a quadratic dispersion law. If the band structure contains a narrow conduction band, the behavior of the NE coefficient is characterized, as with other transport coefficients, by a number of specific features which do not appear in classical theory. To establish the origin of these features, we consider qualitatively the mechanism giving rise to the NE effect in the case of a narrow conduction band.

In the limit of a narrow band, its width W is comparable to k_BT, where k_B is the Boltzmann constant; in other words, the Fermi broadening covers a sizable part of the band. If the chemical potential μ lies near the band center (situation characteristic of HTSC materials [8, 30–36]), the energy interval $\varepsilon = \mu \pm (1–2)k_BT$ includes both the upper and lower parts of the band. Under these conditions, it is unreasonable to introduce the concept of a hole and to study the motion of two types of carriers, electrons and holes, because thermal energy drives the electrons continuously from the lower to the upper half of the band and back. We shall, therefore, assume that all of the transport in a narrow band is governed by one type of carrier, namely, by electrons, which have a positive or a negative effective mass in the lower and upper halves of the band, respectively.

We shall consider, within this condition, a particular case of the band being symmetrical and of the chemical potential level being at its center. Note that, in this case, the dispersion law in the energy region of interest is certainly not quadratic. If a temperature gradient is applied to the sample, the thermal diffusion current, according to the solution to the Boltzmann kinetic equation in the relaxation time approximation, will be given by

$$j = \int\left(e\tau\left(\frac{\partial f_0}{\partial \varepsilon}\right)\bar{V}\frac{\varepsilon-\mu}{T}\frac{\partial T}{\partial R}D(\varepsilon)\right)\bar{V}d\varepsilon, \qquad (1)$$

where f_0 is the equilibrium Fermi–Dirac distribution function, $\bar{V}$ is the mean electron velocity, and $D(\varepsilon)$ is the density-of-states function; the energy is reckoned from the band center and integration is run over the whole band, i.e., from $–W/2$ to $+W/2$.

As seen from Eq. (1), electrons with an energy above the chemical potential will move in one direction; those located below the level, in the opposite direction. Because the chemical-potential level lies at the band center, the effective mass of the electrons with $\varepsilon < \mu$ will be positive and that of the electrons with $\varepsilon > \mu$ will be negative. The integrand of Eq. (1) contains the product of two even and one odd function of energy; hence, the integral is zero, which means that the Seebeck coefficient is zero (similarly, the Hall coefficient in this case is zero). However, although the net thermal diffusion current is zero, the sample is traversed by two counter-propagating flows of electrons with energies above and below the chemical potential, respectively. Because these flows consist of electrons with a positive and a negative mass, a magnetic field applied to the sample will deflect them to the same side. As a result, a carrier flow will form along an axis perpendicular to the temperature gradient and the magnetic field vector and, therefore, an oppositely directed drift current will arise. This is the Nernst–Ettingshausen effect. In this particular case, the existence of the effect is due not to the character of the energy dependence of the relaxation time but to the dispersion law for the narrow band not being quadratic. Note that the sign of the NE coefficient in our particular case of a symmetric and half-filled band will be positive at any temperature.

Thus, the narrowness of the conduction band brings about a qualitative change in both the mechanism

responsible for the NE effect and the behavior of the NE coefficient compared to the classical case of a wide conduction band. To make a more comprehensive analysis, we consider the expression for the NE coefficient in terms of the narrow-band model.

3. THE NERNST–ETTINGSHAUSEN COEFFICIENT IN THE NARROW-BAND MODEL

Adopting a relaxation time approximation and assuming a temperature field and a weak magnetic field to be present, the Boltzmann kinetic equation can be solved in the standard way and yields the following expression for the NE coefficient:

$$Q = -\frac{1}{eT}\left(\frac{I_{\sigma_{H1}}}{I_{\sigma_0}} - \frac{I_{\sigma_{H0}} I_{\sigma_1}}{I_{\sigma_0}^2}\right), \tag{2}$$

where we accept the notation

$$I_{\sigma_0} = \int \sigma(\varepsilon)\left(-\frac{\partial f_0}{\partial \varepsilon}\right)d\varepsilon, \quad I_{\sigma_1} = \int \sigma(\varepsilon)\left(-\frac{\partial f_0}{\partial \varepsilon}\right)\varepsilon d\varepsilon,$$
$$I_{\sigma_{H0}} = \int \sigma_H(\varepsilon)\left(-\frac{\partial f_0}{\partial \varepsilon}\right)d\varepsilon, \quad I_{\sigma_{H1}} = \int \sigma_H(\varepsilon)\left(-\frac{\partial f_0}{\partial \varepsilon}\right)\varepsilon d\varepsilon \tag{3}$$

and $\sigma(\varepsilon) = \frac{\tau e^2 V^2}{3} D(\varepsilon)$ is the differential conductivity, $\sigma_H(\varepsilon) = -\frac{\tau^2 e^3 V^2}{3m^*} D(\varepsilon) = u\sigma(\varepsilon)$ is the Hall differential conductivity, $D(\varepsilon)$ is the electronic density-of-states function, u is the electron mobility, and m^* is the electron effective mass; the integration in Eq. (3) is performed throughout the band.

Relation (2) is general and valid for band spectra of any kind. The only constraint is the condition of isotropy. In an anisotropic case, the expression for the NE coefficient becomes complicated because of the need to take different dispersion relations for different directions into account. As for the HTSC materials, their strong anisotropy results in the conduction becoming two-dimensional; taking into account this factor and considering the conduction in the *ab* plane may give rise only to an insignificant change in the coefficients entering the expressions for the integrals in Eq. (2) while not affecting their general form. For simplicity, we shall limit ourselves to an analysis of the expression for Q in the isotropic case in what follows.

To make a quantitative analysis of the NE coefficient, one should first prescribe the form of the $D(\varepsilon)$, $\sigma(\varepsilon)$, and $\sigma_H(\varepsilon)$ functions in the integrals in Eq. (3). We shall approximate them in terms of the narrow-band model. As shown in [8], if the band spectrum contains a narrow density-of-states peak $W \sim 100$ meV broad, it is the narrowness of this peak, rather than any features in the band structure and in the properties of the carrier system, that determines, in a first approximation, the behavior of the transport coefficients. This permits one to use the simplest rectangular approximation of the $D(\varepsilon)$, $\sigma(\varepsilon)$, and $\sigma_H(\varepsilon)$ functions:

$$\begin{aligned} D(\varepsilon) &= \langle D\rangle \ \text{ for } \ -W_D/2 < \varepsilon < W_D/2, \\ D(\varepsilon) &= 0 \ \text{ for } \ \varepsilon < -W_D/2 \ \text{ and } \ \varepsilon > W_D/2, \\ \sigma(\varepsilon) &= \langle \sigma\rangle \ \text{ for } \ -W_\sigma/2 < \varepsilon < W_\sigma/2, \\ \sigma(\varepsilon) &= 0 \ \text{ for } \ \varepsilon < -W_\sigma/2 \ \text{ and } \ \varepsilon > W_\sigma/2, \\ |\sigma_H(\varepsilon)| &= \langle \sigma_H\rangle \ \text{ for } \ -W_\sigma/2 < \varepsilon < W_\sigma/2, \\ \sigma_H(\varepsilon) &= 0 \ \text{ for } \ \varepsilon < -W_\sigma/2 \ \text{ and } \ \varepsilon > W_\sigma/2, \end{aligned} \tag{4}$$

where $\sigma_H(\varepsilon) < 0$ for $\varepsilon < 0$, $\sigma_H(\varepsilon) > 0$ for $\varepsilon > 0$, and

$$\langle D\rangle = \frac{1}{W_D}\int_{-W_D/2}^{W_D/2} D(\varepsilon)d\varepsilon, \quad \langle \sigma\rangle = \frac{1}{W_\sigma}\int_{-W_\sigma/2}^{W_\sigma/2} \sigma(\varepsilon)d\varepsilon,$$
$$\langle \sigma_H\rangle = -\frac{2}{W_\sigma}\int_{-W_\sigma/2}^{0} \sigma_H(\varepsilon)d\varepsilon = \frac{2}{W_\sigma}\int_{0}^{W_\sigma/2} \sigma_H(\varepsilon)d\varepsilon.$$

With this approximation, the relaxation times, electron velocities, and electronic masses (to within the sign) become averaged in a narrow interval of energies, ε from $-W_\sigma/2$ to $W_\sigma/2$, comparable to the Fermi broadening. This permits one to derive fairly simple analytical expressions describing the temperature dependences of the chemical potential and of the three transport coefficients [8]. The merits inherent in the application of a similar approach to the analysis of the NE coefficient are obvious: indeed, it simplifies the calculation of the coefficient substantially and, hence, makes possible a qualitative and quantitative consideration of its behavior. In addition, this approach permits one to carry out a joint analysis of the behavior of the four transport coefficients in terms of the same model.

The narrow-band model contains three main parameters, namely, the total effective band width W_D, the effective band width in conduction W_σ (with the ratio $C = W_\sigma/W_D$ characterizing the degree of carrier localization), and the band filling by electrons F, which is the ratio of the total number of carriers to the total number of states in the band and, together with W_D, determines the temperature dependence of the chemical potential:

$$\mu^* \equiv \frac{\mu}{k_B T} = \ln\frac{F W_D/2k_B T}{(1-F)W_D/2k_B T}. \tag{5}$$

To take into account the possible weak asymmetry of a narrow band, these three main parameters should be complemented by an additional parameter b, which characterizes the shift of the center of the differential conductivity rectangle relative to the band center (the degree of band asymmetry). In this case, the value of μ^*

obtained from Eq. (5) to calculate the transport coefficients should be replaced by

$$(\mu^*)' = \mu^* - bW_D/k_BT. \quad (6)$$

Note that, as shown in our previous publications, the values of all four model parameters for HTSC materials belonging to different families can be derived from a quantitative analysis of experimental data on the Seebeck coefficient [8, 30–36].

Within approximation (4), the integrals in Eq. (3) are simplified considerably, thus permitting a qualitative analysis of the specific features in the behavior of the NE coefficient in the narrow-band model. We shall start by studying the change in the character of the $Q(T)$ relation when taking the limits of a wide and a narrow band.

In the high-temperature limit (i.e., when the $k_BT > W_D/2$ condition is met), we substitute Eq. (4) into Eq. (3) and integrate Eq. (3) within the limits $-W_\sigma < \varepsilon < W_\sigma$, taking into account that $\langle\sigma_H\rangle = \bar{u}\langle\sigma\rangle$, where $\bar{u}$ is the band-averaged electron mobility, to obtain

$$\lim_{T\to\infty} Q = -\frac{1}{eT} \times u\left(\frac{\int\frac{1}{4}\mathrm{sgn}(\varepsilon)\varepsilon d\varepsilon}{\int\frac{1}{4}\varepsilon d\varepsilon} - \frac{\int\frac{1}{4}\mathrm{sgn}(\varepsilon)d\varepsilon\int\frac{1}{4}\varepsilon d\varepsilon}{\left(\int\frac{1}{4}\varepsilon d\varepsilon\right)^2}\right) = 0.$$

Thus, irrespective of any features in the narrow-band structure and of the extent of the band filling by electrons, the high-temperature NE coefficient tends to zero as $Q \propto 1/T$.

In the other limiting case of $T \longrightarrow 0$ (i.e., for $W_D/2 \gg k_BT$), our approximation reduces to the classical situation of a wide band with an energy-independent relaxation time. When taking integrals in Eq. (3), one can limit the integration to the energy interval within which the function $\left(-\frac{\partial f_0}{\partial\varepsilon}\right)$ is nonzero. Clearly enough, if the chemical-potential level lies far enough from the band center, where the quadratic dispersion law is no longer valid, i.e., if the condition $|\mu| \gg k_BT$ is satisfied, the energy ε in integrals in Eq. (3) retains its sign within the interval under consideration. As a result, $I_{\sigma_{H1}} = \bar{u}I_{\sigma_1}$, $I_{\sigma_{H0}} = \bar{u}I_{\sigma_0}$, and the expression in parentheses in Eq. (3) vanishes. Hence, as considered in the wide-band limit, the NE coefficient is zero irrespective of which half of the band contains the chemical-potential level. This behavior of Q coincides fully with the classical wide-band case if the relaxation time is assumed to be energy independent.

Thus, in the case of a band of intermediate width, the NE coefficient calculated by the narrow-band model will tend to zero at both high and low temperatures and the $Q(T)$ relation will have a maximum at an intermediate temperature. In the intermediate-temperature region, the $Q(T)$ dependence will be affected considerably, in addition to the narrowness of the band, both by the magnitude of the main model parameters (F, W_D, C, b) and by finer features in the band structure, which can be taken into account within the model in question by properly varying the model functions $D(\varepsilon)$, $\sigma(\varepsilon)$, and $\sigma_H(\varepsilon)$. The results of quantitative analysis of these effects are considered below.

4. SPECIFIC FEATURES IN THE TEMPERATURE DEPENDENCES OF THE NERNST–ETTINGSHAUSEN COEFFICIENT IN THE CASE OF A NARROW CONDUCTION BAND

Let us analyze the character of the $Q(T)$ dependences for a narrow-band material and consider the possibility of describing the experimental data on HTSC compounds in terms of a narrow-band model. To do this, we have first to choose model approximations of the functions $\sigma(\varepsilon)$ and $\sigma_H(\varepsilon)$, which, on the one hand, are physically meaningful and, on the other, permit one to obtain calculated $Q(T)$ relations that qualitatively fit observations. Moreover, the approximations used and the values of the main model parameters should make it possible to calculate curves which fit experimental data for the $\rho(T)$, $S(T)$, and $R_H(T)$ dependences. A comprehensive analysis of our experimental data on the $Q(T)$ dependences in doped HTSCs of the $YBa_2Cu_3O_y$ system will be given in another paper. Without discussing these results here in any detail, we limit ourselves to pointing out the following main characteristic features of the $Q(T)$ dependences found by us in [37, 38] and observed in [5] on samples of various compositions:

The NE coefficient of $YBa_2Cu_3O_y$ at $T = 300$ K is always positive; in the low-temperature region, a crossover to negative values of Q takes place in some compositions.

The magnitude of Q grows weakly as the temperature decreases from $T = 300$ K.

The $Q(T)$ dependence passes through a broad maximum at $T = 200$–260 K depending on the sample composition.

The magnitude of Q drops sharply as the temperature is lowered even more.

Any model developed to describe the behavior of the NE coefficient in HTSCs should take into account all these features.

First, let us consider a symmetric narrow band with the Fermi level near the band center, a case that we have already discussed. The temperature dependence of the NE coefficient calculated for various values of F and C in terms of the model approximation (4) is displayed in Figs. 1a and 1b, respectively. The band width was assumed equal to $W_D = 100$ meV; the carrier mobility,

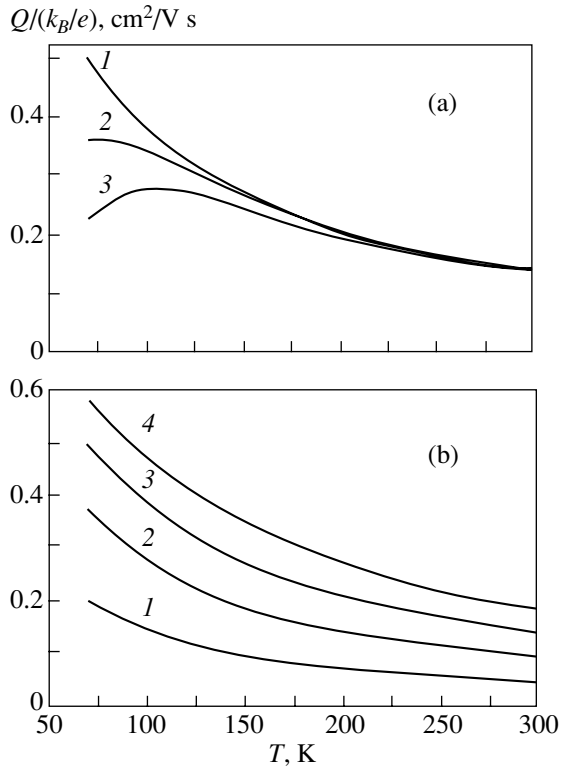

Fig. 1. $Q(T)$ dependences for a symmetric narrow band calculated (a) for various band fillings F: (*1*) 0.5, (*2*) 0.4, 0.6, and (*3*) 0.3, 0.7; and (b) for various degrees of carrier localization C: (*1*) 0.1, (*2*) 0.2, (*3*) 0.3, and (*4*) 0.4. The model parameters used were $W_D = 100$ meV, $u = 0.5$ cm^2/V s; (a) $C = 0.3$ and (b) $F = 0.5$.

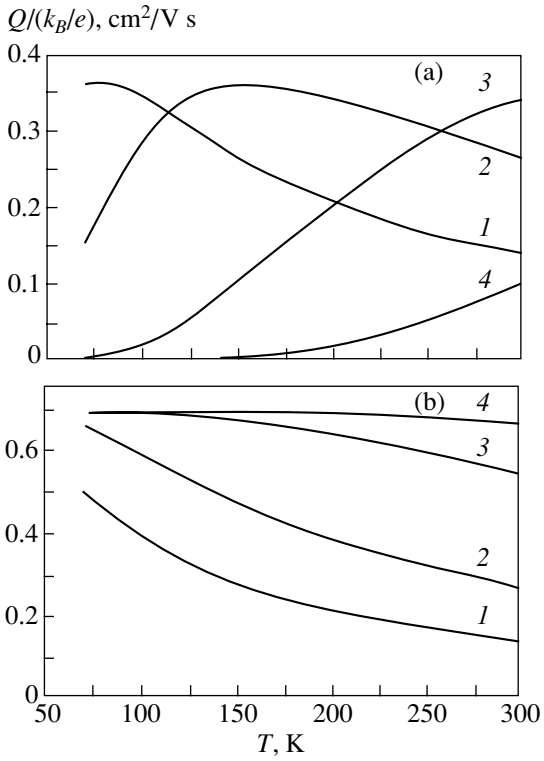

Fig. 2. $Q(T)$ dependences for a symmetric narrow band calculated for various band widths. The model parameters used were $C = 0.3$, $u = 0.5$ cm^2/V s; F = (a) 0.6 and (b) 0.5; W_D = (*1*) 100, (*2*) 200, (*3*) 500, and (*4*) 1000 meV.

to $u = 0.5$ cm^2/V s. As seen from Fig. 1a, at high temperatures, the NE coefficient scales as T^{-1} and its value, as already pointed out, does not depend on the band filling. Irrespective of the band filling, the NE coefficient is always positive. For instance, for $F = 0.3$, where the Seebeck and Hall coefficients calculated within the narrow-band model are negative, the NE coefficient remains positive. As the band filling changes, the $Q(T)$ dependence also changes; significantly, both an increase and a decrease in F relative to the half-filling brings about the same change in the character of the $Q(T)$ dependence and, in the low-temperature domain, the NE coefficient reaches a maximum at $F = 0.5$, i.e., the value at which μ is located in the region with the strongest deviation of dispersion from the quadratic law. Thus, as F is varied, the $Q(T)$ dependence varies symmetrically relative to the band half-filling. Note that these features of the $Q(T)$ dependence agree with the results reported in [29]. As for the degree of carrier localization C, the value of Q, as seen from Fig. 1b, increases with one increase in the fraction of extended states throughout the temperature interval covered, but the $Q(T)$ dependence retains its qualitative pattern.

Consider the effect of the band width on the $Q(T)$ dependence. Figure 2a presents $Q(T)$ plots calculated for various values of W_D and fixed $F = 0.6$ and $C = 0.3$. As shown earlier, the Q coefficient should vanish in both the high- and the low-temperature limit. In the low-temperature limit, we have $|\mu| \gg k_B T$; i.e., this limit is realized in the case where the Fermi broadening of the distribution function does not extend to the center of the narrow band, where the quadratic dispersion law breaks down, and the effective mass reverses its sign. The band broadening at a fixed F initiates an increase in $|\mu|$, and, accordingly, the $|\mu| \gg k_B T$ condition is satisfied at higher temperatures. This brings about a shift in the part of the $Q(T)$ dependence where the NE coefficient increases with increasing temperature toward higher temperatures.

The decrease in Q with increasing temperature observed to occur in curves *1* and *2* in Fig. 2a is connected with the onset of the high-temperature limit, where the half-width of the narrow band becomes comparable to the Fermi broadening. As the band width continues to grow, this condition becomes satisfied at increasingly higher temperatures. Therefore, curves *3* and *4* do not exhibit the part of the dependence where

Q falls with increasing temperature, because it lies beyond the temperature interval shown (50–300 K).

A particular case is the band half-filling ($F = 0.5$) where the Fermi level lies at the band center, i.e., directly in the region in which the quadratic dispersion law breaks down. Under these conditions, the chemical potential calculated from Eq. (4) is zero and the condition $|\mu| \gg k_BT$ is not met at any temperature; this means that the low-temperature limit is not realized. Accordingly, the calculated $Q(T)$ dependences do not have a region of Q that grows with increasing temperature (Fig. 2b). In the high-temperature limit, the band half-filling does not qualitatively affect the behavior of the NE coefficient. The calculated curves fall off to zero the faster, the smaller the band width.

Most of the $Q(T)$ dependences plotted in Figs. 1 and 2 do not agree with the ones observed experimentally in HTSC materials. The exceptions to the rule are curves *3* in Fig. 1a and *2* in Fig. 2a. However, as already mentioned, an analysis of experimental $Q(T)$ dependences within the narrow-band model does not offer a wide choice of values for the model parameters, because they are rigidly determined from the $S(T)$ relations obtained for the same samples. The values of the parameters $F = 0.6$ and $W_D = 200$ meV, for which curve *2* in Fig. 2a was calculated, and, especially, the values $F = 0.3$ and $W_D = 100$ meV (curve *3* in Fig. 1a) are not realized for $YBa_2Cu_3O_y$ samples at $y \approx 7$ [8].

Thus, a joint analysis of the $S(T)$ and $Q(T)$ dependences made within the symmetric narrow-band model does not provide qualitative agreement between the calculations and experimental data. At the same time, as pointed out in publications [8, 34, 36], in which the narrow-band model was used to describe the transport properties of HTSCs in the $YBa_2Cu_3O_y$ system, the conduction band in these compounds is close to symmetric. A possible way out lies in assuming that the band spectrum has features which, while not affecting the behavior of the electrical resistivity and the Seebeck coefficient (or affecting them only weakly), influence the NE coefficient. The most natural approach appears to be to take into account the effect of the energy dependence of the relaxation time, the asymmetry in the dispersion relation $\varepsilon(k)$ and, accordingly, in $m^*(k)$, and the asymmetry in the density-of-states function. Consider possible versions of the model approximation of the $D(\varepsilon)$, $\sigma(\varepsilon)$, and $\sigma_H(\varepsilon)$ functions, which result from taking into account these factors, while at the same time leaving the general characteristics of the model unchanged.

First of all, we consider the effect of the $\tau(\varepsilon)$ dependence on the form of the calculated $Q(T)$ curves. The relaxation time enters into the expression for the differential electrical conductivity $\sigma(\varepsilon)$ as a factor and into the Hall differential electrical conductivity $\sigma_H(\varepsilon)$ quadratically. This means that the energy dependence of the relaxation time should affect the form of $\sigma_H(\varepsilon)$ more strongly. Retaining the rectangular approximation, one can simulate the case where the relaxation time varies in going from the lower to the upper band edge by assuming the $\sigma(\varepsilon)$ and $\sigma_H(\varepsilon)$ rectangles in the upper and lower band halves to be of different height. The difference between the heights of the rectangles approximating $\sigma_H(\varepsilon)$ should be larger than in the case of $\sigma(\varepsilon)$ approximation, as shown in Fig. 3a. If τ varies in going from the edges of the band to its center, this should change the dimensions of the rectangles approximating $\sigma_H(\varepsilon)$ relative to those of the $\sigma(\varepsilon)$ rectangle (by analogy with the difference between the rectangles approximating $D(\varepsilon)$ and $\sigma(\varepsilon)$ within the narrow-band model in [8]), as shown in Fig. 3b.

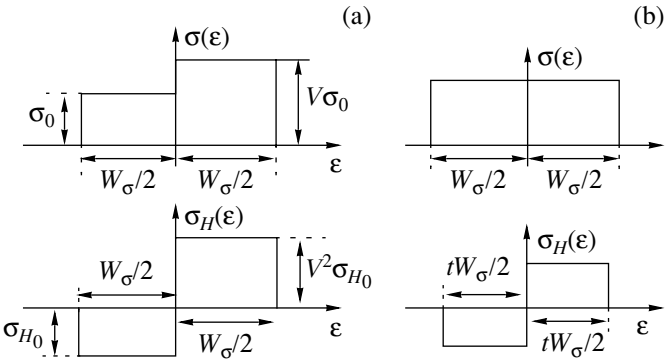

Fig. 3. Different modeling of the energy dependence of the relaxation time in a narrow band. The magnitude of τ varies (a) from the lower to the upper band edge or (b) from the band edges to the band center.

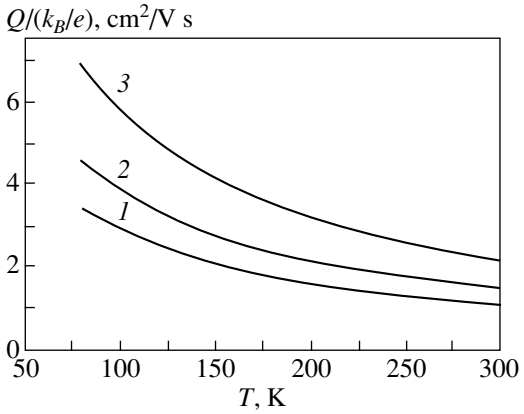

Fig. 4. $Q(T)$ dependences calculated within the approximation shown in Fig. 3a. The model parameters used were $F = 0.51$, $W_D = 100$ meV, $C = 0.3$, $u = 0.5$ cm^2/V s, and $V =$ (*1*) 0.5, (*2*) 1.0, and (*3*) 2.0.

The calculated $Q(T)$ for the first case is displayed in Fig. 4 for different values of the V parameter describing the character and degree of τ variation with increasing carrier energy in the band. Figure 5 plots the calculations performed within the approximation presented in Fig. 3b. It is seen that both scenarios of taking into account the character of the $\tau(\varepsilon)$ dependence do not

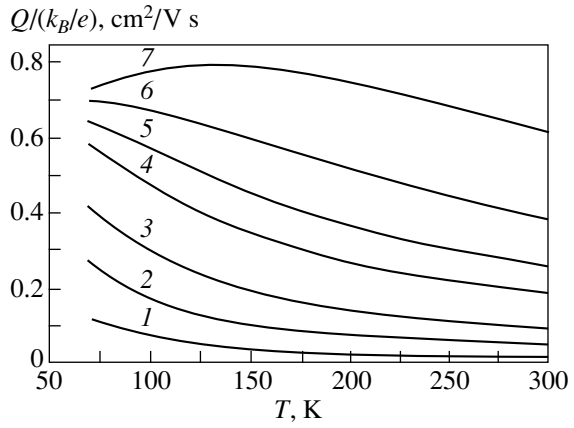

Fig. 5. $Q(T)$ dependences calculated within the approximation shown in Fig. 3b. The model parameters used were F = 0.51, W_D = 100 meV, C = 0.3, u = 0.5 cm^2/Vs, and t = (*1*) 0.3, (*2*) 0.5, (*3*) 0.7, (*4*) 1, (*5*) 1.2, (*6*) 1.5, and (*7*) 2.

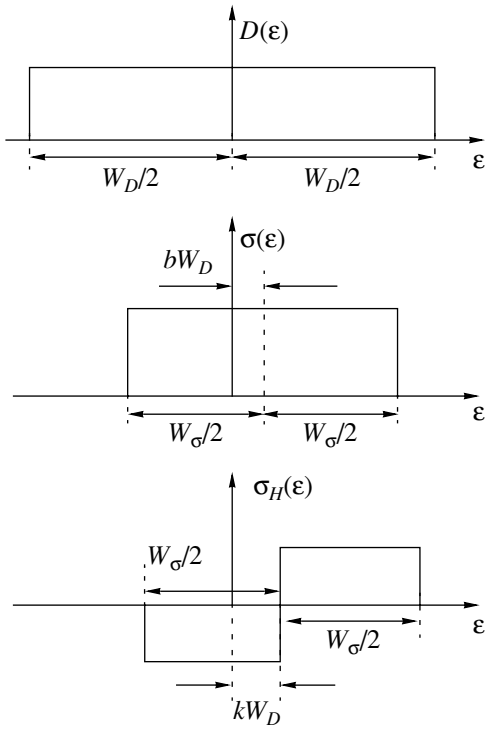

Fig. 6. Approximation of the density-of-states, differential conductivity, and Hall conductivity functions used in the calculation of the $Q(T)$ dependence within the narrow-band model.

change, in most cases, the form of the $Q(T)$ dependence, which still does not fit the experiment. An exception is curve *7* in Fig. 5; however, an analysis of the Hall coefficient showed that the $R_H(T)$ dependences calculated in terms of the model approximation presented in Fig. 3b disagree qualitatively with experimental data obtained on $YBa_2Cu_3O_y$.

Thus, in the case of a narrow conduction band, the character of the energy dependence of the relaxation time does not exert, in contrast to the classical case, any noticeable effect on the behavior of the NE coefficient. As follows from our calculations, a weak asymmetry in the density-of-states function, while somewhat changing the behavior of the Q coefficient, also does not affect the $Q(T)$ dependence qualitatively.

The effect of the dispersion relation $\varepsilon(k)$ on the NE coefficient is of interest. The expression for $\sigma(\varepsilon)$ contains the squared velocity V^2, where $V = \partial\varepsilon/\partial k$, and the expression for $\sigma_H(\varepsilon)$ involves, in addition, the effective electron mass $m^* = \hbar^2/(\partial^2\varepsilon/\partial k^2)$. In a standard band and for a symmetric $\varepsilon(k)$ relation, V^2 is maximum at the band center (on the energy scale) and falls off toward the edges and m^* reverses its sign at the band center. If $\varepsilon(k)$ is asymmetric, the $V^2(\varepsilon)$ dependence shifts relative to the band center and, in the case of a rectangular approximation, this asymmetry brings about a shift in the $\sigma(\varepsilon)$ rectangle, as well as in the upper and lower boundaries of the $\sigma_H(\varepsilon)$ rectangles, with respect to the center of the $D(\varepsilon)$ rectangle. We note that the energy position of the point at which the $\sigma_H(\varepsilon)$ function reverses its sign is determined by the energy at which the effective mass reverses sign; therefore, taking into account the asymmetry in the $\varepsilon(k)$ function will shift not only the boundaries of the $\sigma_H(\varepsilon)$ rectangles but also, which is particularly important, the position of the sign reversal point. This will transform the model approximation of the above functions as shown in Fig. 6. Expression (2) for the NE coefficient can be written in terms of this approximation as

$$Q = -\frac{1}{eT}\bar{u}\left(\frac{I_{H_1}}{I_0} - \frac{I_{H_0}I_1}{I_0^2}\right), \tag{7}$$

where

$$I_0 = \int_{-W_\sigma/2 + bW_D}^{W_\sigma/2 + bW_D}\left(-\frac{\partial f_0}{\partial\varepsilon}\right)d\varepsilon,$$

$$I_{H_0} = \int_{-W_\sigma/2 + kW_D}^{W_\sigma/2 + kW_D}\left(-\frac{\partial f_0}{\partial\varepsilon}\right)\mathrm{sgn}(\varepsilon - kW_D)d\varepsilon, \tag{8}$$

$$I_1 = \int_{-W_\sigma/2 + bW_D}^{W_\sigma/2 + bW_D}\left(-\frac{\partial f_0}{\partial\varepsilon}\right)\varepsilon d\varepsilon,$$

$$I_{H_1} = \int_{-W_\sigma/2 + kW_D}^{W_\sigma/2 + kW_D}\left(-\frac{\partial f_0}{\partial\varepsilon}\right)\mathrm{sgn}(\varepsilon - kW_D)\varepsilon d\varepsilon.$$

Obviously enough, such a change in the $\sigma_H(\varepsilon)$ function should produce a very strong effect on the Hall and NE coefficients, whereas a weak asymmetry in the $\sigma(\varepsilon)$

function, as shown in [8], does not influence in any way the form of the $R_H(T)$ dependence and affects $S(T)$ only weakly for band fillings above $F = 0.505$. This permits one, in a first approximation, to disregard, in calculations, the asymmetry of the $\sigma(\varepsilon)$ function and to use, in most cases, the approximation presented in Fig. 6 and expressions (7) and (8) for $b = 0$ but $k \neq 0$. The value of the model parameter k characterizes the degree of asymmetry of the dispersion curve. In a general case, where an analysis of the $S(T)$ dependences indicates the presence of asymmetry in the density-of-states function (which, as shown by us earlier, is observed in the HTSCs of bismuth [32] and lanthanum [39] systems, as well as in calcium-doped $YBa_2Cu_3O_y$ [33, 35]), one should also take this factor into account and use, in calculating the NE coefficient, the value $b \neq 0$ found from the analysis of the $S(T)$ dependences.

This correction dramatically changes the qualitative pattern of the behavior of the NE coefficient. Figure 7 displays $Q(T)$ dependences calculated within the approximation shown in Fig. 6 with the use of Eqs. (5), (7), and (8) for $b = 0$ and for different asymmetries in $\varepsilon(k)$ (i.e., different values of the k parameter). In the high-temperature domain, the NE coefficient remains positive as before; however, as the temperature decreases, a broad maximum appears in the $Q(T)$ dependence beyond the region of its growth (this region is also observed with other model approximations), whereupon Q falls off fairly rapidly. For certain values of the model parameters, the NE coefficient reverses its sign at low temperatures. Thus, the $Q(T)$ dependence has undergone a substantial change and it now exhibits all the above features, which are characteristic of $Q(T)$ curves measured experimentally on doped HTSCs of yttrium systems.

As seen from Fig. 7, the $Q(T)$ dependences calculated within this approximation that fit the experiment qualitatively are observed at both positive and negative values of the model parameter k (curves *4*, *5*). To get rid of the ambiguity in determination of the band parameters, we carried out a calculation of the temperature dependence of the Hall coefficient using the same approximation and values of k differing in sign. As follows from these calculations, the $R_H(T)$ dependence calculated for $k < 0$ fits the Hall experimental data [2], i.e., $R_H > 0$ and $R_H(T) \propto T^{-1}$, whereas in the case of $k > 0$, the values of R_H are negative throughout the temperature range covered. Thus, it is the use of negative values of k in model calculations that permits one to reach qualitative agreement between experimental data and calculations in the case of HTSC materials not only for $Q(T)$ but also for the temperature dependences of other transport coefficients, including the Hall coefficient. Hence, when choosing the values of the model parameters to fit the $Q(T)$ dependence, one should set $k < 0$.

We should point out the extremely high sensitivity of the NE coefficient to the details in the band spectrum. Taking into account a fairly weak asymmetry in

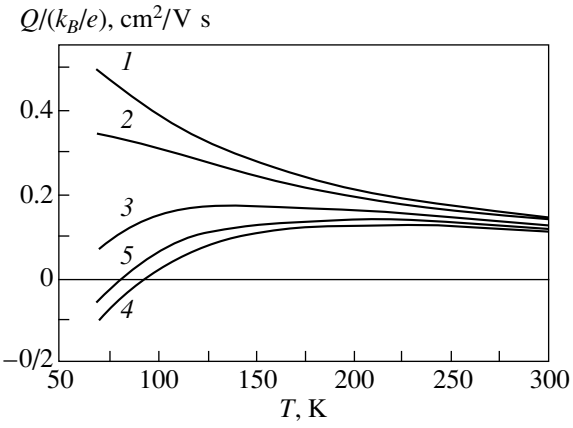

Fig. 7. $Q(T)$ dependences calculated in terms of the approximation presented in Fig. 6 for $b = 0$. The model parameters used were $F = 0.51$, $W_D = 100$ meV, $C = 0.3$, $u = 0.5$ cm^2/V s, and $k =$ (*1*) 0, (*2*) –0.05, (*3*) –0.1, (*4*) –0.14, and (*5*) 0.14.

$\varepsilon(k)$ gives rise to a qualitative change in the shape of the calculated $Q(T)$ dependences. Note that this asymmetry does not affect the character of the $\rho(T)$ and $S(T)$ dependences, because the model approximation of the $D(\varepsilon)$ and $\sigma(\varepsilon)$ functions entering the expressions for these coefficients within the narrow-band model remains unchanged and, as already mentioned, does not affect the shape of the $R_H(T)$ dependences, which fit the experimental data as within the standard model of a symmetric narrow band. Thus, the proposed model approximation of the density-of-states functions and of the differential and Hall conductivities can be used to advantage not only in describing the $Q(T)$ dependences but also in a combined analysis of the totality of experimental data on the temperature dependences of the electrical resistivity and the Seebeck, Hall, and Nernst–Ettingshausen coefficients obtained on $YBa_2Cu_3O_y$ HTSC samples of different composition.

To make a quantitative analysis of the temperature dependences of the NE coefficient in the case of a narrow conduction band, one should use Eqs. (5)–(8) on expressing Q through the narrow-band model parameters F, W, C, b, k, and u. One more point should be mentioned. As already noted, in a combined analysis of experimental data on the Seebeck and NE coefficients, the values of the main model parameters, namely, F, W, and C (and, if needed, b), can be derived unambiguously from $S(T)$ relations to be subsequently used to analyze $Q(T)$ by means of Eqs. (7) and (8). As a result, the behavior of the NE coefficient is determined only by two additional parameters, namely, k and u. Note that the mobility, which enters Eq. (7) as a factor, turns out to be essential only when calculating the magnitude of the NE coefficient and does not change the form of its temperature dependence. Thus, if the parameters F, W_D, W_σ, and b are fixed, the character of the $Q(T)$ dependence is fully determined by the magnitude of the

parameter k; the absolute values of Q, by the value of u, which permits one to unambiguously extract these parameters from experimental data for $Q(T)$. The results of an analysis of experimental data obtained on doped HTSCs of the $YBa_2Cu_3O_y$ system will be presented in another publication.

5. DETERMINATION OF THE PARAMETERS OF THE CARRIER SYSTEM FROM AN ANALYSIS OF THE $Q(T)$ RELATIONS IN TERMS OF THE NARROW-BAND MODEL

An analysis of the effect of various features in the band spectrum on the behavior of the NE coefficient showed that the most significant factor in the case of a narrow conduction band is the character of the dispersion relation $\varepsilon(k)$. Other features in the band structure and in the properties of the carrier system (the asymmetry in the density-of-states function or the character of the energy dependence of the relaxation time) are less significant and may be disregarded in a first approximation. In particular, the coefficient Q does not vanish even if τ is independent of ε. This means that an analysis of the NE coefficient cannot give information on the carrier scattering mechanism and the character of the $\tau(\varepsilon)$ dependence in materials with a narrow conduction band, unlike the classical case of semiconductors and metals, where measurements of the $Q(T)$ relations and their analysis in terms of the classical transport theory are performed primarily with this purpose in mind. At the same time, analyzing the $Q(T)$ relations within the narrow-band model in samples with a purposefully varied composition offers the possibility of following the variation of the degree of asymmetry in the dispersion relation.

When deriving the carrier mobility from an analysis of the $Q(T)$ dependence, one should bear in mind the following. In a classical case of a broad band, the electron energy interval of the order of a few k_BT that is of importance in treating transport phenomena is small compared to the total band width, which permits one to neglect the $m^*(\varepsilon)$ dependence and, using the band-averaged relaxation time $\langle\tau\rangle$, to determine the carrier mobility $u = \langle\tau\rangle e/m^*$. In the narrow-band case, one can also use the relaxation time averaged over energy, but the $m^*(\varepsilon)$ dependence cannot be neglected. In particular, the effective mass at the band center reverses its sign, and it is this energy region that plays a crucial role in the HTSC materials whose band is close to being half filled. Assuming the effective masses in the upper and lower halves of the band to be equal to within the sign, i.e., approximating the $m^*(\varepsilon)$ dependence with rectangles, the magnitude of u can be defined as the mean electron mobility in the narrow band. It is this mobility that enters Eq. (7) and that can be derived from the experimental $Q(T)$ dependence within the narrow-band model. Hence, as in the classical case, a study of the NE effect in narrow-band conductors can be employed to determine the carrier mobility. Note the following circumstances. First, intercrystallite layers in polycrystalline samples affect the electrical resistivity substantially, which entails errors in the determination of the absolute values of σ. Second, in the narrow-band case, the Hall concentration is not actually the true carrier concentration [8]. Both these factors are essential in analyzing the experimental data obtained on HTSC materials, so that the determination of the mobility from resistivity and Hall measurements as $u = \sigma R_H$ appears invalid. Therefore, experimental investigation and analysis of the NE coefficient is, in this case, a very efficient and informative method for determining the carrier mobility.

6. ANALYSIS OF THE APPLICABILITY OF THE TRANSPORT EQUATION

Because in the analysis of the $Q(T)$ dependence we made use of the Boltzmann transport equation and solved it in the relaxation time approximation, it appears necessary to verify the validity of this approach in the case of narrow-band materials in general and as applied to HTSC materials in particular.

The first condition for applicability of the transport equation is based on accepting the concept of the mean free time, i.e., on assuming that collisions are fairly rare events. Because the distribution function, which varies strongly within an energy interval of the order of k_BT, can be used only if the uncertainty in energy satisfies the inequality $\Delta\varepsilon < k_BT$ and the first approximation of perturbation theory that is employed in calculating the collision integral is invalid if the electron suffers more than one collision, the time $\Delta t \approx \hbar/\Delta\varepsilon$ should be less than τ. As a result, we conclude that the following inequality should be met:

$$k_BT > \hbar/\tau. \tag{9}$$

This may be considered the condition for shortness of the collision time compared to the time between two successive collisions. Using the expression $u = e\langle\tau\rangle/m^*$, where $\langle\tau\rangle$ is the relaxation time averaged in the corresponding way, criterion (9) can be recast in the form

$$k_BT > e\hbar/m^*u. \tag{10}$$

Condition (9) is satisfied for a broad class of high-conductivity semiconductors. Assuming the effective mass to be approximately equal to the free-electron mass, the carrier mobility at $T = 300$ K should be, according to (10), more than 40 $cm^2/V\,s$. In the case of $YBa_2Cu_3O_y$, however, evaluation of the mobility by using the expression $u = R_H\sigma$ yields very small values $u = 1$–10 $cm^2/V\,s$. As a result, the carrier mean free path l can turn out to be less than the interatomic distance, which invalidates the assumption of free electron motion within the length l.

As a way out of this situation, one can take into account that the narrow-band case is characterized by large effective carrier masses. The low mobilities may

not only result from small mean free paths, which is in conflict with the uncertainty relation, but may also be caused by large effective masses. In this case, the relaxation time can remain long enough, $\tau > 10^{-14}$–10^{-15} s, to leave criterion (9) satisfied.

If the band is narrow enough, it may turn out that the uncertainty in the energy of a scattered electron becomes larger than the width of the band responsible for conduction, $W < \hbar/\tau$, thus making the band pattern meaningless. Estimation of the width of the narrow band in HTSC compounds yields $W \geq 100$ meV [8, 33–36, 39]. In this case, if criterion (9) is satisfied, the condition $W \gg \hbar/\tau$ will be certain to be met.

Another possible problem consists in that, in the case of very narrow conduction bands with a width $W < k_B\Theta_D$ (Θ_D is the Debye temperature), carrier interaction with lattice vibrations cannot be treated using the methods of perturbation theory. In these conditions, electron–phonon interaction cannot be considered a small perturbation and electrons can transfer to polaron states. For $YBa_2Cu_3O_y$, we have $\Theta_D \approx 400$ K [40] and the condition $W > k_B\Theta_D$ is certain to be met. Moreover, $YBa_2Cu_3O_y$-based superconductors are structures with strong site disorder, which permits the assumption that scattering from lattice defects is a dominant scattering process.

A magnetic field imposes certain limitations on the applicability of the transport equation. The Boltzmann equation is essentially classical, which is indicated by the coordinate and momentum being simultaneously set in the distribution function. The condition for applicability of classical mechanics is known to reduce to the following requirement on the particle wavelength: $\lambda < L$, where L is a characteristic length determining the extent of action of forces, i.e., the region of space within which the potential energy changes noticeably. In a magnetic field, such a characteristic length is the electron orbital radius $r = V/\omega$. Because $\lambda \approx \hbar/m^*V$ and $m^*V^2 \approx k_BT$, we come to the condition $\hbar\omega < k_BT$, where the carrier rotation rate in a plane perpendicular to the magnetic field vector H is $\omega = eH/m^*$. In the narrow-band case under consideration, where the carrier mass is large, the condition $\hbar\omega < k_BT$ will be met within a broad range of H and, even at high H electronic orbits, will not be quantized.

Thus, the band theory and the Boltzmann equation can be used, although with certain reservations, in analyzing experimental data on transport coefficients in HTSC materials, including the NE coefficient.

7. CONCLUSIONS

Thus, we have carried out a comprehensive analysis of the Nernst–Ettingshausen effect in conductors with a narrow conduction band and considered some aspects of this analysis as applied to describing the temperature dependences of the NE coefficient in the normal phase of high-temperature superconductors of the $YBa_2Cu_3O_y$ family. The main results obtained and the conclusions drawn are as follows.

(1) We have qualitatively analyzed the reasons for the onset of the NE effect, as well as the features in the $Q(T)$ dependence originating from the narrowness of the conduction band. It was shown that the NE coefficient tends in this case to zero in both the low- and high-temperature limits. The applicability of the approach employed to HTSC materials is validated.

(2) An analysis of the NE coefficient made in terms of the narrow-band model has revealed a number of features in its behavior compared to the classical wide-band case. It was shown that the temperature dependence and the sign of the NE coefficient are determined not by the energy dependence of the relaxation time but rather by the extent to which the dispersion relation $\varepsilon(k)$ deviates from the quadratic law. In a symmetric narrow band, the NE coefficient assumes, irrespective of the energy dependence of the relaxation time and of the degree of band filling by electrons, only positive values and it does not vanish even if τ is independent of ε.

(3) The $Q(T)$ dependence in the narrow-band model has been calculated. An analysis of the effect of various features in the band spectrum showed that only taking into account the asymmetry in the dispersion relation $\varepsilon(k)$ permits one to obtain calculated temperature dependences $Q(T)$ which fit qualitatively the relations observed experimentally in the $YBa_2Cu_3O_y$ HTSC system. Other features of the band spectrum and of the properties of the carrier system [an asymmetry in the density-of-states function or the character of the $\tau(\varepsilon)$ dependence] were found to be less significant and can be neglected in a first approximation.

(4) It was shown that the narrow-band model can be used to advantage in a combined analysis of the temperature dependences of the four transport coefficients in the normal phase of HTSC materials. Including experimental data on the NE coefficient into the analysis permits one to estimate, in addition to the main band-spectrum parameters, the degree of asymmetry of the dispersion relation and to determine the average carrier mobility in a narrow band.

ACKNOWLEDGMENTS

This study was supported by the Ministry of Education of Russia, grant no. E00-3.4-546.

REFERENCES

1. Y. Iye, in *Physical Properties of High Temperature Superconductors*, Ed. by D. M. Ginsberg (World Sci., Singapore, 1992), Vol. III.
2. N. P. Ong, in *Physical Properties of High Temperature Superconductors*, Ed. by D. M. Ginsberg (World Sci., Singapore, 1990), Vol. II.
3. A. B. Kaiser and C. Ucher, in *Studies of High Temperature Superconductors*, Ed. by A. V. Narlikar (Nova Sci. Publ., New York, 1991), Vol. 7.

4. S. Lambrecht and M. Ausloos, Phys. Rev. B **53** (21), 14047 (1996).
5. J. A. Clayhold, Phys. Rev. B **54** (9), 6103 (1996).
6. P. Fournier, X. Jiang, W. Jiang, *et al.*, Phys. Rev. B **56** (21), 14149 (1997).
7. S. A. Kaz'min, V. I. Kaĭdanov, and G. Leĭsing, Fiz. Tverd. Tela (Leningrad) **30** (10), 2955 (1988) [Sov. Phys. Solid State **30**, 1703 (1988)].
8. V. E. Gasumyants, V. I. Kaidanov, and E. V. Vladimirskaya, Physica C (Amsterdam) **248** (2–3), 255 (1995).
9. S. Bar-Ad, B. Fisher, J. Ashkenazi, and J. Genossar, Physica C (Amsterdam) **156** (5), 741 (1988).
10. V. V. Moshchalkov, Solid State Commun. **73** (11), 777 (1990).
11. B. Fisher, J. Genossar, L. Patlagan, and G. M. Reisner, Phys. Rev. B **48** (21), 16056 (1993).
12. K. R. Krylov, A. I. Ponomarev, I. M. Tsidilkovski, *et al.*, Phys. Lett. A **131** (3), 203 (1988).
13. A. S. Alexandrov, A. M. Bratkovsky, and N. F. Mott, Phys. Rev. Lett. **72** (11), 1734 (1994).
14. M. A. van Veenendaal, G. A. Sawatzky, and W. A. Groen, Phys. Rev. B **49** (2), 1407 (1994).
15. C. Quitmann, D. Andrich, C. Jarchow, *et al.*, Phys. Rev. B **46** (18), 11813 (1992).
16. M. Sato, R. Horida, and K. Nagasaka, Phys. Rev. Lett. **70** (8), 1175 (1993).
17. M. Boekholt and G. Guntherodt, Physica C (Amsterdam) **181** (1–3), 179 (1991).
18. D. N. Aristov and A. G. Yashenkin, Physica C (Amsterdam) **248** (1–2), 22 (1995).
19. G. V. M. Williams, J. T. Tallon, R. Michalak, and R. Dupree, Phys. Rev. B **57** (14), 8696 (1998).
20. H. Verweij and L. F. Feiner, Phys. Rev. B **41** (7), 4302 (1990).
21. C. C. Tsuei, C. C. Chi, D. M. Newns, *et al.*, Phys. Rev. Lett. **69** (14), 2134 (1992).
22. H. Jichu, T. Matsuura, and Y. Kuroda, J. Phys. Soc. Jpn. **59** (8), 2820 (1990).
23. M. Tachiki and H. Matsumoto, J. Magn. Magn. Mater. **90–91**, 597 (1990).
24. G. Dopf, J. Wagner, P. Dieterich, *et al.*, Phys. Rev. Lett. **68** (13), 2082 (1992).
25. S. Ishihara, H. Matsumoto, S. Odashima, *et al.*, Phys. Rev. B **49** (2), 1350 (1994).
26. T. Hotta, J. Phys. Soc. Jpn. **64** (8), 2923 (1995).
27. N. Bulut, D. J. Scalapino, and S. R. White, Phys. Rev. B **50** (10), 7215 (1994).
28. A. Georges, G. Kotliar, W. Krauth, and M. Rozenberg, Rev. Mod. Phys. **68** (1), 13 (1996).
29. M. I. Klinger, V. G. Novikova, and V. N. Agarkova, Zh. Tekh. Fiz. **26** (10), 2185 (1956).
30. V. E. Gasumyants, E. V. Vladimirskaya, and I. B. Patrina, Physica C (Amsterdam) **235–240** (2), 1467 (1994).
31. N. V. Ageev, V. É. Gasumyants, and V. I. Kaĭdanov, Fiz. Tverd. Tela (St. Petersburg) **37** (7), 2152 (1995) [Phys. Solid State **37**, 1171 (1995)].
32. V. E. Gasumyants, N. V. Ageev, E. V. Vladimirskaya, *et al.*, Phys. Rev. B **53** (2), 905 (1996).
33. V. É. Gasumyants, E. V. Vladimirskaya, M. V. Elizarova, and N. V. Ageev, Fiz. Tverd. Tela (St. Petersburg) **40** (12), 2145 (1998) [Phys. Solid State **40**, 1943 (1998)].
34. V. É. Gasumyants, E. V. Vladimirskaya, M. V. Elizarova, and I. B. Patrina, Fiz. Tverd. Tela (St. Petersburg) **41** (3), 389 (1999) [Phys. Solid State **41**, 350 (1999)].
35. M. V. Elizarova and V. É. Gasumyants, Fiz. Tverd. Tela (St. Petersburg) **41** (8), 1363 (1999) [Phys. Solid State **41**, 1248 (1999)].
36. V. E. Gasumyants, M. V. Elizarova, and R. Suryanarayanan, Phys. Rev. B **61** (18), 12404 (2000).
37. V. E. Gasumyants, N. V. Ageev, I. E. Goldberg, and V. I. Kaydanov, Physica C (Amsterdam) **282–289** (3), 1279 (1997).
38. V. Gasumyants, N. Ageev, E. Vladimirskaya, and V. Kaydanov, Superlattices Microstruct. **24** (6), 443 (1998).
39. M. V. Elizarova and V. E. Gasumyants, Phys. Rev. B **62** (9), 5989 (2000).
40. J. P. Emerson, D. A. Wright, R. A. Fisher, and N. E. Phillips, Czech. J. Phys., Suppl. S3 **46**, 1209 (1996).

Translated by G. Skrebtsov

Physics of the Solid State, Vol. 43, No. 10, 2001, pp. 1845–1849. Translated from Fizika Tverdogo Tela, Vol. 43, No. 10, 2001, pp. 1772–1775.

METALS AND SUPERCONDUCTORS

Superconductivity of $(Sn_{1-z}Pb_z)_{1-x}In_xTe$ Alloys

R. V. Parfen'ev*, D. V. Shamshur*, and S. A. Nemov**

**Ioffe Physicotechnical Institute, Russian Academy of Sciences, ul. Politekhnicheskaya 26, St. Petersburg, 194021 Russia*
e-mail: D.Shamshur@shuvpop.ioffe.rssi.ru
***St. Petersburg State Technical University, ul. Politekhnicheskaya 29, St. Petersburg, 195251 Russia*
e-mail: Nemov@twonet.stu.neva.ru
Received April 3, 2001

Abstract—The temperature dependences of the electrical resistivity of $(Sn_{1-z}Pb_z)_{1-x}In_xTe$ alloys with different concentrations of lead (z = 0–0.60) and indium (x = 0.03–0.20) were studied at temperatures T = 0.4–4.2 K in magnetic fields from zero to H = 15 kOe. A resistivity drop of no less than three–four orders of magnitude was observed in this range of alloy compositions. Application of a magnetic field above a critical level resulted in a recovery of the sample resistivity to the original value. The observed resistivity drop is identified with a superconducting transition. The critical parameters of the superconducting transition (T_c and H_{c2}) were determined at the drop to one half the normal resistivity level. Experimental dependences of the critical superconducting-transition temperature T_c and of the second critical magnetic field H_{c2} on the contents of lead (z) and indium (x) were measured. The data obtained confirm a strong localization of the In impurity states and are evidence of the extrinsic nature of superconductivity in the class of materials under study. It was established that as the Pb content in $(Sn_{1-z}Pb_z)_{1-x}In_xTe$ increases, T_c and H_{c2} decrease as the Fermi level E_F (fixed in the In impurity resonance band) leaves the Δ extremum and the superconductivity breaks down when E_F leaves the $L\Sigma$ saddle point in the valence-band energy spectrum. © *2001 MAIK "Nauka/Interperiodica".*

1. INTRODUCTION

Resonance states of Group III impurities (In and Tl) have been revealed experimentally and studied in narrow-bandgap materials based on the chalcogenides of lead (PbTe, PbSe, PbS) and tin (SnTe) [1, 2]. Some compositions of these materials (with the Fermi level lying within the resonance state band, i.e., with the latter filled partially by electrons) exhibit a superconducting transition with critical temperatures T_c and critical magnetic fields H_{c2} which exceed, by an order of magnitude (see, e.g., [1–5]), the critical parameters of superconducting semiconductor compounds free of impurities that create resonance states within the allowed electron spectrum in crystals. Note that the volume character of superconductivity in $Sn_{1-x}In_xTe$ was established independently in studies of low-temperature heat capacity [6].

This paper reports on a systematic investigation into the effect of the content of lead z and indium impurity x in $(Sn_{1-z}Pb_z)_{1-x}In_xTe$ alloys on the critical parameters of the superconducting transition.

2. SAMPLES AND EXPERIMENTAL TECHNIQUES

Samples with the chemical formula $(Sn_{1-z}Pb_z)_{1-x}In_xTe$ (z = 0–0.60 and x = 0.03–0.20) were prepared using ceramic technology [1, 2]. The preparation procedure consisted of alloying the starting components of semiconductor-grade purity in vacuum, with subsequent room-temperature quenching. The ingots were crushed to a grain size of $d \sim 0.1$ mm, and the material was hot-pressed (P = 2000 kg/cm^2). Next, the samples were annealed in vacuum at 600°C for 200 h. X-ray microprobe analysis did not reveal any traces of a second phase in the samples studied.

The low-temperature measurements were carried out directly in liquid He^3. The temperature of 0.4 K was reached by evacuating saturated He^3 vapor with an adsorption charcoal pump cooled by liquid He^4. The temperature dependences of the electrical resistivity ρ of the samples were studied at 0.4–4.2 K in magnetic fields H up to 15 kOe. The jump in the $\rho(T)$ dependences observed within a narrow temperature interval $\Delta T \sim 0.1$ K and the recovery of the sample resistance in a magnetic field at temperatures below T_c indicated a superconducting transition. The transition to the superconducting state was also observed to occur in studies of the temperature dependence of the magnetic susceptibility of some samples. The critical parameters T_c and $H_{c2}(T)$ were determined from the condition $\rho = 0.5\rho_N$ (ρ_N is the normal-state resistance at $T \le 4.2$ K). The $H_{c2}(T)$ dependences were used to find the derivatives $|\partial H_{c2}/\partial T|_{T \to T_c}$ for each sample, after which one could estimate the critical magnetic field $H_{c2}(0)$ at T = 0 K using the extrapolation expression

$$H_{c2}(T) = H_{c2}(0)[1 - (T/T_c)^2] \quad (1)$$

1063-7834/01/4310-1845$21.00 © 2001 MAIK "Nauka/Interperiodica"

and the relation $H_{c2}(0) = 0.69T_c(dH_{c2}/dT)|_{T_c}$.

The hole concentration was determined at room temperature from Hall effect data by means of the relation

$$p = (eR)^{-1}, \quad (2)$$

where R is the Hall coefficient and e is the absolute value of the electronic charge. The experimental data obtained in this work are presented graphically in Figs. 1–6.

3. EXPERIMENTAL DATA AND DISCUSSION

We consider our experimental data. Figures 1–3 present the dependences of the critical temperature T_c [7], $|\partial H_{c2}/\partial T|_{T \to T_c}$, and $H_{c2}(0)$, respectively, on the lead content z in solid solution. These relations bear a clearly pronounced nonmonotonic character but follow a similar pattern. They have maxima whose magnitude and position depend substantially on the alloy composition (z, x). The following trends are observed: the parameters of the superconducting transition grow with increasing the In content and the maxima of the abovementioned dependences shift toward higher lead contents in the alloys. As the indium content x increases, the superconductivity breakdown is also observed to occur at higher lead contents z.

These data, combined with the values of ρ_N (Fig. 4), were used to estimate the density of states at the Fermi

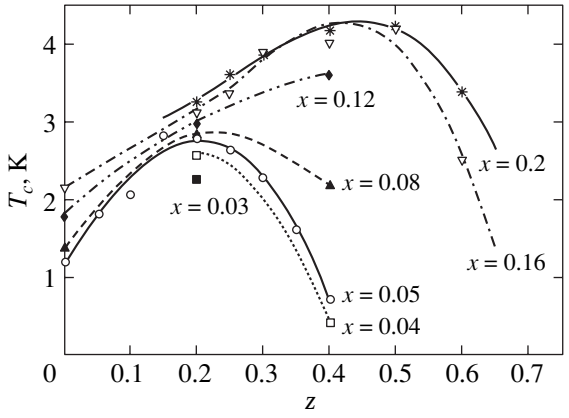

Fig. 1. Dependences of the critical temperature of the superconducting transition T_c on lead content z in $(Sn_{1-z}Pb_z)_{1-x}In_xTe$ solid solutions. Here and in the other figures, the indium content x is identified at the corresponding curve for each lot.

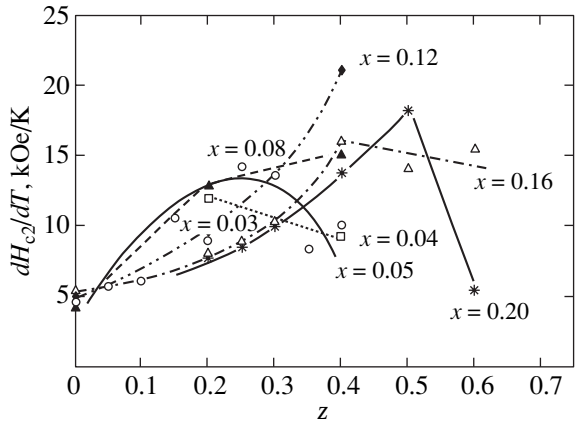

Fig. 2. Dependences of the derivative of the second critical magnetic field with respect to temperature, $|\partial H_{c2}/\partial T|_{T \to T_c}$, on lead content z in $(Sn_{1-z}Pb_z)_{1-x}In_xTe$ solid solutions.

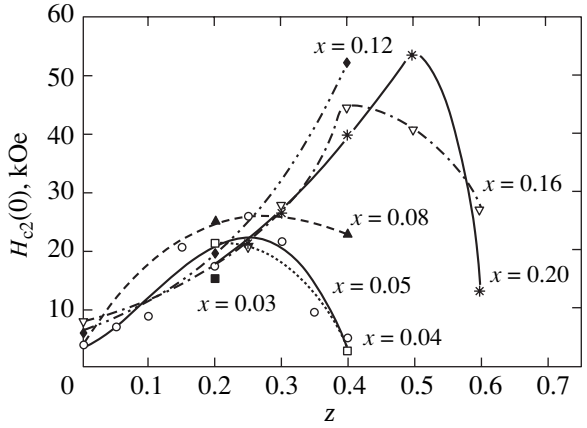

Fig. 3. Dependences of the second critical magnetic field extrapolated to zero temperature, $H_{c2}(0)$, on lead content z in $(Sn_{1-z}Pb_z)_{1-x}In_xTe$ solid solutions.

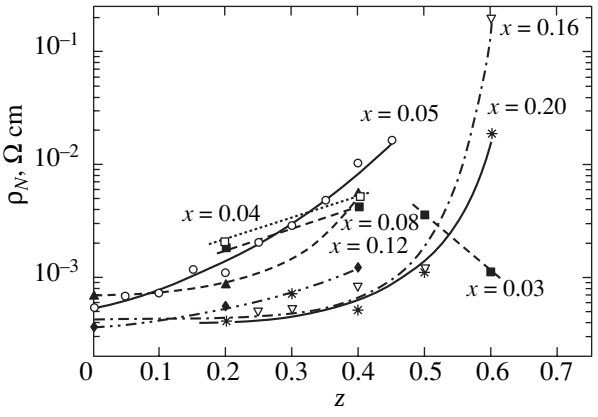

Fig. 4. Dependences of the electrical resistivity in the normal state (T = 4.2 K) ρ_N on lead content z in $(Sn_{1-z}Pb_z)_{1-x}In_xTe$ solid solutions.

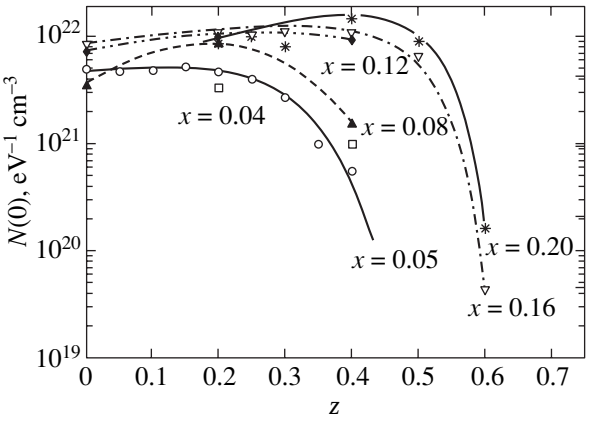

Fig. 5. Dependences of the density of states at the Fermi level $N(0)$ on lead content z in $(Sn_{1-z}Pb_z)_{1-x}In_xTe$ solid solutions.

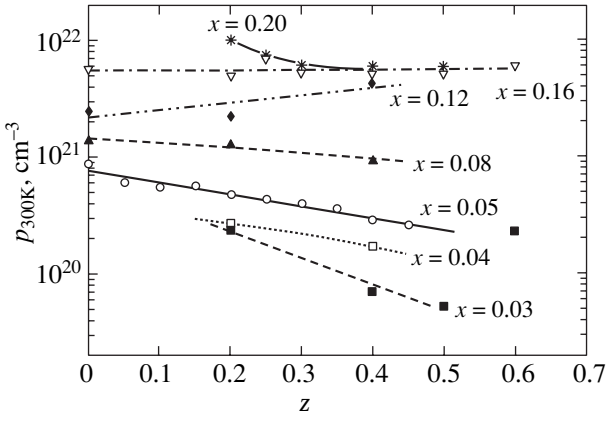

Fig. 6. Dependence of the Hall concentration of holes p on lead content z in $(Sn_{1-z}Pb_z)_{1-x}In_xTe$ solid solutions.

level in the normal state, $N(0)$, from the expressions

$$N(0) = 2.84 \times 10^{14} |\partial H_{c2}/\partial T|_{T \to T_c} \rho_N^{-1}, \quad (3)$$

$$N(0) = 4.83 \times 10^{14} H_{c2}(0)/(T_c \rho_N). \quad (4)$$

The estimation yielded similar results, which are plotted in Fig. 5. As seen from Figs. 1 and 5, there is a correlation between the dependences of the critical temperature and density of states on the composition (z and x) of the alloys studied.

We consider the effect of the In impurity on the properties of the samples. As follows from the data on the Hall concentration of holes presented in Fig. 6, an increase in the indium content x in the $(Sn_{1-z}Pb_z)_{1-x}In_xTe$ alloys results in an increase in the hole concentration p and, accordingly, in the Fermi level E_F being displaced deeper into the valence band. We note that in $(Sn_{1-z}Pb_z)_{1-x}In_xTe$ alloys with fixed lead and indium contents, the hole concentration and the Fermi level remain unchanged when an excess of tellurium (which behaves as an acceptor in IV–VI compounds) is added to the sample charge. We studied this effect in more detail on a $(Sn_{0.8}Pb_{0.2})_{0.95}In_{0.05}Te_{1+y}$ alloy [8]. The stabilization of E_F and the superconducting transition at liquid–helium temperatures, observed by us in the $(Sn_{1-z}Pb_z)_{1-x}In_xTe$ alloys, are typical of IV–VI compounds doped with Group III impurities, which produce resonance states deep in the valence band [1–5]. Based on this, we shall attempt interpretation of our data in terms of the concept of In resonance states, taking into account the band structure rearrangement in $(Sn_{1-z}Pb_z)_{1-x}In_xTe$ alloys induced by increasing lead content.

We consider the data on the critical temperature in more detail. For a fixed indium content in the alloy (for instance, $x = 0.05$), an increase in the lead content in the solid solution entails a growth of T_c, which for $z > 0.2$ is replaced by its decrease, so that for $z > 0.4$ the critical temperature becomes less than 0.4 K (Fig. 1) and the Hall concentration of holes falls off monotonically (Fig. 6). Because the Fermi level in our alloys, as already mentioned, is fixed in the band of In impurity states, the decrease in p should be assigned to a displacement of the In resonance states toward the valence-band top.

Earlier studies [1, 2] showed the resonance state band to contain two states per Group III impurity atom and one valence electron not involved in the chalcogen bonds. In the IV–VI compounds, metals (Pb, Sn) have a valence of 2^+ and the In substituting for metal atoms on the cation sublattice has only three valence electrons, with two of them being involved in chemical bonds with the chalcogen atoms. Therefore, the In resonance band is exactly half-filled by its electrons and the Fermi level lies at its center.

When the impurity band is within the valence band (below its top), electrons transfer from higher-lying band states to the impurity states and increase their filling by electrons, so that the hole concentration in the valence band is equal to the number of electrons transferred to the impurity states. In this case, the degree of the In band filling by electrons can be roughly estimated from the expression (similar to [3])

$$k = 0.5 + p/2N_{In}. \quad (5)$$

In equation (5), we have used for p the Hall concentration of holes and N_{In} is the concentration of the indium impurity in the alloy.

As the In band shifts toward the valence-band top, the concentration of electrons transferred to the impurity states (and the concentration of the holes in the valence band) decreases. In accordance with Eq. (5), the filling of the impurity band k approaches 0.5 and the

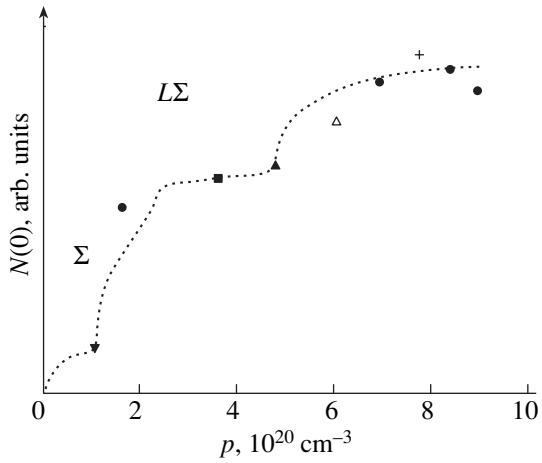

Fig. 7. Qualitative pattern of the hole band spectrum of $Sn_{1-z}Pb_zTe$ alloys (after [10, 11]).

Fermi level E_F shifts toward the impurity band center; this is what accounts for the observed growth in the critical parameters of the superconducting transition in the alloys under study with increasing lead content (Figs. 1–3). Note that the pattern of the experimental relations does not change with an increase in the amount of indium, N_{In}, from 4 to 20 at. %, which suggests that the In impurity states retain their resonance character in the alloys studied and, thus, confirms their strong localization. According to [9], the localization radius of the In impurity states in the $Pb_{0.78}Sn_{0.22}Te$ solid solution is approximately 6 Å.

Our estimates of the density of states at the Fermi level (Fig. 6) are in agreement with the model under consideration. As already mentioned, E_F shifts toward the valence-band top with increasing z, which is accompanied by a decrease in the density of band states. This should result in a weaker coupling between the band and impurity states [2, 3] and, accordingly, in a narrowing of the indium energy band and a growth in the density of impurity states. These processes apparently compensate one another to a considerable extent, as a result of which the total density of states is observed to vary only weakly (for $z < 0.3$–0.4, depending on the In content in the alloys, see Fig. 5).

As the lead content is increased still more in all samples with different indium concentrations, the critical parameters T_c, $H_{c2}(0)$, and $|\partial H_{c2}/\partial T|_{T \to T_c}$ and the density of states are observed to decrease rapidly, which we assign to the Fermi level leaving the additional valence-band extrema.

We consider alloy samples with a comparatively low indium content ($x \le 0.05$). In the lot of $(Sn_{1-z}Pb_z)_{0.95}In_{0.05}Te$ samples studied in most detail, the dependences of the critical parameters and of the density of states on the lead content z in the alloys exhibit a distinct correlation with the Fermi level position (the hole concentration p, see Fig. 6) in the valence-band spectrum of the alloys not doped with indium (Fig. 7). A comparison of the data in Figs. 6 and 7 shows that T_c, $H_{c2}(0)$, and $N(0)$ begin to drop as E_F leaves the Δ extremum corresponding to the hole concentration $p \approx 5 \times 10^{20}$ cm^{-3}. The superconductivity is observed to break down as the Fermi level leaves the $L\Sigma$ saddle point, which corresponds to $p \approx (2$–$3) \times 10^{20}$ cm^{-3}.

At higher indium concentrations in the $(Sn_{1-z}Pb_z)_{1-x}In_xTe$ solid solutions, $x \ge 0.08$, no such quantitative agreement between the data on the superconducting transition (Figs. 1–3) and that on the Hall concentration of holes (Fig. 6) with the concentrations corresponding to the critical band-structure points of the alloys (Fig. 7) is observed. This may be associated with the In impurity affecting the band spectrum of the alloys.

4. CONCLUSION

The results of this work can be summed up as follows. The critical temperature of the superconducting transition T_c and the second critical magnetic field H_{c2} in the $(Sn_{1-z}Pb_z)_{1-x}In_xTe$ alloys have been experimentally established to depend on the contents of lead (z) and indium (x). The data obtained support the presence of a correlation between the position of the In impurity states in the band spectrum of the alloys and the parameters of the superconducting state, thus indicating the extrinsic character of the superconductivity in the class of materials under study. It has been found that the superconductivity in $(Sn_{1-z}Pb_z)_{1-x}In_xTe$ samples breaks down when the Fermi level, fixed at the band of In resonance states, leaves the Δ extremum and the $L\Sigma$ saddle point of the hole energy spectrum.

ACKNOWLEDGMENTS

This study was partially supported by the Russian Foundation for Basic Research, project no. 99-02-18156.

REFERENCES

1. V. I. Kaĭdanov and Yu. I. Ravich, Usp. Fiz. Nauk **145** (1), 51 (1985) [Sov. Phys. Usp. **28**, 31 (1985)].
2. S. A. Nemov and Yu. I. Ravich, Usp. Fiz. Nauk **168** (8), 817 (1998) [Phys. Usp. **41**, 735 (1998)].
3. V. I. Kaĭdanov, S. A. Nemov, R. V. Parfen'ev, and D. V. Shamshur, Pis'ma Zh. Éksp. Teor. Fiz. **35** (12), 517 (1982) [JETP Lett. **35**, 639 (1982)].
4. G. S. Bushmarina, I. A. Drabkin, V. V. Kompaniets, *et al.*, Fiz. Tverd. Tela (Leningrad) **28** (4), 1094 (1986) [Sov. Phys. Solid State **28**, 612 (1986)].
5. P. P. Konstantinov, R. V. Parfeniev, M. O. Safonchik, *et al.*, Physica C (Amsterdam) **333**, 31 (2000).
6. H. Miyauchi, T. Nakaima, and E. Kanda, J. Phys. Soc. Jpn. **34**, 282 (1973).

7. R. V. Parfeniev, D. V. Shamshur, and S. A. Nemov, in *Proceedings of the 24th International Conference on the Physics of Semiconductors, ICPS 24, Jerusalem, 1998*, Ed. by D. Gershoni (World Sci., Singapore, 1998), on CD-ROM.
8. S. A. Nemov, R. V. Parfen'ev, and D. V. Shamshur, Fiz. Tverd. Tela (St. Petersburg) **41** (12), 2132 (1999) [Phys. Solid State **41**, 1956 (1999)].
9. Yu. I. Ravich, S. A. Nemov, and V. I. Proshin, Fiz. Tekh. Poluprovodn. (St. Petersburg) **29** (8), 1448 (1995) [Semiconductors **29**, 754 (1995)].
10. G. S. Bushmarina, I. A. Drabkin, M. A. Kvantov, and O. E. Kvyatkovskiĭ, Fiz. Tverd. Tela (Leningrad) **32** (10), 28 (1990) [Sov. Phys. Solid State **32**, 1666 (1990)].
11. A. V. Berezin, S. A. Nemov, R. V. Parfen'ev, and D. V. Shamshur, Fiz. Tverd. Tela (St. Petersburg) **35** (1), 53 (1993) [Phys. Solid State **35**, 28 (1993)].

Translated by G. Skrebtsov

Physics of the Solid State, Vol. 43, No. 10, 2001, pp. 1850–1852. Translated from Fizika Tverdogo Tela, Vol. 43, No. 10, 2001, pp. 1776–1778.

SEMICONDUCTORS AND DIELECTRICS

Thermopower of a Semiconductor Film with Parabolic Potential in a Strong Magnetic Field

F. M. Gashimzade, A. M. Babaev, and Kh. A. Gasanov

Institute of Physics, Academy of Sciences of Azerbaijan, pr. Dzhavida 33, Baku, 370143 Azerbaijan

Received February 8, 2001

Abstract—Relationships for the transverse magnetothermopower of a semiconductor film with parabolic potential are derived for the cases of nondegenerate statistics and strong degeneracy. It is demonstrated that, in the case of strong degeneracy, quantum levels lying below the Fermi level intersect the Fermi level with an increase in the magnetic field, which leads to jumpwise oscillations of the thermopower magnitude. © *2001 MAIK "Nauka/Interperiodica".*

1. INTRODUCTION

In the past few decades, numerous experimental and theoretical investigations have been focused on the thermopower in low-dimensional systems (films, nanowires, and quantum dots) [1–3]. Bogachek *et al.* [2] theoretically studied the longitudinal magnetothermopower. It was revealed that the longitudinal magnetothermopower exhibits an oscillatory behavior under variations in the magnetic field. According to [2], this behavior of the longitudinal magnetothermopower can be explained by the sequential switching on (switching off) the energy levels with a change in the magnetic field.

It is assumed that a similar behavior should also be observed in the case of transverse magnetothermopower under the conditions of strong degeneracy. This assumption stems from the fact that, under these conditions, the dependence of the nondissipative magnetothermopower simply reproduces the behavior of the density of states at the Fermi level [4].

In the present work, we calculated the magnetothermopower in a semiconductor film with a parabolic potential and a magnetic field applied along the film plane. Since we considered the case of partial band occupation, the nonparabolicity of the light-carrier band was disregarded. In principle, the nonparabolicity can easily be included in the calculation by using the results obtained in [5].

Let us first derive the relationships for the electron spectrum and the density of states and then calculate the transverse magnetothermopower for the cases of nondegenerate statistics and strong degeneracy.

2. ELECTRON SPECTRUM FOR A PARABOLIC QUANTUM WELL IN A LONGITUDINAL MAGNETIC FIELD

For the standard electron dispersion law, the sought spectrum can be represented in the following form [5, 6]:

$$\varepsilon_{N,k_y,k_z,\sigma} = (N+1/2)\hbar\omega + \frac{\hbar^2 k_z^2}{2m} + \frac{\omega_0^2\hbar^2 k_y^2}{\omega^2 2m} + \sigma g\mu_B H. \quad (1)$$

Here, the Landau gauge is chosen for the vector potential $\bar{A}(0, x\cdot H, 0)$, ω_0 characterizes the parabolic potential of the film

$$U = \frac{m\omega_0^2 x^2}{2}, \quad (2)$$

$\omega = \omega_0\sqrt{1+z^2}$ (where $z = \frac{\omega_c}{\omega_0}$ and $\omega_c = \frac{eH}{mc}$ is the cyclotron frequency), μ_B is the Bohr magneton, g is the factor of spectroscopic splitting, $\sigma = \pm 1/2$, and N is the number of the quantum level.

For semiconductors of the InSb type, this formula can be used in the case of partial occupation of the conduction band [7].

The coordinate wave function, which corresponds to the energy eigenvalue (1), has the form

$$\varphi_{N,K_y,K_z}(r) = \varphi_N(x-x_0)\exp(ik_y y + ik_z z), \quad (3)$$

where

$$\varphi_N(x-x_0) = \frac{1}{\pi^{1/4}a^{1/2}\sqrt{2^N N!}} \times \exp\left(-\frac{(x-x_0)^2}{2a^2}\right)H_N\left(\frac{x-x_0}{a}\right), \quad (4)$$

$$a = \sqrt{\frac{\hbar}{m\omega}}, \quad (5)$$

1063-7834/01/4310-1850$21.00

$$x_0 = -\frac{\omega_c}{\omega}\frac{\hbar k_y}{m\omega} = -\frac{\omega_c}{\omega}a^2 k_y. \quad (6)$$

The density of states is defined by the expression

$$\rho(\varepsilon) = \sum_{N, k_y, k_z, \sigma} \delta(\varepsilon_{N, k_y, k_z, \sigma} - \varepsilon). \quad (7)$$

Then, by changing over from the summation over k_z and k_y to integration and adopting expression (6), we obtain

$$\rho(\varepsilon) = \frac{L_y L_Z}{(2\pi)^2}\frac{\sqrt{2m}}{\hbar}2\frac{m\omega}{\hbar}\frac{\omega}{\omega_c}\sum_{N,\sigma}\int_0^{x_0^m}\frac{dx_0}{\sqrt{\varepsilon - \varepsilon_{N\sigma} - bx_0^2}}. \quad (8)$$

Here,

$$\varepsilon_{N\sigma} = (N + 1/2)\hbar\omega + \sigma g\mu_B H, \quad (9)$$

$$b = \frac{m\omega_0^2}{\omega_c}\omega^2. \quad (10)$$

For a typical quantum well in $Ga_xAl_{1-x}As$ (see Fig. 1 in [8]), the upper limit of integration x_0^m is determined by the degree of well occupation. Specifically, if $\varepsilon - \varepsilon_{N\sigma} < b\left(\frac{L_x}{2}\right)^2$, the result of integration does not depend on the quantum well width and is equal to $\frac{\pi}{\sqrt{b}}$. Otherwise, if $\varepsilon - \varepsilon_{N\sigma} > b\left(\frac{L_x}{2}\right)^2$, the result of integration depends on the well width, i.e., $W \equiv L_x$. Note that, according to Fig. 1 in [8], $\Delta_1 \equiv \frac{m\omega_0^2}{2}\left(\frac{L_x}{2}\right)^2$ in a zero magnetic field. These relationships will be used below to determine ω_0.

Therefore, we have

$$\rho(\varepsilon) = \frac{L_y L_z}{2\pi\hbar^2}\frac{m\omega}{\omega_0}, \quad (11)$$

$$\times\left\{\sum_{N,\sigma} H(-\varepsilon + \varepsilon_{N,\sigma} + bL_x^2/4)\right.$$

$$\left.\frac{2}{\pi}\sum_{N,\sigma}\arcsin\left(\sqrt{\frac{bL_x^2/4}{\varepsilon - \varepsilon_{N,\sigma}}}\left(\varepsilon - \varepsilon_{N,\sigma} - b\frac{L_x^2}{4}\right)\right)\right\},$$

where $H(x)$ is the Heaviside function.

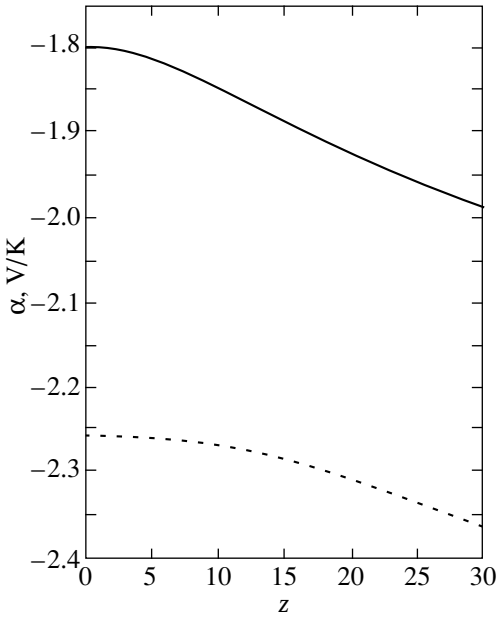

Fig. 1. Dependences of the magnetothermopower $\alpha(H)$ (V/K) on the magnetic field $z = \omega_c(H)/\omega_0$ for InSb (solid line) and GaAs (dashed line).

3. THE CASE OF CLASSICAL STATISTICS

In his monograph, Askerov [4] showed that the transverse magnetothermopower can be calculated using the Obraztsov formula [9]

$$\alpha(H) = -\frac{S}{en}. \quad (12)$$

Here, S is the entropy of the electron gas

$$S = -\left(\frac{\partial\Omega}{\partial T}\right)_{\xi, H}, \quad (13)$$

$$\Omega = -k_0 T\sum_{N, k_y, k_Z, \sigma}\ln\left(1 + \exp\left(\frac{\xi - \varepsilon_{N, k_y, k_Z, \sigma}}{k_0 T}\right)\right), \quad (14)$$

where Ω is the Gibbs thermodynamic potential and ξ is the chemical potential.

For the nondegenerate statistics,

$$\Omega = -n\kappa_0 T, \quad (15)$$

where n is the electron concentration (in our case, n is the two-dimensional electron concentration).

From formulas (12), (13), and (15), we obtain the following relationship for the transverse magnetothermopower in a semiconductor film:

$$\alpha(H) = -\frac{k_0}{e}$$

$$\times\left(2 - \eta + \nu\coth\nu - \nu_s\coth\nu_s - \frac{t\exp(-t^2)}{\sqrt{\pi}\,\mathrm{erf}(t)}\right). \quad (16)$$

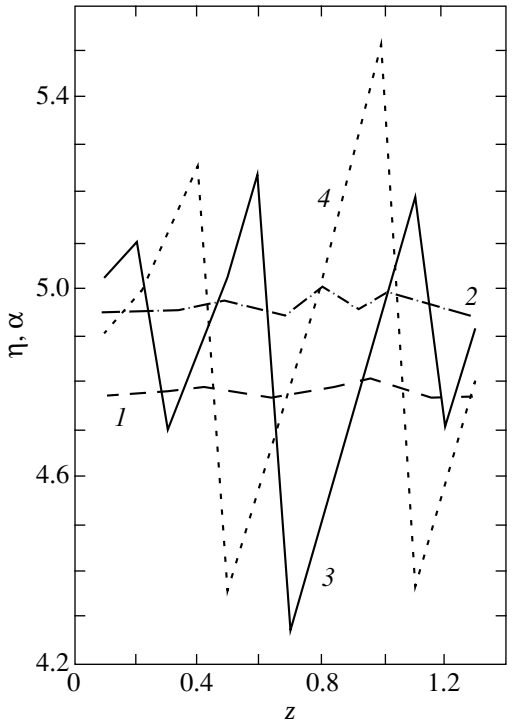

Fig. 2. Dependences of (*1*, *2*) the normalized Fermi level $\eta = \xi/k_0T$ and (*3*, *4*) the magnetothermopower $\alpha(H)$ (arb. units) on the magnetic field $z = \omega(H)_c/\omega_0$ for (*1*, *3*) InSb and (*2*, *4*) GaAs.

Here,

$$t = \sqrt{\frac{bL_x^2}{4k_0T}}, \qquad (17)$$

erf(*t*) is the probability integral [10],

$$\nu = \frac{\hbar\omega}{2k_0T}, \quad \nu_s = \frac{g\mu_B H}{2k_0T}, \quad \eta = \frac{\xi}{k_0T}, \qquad (18)$$

and k_0 is Boltzmann's constant.

In our calculations, we used the available data [8] on the well width (L_x = 4000 Å), the parabolic well height (Δ_1 = 150 meV), and the electron mass ($m = 0.067m_0$) to obtain the estimate $\omega_0 = 4.437 \times 10^{12}$ s^{-1}.

For InSb semiconductors, we assumed that $m = 0.016m_0$ and $\hbar\omega_0$ = 7.5 meV in accordance with [7]. In addition, we set $n = 2 \times 10^{10}$ and 5×10^{10} cm^{-2} for InSb and GaAs, respectively. The calculated dependences $\alpha(H)$ for GaAs (g = –0.44) and InSb (g = –51.2) at T = 300 K are shown in Fig. 1.

4. THE CASE OF STRONG DEGENERACY

In this case, the transverse magnetothermopower is proportional to the density of states [4]:

$$\alpha(H) = -\frac{\pi^2\kappa_0}{3e}\frac{\kappa_0 T}{n}\rho(\xi_F), \qquad (19)$$

where the Fermi level ξ_F is determined from the expression for the electron concentration and depends, even if only slightly, on the magnetic field,

$$n = \sum_{N,\sigma}(\xi_F - \varepsilon_{N,\sigma})\rho(\xi_F).$$

This formula makes allowance for the fact that the Fermi levels at actual concentrations are located considerably below $b(L_x/2)^2$.

As the magnetic field increases, the quantum levels lying below the Fermi level intersect the Fermi level, which leads to a jumpwise decrease in the thermopower magnitude. However, the density of states and the magnetothermopower between the jumps increase proportionally with $\omega(H)$. Hence, the dependence $\alpha(H)$ exhibits an oscillatory behavior.

Figure 2 displays the oscillatory dependences for GaAs ($n = 10^{12}$ cm^{-2}) and InSb ($n = 5 \times 10^{11}$ cm^{-2}) at T = 4.2 K.

The concentrations are higher than in the nondegenerate case as our aim was to observe several oscillations of the magnetothermopower.

For InSb, the jumps are nonuniform due to a considerable confluence of the quantum level splitting.

As was noted above, the magnetothermopower of a quantum wire also exhibits a similar oscillatory behavior. However, unlike the nondissipative transverse magnetothermopower studied in the present work, Beenakker and Staring [1] considered the longitudinal magnetothermopower.

REFERENCES

1. C. W. Z. Beenakker and A. A. M. Staring, Phys. Rev. B **46** (15), 9667 (1992).
2. E. N. Bogachek, A. G. Scherbakov, and Uzi Landman, Phys. Rev. B **54** (16), 11094 (1996).
3. I. Heremans and O. P. Gansen, J. Phys. C **12**, 3483 (1979).
4. B. M. Askerov, *Electron Transport Phenomena in Semiconductors* (Nauka, Moscow, 1985).
5. J. Hammersberg and H. Weman, Phys. Rev. B **54** (7), 4835 (1996).
6. V. M. Galitskiĭ, B. M. Karnakov, and V. I. Kogan, *Problems on Quantum Mechanics* (Nauka, Moscow, 1981).
7. T. Darnhofer and U. Rossller, Phys. Rev. B **47** (23), 16020 (1993).
8. M. P. Stopa and S. D. Sarma, Phys. Rev. B **40** (14), 10048 (1989).
9. Yu. Obraztsov, Fiz. Tverd. Tela (Leningrad) **6**, 414 (1964) [Sov. Phys. Solid State **6**, 331 (1964)]; Fiz. Tverd. Tela (Leningrad) **7**, 573 (1965) [Sov. Phys. Solid State **7**, 455 (1965)].
10. *Handbook of Mathematical Functions*, Ed. by M. Abramowitz and I. A. Stegun (Dover, New York, 1971; Nauka, Moscow, 1979).

Translated by N. Korovin

Physics of the Solid State, Vol. 43, No. 10, 2001, pp. 1853–1859. Translated from Fizika Tverdogo Tela, Vol. 43, No. 10, 2001, pp. 1779–1784.

SEMICONDUCTORS AND DIELECTRICS

The Role of Extended Defects in the Formation of the Spectrum of Electronic States in High-Purity *p*-CdTe Polycrystals with Stoichiometric Composition

V. S. Bagaev*, V. V. Zaĭtsev, Yu. V. Klevkov, S. A. Medvedev, E. E. Onishchenko, M. L. Skorikov, and V. A. Tsvetkov

Lebedev Physical Institute, Russian Academy of Sciences, Leninskiĭ pr. 53, Moscow, 117924 Russia

**e-mail: bagaev@lebedev.ru*

Received March 5, 2001

Abstract—The spectra of the low-temperature photoluminescence in the cases of band-to-band and subgap laser excitation and the luminescence-excitation spectra of high-purity [111]-textured *p*-CdTe polycrystals with stoichiometric composition were measured. The spectrum of electronic states in the 1.3–1.6 eV energy range and the changes in this spectrum as a result of annealing of the samples in cadmium vapor were studied. It is shown that the electron levels located in the CdTe band gap that are responsible for the *Z* and *Y* luminescence bands ($\hbar\omega$ = 1.36 and 1.47 eV) are formed as a result of interaction of extended defects with background impurities. © *2001 MAIK "Nauka/Interperiodica"*.

1. INTRODUCTION

Despite the long-standing comprehensive studies of wide-gap II–VI semiconductors, the field of their practical applications is still very limited. The reasons for this are well known and stimulate further investigation of these materials. The phenomenon of self-compensation, characteristic to the entire family of wide-gap II–VI compounds, is related to the origin of deep electron states in the band gap and brings about an increase in the resistivity. Determination of the origin of deep electronic states remains a major fundamental problem at present; successful practical application of the II–VI compounds depends on solution of this problem. According to widely accepted concepts, the deep electronic states are formed as a result of complex processes of interaction between impurities and structural defects during crystal growth. In nonstoichiometric bulk crystals grown at high temperatures using the liquid- and vapor-phase methods, the concentration of native defects is ~10^{15}–10^{16} cm^{-3} [1] and the concentration of background impurities is no lower than ~10^{16} cm^{-3}.

The self-compensation models developed previously were based on consideration of the interaction between intrinsic and extrinsic defects [2, 3]. As the technologies for producing crystals and epitaxial films of the II–VI compounds became more sophisticated, notions on compensation were reconsidered on the basis of quasi-chemical models and of lattice-relaxation effects as a result of doping [4, 5]. The search for new approaches to explaining the compensation mechanism is stimulated by a number of recent experimental data that are difficult to interpret in terms of the existing models. This can be exemplified by the development of technology for growing nominally undoped CdTe crystals with nearly stoichiometric composition using high-purity components; the resistivity of these crystals was shown to be as high as 10^9–10^{10} Ω cm [6, 7].

Few publications [8–12] concern themselves with the effect of extended defects (dislocations, twins, subgrains, and grain boundaries) on the optical and, especially, transport properties of undoped II–VI compound crystals. Much more data have been accumulated from studying the optical properties of the II–VI epilayers [13–17].

It is well known [18] that extended defects are involved in the scattering of free charge carriers, are the sites where impurities (and intrinsic defects) accumulate, and give rise to local stresses and internal electric fields that affect the potential relief. Both in bulk crystals and in films, the density of extended defects varies in a wide range and may be quite high. The density and type of a defect depend on the conditions of crystal and film grow.

The vast majority of the studied objects (crystals and films) contain a large number of extended defects in addition to point impurities and nonstoichiometric defects [19–22].

The results of annealing the crystals in the saturated vapor of the components are indicative of an intricate interaction between all types of defects. Redistribution of segregated impurities and intrinsic defects in the vicinity of extended defects may profoundly affect the electrical and optical properties of the crystals.

Recently, clarification of the relation between the presence of extended defects in undoped II–VI crystals and the emergence of the characteristic *Y* and *Z* bands

in the optical spectra of these crystals was attempted. An increase in the intensity of the *Y* band in undoped CdTe crystals was observed in the regions with increased dislocation density [23]. A relation between the dislocations and *Y* band was also established in the deformed *n*-ZnSe samples [24]. Similar studies have been performed for ZnTe crystals [25]. An increase in the importance of the role played by nonradiative recombination and the quenching of emission in the excitonic region of the spectrum have been observed. Scanning microprobe photoluminescence (PL) was used at 100 K to show that the intensities of the lines at 1.47 and 1.36 eV (the *Z* line) excited by the radiation of an He–Ne laser increased sharply at the sites where dislocations emerged to the surface of CdTe samples [26]. In heteroepitaxial CdTe films, the intensity of the *Y* line in the PL spectrum is uniquely related to specially introduced layers, with their crystal orientation differing from the main film orientation [27]. Although the mechanism of forming localized deep states is not yet clear, the involvement of extended defects in the formation of some of these states has been verified.

In this study, we analyzed the spectra of low-temperature PL in polycrystalline *p*-CdTe samples with extremely low concentrations of native point defects and background impurities in order to assess the contribution of extended defects to the formation of localized electronic states.

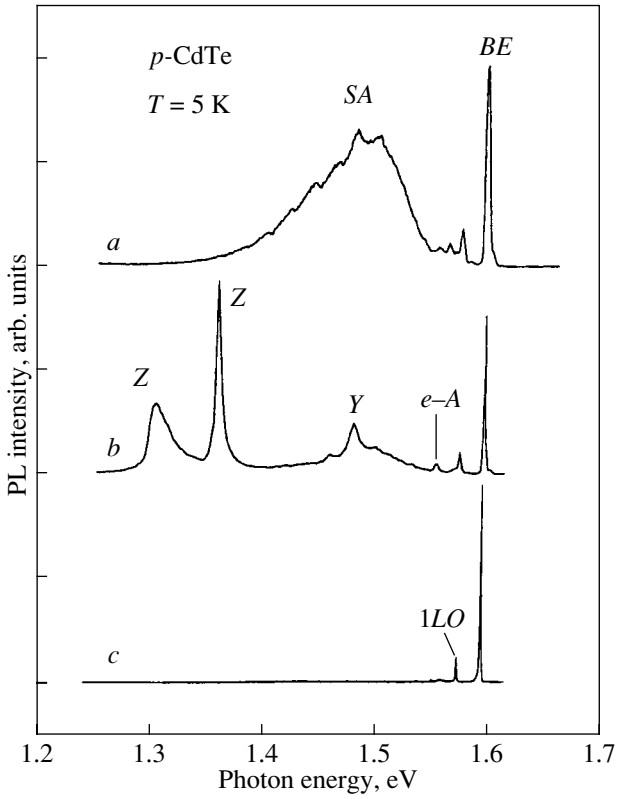

Fig. 1. Photoluminescence (PL) spectra demonstrating the results of purifying the CdTe polycrystals of residual impurities.

2. EXPERIMENTAL

Polycrystalline *p*-CdTe ingots were obtained at the stage of finishing purification of the compound through vacuum sublimation at a crystallization temperature of ~620°C; the ingots were synthesized from high-purity components [28], had stoichiometric composition (the composition corresponding to the P_{min} point), and were textured in the [111] direction. The average diameter of a single-crystal grain in the texture was 2 mm. The dislocation density in the grain was no higher than 10^2 cm^{-2}. Twinning lamellas were present in some of the grains. The total concentration of background impurities in purified CdTe did not exceed 10^{14} cm^{-3}.

We measured the low-temperature PL either on freshly prepared cleaved surfaces or in samples subjected preliminarily to lapping, polishing, and chemical etching in a solution of bromine in methanol. Some of the samples were annealed in saturated cadmium vapor for 72 h at $T \cong 600$°C in order to study the behavior of background impurities at the grain boundaries.

In order to study the spectrum of localized deep states, the density of which was low in the CdTe samples under investigation, we used optical methods: PL measurements under band-to-band and resonance excitation in the excitonic region of the spectrum and the method of excitation PL. In addition, we measured the electrical conductivity of the samples at $T = 300$ K. The PL spectra were measured in the temperature range of 2–100 K using the conventional method [29]. The PL was excited by Ar laser radiation with lines at 515 and 488 nm or by a He–Ne laser.

We used a tunable titanium–sapphire laser for resonance excitation of PL and for measuring the excitation PL spectra; the emission was detected using a cooled photomultiplier with a GaAs cathode.

3. RESULTS AND DISCUSSION

In Fig. 1, we show three spectra of the *p*-CdTe low-temperature PL, which characterize the quality of the material after various stages of purification. The upper spectrum (curve *a*) corresponds to the material after low-temperature synthesis and the first-stage of purification. Spectrum *b* was obtained after several stages of purification. Spectrum *c* corresponds to the ingot after the final purification stage.

The samples have a composition close to stoichiometric even after the first stage of purification; this composition is retained after all the subsequent purification stages. It is notable that only the concentration of background impurities decreases from stage to stage.

The PL was measured at $T = 5$ K on freshly cleaved surfaces. The intense emission related to bound excitons (*BE*) is observed in all the spectra. As the content of background impurities is lowered (spectrum *b*), the so-called self-activated (*SA*) band disappears and the intensities of emission bands related to band–impurity (*e–A*) transitions and to donor–acceptor pairs and also

of the *Y* (~1.47 eV) and *Z* (~1.36 and 1.3 eV) bands decrease. These bands are almost indistinguishable in the final (*c*) spectrum. All three samples were of the *p*-type conductivity; their resistivity increased from ~10^3 to 10^6 Ω cm as the purification became more profound. The behavior of the *Z* and *Y* bands, the formation of which involves extended defects, is noteworthy.

Measurements of PL under local excitation of a sample with sharply focused radiation ($d \sim 5$ μm) of a He–Ne laser at $T = 100$ K showed that the *Z* and *Y* bands were dependably detected only when the excitation spot was in the vicinity of the grain boundary.

Electronic levels with ionization energies of 246 meV (the *Z* band) and 136 meV (the *Y* band) in these samples manifest themselves in the photoconductivity spectra and in the temperature dependence of resistivity [30].

It is well known that inversion of the conductivity type occurs in undoped and fairly pure *p*-CdTe crystals as a result of annealing in Cd vapor [31]. We repeatedly observed this effect after heat treatment of CdTe samples subjected to the initial stages of purification. Annealing of samples with a low concentration of residual impurities does not result in a change in the conductivity type; at the same time, the resistivity of the samples increases by two–three times.

3.1. Shallow Acceptor and Donor States in p-CdTe Polycrystals with Stoichiometric Composition

The low-temperature PL spectra provide a rough idea of the purity and structural quality of the crystals under investigation and also of the type of shallow-level substitutional impurities present in the samples. The chemical nature of the impurities can be inferred from the spectral positions of the lines A^0X related to excitons bound to acceptor impurities (the lines of excitons D^0X bound to the shallow-level donors cannot be resolved for various types of these donors), the lines corresponding to the *e–A* and *D–h* transitions, and from the emission related to the donor–acceptor pairs and to the two-hole transitions (THTs) and two-electron transitions (TETs). In the samples under consideration with donor and acceptor concentrations lower than 10^{14} cm^{-3}, analysis of the impurity composition is extremely difficult.

The impurity-related transitions and the emission of donor–acceptor pairs make themselves barely evident in the PL spectra. The two-hole and two-electron transitions are typically clearly pronounced in the PL spectra for impurity concentrations of $\geq 10^{15}$ cm^{-3}. However, the observation of such transitions becomes almost impossible for a volume charge-carrier concentration lower than 10^{14} cm^{-3}. The probability of observation of THT and TET processes may increase if the impurities are preferentially concentrated in the vicinity of extended defects, which is aided by annealing of the sample in Cd vapor. The transitions involving bound excitons are most sensitive to low impurity concentrations owing to the high oscillator strengths of these transitions. However, the spectral positions of the peaks related to excitons bound to impurities such as Na, Li, and N differ by mere several hundredths of millielectronvolts.

The following special feature of the obtained *p*-CdTe PL spectra, which indirectly substantiates our inference as to the role of extended defects (the small-angle crystallite boundaries), is noteworthy. The spectral width of the bound-exciton lines (D^0X and A^0X) depends on the excitation-spot diameter and varies in the 0.5–1.2 meV range, whereas the position of the line peaks varies within ~0.2 meV. The peak of the A^0X line in the low-temperature PL spectra of high-purity stoichiometric CdTe polycrystals is located within 1.589–1.5893 eV. This suggests that the main shallow-level acceptors in the samples are related to Li and Na impurities, because the nitrogen concentration becomes so low even after the initial stages of purification that it cannot be detected using spectral analysis.

In Fig. 2, we show a typical full-range PL spectrum for polycrystalline stoichiometric CdTe samples annealed in an atmosphere of Cd vapor. The measurements were performed on samples polished perpendic-

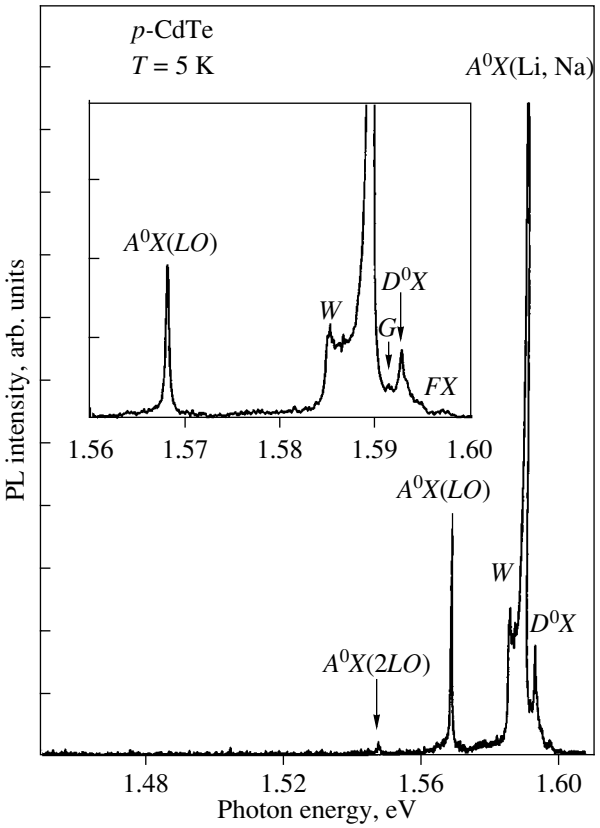

Fig. 2. The full-range photoluminescence (PL) spectrum of the purest samples after annealing in an atmosphere of Cd vapor. Details of the spectrum in the excitonic region are shown in the inset.

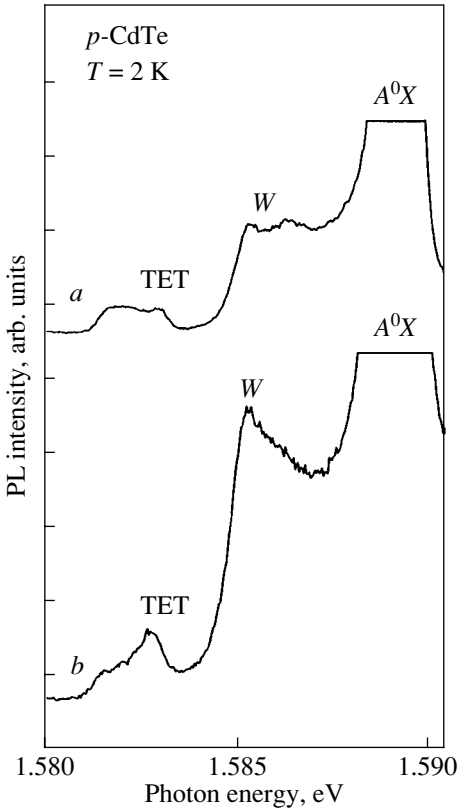

Fig. 3. Shape of the photoluminescence (PL) spectra in the region of a two-electron-transition emission and the *W* band for two different sites at the sample surface in the case of D^0X-line resonance excitation.

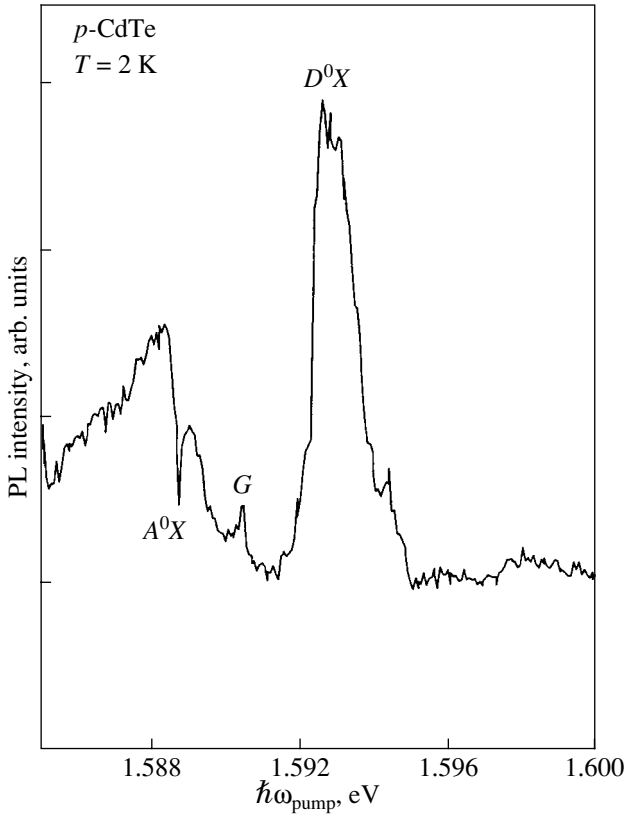

Fig. 4. The excitation spectrum for two-electron-transition luminescence (at 1.582 eV).

ularly to the direction of the texture growth with subsequent etching in a solution of bromine in methanol. A barely distinguishable *G* line (at 1.5902 eV) and a *W* line (at ~1.586 eV) are observed in the excitonic region of the spectrum in addition to the low-intensity free-exciton line (*FX*) and the bound-exciton lines D^0X (at 1.5928 eV) and A^0X (at 1.5891 eV). The intense *G* line is commonly observed in the spectra of high-resistivity Cl-doped CdTe crystals, and its interpretation is controversial [32]. The *W* line is observed in the spectra of *p*-CdTe samples annealed in an atmosphere of Cd vapor. We discuss the *W* line below.

In order to reduce the role played by the surface recombination and to attempt to detect the TET and THT processes, we measured the PL spectra under the conditions of resonance excitation of the excitons bound to impurities; we also measured the excitation PL spectra. We failed to detect the THT-related processes with involvement of Cu, Ag, P, and As under the resonance excitation of PL in the frequency range corresponding to the A^0X line. It is difficult to reliably detect the two-hole transitions with involvement of Li and Na (the line for Li peaks at 1.5463 eV) because the corresponding lines are obscured by the $A^0X_{\mathrm{Li,\,Na}} + 2LO$ line, which has a higher intensity.

Two low-intensity doublet lines (in addition to the A^0X line at 1.5891 eV) are observed in the PL spectrum (Fig. 3, curve *a*) under resonance excitation of the D^0X line (1.5928 eV). The short-wavelength doublet features two peaks at 1.5863 and 1.5953 eV. In the majority of publications, the peak of the *W* line is typically reported at 1.586 eV [33, 34]. The doublet band at a longer wavelength lies in the region of the TET-related emission. One of the peaks of the band near 1.582 eV corresponds to TET processes with the involvement of chlorine atoms. The peak at a shorter wavelength is close to the spectral position of the TET processes that involve fluorine [35]. The insufficiently purified deionized water used in the technological process may constitute the source of the above impurities (although their concentrations are low). Spectrum *b* in Fig. 3 was measured after the excitation spot had been slightly shifted. A marked redistribution of the line intensities in both doublets may be indicative of nonuniform impurity distribution in the vicinity of an extended defect.

The dominant contribution of donors to the formation of the emission bands shown in Fig. 3 is also indicated by the excitation spectra of PL in the TET and *W* bands. In Fig. 4, we show the excitation spectrum of PL for two-electron transitions (at 1.582 eV). The high-

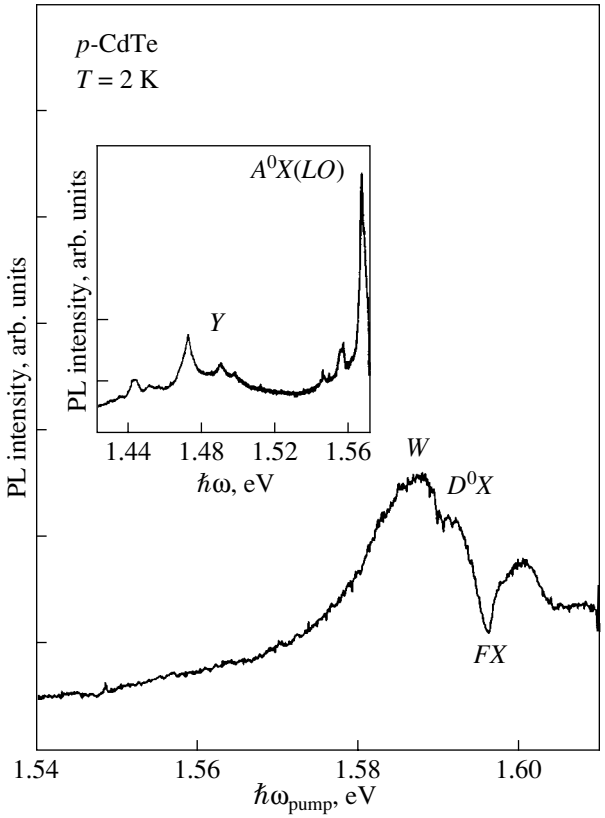

Fig. 5. The excitation spectrum for *Y*-band luminescence (1.47 eV). The luminescence-spectrum region in the vicinity of the *Y* band is shown in the inset.

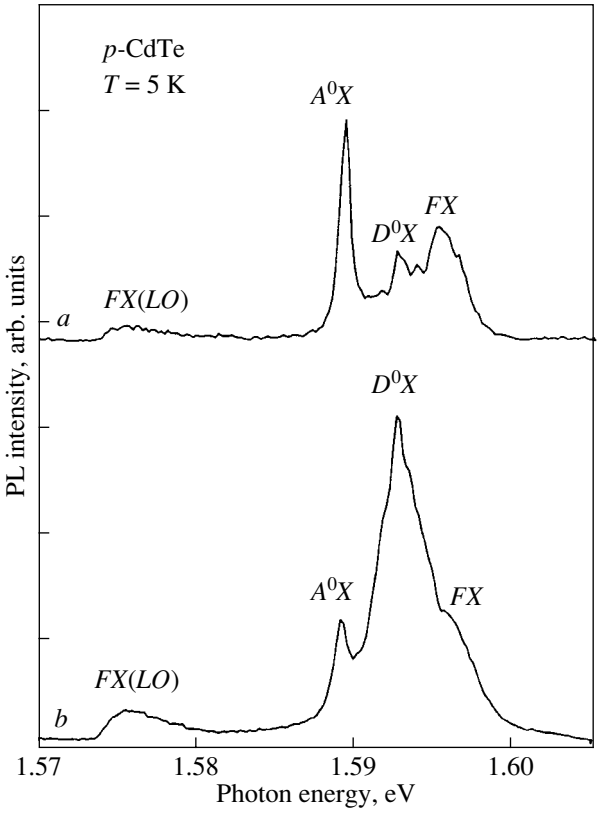

Fig. 6. Redistribution of emission intensities between the luminescence excitonic lines for CdTe single-crystallite excitation levels of (*a*) 0.25 and (*b*) 1 W/cm^2.

est intensity of the TET PL line is observed under the conditions of resonance excitation of excitons bound to donors (1.5928 eV). An almost identical excitation spectrum is observed for one of the *W* lines (at 1.5863 eV). In addition to an increase in intensity under excitation of the D^0X line, common special features in the excitation spectra consist in sharp dips of the excitation at the emission frequency of an exciton bound to an acceptor (at 1.5891 eV for Li acceptor) and in the absence of a response to the excitation of free excitons. The sharp dip at the A^0X frequency can be explained by the high oscillator strengths for radiative transitions related to excitons bound to acceptors, whereas the absence of a response to excitation of free excitons may indicate that the radiative-channels represented by the *FX* line, on the one hand, and the D^0X and A^0X lines, on the other hand, are spatially separated.

3.2. Relation between the D^0X, W, and Y Emission Bands

If the excitation is such that the incident-photon energy is less than the band gap and is not at resonance with excitonic lines, the radiative channels of excitonic recombination are highly depressed. As a result, a number of low-intensity emission lines are observed in the long-wavelength region of the spectrum; analysis of these lines is beyond the scope of this study. We briefly dwell on one of the above lines (the *Y* line peaked at 1.476 eV), the relation of which to extended defects in undoped *p*-CdTe samples has been reliably established [23]. The *Y* band is also observed in *p*-CdTe samples doped moderately with chlorine, in which case the intensity of this band depends on Cl concentration [32]. In Fig. 5, we show the spectrum of PL excitation for this line. A characteristic feature of this spectrum consists in the fact that the intensity of the *Y* line emission depends on the resonance excitation of the *W* line in addition to the band-to-band and D^0X-line excitation. Thus, the *W*-line emission is also formed with the involvement of extended defects. Furthermore, the deep dip in the spectrum at the *FX*-emission frequency is noteworthy. The PL spectra of the same CdTe samples (Fig. 6) support the inference as to the spatial separation of recombination channels for free excitons and those bound to impurities. If a crystallite is primarily excited, a high intensity of the free-exciton PL is observed, which is characteristic of perfect crystals with a low impurity concentration. In addition, the reported spectra support the inference as to the almost

identical concentrations of the shallow-level donors and acceptors in the samples we studied. This is suggested by the fact that, as the intensity of the band-to-band excitation increases by a mere factor of 4 (cf. spectra *a*, *b* in Fig. 6), the intensities of the lines related (one way or another) to donors in *p*-CdTe increase sharply in addition to the *FX*-line intensity. This may indicate that the charged donors are neutralized by generated free electrons, which brings about a nonlinear increase in the intensity of the D^0X line [36]. The relation of the *W* line to donors is clearly observed in the resonance PL and the excitation PL spectra, whereas the relation between the *G* band and the presence of donors manifests itself in the form of a peak in the TET excitation spectrum (Fig. 4). Moreover, a sharp peak in the emission intensity in the A^0X-line excitation spectrum is observed under the conditions of *G*-line resonance excitation. Both of the above facts may indicate that the recombination centers under consideration are primarily localized in the same regions (specifically, in the vicinity of extended defects) and that the origin of the *G* line is related to excitons.

4. CONCLUSIONS

Thus, on the basis of the results reported above, we may draw the following conclusions:

(1) The concentrations of the electrically and optically active centers are no higher than 10^{13} cm^{-3} in the studied high-purity stoichiometric textured CdTe polycrystals.

(2) For a low dislocation density (<100 cm^{-2}), the main types of extended defects in a single-crystal grain are the boundaries of textured crystallites with an angular misorientation of 1°–4° and, to a lesser extent, the twinning lamellas.

(3) A decrease in the intensity of the *Z* and *Y* lines in the PL spectra measured after successive stages of purification of the CdTe samples indicates that impurities and extended defects interact and give rise to deep electronic states with activation energies of 246 and 136 meV.

(4) The results of annealing CdTe samples in an atmosphere of Cd vapor and the analysis of the photoluminescence spectra suggest that, for a low total concentration of background impurities, the concentrations of the shallow-level donors and acceptors are close to each other, and that the impurities are mainly located in the vicinity of extended defects.

(5) The detected relation between the *Y*-line intensity and the *W*-line resonance excitation is indicative of the involvement of extended defects in the formation of the electronic states responsible for the *W* photoluminescence band.

(6) The observed relation between the intensities of the D^0X, *Y*, and *W* lines may indicate that the electronic states responsible for the *Y*- and *W*-line photoluminescence emission are formed as a result of interaction between residual donors and extended defects in *p*-CdTe.

ACKNOWLEDGMENTS

We thank V.V. Ushakov for measurements of the microprobe scanning photoluminescence and A.V. Kvit and A.F. Plotnikov for their helpful comments when discussing the results.

This study was supported by the Russian Foundation for Basic Research (project nos. 98-02-16980 and 00-02-17335), the Program "Leading Scientific Schools" (grant no. 00-15-96568), and the Interdisciplinary Program "Physics of Solid-State Nanostructures" of the Ministry of Science of the Russian Federation (project no. 97-1045).

REFERENCES

1. B. K. Meger and W. Stadler, J. Cryst. Growth **161**, 119 (1996).
2. F. A. Kroger, *The Chemistry of Imperfect Crystals* (North-Holland, Amsterdam, 1964).
3. Y. Marfaing, Prog. Cryst. Growth Charact. **4**, 317 (1981).
4. R. M. Park, M. B. Troffer, C. M. Rouleau, *et al.*, Appl. Phys. Lett. **57**, 2127 (1990).
5. Y. Marfaing, J. Cryst. Growth **161**, 205 (1996).
6. P. Rudolph, S. Kawasaki, S. Yamasita, *et al.*, J. Cryst. Growth **161**, 28 (1996).
7. P. Rudolph, S. Kawasaki, S. Yamasita, *et al.*, J. Cryst. Growth **149**, 201 (1995).
8. H. Muller, P. Haasen, and W. Schroter, Phys. Status Solidi A **80**, 223 (1983).
9. K. Ohba, T. Taguchi, C. Onodera, *et al.*, Jpn. J. Appl. Phys. **28** (7), L1246 (1989).
10. K. Terashima, M. Kawachi, and M. Takena, J. Cryst. Growth **104**, 467 (1990).
11. T. I. Milenov and M. M. Gospodinov, Nucl. Instrum. Methods Phys. Res. A **322**, 363 (1992).
12. F. Gelsdorf and W. Schroter, Philos. Mag. A **49**, L35 (1984).
13. N. Shibata, A. Ohki, S. Zembutsu, and A. Katsui, Jpn. J. Appl. Phys. **27** (3), L441 (1988).
14. S. Fujii, T. Terada, Y. Fujita, and T. Iuchi, Jpn. J. Appl. Phys. **28** (10), L1712 (1989).
15. J. Saraie, N. Matsumura, M. Tsubokura, *et al.*, Jpn. J. Appl. Phys. **28** (1), L108 (1989).
16. K. Chahzad, J. Petruzzello, D. J. Olego, *et al.*, Appl. Phys. Lett. **57** (3), 2452 (1990).
17. K. Wolf, A. Naumov, T. Reisinger, *et al.*, J. Cryst. Growth **135**, 113 (1994).
18. H. F. Matare, J. Appl. Phys. **56** (10), 2605 (1984).
19. K. Durose, G. J. Russell, and J. Woods, J. Cryst. Growth **72**, 85 (1985).
20. K. Durose, G. J. Russell, and J. Woods, J. Cryst. Growth **86**, 471 (1988).

21. M. Samimi, B. Biglari, M. Hage-Ali, *et al.*, Nucl. Instrum. Methods Phys. Res. A **289**, 243 (1989).
22. G. Brandt, H. Ennen, R. Miritz, and W. Rothemund, J. Cryst. Growth **101**, 226 (1990).
23. S. Seto, A. Tanaka, F. Takeda, and K. Matsuura, J. Cryst. Growth **138**, 346 (1994).
24. Y. G. Shreter, Y. T. Rebane, O. V. Klyaniv, *et al.*, J. Cryst. Growth **159**, 833 (1996).
25. J. A. García, A. Remon, V. Munoz, and R. Triboulet, J. Cryst. Growth **197**, 794 (1999).
26. A. Gukasyan, A. Kvit, Y. Klevkov, and S. Kazaryan, Mater. Sci. Eng. B **B47**, 87 (1997).
27. D. J. Brink and H. W. Kunert, J. Appl. Phys. **78** (11), 6720 (1995).
28. S. A. Medvedev and Yu. V. Klevkov, RF Patent No. 2,143,014 (1999).
29. V. V. Zaĭtsev, V. S. Bagaev, and E. E. Onishchenko, Fiz. Tverd. Tela (St. Petersburg) **41** (4), 717 (1999) [Phys. Solid State **41**, 647 (1999)].
30. Yu. V. Klevkov, S. A. Kolosov, S. A. Medvedev, and A. F. Plotnikov, Fiz. Tekh. Poluprovodn. (St. Petersburg) **35** (2001) (in press) [Semiconductors **35** (2001) (in press)].
31. R. Triboulet, A. Aoudia, and A. Lusson, J. Electron. Mater. **24** (9), 1061 (1995).
32. S. Seto, A. Tanaka, Y. Masa, and M. Kawashima, J. Cryst. Growth **117**, 271 (1992).
33. K. Saminadayar, J. Francou, and J. Pautrat, J. Cryst. Growth **72**, 236 (1985).
34. A. Burchard, R. Magerle, J. Freidinger, *et al.*, J. Cryst. Growth **161**, 128 (1996).
35. J. M. Francou, K. Saminadayar, and J. Pautrat, Phys. Rev. B **41** (7), 12035 (1990).
36. T. Schmidt, K. Lischka, and W. Zulehner, Phys. Rev. B **45** (16), 8989 (1992).

Translated by A. Spitsyn

Physics of the Solid State, Vol. 43, No. 10, 2001, pp. 1860–1866. Translated from Fizika Tverdogo Tela, Vol. 43, No. 10, 2001, pp. 1785–1790.

SEMICONDUCTORS AND DIELECTRICS

Temperature Effect on Spatial Correlations of Impurity Ions in HgSe : Fe Crystals

V. M. Mikheev

Institute of Metal Physics, Ural Division, Russian Academy of Sciences, ul. S. Kovalevskoĭ 18, Yekaterinburg, 620219 Russia
e-mail: mikheev@imp.uran.ru

Received March 11, 2001

Abstract—The spatial correlations in the arrangement of iron ions in HgSe : Fe compounds are described by the pair correlation function calculated within the hard sphere model. The temperature effect is taken into account by substituting the thermodynamic mean for the correlation sphere radius. The thermodynamic averaging is performed using the Einstein approach. The temperature dependences of the mobility of electrons scattered by a spatially correlated distribution of iron ions are calculated, and the results of these calculations are compared with the experimental data. © *2001 MAIK "Nauka/Interperiodica".*

1. INTRODUCTION

In HgSe : Fe crystals, the resonance level of iron atoms is located in the conduction band and the iron atoms themselves are donors, each giving up one electron to the conduction band. At a critical concentration of iron atoms $n_c \simeq 4.5 \times 10^{18}$ cm^{-3}, the Fermi level of conduction electrons coincides with the resonance level. In the case when the iron concentration is less than the critical value, all the iron atoms are ionized. It is assumed that iron atoms are spatially distributed in a random way. Hence, it follows that, at $n_{Fe} < n_c$, iron ions are also arranged in a random manner. When the concentration of iron atoms is higher than the critical concentration, only a portion of iron atoms occurs in the ionization state and the concentration of iron ions n_{Fe}^{+} is equal to n_c. Therefore, even for a random distribution of iron atoms, the spatial distribution of impurity ions can be considered to be correlated. This distribution appears very specific, because it substantially depends on the number of vacant sites (neutral iron atoms). The effect of spatial correlations in the arrangement of impurity ions on the electron mobility in HgSe : Fe crystals has been studied extensively over the last decade [1]. In recent works dealing with HgSe : Fe crystals [1–4], these specific distributions of impurity ions at low temperatures (in the limiting case, $T = 0$) have been calculated within the hard sphere model.

In the low-temperature range $0 \le T \le 50$ K, the HgSe : Fe compounds are characterized by an anomalously rapid decrease in the electron mobility with an increase in temperature [1]. Since, in this temperature range, the degree of degeneracy of an electron gas is rather high ($\varepsilon_F \approx 210$ meV) and the contribution of electron scattering by phonons is small compared to the impurity scattering, this anomaly is usually explained by the weakening of correlations in the arrangement of iron ions due to the increase in temperature. Ablyazov and Éfros [5] analyzed similar anomalies in the temperature dependence of the mobility $\mu(T)$ under the assumption that iron ions form a Wigner lattice. Tsidil'kovskiĭ *et al.* [6] calculated the temperature dependence of the mobility with the use of the Mayer function in describing interionic correlations. In both cases [5, 6], the authors used fitting parameters for a quantitative description of the observed temperature dependence $\mu(T)$.

In the present work, I propose a rigorous procedure for calculating the temperature dependences of the pair correlation functions describing the spatial distribution of iron ions. It should be noted that, unlike the calculations performed in [5, 6], I did not resort to any new model concepts and restricted my consideration to the models already used for calculating the spatial correlations of iron ions at $T = 0$ [3].

2. ENERGY OF CORRELATION IN THE SPATIAL ARRANGEMENT OF IRON IONS

At $T = 0$, iron ions adopt a configuration in which the energy of the Coulomb repulsion is minimum. In the case when the lattice temperature is nonzero, there exist all possible configurations that can be formed by iron ions. For a given configuration of ions, the correlation energy can be defined as the difference between the energy of interionic interaction in this configuration and the energy of the interaction of impurity ions spatially distributed in a random manner. The probability of finding a system of ions in the given configuration depends on the correlation energy corresponding to this configuration. Therefore, first of all, it is necessary to evaluate the correlation energy for the given configuration of impurity ions.

1063-7834/01/4310-1860$21.00

Let us assume that n_{Fe}^{+} is the concentration of iron ions (for simplicity, the crystal volume V is taken equal to unity). In this case, the energy of interionic interaction is given by

$$E_{ii} = \frac{1}{2}\sum_{j}\sum_{i\neq j} V(r_{ij}), \tag{1}$$

where $V(r_{ij})$ is the energy of the interaction between two ions. The interaction between ions will be described by the potential calculated in the framework of the Thomas–Fermi model, that is,

$$V(r) = \frac{e^2}{\kappa r}\exp\left(-\frac{r}{r_{TF}}\right),$$

where $r_{TF}^{-2} = 6\pi n_e e^2/\kappa\varepsilon_F$. For HgSe : Fe crystals, these parameters are as follows: the permittivity $\kappa = 20$, the electron concentration $n_e = n_c \simeq 4.5 \times 10^{18}$ cm^{-3} (at $n_{Fe} > n_c$), $\varepsilon_F \approx 210$ meV, and $r_{TF} = 5.8 \times 10^{-7}$ cm. The mean energy of interionic interaction $\langle E_{ii}\rangle$ is calculated by the formula [7]

$$\langle E_{ii}\rangle = \left\langle \frac{1}{2}\sum_{j}\sum_{i\neq j} V(r_{ij})\right\rangle = \frac{1}{2}\int dr_1 dr_2 n(r_1) n(r_2) V(r_{12}) g(r_1, r_2), \tag{2}$$

where $g(r_1, r_2)$ is the pair correlation function describing the spatial distribution of particles. For a homogeneous and isotropic spatial distribution of iron ions, formula (2) takes the form

$$\langle E_{ii}\rangle = 2\pi n_{Fe}^{+2}\int_0^\infty r^2 dr V(r) g(r). \tag{3}$$

The energy of correlation E_c in the arrangement of iron ions is defined as the difference

$$E_c = \langle E_{ii}\rangle - \langle E_{ii}^h\rangle, \tag{4}$$

where $\langle E_{ii}\rangle$ is the mean energy of the interaction between iron ions whose distribution is described by the correlation function $g(r)$ and $\langle E_{ii}^h\rangle$ is the mean energy of the interaction between iron ions spatially distributed in a random manner ($g^h(r) = 1$). By substituting expression (3) into formula (4), we obtain the relationship for the energy of correlation in the ion arrangement per ion, ε_c; that is,

$$E_c = n_{Fe}^{+}\varepsilon_c = 2\pi n_{Fe}^{+2}\int_0^\infty r^2 dr V(r)[g(r) - 1]. \tag{5}$$

The correlation energy for iron ions in HgSe : Fe crystals was calculated in [8, 9]. Wilamowski [8] determined the correlation energy according to formula (5). The author of [9] was not satisfied with the standard expression (5) for the correlation energy and proposed his own rather strange relationship (see formula (9) in [9]):

$$U(R_i) = \sum_{i\neq j} V(R_{ij})(g(R_{ij}) - 1).$$

Here, $U(R_i)$ is the correlation potential and $V(R_{ij})$ is the potential produced by the jth Fe^{3+} ion at the point R_i.

The correlations in the arrangement of iron ions emerge at a sufficiently high doping when $n_{Fe} > n_c$. In this case, the concentration of iron ions n_{Fe}^{+} is constant and equal to the critical concentration n_c. Note that any configuration formed by a system of ions is described by the correlation function $g(r)$. In the hard sphere model, the correlation function depends on two parameters, namely, the concentration of iron ions and the hard sphere diameter r_c. The latter quantity is treated as the minimum distance between the iron ions. Therefore, at a constant concentration of iron ions, the configuration adopted by the system of iron ions is uniquely determined by the parameter r_c and the correlation energy is the single-valued function $\varepsilon_c(r_c)$ of this parameter. The r_c parameter depends on the concentration ratio between iron ions and iron atoms [1–3]. In my earlier work [3], the equation relating the r_c parameter to the concentration ratio n_{Fe}^{+}/n_{Fe} was derived in terms of statistical physics in the following form:

$$n_{Fe}^{+} = n_{Fe} W(n_{Fe}^{+}, r_c, r_1),$$
$$W(n_{Fe}^{+}, r_c, r_1) = \left(1 - \left(\frac{r_c}{r_1}\right)^3\right)^a. \tag{6}$$

Here, (n_{Fe}^{+}, r_c, r_1) is the probability of finding an iron atom at a distance larger than $r_c$from the nearest-neighbor iron ion, $a = 4\pi r_1^3 n_{Fe}^{+}/3 = 5.92$, and r_1 is the radius of the first correlation sphere for a face-centered cubic lattice.

In the hard sphere model, the pair correlation function can be calculated using standard computational techniques with the required accuracy [7]. In [2], the spatial distribution of iron ions was described by the correlation function calculated by retaining only the zeroth term in the density expansion, which corresponds to the first virial coefficient; that is,

$$g(r_c, r) = \begin{cases} 0, & r < r_c \\ 1, & r \geq r_c. \end{cases} \tag{7}$$

Wilamowski [8] calculated the correlation energy ε_c according to formula (5) with the use of the correlation function (7). Curve *1* in Fig. 1 represents the results of this calculation performed with the parameters

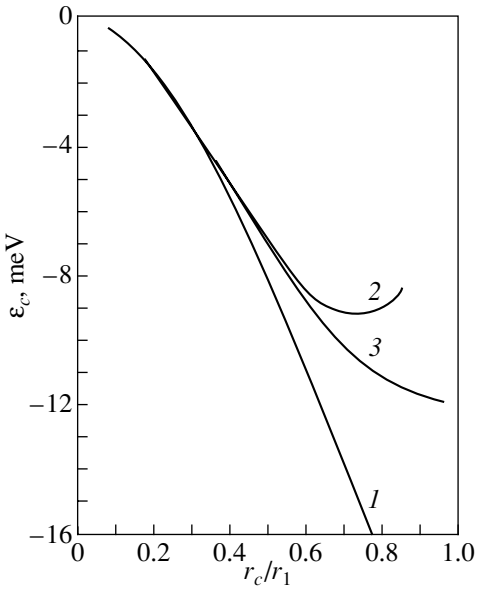

Fig. 1. Dependences of the correlation energy on the correlation radius for (*1*) correlation function (7), (*2*) correlation function (8), and (*3*) the correlation function in the Percus–Yevick approximation.

$\varepsilon_F = 210$ meV, $\kappa = 20$, and $n_{Fe}^+ = n_e = 4.5 \times 10^{18}$ cm^{-3}. In [3], the pair correlation function $g(r_c, r)$ was calculated with inclusion of the first term in the density expansion, which corresponds to the second virial coefficient [7]; that is,

$$g(r_c, r) = \begin{cases} 0, & r < r_c \\ 1 + 8\eta\left[1 - \dfrac{3r}{4r_c} + \dfrac{1}{16}\left(\dfrac{r}{r_c}\right)^3\right], & r_c \le r \le 2r_c \\ 1, & 2r_c < r. \end{cases} \quad (8)$$

Here, $\eta = \pi r_c^3 n_{Fe}^+/6$ is the packing coefficient. The correlation energy ε_c calculated from formula (5) with the correlation function (8) is shown by curve *2* in Fig. 1. Kuleev [9] calculated the correlation energy with the use of the correlation function obtained within the Percus–Yevick approximation [7]. The results of calculations with this correlation function are represented by curve *3* in Fig. 1. It can be seen that the results of all the calculations virtually coincide at a correlation sphere radius in the range $0 < r_c/r_1 < 0.5$. As follows from expression (6), which relates the correlation sphere radius r_c to the iron concentration n_{Fe}, the r_c values lying in this range correspond to iron concentrations in the range $4.5 \times 10^{18} < n_{Fe} < 10^{19}$ cm^{-3}. The experimental investigations of HgSe : Fe crystals [1, 2] revealed that, in the concentration range $4.5 \times 10^{18} < n_{Fe} \le 2 \times 10^{19}$ cm^{-3}, the electron mobility increases with an increase in the iron concentration. According to formula (6), these concentrations of iron atoms correspond to the range $0 \le r_c/r_1 \le 0.6$. In this r_c range, expression (7) for the correlation function appears to be no more than a very rough approximation and leads to overestimated correlation energies. It follows from Fig. 1 that, in the experimentally important range of iron concentrations, the correlation energies calculated with the correlation function (8) virtually coincide with the correlation energies found from the correlation function in the Percus–Yevick approximation. At higher iron concentrations, the results of calculations disagree. However, according to the estimates made in [3], the applicability of the hard sphere model itself in this case becomes problematic. For this reason, I restricted my consideration to the experimentally important range of iron concentrations in which calculations with the use of the pair correlation function (8) ensure sufficiently reliable estimates.

3. CALCULATIONS OF THE MEAN PHYSICAL QUANTITIES

The pair correlation function $g(r_c, r)$ depends on the sole parameter r_c. By varying this parameter, we specify the configuration of iron ions. Recall that, by definition, the r_c quantity is the minimum distance between iron ions (for a random distribution of ions, the r_c parameter is equal to zero). At $T = 0$, there exists only one configuration corresponding to the r_c parameter which is calculated by relationship (6). At a finite temperature, there exist all possible configurations that correspond to all possible correlation radii in the range $0 < r_c^T < r_c$. In this case, the mean correlation radius is a function of temperature: $\langle r_c^T \rangle = r_c(T)$.

At a nonzero temperature, the correlations in a system of iron ions will be described in terms of the pair correlation function $g(r_c(T), r)$ calculated within the hard sphere model, in which the correlation radius r_c is replaced by the mean value $\langle r_c^T \rangle = r_c(T)$. This method is widely used in the study of equilibrium liquids and melts in the framework of the hard sphere model (see [10] and references therein). When calculating the temperature dependences for melts, the hard sphere diameter r_c is usually replaced by the equilibrium value $r_c(T)$, which can be obtained by minimizing the free energy of the system.

Unlike liquids and melts, systems of impurity ions in semiconductors, as a rule, are nonequilibrium. Samples have been prepared at high temperatures ($T \approx 1000$ K). At very high temperatures, impurities are ionized and the ion distribution is nearly random. As the temperature decreases, the impurity ions are fixed; i.e., the spatial distribution of these ions becomes frozen. This frozen distribution is described as a random distri-

bution with the use of the pair correlation function $g^h(r) = 1$. At low temperatures, this frozen random distribution of interacting ions is nonequilibrium. It is necessary to distinguish two cases: (a) all the impurity centers are ionized and (b) one portion of the impurity centers is ionized while the other portion is neutral. In the case of complete ionization, the impurity ions are spatially distributed in a random manner. For partial ionization of the impurity centers, the impurity ions undergo a spatial redistribution owing to the presence of vacant sites (neutral impurities) and their stable distribution turns out to be correlated. An equilibrium distribution is attained when the fraction of ions is sufficiently small and the number of vacant sites is large.

In HgSe : Fe compounds at an iron concentration $n_{Fe} > n_c$, the concentration of iron ions is fixed ($n_{Fe}^+ = n_c \simeq 4.5 \times 10^{18}$ cm^{-3}) and the vacant sites (neutral impurities) give rise to a correlation in the spatial distribution of iron ions. The point of the matter can be easily understood from Fig. 1. An increase in the iron concentration brings about an increase in the number of vacant sites, and the iron ions undergo a redistribution. According to relationship (6), this is accompanied by an increase in the parameter r_c/r_1 and, correspondingly, an increase in the magnitude of the correlation energy ε_c. All the calculated curves (*1–3*) in Fig. 1 demonstrate that the correlation energy decreases in the experimentally important range of variations in the r_c/r_1 parameter. Although these curves over the entire range $0 < r_c/r_1 < 1$ are only illustrative in character, they suggest that there are at least two alternatives. In the first case, the correlation energy at a certain iron concentration $n_{Fe} = n_m$ exhibits an extremum that corresponds to the minimum free energy. In turn, this iron concentration corresponds to an equilibrium correlated distribution of impurity centers (curve *2*). In the second case, the correlation energy decreases monotonically as the r_c/r_1 parameter increases to $r_c/r_1 = 1$, at which the equilibrium state of the system of iron ions corresponds to a Wigner crystal (curve *3*). In the framework of the simple model used in calculations, it is impossible to decide between these alternatives. However, all the computational variants represented in Fig. 1 suggest that, in the experimentally important range of variations in the r_c/r_1 parameter, the correlation energy is a monotonically decreasing function of this parameter (and, hence, the iron concentration) and the system of iron ions is nonequilibrium.

Therefore, in our case of a nonequilibrium distribution of iron ions, unlike equilibrium liquids and melts, the procedure of minimizing the free energy cannot be used to determine the steady-state value of $r_c(T)$. In the present work, the steady-state value of the correlation sphere radius $r_c(T)$ is identified with the thermodynamic mean.

When averaging the correlation radius, we will follow the Einstein approach [11], which is based on the generalized Boltzmann principle in the description of nonequilibrium systems. The known Boltzmann formula is used as the initial expression

$$S = k_B \ln \Gamma,$$

where S is the entropy of an isolated macrosystem in the thermodynamic equilibrium and Γ is the statistical weight of this macrosystem. According to the Einstein concept, the probability of occurring a complete system (thermostat + studied subsystem) in a nonequilibrium macroscopic state is represented by the formula

$$W \propto \exp\left(\frac{1}{k_B} S_h\right),$$

where S_h is the entropy of the complete system. In the *Course of Theoretical Physics* by Landau and Lifshitz [12], the Einstein approach is used in the description of fluctuations. In the subsequent presentation of the theory, we will follow the monograph [12]. (The Einstein and Gibbs approaches and the current state of the art in the study of this problem have been discussed thoroughly in the recent review by Rudoĭ and Sukhanov [13].)

Let us now assume that the system composed of n_{Fe}^+ iron ions is in equilibrium with a thermostat at temperature T. The probability of finding this system in the configuration corresponding to the correlation radius r_c^T is defined by the relationship

$$W(r_c) \propto \exp\left(-\frac{\Delta E - T\Delta S + P\Delta V}{T}\right),$$

where ΔE, ΔS, and ΔV are the changes in the energy, entropy, and volume of the iron ion system, respectively, under variations in the correlation radius from zero to a specified value r_c^T and P and T are the pressure and the temperature of the medium, respectively [12]. The volume occupied by iron ions coincides with the volume occupied by iron atoms and remains unchanged upon ion ordering. Hence, it follows that $\Delta V = 0$.

All quantities that are independent of the r_c^T parameter and appear in the exponent cancel out upon normalization of the expression for the probability W. As a result, we obtain

$$W(r_c^T) \propto \exp\left(-\frac{E_c - TS(r_c^T)}{T}\right), \quad (9)$$

where E_c is the correlation energy for the system of iron ions and $S(r_c^T)$ is the entropy component depending on the r_c^T parameter.

For a homogeneous and isotropic distribution of iron ions, the correlation energy $E_c = n_{Fe}^+ \varepsilon_c$ is deter-

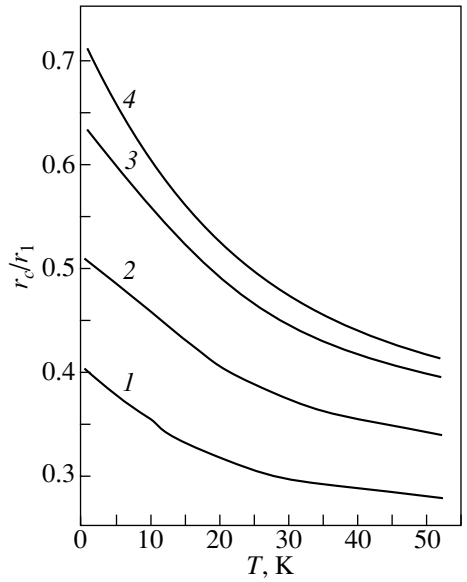

Fig. 2. Temperature dependences of the correlation radius for HgSe : Fe samples at different concentrations of iron atoms n_{Fe}, 10^{18} cm^{-3}: (*1*) 7, (*2*) 11, (*3*) 29, and (*4*) 85.

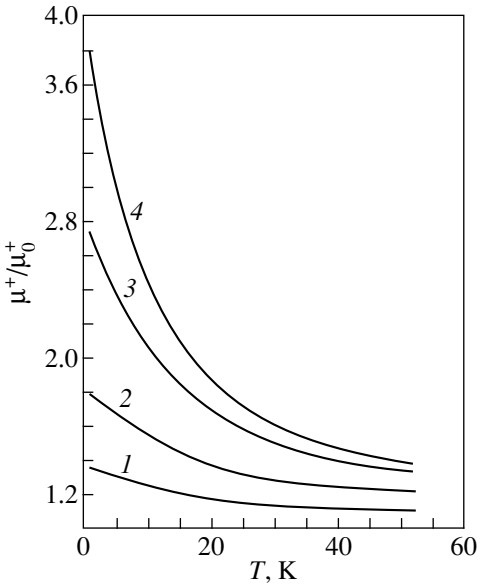

Fig. 3. Temperature dependences of the electron mobility μ^+ upon scattering by iron ions in HgSe : Fe samples at different concentrations of iron atoms. Designations of the curves are the same as in Fig. 2.

mined according to formula (5). The entropy component $S(r_c^T)$ for the system of iron ions has the form

$$S(r_c^T) = n_{Fe}^+ \ln W(n_{Fe}^+, r_c^T, r_1), \qquad (10)$$

where the probability $W(n_{Fe}^+, r_c^T, r_1)$ is calculated from formula (6). Substitution of the expressions for the correlation energy and the entropy into relationship (9) leads to the factorization of the formula for the probability $W(r_c^T)$, that is

$$W(r_c^T) = \prod_1^{n_{Fe}^+} W_0(r_c^T).$$

Here, $W_0(r_c^T)$ is the probability that a particular iron ion at a temperature T is located at a distance larger than r_c^T from the nearest-neighbor ion. This probability is defined by the formula

$$W_0(r_c^T) = W(n_{Fe}^+, r_c^T, r_1)\exp\left(-\frac{\varepsilon_c}{T}\right). \qquad (11)$$

Formula (11) makes it possible to perform thermodynamic averaging of the r_c^T parameter as follows:

$$\langle r_c^T \rangle = r_c(T) = \frac{\int_0^{r_c} x W_0(x)dx}{\int_0^{r_c} W_0(x)dx}. \qquad (12)$$

From relationships (5), (6), (8), (11), and (12), we calculated the temperature dependences of the correlation radius $r_c(T)$ for HgSe : Fe samples at iron concentrations ranging from $n_{Fe} = 7 \times 10^{18}$ cm^{-3} (Fig. 2, curve *1*) to $n_{Fe} = 8.5 \times 10^{19}$ cm^{-3} (Fig. 2, curve *4*). It can be seen from Fig. 2 that, as the temperature increases in the range $0 < T < 50$ K, the mean correlation radius $r_c(T)$ decreases by 30–40%. Therefore, we can assert that, in the system of iron ions, the spatial correlations in the iron ion distribution described by the pair correlation function $g(r_c(T), r)$ weaken with an increase in the temperature.

4. EFFECT OF TEMPERATURE ON THE ELECTRON MOBILITY

The electron mobility at a nonzero temperature was calculated by the same methods and with the same correlation function as were used earlier in the calculation of the electron mobility at $T = 0$ [3]. The sole difference from the calculations carried out in [3] resided in the fact that the r_c parameter in the correlation function was replaced by the thermodynamic mean $r_c(T)$, which was calculated from formulas (5), (6), (8), (11), and (12). Now, we recall the scheme used for calculating the electron mobility μ [1–3]. The differential cross section of electron scattering $\sigma(\mathbf{q})$ (where $\mathbf{q}$ is the scattering vector) can be expressed through the cross section $\delta_0(\mathbf{q})$ for scattering by one of the centers, that is,

$$\sigma(\mathbf{q}) = \sigma_0(\mathbf{q})S(\mathbf{q}). \qquad (13)$$

In turn, the structure factor $S(\mathbf{q})$ and the Fourier transform of the pair correlation function, which describes the spatial distribution of scatterers, are related by the equation

$$S(\mathbf{q}) = 1 + n_{\mathrm{Fe}}^{+}\int [g(r_c(T), r) - 1]\exp(iqr)dr. \quad (14)$$

In the framework of the Thomas–Fermi model, the mobility μ_0^+ of electrons scattered by a random distribution of impurity ions is described by the Brooks–Herring formula [14]. According to expression (13), the ratio between the mobility μ^+ of electrons scattered by a spatially correlated distribution of ions and the mobility μ_0^+ of electrons scattered by random ion distribution ions can be written in the form [3]

$$\frac{\mu^+}{\mu_0^+} = \int_0^{2k_{\mathrm{F}}} \frac{q^3 dq}{[q^2 + r_{\mathrm{TF}}^{-2}]^2} \Big/ \int_0^{2k_{\mathrm{F}}} \frac{S(\mathbf{q})q^3 dq}{[q^2 + r_{\mathrm{TF}}^{-2}]^2}. \quad (15)$$

By using formulas (5), (6), (8), (11), (12), (14), and (15), we calculated the temperature dependences of the electron mobility μ^+ for HgSe : Fe samples at different iron concentrations.

Figure 3 displays the temperature dependences of the mobility μ^+/μ_0^+ for HgSe : Fe samples at iron concentrations ranging from $n_{\mathrm{Fe}} = 7 \times 10^{18}$ cm^{-3} (curve *1*) to $n_{\mathrm{Fe}} = 8.5 \times 10^{19}$ cm^{-3} (curve *4*). The results of calculations (Fig. 3) demonstrate that the weakening of correlations in the arrangement of scatterers with an increase in the temperature leads to a substantial decrease in the mobility of degenerate electrons in the temperature range $0 < T < 20$ K, in which electron scattering by phonons is negligibly small. This effect depends on the degree of correlation in the arrangement of scatterers at $T = 0$. At the iron concentration $n_{\mathrm{Fe}} = 8.5 \times 10^{19}$ cm^{-3} (curve *4*), the packing coefficient $\eta(0)$ at $T = 0$ is equal to 0.29 and the decrease in the electron mobility is 50%. For $n_{\mathrm{Fe}} = 7 \times 10^{18}$ cm^{-3} (curve *1*), $\eta(0) = 0.05$ and the mobility is decreased by 15%.

The temperature dependences of the electron mobility for the $Hg_{1-x}Fe_xSe$ sample at the iron concentration $x = 0.003$ ($n_{\mathrm{Fe}} = 4.5 \times 10^{19}$ cm^{-3}) are plotted in Fig. 4. The experimental data are taken from [15]. The mobility μ_0^+ of electrons scattered by a random ion distribution corresponds to the experimental mobility in the sample at the iron concentration $n_{\mathrm{Fe}} = n_c = 4.5 \times 10^{18}$ cm^{-3}. According to the data obtained by Pool *et al.* [15], $\mu_0^+ = 3.5 \times 10^4$ cm^2/(V s). The calculated temperature dependence of the mobility μ^+/μ_0^+ is shown by the solid line in Fig. 4. The dashed line represents the

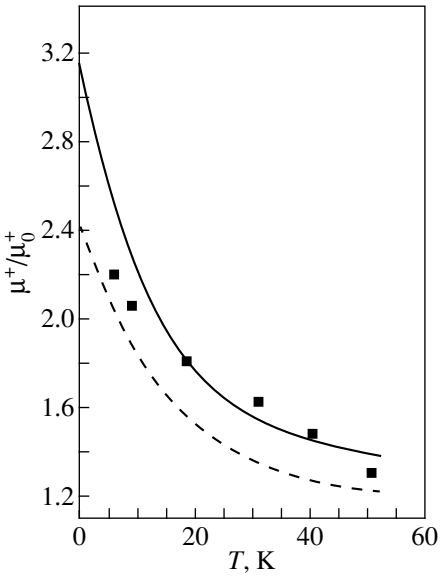

Fig. 4. Temperature dependences of the electron mobility for the $Hg_{1-x}Fe_xSe$ sample with $x = 0.003$ ($n_{\mathrm{Fe}} = 4.5 \times 10^{19}$ cm^{-3}). The solid line shows the mobility of electrons upon scattering by iron ions. The dashed line corresponds to electron scattering by iron ions and neutral iron atoms. Points are the experimental data taken from [15].

dependence of the mobility μ/μ_0^+ calculated with due regard for electron scattering by neutral iron atoms:

$$\mu^{-1} = \mu^{+-1} + \mu_0^{-1}. \quad (16)$$

The electron mobility associated with scattering by neutral iron atoms is calculated according to the relationship [4]

$$\mu_0 = A/(n_{\mathrm{Fe}} - n_{\mathrm{Fe}}^{+}), \quad (17)$$

where the constant A is equal to 1.46×10^{25} cm^{-1} V^{-1} s^{-1}. A comparison of the theoretical curves and the experimental points (Fig. 4) demonstrates reasonable agreement between theory and experiment. In conclusion, it should be noted that, unlike the calculations performed in [5, 6], we calculated the temperature dependence of the electron mobility without recourse to fitting parameters.

ACKNOWLEDGMENTS

The author is grateful to G.I. Kharus for his participation in extended discussions of the results.

REFERENCES

1. I. M. Tsidil'kovskii, *Electron Spectrum of Gapless Semiconductors* (Akad. Nauk SSSR, Sverdlovsk, 1991; Springer-Verlag, Berlin, 1997), Springer Series in Solid-State Sciences, Vol. 116.

2. Z. Wilamowski, K. Swatek, T. Dietl, and J. Kossut, Solid State Commun. **74** (8), 833 (1990).
3. V. M. Mikheev, Fiz. Tverd. Tela (St. Petersburg) **41** (11), 1994 (1999) [Phys. Solid State **41**, 1830 (1999)].
4. V. M. Mikheev, Fiz. Tverd. Tela (St. Petersburg) **43** (3), 414 (2001) [Phys. Solid State **43**, 430 (2001)].
5. N. N. Ablyazov and A. L. Éfros, Zh. Éksp. Teor. Fiz. **95** (4), 1450 (1989) [Sov. Phys. JETP **68**, 837 (1989)].
6. I. M. Tsidil'kovskiĭ, I. G. Kuleev, and I. I. Lyapilin, Zh. Éksp. Teor. Fiz. **102** (1), 326 (1992) [Sov. Phys. JETP **75**, 172 (1992)].
7. R. Balescu, *Equilibrium and Nonequilibrium Statistical Mechanics* (Wiley, New York, 1975; Mir, Moscow, 1978), Vol. 1.
8. Z. Wilamowski, Acta Phys. Pol. A **77** (1), 133 (1989).
9. I. G. Kuleev, Fiz. Tverd. Tela (St. Petersburg) **40** (3), 425 (1998) [Phys. Solid State **40**, 389 (1998)].
10. E. I. Khar'kov, I. I. Lysov, and I. E. Fedorov, *Physics of Liquid Metals* (Kiev, 1979).
11. A. Einstein, *Selected Works* (Nauka, Moscow, 1966), Vol. 3.
12. L. D. Landau and E. M. Lifshitz, *Course of Theoretical Physics*, Vol. 5: *Statistical Physics* (Nauka, Moscow, 1976; Pergamon, Oxford, 1980), Part 1.
13. Yu. G. Rudoĭ and A. D. Sukhanov, Usp. Fiz. Nauk **170** (12), 1265 (2000).
14. F. J. Blatt, *Physics of Electronic Conduction in Solids* (McGraw-Hill, New York, 1968; Mir, Moscow, 1971).
15. F. S. Pool, J. Kossut, U. Debska, and R. Reifenberger, Phys. Rev. B **35** (8), 3900 (1987).

Translated by O. Borovik-Romanova

Physics of the Solid State, Vol. 43, No. 10, 2001, pp. 1867–1875. Translated from Fizika Tverdogo Tela, Vol. 43, No. 10, 2001, pp. 1791–1798.

SEMICONDUCTORS AND DIELECTRICS

A Tight-Binding Representation of Electron–Hole Exchange Interaction in Semiconductors

S. V. Goupalov[1, 2]* and E. L. Ivchenko[1]

[1]*Ioffe Physicotechnical Institute, Russian Academy of Sciences, Politekhnicheskaya ul. 26, St. Petersburg, 194021 Russia*

[2]*Department of Physics, Washington State University, Pullman, WA 99164-2814, USA*

e-mail: ivchenko@coherent.ioffe.rssi.ru

Received March 15, 2001

Abstract—The electron–hole exchange interaction in semiconductors is analyzed in the framework of the empirical tight-binding method. It is demonstrated that intra-atomic and interatomic contributions to the long-range exchange interaction enter in an inequivalent way. In particular, for the $\Gamma_6 \times \Gamma_7$ exciton in a spherical nanocrystal with a cubic lattice, the dipole–dipole contribution associated only with the intra-atomic (or intra-site) transitions does not lead to singlet–triplet splitting of the exciton level. The interatomic transitions, for example, anion-to-cation transitions between the nearest neighbors in binary semiconductor compounds, determine the so-called monopole–monopole contribution to the exchange splitting of the $\Gamma_6 \times \Gamma_7$ exciton, and this contribution does not vanish in a spherical nanocrystal. © *2001 MAIK "Nauka/Interperiodica".*

1. INTRODUCTION

The exchange interaction between an electron and a hole bound into an exciton in a semiconductor crystal was extensively investigated in the early 1970s in relation to the study of the fine structure of exciton levels [1–6]. It is common practice to consider two contributions to matrix elements of the exchange interaction operator. The first (long-range) contribution only slightly varies at distances of the order of the lattice constant and depends on the wave vector of the electron–hole pair involved. The second contribution is governed by the short-range part of the Coulomb potential and does not depend on the wave vectors of the electrons and holes. The matrix elements of the long-range exchange interaction operator between Bloch wave functions are calculated either within the effective mass method [1, 2, 4, 7] or with the use of an expansion in Wannier functions (see [5, 6] and references therein). Note that the matrix elements of the velocity (momentum) operator between Bloch functions at band extrema in the former case and the coordinate matrix elements between Wannier functions in the latter case are identified with the corresponding interband optical matrix elements. However, these two methods give different matrix elements of the long-range exchange interaction. This difference is usually explained by the inequivalent separation of the initial exchange interaction operator into the long-range and short-range parts in the former and latter methods [6, 8]. However, our analysis (performed in the first part of the present work) of the long-range exchange interaction in the framework of the empirical tight-binding method shows that a different factor is responsible for this difference. It turns out that the velocity operator matrix element components associated with interatomic and intra-atomic transitions, which are naturally separated in the tight-binding method, make inequivalent contributions to the matrix element of the long-range exchange interaction. At the same time, in both the effective mass method and the Wannier function expansion method, we deal with functions that characterize band states and different contributions to the velocity operator matrix element cannot be separated within the framework of these methods. It has been demonstrated that intra-atomic transitions are not included in the velocity operator matrix element in the effective mass method. By contrast, the interatomic component of the velocity operator is ignored in the Wannier function expansion method. The matrix elements of the long-range exchange interaction in these two methods can be derived upon changing over to the corresponding limits in the relationship obtained within the empirical tight-binding method for similar matrix elements.

In recent years, the electron–hole exchange interaction in semiconductors has attracted considerable attention in connection with extensive investigations into quasi-zero-dimensional structures (quantum dots). In these objects, the quantum confinement effect can lead to an increase in the exchange splitting of exciton levels by a factor of several tens compared to the splitting observed in bulk semiconductors. The theory of the exchange interaction in quantum dots was constructed either within the effective mass method [9–12], or with the use of the expansion in Wannier functions [13, 14]. The approaches proposed in [15–17] were also based on the results obtained in [13]. As for bulk semiconductors, these approaches led to different results. In this

* Present address: School of Electrical and Computer Engineering, Georgia Institute of Technology, Atlanta, GA 30332-0250 USA.

respect, the theory developed in the first part of the present work is applied to an exciton localized in a quantum dot. As an example, we consider a $\Gamma_6 \times \Gamma_7$ exciton in a spherical semiconductor nanocrystal of the T_d crystal class with a radius R, which is small compared to the exciton Bohr radius a_B.

2. THE TIGHT-BINDING MODEL FOR A BULK SEMICONDUCTOR

In the tight-binding model, the Bloch electronic state $|n\mathbf{k}\rangle$ is expanded in terms of atomic orbitals (AOs) (see [18–22] and references therein):

$$\langle \mathbf{r}|n\mathbf{k}\rangle = \frac{1}{\sqrt{N}}\sum_{\mathbf{a}b\alpha}\exp[i\mathbf{k}(\mathbf{a}+\boldsymbol{\tau}_b)] \times C_{b\alpha}(n,\mathbf{k})\Phi_{b\alpha}(\mathbf{r}-\mathbf{a}-\boldsymbol{\tau}_b). \quad (1)$$

Here, $\mathbf{k}$ is the electron wave vector, n is the band index, $\mathbf{a}$ is the vector specifying the position of a unit cell, b is the index for numbering of atoms in a particular unit cell, $\boldsymbol{\tau}_b$ is the vector determining the site of the b atom inside the unit cell, and α is the AO index. Taking into account the spin and spin–orbit splitting, α involves the indices of the orbital angular momentum $l = s, p, d, s^*...$; the total angular momentum j; and the projection j_z of the total angular momentum onto the z axis. In the sp^3 model for a homogeneous semiconductor crystal with a zinc blende lattice, the above designations have the following meaning [18]: b labels the sort of atoms, i.e., cations ($b = c$) or anions ($b = a$); $\alpha = l, j, j_z$ at $l = s$ or p; $j = 1/2$ at $l = s$ and $j = 1/2$ and 3/2 at $l = p$; and $j_z = \pm 1/2$ at $j = 1/2$ and $j_z = \pm 1/2$ and $\pm 3/2$ at $j = 3/2$. Sometimes, AOs will be denoted using one vector $\mathbf{R} = \mathbf{a} + \boldsymbol{\tau}_b$ rather than the pair $\mathbf{a}$ and b. For convenience, the multiplier $1/\sqrt{N}$ (where N is the number of unit cells in the Born–Karman quantization box) is introduced into relationship (1). In this case, the expansion coefficients $C_{b\alpha}(n, \mathbf{k})$ satisfy the normalization condition

$$\sum_{b\alpha}|C_{b\alpha}(n\mathbf{k})|^2 = 1. \quad (2)$$

Now, we introduce the tight-binding parameters $H^{b'b}_{\alpha'\alpha}(\mathbf{R}' - \mathbf{R})$. In the $\mathbf{k}$ representation, the Schrödinger equation takes the form

$$\sum_{b\alpha}H^{b'b}_{\alpha'\alpha}(\mathbf{k})C_{b\alpha}(n,\mathbf{k}) = E_{n\mathbf{k}}C_{b'\alpha'}(n,\mathbf{k}) \quad (3)$$

with the electronic Hamiltonian

$$H^{b'b}_{\alpha'\alpha}(\mathbf{k}) = \sum_{\mathbf{a}}\exp[i\mathbf{k}(\mathbf{a}+\boldsymbol{\tau}_b-\boldsymbol{\tau}'_b)]H^{b'b}_{\alpha'\alpha}(\boldsymbol{\tau}'_b-\mathbf{a}-\boldsymbol{\tau}_b). \quad (4)$$

Specifically, in the sp^3 model, when only the interaction between the nearest neighbors is taken into consideration, there are the following ten linearly independent parameters: the diagonal energies E_{sa}, E_{sc}, E_{pa}, and E_{pc} for the s and p orbitals on an anion and a cation (without regard for the spin–orbit interaction); the spin–orbit splittings Δ_a and Δ_c of the p orbitals; and four interaction matrix elements V_{ss}, V_{pp}, $V_{pc,\,sa} \equiv V_{sa,\,pc}$ and $V_{pa,\,sc} \equiv V_{sc,\,pa}$ for the nearest cation and anion (for simplicity, the interatomic spin–orbit interaction is neglected).

In the tight-binding method, the coordinate matrix elements

$$\langle \mathbf{a}'b'\alpha'|\mathbf{r}|\mathbf{a}b\alpha\rangle = \langle \mathbf{R}'\alpha'|\mathbf{r}|\mathbf{R}\alpha\rangle$$

in the AO basis set are defined by the expression

$$\langle \mathbf{R}'\alpha'|\mathbf{r}|\mathbf{R}\alpha\rangle = (\mathbf{R}\delta_{\alpha'\alpha} + \mathbf{r}^b_{\alpha'\alpha})\delta_{\mathbf{R}'\mathbf{R}}, \quad (5)$$

which is diagonal with respect to $\mathbf{R}$ and includes two terms. The first term is diagonal with respect to the αth orbital, proportional to the $\mathbf{R}$ vector, and independent of α. The second term does not depend on the position of the unit cell and describes the intra-atomic (intrasite) transitions:

$$\mathbf{r}^b_{\alpha'\alpha} = \langle \mathbf{R}\alpha'|\mathbf{r}-\mathbf{R}|\mathbf{R}\alpha\rangle \equiv \langle \mathbf{a}b\alpha'|\mathbf{r}-\mathbf{a}-\boldsymbol{\tau}_b|\mathbf{a}b\alpha\rangle. \quad (6)$$

With due regard for the relationship

$$\mathbf{v} = \frac{i}{\hbar}(H\mathbf{r}-\mathbf{r}H)$$

between the velocity ($\mathbf{v}$) and coordinate ($\mathbf{r}$) operators, the velocity operator matrix elements in the tight-binding method can be represented in the form of two terms $\mathbf{v}^{(1)}_{b'\alpha',\,b\alpha}(\mathbf{R}', \mathbf{R})$ and $\mathbf{v}^{(2)}_{b'\alpha',\,b\alpha}(\mathbf{R}', \mathbf{R})$. The first term

$$\mathbf{v}^{(1)}_{b'\alpha',\,b\alpha}(\mathbf{R}', \mathbf{R}) = \frac{i}{\hbar}(\mathbf{R}-\mathbf{R}')H^{b'b}_{\alpha',\,\alpha}(\mathbf{R}'-\mathbf{R}) \quad (7)$$

is uniquely determined by the tight-binding parameters and describes the electron transfer from the atom ($\mathbf{a}$, b) to the atom ($\mathbf{a}'$, b'). The vector $\mathbf{v}^{(1)}_{b'\alpha',\,b\alpha}$ is oriented along a straight line connecting these atoms and is proportional to the corresponding tight-binding matrix element. The second term

$$\mathbf{v}^{(2)}_{b'\alpha',\,b\alpha}(\mathbf{R}', \mathbf{R}) = \frac{i}{\hbar}\begin{cases}(E_{b\alpha'}-E_{b\alpha})\mathbf{r}^b_{\alpha'\alpha} & \text{at } \mathbf{R}' = \mathbf{R}\\ \sum_{\alpha''}[H^{b'b}_{\alpha'\alpha''}(\mathbf{R}'-\mathbf{R})\mathbf{r}^b_{\alpha''\alpha} & \\ -\mathbf{r}^{b'}_{\alpha'\alpha''}H^{b'b}_{\alpha''\alpha}(\mathbf{R}'-\mathbf{R})] & \text{at } \mathbf{R}' \neq \mathbf{R}\end{cases} \quad (8)$$

is proportional to the intra-atomic coordinate matrix elements and differs from zero for both intra-atomic and interatomic transitions. Relationship (8) takes into account that the $H^{b'b}_{\alpha'\alpha}(\mathbf{R}'-\mathbf{R})$ matrix element at $\mathbf{R}' = \mathbf{R}$ is diagonal with respect to α and is equal to the energy $E_{b\alpha}$

of an electron on the α orbital of the *b* atom. In the **k** representation, the velocity operator matrix elements are given by

$$\mathbf{v}^{b'b}_{\alpha'\alpha}(\mathbf{k}) = \sum_{\mathbf{a}} \exp[i\mathbf{k}(\mathbf{a}+\boldsymbol{\tau}_b-\boldsymbol{\tau}'_b)]\langle 0b'\alpha'|\mathbf{v}|\mathbf{a}b\alpha\rangle. \quad (9)$$

Specifically, term (7) in this representation at $\mathbf{k}=0$ has the form

$$\mathbf{v}^{(1)}_{b'\alpha',b\alpha}(\mathbf{k}=0) = \frac{i}{\hbar}\sum_{\mathbf{a}}(\mathbf{a}+\boldsymbol{\tau}_b-\boldsymbol{\tau}'_b)H^{b'b}_{\alpha'\alpha}(\boldsymbol{\tau}'_b-\mathbf{a}-\boldsymbol{\tau}_b). \quad (10)$$

The set of the $C_{b\alpha}(n, \mathbf{k})$ coefficients can be represented as the multicomponent column vector $\hat{C}(n, \mathbf{k})$. The $\hat{C}(n, 0)$ column vector is the eigenvector of the $H^{b'b}_{\alpha'\alpha}(0)$ matrix, with the eigenvalue $E^0_n \equiv E_{n,0}$ corresponding to an extremum of the *n*th band. From relationships (4) and (10), it follows that, to the first order of the perturbation theory in ka_0 (where a_0 is the lattice constant), the tight-binding Hamiltonian takes the form

$$H^{b'b}_{\alpha'\alpha}(\mathbf{k}) = H^{b'b}_{\alpha'\alpha}(0) + \hbar\mathbf{k}\mathbf{v}^{(1)}_{b'\alpha',b\alpha}(\mathbf{k}=0). \quad (11)$$

The $C_{b\alpha}(n, \mathbf{k})$ coefficients in the *n*th nondegenerate band are defined by the formula

$$C_{b\alpha}(n,\mathbf{k}) = C_{b\alpha}(n,0) + {\sum_l}' \frac{\hbar\mathbf{k}\mathbf{v}^{(1)}_{ln}}{E^0_n - E^0_l}C_{b\alpha}(l,0), \quad (12)$$

where

$$\mathbf{v}^{(1)}_{ln} = \sum_{bb'\alpha\alpha'} C^*_{b'\alpha'}(l,0)\mathbf{v}^{(1)}_{b'\alpha',b\alpha}(0)C_{b\alpha}(n,0)$$

and the prime indicates summation over the states with $E^0_l \neq E^0_n$. Note that, unlike expression (12), the expansion of the periodic Bloch amplitude $u_{n,\mathbf{k}} = e^{-i\mathbf{k}\mathbf{r}}|n\mathbf{k}\rangle$ in powers of **k** contains the full matrix element of the velocity operator:

$$u_{n,\mathbf{k}}(\mathbf{r}) = u_{n,0}(\mathbf{r}) + {\sum_l}' \frac{\hbar\mathbf{k}\mathbf{v}_{ln}}{E^0_n - E^0_l}u_{l,0}(\mathbf{r}) + \ldots, \quad (13)$$

where

$$\mathbf{v}_{ln} = \mathbf{v}^{(1)}_{ln} + \mathbf{v}^{(2)}_{ln},$$

$$\mathbf{v}^{(i)}_{ln} = \sum_{bb'\alpha\alpha'} C^*_{b'\alpha'}(l,0)\mathbf{v}^{(i)}_{b'\alpha',b\alpha}(k=0)C_{b\alpha}(n,0). \quad (14)$$

For completeness, we also write an expression to relate the Wannier functions $w_n(\mathbf{r})$ to the AOs [5], that is,

$$w_n(\mathbf{r}-\mathbf{a}') = \frac{1}{N}\sum_{\mathbf{k}\mathbf{a}b\alpha} C_{b\alpha}(n,\mathbf{k}) \times \exp[i\mathbf{k}(\mathbf{a}-\mathbf{a}'+\boldsymbol{\tau}_b)]\Phi_{b\alpha}(\mathbf{r}-\mathbf{a}-\boldsymbol{\tau}_b), \quad (15)$$

where summation is performed over all wave vectors of the Brillouin zone. It is evident that the use of the Wannier functions characterizing the band states *n* complicates the separation of the contributions from interatomic and intra-atomic transitions to the velocity matrix element.

In tight-binding calculations, the question that necessarily arises is what are the relative contributions from intra-atomic and interatomic transitions to the interband matrix elements of the electron velocity (or electron momentum) operator and, what is the same, what is the probability of optical absorption or emission in semiconductors? Chang *et al.* [23–25] accounted for both transitions, but used intra-atomic matrix elements of the momentum operator that were larger than the analogous elements for anion-to-cation transitions. In [26, 27], the contribution from interatomic transitions was ignored altogether. At the same time, many authors [28–32] have completely neglected intra-atomic transitions. We will show below that the intra-atomic and interatomic contributions are inequivalently included in the matrix elements of the long-range electron–hole exchange interaction in semiconductors, unlike the matrix elements of the optical transitions in which these contributions cannot be separated.

3. THE ELECTRON–HOLE EXCHANGE INTERACTION OPERATOR

The operator of the electron–hole exchange Coulomb interaction in a semiconductor crystal can be specified by the matrix elements [1, 2]

$$\begin{aligned}\left\langle m', \mathbf{k}'_e; n', \mathbf{k}'_h\middle|U^{eh}_{\text{exch}}\middle|m, \mathbf{k}_e; n\mathbf{k}_h\right\rangle &= -\left\langle m', \mathbf{k}'_e; \bar{n}, -\mathbf{k}_h\middle|U^{ee}_{\text{exch}}\middle|m, \mathbf{k}_e; \bar{n}', -\mathbf{k}'_h\right\rangle \\ &= \int \psi^\dagger_{m',\mathbf{k}'_e}(\mathbf{r}_1)\psi_{\bar{n}',-\mathbf{k}'_h}(\mathbf{r}_1)\frac{e^2}{\kappa|\mathbf{r}_1-\mathbf{r}_2|} \\ &\quad\times\psi^\dagger_{\bar{n},-\mathbf{k}_h}(\mathbf{r}_2)\psi_{m,\mathbf{k}_e}(\mathbf{r}_2)d\mathbf{r}_1 d\mathbf{r}_2.\end{aligned} \quad (16)$$

Here, the indices *ee* and *eh* refer to the electron–electron and electron–hole representations of operators [2], respectively; κ is the (high-frequency) permittivity; $|m, \mathbf{k}_e; n, \mathbf{k}_h\rangle$ is the two-particle excited state of the crystal; the states $|n, \mathbf{k}\rangle$ and $|\bar{n}, -\mathbf{k}\rangle$ are related through the time reversal operation; and $\psi_{m,\mathbf{k}_e}(\mathbf{r}) \equiv \langle\mathbf{r}|m, \mathbf{k}_e\rangle$ and $\psi_{n,\mathbf{k}_h}(\mathbf{r}) \equiv \langle\mathbf{r}|n, \mathbf{k}_h\rangle$ are the Bloch wave functions in the electron and hole representations, respectively. As follows from the translational invariance of a bulk crystal,

the matrix elements (16) are nonzero only for coinciding resultant wave vectors of an electron–hole pair:

$$\mathbf{K} = \mathbf{k}_e + \mathbf{k}_h = \mathbf{k}'_e + \mathbf{k}'_h. \quad (17)$$

The Bloch functions in the form of expression (1) with the coefficients $C_{b\alpha}(m, \mathbf{k}_e)$ and $C_{b\alpha}(n, \mathbf{k}_h)$ for electrons and holes are used in the tight-binding method. The calculation of the exchange integral in this method reduces to summation over six discrete variables:

$$\sum_{\mathbf{R}_1\mathbf{R}_2} e^{i\mathbf{K}(\mathbf{R}_2-\mathbf{R}_1)} \sum_{\alpha'_1,\alpha_1,\alpha'_2,\alpha_2} U(\mathbf{R}_1, \alpha'_1, \alpha_1; \mathbf{R}_2, \alpha'_2, \alpha_2) \quad (18)$$
$$\times C^*_{b_1\alpha'_1}(m', \mathbf{k}'_e) C_{b_1\alpha_1}(\bar{n}', -\mathbf{k}'_h) C_{b_2\alpha'_2}(m, \mathbf{k}_e) C^*_{b_2\alpha_2}(n, -\mathbf{k}_h),$$

where

$$U(\mathbf{R}_1, \alpha'_1, \alpha_1; \mathbf{R}_2, \alpha'_2, \alpha_2)$$
$$= \frac{e^2}{\kappa}\iint \frac{d\mathbf{r}_1 d\mathbf{r}_2}{|\mathbf{r}_1-\mathbf{r}_2|} \Phi^\dagger_{b_1\alpha'_1}(\mathbf{r}_1-\mathbf{R}_1)\Phi_{b_1\alpha_1}(\mathbf{r}_1-\mathbf{R}_1) \quad (19)$$
$$\times \Phi_{b_2\alpha'_2}(\mathbf{r}_2-\mathbf{R}_2)\Phi^\dagger_{b_2\alpha_2}(\mathbf{r}_2-\mathbf{R}_2).$$

Hereafter, we will focus our attention only on the long-range exchange interaction (sometimes referred to as the nonanalytical exchange interaction). Hence, we assume that k_e and k_h are small compared to the reciprocal a_0^{-1} of the lattice constant and the terms with $\mathbf{R}_1 = \mathbf{R}_2$ do not enter into sum (18). The corresponding operator will be denoted as $U^{(\mathrm{long})}_{\mathrm{exch}}$. Apparently, when formulating the tight-binding model, we should eliminate the terms with $\mathbf{R}_1 = \mathbf{R}_2$ from the general formulas (16) and (18) beforehand. Instead of these terms, we should add the independent short-range contribution $U^{(\mathrm{short})}_{\mathrm{exch}}$ to expression (18) and introduce additional parameters (describing the intrasite exchange interaction) into the theory.

In order to determine the tight-binding exchange integral (19), we expand the Coulomb potential in a power series of $\mathbf{r} - \mathbf{R}$ in the vicinity of the points $\mathbf{R}_1 = \mathbf{a}_1 + \boldsymbol{\tau}_{b_1}$ and $\mathbf{R}_2 = \mathbf{a}_2 + \boldsymbol{\tau}_{b_2}$ ($\mathbf{R}_1 \neq \mathbf{R}_2$), that is,

$$\frac{1}{|\mathbf{r}_1-\mathbf{r}_2|} \approx \frac{1}{|\mathbf{R}_1-\mathbf{R}_2|} - [(\mathbf{r}_1-\mathbf{R}_1)-(\mathbf{r}_2-\mathbf{R}_2)]$$
$$\times \frac{\mathbf{R}_1-\mathbf{R}_2}{|\mathbf{R}_1-\mathbf{R}_2|^3} + (\mathbf{r}_1-\mathbf{R}_1)_\lambda(\mathbf{r}_2-\mathbf{R}_2)_\eta \quad (20)$$
$$\times \frac{|\mathbf{R}_1-\mathbf{R}_2|^2\delta_{\lambda\eta} - 3(\mathbf{R}_1-\mathbf{R}_2)_\lambda(\mathbf{R}_1-\mathbf{R}_2)_\eta}{|\mathbf{R}_1-\mathbf{R}_2|^5}.$$

By using the orthonormality of AOs for a particular site and formula (6), relationship (19) can be rearranged to give

$$U(\mathbf{R}_1, \alpha'_1, \alpha_1; \mathbf{R}_2, \alpha'_2, \alpha_2)$$
$$= \frac{e^2}{\kappa}\left[\frac{1}{R}\delta_{\alpha'_1\alpha_1}\delta_{\alpha'_2\alpha_2} - (\mathbf{r}^{b_1}_{\alpha'_1\alpha_1}\delta_{\alpha'_2\alpha_2} - \delta_{\alpha'_1\alpha_1}\mathbf{r}^{b_2*}_{\alpha'_2\alpha_2})\frac{\mathbf{R}}{R^3}\right. \quad (21)$$
$$\left. + r^{b_1}_{\alpha'_1\alpha_1;\lambda} r^{b_2*}_{\alpha'_2\alpha_2;\eta} \frac{R^2\delta_{\lambda\eta} - 3R_\lambda R_\eta}{R^5}\right],$$

where $\mathbf{R} = \mathbf{R}_1 - \mathbf{R}_2$ and $R = |\mathbf{R}|$. In calculating the long-range exchange interaction, the summation in expression (18) over $\mathbf{R}_1$ and $\mathbf{R}_2$ can be replaced by integration according to the scheme

$$\sum_{\mathbf{R}_1\mathbf{R}_2} \longrightarrow \sum_{b_1b_2}\sum_{\mathbf{a}_1\mathbf{a}_2} \longrightarrow \sum_{b_1b_2}\iint \frac{d\mathbf{r}_1 d\mathbf{r}_2}{\Omega_0^2},$$

where Ω_0 is the unit cell volume. It is worth noting that the regions of the $\mathbf{r}_1$ and $\mathbf{r}_2$ variables inside the same unit cell make a negligibly small contribution to the double integral. Hence, the difference $\mathbf{R}_1 - \mathbf{R}_2 = \mathbf{a}_1 - \mathbf{a}_2 + \boldsymbol{\tau}_{b_1} - \boldsymbol{\tau}_{b_2}$ in the integrand can be replaced by $\mathbf{r}_1 - \mathbf{r}_2$, irrespective of whether b_1 and b_2 coincide or differ.

Next, we use the identities

$$\frac{\mathbf{r}_1-\mathbf{r}_2}{|\mathbf{r}_1-\mathbf{r}_2|^3} = -\frac{\partial}{\partial\mathbf{r}_1}\frac{1}{|\mathbf{r}_1-\mathbf{r}_2|},$$
$$\frac{\partial^2}{\partial r_{1,\lambda}\partial r_{2,\eta}}\frac{1}{|\mathbf{r}_1-\mathbf{r}_2|} = -\frac{\partial^2}{\partial r_{1,\lambda}\partial r_{1,\eta}}\frac{1}{|\mathbf{r}_1-\mathbf{r}_2|}$$
$$= \frac{|\mathbf{r}_1-\mathbf{r}_2|^2\delta_{\lambda\eta} - 3(\mathbf{r}_1-\mathbf{r}_2)_\lambda(\mathbf{r}_1-\mathbf{r}_2)_\eta}{|\mathbf{r}_1-\mathbf{r}_2|^5} \quad (22)$$
$$+ \frac{4\pi}{3}\delta_{\lambda\eta}\delta(\mathbf{r}_1-\mathbf{r}_2),$$
$$\iint d\mathbf{r}_1 d\mathbf{r}_2 \frac{e^{i\mathbf{K}(\mathbf{r}_2-\mathbf{r}_1)}}{|\mathbf{r}_1-\mathbf{r}_2|} = V\frac{4\pi}{K^2}$$

and the relationships

$$\sum_{b\alpha} C^*_{b\alpha}(m, \mathbf{k}_e) C_{b\alpha}(\bar{n}, -\mathbf{k}_h) = \frac{\hbar(\mathbf{k}_e+\mathbf{k}_h)\mathbf{v}^{(1)}_{m\bar{n}}}{E^0_m - E^0_n}, \quad (23)$$

$$\sum_{b\alpha'\alpha} C^*_{b\alpha'}(m, 0)\mathbf{r}^b_{\alpha'\alpha} C_{b\alpha}(\bar{n}, 0) = -\frac{i\hbar\mathbf{v}^{(2)}_{m\bar{n}}}{E^0_m - E^0_n}, \quad (24)$$

where the matrix elements $\mathbf{v}^{(j)}_{m\bar{n}}$ ($j = 1, 2$) are defined by formula (14) and V is the crystal volume. Relationship (23) was derived with due regard for expansion (12) and the orthonormality of the $\hat{C}(n, 0)$ column vectors.

Formula (24) was deduced by multiplying and dividing the $\mathbf{r}^b_{\alpha'\alpha}$ vector into $E^0_m - E^0_n$ and using the identity

$$\sum_{b\alpha'\alpha} C^*_{b\alpha'}(m,0)(E^0_m \mathbf{r}^b_{\alpha'\alpha} - \mathbf{r}^b_{\alpha'\alpha} E^0_n) C_{b\alpha}(\bar{n},0)$$
$$= \hat{C}^\dagger(m,0)(H\hat{\mathbf{r}} - \hat{\mathbf{r}}H)\hat{C}(\bar{n},0),$$

where H is the tight-binding Hamiltonian (4) at $\mathbf{k} = 0$ and $\hat{\mathbf{r}}$ is the vector matrix with the components $\mathbf{r}^b_{\alpha'\alpha}\delta_{b'b}$. As a result, we obtain the matrix element of the long-range exchange interaction in the following form:

$$\langle m', \mathbf{k}'_e; n', \mathbf{k}'_h | U^{(\mathrm{long})}_{\mathrm{exch}} | m, \mathbf{k}_e; n, \mathbf{k}_h \rangle$$
$$= \frac{4\pi e^2}{\kappa V} \frac{\hbar^2}{(E^0_m - E^0_n)^2} \left\{ \frac{(\mathbf{K}\mathbf{v}^{(1)}_{m'\bar{n}'})(\mathbf{K}\mathbf{v}^{(1)}_{m\bar{n}})^*}{K^2} \right.$$
$$+ \frac{(\mathbf{K}\mathbf{v}^{(1)}_{m'\bar{n}'})(\mathbf{K}\mathbf{v}^{(2)}_{m\bar{n}})^* + (\mathbf{K}\mathbf{v}^{(2)}_{m'\bar{n}'})(\mathbf{K}\mathbf{v}^{(1)}_{m\bar{n}})^*}{K^2} \quad (25)$$
$$\left. + \left[\frac{(\mathbf{K}\mathbf{v}^{(2)}_{m'\bar{n}'})(\mathbf{K}\mathbf{v}^{(2)}_{m\bar{n}})^*}{K^2} - \frac{1}{3}\mathbf{v}^{(2)}_{m'\bar{n}'}\mathbf{v}^{(2)*}_{m\bar{n}} \right] \right\},$$

where the first, second, and third terms in the curly brackets correspond to the contributions from the first, second, and third terms in the square brackets in relationship (21). Expression (25) can be conveniently rewritten as

$$\left\langle m', \mathbf{k}'_e; n', \mathbf{k}'_h \middle| U^{(\mathrm{long})}_{\mathrm{exch}} \middle| m, \mathbf{k}_e; n, \mathbf{k}_h \right\rangle = \frac{4\pi e^2}{\kappa V}$$
$$\times \frac{\hbar^2}{(E^0_m - E^0_n)^2} \left[\frac{(\mathbf{K}\mathbf{v}_{m'\bar{n}'})(\mathbf{K}\mathbf{v}_{m\bar{n}})^*}{K^2} - \frac{1}{3}\mathbf{v}^{(2)}_{m'\bar{n}'}\mathbf{v}^{(2)*}_{m\bar{n}} \right] \delta_{\mathbf{K}'\mathbf{K}}, \quad (26)$$

where the full matrix element $\mathbf{v}_{ln}$ of the velocity operator is given by formula (14).

Relationship (26) is convenient for analyzing the validity range of the effective mass and Wannier function expansion methods. In the effective mass method, the expression for the matrix element of the long-range exchange interaction [1–4, 10–12] coincides with the first term in the square brackets in formula (26). This implies that, in the effective mass the method, the intraatomic transitions are ignored, $\mathbf{v}^{(2)}_{ln} = 0$, and $\mathbf{v}_{ln} = \mathbf{v}^{(1)}_{ln}$. In the case of the expansion of the Bloch functions in terms of the Wannier functions, the interatomic transitions are neglected and it is actually assumed that $\mathbf{v}^{(1)}_{ln} = 0$ and $\mathbf{v}_{ln} = \mathbf{v}^{(2)}_{ln}$. This is also indicated by the fact that the solution obtained within this approach involves interband coordinate matrix elements between the Wannier functions centered on the same unit cell [5, 6]. The higher the degree of localization of the Wannier functions, the stronger the grounds to disregard the interband coordinate matrix elements between the functions centered on different cells. Therefore, this approximation should be best fulfilled in the limit when the Wannier functions are localized within one unit cell and the interatomic transitions can be ignored. Many authors have noted the difference between the matrix elements of the long-range exchange interaction in the effective mass and Wannier function expansion methods [6, 8]. This difference was attributed to different separations of the exchange interaction into long-range and short-range contributions with due regard for the δ function that arises upon inverse Fourier transform of the first term in the square brackets in relationship (26) [see also formula (22)]. In actual fact, the general formula (26) includes the solutions from both methods as limiting cases. Moreover, as is shown in the Appendix in considering the exchange interaction in quantum dots, the above δ function is unrelated to the short-range interaction associated with scales of the order of the lattice constant and less.

With the aim of illustrating formula (26), let us consider a pair of simple bands, namely, the conduction band Γ_6 and the valence band Γ_7 in semiconductors of the GaAs type. Taking into account the twofold spin degeneracy of the Γ_6 conduction and Γ_7 valence bands, the ground exciton level consists of four sublevels characterized by the total angular momenta $J = 0$ (singlet, Γ_2 representation) and $J = 1$ (triplet, Γ_5 representation). It is convenient to change over to the electron–hole excitation basis set, in which the three states $|\nu, \mathbf{k}_e, \mathbf{k}_h\rangle$ (where $\nu = x, y$, and z) are optically active at the polarization $\mathbf{e} \parallel \nu$ and the optical transition to the fourth state $|\Gamma_2, \mathbf{k}_e, \mathbf{k}_h\rangle$ is forbidden. The long-range exchange interaction (26) affects only the $|\nu, \mathbf{k}_e, \mathbf{k}_h\rangle$ state and, in the new basis set, has the form

$$\langle \nu', \mathbf{k}'_e, \mathbf{k}'_h | U^{(\mathrm{long})}_{\mathrm{exch}} | \nu, \mathbf{k}_e, \mathbf{k}_h \rangle = \frac{4\pi}{\kappa V}\left(\frac{e\hbar}{E'_g}\right)^2$$
$$\times \left[\frac{K_{\nu'}K_\nu}{K^2} |v_{cv}|^2 - \frac{1}{3}|v^{(2)}_{cv}|^2 \delta_{\nu',\nu} \right] \delta_{\mathbf{K}',\mathbf{K}}, \quad (27)$$

where v_{cv} is the interband matrix element of the velocity operator, $v^{(2)}_{cv}$ is the contribution [defined by expressions (8) and (14)] to v_{cv}, and E'_g is the energy gap between the Γ_6 and Γ_7 bands. For a 1s exciton, we have

$$\left\langle 1s, \mathbf{K} \middle| U^{(\mathrm{long})}_{\mathrm{exch}} \middle| 1s, \nu, \mathbf{K} \right\rangle$$
$$= \hbar\omega_{LT} \frac{K_{\nu'}K_\nu}{K^2} - \frac{1}{3}\hbar\omega^{(2)}_{LT}\delta_{\nu',\nu}, \quad (28)$$

where $\hbar\omega_{LT} = (4/\kappa a_B^3)(e\hbar|v_{cv}|/E'_g)^2$ is the longitudinal–transverse exciton splitting, a_B is the Bohr radius of the

1*s* exciton in a bulk semiconductor, and

$$\hbar\omega_{LT}^{(2)} = \hbar\omega_{LT}\left(\frac{V_{cv}^{(2)}}{V_{cv}}\right)^2. \quad (29)$$

4. EXCHANGE INTERACTION IN A SPHERICAL QUANTUM DOT

Now, let us consider the exchange splitting of a level of a $\Gamma_6 \times \Gamma_7$ zero-dimensional exciton with the wave function

$$\Psi_{\text{exc}}(\mathbf{r}_e, \mathbf{r}_h) = \phi_{e,m}(\mathbf{r}_e)\phi_{h,n}(\mathbf{r}_h), \quad (30)$$

which is the product of the electron and hole one-particle wave functions localized on the ground size-quantization levels *e*1 and *h*1 in a spherical quantum dot. The indices *m* and *n* in expression (30) take the values of the projections of the electron spin (±1/2) in the conduction band and the angular momentum of the hole ($j = 1/2$) in the Γ_7 valence band that is split out from the Γ_8 band owing to the spin–orbit interaction. It is assumed that the quantum dot radius *R* is large compared to the lattice constant a_0 and, at the same time, is sufficiently small; therefore, the admixture of the electron–hole states of the upper size-quantization levels to function (30) due to the Coulomb interaction can be ignored. For the simple bands Γ_6 and Γ_7, the envelopes of the two wave functions $\phi_{e,m}(\mathbf{r}_e)$ and $\phi_{h,n}(\mathbf{r}_e)$ in the effective mass method at infinitely high barriers coincide and have the form

$$F(\mathbf{r}) = \frac{\sin(\pi r/R)}{r\sqrt{2\pi R}}. \quad (31)$$

Earlier [10, 12], within the effective mass method, we obtained the following expression for the singlet–triplet splitting of the ground level of the $\Gamma_6 \times \Gamma_7$ exciton in a nanocrystalline ball:

$$\Delta_{ST}^{QD}(R) = \pi C\left(\Delta_{ST}^{\text{bulk}} + \frac{1}{3}\hbar\omega_{LT}\right)\left(\frac{a_{\text{B}}}{R}\right)^3. \quad (32)$$

Here,

$$C = \int_0^\pi \frac{\sin^4 x}{x^2}dx \approx 0.672, \quad (33)$$

$\Delta_{ST}^{\text{bulk}}$ is the short-range exchange interaction constant, $\hbar\omega_{LT}$ is the longitudinal–transverse exciton splitting, a_{B} is the exciton Bohr radius in the bulk semiconductor, and the background permittivity κ of the nanocrystal is assumed to be equal to the permittivity κ_m of the matrix (the formula derived in [10, 12] is also valid at $\kappa \neq \kappa_m$).

Taking into account that the $\phi_{e,m}(\mathbf{r})$ [or $\phi_{h,n}(\mathbf{r})$] function can be represented as the sum

$$\sqrt{V}\sum_{\mathbf{k}} F_{\mathbf{k}}|m\mathbf{k}\rangle,$$

[where $F_{\mathbf{k}}$ is the Fourier transform of envelope (31) and *V* is the Born–Karman box volume] and using relationship (1) for $|m\mathbf{k}\rangle$, we obtain that, in the tight-binding method,

$$\phi_{e,m}(\mathbf{r}) = \sum_{\mathbf{a}b\alpha} S_{b\alpha}(m, \mathbf{a})\Phi_{b\alpha}(\mathbf{r} - \mathbf{a} - \boldsymbol{\tau}_b), \quad (34)$$

$$S_{b\alpha}(m, \mathbf{a}) = \sqrt{\Omega_0}\sum_{\mathbf{k}} \exp[i\mathbf{k}(\mathbf{a} + \boldsymbol{\tau}_b)]C_{b\alpha}(m, \mathbf{k})F_{\mathbf{k}}.$$

At $R \gg a_0$, we can neglect the difference of $\exp(i\mathbf{k}\boldsymbol{\tau}_b)$ from unity and use expansion (12). Then, the expression for the $S_{b\alpha}$ coefficients written as a multicomponent column can be transformed to the form

$$\hat{S}(m, \mathbf{a}) = \sqrt{\Omega_0}$$
$$\times\left[\hat{C}(m, 0) + \sum_l{}' \frac{\hbar\mathbf{v}_{lm}^{(1)}}{E_m^0 - E_l^0}\hat{C}(l, 0)\left(-i\frac{\partial}{\partial\mathbf{a}}\right)\right]F(\mathbf{a}), \quad (35)$$

where $F(\mathbf{a})$ is the envelope $F(\mathbf{r})$ at the discrete values $\mathbf{r} = \mathbf{a}$. It should be emphasized that, with due regard for the second term in the square brackets in relationship (35), the $\hat{S}(m, \mathbf{a})$ and $\hat{S}(\bar{n}, \mathbf{a})$ columns are nonorthogonal,

$$\hat{S}^\dagger(m, \mathbf{a})\hat{S}(\bar{n}, \mathbf{a}) = i\Omega_0\frac{\hbar\mathbf{v}_{m\bar{n}}^{(1)}}{E_g'}\frac{\partial}{\partial\mathbf{a}}F^2(\mathbf{a}), \quad (36)$$

just as the $\hat{C}(m, \mathbf{k}_e)$ and $\hat{C}(\bar{n}, -\mathbf{k}_h)$ columns are nonorthogonal at $\mathbf{k}_e + \mathbf{k}_h \neq 0$ [see formula (23)].

The exchange interaction matrix elements between functions (30) are calculated in much the same manner as in the preceding section for the Bloch states in the bulk crystal. For brevity, we will present only the result for the specific case $\mathbf{r}_{\alpha'\alpha}^b = 0$ and then discuss what happens when the intrasite matrix elements $\mathbf{r}_{\alpha'\alpha}^b$ are taken into consideration. In our specific case, the exchange interaction matrix elements are given by

$$\frac{e^2}{\kappa}\sum_{\mathbf{R}_1 \neq \mathbf{R}_2}\sum_{\alpha_1, \alpha_2} S_{b_1\alpha_1}^*(m', \mathbf{a}_1)S_{b_1\alpha_1}(\bar{n}', \mathbf{a}_1)$$
$$\times\frac{1}{|\mathbf{R}_1 - \mathbf{R}_2|}S_{b_2\alpha_2}(m, \mathbf{a}_2)S_{b_2\alpha_2}^*(\bar{n}', \mathbf{a}_2). \quad (37)$$

For the *m* states in the Γ_6 conduction band and the *n* states in the Γ_7 valence band, the product $S_{b\alpha}^*(m, \mathbf{a})S_{b\alpha}(\bar{n}, \mathbf{a})$ is nonzero only with allowance

made for the derivative in formula (35). Therefore, this product is expressed through the components of the vector $\partial F^2(\mathbf{a})/\partial \mathbf{a}$, which, in particular, leads to identity (36). As is demonstrated in the Appendix, the summation in relationship (37) can be replaced by independent integration over $\mathbf{r}_1$ and $\mathbf{r}_2$ and division into Ω_0^2. With due regard for expression (36), relationship (37) is rearranged as follows:

$$\sum_{\lambda,\eta}\frac{e^2}{\kappa}\left(\frac{\hbar}{E_g'}\right)^2 v^{(1)}_{m'\bar{n}',\lambda}v^{(1)*}_{m\bar{n},\eta} \times\iint\frac{d\mathbf{r}_1 d\mathbf{r}_2}{|\mathbf{r}_1-\mathbf{r}_2|}\left(\frac{\partial}{\partial r_{1,\lambda}}F^2(\mathbf{r}_1)\right)\left(\frac{\partial}{\partial r_{2,\eta}}F^2(\mathbf{r}_2)\right). \tag{38}$$

By changing over to the differentiation of the $|\mathbf{r}_1-\mathbf{r}_2|^{-1}$ function and using identity (22), we obtain the integral

$$\left\langle e,m';\,h,n'\left|U^{(\mathrm{long})}_{\mathrm{exch}}\right|e,m;\,h,n\right\rangle = \frac{4\pi}{3\kappa}\left(\frac{e\hbar}{E_g'}\right)^2\mathbf{v}^{(1)}_{m'\bar{n}'}\mathbf{v}^{(1)*}_{m\bar{n}}\int d\mathbf{r}F^4(\mathbf{r}). \tag{39}$$

Out of two terms on the right-hand side of identity (22), only the second term proportional to the δ function contributes to integral (39). For envelope (31), we have

$$\int d\mathbf{r}F^4(\mathbf{r}) = \frac{C}{R^3},$$

where the C coefficient is defined by formula (33).

The $r^b_{\alpha'\alpha}$ intrasite matrix elements can be allowed for with the use of formula (20). For the $\Gamma_6\times\Gamma_7$ exciton, the third term in relationship (20) after the summation over $\mathbf{R}_1\neq\mathbf{R}_2$ or the equivalent integration does not make a contribution and, instead of expression (39), we obtain

$$\left\langle \mathrm{exc},\nu'\left|U^{(\mathrm{long})}_{\mathrm{exch}}\right|\mathrm{exc},\nu\right\rangle = \frac{\pi C}{3}\hbar(\omega_{LT}-\omega^{(2)}_{LT})\frac{a_\mathrm{B}^3}{R^3}\delta_{\nu',\nu}, \tag{40}$$

where ω_{LT} and $\omega^{(2)}_{LT}$ are introduced into expression (28). The long-range contribution (40) differs from a similar contribution in formula (32) in its multiplier,

$$\gamma = \frac{\omega_{LT}-\omega^{(2)}_{LT}}{\omega_{LT}} = 1-\left(\frac{v^{(2)}_{cv}}{v_{cv}}\right)^2. \tag{41}$$

Franceschetti *et al.* [33] numerically calculated the exchange interaction in spherical nanocrystals by using the pseudopotential method. Relationship (37) or (39) corresponds to the monopole–monopole contribution to the exchange interaction according to the terminology used in [33]. In turn, the terms linear and quadratic in $\mathbf{r}^b_{\alpha'\alpha}$ correspond to the monopole–dipole and dipole–dipole contributions. Furthermore, it should be noted that the quantity q_n in formula (6) in [33], to within the common factor, coincides with the quantity defined by formula (36). For the $\Gamma_6\times\Gamma_7$ exciton in the spherical quantum dot, the dipole–dipole contribution vanishes and the monopole-dipole contribution is proportional to $\omega_{LT}-\omega^{(1)}_{LT}-\omega^{(2)}_{LT}\propto\left|v^{(1)}_{cv}v^{(2)}_{cv}\right|$. In the case of the $\Gamma_6\times\Gamma_8$ exciton, the dipole–dipole contribution is nonzero even for spherical nanocrystals. The pseudopotential calculations show that the monopole–monopole contribution to the long-range exchange interaction in the typical semiconductors CdSe, InP, and GaAs is predominant (see Table 1 in [33]). Therefore, the results of our earlier calculations (within the effective mass method) of the fine structure of exciton levels in CdSe nanocrystals [10, 12] remain valid. It can be expected that, for wide-gap semiconductors, the relative role of the $\mathbf{r}^b_{\alpha'\alpha}$ intrasite matrix elements introduced into relationships (5) and (6) will become more important and the γ coefficient will noticeably differ from unity.

Thus, we demonstrated that, for the $\Gamma_6\times\Gamma_7$ exciton in the spherical semiconductor nanocrystal, the interatomic transitions determined by the velocity operator matrix elements $\mathbf{v}^{(1)}_{mn}$ lead to the monopole–monopole contribution (38). In the coordinate representation, the corresponding contribution to the long-range exchange interaction is made by the second derivative,

$$\frac{\partial^2}{\partial r_{1,\lambda}\partial r_{2,\eta}}\frac{1}{|\mathbf{r}_1-\mathbf{r}_2|},$$

which, according to identity (22), can be written as the sum of two terms. The first term describes an interaction of the dipole–dipole type and does not affect the singlet–triplet splitting (32). The second term has the form of a δ function. However, physically, this δ function does not imply that the contribution associated with it is of a contact character and is governed by the regions with $\mathbf{r}_1$ and $\mathbf{r}_2$ lying within one or two unit cells, as is the case with short-range exchange interaction. We emphasize that the main contribution to sum (37) or integral (38) is made by the points $\mathbf{r}_1$ and $\mathbf{r}_2$ located at distances comparable to R.

In earlier works, the electron–hole exchange interaction was considered under the explicit or implicit assumption that either only interatomic [1–4, 9–12] or only intra-atomic [5, 6, 13–17] transitions contribute to the interband matrix elements of the velocity (or momentum) operator. In the present work, the analytical theory of the long-range exchange interaction with due regard for transitions of both types was constructed for the first time. Formulas (26), (27), and (40) are original.

Platonov *et al.* [32] noted that the interatomic and intra-atomic contributions to the matrix elements of optical transitions in type-II heterostructures enter in an inequivalent way. In this respect, in addition to the

investigation into the exchange interaction in type-I heterostructures, the experimental study of the lateral optical anisotropy in type-II multilayer nanostructures, such as ZnSe/BeTe or CdS/ZnSe [32, 34, 35], can be of help in assessing the role of intra-atomic transitions.

APPENDIX

Let us analyze the double sum

$$I = \sum_{\mathbf{a}_1 \neq \mathbf{a}_2} \left(\frac{\partial}{\partial a_{1,\lambda}} H_{\mathbf{a}_1}\right) \frac{1}{|\mathbf{a}_1 - \mathbf{a}_2|} \left(\frac{\partial}{\partial a_{2,\lambda}} H_{\mathbf{a}_2}\right), \quad \text{(A1)}$$

where $\mathbf{a}_{1,2}$ are the vectors of a cubic Bravais lattice and $H_{\mathbf{a}}$ is the invariant function localized within a sphere of radius R. When the radius R is considerably larger than the lattice constant a_0, the summation can be replaced by integration with division into the unit cell volume squared Ω_0^2:

$$I = \iint \frac{d\mathbf{r}_1 d\mathbf{r}_2}{\Omega_0^2} \left(\frac{\partial}{\partial r_{1,\lambda}} H_{\mathbf{r}_1}\right) \frac{1}{|\mathbf{r}_1 - \mathbf{r}_2|} \left(\frac{\partial}{\partial r_{2,\lambda}} H_{\mathbf{r}_2}\right). \quad \text{(A2)}$$

This integral can be calculated by using integration by parts and relationship (22) for the second derivative of the Coulomb potential. From symmetry considerations, it immediately follows that the first term in formula (22) does not contribute to integral (A2). The second term in formula (22) leads to the contribution

$$I = \iint \frac{d\mathbf{r}_1 d\mathbf{r}_2}{\Omega_0^2} H_{\mathbf{r}_1} \frac{4\pi}{3} \delta(\mathbf{r}_1 - \mathbf{r}_2) H_{\mathbf{r}_2} = \frac{4\pi}{3\Omega_0^2} \int d\mathbf{r} H_{\mathbf{r}}^2. \quad \text{(A3)}$$

It should be emphasized that the change-over from the differentiation of the $H_{\mathbf{a}}$ functions to the differentiation of $|\mathbf{a}_1 - \mathbf{a}_2|^{-1}$ in sum (A1) is incorrect, that is,

$$\sum_{\mathbf{a}_1 \neq \mathbf{a}_2} \left(\frac{\partial}{\partial a_{1,\lambda}} H_{\mathbf{a}_1}\right) \frac{1}{|\mathbf{a}_1 - \mathbf{a}_2|} \left(\frac{\partial}{\partial a_{2,\lambda}} H_{\mathbf{a}}\right)$$

$$\neq \sum_{\mathbf{a}_1 \neq \mathbf{a}_2} H_{\mathbf{a}_1} H_{\mathbf{a}_2} \frac{\partial^2}{\partial a_{1,\lambda} \partial a_{2,\lambda}} \frac{1}{|\mathbf{a}_1 - \mathbf{a}_2|}.$$

The left-hand sum is nonzero, whereas the right-hand side sum (at the invariant function $H_{\mathbf{a}}$) is equal to zero.

It is instructive to estimate the used approximations. When H is estimated in the order of magnitude at R^{-3}, we obtain $I \sim (\Omega_0^2 R^3)^{-1}$. According to relationship (A2), compared to the integral I, the smallness of the contribution from the $\mathbf{r}_1$ and $\mathbf{r}_2$ regions within the same unit cell to this integral can be estimated at $(a_0/R)^2 \propto (\Omega_0/R^3)^{2/3}$. Apparently, the same smallness occurs for the difference between sum (A1) over the discrete variables $\mathbf{a}_1 \neq \mathbf{a}_2$ and the double integral (A2), in which the integration variables $\mathbf{r}_1$ and $\mathbf{r}_2$ independently vary throughout the volume of the sphere with radius R. The main contribution to the integral is made by the $\mathbf{r}_1$ and $\mathbf{r}_2$ points located at distances of the order of R. Consequently, the formal use of the δ function, when changing over from formula (A2) to formula (A3), does not indicate the particular role of regions with closely spaced $\mathbf{r}_1$ and $\mathbf{r}_2$ points in distinction to short-range exchange interactions, which are intrasite in character. Therefore, at $R \gg a_0$, sum (A1) and integral (A2) remain virtually constant when the denominator $|\mathbf{a}_1 - \mathbf{a}_2|$ under the double summation sign or $|\mathbf{r}_1 - \mathbf{r}_2|$ in the integrand is replaced by $|\mathbf{a}_1 - \mathbf{a}_2 + \boldsymbol{\tau}_{b_1} - \boldsymbol{\tau}_{b_2}|$ or $|\mathbf{r}_1 - \mathbf{r}_2 + \boldsymbol{\tau}_{b_1} - \boldsymbol{\tau}_{b_2}|$, respectively, at arbitrary $\boldsymbol{\tau}_{b_1}$ and $\boldsymbol{\tau}_{b_2}$. This circumstance was already noted in Section 4 in considering the exchange interaction in a homogeneous crystal.

ACKNOWLEDGMENTS

This work was supported by the Russian Foundation for Basic Research (project no. 00-02-16997) and the Ministry of Science and Technology of the Russian Federation (Program "Physics of Nanostructures"). S.V. Goupalov acknowledges the support of the Office of Naval Research and the National Science Foundation (grants ECS-0072986, DMR-9705403, and DMR-0073364).

REFERENCES

1. G. E. Pikus and G. L. Bir, Zh. Éksp. Teor. Fiz. **60**, 195 (1971) [Sov. Phys. JETP **33**, 108 (1971)]; Zh. Éksp. Teor. Fiz. **62**, 324 (1972) [Sov. Phys. JETP **35**, 174 (1972)].
2. G. L. Bir and G. E. Pikus, *Symmetry and Strain-Induced Effects in Semiconductors* (Nauka, Moscow, 1972; Wiley, New York, 1975).
3. V. A. Kiselev and A. G. Zhilich, Fiz. Tverd. Tela (Leningrad) **14**, 1438 (1972) [Sov. Phys. Solid State **14**, 1233 (1972)]; Fiz. Tekh. Poluprovodn. (Leningrad) **8**, 641 (1974) [Sov. Phys. Semicond. **8**, 411 (1974)].
4. M. M. Denisov and V. P. Makarov, Phys. Status Solidi B **56**, 9 (1973).
5. F. Bassani and G. Pastori Parravicini, *Electronic States and Optical Transitions in Solids* (Pergamon, New York, 1975; Nauka, Moscow, 1982).
6. K. Cho, Phys. Rev. B **10**, 4463 (1976).
7. U. Rössler and H.-R. Trebin, Phys. Rev. B **23**, 1961 (1981).
8. L. C. Andreani, in *Confined Electrons and Photons*, Ed. by E. Burstein and C. Weisbuch (Plenum, New York, 1995).
9. S. V. Goupalov, E. L. Ivchenko, and A. V. Kavokin, Superlattices Microstruct. **23**, 1205 (1998).
10. S. V. Goupalov and E. L. Ivchenko, J. Cryst. Growth **184/185**, 393 (1998); Acta Phys. Pol. A **94**, 341 (1998).
11. S. V. Goupalov, E. L. Ivchenko, and A. V. Kavokin, Zh. Éksp. Teor. Fiz. **113**, 703 (1998) [JETP **86**, 388 (1998)].

12. S. V. Goupalov and E. L. Ivchenko, Fiz. Tverd. Tela (St. Petersburg) **42**, 1976 (2000) [Phys. Solid State **42**, 2030 (2000)].
13. T. Takagahara, Phys. Rev. B **47**, 4569 (1993); Phys. Rev. B **60**, 2638 (1999).
14. T. Takagahara, J. Lumin. **87–89**, 308 (2000); Phys. Rev. B **62**, 16840 (2000).
15. M. Nirmal, D. J. Norris, M. Kuno, *et al.*, Phys. Rev. Lett. **75**, 3728 (1995).
16. D. J. Norris, Al. L. Efros, M. Rosen, and M. G. Bawendi, Phys. Rev. B **53**, 16347 (1996).
17. Al. L. Efros, M. Rosen, M. Kuno, *et al.*, Phys. Rev. B **54**, 4843 (1996).
18. P. Vogl, H. P. Hjalmarson, and J. D. Dow, J. Phys. Chem. Solids **44**, 365 (1983).
19. E. L. Ivchenko, A. Yu. Kaminski, and U. Rössler, Phys. Rev. B **54**, 5852 (1996).
20. T. B. Boykin, Phys. Rev. B **56**, 9613 (1997).
21. E. L. Ivchenko, A. A. Toropov, and P. Voisin, Fiz. Tverd. Tela (St. Petersburg) **40**, 1925 (1998) [Phys. Solid State **40**, 1748 (1998)].
22. J.-M. Jancu, R. Scholz, F. Beltram, and F. Bassani, Phys. Rev. B **57**, 6493 (1998).
23. Y.-C. Chang and J. N. Schulman, Phys. Rev. B **31**, 2069 (1985).
24. Y.-C. Chang and D. E. Aspnes, Phys. Rev. B **41**, 12002 (1990).
25. G. D. Sanders and Y.-C. Chang, Phys. Rev. B **45**, 9202 (1992).
26. Z. Xu, Solid State Commun. **76**, 1143 (1990).
27. L. M. Ramaniah and S. V. Nair, Phys. Rev. B **47**, 7132 (1993).
28. L. C. Lew Yan Voon and L. R. Ram-Mohan, Phys. Rev. B **47**, 15500 (1993).
29. M. Graf and P. Vogl, Phys. Rev. B **51**, 4940 (1995).
30. B. Koopmans, P. V. Santos, and M. Cardona, Phys. Status Solidi B **205**, 419 (1998).
31. T. Dumitrică, J. S. Graves, and R. E. Allen, Phys. Rev. B **58**, 15340 (1998).
32. A. V. Platonov, V. P. Kochereshko, E. L. Ivchenko, *et al.*, Phys. Rev. Lett. **83**, 3546 (1999).
33. A. Franceschetti, L. W. Wang, H. Fu, and A. Zunger, Phys. Rev. B **58**, 13367 (1998).
34. D. R. Yakovlev, E. L. Ivchenko, V. P. Kochereshko, *et al.*, Phys. Rev. B **61**, 2421 (2000).
35. M. Schmidt, M. Grün, S. Petillon, *et al.*, Appl. Phys. Lett. **77**, 85 (2000).

Translated by O. Borovik-Romanova

Physics of the Solid State, Vol. 43, No. 10, 2001, pp. 1876–1884. Translated from Fizika Tverdogo Tela, Vol. 43, No. 10, 2001, pp. 1799–1807.

SEMICONDUCTORS AND DIELECTRICS

Polarized ARPES Spectra of Undoped Cuprates

V. A. Gavrichkov*, A. A. Borisov, and S. G. Ovchinnikov

Kirensky Institute of Physics, Siberian Division, Russian Academy of Sciences, Akademgorodok, Krasnoyarsk, 660036 Russia

**e-mail: gav@iph.krasn.ru*

Received January 10, 2001

Abstract—The spectral density (SD) in the ARPES spectra of antiferromagnetic (AFM) dielectrics $Sr_2CuO_2Cl_2$ and $Ca_2CuO_2Cl_2$ along the principal symmetry directions of the Brillouin zone was studied by the generalized tight binding method. At the valence band top of these undoped cuprates in the AFM state, there is a pseudogap of magnetic nature with $E_s(\mathbf{k}) \sim 0$–0.4 eV between a virtual level and the valence band proper. The observed similarity of dispersion along the Γ–M and X–Y directions can be explained by the proximity of the $^3B_{1g}$ triplet and the Zhang–Rice singlet levels. The value of parity of the polarized ARPES spectra at the Γ, M, and X points calculated for the AFM phase of undoped cuprates with an allowance for the partial contributions is even. The conditions favoring observation of the partial contributions in polarized ARPES spectra are indicated. Due to the spin fluctuations, the virtual level acquires dispersion and possesses a small spectral weight. Probably, this level cannot be resolved on the background of the main quasi-particle peak as a result of the damping effects. © *2001 MAIK "Nauka/Interperiodica".*

1. INTRODUCTION

Investigation of dielectrics such as $Sr_2CuO_2Cl_2$ and $Ca_2CuO_2Cl_2$ by the method of angle-resolved photoemission spectroscopy (ARPES) is a means of studying evolution of the electron structure of doped high-temperature superconductors. The available ARPES spectra, measured along the principal symmetry directions for various polarizations of synchrotron radiation, allow the valence states to be classified with respect to the symmetry properties. Indeed, data on the electron structures of both $Sr_2CuO_2Cl_2$ and $Ca_2CuO_2Cl_2$ allow three groups of the valence states to be distinguished, the first group being invariant relative to the reflection from the plane of emission and the second and third groups being even and odd with respect to this reflection. According to the selection rules [1], the ARPES spectra measured with a polarization vector parallel to the plane of emission should show only the even group of states, while the spectra recorded for the perpendicular polarization should display only the odd group. In the perpendicular geometry, the polarization vector is always parallel to the CuO_2 plane. Therefore, contributions due to the p_z and d_z valence states binding the planes into a unified tree-dimensional structure will be observed only in the spectra measured in a parallel geometry.

Let us summarize the main ARPES results [2] related to the problem under consideration:

(i) An analysis of the level occupancies $n(\mathbf{k})$ [3] obtained from the ARPES spectra of antiferromagnetic (AFM) dielectrics $Sr_2CuO_2Cl_2$ and $Ca_2CuO_2Cl_2$ shows the presence of a singularity in $n(\mathbf{k})$ at the intersection with a $\mathbf{k}$ contour (close to the Fermi surface) predicted previously based on the results of band calculations. The quasi-particle peak dispersion on the $\mathbf{k}$ contour of the "remnant Fermi surface" is close to a d-like dependence of the $|\cos(k_x a) - \cos(k_y a)|$ type. Since the last function is analogous to a d-like dispersion of the pseudogap in undoped $Bi_2Sr_2CaCu_2O_{8+\delta}$(*Dy*)and the superconducting gap in the optimum doped compound, there is an evident relationship between the three energy gap values.

(ii) On the other hand, the $|\cos(k_x a) - \cos(k_y a)|$ relationship has a linear character in the vicinity of the point $M = (\pi/2; \pi/2)$. A similar linear relationship $\sim J\sqrt{\cos^2(k_x a) - \cos^2(k_y a)}$ was observed for the dispersion of spinons [4]. However, the experimental dispersion in the vicinity of M seems to be quadratic rather than linear [2].

(iii) Although the observed dispersion is well described within the framework of the t–t'–t''–J model, there is one special point in application of this model to real systems. According to the t–t'–t''–J model, dispersion along the $\Gamma(0, 0)$–$M(\pi, \pi)$ and $X(\pi, 0)$–$Y(0, \pi)$ directions is related to different parameters (J and t', respectively). Therefore, the observed analogy of the dispersion relationships along these different directions poses inexpediently strict limitations on the model parameters. The existing explanations of the observed universality are related to the self-consistent Born approximation in the t–t'–t''–J model theory [5].

(iv) The results of experiments with polarized radiation are indicative of an even parity of the ARPES spectra of dielectrics in the symmetric points Γ, M, X, and Y [6], the value of the parity being dependent on the doping level. However, parity cannot be interpreted within the framework of the t–t'–t''–J model. For this

reason, theoretical investigations devoted to polarized ARPES spectra usually employ the local density approximation (LDA) in the density functional method (DFM) [7]. The results obtained within the framework of LDA allow the parity to be analyzed. Unfortunately, the dispersion law is not treated as successfully as is the t–t'–t''–J model. In particular, the LDA approach fails to reproduce the quasi-particle peak corresponding to the Zhang–Rice state at the valence band top.

The purpose of this study was to analyze the density of states (SD) spectrum for oxychlorides $Sr_2CuO_2Cl_2$ and $Ca_2CuO_2Cl_2$ based on the ARPES data for various polarizations. The results obtained within the framework of the generalized tight binding method (GTBM) [8] offer a natural generalization of the t–t'–t''–J model and allow clear physical interpretation.

The first section of this paper gives a brief outline of the GTBM and introduces basic formulas for the dispersion and SD. The second section presents the result of numerical calculations of the dispersion relationships and the quasi-particle peak amplitude in the spectral density along the Γ–M–X–Y and X–Y directions in the paramagnetic (PM) and AFM phases. Partial contributions to the SD due to various orbitals are calculated, which is important for identification of ARPES spectra that may differ both in the parity and in scattering cross sections for the incident radiation. The nature of the energy gap is established and the shape of dispersion is determined along the **k** contour of the remnant Fermi surface. The third section gives a symmetry analysis of the partial contributions at the Γ, M, X, and Y points and indicates polarizations for which these contributions can be observed, and the even parity of the total contribution is revealed. The fourth section considers the influence of spin fluctuations on the energy band structure of oxychlorides.

2. SPECTRAL DENSITY OF STATES IN THE GENERALIZED TIGHT-BINDING METHOD

Here, we will briefly formulate the GTBM for a CuO_6 (CuO_4Cl_2) cluster considered as a unit cell. The problem of nonorthogonality of the molecular orbitals of neighboring clusters is explicitly solved by constructing the corresponding Wannier functions on the $d_{x^2-y^2}$, $d_{3z^2-r^2}$, p_x, p_y, p_z five-orbital initial basis set of atomic states.

In the new symmetric basis set, a single-cell part of the Hamiltonian is factorized, making it possible to classify, according to symmetry, all the possible effective single-particle excitations in the CuO_2 plane. Subsequent exact diagonalization of the unit-cell Hamiltonian and the transition to the Hubbard operator representation make it possible to take into account the hopping part of the Hamiltonian.

The initial Hamiltonian of a multiband p–d model can be written in the standard form:

$$
\begin{aligned}
H &= H_d + H_p + H_{pd} + H_{pp}, \quad H_d = \sum_r H_d(r), \\
H_d(r) &= \sum_{\lambda\sigma}\Bigg[(\varepsilon_\lambda - \mu)d^+_{\lambda r\sigma}d_{\lambda r\sigma} + \frac{1}{2}U_\lambda n^\sigma_{\lambda r}n^{-\sigma}_{\lambda r} \\
&+ \sum_{\lambda'\sigma'}\left(-J_d d^+_{\lambda r\sigma}d_{\lambda r\sigma'}d^+_{\lambda' r\sigma'}d_{\lambda' r\sigma} + \sum_{r'}V_{\lambda\lambda'}n^\sigma_{\lambda r}n^{\sigma'}_{\lambda' r'}\right)\Bigg], \\
H_p &= \sum_i H_p(i), \quad H_p(i) = \sum_{\alpha\sigma}\Bigg[(\varepsilon_\alpha - \mu)p^+_{\alpha i\sigma}p_{\alpha i\sigma} \\
&+ \frac{1}{2}U_\alpha n^\sigma_{\alpha i}n^{-\sigma}_{\alpha i} + \sum_{\alpha' i'\sigma'}V_{\alpha\alpha'}n^\sigma_{\alpha i}n^{\sigma'}_{\alpha' i'}\Bigg], \\
H_{pd} &= \sum_{\langle i,r\rangle}H_{pd}(i,r), \\
H_{pd}(i,r) &= \sum_{\alpha\lambda\sigma\sigma'}(t_{\lambda\alpha}p^+_{\alpha i\sigma}d_{r\lambda\sigma} + V_{\alpha\lambda}n^\sigma_{\alpha i}n^{\sigma'}_{\lambda r}), \\
H_{pp} &= \sum_{\langle i,j\rangle}\sum_{\alpha\beta\sigma}(t_{\alpha\beta}p^+_{\alpha i\sigma}p_{\beta j\sigma} + \text{H.c.}),
\end{aligned}
\tag{1}
$$

where $n^\sigma_{\lambda i} = d^+_{\lambda i\sigma}d_{\lambda i\sigma}$ and $n^\sigma_{\alpha i} = p^+_{\alpha i\sigma}p_{\alpha i\sigma}$. Here, the indices r and i run through the positions of $d_{x^2-y^2}$, $d_{3z^2-r^2}$ and p_x, p_y, p_z sets of localized atomic orbitals. Similarly, $\varepsilon_\lambda = \varepsilon_{d_x}$ ($\lambda = d_x$), ε_{d_z} ($\lambda = d_z$) and $\varepsilon_\alpha = \varepsilon_p$ ($\alpha = p_x, p_y$), ε_{p_z} ($\alpha = p_z$) are the energies of the corresponding atomic orbitals; $t_{\lambda\alpha} = t_{pd}$ ($\lambda = d_x$; $\alpha = p_x, p_y$) and $t_{pd}/\sqrt{3}$ ($\lambda = d_z$, $\alpha = p_x, p_y$) are the matrix elements for the copper–oxygen hopping; $t_{\alpha\beta} = t_{pp}$ are the matrix elements of hopping between nearest-neighbor oxygen ions; $U_\lambda = U_d$ ($\lambda = d_x, d_z$) and $U_\alpha = U_p$ ($a = p_x, p_y, p_z$) are the interatomic Coulomb interactions on copper and oxygen atoms, respectively; and $V_{\alpha\lambda} = V_{pd}$ ($\alpha = p_x, p_y$; $\lambda = d_x, d_z$) and V'_{pd} ($\alpha = p_z$; $\lambda = d_x, d_z$) are the copper–oxygen Coulomb repulsion energies. All matrix elements of the Coulomb and exchange interaction are assumed to be independent of the shape of the d or p in-plane orbitals. The primed values refer to the interaction with apical oxygen in CuO_6 or with chlorine in CuO_4Cl_2. Subsequent steps in the conversion of Hamiltonian (1) are analogous to those described in [8]. Here, we will only write the key formulas. All calculations were carried out for the CuO_2 plane divided into CuO_6 (CuO_4Cl_2) clusters.

Using the linear transformation $\hat{S}$, we introduce the new operators $a_{k\sigma}$ and $b_{k\sigma}$ of the hole annihilation in the molecular orbitals of oxygen:

$$\begin{pmatrix} b_{k\sigma} \\ a_{k\sigma} \end{pmatrix} = \hat{S}\begin{pmatrix} p_{xk\sigma} \\ p_{yk\sigma} \end{pmatrix} = \begin{pmatrix} is_x/\mu_k & is_y/\mu_k \\ is_y/\mu_k & -is_x/\mu_k \end{pmatrix}\begin{pmatrix} p_{xk\sigma} \\ p_{yk\sigma} \end{pmatrix}, \quad (2)$$

$$\mu_k^2 = s_x^2 + s_y^2, \quad |\hat{S}| = 1.$$

The new operators satisfy the required commutation relationships $\{b_{k\sigma}^+, a_{p\sigma}\} = 0$. In the new representation, Hamiltonian (1) acquires the form of a sum of intracell (H_c) and intercell (H_{cc}) contributions

$$H = H_c + H_{cc}, \; H_c = \sum_{f\sigma} H_{f\sigma}, \; H_{f\sigma} = h^{(a)} + h^{(b)} + h^{(ab)},$$

$$h^{(b)} = (\varepsilon_b n_b^\sigma + \varepsilon_{d_x} n_{d_x}^\sigma) + \frac{1}{2}U_d n_{d_x}^\sigma n_{d_x}^{-\sigma}$$

$$+ \frac{1}{2}U_b n_b^\sigma n_b^{-\sigma} + \sum_{\sigma'} V_{pd} n_{d_x}^\sigma n_b^{\sigma'} - \tau_b(d_{x\sigma}^+ b_\sigma + \text{H.c.}),$$

$$h^{(a)} = (\varepsilon_a n_a^\sigma + \varepsilon_{d_z} n_{d_z}^\sigma + \varepsilon_{p_z} n_{p_z}^\sigma) + \frac{1}{2}U_d n_{d_z}^\sigma n_{d_z}^{-\sigma} + \frac{1}{2}U_a n_a^\sigma n_a^{-\sigma}$$

$$+ \frac{1}{2}U_p' n_{p_z}^\sigma n_{p_z}^{-\sigma} + \sum_{\sigma'}(V_{pd} n_{d_z}^\sigma n_{p_z}^{\sigma'} + V_{pd} n_{d_z}^\sigma n_a^{\sigma'})$$

$$+ \tau_a(d_{z\sigma}^+ a_\sigma + \text{h.c.}) - \tau_{pd}'(d_{z\sigma}^+ + \text{h.c.}) - t_{pp}'(a_\sigma^+ p_{z\sigma} + \text{h.c.});$$

$$h^{(ab)} = \sum_{\sigma'} U_d n_{d_x}^\sigma n_{d_x}^{\sigma'} + U_{ab} n_a^\sigma n_b^{\sigma'}$$

$$+ V_{pd} n_{d_x}^\sigma n_a^{\sigma'} + V_{pd} n_b^\sigma n_{d_z}^{\sigma'} + V_{pd}' n_{d_x}^\sigma n_{p_z}^{\sigma'}, \quad (3)$$

$$H_{cc} = \sum_{(i \neq j)} \sum_\sigma (h_{\text{hop}}^{(b)} + h_{\text{hop}}^{(a)} + h_{\text{hop}}^{(ab)}),$$

$$h_{\text{hop}}^{(b)} = -2t_{pd}\mu_{ij}(d_{xi\sigma}^+ b_{j\sigma} + b_{i\sigma}^+ d_{xi\sigma}) - 2t_{pp}\nu_{ij} b_{i\sigma}^+ b_{j\sigma},$$

$$h_{\text{hop}}^{(a)} = \frac{2t_{pd}}{\sqrt{3}}\lambda_y(d_{zi\sigma}^+ a_{j\sigma} + \text{H.c.})$$

$$+ 2t_{pp}\nu_{ij} a_{i\sigma}^+ a_{j\sigma} - 2t_{pp}'\lambda_{ij}(p_{zi\sigma}^+ a_{j\sigma} + \text{H.c.}),$$

$$h_{\text{hop}}^{(ab)} = \frac{2t_{pd}}{\sqrt{3}}\xi y(d_{zi\sigma}^+ b_{j\sigma} + \text{H.c.})$$

$$+ 2t_{pp}\chi_{ij}(a_{i\sigma}^+ b_{j\sigma} + \text{h.c.}) - 2t_{pp}'\xi_{ij}(p_{zi\sigma}^+ b_{j\sigma} + \text{H.c.}),$$

where

$$\varepsilon_b = \varepsilon_p - 2t_{pp}\nu_{00}, \quad \varepsilon_a = \varepsilon_p + 2t_{pp}\nu_{00},$$

$$\tau_b = 2t_{pd}\mu_{00}, \quad \tau_a = 2t_{pd}\lambda_{00}/\sqrt{3},$$

$$\tau_{pd}' = 2t_{pd}'/\sqrt{3}, \quad \tau_{pp}' = 2t_{pp}'\lambda_{00}.$$

The coefficients μ_{ij}, ν_{ij}, and λ_{ij} concern to the hybridization of states of the same symmetry and depend only on the distance between the ith and jth cells. The coefficients ξ_{ij} and χ_{ij} concern to the hybridization of states belonging to different a_1 and b_1 representations and change sign upon reflection along either the x and y axis. Expressions for these coefficients are derived in [8, 9].

Now let us determine the eigenvalues and eigenstates of the single-cell Hamiltonian H_c, after which the total Hamiltonian can be rewritten in terms of these eigenstates. In the vacuum sector, the eigenstate is $a^{10}p^6$ or $|0\rangle$. In the single-hole b_1 sector on the basis of $|d_{x\sigma}^+|0\rangle$ and $|b_\sigma^+|0\rangle$ states, the eigenvectors $|\tilde{b}_p\rangle = \beta_p(b)|b_\sigma^+|0\rangle + \beta_p(d_x)|d_{x\sigma}^+|0\rangle$ with the energies $\varepsilon_{1\tilde{b}_p}$ (p = 1, 2) can be found through exact diagonalization of the matrix:

$$\hat{h}^{(b)} = \begin{pmatrix} \varepsilon_{d_x} & -\tau_b \\ -\tau_b & \varepsilon_b \end{pmatrix}. \quad (4)$$

In the single-hole a_1 sector on the basis of $|a_\sigma^+|0\rangle$, $|p_{z\sigma}^+|0\rangle$, and $|d_{z\sigma}^+|0\rangle$ states, the eigenvectors $|\tilde{a}_p\rangle = \alpha_p(a)|a_\sigma^+|0\rangle + \alpha_p(p_z)|p_\sigma^+|0\rangle + \alpha_p(d_z)|d_{z\sigma}^+|0\rangle$ with the energies $\varepsilon_{1\tilde{a}_p}$ (p = 1, 2, 3) can be found through exact diagonalization of the matrix:

$$\hat{h}^{(a)} = \begin{pmatrix} \varepsilon_{d_z} & \tau_a & -\tau_{pd}' \\ \tau_a & \varepsilon_a & -t_{pd}' \\ -\tau_{pd}' & -t_{pd}' & \varepsilon_{p_z} \end{pmatrix}. \quad (5)$$

By the same way, we determine the eigenstates $|\tilde{A}_q\rangle$ with the energies $\varepsilon_{2\tilde{A}_q}$ in the two-hole A_1 sector $|\tilde{A}_q\rangle = \sum_i A_{qi}|A_i\rangle$, where the coefficients are the eigenvectors A_i (i, q = 1–9), and the basis set of singlet functions $|\tilde{A}_q\rangle$. One of these basis set states represents the Zhang–Rice singlet $|\text{ZR}\rangle$. In the two-hole B_1 sector, we find the triplet eigenvectors $|\tilde{B}_{qM}\rangle = \sum_i B_{qi}|B_{iM}\rangle$ (q = 1– 6; M = –1, 0, 1) with the energies $\varepsilon_{2\tilde{B}_q}$, coefficients B_{qi}, and basis set functions $|B_{qM}\rangle$. Thus, diagonalization of the Hamiltonian for a CuO_6 (CuO_4Cl_2) cluster is performed separately in various sectors with the number of holes n = 0, 1, or 2.

Previously [10], we found two basic possibilities for stabilizing the $|\tilde{B}_{1M}\rangle$ state as the ground state: (i) with decreasing energy of the p orbitals of O (or Cl) ions in the apical position and (ii) with decreasing crystal-field

parameter $\Delta_d = \varepsilon_{d_z} - \varepsilon_{d_x}$. According to estimates [10], the energy interval between triplet and singlet sates is $\Delta\varepsilon_2 \sim 0.5$ eV. The existence of two states $|\tilde{A}_1\rangle$ and $|\tilde{B}_{1M}\rangle$ with competing energies in the region of realistic values of the parameters implies that both these states have to be taken into account as basis states in our model and that no further reduction to an effective single-band Hubbard model or the *t*–*t*'–*t*"–*J* model is possible. As a result of the exact diagonalization, the Hamiltonian H_c for the AFM phase acquires the following form:

$$H_c = \sum_{pf_G\sigma}(\varepsilon_{1pG} - \mu)X^{pp}_{f_G\sigma} + \sum_{qf_G\sigma}(\varepsilon_{2qG} - 2\mu)X^{qq}_{f_G\sigma}, \qquad f_G = \begin{cases} f_A, & f \in A \\ f_B, & b \in B. \end{cases} \tag{6}$$

Here, *p* and *q* enumerate the single- and two-hole terms of a cell, respectively, and $X^{pq}_f = |p\rangle\langle q|$ are the Hubbard operators constructed on the exact states of the cell. The sublattice levels are split by the field of the AFM state: $\varepsilon_{1pA} = \varepsilon_{1p} - \sigma h$, $\varepsilon_{1pB} = \varepsilon_{1p} + \sigma h$, where the quantity $h \sim J\langle S_z\rangle$ and *J* is the effective exchange interaction between nearest neighbors. As the doping level increases, the *h* value drops to vanish completely in the PM phase. In this paper, the consideration is restricted to a non-self-consistent calculation in which the magnetic state is assumed to be known (AFM or PM at *T* = 0). In the new basis set, the single-electron operators are expressed as

$$c_{f\lambda\sigma} = \sum_m \gamma_{\lambda\sigma}(m)X^m_{f\sigma}, \tag{7}$$

where $c_{\lambda f\sigma} = d_{xf\sigma}, d_{zf\sigma}, a_{f\sigma}, b_{f\sigma}, p_{zf\sigma}$ and *m* is the number of the root vector $\boldsymbol{\alpha}_m(pq)$. To simplify treatment of the Hubbard operators, we use a convenient notation proposed by Zaĭtsev [11]. The matrix elements $\gamma_{\lambda\sigma}(m)$ (m = 0, 1, …, 31) corresponding to the above root vectors can be directly calculated upon exact diagonalization of the Hamiltonian H_c; the results of such a calculation are presented in [8]. We take into account only two lower terms: b_1, a_1 in the single-particle sector and $\tilde{A}_1$, $\tilde{B}_{1M}$ in the two-particle sector. This corresponds to $|p\rangle = |\tilde{a}_1\rangle$, $|\tilde{b}_1\rangle$ and $|q\rangle = |\tilde{A}_1\rangle$, $|\tilde{B}_{1M}\rangle$ in Eq. (6). All other terms correspond to higher energies and can be ignored as far as the physics of low-energy excitations is considered. The corresponding dispersion relationships for the valence band were derived using equations of motion for Green's functions constructed on Hubbard operators:

$$C^{\lambda\lambda'}_{k\sigma} = \langle\langle c_{k\lambda\sigma}|c^+_{k\lambda'\sigma}\rangle\rangle_E = \sum_{mn}\gamma_{\lambda\sigma}(m)\gamma^+_{\lambda'\sigma}(n)D^{mn}_{k\sigma}, \tag{8}$$

where

$$\hat{D}_{k\sigma} = \begin{pmatrix} \hat{D}_{k\sigma}(AA) & \hat{D}_{k\sigma}(AB) \\ \hat{D}_{k\sigma}(BA) & \hat{D}_{k\sigma}(BB) \end{pmatrix},$$

$$D^{mn}_{k\sigma}(AB) = \langle\langle X^m_{k\sigma}|Y^n_{k\sigma}\rangle\rangle_E.$$

In the Hubbard I approximation, the dispersion relationship is determined by the equation

$$\left\| (E - \Omega^G_m)\delta_{mn}/F^G_\sigma(m) - 2\sum_{\lambda\lambda'}\gamma^*_{\lambda\sigma}(m)T^{PG}_{\lambda\lambda'}(\mathbf{k})\gamma_{\lambda'\sigma}(n) \right\| = 0. \tag{9}$$

This relationship is similar to the standard single-electron equation for the tight-binding method but differs from the latter in two respects. First, the single-particle energies are determined as resonances between multielectron states. Second, the occupation factors $F^G_\sigma(m) = \langle X^{pq}_{f_G\sigma}\rangle + \langle X^{qq}_{f_G\sigma}\rangle$ lead to a concentration dependence of both the dispersion relationships and the quasi-particle peak amplitude in the SD. Mathematically, we deal with an equation of the generalized eigenvalue problem, with the matrix of the inverse occupation factors replacing the ordinary "nonorthogonality matrix." Each root vector $\boldsymbol{\alpha}_m$ determines a charged Fermi quasi-particle with spin 1/2 and local energy $\Omega^G_m = \varepsilon_{2qG} - \varepsilon_{1pG}$.

Equation (9) is a convenient means of calculating the dispersion relationships, which allows all possible quasi-particle states to be determined. However, not all of these theoretically possible sates can be observed in experiment. As is known, the ARPES measurements give the amplitude of the quasi-particle peaks in SD

$$A_\sigma(\mathbf{k}, E) = \left(-\frac{1}{\pi}\right)\sum_\lambda \mathrm{Im}(G^{\lambda\lambda}_{k\sigma}) = \left(-\frac{1}{\pi}\right)\sum_{\lambda mn}\gamma_{\lambda\sigma}(m) \times \gamma^+_{\lambda\sigma}(n)\mathrm{Im}(D^{mn}_{k\sigma}(AA) + D^{mn}_{k\sigma}(BB)), \tag{10}$$

rather than a dispersion law as such. Owing to the corresponding occupation factors, the SD may become negligibly small or even vanish for some quasi-particles. As a result, the corresponding peak will be missing from the spectrum. The high dimensionality of the $\hat{D}_{k\sigma}$ matrix (32×32) makes analytical representation of SD impossible. We have performed a numerical calculation of the SD using relationship (10) for the principal symmetry directions of the Brillouin zone at *T* = 0. For the PM phase, the dispersion law and the SD can be obtained using single- sublattice analogs of Eqs. (9) and (10).

3. NUMERICAL CALCULATION OF SPECTRAL DENSITY

Figure 1 shows the results of the numerical calculation of dispersion along the principal symmetry directions of the Brillouin zone for a quasi-particle peak at the valence band top of $Sr_2CuO_2Cl_2$ and $Ca_2CuO_2Cl_2$ compounds in the AFM and PM states at $T = 0$. In the PM phase, the calculated dispersion law is analogous to that observed in optimum doped samples of $Bi_2Sr_2CaCu_2O_{8+\delta}(Dy)$ [12]. The most interesting feature of our theoretical spectrum is the presence of an energy level with a zero SD at the very top of the valence band, which is not manifested in the experimental ARPES spectra. Indeed, the undoped AFM sample contains only $\boldsymbol{\alpha}_{0\sigma}(\tilde{b}_{1\uparrow} - \tilde{A}_1)$ and $\boldsymbol{\alpha}_{0\sigma}(\tilde{b}_{1\downarrow} - \tilde{A}_1)$ quasi-particles at the valence band top. At zero temperature, with neglect of the quantum fluctuations, the filling numbers for a single-hole $|\tilde{b}_{1\sigma}\rangle$ state in one of the spin projections are zero for both *A* and *B* sublattices. Therefore, one of the spin projections in the undoped compound possesses a nondispersive level called the virtual level [8]. Since the transitions between empty states have zero amplitude, a peak corresponding to transitions involving this level is not observed in the SD. This is a typical manifestation of the strong correlation effect.

Thus, the energy gap between the valence and conduction band in oxychlorides at $T = 0$ can be represented as $E_g(\mathbf{k}) = E_{ct}(\mathbf{k}) + E_S(\mathbf{k})$, where $E_{ct}(\mathbf{k})$ is the charge transfer gap and $E_S(\mathbf{k})$ is the gap between the virtual level and the valence band. Since both these terms refer to quasi-particles of the same type (with the same spin projection) existing on the background of different components of the spin doublet $|b_\sigma\rangle$, the gap $E_S(\mathbf{k})$ has a magnetic nature and is absent in the PM phase. Taking into account the absence of the main characteristic signs of the semiconductor gap and the zero value at $\mathbf{k} = M$, the $E_S(\mathbf{k})$ value will be referred to as the pseudogap.

Figure 2 presents the dispersion of the pseudogap $E_S(\mathbf{k})$ along the boundary of the AFM Brillouin zone on the background of the *d*-like dependence of the $|\cos(k_x a) - \cos(k_y a)|$ type. This diagram demonstrates a clear relationship between the pseudogap in AFM dielectrics, the pseudogap in weakly doped compounds, and the superconducting gap in optimum doped samples [2]. Proximity of the calculated law to the experimentally observed dispersion [2] suggests that the **k** contour of the remnant Fermi surface observed by Ronning *et al.* [3] in AFM dielectric $Ca_2CuO_2Cl_2$ can be an ARPES signal from the valence band. A possible reason for this is the purely two-dimensional character of the quasi-particle states on any **k** contour close to the $X \rightleftharpoons Y$ contour. In all other symmetry directions, the calculation reproduces nonzero contributions to SD from the out-of-plane d_z and p_z molecular orbitals (see below). The factors $T_{\lambda\lambda'}(k) = \frac{1}{N}\sum_{R_i} T_{\lambda\lambda'}(\mathbf{R}_i) e^{ikR_i}$ in Eq. (9) contain no inter-sublattice terms for any **k** on the $X \rightleftharpoons Y$ contour, so that the dispersion along this contour can be only of the $\sim\cos(k_x a)\cos(k_y a)$ type. As expected, this dispersion curve precisely fits the results of our numerical calculation (Fig. 2). The experiment more likely corresponds to a linear dispersion in the vicinity of the point *M* [2] and we believe that it is not $|\cos(k_x a) - \cos(k_y a)|$, but it is $\cos(k_x a)\cos(k_y a)$ relationship.

According to the results of our calculations, a reason for the similar dispersion patterns observed in the AFM phase along the Γ–*M* and *X*–*Y* symmetry directions is a

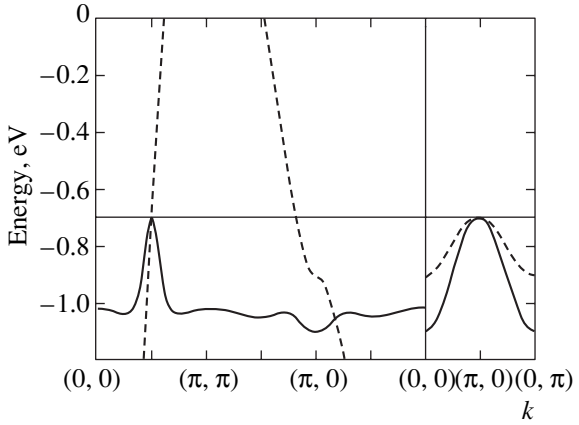

Fig. 1. Dispersion at the valence band top along the main symmetry directions of the Brillouin zone of the AFM (solid curve) and PM (dashed curve) phases at $T = 0$ calculated by Eq. (9).

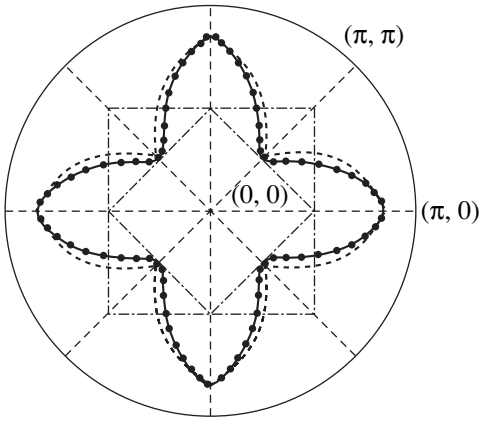

Fig. 2. Dispersion of the $E_S(\mathbf{k})$ pseudogap along the $X \rightleftharpoons Y$ contour, representing $|\cos(k_x a) - \cos(k_y a)|$ (dashed curve), $|\cos(k_x a)\cos(k_y a)|$ (solid curve), and numerical calculations by formula (9) (points). The dispersion is given by the distance from the AFM Brillouin zone boundary to the point of calculation.

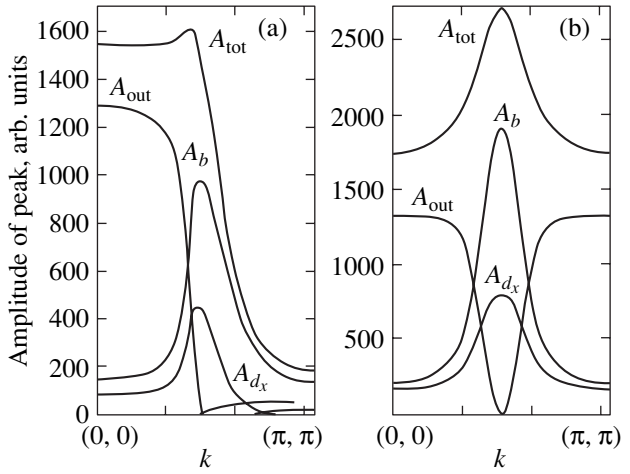

Fig. 3. **k**-Dependences of the partial contributions to the quasi- particle peak amplitude along the Γ–*M* direction for (a) PM and (b) AFM phases.

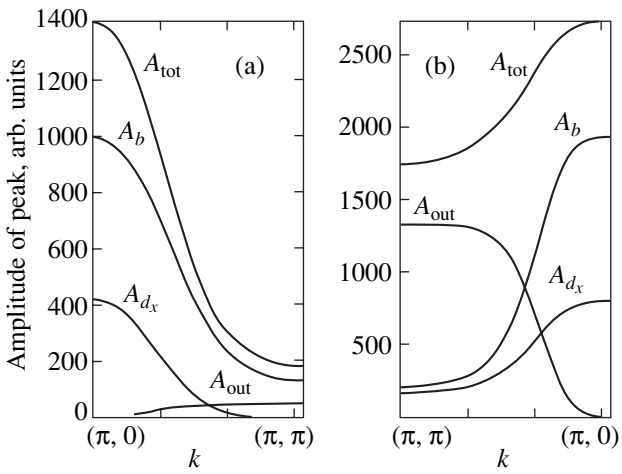

Fig. 4. **k**-Dependences of the partial contributions to the quasi- particle peak amplitude along the *M*–*X* direction for (a) PM and (b) AFM phases.

strong hybridization of the valence band of the Zhang–Rice singlet and the lower band of the $^3B_{1g}$ triplet at the points Γ and *M*. According to our data, the observed similarity is determined only by the values of parameters related to apical Cl or O ions. In addition, our results reveal a strong anisotropy of the effective mass in the vicinity of $\mathbf{k} = M$ ($m_{\text{eff}}^{XY}/m_{\text{eff}}^{\Gamma M} \sim 10$). Therefore, the similarity refers only to the dispersion width in these directions.

The SD $A(\mathbf{k}, E)$ was calculated along the four principal symmetry directions of the Brillouin zone: Γ–*M*, *M*–*X*, *X*–Γ, and *X*–*Y* for PM and AFM phases. According to Eq. (10), the SD is additive. Therefore, we may determine the partial SD contributions due to all orbitals involved in the calculation:

$$A(\mathbf{k}, E) = \sum_{\lambda\sigma} A_{\lambda\sigma}(\mathbf{k}, E),$$

where $\lambda = d_x$, *b*, *a*, d_z, and p_z. As will be demonstrated below, the additive representation offers a convenient approach to analysis of the polarized ARPES spectra.

Figures 3a and 3b show **k**-dependences of the SD amplitude and the partial contributions along the Γ–*M* symmetry direction for AFM and PM phases, respectively. For realistic values of the parameters used in the calculation [8], the $^3B_{1g}$ triplet level is 0.7 eV higher than the A_{1g} level of the Zhang–Rice singlet. As expected, the **k**-profile of the quasi-particle peak amplitude loses symmetry relative to the point *M* upon transition to the PM phase. If the contribution due to the out-of-plane orbitals $A_{\text{out}}(\mathbf{k}, E) = A_{d_z}(\mathbf{k}, E) + A_{p_z}(\mathbf{k}, E)$ is still dominant at $\mathbf{k} = \Gamma$, the quasi-particle peak amplitude at the point *M* significantly decreases. The residual SD at this symmetry point is due to the admixture of states from the conduction band involving only in-plane d_x and *b* orbitals.

Figures 4a and 4b show the **k**-dependences of the quasi-particle peak amplitude along the *M*–*X* symmetry direction of the Brillouin zone. In both AFM and PM phases, only the in-plane *b* and d_x orbitals $A_{\text{pl}}(\mathbf{k}, E) = A_{d_x}(\mathbf{k}, E) + A_b(\mathbf{k}, E)$ contribute at the point $\mathbf{k} = X$, while the contributions from p_z and d_z states at this symmetry point vanish. The total amplitude of SD monotonically increases along the *M*–*X* direction in both AFM and PM phases. Of special interest was the symmetry direction Γ–*X* (Figs. 5a, 5b). Here, in addition to the analogous suppression of the partial contribution $A_{\text{out}}(\mathbf{k}, E)$ at the point $\mathbf{k} = X$, there is a crossover from monotonic growth

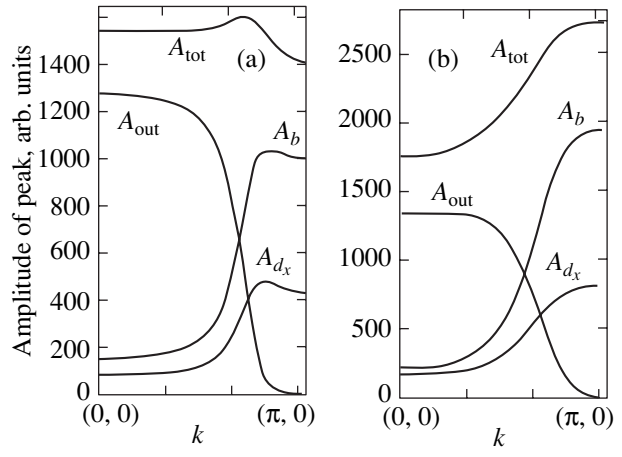

Fig. 5. **k**-Dependences of the partial contributions to the quasi- particle peak amplitude along the Γ–*X* direction for (a) PM and (b) AFM phases.

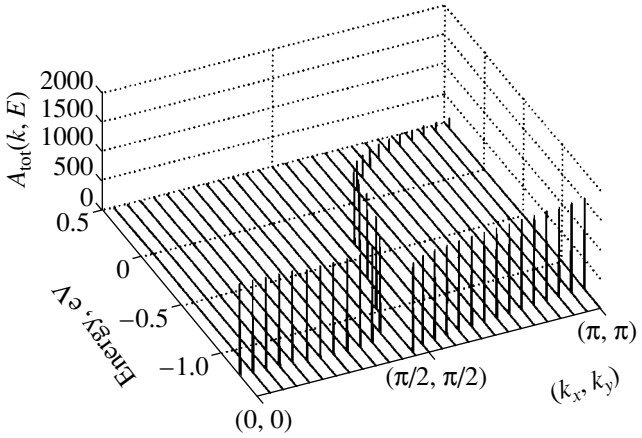

Fig. 6. Three-dimensional **k**-dependences of the amplitude of the quasi-particle peak along the Γ–*M* direction for the PM phase.

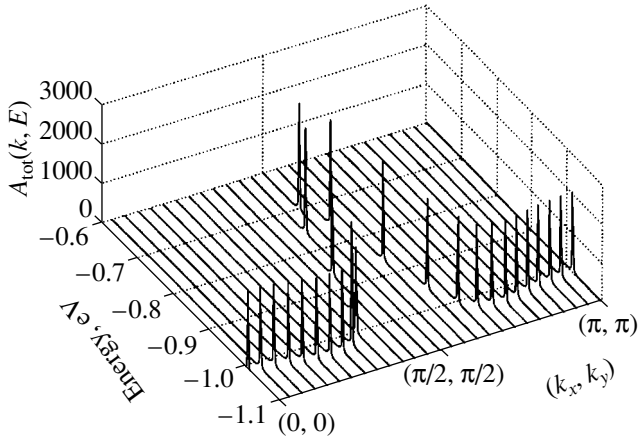

Fig. 7. Three-dimensional **k**-dependences of the amplitude of the quasi-particle peak along the Γ–*M* direction for the AFM phase.

in the quasi-particle peak amplitude in the AFM phase to nonmonotonic behavior with a maximum at **k** = $(2\pi/3, 0)$ in the PM phase. An analogous maximum was observed in the ARPES spectra of $Ca_2CuO_2Cl_2$ at T = 150 K [2]. An analysis of the eigenstates in this symmetry direction showed that a maximum at the point ~$(2\pi/3, 0)$ in the PM phase is related to a maximum admixture of the states from the conduction band. The same factor accounts for a maximum in the partial contributions of the in-plane b and d_x orbitals. Along the *X*–*Y* symmetry direction, the quasi-particle peak amplitude containing only the $A_{d_x}(\mathbf{k}, E)$ and $A_b(\mathbf{k}, E)$ contributions is virtually independent of the wavevector.

Figures 6 and 7 show three-dimensional view of $A(\mathbf{k}, E)$ along the Γ–*M* direction. The spectra of both PM and AFM phases exhibit no quasi-particle peak in the region of virtual level energies. The spectrum of the PM phase shows evidence of a triplet contribution to the quasi-particle peak amplitude.

4. POLARIZATION DEPENDENCE OF THE ARPES SPECTRA

Additional information on the nature of states in the valence band can be obtained by comparing ARPES spectra measured using parallel and perpendicular polarizations of the electric vector relative to the photoemission plane.

Let us analyze the polarization dependence of the SD (10) with allowance for parity and the magnitude of the partial contributions. The ARPES spectra will be considered with neglect of the magnetic scattering effects, which are small compared to the charge scattering effects as reflected by the factor $(\hbar\omega/mc^2)$. However, the charge effects are significantly influenced by the presence and type of magnetic ordering.

Data summarized in the table show the **k** groups, irreducible representations, and parities of the in-plane and out-of-plane orbital contributions to the total SD in the Γ, *X*, and *M* symmetry points of the Brillouin zone for the AFM phase. As is seen from these data, the presence of a nonzero photocurrent at the point Γ is related to a small E_u irreducible representation of the **k** group for $\alpha_{0\sigma}(\tilde{b}_{1,\sigma'}\tilde{A}_1^{-1})$ quasi-particles rather than to an additional (satellite) quasi-particle state. A special feature of the photocurrent observe-d at the center of the Brillouin zone is that this signal is proportional only to the SD contribution from oxygen orbitals. The parity of the total SD $A_{tot}(\mathbf{k}, E)$ is indicated with allowance for the partial contributions at the corresponding points of the Brillouin zone.

The states of different parity in the valence band can be probed separately by changing the sample orientation during the ARPES measurements in combination with the linearly polarized radiation. Moreover, it is even possible to observe evolution of the parity with variation of the doping level [6]. In the SD of oxychlorides, a quasi-particle peak was observed in the Γ–*M* and Γ–*X* directions only for the parallel experimental geometry. This is possible only provided that the valence states are even. A simple comparison with the results of polarized ARPES measurements [6] shows that the calculated parity agrees with that observed for the undoped compounds. Since the even parity at the points Γ and *M* is due to the out-of-plane contribution $A_{out}(\mathbf{k}, E)$, the quasi-particle peak amplitude must also depend on the angle of incidence of a radiation polarized in the parallel direction.

5. EFFECT OF SPIN FLUCTUATIONS ON THE BAND STRUCTURE OF ANTIFERROMAGNETS

In our non-self-consistent approach, dependence of the electron structure on the magnetic ordering is mediated by the occupation factors $F_\sigma(m)$ entering into Eq. (9). At

The characteristics of partial contributions to the total SD amplitude in polarized ARPES

	I	II	III	IV
	$\Gamma(D_{4h})$–$M(D_{4h})$		Γ–$X(D_{2h})$	
A_{d_x}	Odd (B_{1g})	Odd (B_{1g})	Even	Even (A_g)
A_b	0 (E_u)	Odd (B_{1g})	0	Even (A_g)
$A_{\text{in}} = A_{d_x} + A_b$	0 + Odd	Odd	0 + Even	Even
A_a	0 (E_u)	Even (A_{1g})	0	Odd (B_{2u})
$A_{\text{out}} = A_{d_z} + A_{p_z} + A_a$	~Even (A_{1g})	Even (A_{1g})	~Even	~Even (A_g)
$A_{\text{tot}} = A_{\text{in}} + A_{\text{out}}$	~Even	~Even	~Even	~Even

Note: Experimental observation conditions: (columns I and III) A_{d_x}, A_b, and A_{out} are observed using perpendicular, arbitrary, and parallel polarization, respectively; (column II) A_{in} and A_{out} are observed using perpendicular and parallel polarization, respectively; (column IV) A_{in} and A_{out} are observed using parallel polarization.

a valence band top, the determining role belongs to the quasi-particles $\boldsymbol{\alpha}_{0\sigma}(\tilde{b}_{1,\sigma'} - {}^1\tilde{A}_1)$, $\boldsymbol{\alpha}_{1\sigma}(\tilde{b}_{1,\sigma'} - {}^3\tilde{B}_{1,0})$, and $\boldsymbol{\alpha}_{2\sigma}(\tilde{b}_{1,\sigma'} - {}^3\tilde{B}_{1,2\sigma})$; in the case of undoped oxychlorides featuring unoccupied two-hole terms, $F_{\sigma'}(\boldsymbol{\alpha}_{1\sigma}) = \langle n_{\tilde{b},\sigma'}\rangle$. For nonzero matrix elements $\gamma_{\lambda\sigma}(m)$ (m = 0, 1, …, 31) given by (7), the occupation factors in the AFM phase with sublattices A: $\langle S_A^z\rangle = \langle S^z\rangle$ and B: $\langle S_B^z\rangle = -\langle S^z\rangle$ can be written in the following form ($\sigma = \pm 1/2$): $F^G_{-\sigma}(\boldsymbol{\alpha}_{0\sigma}) = F^G_{-\sigma}(\boldsymbol{\alpha}_{1\sigma}) = 1/2 - 2\sigma\langle S_G^z\rangle$, $F^G_{\sigma}(\boldsymbol{\alpha}_{2\sigma}) = 1/2 + 2\sigma\langle S_G^z\rangle$ (where $G = A, B$). To the present moment we restricted the consideration to the Ising order, assuming that $\langle S^z\rangle = 1/2$. The simplest way to provide for a self- consistent calculation is to construct an effective Hamiltonian in the form of a Heisenberg Hamiltonian with an antiferromagnetic exchange term J, followed by a self-consistent calculation of $\langle S^z\rangle$. Thus, we may take into account the local spin fluctuations (zero-point fluctuations in the AFM phase), while allowance for the nonlocal fluctuations of the $\langle S_i^+ S_j^-\rangle$ type would require going beyond the scope of the Hubbard I approximation adopted in this study. A detailed analysis of the applicability of such methods and comparison with the available results on the magnetic polarons in the t–t'–J model were made in [13].

As is known, the presence of the zero-point fluctuations gives rise to quantum spin reduction: $\langle S^z\rangle = 1/2 - n_0$, where the n_0 value can be calculated by different methods. According to the spin wave theory, two-dimensional antiferromagnets are characterized by $n_0 \approx 0.2$ [14]. Allowance for the spin fluctuations significantly modifies the energy band structure (Fig. 8). Indeed, the nondispersed level in Fig. 1 has a zero dispersion and a zero spectral weight because $F^A_{\downarrow}(\boldsymbol{\alpha}_{0\uparrow}) = 0$ in the Ising calculation variant. Owing to the spin fluctuations, the occupation factors are $F^A_{\downarrow}(\boldsymbol{\alpha}_{0\uparrow}) = n_0$ and $F^B_{\downarrow}(\boldsymbol{\alpha}_{0\uparrow}) = 1 - n_0$, which yields a nonzero dispersion and a spectral weight ~n_0. Thus, in the presence of spin fluctuations, the band structure of an undoped antiferromagnet is similar to the band structure of a doped Ising ferromagnet with a hole concentration of $x = n_0$. Because of the small spectral weight of the corresponding band, this band appears as a low-energy satellite in the ARPES spectrum. It is not excluded that the damping effects exclude the possibility of resolving this peak. Nevertheless, such satellites, the intensity of which (as well as of the spin fluctuations) increases with the temperature T,

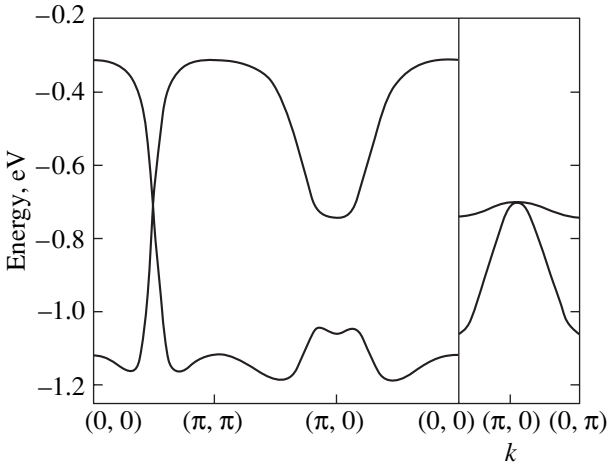

Fig. 8. Dispersion at the valence band top along the main symmetry directions of the Brillouin zone of the AFM phase calculated with an allowance for the spin fluctuations (quantum spin reduction $n_0 = 0.1$).

were recently obtained in calculations performed by the quantum Monte Carlo method within the framework of the Hubbard model [15].

6. CONCLUSIONS

To summarize the results of our calculations, subsequent analysis, and comparison with experimental ARPES data, we point out the following.

(i) Owing to a small energy gap (~0.7 eV) between the $^3B_{1g}$ triplet level and the Zhang–Rice singlet level, a strong hybridization of the singlet valence band and the lower $^3B_{1g}$ triplet band takes place at the Γ and *M* symmetry points. This hybridization accounts for the like patterns of dispersion observed in the Γ–*M* and *X*–*Y* directions of the AFM phase. However, our calculations predict anisotropy of the effective mass at $\mathbf{k} = M$ with a ratio of $m_{\text{eff}}^{XY}/m_{\text{eff}}^{\Gamma M} \approx 10$. On the whole, the valence band does not possess a two-dimensional character. As a result, when the angle of incidence of radiation polarized parallel to the plane of emission deviates from normal, the amplitude of the quasi-particle peak at the Γ and *M* symmetry points in the AFM phase will increase.

(ii) At the valence band top of $Sr_2CuO_2Cl_2$ and $Ca_2CuO_2Cl_2$ in the AFM state, there is a pseudogap of magnetic nature with $E_s(\mathbf{k}) \sim 0$–0.4 eV between a virtual level and the valence band proper; the gap vanishes at the point *M* of the Brillouin zone. The virtual level corresponds to a small SD at $T = 0$, which is proportional to the zero-point spin fluctuation density n_0. Dispersion of the pseudogap in the *X*–*Y* direction agrees well with that on the **k** contour of the remnant Fermi surface. Contribution to the SD in this direction is entirely due to the in-plane d_x and *b* orbitals and, hence, the spectrum has essentially a two-dimensional character. In the PM phase, the pseudogap is absent and the valence band dispersion is analogous to that of $Bi_2Sr_2CaCu_2O_{8+\delta}$(*Dy*) doped to the optimum level [12].

(iii) The parity calculated for the ARPES spectra at the points Γ, *M*, and *X* of the AFM phase with allowance for the partial contributions is even, in agreement with [6]. The presence of a nonzero photocurrent at Γ is related to a small E_u irreducible representation for the $\boldsymbol{\alpha}_{0\sigma}(\tilde{b}_{1,\sigma'} - {}^1\tilde{A}_1)$ quasi-particle state with $\mathbf{k} = \Gamma$ rather than to an additional satellite state. A special feature of the photocurrent observed at the center of the Brillouin zone is that this signal is proportional only to the SD contribution from in-plane oxygen orbitals.

(iv) Allowance for the spin fluctuations significantly modifies the energy band structure. Indeed, the nondispersed level in the AFM phase has a zero dispersion and a zero spectral weight in the Ising calculation scheme. Owing to the spin fluctuations, the level acquires nonzero dispersion and spectral weight. Thus, in the presence of spin fluctuations, the band structure of oxychlorides is similar to the band structure of a doped Ising ferromagnet. Owing to the small spectral weight acquired by the virtual level due to the spin fluctuations, this band appears as a low-energy satellite in the ARPES spectrum. It is not excluded that the damping effects exclude the possibility of observing this peak against the background of the main quasiparticle peak.

ACKNOWLEDGMENTS

The authors are grateful to Prof. A. Lichtehshtein (Holland) for helpful advice, Prof. D.M. Edwards (Great Britain) and Prof. A. Oles (Poland) for their interest in this work, and Prof. W. Nolting (Germany) and his students, T. Hickel and P. Sinyukov, for fruitful discussions.

This study was supported by the Krasnoyarsk Scientific Foundation, project no. 9F0039.

REFERENCES

1. Z. Zangvill, *Physics at Surfaces* (Cambridge Univ. Press, Cambridge, 1988).
2. T. Tohyama and S. Maekawa, Supercond. Sci. Technol. **13**, 17 (2000).
3. F. Ronning, C. Kim, D. I. Feng, *et al.*, Science **282**, 2067 (1998).
4. R. B. Laughlin, Phys. Rev. Lett. **79** (9), 1726 (1997).
5. T. Tohyama, Y. Shibata, S. Maekawa, *et al.*, J. Phys. Soc. Jpn. **69** (9), 3716 (2000).
6. M. Grioni, H. Berger, S. Larosa, *et al.*, Physica B (Amsterdam) **230–232,** 825 (1997).
7. R. Hayn, H. Rosner, V. Yu. Yushankhai, *et al.*, Phys. Rev. B **60** (1), 645 (1999).
8. V. A. Gavrichkov, S. G. Ovchinnikov, A. A. Borisov, and E. G. Goryachev, Zh. Éksp. Teor. Fiz. **118** (2), 422 (2000) [JETP **91**, 369 (2000)].
9. R. Raimondi, J. H. Jefferson, and L. F. Feiner, Phys. Rev. B **53** (13), 8774 (1996).
10. V. A. Gavrichkov and S. G. Ovchinnikov, Fiz. Tverd. Tela (St. Petersburg) **40** (2), 184 (1998) [Phys. Solid State **40**, 163 (1998)].
11. R. O. Zaytsev, Zh. Éksp. Teor. Fiz. **68** (1), 207 (1975) [Sov. Phys. JETP **41**, 100 (1975)].
12. D. S. Marshall, D. S. Dessau, A. G. Loeser, *et al.*, Phys. Rev. Lett. **76** (25), 4841 (1996).
13. S. G. Ovchinnikov, Zh. Éksp. Teor. Fiz. **107** (3), 796 (1995) [JETP **80**, 451 (1995)].
14. P. Horsch and W. von der Linden, Z. Phys. B **72**, 181 (1988).
15. C. Grober, R. Eder, and W. Hanke, Phys. Rev. B **62** (7), 4336 (2000).

Translated by P. Pozdeev

Physics of the Solid State, Vol. 43, No. 10, 2001, pp. 1885–1891. Translated from Fizika Tverdogo Tela, Vol. 43, No. 10, 2001, pp. 1808–1814.

SEMICONDUCTORS AND DIELECTRICS

Luminescence of $CsPbCl_3$ Microcrystals in CsCl:Pb and $PbCl_2$:Cs Crystals under Synchrotron Excitation

A. Voloshinovskiĭ*, S. Myagkota*, A. Gloskovskiĭ*, and S. Zazubovich**

Franko L'vov National University, L'vov, 79005 Ukraine

e-mail: glos@bigfoot.com

***Institute of Physics, Tartu University, Riia 142, Tartu, 51014 Estonia*

Received January 10, 2001; in final form, March 5, 2001

Abstract—This paper reports on a study of the luminescence kinetics in $CsPbCl_3$ microcrystals dispersed in a CsCl or $PbCl_2$ host matrix, which are excited by synchrotron radiation at energies E_{exc} = 4–20 eV. The luminescence decay kinetics of $CsPbCl_3$ microcrystals is found to contain different time components generated by direct excitation of the microcrystals or reabsorption of the luminescence emitted by other centers. It is conjectured that the decreased luminescence decay constant of $CsPbCl_3$ microcrystals dispersed in these hosts as compared to its counterpart of $CsPbCl_3$ single crystals is accounted for by size quantization. © *2001 MAIK "Nauka/Interperiodica".*

1. INTRODUCTION

$CsPbCl_3$ single crystals exhibit strong free-exciton luminescence with a main decay time of the order of 0.5 ns [1, 2]; this could make them potentially promising for application as fast high-energy radiation converters. Nanocrystals are characterized by still faster decay kinetics due to the size quantization effect. It was shown [3–5] that subjecting CsCl:Pb and $PbCl_2$:Cs crystals to specific heat treatment gives rise to the formation of $CsPbCl_3$ nanocrystals dispersed, respectively, in the CsCl and $PbCl_2$ host matrices.

Investigation of the luminescence kinetics of $CsPbCl_3$ microcrystals dispersed in an insulator matrix and excited by synchrotron radiation is needed in order to establish the mechanism of transformation of the excited radiation to the intrinsic electronic excitation of the CsCl or $PbCl_2$ matrix and of the $CsPbCl_3$ microcrystals. Such studies also offer the possibility of determining the application potential of these materials for the detection and visualization of high-energy radiation.

We present the results of a study of the luminescence spectra and kinetics of $CsPbCl_3$ microcrystals dispersed in a CsCl or $PbCl_2$ matrix and excited by synchrotron radiation within the 4–20 eV range.

2. EXPERIMENTAL

The CsCl:Pb (C_{Pb} = 0.5 mol %) and $PbCl_2$:Cs (C_{Cs} = 0.05 and 0.5 mol %) crystals used were grown by the Stockbarger method (the figures in parentheses are the corresponding impurity concentrations in the melt). To produce $CsPbCl_3$ microcrystals dispersed in CsCl or $PbCl_2$ host matrices, a CsCl:Pb or $PbCl_2$:Cs crystal was subjected to prolonged high-temperature annealing (20–100 h, 180–220°C). Such heat treatment activates thermal motion of the anion and cation vacancies; clusters of the type of the $CsPbCl_3$ molecule are formed in the CsCl and $PbCl_2$ matrices and combine subsequently in microcrystals of a certain size that become dispersed in the above matrices.

The luminescence kinetics of the crystals was measured using time-resolved spectroscopy on a SUPERLUMI station at HASYLAB (Hamburg, Germany). The synchrotron beam was directed onto the crystal through a 2 m long normal-incidence vacuum monochromator (with an entrance slit spectral width of ~0.2 nm). The luminescence of crystals fixed on the holder of a helium cryostat was passed through a secondary B & M monochromator [6] and measured with a PM tube. The luminescence decay kinetics was studied using the correlated photon counting technique. The mathematical treatment of the luminescence decay curves, which takes into account the temporal parameters of the exciting synchrotron pulse, permits one to estimate time constants down to 0.15 ns. The luminescence spectra were measured within time gate of Δt = 5 ns (referred to subsequently as the fast luminescence component) and of Δt = 50 ns and with a time delay of δt = 150 ns relative to the beginning of the exciting pulse (the delayed luminescence component).

3. RESULTS OF THE EXPERIMENT AND DISCUSSION

3.1. Luminescence Spectra of $CsPbCl_3$ Microcrystals

Figure 1 displays luminescence spectra of CsCl:Pb and $PbCl_2$:Cs crystals excited in the transmission

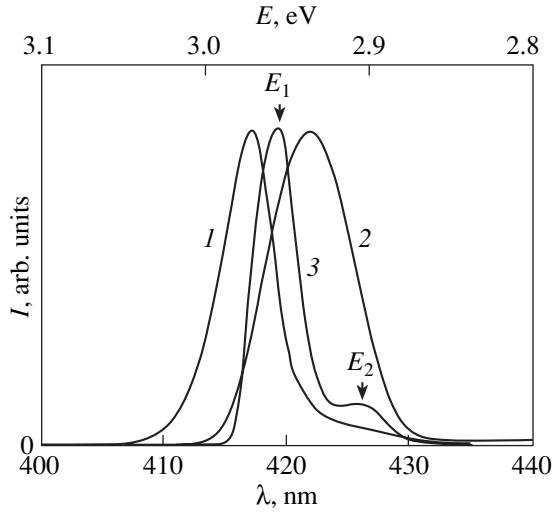

Fig. 1. Luminescence spectra of $CsPbCl_3$ microcrystals dispersed in (*1*) CsCl and (*2*) $PbCl_2$ matrices and (*3*) of a $CsPbCl_3$ single crystal measured at E_{exc} = (*1*, *3*) 5.12 and (*2*) 3.87 eV. T = 10 K.

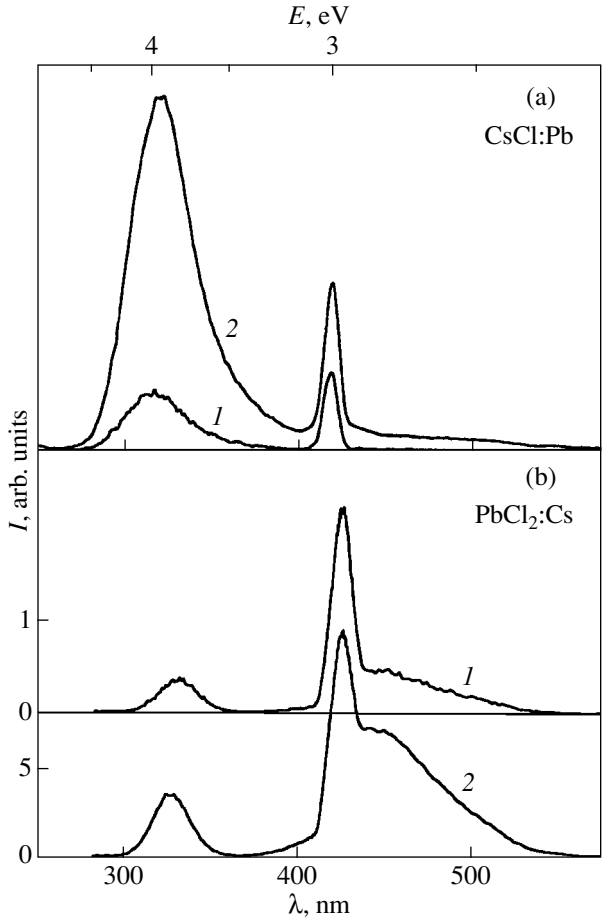

Fig. 2. Spectra of (*1*) the prompt and (*2*) the delayed luminescence component of microcrystals (a) in a CsCl matrix measured at E_{exc} = 7.29 eV and (b) in a $PbCl_2$ matrix at E_{exc} = 10.77 eV (115 nm). T = 10 K.

regions of CsCl:Pb by photons of energy E_{exc} = 5.12 eV (λ_{exc} = 242 nm) and of $PbCl_2$:Cs by photons of energy E_{exc} = 3.87 eV (λ_{exc} = 320 nm) at T = 10 K (curves *1*, *2*, respectively). The narrow bands with a half-width ΔH = 0.03 and 0.05 eV that peak at E_{em} = 2.98 eV (λ_{em} = 416 nm) in CsCl:Pb and at E_{em} = 2.93 eV (λ_{em} = 423 nm) in $PbCl_2$:Cs are similar in spectral position and half-width to those of the free-exciton emission band in single-crystal $CsPbCl_3$ (E_{em} = 2.954 eV, λ_{em} = 419.6 nm, and ΔH = 0.025 eV) (curve *3*), whose position does not depend on excitation wavelength.

The increased half-width of the luminescence band of $CsPbCl_3$ microcrystals dispersed in the CsCl or $PbCl_2$ matrix compared to that of single-crystal $CsPbCl_3$ is accounted for by the formation of $CsPbCl_3$ microcrystals that vary in size in the course of heat treatment. The short-wavelength shift of the free-exciton emission band maximum of $CsPbCl_3$ microcrystals in the CsCl matrix relative to that of single-crystal $CsPbCl_3$ by ΔE = 26 meV is regarded as a manifestation of the size quantization effect [3]. An expression relating the short-wavelength shift to the microcrystal radius R_{QD} [7],

$$\Delta E = \frac{\hbar^2\pi^2}{2\mu R_{QD}^2},$$

where $\mu \approx 0.65m_0$ is the reduced exciton mass [8, 9] (m_0 is the free-electron mass), yields $R_{QD} \approx 5$ nm for the average radius of $CsPbCl_3$-type microcrystals dispersed in the CsCl matrix.

To find an explanation for the long-wavelength shift of the emission spectrum of $CsPbCl_3$ microcrystals dispersed in a $PbCl_2$ matrix, we consider the structure of the emission spectrum of $CsPbCl_3$ single crystals in more detail (curve *3* in Fig. 1). The short-wavelength maximum at E_1 = 2.954 eV (419.6 nm) is assigned to free-exciton emission; the long-wavelength maximum at E_2 = 2.91 eV (426 nm), to trapped exciton emission [2, 9]. It is possible that the formation of $CsPbCl_3$ microcrystals in a $PbCl_2$ matrix distorts the structure of clusters of the type of the $CsPbCl_3$ molecule to the extent to which free-exciton emission is suppressed and only trapped excitons can produce emissions. In this case, the luminescence band of the $CsPbCl_3$ microcrystal with E_{em} = 2.93 eV (423 nm) is due to trapped excitons and, hence, is shifted to shorter wavelengths by ΔE = 21 meV with respect to the bound-exciton emission band of single-crystal $CsPbCl_3$ with E_{em} = 2.91 eV (426 nm).

The luminescence spectra of CsCl:Pb and $PbCl_2$:Cs crystals excited within the exciton or intrinsic absorption bands of the corresponding matrix contain, in addition to the above-mentioned band of $CsPbCl_3$ microcrystal luminescence, a broad luminescence band that peaks at E_{em} = 3.93 eV (315 nm) (Fig. 2a) or broad

luminescence bands at E_{em} = 3.75 eV (330 nm) and 2.69–2.58 eV (460–480 nm), depending on the energy of excitation quanta (Fig. 2b). The luminescence band at E_{em} = 3.93 eV of a CsCl:Pb crystal is assigned in [10] to radiative transitions from the Jahn–Teller minima of a relaxed excited state of a single $Pb^{2+}-V_c^-$ emission center to the impurity ground state.

The studies reported in [11, 12] indicate that the luminescence band at E_{em} = 3.75 eV and the short-wavelength wing of the band at E_{em} = 2.69–2.58 eV in a $PbCl_2$:Cs crystal (Fig. 2b) should be assigned to the emission of two types of self-trapped excitons (STE) and that the long-wavelength wing of the latter band is due to the emission of a defect. At the same time, the bands at E_{em} = 3.75 and 2.69–2.58 eV are interpreted in [13] as being due to the emission of two type of STEs.

As seen from Fig. 2, the narrow-band luminescence of the crystals under study, unlike the $CsPbCl_3$ single crystal characterized by only a fast luminescence component with E_{em} = 2.954 eV, contains both a prompt and a delayed luminescence component.

The origin of the delayed component in the luminescence spectra of microcrystals can be explained by analyzing the luminescence excitation spectra of single crystals, as well as the excitation spectra of the prompt and delayed luminescence components of $CsPbCl_3$ microcrystals.

3.2. Excitation Spectra of $CsPbCl_3$ Microcrystals

3.2.1. The CsCl:Pb crystal. The luminescence excitation spectra of microcrystals contain characteristic ranges associated with the transmission region of the matrix (E_{exc} = 4–7.8 eV) and with band-to-band transitions (E_{exc} > 8.3 eV). The first thing one notices in the matrix transmission region is that some of the maxima in the excitation spectrum (identified by arrows in Fig. 3, curve *1*) of the prompt luminescence-band component of $CsPbCl_3$ microcrystals coincide with the corresponding minima in the excitation spectrum of the free-exciton luminescence band of single-crystal $CsPbCl_3$ (curve *3* in Fig. 3). Minima in a luminescence excitation spectrum are usually associated with reflection losses and nonradiative exciton decay at near-surface defects. The inverse shape of the luminescence excitation band can be readily interpreted if the microcrystals are so small that the exciting light passes through them without noticeable absorption. In this case, the excitation spectrum of the intrinsic luminescence band of $CsPbCl_3$ microcrystals reproduces the pattern of the absorption spectrum rather than being distorted by the absorption due to surface defects, as in a $CsPbCl_3$ single crystal.

The strong decrease in the excitation efficiency of the prompt luminescence component in $CsPbCl_3$ microcrystals that was observed to occur with photons of energy E_{exc} > 6.8 eV (curve *1* in Fig. 3) can be interpreted as being due to a more efficient excitation, in this energy region, of the luminescence of single $Pb^{2+}-V_c^-$ centers in the CsCl:Pb crystal (curves *4*, *5*).

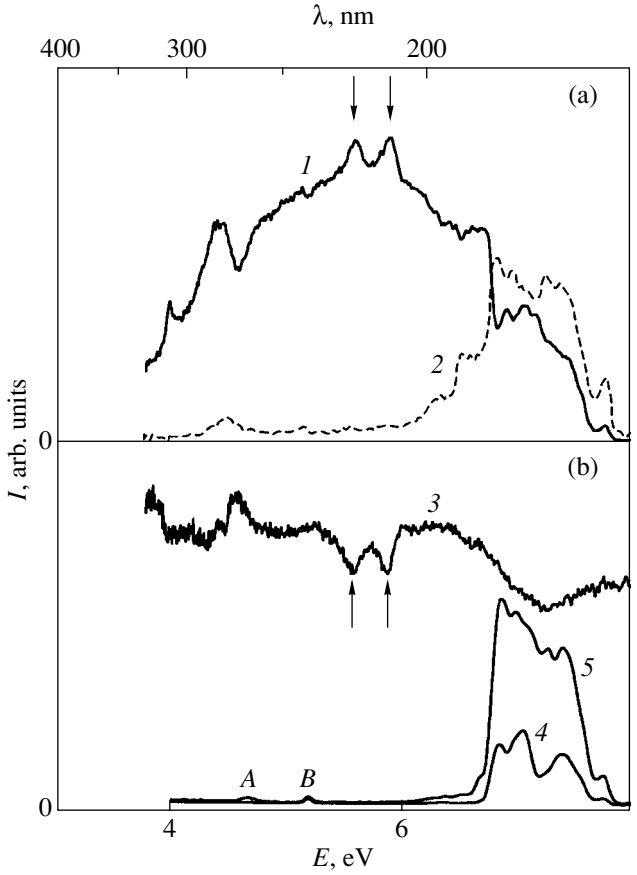

Fig. 3. (a) Excitation spectra of (*1*) the prompt and (*2*) the delayed component of the CsCl:Pb crystal luminescence band (C_{Pb} = 0.5 mol %) obtained at E_{em} = 2.98 eV; and (b) (*3*) free-exciton luminescence bands of single-crystal $CsPbCl_3$ obtained at E_{em} = 2.954 eV and (*4*) prompt and (*5*) delayed luminescence components of single $Pb^{2+}-V_c^-$ emitting centers in a CsCl matrix obtained at E_{em} = 3.93 eV. Symbols *A* and *B* identify the absorption bands of single emitting centers. *T* = 10 K.

The similarity between the excitation spectra of the delayed luminescence component of $CsPbCl_3$ microcrystals (curve *2* in Fig. 3) and the luminescence excitation spectrum of single $Pb^{2+}-V_c^-$ centers suggests that the lead centers are involved in the formation of the delayed luminescence component in microcrystals.

Within the 8 eV ≤ E_{exc} ≤ 14 eV energy range, the prompt luminescence component of $CsPbCl_3$ microcrystals is not excited (curve *1* in Fig. 4). This is due to the fact that there is no direct optical excitation of $CsPbCl_3$ microcrystals and to direct electron–hole recombination with $CsPbCl_3$ microcrystals.

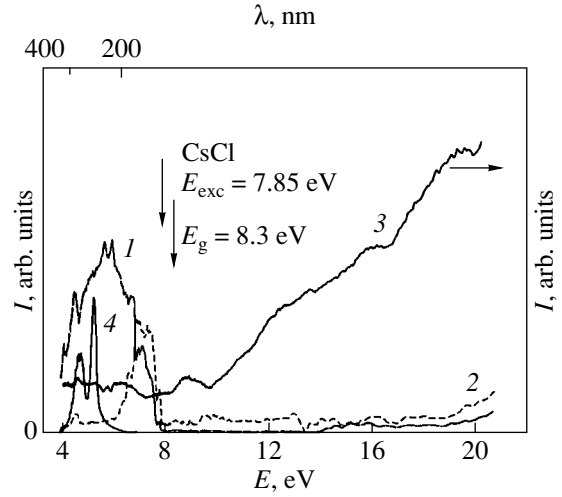

Fig. 4. Excitation spectra of (*1*) the prompt and (*2*) the delayed component of the CsCl:Pb crystal luminescence band obtained at E_{em} = 2.98 eV and (*3*) of the luminescence band of single-crystal $CsPbCl_3$ obtained at E_{em} = 2.954 eV; and (*4*) a core–valence luminescence spectrum of the CsCl matrix. T = 10 K. The arrows identify the position of the long-wavelength exciton-absorption band and the onset of interband transitions in the CsCl matrix at the same temperature.

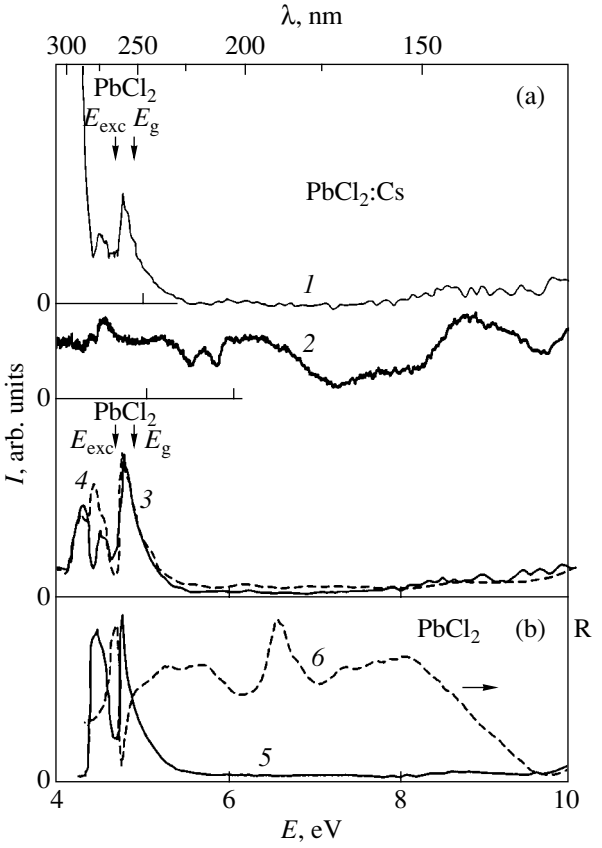

Fig. 5. (a) Excitation spectra of (*1*) the prompt and (*3*) the delayed luminescence component of a $PbCl_2$:Cs crystal (C_{Cs} = 0.05 mol %) obtained at E_{em} = 2.93 eV, (*2*) of the free-exciton luminescence band of single-crystal $CsPbCl_3$ obtained at E_{em} = 2.954 eV and (*4*) of the luminescence band of a $PbCl_2$:Cs crystal (C_{Cs} = 0.05 mol %) obtained at E_{em} = 3.75 eV; and (b) (*5*) excitation spectrum of the $PbCl_2$ matrix luminescence band obtained at E_{em} = 3.75 eV and (*6*) the reflectance spectrum of the $PbCl_2$ matrix. T = 10 K.

Excitation of the CsCl:Pb crystal by photons with energies above 14 eV brings about excitation of the core–valence luminescence (CVL) of the CsCl matrix, which is reabsorbed efficiently by the $CsPbCl_3$ microcrystals, because the excitation spectrum of the luminescence of $CsPbCl_3$ microcrystals coincides with that of the CVL of the CsCl matrix (curves *1*, *4* in Fig. 4). This channel of the $CsPbCl_3$ microcrystal excitation accounts for the prompt x-ray-induced luminescence of $CsPbCl_3$ microcrystals dispersed in the CsCl matrix [4].

3.2.2. The $PbCl_2$:Cs crystal. Figure 5a presents the excitation spectra of the prompt and the delayed component of the luminescence with E_{em} = 2.93 eV of the $CsPbCl_3$ microcrystals, of the intrinsic luminescence of the $CsPbCl_3$ single crystal (E_{em} = 2.954 eV), and of the STE luminescence of the $PbCl_2$:Cs crystal with E_{em} = 3.75 eV in the E_{exc} = 4–10 eV region. The excitation spectrum of the STE luminescence band of the $PbCl_2$ matrix with E_{em} = 3.75 eV and its reflectance spectrum are shown in Fig. 5b.

The structure of the excitation spectrum of the prompt and delayed components of the luminescence band of $CsPbCl_3$ microcrystals with E_{em} = 2.93 eV (curves *1*, *3* in Fig. 5) shown in the $4.4 < E_{exc} < 4.9$ eV region is identical to that of the STE luminescence with E_{em} = 3.75 eV of the $PbCl_2$ matrix (curves *4*, *5*). The similarity between the excitation spectra of the $CsPbCl_3$ microcrystal luminescence and of the intrinsic STE luminescence of the $PbCl_2$ matrix with E_{em} = 3.75 eV observed in this range implies the existence of a certain mechanism of electron excitation energy transfer from the $PbCl_2$ matrix to the $CsPbCl_3$ microcrystals. That the excitation spectrum of the prompt component of the $CsPbCl_3$ microcrystal luminescence with E_{em} = 2.93 eV reproduces that of the STE luminescence in the $PbCl_2$ matrix with E_{em} = 3.75 eV is possibly the result of the presence of a prompt component in the matrix STE luminescence. Indeed, studies reported in [14] suggest that the STE decay kinetics of the $PbCl_2$ matrix with E_{em} = 3.75 eV has a prompt (τ_f = 0.61 ns) and a delayed (slow) component (τ_s = 11.8 μs).

The low excitation efficiency of the delayed and the prompt luminescence component of $CsPbCl_3$ microcrystals produced by photons of energy of the range $5.5 \text{ eV} \le E_{exc} \le 10$ eV is accounted for by the low excitation efficiency of the intrinsic STE luminescence of the $PbCl_2$ matrix in this energy range.

The specific features of the mechanism responsible for the luminescence excitation in $CsPbCl_3$ microcrystals in the energy range under study were established when investigating the luminescence decay kinetics of microcrystals.

3.3. Luminescence Decay Kinetics of $CsPbCl_3$ Microcrystals

3.3.1. Luminescence decay kinetics of $CsPbCl_3$ microcrystals dispersed in a CsCl matrix. Figure 6 (curve *1*) shows the luminescence decay kinetics of $CsPbCl_3$ microcrystals excited in the transmission region of the CsCl matrix (E_{exc} = 3.5–6.0 eV). The decay curves of micro- and single-crystal $CsPbCl_3$ excited in the same spectral region can be fitted by a combination of two exponentials with decay times of $\tau_{f1} \approx 0.15$ ns, $\tau_{f2} = 12.1$ ns and $\tau_{f1} = 0.48$ ns, $\tau_{f2} = 7.0$ ns, respectively. The decrease in the luminescence decay time τ_{f1} of $CsPbCl_3$ microcrystals compared to that of single-crystal $CsPbCl_3$ could be due to the size quantization effect.

The luminescence decay kinetics of $CsPbCl_3$ microcrystals excited in the 6.0–7.8 eV region is identical to that of the emission band of single Pb^{2+}–V_c^- centers with E_{em} = 3.93 eV (curves *2*, *4* in Fig. 6). The luminescence decay curves of the microcrystals are described by the decay times $\tau_{f1} = 2.6$ ns and $\tau_{f2} = 25$ ns; those of single Pb^{2+}–V_c^- centers, by $\tau_{f1} = 2.4$ ns and $\tau_{f2} = 27$ ns. In both cases, there is a delayed component τ_s, which is too long to be measured by the technique we used to study the delayed luminescence component. The existence of a prompt and a delayed luminescence component in the band with E_{em} = 3.93 eV in the CsCl:Pb crystal supports the existence of a radiative and a metastable sublevel in the relaxed state of the Pb^{2+} ion. The coincidence of the luminescence decay curves of the microcrystals and single centers suggests that the delayed component in the microcrystal luminescence decay kinetics is on the millisecond time scale, as is the case with single Pb^{2+}–V_c^- centers. That the temporal luminescence parameters of microcrystals and single centers coincide indicates that no multipole mechanisms of energy transfer from single Pb^{2+}–V_c^- centers to $CsPbCl_3$ microcrystals operate here, i.e., that the luminescence of the microcrystals excited in the absorption bands of the Pb^{2+}–V_c^- centers is due to reabsorption of the radiation emitted by the single centers.

The luminescence decay kinetics of $CsPbCl_3$ microcrystals produced when the CsCl:Pb crystal is excited by photons of energy $E_{exc} > 14$ eV contains a main decay constant with $\tau_f = 1.4$ ns (curve *3* in Fig. 6). This is accounted for by the excitation, for $E_{exc} > 14$ eV, of the CVL with a decay constant $\tau \approx 1.4$ ns in the CsCl matrix, which is reabsorbed efficiently by the $CsPbCl_3$ microcrystals.

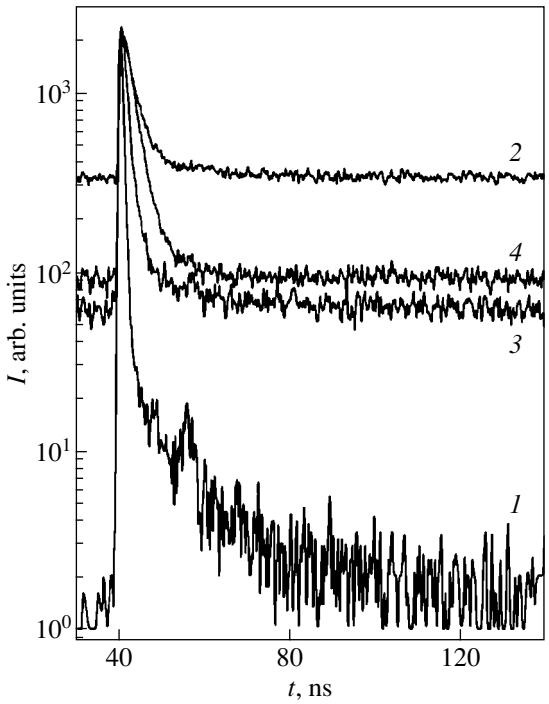

Fig. 6. Luminescence decay kinetics of $CsPbCl_3$ microcrystals dispersed in a CsCl matrix. The excitation is made at E_{exc} = (*1*) 3.5–6.0, (*2*) 7.7, and (*3*) >14 eV. Curve *4* illustrates the decay kinetics of the luminescence of single Pb^{2+}–V_c^- centers in the CsCl matrix, which peaks at E_{em} = 3.93 eV and was excited in the spectral region E_{exc} = 6.0–7.8 eV. T = 10 K.

Thus, the luminescence decay kinetics of $CsPbCl_3$ microcrystals with $\tau_f = 0.15$ ns is observed only under direct optical excitation in the transmission region of the CsCl matrix. The component with the decay time $\tau_f = 1.4$ ns originates from reabsorption of the matrix CVL excited for $E_{exc} > 14$ eV. The overlap of the excitation spectrum of the microcrystals with emission spectra of single Pb^{2+}–V_c^- centers in the CsCl:Pb crystal gives rise to the formation of a delayed component in the luminescence decay kinetics of $CsPbCl_3$ microcrystals with time constants of $\tau_{f1} = 2.6$ ns, $\tau_{f2} = 25$ ns, and $\tau_s \approx 1$ ms. Size quantization possibly brings about a slight decrease in the luminescence decay time of $CsPbCl_3$ microcrystals dispersed in the CsCl matrix ($\tau_f = 0.15$ and 0.48 ns for $CsPbCl_3$ microcrystals and single crystals, respectively).

3.3.2. Luminescence decay kinetics of the $CsPbCl_3$ microcrystals dispersed in a $PbCl_2$ matrix. Figure 7 presents luminescence decay curves of $CsPbCl_3$ microcrystals excited in the regions of transmission and intrinsic absorption of the $PbCl_2$ matrix. In both cases, one can discriminate a prompt component

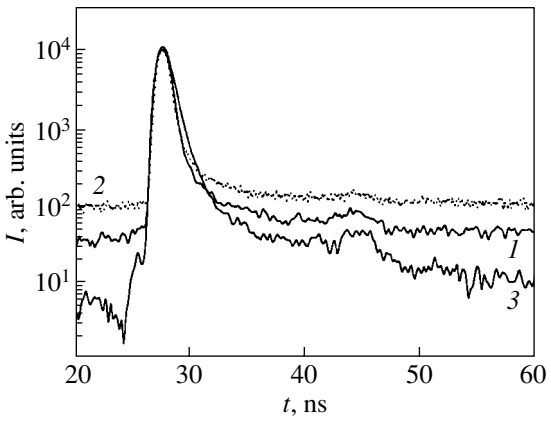

Fig. 7. Decay kinetics of the luminescence of $CsPbCl_3$ microcrystals dispersed in a $PbCl_2$ matrix, which was excited in the regions of (*1*) transmission (E_{exc} = 3.8 eV) and (*2*) intrinsic absorption of the $PbCl_2$ matrix (E_{exc} = 14.0 eV), as well as of the luminescence of (*3*) single-crystal $CsPbCl_3$ excited by E_{exc} = 3.8 eV photons. T = 10 K.

with τ_{f1} = 0.30 ns and longer components with time constants $\tau_{f2} \approx 2$ ns and $t_{f3} \approx 23$ ns in the luminescence decay curves. The presence of a prompt component with τ_{f1} = 0.30 ns in the decay kinetics of $CsPbCl_3$ microcrystals excited in the transmission region of the matrix originates from direct excitation of the microcrystals both on the surface and in the bulk of the matrix; when excited in the region of intrinsic absorption of the matrix, the prompt component is possibly caused by the presence of a small amount of microcrystals on the surface of the $PbCl_2$ matrix. The luminescence decay kinetics of a $CsPbCl_3$ single crystal excited at E_{exc} = 3.8 eV are illustrated by curve *3* in Fig. 7. As in the case of $CsPbCl_3$ microcrystals dispersed in the CsCl matrix, the slightly shorter luminescence decay time of $CsPbCl_3$ microcrystals in the $PbCl_2$ matrix (τ_{f1} = 0.30 and 0.48 ns for the micro- and single-crystal $CsPbCl_3$, respectively) could be due to the size quantization effect.

There is also a delayed component τ_s, which is too long to be measured using the technique employed. The existence of a delayed component τ_s in the luminescence decay kinetics of $CsPbCl_3$ microcrystals in the $PbCl_2$:Cs crystal is apparently due to reabsorption of the $PbCl_2$ STE luminescence by $CsPbCl_3$ microcrystals. Indeed, the STE luminescence decay kinetics of the $PbCl_2$ matrix was shown to be dominated by a delayed component with τ_s = 11.8 ns [14].

Thus, the prompt component in the luminescence decay kinetics of $CsPbCl_3$ microcrystals with τ_{f1} = 0.30 ns is detected within a broad energy range, including the regions of both transmission and intrinsic absorption of the $PbCl_2$ matrix.

4. CONCLUSIONS

Our present study permits the following conclusions.

(1) Long, high-temperature annealing (20–100 h, 180–220°C) of CsCl:Pb (C_{Pb} = 0.5 mol %) and $PbCl_2$:Cs (C_{Cs} = 0.05 and 0.5 mol %) crystals initiates the formation of $CsPbCl_3$ microcrystals dispersed in the CsCl and $PbCl_2$ matrices, respectively.

(2) The luminescence of $CsPbCl_3$ microcrystals excited in the transmission region of the CsCl matrix originates from direct excitation or reabsorption of the emission of single Pb^{2+}–V_c^- centers. In the first case, the luminescence decay constant is $\tau_f \approx 0.15$ ns; in the second, the decay kinetics follows a curve characteristic of single Pb^{2+}–V_c^- centers.

(3) The prompt component with the decay time constant τ_f = 0.30 ns excited in the regions of transmission and intrinsic absorption of the $PbCl_2$ matrix is caused by direct excitation of the $CsPbCl_3$ microcrystals; the delayed component, with $\tau_s \approx 10$ μs, is due to reabsorption of the STE emission in the $PbCl_2$ matrix.

(4) The slight shortening of the luminescence decay constants of $CsPbCl_3$ microcrystals dispersed in CsCl and $PbCl_2$ matrices compared to the corresponding constant for single-crystal $CsPbCl_3$ is possibly due to the size quantization effect.

ACKNOWLEDGMENTS

The authors are grateful to Prof. G. Zimmerer for his assistance in the synchrotron measurements and valuable discussions.

This study was partly supported by the INTAS program, grant no. 99-01350, and the Estonian Scientific Foundation, grant no. 3875.

REFERENCES

1. A. S. Voloshinovs'kiĭ, V. B. Mikhaĭlik, S. V. Myagkota, *et al.*, Ukr. Fiz. Zh. **38** (7), 46 (1993).
2. M. Nikl, E. Mihokova, K. Nitsch, *et al.*, Chem. Phys. Lett. **220** (1/2), 14 (1994).
3. M. Nikl, K. Nitsch, K. Polak, *et al.*, Phys. Rev. B **51** (8), 5192 (1995).
4. S. V. Myagkota, Opt. Spektrosk. **87** (2), 311 (1999) [Opt. Spectrosc. **87**, 290 (1999)].
5. S. V. Myagkota, A. S. Voloshinovskiĭ, and A. V. Gloskovskiĭ, Opt. Spekrosk. **88** (4), 598 (2000) [Opt. Spectrosc. **88**, 538 (2000)].
6. G. Zimmerer, Nucl. Instrum. Methods Phys. Res. A **308** (1/2), 178 (1991).

7. Al. L. Éfros and A. L. Éfros, Fiz. Tekh. Poluprovodn. (Leningrad) **16** (7), 1209 (1982) [Sov. Phys. Semicond. **16**, 772 (1982)].
8. L. N. Amitin, A. T. Anistratov, and A. I. Kuznetsov, Fiz. Tverd. Tela (Leningrad) **21** (12), 3535 (1979) [Sov. Phys. Solid State **21**, 2041 (1979)].
9. I. P. Pashuk, N. S. Pidzyrailo, and M. G. Matsko, Fiz. Tverd. Tela (Leningrad) **23** (7), 2162 (1981) [Sov. Phys. Solid State **23**, 1263 (1981)].
10. R. Aceves, V. Babin, M. Barboza Flores, *et al.*, J. Phys.: Condens. Matter **10** (24), 5449 (1998).
11. R. Kink, G. Liidja, and V. Plekhanov, Tr. Inst. Fiz. Akad. NaukÉst. SSR **40**, 132 (1972).
12. R. Kink, T. Avarmaa, V. Kisand, *et al.*, J. Phys.: Condens. Matter **10** (3), 693 (1998).
13. M. Kitaura and H. Nakagawa, J. Lumin. **72**, 883 (1997).
14. K. Polak, D. J. S. Birch, and M. Nikl, Phys. Status Solidi B **145**, 741 (1988).

Translated by G. Skrebtsov

Physics of the Solid State, Vol. 43, No. 10, 2001, pp. 1892–1897. Translated from Fizika Tverdogo Tela, Vol. 43, No. 10, 2001, pp. 1815–1820.

DEFECTS, DISLOCATIONS, AND PHYSICS OF STRENGTH

Inherent Submicroporosity and Crystallization of Amorphous Alloys

V. I. Betekhtin*, A. G. Kadomtsev*, and O. V. Tolochko**

** Ioffe Physicotechnical Institute, Russian Academy of Sciences, Politekhnicheskaya ul. 26, St. Petersburg, 194021 Russia*

*** St. Petersburg State Technical University, Politekhnicheskaya ul. 29, St. Petersburg, 195251 Russia*

e-mail: Vladimir.Betekhtin@pop.ioffe.rssi.ru

Received April 2, 2001

Abstract—The effect of inherent submicroporosity (regions with an excess free volume) in amorphous alloys on the regularities of their crystallization is investigated. Inherent submicroporosity arises in amorphous alloys prepared by quenching under different conditions. It is proved that this effect should be taken into account in the first stage of crystallization of amorphous alloys. © *2001 MAIK "Nauka/Interperiodica".*

1. INTRODUCTION

Amorphous alloys are very promising materials owing to their physical and mechanical properties. The chief disadvantage of these alloys is their low thermal stability, because amorphous alloys produced by ultrafast quenching (the most widely used method of their preparation) can occur either in an unstable state or in a metastable state. The transition to an equilibrium crystalline state leads to a considerable change in all properties of the amorphous alloy. This explains why a large number of works is concerned with investigation into the crystallization kinetics of amorphous alloys. At present, the general regularities of crystallization of amorphous alloys are known [1–7]. However, a number of problems, in particular, the problem of the effect of excess free volume on crystallization processes, remain unsolved.

As is known, the presence of a free volume (1–2%) in an amorphous structure is an important structural feature that distinguishes amorphous alloys from their crystalline analogs. The free volume in amorphous alloys can be separated into two components, namely, the structure-sensitive volume and excess free volume [3, 4, 8]. The former component of the free volume is an integral characteristic of the amorphous state. The structure-sensitive free volume is involved in the atomic complexes responsible for the topological and compositional characteristics of the amorphous state. This part of the free volume completely annihilates only after the completion of crystallization of the alloy. The excess free volume is considered to be a structural defect (submicropores) whose elimination leaves the symmetry and topological characteristics of the amorphous state unchanged. At the same time, the evolution of this mobile component of the free volume substantially affects the physical and mechanical properties of amorphous alloys [8–10]. Therefore, it can be assumed that the inherent submicroporosity and other characteristics of the defect structure of amorphous alloys also have an effect on their crystallization kinetics.

The concept of inherent submicropores agrees well with the ideas of Ya.I. Frenkel [11], according to which an amorphous state, like a liquid, is characterized by local microdiscontinuities, i.e., holes. These holes are not identical to vacancies in crystals and should occur in the form of incipient microcracks or pores. The presence of microdiscontinuities (holes) already in the melt prior to rapid cooling suggests that the quenching conditions (temperature of the melt, cooling rate, and other factors) can affect the parameters of structural defects in the "frozen" melt, i.e., in the amorphous alloy.

In this work, we investigated the influence of specific quenching conditions on the parameters of structural defects (primarily, submicropores) and, as a consequence, on the regularities of the early stage of crystallization during heat treatment of amorphous alloys.

2. SAMPLE PREPARATION AND EXPERIMENTAL TECHNIQUE

Amorphous alloys in the Fe–B system served as the main objects of our investigation. In addition, we studied alloys in the Fe–Co–B and Ni–P systems. The alloy samples in the form of ribbons approximately 40 μm thick were prepared by quenching on the outside of a rapidly spinning copper disk. In order to choose the appropriate conditions of quenching, the kinematic viscosity ν of the melts was measured by the oscillating sample method [12]. It was revealed that the temperature dependence of the kinematic viscosity ν exhibits an anomalous behavior at a certain temperature T_1' and a branching into two curves $\nu(T)^+$ and $\nu(T)^-$ upon heating and cooling, i.e., the kinematic viscosity hysteresis (Fig. 1). The temperature dependences of the viscosity of the Fe–Co–B and Ni–P alloys upon heating and cool-

ing show a qualitatively similar behavior. These findings indicate that the structure of the melt undergoes an irreversible transformation which starts at a temperature close to T_1' and ceases (at a heating rate of 9 K/min) near the hysteresis point T_2' in polytherms, i.e., the point at which the temperature dependence branches into the curves $\nu(T)^+$ and $\nu(T)^-$. The results obtained were used for choosing the temperature–time conditions of heat treatment of the melts prior to quenching. The alloys of each composition were prepared according to the following three regimes: (1) quenching from $T_1 = T_1' -$ (40–50 K) (alloy 1), (2) quenching from $T_2 = T_2' +$ (30–50 K) (alloy 2), and (3) heating to T_2 and quenching from T_1 (alloy 3). The specific quenching regimes for the $Fe_{85}B_{15}$ alloy are presented in Table 1.

The structure of the amorphous alloys prepared under different quenching conditions was studied by the small-angle x-ray scattering (SAXS) technique, x-ray diffraction, and transmission electron microscopy (TEM).

The experiments were carried out using a small-angle x-ray camera with the Kratky collimation (MoK_α radiation). The setup made it possible to determine the parameters of scattering inhomogeneities ranging in size from ~3 to 300 nm. The SAXS data were processed by the Guinier method. Moreover, scattering indicatrix invariants were constructed and analyzed. With the aim of elucidating the nature of inhomogeneities, the scattering indicatrices of the alloys were analyzed prior to and after treatment under a hydrostatic pressure of 1 GPa. Earlier [8], it was shown that the treatment under pressure leads to a considerable decrease in the intensity of scattering by submicropores due to their partial healing, whereas the scattering by inhomogeneities unrelated to holes remains unchanged. The TEM

Table 1. Temperature–time conditions for preparation of the $Fe_{85}B_{15}$ amorphous alloys

No. of quenching regime	Heating temperature of the melt, °C	Isothermal treatment time, min	Quenching temperature, °C
1	1250	5	1250
2	1395	5	1395
3	1400	5	1250

examination of the samples was performed with a JEOL 2000-EX instrument at an accelerating voltage of 200 kV. The samples were prepared using an argon-etch apparatus with a gun tilt angle of 20°. The crystallization was investigated in the course of isothermal treatment. The phase composition and transformation kinetics were determined by x-ray structure analysis on a DRON-3 diffractometer (FeK_α radiation). The viscosity was measured in the tensile test. The apparent viscosity η was calculated according to the formula $\eta = (PL/3S\Delta L)\Delta t$, where P is the load, L is the sample length, ΔL is the viscous (irreversible) deformation for the time Δt (1 h), and S is the cross-sectional area of the sample. The glass transition temperature was determined as the abscissa of the point of intersection between the temperature dependences of the linear expansion coefficient above and below the glass transition range.

3. EXPERIMENTAL RESULTS

First, we consider how the temperature–time conditions of preparation of the $Fe_{85}B_{15}$ alloy affect the regularities of its crystallization. It is found that, irrespective of the quenching conditions, the crystallization of all the alloys begins with the precipitation of a solid

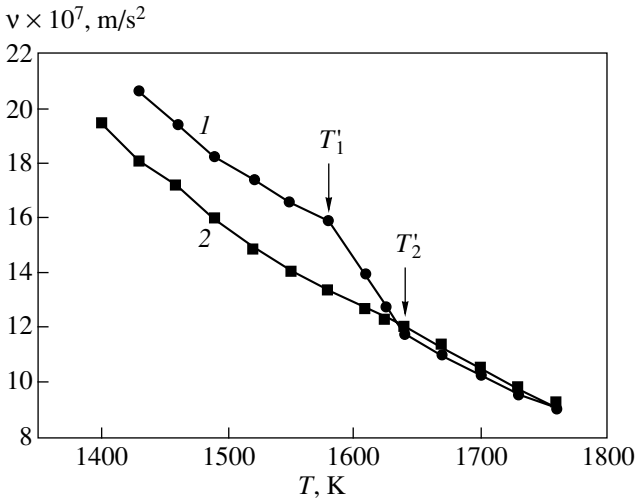

Fig. 1. Polytherms of the kinematic viscosity ν for the $Fe_{85}B_{15}$ alloy upon (*1*) heating and (*2*) cooling.

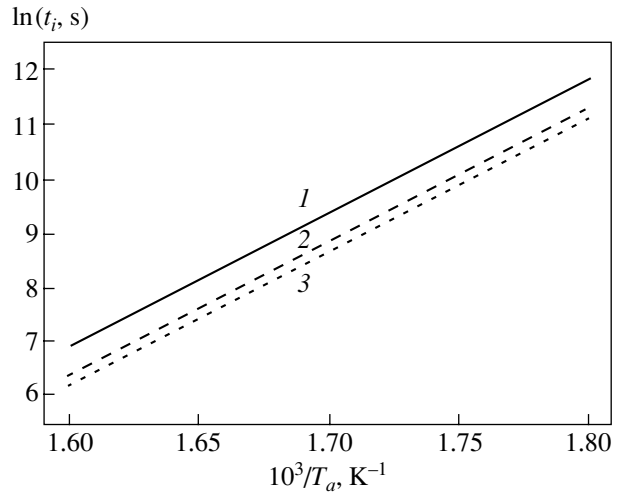

Fig. 2. Dependences of the time ($\ln t_i$) prior to the onset of crystallization on the isothermal treatment temperature for the $Fe_{85}B_{15}$ alloys prepared according to regimes 1–3.

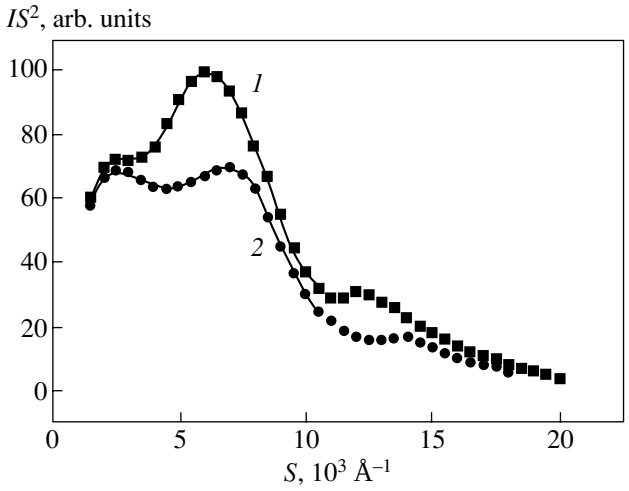

Fig. 3. Scattering indicatrices for the $Fe_{85}B_{15}$ alloy (*1*) prior to and (*2*) after treatment under hydrostatic pressure.

solution based on the body-centered cubic (bcc) iron phase. (In the course of the second stage, the amorphous matrix is decomposed into metastable boride Fe_3B and a solid solution with a structure based on the iron bcc lattice.) The experimental results obtained at the first stage of crystallization upon isothermal treatment are shown in Fig. 2 in the $\ln(t_i)$–$1/T_a$ coordinates, where T_a is the temperature of isothermal treatment and t_1 is the time corresponding to the appearance of the crystalline phase (the solid solution with a structure based on the iron bcc lattice) in the amorphous matrix at a given temperature of isothermal treatment. Note that the values of t_1 were determined during successive isothermal treatments from the data of qualitative x-ray powder diffraction analysis. As can be seen from Fig. 2, the alloy prepared from the not-too-heated melt (regime 1) possesses the highest stability against crystallization over the entire temperature range. The alloys prepared according to regime 2 (and, especially, regime 3) crystallize somewhat earlier.

The characteristics calculated from the experimental data for the amorphous alloys prepared according to the three quenching regimes are summarized in Table 2. It is seen from this table that, within the limits of experimental error, the activation energies E_{cryst} of the first crystallization stage are equal to each other. At the same time, the viscosities of all the alloys (specifically of alloys 1 and 3) differ substantially. The enthalpy of the first crystallization stage for alloy 3 slightly differs form the enthalpies of alloys 1 and 2, and the glass transition temperature T_g of alloy 2 differs from the corresponding temperatures of alloys 1 and 3.

It can be assumed that the differences revealed in the kinetics of the first crystallization stage and in the properties of the alloys under investigation are associated with the structural features inherited by amorphous ribbons after ultrafast quenching. In frozen melts, these features are electron density inhomogeneities of the hole nature and others.

The systematic small-angle x-ray scattering investigations demonstrated that the alloys prepared with the use of all three regimes involve two or three fractions of scattering inhomogeneities. Figure 3 depicts typical scattering indicatrix invariants for alloy 1 prior to and after treatment under hydrostatic pressure. It can be seen that this treatment results in a considerable decrease in the intensity of two out of the three observed maxima and in a change in their location. According to the analysis of the intensity and the shape of the invariant curves for the amorphous alloys prior to and after the treatment under pressure [8], we deal with

Table 2. Characteristics of the $Fe_{85}B_{15}$ alloys

No. of quenching regime	1	2	3
Activation energy of the first crystallization stage, kJ/mol	180 ± 18	180 ± 10	178 ± 10
Glass transition temperature, K	621 ± 3	601 ± 4	620 ± 3
Viscosity at 583 K, Pa	$(8.9 \pm 0.6) \times 10^{13}$	$(6.6 \pm 0.6) \times 10^{13}$	$(1.4 \pm 0.4) \times 10^{13}$
Enthalpy of the first crystallization stage, J/g	65 ± 3	68 ± 3	56 ± 4

Table 3. Parameters of structural inhomogeneities for the $Fe_{85}B_{15}$ alloys

No. of quenching regime	Submicropores			Quenching inhomogeneities	
	diameter, nm		relative number	diameter, nm	relative number
	near the surface	in the bulk			
1	100 ± 9	15 ± 2	1	240 ± 20	1
2	97 ± 10	15 ± 2	1.9	220 ± 15	1.8
3	62 ± 14	15 ± 2	1.6	–	–

scattering by two fractions of inhomogeneities of the hole nature, i.e., with scattering by submicropores. The treatment under pressure brings about a partial healing of micropores, which leads to a change in the scattering indicatrices. Inhomogeneities of the third fraction, whose parameters remain unchanged under pressure, have a nonhole nature.

Table 3 presents data on the size and relative number of submicropores and nonhole-type scattering inhomogeneities in the studied alloys. It is seen from this table that each of the alloys contains submicropores with mean sizes of approximately 10 and 100 nm.

Analysis of the distribution of fine and coarse submicropore fractions over the thickness of amorphous ribbons revealed that submicropores of the coarse fraction are localized in thin (about 1–3 μm) surface layers of amorphous ribbons, whereas submicropores of the fine fraction are rather uniformly distributed throughout the ribbon thickness. These data are in agreement with the results of our earlier investigations [8, 13] of the scattering indicatrices for amorphous ribbons prior to and after electrolytic etching of thin surface layers. Therefore, the effect of the coarse submicropore fraction can be ignored in analyzing the regularities of bulk crystallization. As was shown earlier in [13], this effect should be included in the analysis of the specific features of surface crystallization (as compared to bulk crystallization).

It follows from Table 3 that the bulk concentrations of submicropores (about 15 nm in size) in the amorphous alloys produced under different quenching conditions differ significantly: higher concentrations are observed in alloys 2 and 3, whereas alloy 1 has the lowest concentration of submicropores. The concentrations of scattering centers of the nonhole nature are also different in alloys 1–3. The scattering center concentration in alloy 2 is nearly twice as high as that in alloy 1. As regards alloy 3, the nonhole-type scattering inhomogeneities are not found in this alloy to within the experimental error of their determination.

Now, we dwell on the results of structural investigations of the amorphous alloys with the use of transmission electron microscopy. A detailed comparison of the microstructures obtained after the first stage of crystallization was performed for alloys 1 and 3. This choice is explained by the substantial difference in the thermal effects of the first crystallization stage in alloys 1 and 3 despite the fact that the quenching rates for these alloys are identical. (Compared to alloys 1 and 3, alloy 2 has a lower glass transition temperature and, hence, a lower cooling rate.)

Figures 4a and 4b show the characteristic microstructures formed in the Fe–B alloys immediately after completion of the first crystallization stage in amorphous ribbons prepared according to regimes 1 and 3, respectively. The histograms of the size distribution of crystals are depicted in Figs. 5a and 5b. The size of a crystal was taken equal to the averaged (over the results of two measurements) maximum size of its diagonals.

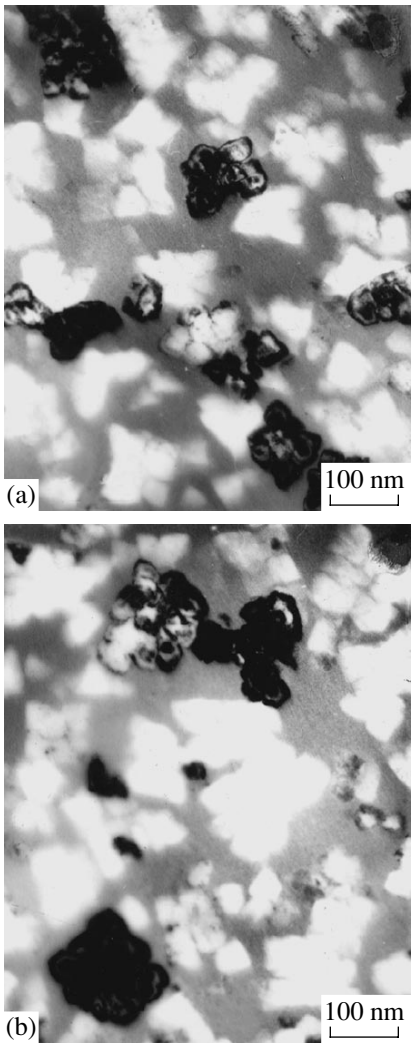

Fig. 4. Micrographs of bcc crystals of the $Fe_{85}B_{15}$ alloys prepared according to regimes (a) 1 and (b) 3.

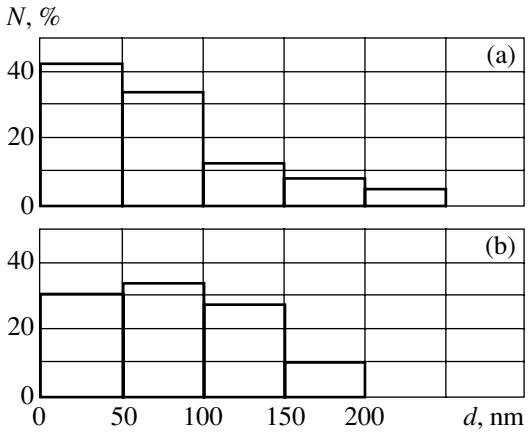

Fig. 5. Histograms of the particle sizes d after completion of the first stage of crystallization in the $Fe_{85}B_{15}$ alloys prepared according to regimes (a) 1 and (b) 3.

4. DISCUSSION

Let us consider the physical prerequisites that can shed light on the origin of the observed effect of the quenching conditions on the concentration, size, and distribution of submicropores (regions with an excess free volume) over the cross section of amorphous ribbons and, as a consequence, on the kinetics of the first crystallization stage. We proceed from the assumption that the melt prior to rapid cooling on the spinning disk contains discontinuities, so that the higher the temperature of the melt, the larger the number of discontinuities [11]. Therefore, an increase in the temperature of the melt should lead to an increase in the number of frozen discontinuities (submicropores). Moreover, the effective quenching rate should also affect the parameters of these discontinuities. In the framework of the above concepts and with due regard for the action of centrifugal forces arising upon pouring of the melt onto a rapidly spinning disk (refrigerator) [8], the distribution of excess free volume regions over the cross section of amorphous ribbons should not be uniform: the mean sizes of regions in surface layers should be larger.

Thus, the obtained data on the influence of quenching conditions on the size, concentration, and distribution of submicropores in amorphous ribbons are well explained in terms of the general physical concepts.

Now, we analyze the possible reasons for the different thermal stabilities of the amorphous alloys prepared under different quenching conditions. First, we compare the alloys prepared according to regimes 1 and 3. It can be seen from Tables 1 and 2 that many characteristics of these alloys differ substantially. Since the quenching rates of alloys 1 and 3 are identical, the differences in the other parameters can be explained by the fact that alloy 3 inherits the defect structure of the higher-temperature (1400°C) melt. The structure of alloy 3 virtually does not involve electron density inhomogeneities of the nonhole nature, which can be interpreted as quenching nuclei, and, what is especially important, is characterized by a larger number of submicropores. It seems likely that the difference in the stability (crystallization kinetics) of alloys 1 and 3 is associated with the difference in the number of initial submicropores in the inner layers of the amorphous ribbons. This difference (by a factor of 1.6) can lead to a somewhat earlier (easier) onset of the formation of crystalline regions. Note that, owing to the low viscosity of alloy 3 (most likely, due to the small concentration of quenching nuclei), the induction period of crystallization of this alloy can also be shorter than that of alloy 1.

Another feature distinguishing the amorphous alloys prepared in regime 3 from those produced in regime 1 is a weaker thermal effect of the first crystallization stage, which can be caused by a higher density of crystal boundaries. In [14], the retardation of transformation, low latent heats of crystallization, and a clear-cut separation of two stages were treated as characteristic features of the crystallization process with the formation of a nanocrystalline structure. Therefore, it can be assumed that, after the first crystallization stage, the structure of the amorphous ribbons prepared according to regime 3 should involve a large number of tiny crystals whose sizes are less than those in the alloys produced in regime 1.

However, the TEM investigations showed that the quenching regime (1 or 3) does not substantially affect the size of crystals formed after the first crystallization stage. When passing from regime 1 to regime 3, the density and size distributions of crystals in the amorphous matrix becomes only more uniform. It can be seen from Figs. 5a and 5b that, after quenching of the alloys according to regime 3, the structure involves a smaller number (in percentage terms) of crystals less than 50 nm in size and contains no crystals more than 200 nm in size.

The complex shape of crystals makes evaluation of their surface area difficult. In order to compare these parameters for alloys 1 and 3, the crystal shape was simulated using simple geometric figures. It turned out that, for any model shape, the surface area of crystals in alloy 3 is 1.25 times as large as that in alloy 1. This difference in the interfacial area explains the difference (by a factor of approximately 1.2) between the enthalpies of the first crystallization stage in alloys 1 and 3.

Let us now consider the specific features in the structure and properties of the alloy produced by quenching in regime 2. The concentration of submicropores formed in the inner layers of the amorphous ribbon is nearly twice the submicropore concentration in alloy 1 and is even somewhat higher than that in alloy 3 (Table 3). Consequently, the faster crystallization of alloy 2 as compared to that of alloy 1 can also be associated with an increase in the inherent porosity. Alloy 2 differs from alloys 1 and 3 in that it has a lower glass transition temperature, which, in principle, suggests a lower cooling rate in the glass transition range. As a result, the number of quenching nuclei formed in alloy 2 is larger than those in alloys 1 and 3 (Table 3). Despite a considerably larger number of quenching nuclei, the viscosity of alloy 2 at a temperature of 533 K is slightly less than the viscosity of alloy 1, which can be explained by the substantially higher value of the reduced temperature T/T_g.

Therefore, variations in the quenching conditions (temperature of the melt and cooling rate) affect the specific features in the formation of the amorphous structure and, as a consequence, its thermal stability. A simultaneous change in two quenching parameters (temperature and rate) makes analysis of their influence on the structure and properties difficult. However, for the alloys prepared with the use of all three regimes, we can draw the common inference that an increase in the inherent porosity in the inner layers of amorphous ribbons leads to an earlier (easier) onset of formation of crystalline regions.

It is evident that other structural features of the amorphous alloys prepared by ultrafast quenching can also affect the thermal stability. However, it seems likely that the inherent submicroporosity is one of the most universal structural factors that has an effect on the onset of crystallization. This is also supported by the results obtained in the study of the fast surface crystallization in amorphous alloys [13] and the preliminary data on the influence of pressure on the crystallization process. It is known that the surface crystallization is a specific type of crystallization which occurs in amorphous alloys produced by ultrafast quenching; these alloys are characterized by fast surface crystallization [1]. In our previous work [13], the $Fe_{58}Ni_{20}Si_9B_{13}$ alloy was investigated by the SAXS technique and Auger spectroscopy. It was shown that the submicroporosity in outer surface layers (in contact with the atmosphere in the course of quenching) approximately 1–3 nm thick is substantially higher than that in the bulk, whereas the concentrations of chemical elements (forming this alloy) in the surface layers and in the bulk are close to each other. These results allowed us to conclude that it is this increased submicroporosity that is responsible for the fast crystallization of the outer surface in the $Fe_{58}Ni_{20}Si_9B_{13}$ alloy. (The fast crystallization of the inner surface of this alloy was brought about primarily by the change in the chemical composition, because no noticeable features of the pore structure on this surface were revealed.) This conclusion is confirmed by our preliminary data, according to which the treatment under pressure leads to a decrease in the excess free volume and slows down crystallization processes.

In conclusion, we dwell briefly on general considerations that can elucidate the influence of the submicroporosity (excess free volume) on the crystallization kinetics in amorphous alloys. It is known that the crystallization, i.e., the transition of the alloy from a metastable state to a stable state, is attended by a decrease in the free volume. This change in the volume brings about a decrease in the elastic energy, which, according to [1], more rapidly decreases near the surface.

Thus, the increase in submicroporosity, i.e., in the free surfaces of submicropores, should lead to an earlier (easier) onset of the formation of crystalline regions.

ACKNOWLEDGMENTS

This work was supported by the Russian Foundation for Basic Research, project no. 99-02-18287.

REFERENCES

1. *Glassy Metals*, Ed. by H.-J. Güntherodt and H. Beck (Springer-Verlag, Berlin, 1981; Mir, Moscow, 1983).
2. K. Suzuki, H. Fuzimori, and K. Hasimoto, *Amorphous Metals*, Ed. by Ts. Masumoto (Metallurgiya, Moscow, 1987), translated from Japanese.
3. *Metastable and Nonequilibrium Alloys*, Ed. by Yu. V. Efimov (Metallurgiya, Moscow, 1988).
4. A. M. Glezer and B. V. Molotilov, *Structure and Mechanical Properties of Amorphous Alloys* (Metallurgiya, Moscow, 1992).
5. Gropal Venu and G. Bhathager Rao, J. Mater. Sci. Lett. **13** (2), 99 (1994).
6. G. E. Abrosimova, S. A. Aronin, and A. V. Serebryakov, Fiz. Met. Metalloved. **68** (3), 552 (1989).
7. T. V. Larionova, O. V. Tolochko, N. O. Gonchukova, and E. V. Novikov, Fiz. Khim. Stekla **22** (3), 334 (1996) [Glass Phys. Chem. **22** (3), 248 (1996)].
8. V. I. Betekhtin, A. M. Glezer, A. G. Kadomtsev, and A. Yu. Kipyatkova, Fiz. Tverd. Tela (St. Petersburg) **40** (1), 85 (1998) [Phys. Solid State **40**, 74 (1998)].
9. A. M. Glezer and V. I. Betekhtin, Fiz. Tverd. Tela (St. Petersburg) **38** (6), 1784 (1996) [Phys. Solid State **38**, 983 (1996)].
10. V. I. Betekhtin, E. L. Gyulikhandanov, A. G. Kadomtsev, *et al.*, Fiz. Tverd. Tela (St. Petersburg) **42** (8), 1420 (2000) [Phys. Solid State **42**, 1460 (2000)].
11. Ya. I. Frenkel, *Introduction to the Theory of Metals* (Moscow, 1958).
12. O. V. Tolochko, T. V. Larionova, N. O. Gonchukova, and I. V. Polents, Fiz. Khim. Stekla **24** (5), 610 (1998) [Glass Phys. Chem. **24** (5), 432 (1998)].
13. V. I. Betekhtin, A. G. Kadomtsev, V. E. Korsukov, *et al.*, Pis'ma Zh. Tekh. Fiz. **24** (23), 58 (1998) [Tech. Phys. Lett. **24**, 932 (1998)].
14. T. Kulik, Mater. Sci. Eng. A **159** (1), 95 (1992).

Translated by O. Borovik-Romanova

Physics of the Solid State, Vol. 43, No. 10, 2001, pp. 1898–1904. Translated from Fizika Tverdogo Tela, Vol. 43, No. 10, 2001, pp. 1821–1827.

DEFECTS, DISLOCATIONS, AND PHYSICS OF STRENGTH

Electromagnetic Emission of Mobile Dislocation Segments in an Ionic Crystal

O. V. Charkina and K. A. Chishko

Physicotechnical Institute of Low Temperatures, National Academy of Sciences of Ukraine, Kharkov, 61164 Ukraine
e-mail: chishko@ilt.kharkov.ua

Received February 1, 2001

Abstract—The problem of electromagnetic emission of an edge dislocation segment moving in an ionic lattice with a NaCl-type structure is considered. The proposed mechanism of electromagnetic emission is associated with the appearance of macroscopic alternating polarization currents along the extraplane edge of the edge dislocation in the course of its motion between adjacent valleys of the Peierls relief. The relationships for electromagnetic radiation fields of an arbitrarily moving segment are derived, and the problem of electromagnetic emission of a segment that executes harmonic oscillations in the field of an external quasi-stationary elastic wave with a frequency $\Omega \ll c/l$ (where l is the segment length and c is the velocity of sound) is treated in detail. The power of the emitted electromagnetic signal and the "acoustoelectromagnetic transformation" coefficient (the ratio between the electromagnetic radiation power and the mechanical power required for setting the segment in motion) are determined. © *2001 MAIK "Nauka/Interperiodica".*

1. INTRODUCTION

Electromagnetic effects that accompany the motion of defects in crystals have been the subject of extensive investigations in modern solid-state physics. Over the last few years, considerable advances have been made in this area of science. First and foremost, these are experimental observations [1–3] and theoretical interpretation [3, 4] of the magnetoplastic effect in ionic crystals and metals and also detailed experimental investigations into the electromagnetic emission of dislocations and cracks [5, 6]. It should be emphasized that these phenomena are essentially dynamic in character and, hence, are of particular importance in the understanding of the nature of plastic deformation in solids. Electromagnetic phenomena in deformed solids have long been studied both from the standpoint of basic research [7] and in relation to applied problems arising, for example, in geophysics [8] and fracture mechanics of structural materials [9, 10].

An interesting dynamic effect in strained crystals is the emission of electromagnetic waves during dislocation motion and the nucleation and growth of cracks. In principle, it is clear that, for example, dislocation motion brings about disturbances in both the crystal lattice and the electronic subsystem of the crystal. As is known, the former disturbance leads to the generation of elastic waves in the sample and the latter disturbance gives rise to electromagnetic emission whose character is determined by the specific properties of dislocations and the medium in which the electromagnetic wave propagates. It seems likely that ionic crystals are the most convenient objects for the investigation of electromagnetic emission of dislocations, because they are dielectrics in which absorption of an electromagnetic signal is virtually absent down to the IR frequency range. On the other hand, dislocations of the majority of the types in these crystals have a charged core [11, 12], so that their motion is naturally attended by effective currents. Therefore, in this case, it is rather simple to construct adequate physical models in which a dislocation is interpreted as a source of electromagnetic waves in the crystal.

Kosevich and Margvelashvili [13] studied the emission of electromagnetic waves by mobile dislocations in ionic crystals and explained this phenomenon in terms of a mechanism based on electroelastic effects in deformed lattices consisting of oppositely charged ions. In our earlier work [14], we proposed an alternative mechanism of electromagnetic emission of edge dislocations in ionic crystals, according to which the electromagnetic emission is due to the occurrence of macroscopic polarization currents along the line of a moving rectilinear dislocation. It turned out that the emission intensity in the latter case is five orders of magnitude higher than that in the former case. Therefore, it can be expected that the mechanism proposed in [14] is responsible for experimentally observable effects.

In [13, 14], the electromagnetic emission was considered for rectilinear edge dislocations. It is clear that, in a real crystal, a dislocation moving through a stopper network is actually a set of oscillating segments. In this respect, it was of interest to solve the problem of electromagnetic emission of a curvilinear dislocation whose configuration is an arbitrary function of time. The aim of the present work was to analyze the formulated problem and to elucidate the contribution from this emission mechanism to the total electromagnetic emission.

1063-7834/01/4310-1898$21.00

2. FORMULATION OF THE PROBLEM

Let us consider an edge dislocation in a cubic cell of the NaCl type with a glide plane coinciding with one of the {110} planes. The Cartesian coordinate system is chosen in such a way that the dislocation glides in the plane $y = 0$ and its line in the absence of external disturbances coincides with the z axis. We assume that the dislocation line in the course of motion is so curved that its configuration in the laboratory coordinate system at any instant of time can be described by the function $x = x_0(z, t)$, which is single-valued with respect to the z coordinate. This means that the dislocation during the motion cannot generate loops of the Frank–Read source type. Therefore, the charge density $\rho(\mathbf{r}, t)$ at the extraplane edge of the curvilinear dislocation (in the core) can be represented as

$$\rho(\mathbf{r}, t) = e^*\delta(y)F(x)\delta(x - x_0(z, t)) \times \sum_{m=-\infty}^{\infty} \{\delta(z - 2ma) - \delta[z - (2m + 1)a]\}. \quad (1)$$

Here, e^* is the effective charge of a node at the extraplane edge, $2a$ is the distance between likely charged ions along the z axis [positive ions are located at the sites $z = 2ma$ and negative ions occupy the sites $z = (2m + 1)a$], and the period of the function $F(x)$ [$|F(x)| \le 1$] in the direction of the dislocation motion is equal to $2b$ (where b is the distance between adjacent minima of a Peierls relief in the direction of the Ox axis). The multiplier $F(x)$ allows for the effective "recharging" of the node located at the dislocation line when this node is displaced to the adjacent valley of the Peierls relief [14]. It is worth noting that, unlike the rectilinear dislocation [14], the sign of the effective charge at the node through which the line of a curvilinear dislocation segment passes [see formula (1)] depends on two coordinates (x_0 and z).

It is evident that the evolution of the charge in the core of a curvilinear dislocation should satisfy the continuity equation

$$\frac{\partial\rho(\mathbf{r}, t)}{\partial t} + \mathrm{div}\mathbf{j}(\mathbf{r}, t) = 0, \quad (2)$$

where $\mathbf{j}$ is the effective current density in the dislocation core. By differentiating relationship (1) with respect to time and rearranging it, we have

$$\frac{\partial\rho}{\partial t} = -ae^*\delta(y)\left\{\frac{\partial}{\partial z}\left[F(x)\frac{\partial}{\partial x}\delta(x - x_0(z, t))V(z, t) \times \sum_{m=-\infty}^{\infty}\delta(z - 2ma)\right] - F(x)\frac{\partial}{\partial z} \times \left[V(z, t)\frac{\partial}{\partial x}\delta(x - x_0(z, t))\right]\sum_{m=-\infty}^{\infty}\delta(z - 2ma)\right\}. \quad (3)$$

Here, we used the approximate expression

$$\sum_{m=-\infty}^{\infty}[\delta(z - 2ma) - \delta[z - (2m + 1)a]] \simeq a\frac{\partial}{\partial z}\sum_{m=-\infty}^{\infty}\delta(z - 2ma),$$

which implies that we are interested only in microscopic quantities that vary slowly at distances of the order of interatomic distances. This corresponds to the usual procedure of microcurrent averaging accepted in electrodynamics of continua [15]. Comparison of relationships (3) and (2) demonstrates that the term under the sign of the total derivative with respect to z in formula (3) is the current density component j_z, that is,

$$j_z(\mathbf{r}, t) = \frac{e^*}{2}\delta(y)F(x)V(z, t)\frac{\partial}{\partial x}\delta(x - x_0(z, t)), \quad (4)$$

where $V(z, t) = \partial x_0(z, t)/\partial t$ is the distribution of velocities of motion of dislocation segment points. The other part of expression (3) is naturally attributed to $\partial j_x/\partial x$. By integrating it over x, we find

$$j_x(\mathbf{r}, t) = -\frac{e^*}{2}\delta(y) \times \int_{-\infty}^{x_0(z, t)} dx'F(x')\frac{\partial}{\partial z}\left[V(z, t)\frac{\partial}{\partial x'}\delta(x' - x_0(z, t))\right] \quad (5)$$

$$= -\frac{e^*}{2}\delta(y)\frac{\partial}{\partial z}\left[V(z, t)\frac{\partial}{\partial x_0}F(x_0(z, t))\Theta(x_0(z, t) - x)\right].$$

When writing relationships (4) and (5), we performed averaging of the corresponding terms in expression (3) over the z coordinate.

Now, it is easy to calculate the components (necessary for further analysis) of the dipole moment vector $\mathbf{d}(t)$ of the dislocation segment. This vector is related to the current density $\mathbf{j}$ by the usual expression [16]

$$\frac{\partial\mathbf{d}}{\partial t} = \int\mathbf{j}(\mathbf{r}, t)dV. \quad (6)$$

With due regard for relationships (4) and (6), the dipole moment component dz is given by

$$\frac{\partial d_z}{\partial t} = \frac{e^*}{2}\int dz'V(z', t)\frac{\partial}{\partial x_0}F(x_0(z', t)) = \frac{e^*}{2}\frac{\partial}{\partial t}\int F(x_0(z', t))dz'. \quad (7)$$

For d_x, after the integration of expression (5) over y and z, we obtain

$$d_x = \frac{e^*}{2}\int_{-\infty}^{+\infty} dx\Big[V(z_1, t)\frac{\partial}{\partial x_0}F(x_0(z_1, t))\Theta(x_0(z_1, t) - x) - V(z_2, t)\frac{\partial}{\partial x_0}F(x_0(z_2, t))\Theta(x_0(z_2, t) - x)\Big], \quad (8)$$

where $z = z_{1,2}$ are the coordinates of the dislocation ends (formally, we can set $|z_{1,2}| \longrightarrow \infty$). For the calculation of integral (8), we assume that the motion of the curvilinear dislocation can be considered a superposition of displacements $u(z, t)$ of dislocation points in a certain accompanying coordinate system and the displacement $X(t)$ of this system in space; i.e., $x_0(z, t) = X(t) + u(z, t)$. To state this differently, the dislocation motion can be treated as a superposition of the motion of a rectilinear (on the average) dislocation and the dislocation point oscillations $u(z, t)$ about the $oX(t)$ axis of the accompanying coordinate system. The oX axis of this system can be chosen, for example, from the condition

$$\int_{z_1}^{z_2} u(z, t)dz = 0.$$

Here, we will not discuss the question as to whether this definition of the accompanying system is unique. For our purposes, it is sufficient that such a system exists in principle. Since integrand (8) involves the δ function, the range of integration in this integrand is actually limited from above by $x = X(t) + u(z, t)$. In this case, the integral over x from $-\infty$ to $X(t)$ becomes zero under the assumption that $V(z_1, t) = V(z_2, t) = dX/dt$ at $|z_{1,2}| \longrightarrow \infty$ and the dislocation ends are simultaneously located in valleys of the Peierls relief; i.e., $F[x_0(z_1, t)] = F[x_0(z_2, t)]$. Then,

$$d_x = -\frac{e^*}{2}u(z, t)[V(z_1, t) - V(z_2, t)]\frac{\partial}{\partial x_0}F(x_0(z_1, t)). \quad (9)$$

Finally, when the segment ends are fixed at stoppers, we obtain $V(z_1, t) = V(z_2, t) = 0$ and the dipole moment component d_x vanishes. It is this case that will be considered in the following discussion.

3. ELECTROMAGNETIC EMISSION OF A DISLOCATION SEGMENT

In this section, we will derive the relationships that describe the electromagnetic fields induced in the crystal by a single dislocation segment, which has the initial length l and is fixed at the points $z = \pm l/2$ on the Oz axis. The dislocation, as before, glides in the plane $y = 0$. As can be seen from formula (5), the current density component j_x for the segment with fixed ends vanishes, so that the evolution of the radiation fields is governed only by the dipole moment component $d_z(t)$.

It is convenient to represent the radiation fields of the segment in the spherical coordinates r, θ, and φ, where the azimuthal angle θ is measured from the Oz axis of the Cartesian coordinate system. The formulas for the strengths $\mathbf{E}(\mathbf{r}, t)$ and $\mathbf{H}(\mathbf{r}, t)$ of electric and magnetic fields of an elementary dipole in the wave zone are given in [17]. The spectral components (Fourier transforms with respect to time) $\mathbf{E}^\omega(r, \theta, \varphi) = (0, E_\theta^\omega(r, \theta, \varphi), 0)$ and $\mathbf{H}^\omega(r, \theta, \varphi) = (0, 0, H_\varphi^\omega(r, \theta, \varphi))$ of the radiation fields have the form

$$E_\theta^\omega(r, \theta, \varphi) = H_\varphi^\omega(r, \theta, \varphi) = \frac{\omega^2}{c^2 r}d_z^\omega \sin\theta \exp\left(i\frac{\omega r}{c}\right). \quad (10)$$

The E_θ^ω, H_φ^ω, and d_z^ω spectral components introduced into expression (10) are determined in the usual manner. For example,

$$d_z^\omega = \int_{-\infty}^{+\infty} dt d_z(t)\exp(-i\omega t)$$

(the spectral components of all the other functions of time are determined in a similar way).

Thus, the problem of calculating the spectral components of the dipole moment reduces to calculation of integral (7) under the most general assumptions about the form of the $u(z, t)$ function that determines the displacements of dislocation segment points. It is clear that the displacements u far from the fixed points can be sufficiently large ($\sim L$). In any case, it is evident that, for macroscopic segments with $l > 10^{-6}$ cm, the inequality $|u(z, t)| \gg b$ is true virtually for all segment points (except for small neighborhoods of fixed points). This allows us to evaluate integral (7) by using the large parameter $|u(z, t)|/b \gg 1$. With the aim of simplifying further calculations, we assume, as was earlier done in [13], that $F(x) = -\cos(\pi x/b)$ and write d_z as

$$d_z = \frac{e^*}{2}\int_{-l/2}^{l/2} \cos\left(\frac{\pi}{b}u(z, t)dx\right). \quad (11)$$

Integral (11) includes the large parameter $u(z, t)/b$ in the argument of the cosine and can be estimated within the stationary phase approximation [18]. As a result, we obtain

$$d_z(t) = -e^*\left(\frac{b}{2l}\right)^{1/2} \times \sum_\alpha \frac{1}{\sqrt{u''_{zz}(z_\alpha, t)}}\cos\left(\frac{\pi}{b}u(z_\alpha, t) + \frac{\pi}{4}\right), \quad (12)$$

where z_α is a set of stationary points determined by the condition $u'_z = 0$ [hereafter, the prime designates the derivative of the $u(z, t)$ function and the subscript indicates the variable with respect to which the derivative is taken]. Therefore, horizontal ($u' = 0$) and weakly curved ($u'' \longrightarrow 0$) portions of the oscillating segment make the main contribution to the emission.

In order to obtain a more concrete result, we calculate the segment motion in the framework of the string dislocation model [19]. In this approximation, the equation of segment motion takes the form

$$\rho_D u''_{tt} + Bu'_t - Gu''_{zz} = -b\sigma(z, t). \quad (13)$$

Here, $\rho_D = (\rho b^2/4\pi)\ln(l/b)$ and $G = (\mu b^2/4\pi)\ln(l/b)$ are the mass per unit length and the line tension of dislocation, respectively; ρ is the density; μ is the shear modulus of the medium; B is the coefficient of dislocation friction; and σ is the external stress. Equation (13) should be complemented by the boundary conditions at the segment ends $u(\pm l/2, t) = 0$ and the initial conditions, which are conveniently written as $u(z, 0) = 0$ and $u'_t(z, 0) = 0$.

In the case of the boundary-value problem (13), its solution, which is usually represented as a series, is of limited utility for obtaining the pictorial results of interest. Since our prime concern is in the construction of particular qualitative dependences, we consider the situation when the segment either is set in motion by a quasi-uniform (on a scale of the order of segment sizes) external field or executes thermofluctuation displacements at low temperatures at which the contribution from higher harmonics to the configuration of a dislocation string is negligibly small. Within these approximations, the law of dislocation segment motion for calculating the dipole moment can be deduced according to the following scheme.

Let us construct the approximate solution to Eq. (13) by using the direct variational procedure. The action for the dislocation string can be written as

$$S = \int dt \int_{-l/2}^{l/2} dz \mathcal{L}(u, u'_t, u'_z, t), \quad (14)$$

where $\mathcal{L}$ is the Lagrangian density defined by the expression

$$\mathcal{L}(u, u'_t, u'_z, t) = \frac{\rho_D}{2}(u'_t)^2 - \frac{G}{2}(u'_z)^2 - bu\sigma(z, t). \quad (15)$$

The Euler equation corresponding to this variational problem in the presence of friction forces is given by

$$\frac{d}{dt}\left[\frac{\partial \mathcal{L}}{\partial u'_t}\right] + \frac{d}{dz}\left[\frac{\partial \mathcal{L}}{\partial u'_z}\right] - \frac{\partial \mathcal{L}}{\partial u} = -\frac{\partial \mathcal{F}}{\partial u'_t}. \quad (16)$$

The term on the right-hand side of Eq. (16) describes the friction forces expressed in terms of the dissipative function

$$F = \int dt \int_{-l/2}^{l/2} dz \mathcal{F}(u'_t, z, t) \quad (17)$$

with the density

$$\mathcal{F} = \frac{B}{2}(u'_t)^2. \quad (18)$$

It is easy to demonstrate that the formulated variational problem is equivalent to Eq. (13).

Note that, in the majority of practically applicable cases, the external stress field that excites the segment oscillations can be treated as uniform in regions of size ~l. Then, the segment shape at each instant of time is nearly parabolic. Indeed, in the uniform static field $\sigma = \text{const}$, the segment shape is determined by the equation

$$Gu''_{zz} = -b\sigma,$$

The solution to this equation under zero boundary conditions at the ends (at $z = \pm l/2$) is represented by the function

$$u(z) = \frac{\sigma b l^2}{2G}\gamma(z), \quad \gamma(z) = \left(\frac{1}{4} - \frac{z^2}{l^2}\right). \quad (19)$$

Apparently, in a quasi-stationary external elastic field, the oscillating segment has a shape similar to that described by relationships (19), but the bending deflection varies with time, because the stress σ is time dependent.

Therefore, the configuration of the segment, which moves under the changing external load $\sigma(z, t)$ at any instant of time is approximately described by the solution of the direct variational problem with a family of trial functions of the type

$$u(z, t) = U(t)\gamma(z). \quad (20)$$

Substitution of expression (20) into relationship (14) and integration over the z coordinate give the averaged Lagrangian function

$$\begin{aligned} \ell < (U'_t, U, t) &= \int_{-l/2}^{l/2} dz \mathcal{L}(u, u'_t, u'_z, t) \\ &= \frac{l}{6}\left\{\frac{\rho_D}{10}(U'_t)^2 - \frac{G}{l^2}U^2(t) - b\bar{\sigma}(t)U(t)\right\}, \end{aligned} \quad (21)$$

where

$$\bar{\sigma}(t) = \frac{1}{l}\int_{-l/2}^{l/2} dz\sigma(z, t).$$

After varying the action $S = \int dt \ell(U'_t, U, t)$ with respect to U, we obtain the equation

$$\frac{d^2U}{dt^2} + 2\beta\frac{dU}{dt} + \omega_0^2 U = f(t), \quad (22)$$

where

$$\beta = (B/2\rho_D), \quad \omega_0^2 = (10G/\rho_D l^2),$$
$$f(t) = (5b\bar{\sigma}(t)/\rho_D).$$

Consequently, the problem of the segment motion reduces to the equation of motion of an effective harmonic oscillator under the action of a variable external force.

The solution of Eq. (22) can be written for an arbitrary function $f(t)$ on the right-hand side. Thereafter, substitution of expression (20) into relationship (11) and integration over the z coordinate lead to the following formula for the dipole moment:

$$d_z(t) = -e^* l\left(\frac{\pi}{8s(t)}\right)^{1/2} \times [\cos(s(t))C(s(t)) + \sin(s(t))S(s(t))], \quad (23)$$

where $s(t) = \pi U(t)/4b$ and $C(s)$ and $S(s)$ are the Fresnel integrals [20]. By using relationship (23), the radiation fields in the dipole approximation can be written in the ordinary manner [16].

Now, we consider, in greater detail, the important specific case of segment motion when the segment executes harmonic oscillations under the action of a sinusoidal external stress with frequency Ω, that is,

$$\bar{\sigma}(t) = \sigma_0 \cos(\Omega t + \delta).$$

In this case, the solution of Eq. (22) is conveniently represented in the form

$$U(t) = A\cos(\Omega t + \Delta), \quad (24)$$

where

$$A = \frac{5b\sigma_0}{\rho_D}\frac{1}{\sqrt{(\omega_0^2 - \Omega^2)^2 + 4\beta^2\Omega^2}},$$
$$\Delta = \delta + \delta', \quad \tan\delta' = -\frac{2\beta\Omega}{\omega_0^2 - \Omega^2}.$$

The dipole moment of the segment executing harmonic oscillations can be determined from relationship (23) with allowance made for expression (24). In this case, it is also of interest to derive the formulas that describe the spectral composition of radiation. To accomplish this, the dipole moment can be written in the form of a Fourier series:

$$d_z = \sum_{n=-\infty}^{\infty} d_n \exp(in\Omega t). \quad (25)$$

The Fourier amplitudes d_n of the harmonics of the dipole moment with frequencies $\omega_n = n\Omega$ are defined by the formulas

$$d_n = \frac{e^*}{2\pi}\int_0^{2\pi} d\tau \int_0^{l/2} dz \exp(-in\tau)\cos\left[\frac{\pi A}{b}\gamma(z)\cos(\tau + \Delta)\right] \quad (26)$$
$$= \frac{e^*}{2}\exp\left[-in\left(\Delta - \frac{\pi}{2}\right)\right]\int_0^{l/2} dz[J_n(p(z)) + J_n(-p(z))],$$

where

$$p(z) = \frac{\pi A}{b}\gamma(z)$$

and $J_n(x)$ is the nth-order Bessel function of the first kind [20]. As a result, we find that, in the case under consideration, only the amplitudes of even harmonics are nonzero, that is,

$$d_{2n} = -e^*\exp\left[-2in\left(\Delta - \frac{\pi}{2}\right)\right]\int_0^{l/2} J_{2n}(p(z))dz$$
$$= \frac{\pi e^* l}{2\sqrt{2}}\exp\left[-2in\left(\Delta - \frac{\pi}{2}\right)\right]J_{n+\frac{1}{4}}\left(\frac{\alpha}{2}\right)J_{n-\frac{1}{4}}\left(\frac{\alpha}{2}\right), \quad (27)$$
$$\alpha = \frac{\pi A}{4b},$$

and $d_{2n-1} = 0$ (the integral in expression (27) is transformed in accordance with the known rules [21]).

Evidently, the amplitude of the dislocation segment oscillations is high compared to the Burgers vector; i.e., $\alpha \gg 1$. Taking into account this circumstance, the expressions for the electromagnetic radiation fields can be somewhat simplified by calculating the corresponding asymptotics at $\alpha \longrightarrow \infty$. However, this procedure cannot be performed immediately in relationship (27), because the Fourier amplitudes d_{2n} enter into infinite sums and the asymptotics of the Bessel functions of an arbitrary order in these sums considerably depend on the order-to-argument ratio [20]. Consequently, in order to deduce the formulas for the space–time evolution of the radiation fields, it is necessary to substitute expression (27) into relationship (10) and to carry out exact summation over the harmonics $\omega_n = n\Omega$. As a result, we find

$$E_\theta(r, \theta, \varphi) = -\frac{\pi e^* l}{\sqrt{2}c^2 r}\sin\theta\frac{\partial^2}{\partial t^2}\sum_{n=1}^{\infty}(-1)^n J_{n+\frac{1}{4}}\left(\frac{\alpha}{2}\right)$$
$$\times J_{n-\frac{1}{4}}\left(\frac{\alpha}{2}\right)\cos 2n\tau = -\frac{\sqrt{\pi}e^* l}{\sqrt{2\alpha}c^2 r}\sin\theta\frac{\partial^2}{\partial t^2} \quad (28)$$
$$\times \frac{\cos(\alpha\cos\tau)C(\alpha\cos\tau) + \sin(\alpha\cos\tau)S(\alpha\cos\tau)}{\sqrt{\cos\tau}},$$

where

$$\tau = \Omega\left(t - \frac{r}{c}\right) - \Delta. \text{ e} \quad (29)$$

Relationship (28) for the electromagnetic radiation fields remains finite, in particular, at $\cos\tau \longrightarrow 0$, because the Fresnel integrals in this case also tend to zero [20].

In the asymptotic limit $\alpha \longrightarrow \infty$, relationship (28) can be simplified only by retaining the terms of higher order in the α parameter after differentiation with respect to time. The Fresnel integrals $C(\alpha\cos\tau)$ and $S(\alpha\cos\tau)$ cannot be replaced by the corresponding asymptotics, since their arguments are not necessarily large (due to the arbitrariness of $\cos\tau$. Therefore, at $\alpha \gg 1$, we have

$$E_\theta(r, \theta, \varphi) \simeq \frac{\sqrt{\pi}e^* l\alpha^{3/2}\Omega^2\sin\theta}{\sqrt{2}c^2 r}\frac{\sin^2 r}{\sqrt{\cos\tau}} \quad (30)$$

$$\times[\cos(\alpha\cos\tau)C(\alpha\cos\tau) + \sin(\alpha\cos\tau)S(\alpha\cos\tau)].$$

Note also that formulas (28) and (30), which are the result of complex calculations, are similar in form to the aforementioned expression (23).

The peak strength of the electric component of the radiation field is determined from formula (30) at $\cos\tau = 0$, that is,

$$E_\theta \sim \frac{e^* l\Omega^2}{\sqrt{2}c^2 r}\left(\frac{\pi A}{4b}\right)^2 \sin\theta. \quad (31)$$

We now estimate the radiation field strength for a system of dislocation segments in a certain typical case. For one segment with length $l \sim 10^4 b \sim 10^{-4}$ cm, oscillation amplitude $A \sim 10^2 b$, and oscillation frequency $\Omega \sim 10^4$ s^{-1} (pumping in the kilohertz frequency range, i.e., at $\Omega \ll \Omega_0$), we find $E \sim 10^{-17}$ V/m at distances $r \sim$ 1 cm. For a moderate dislocation density ($\sim 10^8$ cm^{-2}) in a crystal, the sample 1 cm^3 in volume contains $\sim 10^{12}$ dislocation segments and the total radiation field strength E of these segments is equal to $E \sim 10$ μV/m. This can be measured with instruments of a standard medium accuracy class (with a sensitivity of ~1 μV/m). Moreover, the amplitude of the electromagnetic emission sharply ($\sim\Omega^2$) increases with an increase in the pumping frequency. Thus, it is obvious that the effects under consideration can be observed directly in experiments.

The spectral intensity of radiation (the intensity of the 2*n*th harmonic of radiation) is represented as

$$dI_{2n} = \frac{4n^4\Omega^4|d_{2n}|^2}{\pi c^3}\sin^3\theta d\theta d\varphi. \quad (32)$$

The total intensity (power) of radiation of the segment is obtained through integrating relationship (28) over angles followed by summation over the frequencies, which leads to the expression

$$I = \frac{4\pi^2 e^{*2} l^2\Omega^4}{3c^3}\sum_{n=1}^{\infty} n^4 J^2_{n+\frac{1}{4}}\left(\frac{\alpha}{2}\right)J_{n-\frac{1}{4}}\left(\frac{\alpha}{2}\right). \quad (33)$$

At $\alpha \gg 1$, the estimate

$$I \sim \frac{2e^{*2} l^2}{3c^3}\Omega^4\left(\frac{\pi A}{4b}\right)^4. \quad (34)$$

is valid. Substitution of the corresponding values (used above for estimating the radiation field strength) into expression (34) gives $I \sim 10^{-25}$ erg/s.

Finally, we determine the acoustoelectromagnetic transformation coefficient, which is equal to the ratio between the electromagnetic radiation power and the mechanical power required for setting segments in motion ($\sigma_0/\mu \sim 10^{-5}$), that is,

$$\eta \simeq \frac{2\pi}{15}\frac{e^{*2}\Omega^3}{c^3\sigma_0 l}\left(\frac{l}{b}\right)^2 \sim 10^{-31}. \quad (35)$$

As is seen, only a very small portion of the mechanical power expended for deforming the crystal is transformed into the energy of electromagnetic radiation of dislocations. However, as can be seen from the above results, the strengths of electromagnetic fields generated by dislocations appear to be quite sufficient for experimental detection of the effects under discussion.

4. DISCUSSION

The results obtained in the present work demonstrate that any dislocation motion in ionic crystals should be attended by an electromagnetic emission whose intensity can be sufficiently high even for a moderate dislocation density ($\sim 10^8$ cm^{-2}) in the sample. The emission mechanism discussed in this work is associated with alternating the polarization macrocurrents in the core of the moving dislocation and does not imply the presence of any static charges of the charged jog type at the dislocation line [11, 12]. Therefore, the proposed mechanism can be realized in any nonpiezoelectric ionic crystal in which dislocations have edge components. In principle, the electromagnetic emission accompanies any motion of dislocation segments and, in particular, thermal fluctuations of dislocation lines. According to the estimates made in the present work, this emission can be recorded in a properly performed experiment. The coefficient of transformation of the mechanical dislocation energy into the electromagnetic radiation is very small. However, the electromagnetic radiation intensity rapidly increases with an increase in the frequency and amplitude of dislocation segment oscillations.

The most efficient technique of detecting electromagnetic emission of dislocations in ionic crystals most likely involves simultaneous and coherent excita-

tion of a large number of dislocation segments in order to obtain an electromagnetic signal with a sufficient amplitude. Such an excitation in a crystal can be achieved by applying an alternate external stress with a known frequency (for example, as is the case of experiments on internal friction). This also makes it possible to analyze the amplitude, intensity, and spectral composition of electromagnetic radiation as functions of the frequency and amplitude of the mechanical pumping. The experimental verification of the predicted dependences of the radiation intensity [relationship (33)] on the frequency and the amplitude of external pumping is of considerable interest in relation to the validation of the proposed dislocation models of electromagnetic emission in strained crystals in its adequacy. It should be emphasized once again that the problem of electromagnetic emission in solids has been rather widely discussed in respect to various applications in materials science and geophysics. However, the development of physical aspects of phenomena associated with this problem (their experimental study and adequate theoretical description of the electromagnetic emission mechanisms in deformed solids) is, in essence, still in its infancy. The present work is a continuation of a series of investigations aimed at solving the aforementioned interesting and important physical problems.

REFERENCES

1. V. I. Al'shits, E. V. Darinskaya, and O. L. Kazakova, Fiz. Tverd. Tela (St. Petersburg) **40** (1), 81 (1998) [Phys. Solid State **40**, 70 (1998)].
2. Yu. I. Golovin and R. B. Mironov, Fiz. Tverd. Tela (St. Petersburg) **37** (7), 2118 (1995) [Phys. Solid State **37**, 1152 (1995)].
3. V. I. Al'shits, E. V. Darinskaya, I. V. Gektina, and F. F. Lavrent'ev, Kristallografiya **35** (4), 1014 (1990) [Sov. Phys. Crystallogr. **35**, 597 (1990)].
4. M. I. Molotskiĭ, Fiz. Tverd. Tela (Leningrad) **33** (10), 3112 (1991) [Sov. Phys. Solid State **33**, 1760 (1991)].
5. Yu. I. Golovin and A. A. Shibkov, Fiz. Tverd. Tela (Leningrad) **28** (11), 3492 (1986) [Sov. Phys. Solid State **28**, 1964 (1986)].
6. Yu. I. Golovin, A. V. Gorbunov, and A. A. Shibkov, Fiz. Tverd. Tela (Leningrad) **30** (7), 1931 (1988) [Sov. Phys. Solid State **30**, 1116 (1988)].
7. W. Nowacki, *Electromagnetic Effects in Solids* (PWN, Warsaw, 1983; Mir, Moscow, 1986), translated from Polish.
8. M. B. Gokhberg, V. A. Morgunov, and O. A. Pokhotelov, *Seismoelectromagnetic Phenomena* (Nauka, Moscow, 1988).
9. A. I. Goncharov, V. P. Koryavov, V. M. Kuznetsov, *et al.*, Dokl. Akad. Nauk SSSR **255** (4), 821 (1980).
10. Yu. P. Malyshkov, V. F. Gordeev, V. P. Dmitriev, *et al.*, Zh. Tekh. Fiz. **54** (2), 336 (1984) [Sov. Phys. Tech. Phys. **29**, 197 (1984)].
11. R. W. Whitworth, Adv. Phys. **24**, 203 (1975).
12. R. W. Whitworth, Philos. Mag. **11** (109), 83 (1965).
13. A. M. Kosevich and I. G. Margvelashvili, Ukr. Fiz. Zh. **12** (12), 2007 (1967).
14. K. A. Chishko and O. V. Charkina, Fiz. Tverd. Tela (St. Petersburg) **38** (9), 2775 (1996) [Phys. Solid State **38**, 1521 (1996)].
15. L. D. Landau and E. M. Lifshitz, *Course of Theoretical Physics*, Vol. 8: *Electrodynamics of Continuous Media* (Fizmatgiz, Moscow, 1959; Pergamon, New York, 1984).
16. L. D. Landau and E. M. Lifshitz, *The Classical Theory of Fields* (Nauka, Moscow, 1965; Pergamon, Oxford, 1975).
17. I. E. Tamm, *Priciples of the Electricity Theory* (GITTL, Moscow, 1954).
18. A. Erdelyi, *Asymptotic Expansions* (Dover, New York, 1956; Fizmatgiz, Moscow, 1962).
19. A. Granato and K. Lücke, J. Appl. Phys. **27** (2), 583 (1956).
20. E. Jahnke, F. Emde, and F. Lösch, *Tables of Higher Functions* (McGraw-Hill, New York, 1960; Nauka, Moscow, 1968).
21. A. P. Prudnikov, Yu. A. Brychkov, and O. I. Marichev, *Integrals and Series* (Nauka, Moscow, 1983; Gordon and Breach, New York, 1986).

Translated by O. Borovik-Romanova

Physics of the Solid State, Vol. 43, No. 10, 2001, pp. 1905–1908. Translated from Fizika Tverdogo Tela, Vol. 43, No. 10, 2001, pp. 1828–1831.

DEFECTS, DISLOCATIONS, AND PHYSICS OF STRENGTH

Spin-Flip Scattering of Conduction Electrons by Dislocations in a Metal

V. M. Zholkevskiĭ and G. A. Denisenko

Shubnikov Institute of Crystallography, Russian Academy of Sciences, Leninskiĭ pr. 59, Moscow, 117333 Russia

Received November 23, 2000; in final form, March 7, 2001

Abstract—The spin-flip scattering of conduction electrons by dislocations in metals with a strong spin–orbit coupling is considered. Calculations are performed in terms of the model spin–orbit potential describing the spin-flip scattering of conduction electrons. It is shown that deformation of the crystal lattice in a metal leads to a change in the structure factor. The core of a rectilinear edge dislocation is calculated by the molecular dynamics method. The results obtained are compared with the experimental data on conduction-electron spin resonance (CESR) in copper. *© 2001 MAIK "Nauka/Interperiodica".*

1. INTRODUCTION

In the problem of charge carrier scattering in metals and semiconductors, the case of spin-flip scattering has attracted the particular interest of researchers [1]. Spin-flip scattering is of considerable importance in the understanding of the mechanism of conduction-electron spin resonance (CESR) [2]. It is this scattering that is responsible for the broadening of resonance lines in the CESR method. Spin flips are associated with changes in the spin–orbit interaction in metals, thermal lattice vibrations, impurity atoms, and intrinsic structural defects (vacancies, grain boundaries, dislocations, stacking faults, etc.). Dislocations are among the most interesting types of structural defects. The problems that arise in calculating the electrical resistance caused by dislocations (in particular, the problems concerning the role of the dislocation core and the possible resonance scattering by localized levels) and in interpretating the experimental results are well known. In the case of spin–orbit interaction, the angular dependences on the directions of incident and scattered electrons differ from those observed in conventional (without a spin flip) scattering, which makes a dominant contribution to the measured electrical resistance. In this respect, the investigation of spin-flip scattering can provide additional information on the geometric characteristics of scattering centers.

The spin-flip scattering of conduction electrons by dislocations in plastically strained metals with a strong spin–orbit coupling (Ag, Cu, and Al) was experimentally investigated by Beuneu and Monod [3]. It should be noted that the conventional techniques successfully used for observation of electron paramagnetic resonance in metals with a weak spin–orbit coupling (alkali metals) are unsuitable in this case because of the large width of the resonance line. The necessity of using special techniques and equipment (for example, the "spin transparency" method [4]) apparently explains why there is only a small number of works dealing with conduction-electron spin resonance in metals with a strong spin–orbit coupling, especially, studies on spin-flip scattering by structural defects of metals.

Unfortunately, no theoretical analysis of the results obtained was performed in [3]. The attempt made by these authors to interpret the experimental data in terms of the phonon scattering mechanism can only be considered qualitative.

The calculations of spin-flip scattering of conduction electrons by dislocations were carried out in [5–7] within the framework of the method applied earlier to liquid metal alloys [8] and phonon scattering [9]. In this approach, information on the spatial features of a defect is contained in the structure factor. The theoretical treatment was performed either using the standard spin–orbit operator and the orthogonalized-plane-wave theory for the description of conduction electrons [5, 6] or with the model spin–orbit pseudopotential (proposed by Animalu [10]) [5, 7]. The spin-flip scattering was calculated in the Born approximation. A dislocation core (the region where the linear theory of elasticity is inapplicable) was simulated by a hollow cylinder, as was done in previous works on the electrical resistance caused by dislocations. The cylinder diameter was chosen by fitting the calculated electrical resistance to the experimental data.

These calculations for copper and silver demonstrated reasonable agreement between the theoretical and experimental values of the spin relaxation time, the quantity characterizing the spin-flip scattering. However, the calculated time of spin relaxation for aluminum was found to be considerably shorter than the experimental spin-relaxation time.

In the present work, the spin-flip scattering of conduction electrons by dislocations was considered using the numerical molecular dynamics simulation of the core of a rectilinear edge dislocation without invoking the dislocation core model mentioned above.

2. CALCULATION TECHNIQUE

Let us assume that the metal lattice potential can be approximated by the sum of spherically symmetric nonoverlapping potentials. In this case, the model pseudopotential V_M [10], which accounts for the spin–orbit interaction, can be represented in terms of the conventional model Heine–Abarenkov potential V_{HA} [11] and the potential $V_{s\text{-}o}$ (characterizing the spin–orbit interaction) according to the relationship

$$V_M = V_{\mathrm{HA}} + V_{s\text{-}o}, \tag{1}$$

where

$$V_{s\text{-}o} = \sum_j \mathbf{s}\mathbf{l}_j \sum_l \lambda_l f_l(|\mathbf{r} - \mathbf{r}_j|) P_l. \tag{2}$$

Here, $\mathbf{l}_j$ is the operator of the angular momentum of a conduction electron with respect to the ion located in the position $\mathbf{r}_j$, $\mathbf{s}$ is the electron spin, λ_l stands for the parameters of the model potential, and P_l is the projection operator on the space of states with the orbital quantum number l. It is assumed that $f_l(r) = 1$ at $r \le R_M$ and $f_l(r) = 0$ at $r > R_M$ (where R_M is the model radius).

In the Born approximation, the relaxation time T_1 of the longitudinal magnetization component (the quantity characterizing the spin-flip scattering of electrons due to the spin–orbit interaction $H_{s\text{-}o}$) is defined by the relationship [2]

$$T_1^{-1} = \frac{2\pi\rho_0(E_{\mathrm{F}})}{\hbar}\iint \frac{d\Omega d\Omega'}{(4\pi)^2}\left|\langle \Psi_{\mathbf{k}_{\mathrm{F}}'s'}|H_{s\text{-}o}|\Psi_{\mathbf{k}_{\mathrm{F}}s}\rangle\right|^2, \tag{3}$$

where $\rho_0(E_{\mathrm{F}}) \equiv \rho(E_{\mathrm{F}})V$ is the density of states near the Fermi level, V is the sample volume, $\Psi_{\mathbf{k}_{\mathrm{F}}s}$ is the conduction-electron wave function, s is the spin state, and $\mathbf{k}_{\mathrm{F}}$ is the Fermi wave vector. In this expression, the integral is to be taken along the directions of the wave vectors of incident and scattered electrons.

In the spin-flip scattering of electrons, both interactions described by relationship (1) should be taken into account. In the case of dislocations, spin-flip scattering arises from the perturbation of potential (1) due to displacements of ions from the initial positions. This means that the displaced ions of the host lattice play the role of scattering centers. In this case (see the discussion of the efficiency of two spin-flip mechanisms in [1]), the spin-flip scattering can be evaluated by doubling the numerical value of the matrix element in expression (3). The same conclusion was made by Animalu [10].

On this basis, we now substitute $V_{s\text{-}o}$ and $\Psi_{\mathbf{k}_{\mathrm{F}}s}$ for $H_{s\text{-}o}$ and the pseudowave function, respectively, and then approximate the orbital part of the pseudowave function by a plane wave. Using the relationship derived in [10] for the model pseudopotential matrix element calculated in terms of plane waves, we obtain the following expression:

$$T_1^{-1} = \frac{\rho_0(E_{\mathrm{F}})}{8\pi\hbar k_{\mathrm{F}}^4}\iint d\Omega\delta\Omega'\left|g\delta S(\mathbf{q})\langle s'|\mathbf{s}[\mathbf{k}_{\mathrm{F}}\times\mathbf{k}_{\mathrm{F}}']s\rangle\right|^2, \tag{4}$$

Here,

$$g = \frac{8\pi}{\Omega_0}\sum_l 2\lambda_l(2l+1)\Lambda_l P_l'(\cos(\mathbf{k}_{\mathrm{F}}', \mathbf{k}_{\mathrm{F}})),$$

where Ω_0 is the unit cell volume, $P_l' \equiv dP_l/dx$, and P_l stands for the Legendre polynomials.

In the spherical Fermi surface approximation, the expression for Λ_l can be written as

$$\Lambda_l = \int_0^{R_M} j_l^2(k_{\mathrm{F}}r)r^2 dr. \tag{5}$$

In expression (4), $\delta S(\mathbf{q})$ is the change in the structure factor $S(\mathbf{q})$ of a perfect crystal lattice of the metal due to the deformation produced by dislocations. The structure factor $S(\mathbf{q})$ is given by the usual relationship,

$$S(\mathbf{q}) = \frac{1}{N}\sum_j \exp\{-i(\mathbf{q}\mathbf{r}_j)\}, \tag{6}$$

where $\mathbf{q} = \mathbf{k}_{\mathrm{F}}' - \mathbf{k}_{\mathrm{F}}$ and N is the total number of ions in the volume V.

The dislocation core is calculated by the molecular dynamics technique with the use of the pair central Morse potential [11]

$$U(r_{ij}) = D[\exp\{-2\alpha(r_{ij} - r_0)\} - 2\exp\{-\alpha(r_{ij} - r_0)\}], \tag{7}$$

where r_{ij} is the distance between two ions, r_0 is the equilibrium distance between two ions, D is the dissociation energy of an ion pair, and α is the constant characterizing the "rigidity" of the interaction.

Now, we assume that atomic displacements along a rectilinear dislocation are equal to zero; i.e., we consider the two-dimensional problem in the plane perpendicular to the dislocation line ($z = 0$). The initial atomic displacements about the rectilinear edge dislocation are specified by solving the problem in terms of the elasticity theory [12], that is,

$$\begin{aligned} u_x &= \frac{b}{2\pi}\left[\arctan\left(\frac{y}{x}\right) + \frac{xy}{2(1-\sigma)r^2}\right] + C_1, \\ u_y &= \frac{b}{4\pi(1-\sigma)}\left[\frac{1-2\sigma}{2}\ln(r^2) + \frac{x^2}{r^2}\right] + C_2, \end{aligned} \tag{8}$$

where $r^2 = x^2 + y^2$, σ is the Poisson ratio, b is the strength of the dislocation, and C_1 and C_2 are the constants of integration. The starting configuration is constructed in such a way that the dislocation intersects the

plane $z = 0$ at the point with coordinates $x = 0$ and $y = 0.5$. The C_1 constant is determined from the condition

$$u_x\big|_{\substack{x \to +0 \\ y > 0}} = 0, \quad u_x\big|_{\substack{x \to -0 \\ y > 0}} = 0,$$

$$u_x\big|_{\substack{x > 0 \\ y \to -\infty}} = -b/2, \quad u_x\big|_{\substack{x < 0 \\ y \to -\infty}} = b/2.$$

The condition $u_y(x, y) = u_y(-x, y)$ is satisfied at any C_2. Therefore, $C_1 = b/2$ at $x > 0$ and $y > 0$, $C_1 = -b/2$ at $x < 0$ and $y > 0$, and $C_2 = 0$ at any values of x and y.

The plane $z = 0$ is separated into two regions: the interior region *I* (the computational cell) and the matrix region *II*. The atomic displacements in region *II* obey the linear theory of elasticity, and the atomic positions in region *I* are determined by solving the dynamic equations [12] with the chosen interatomic potential. This method, as applied to the calculation of the dislocation core with a fixed boundary between regions *I* and *II*, has certain limitations. The chief limitation of the method lies in the fact that the boundary conditions at the interface between these regions are ignored in the elastic solution for region *II*. Different improvements of this model that account for many of the subtle effects of the interplay between the regions under consideration and the construction of models with a mobile boundary have been described by Teodosiu [13]. In our case, the spin relaxation times were estimated by the fixed boundary method. As criteria for choosing the radius R of region *I*, we used the smallness of the difference between the atomic displacements determined from dynamic equations and relationships (8) for the corresponding atoms at the boundary and the smallness of the strain arising at the same boundary (which makes it possible to use the linear theory of elasticity in our calculation). It was found that, for the potential defined by Eq. (7), the region with a radius of the order of ten interatomic distances satisfies the above criteria. The strain at the boundary of this computational cell did not exceed 0.01.

In the course of molecular dynamics calculations of the atomic positions in the computational cell region, we used the procedure of artificial energy dissipation (artificial damping) [14]. This procedure consists in setting all the velocity components equal to zero at the instant the kinetic energy of the system reaches a maximum. In addition, the velocity of the jth particle was taken equal to zero at the instant of time t when the particle began to move in a direction opposite to the force $F_j(t)$ acting between the other particles [12], that is,

$$\mathbf{F}_j(t)\mathbf{v}_j(t) \le 0, \quad j = 1, 2, \ldots, N, \tag{9}$$

where $\mathbf{v}_j$ is the particle velocity.

The criterion for completion of the calculations is the small accumulation of the kinetic energy of the system between the damping procedures.

A theoretical analysis showed [5, 7] that, in the case of copper and silver, it is sufficient to leave the term with $l = 1$ in expression (4). In order to calculate the time of spin relaxation due to dislocations, it is necessary to carry out averaging of expression (4) over the angles (which allows for arbitrariness in the direction of the external constant magnetic field with respect to the dislocation axis in the experiment with conduction-electron spin resonance), to integrate the resulting expression along the dislocation axis, and to average it over the directions of the incidence and scattering of electrons.

After this averaging in our special case, we obtain

$$T_1^{-1} = \frac{128\pi^2\rho(E_F)}{k_F r_0^2}\lambda_1^2\Lambda_1^2 X\rho_d, \tag{10}$$

$$X = N^{4/3}\iint d\varphi d\varphi' |\delta S(\varphi, \varphi')|^2 \times [1 - \cos(\varphi - \varphi') + 2\sin^2(\varphi - \varphi')], \tag{11}$$

where φ and φ' are the polar angles of the vectors $\mathbf{k}_F$ and $\mathbf{k}_F'$, respectively, and ρ_d is the dislocation density. The quantity $\delta S(\varphi, \varphi')$ in formula (11) represents the change in the part of the structure factor (6) that describes the atomic positions in the plane ($z = 0$) perpendicular to the dislocation axis. This quantity is proportional to $N^{-2/3}$, where $N^{2/3}$ is the number of atoms in the plane.

3. NUMERICAL ESTIMATES AND DISCUSSION

Let us now carry out the numerical evaluation for copper. When calculating the X parameter defined by relationship (11), the quantity $\delta S(\varphi, \varphi')$ was determined from the atomic positions obtained using the molecular dynamics method for a distorted crystal lattice. The calculation was performed for the following parameters of potential (7): $D = 0.3429$ eV, $\alpha = 1.3588$ Å^{-1}, and $r_0 = 2.866$ Å [11]. The Poisson ratio σ and the strength of dislocation b in expression (8) for atomic displacements were taken as follows: $\sigma = 0.345$ [7] and $b \approx r_0$. With these parameters, the X parameter was found to be equal to 10. The estimate for copper was obtained using the following parameters: $\lambda_1 = 0.003$ au, $R_M = 4.3$ au, $\rho(E_F) = 1.35 \times 10^{34}$ erg^{-1} cm^{-3}, and $k_F = 1.36 \times 10^8$ cm^{-1} [7]. As a result, the spin relaxation time T_1^{-1} per unit density of dislocations was estimated at 4×10^{-3} s^{-1} cm^2. According to [3], the experimental half-width of the resonance line per unit dislocation density is equal to 1.5 ± 0.3 G cm^2, which corresponds to $T_1^{-1} \approx 2.7 \times 10^{-3}$ s^{-1} cm^2. It is clear that the real structure of dislocation networks under deformations used in the experiment is more complex than the structure of the rectilinear edge dislocations used in our model. From this viewpoint, agreement between the results of calculations and the experimental data is wholly satisfactory.

A number of general remarks need to be made. In the present work, we used the Born approximation. It is evident that this approximation fails to account for scattering when the condition $qa \ll 1$ (where q is the magnitude of the change in the wave vector and a is the characteristic size of the scattering region) is not satisfied. Since, in our case, $a \approx k_F^{-1}$ for the dislocation core, the above condition means that large-angle scattering is disregarded. Apparently, this factor is not of critical importance in interpreting the experimental CESR data, because, in this case, the observed resonance line width is determined by the scattering of all conduction electrons (i.e., the fraction of electrons involved in large-angle scattering is small) and the dislocation structure in the sample is disordered. Note that the used assumption as to the dominant role of small-angle scattering made it possible to compare the scatterings by dislocations and phonons [1, 3].

The calculated value of T_1^{-1} is close to the estimates obtained by Contreras and Helman [6] (0.54×10^{-3} s^{-1} cm^2) and Denisenko and Ermakov [7] (4.6×10^{-3} s^{-1} cm^2). Nonetheless, this result is of undeniable interest, because it has been derived without invoking the model concept of dislocation core.

REFERENCES

1. V. F. Gantmakher and Y. B. Levinson, *Carrier Scattering in Metals and Semiconductors* (Nauka, Moscow, 1984; North-Holland, New York, 1987).
2. B. M. Khabibullin and É. G. Kharakhash'yan, Usp. Fiz. Nauk **111** (3), 483 (1973) [Sov. Phys. Usp. **16**, 806 (1973)].
3. F. Beuneu and P. Monod, Phys. Rev. **13** (8), 3424 (1976).
4. J. Winter, *Magnetic Resonance in Metals* (Clarendon, Oxford, 1971).
5. G. A. Denisenko, Fiz. Tverd. Tela (Leningrad) **19** (6), 1613 (1977) [Sov. Phys. Solid State **19**, 942 (1977)].
6. D. A. Contreras and J. S. Helman, Phys. Rev. B **16** (6), 3493 (1977).
7. G. A. Denisenko and Yu. A. Ermakov, J. Phys. F **10** (8), 1303 (1980).
8. J. S. Helman and R. A. B. Devine, Phys. Rev. B **4** (4), 1153 (1971).
9. R. A. B. Devine and J. S. Helman, Phys. Rev. B **4** (12), 4384 (1971).
10. A. O. E. Animalu, Philos. Mag. **13** (121), 53 (1966).
11. R. M. J. Cotterill and M. Doyama, Phys. Rev. **145** (1), 465 (1966).
12. *Crystal Defects and Their Computer Simulation*, Ed. by Yu. A. Osip'yan (Nauka, Leningrad, 1980).
13. C. Teodosiu, *Elastic Models of Crystal Defects* (Springer-Verlag, Berlin, 1982; Mir, Moscow, 1985).
14. P. C. Gehlen, A. R. Rosenfield, and G. T. Hahn, J. Appl. Phys. **39** (11), 5246 (1968).

Translated by O. Borovik-Romanova

Physics of the Solid State, Vol. 43, No. 10, 2001, pp. 1909–1916. Translated from Fizika Tverdogo Tela, Vol. 43, No. 10, 2001, pp. 1832–1838.

DEFECTS, DISLOCATIONS, AND PHYSICS OF STRENGTH

Analysis of Strain Hardening of Crystals under Large Plastic Strains

G. A. Malygin

Ioffe Physicotechnical Institute, Politekhnicheskaya ul. 26, St. Petersburg, 194021 Russia

e-mail: malygin.ga@pop.ioffe.rssi.ru

Received March 1, 2001

Abstract—A strain-hardening mechanism is considered theoretically for crystals with large shear strains (γ = 1–10). According to this mechanism, the emergence of the fourth and fifth stages in the strain-hardening curve for a crystal is associated with geometrically essential dislocations (GEDs) appearing as a result of accommodation processes accompanying large plastic deformations. Geometrically essential dislocations are concentrated in the boundaries of strongly disoriented fragments of the crystal. A comparison of the experimental and theoretical results leads to the conclusion that the density evolution of GEDs with deformation at the fourth and fifth stages is described by the same kinetic equation as for the evolution of the density of statistically random dislocations at the second and third stages, but with lower values of the kinetic coefficients. © *2001 MAIK "Nauka/Interperiodica".*

1. INTRODUCTION

The strain hardening of crystals with large shear strains (γ = 1–10) [1–6] and dislocation structures [7–15] has become an object of intensive study over the last two decades. These strains emerge as a result of rolling and drawing of a material and under torsion of cylindrical samples with a special annular cut [2, 3, 6]. Experiments on torsion make it possible to obtain strain-hardening curves $\tau(\gamma)$ under various conditions and to analyze them quantitatively.

An analysis shows [1–6] that the dependence of the strain-hardening coefficients $\theta = d\tau/d\gamma$ on the flow stress τ (Fig. 1) exhibits, in addition to the three hardening stages studied earlier, two more stages for $\gamma > 1$. These stages are denoted by numerals *4* and *5* in Fig. 1. The strain-hardening coefficient θ_4 at the fourth stage for metals with a face-centered cubic (fcc) lattice is approximately equal to $0.05\theta_2$, where θ_2 is the strain-hardening coefficient at the second stage. At the end of the fifth stage, this coefficient vanishes and the flow stress acquires the steady-state value τ_5.

It is well known that the second stage of hardening is associated with the interaction and multiplication of dislocations at forest dislocations, while the third stage is associated with the annihilation of screw dislocations through cross slip [16–21]. Annihilation of screw dislocations constrains the dislocation accumulation rate in a strained crystal and ensures equilibrium between hardening and recovery at low and moderate temperatures. The steady stress τ_s corresponding to this equilibrium (Fig. 1) is not attained in actual practice due to the fourth stage of hardening being followed by the fifth stage; at the end of the last stage, this equilibrium sets in. By analogy with the third stage (of dynamic recovery), the fifth stage is called the second stage of dynamic recovery.

There exist various opinions concerning the processes and mechanisms responsible for the emergence of the fourth and fifth stages [2, 22–27]. These hypotheses will be considered in Section 3 of this work. In Section 2, the experimental data on the strain-hardening coefficient are analyzed for a number of metals with an fcc lattice under large plastic strains [3, 5, 6]. In light of this analysis, the proposed models of the new stages are revised in Section 3. A new possible approach to analyzing strain hardening is considered in Section 4 for crystalline materials under large plastic deformations. In Section 5, the dependence of the strain-rate

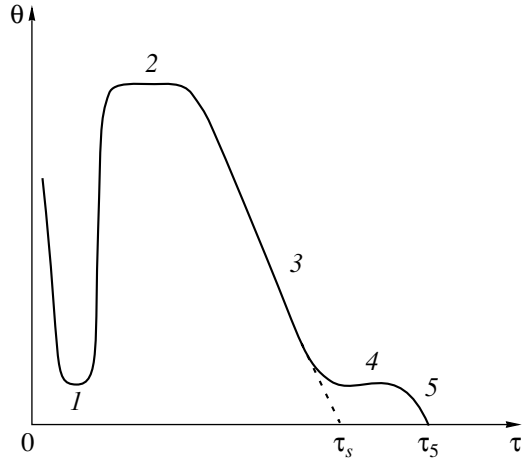

Fig. 1. Schematic dependence of the stress-hardening coefficient on the flow stress. Numerals near the curve indicate different stages of strain hardening.

sensitivity of flow stresses on the stress for large plastic deformations is considered taking this approach into account.

2. ANALYSIS OF EXPERIMENTAL DATA

It is important to find out, at the very outset, whether the recovery mechanisms at the third and fifth stages are interrelated or are basically different mechanisms, as has been proposed by a number of authors [22, 24, 26]. Figure 2a shows the results of processing data [3] on the $\theta(\tau)$ dependence at various temperatures in experiments on the torsion of copper and aluminum polycrystalline samples. The straight line *1* in this figure indicates that there exists a linear correlation between the steady stresses τ_s at the third stage, which are extrapolated to $\theta = 0$ (dashed line in Fig. 1), and the steady stresses τ_5 at the fifth stage for variation in the experimental temperature over a wide range 77–473 K:

$$\frac{\tau_5}{\mu} = 10^{-3} + c_1\frac{\tau_s}{\mu}, \tag{1a}$$

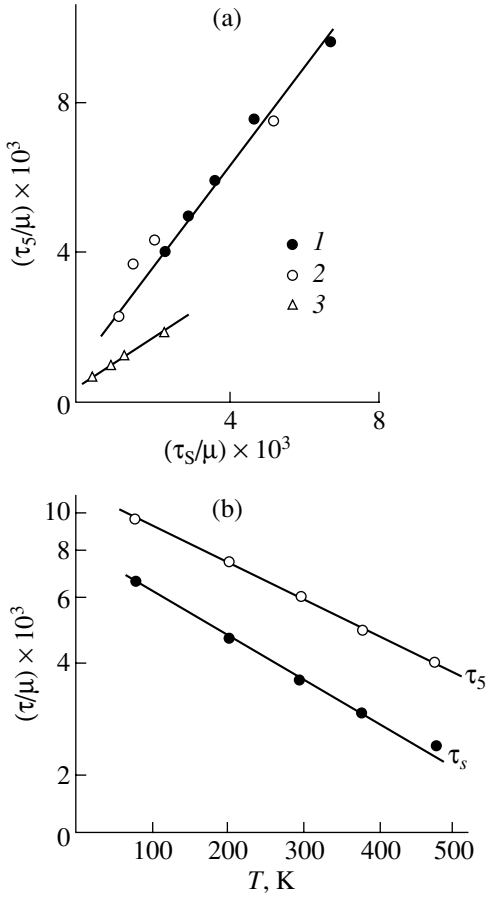

Fig. 2. (a) Correlation between stresses τ_s and τ_5 corresponding to the limit stresses at the third and fifth strain-hardening stages: (*1*) Cu [3], (*2*) Al [3], and (*3*) Au [5]. (b) Temperature dependences of these stresses for copper [3].

where μ is the shear modulus and $c_1 = 1.34$. A similar dependence is also observed for gold single crystals [5] in the temperature range 296–675 K (straight line *3* in Fig. 2a). These results indicate that the recovery mechanisms at the third and fifth hardening stages differ insignificantly. The empirical expression (1a) should be supplemented with the empirical relationship between the strain-hardening coefficient θ_4 at the fourth stage and stress τ_s, which was derived earlier in [2, 3, 6]:

$$\theta_4 = c_2\tau_s, \tag{1b}$$

where $c_2 = 0.05$–0.1 in the case of metals with an fcc lattice.

It was mentioned above that the dynamic recovery mechanisms in these metals is associated with the annihilation of screw dislocations through the cross slip. According to [16, 18, 21], the temperature and strain-rate dependences of τ_s are defined by the formula

$$\tau_s(T, \dot\gamma) = \tau_s(0)\exp\left(-\frac{kT}{A}\ln\frac{\dot\gamma_0}{\dot\gamma}\right), \tag{2}$$

where $\tau_s(0)$ is the flow stress at temperature $T = 0$, $\dot\gamma$ is the plastic strain rate, $\dot\gamma_0$ is the preexponential factor, A is the energy constant depending on the number of stacking faults in the metal [28], and k is the Boltzmann constant. Figure 2b shows the results of processing the data obtained in [3] for stresses τ_s and τ_5 in copper at various temperatures on the basis of formula (2). It can be seen that in accordance with this relationship, the experimental points for τ_s and τ_5 fall on straight lines in the semilogarithmic coordinates. For $\ln(\dot\gamma_0/\dot\gamma) = 23$, we find from the slopes of the straight lines that constants A in Eq. (2) for stresses τ_s and τ_5 are equal to 0.75 and 0.87 eV, respectively.

At the second and third stages, the change in the dislocation density ρ under strains is described by the following equation [16, 21]:

$$\frac{d\rho}{d\gamma} = k_f\rho^{1/2} - k_a\rho, \tag{3}$$

where $bk_f = 10^{-2}$, b is the Burgers vector, k_f is the coefficient determining the intensity of dislocation multiplication at forest dislocations, and k_a is the coefficient of annihilation of screw dislocations through cross slip [21, 29]:

$$k_a(T, \dot\gamma) = k_a(0)\exp\left(\frac{kT}{A}\ln\frac{\dot\gamma_0}{\dot\gamma}\right), \tag{4}$$

where $k_a(0)$ is the annihilation coefficient at $T = 0$. Taking into account the fact that the flow stress depends on the dislocation density as

$$\tau = \alpha\mu b\rho^{1/2} \tag{5}$$

and relationship (3), we find that the strain-hardening coefficient at the third stage decreases linearly with an increase in the stress [16]:

$$\theta(\tau) = \theta_2\left(1-\frac{\tau}{\tau_s}\right). \quad (6)$$

Here, $\theta_2 = (1/2)\alpha\mu b k_f$ is the strain-hardening coefficient at the second stage, $\tau_s = \alpha\mu b k_f/k_a$ is the steady stress at the third stage, and α is the coefficient of interaction between dislocations.

Equations (3), (5), and (6) lead to the following two relationships [17]:

$$\tau\theta = \theta_2\tau_s\left(1-\frac{\tau}{\tau_s}\right)\frac{\tau}{\tau_s}, \quad (7)$$

$$\tau\theta = \frac{1}{2}(\alpha\mu b)^2\frac{d\rho}{d\gamma}. \quad (8)$$

The parabolic nature of variation in the product $\tau\theta$ with a change in the stress at the second and third stages has been confirmed by numerous experiments [16–20]. Relationship (8) shows that the parabolic form of this dependence is associated with the kinetics of multiplication and annihilation of dislocations.

Figure 3 shows the results of data processing on the basis of formula (7) for the dependences $\theta(\tau)$ obtained in experiments [6] on the torsion of polycrystalline copper samples at various temperatures. It can be seen that the $\tau\theta(\tau)$ dependences have a clear parabolic shape within the second and third strain-hardening stages. The curves plotted for various temperatures in the $\tau\theta/(\tau\theta)_{max} - \tau/\tau_s$ coordinates (Fig. 4a), where $(\tau\theta)_{max} = (1/4)\theta_2\tau_s$ are the values of this product that correspond to peaks of the parabolas, confirm this fact. The solid curve in this figure illustrates the theoretical relationship

$$\frac{\tau\theta}{(\tau\theta)_{max}} = 4\left(1-\frac{\tau}{\tau_s}\right)\frac{\tau}{\tau_s}. \quad (9)$$

The results presented in Figs. 3 and 4a show that, for flow stresses at the end of the third stage, the $\tau\theta(\tau)$ curves deviate from the parabolic law (9). The fourth stage corresponds to a slight ascent in the curves, while at the fifth stage, the value of $\tau\theta(\tau)$ becomes zero at stresses $\tau_5 = 1.5\tau_s$. This relationship is similar to the above relationship (1) connecting τ_5 and τ_s. It can also be seen that at the fourth and fifth stages, the dependences $\tau\theta(\tau)$ at various temperatures do not fall on the same curve in the coordinates specified by expression (9).

In Fig. 4b, the dependences $\tau\theta(\tau)$ at the fourth and fifth stages are given in the $\tau\theta_{4-5}/(\tau\theta_{4-5})_{max} - \tau/\tau_s$ coordinates, where $\theta_{4-5}(\tau)$ is the strain-hardening coefficient at $\tau > \tau_s$. In these coordinates, the $\tau\theta_{4-5}(\tau)$ dependences at various temperatures can be approximated by the same curve within the experimental spread of points.

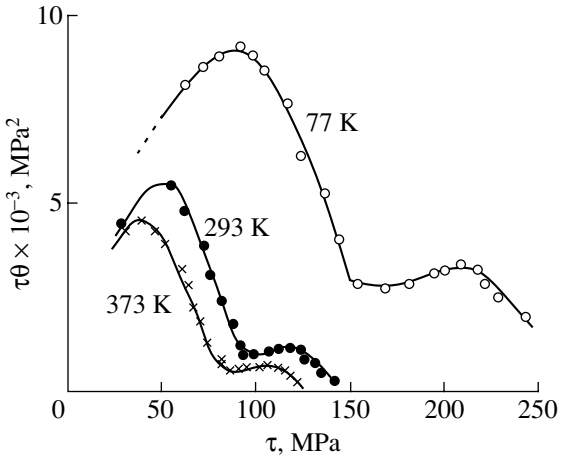

Fig. 3. Product $\tau\theta(\tau)$ as a function of stress for copper at different temperatures [6].

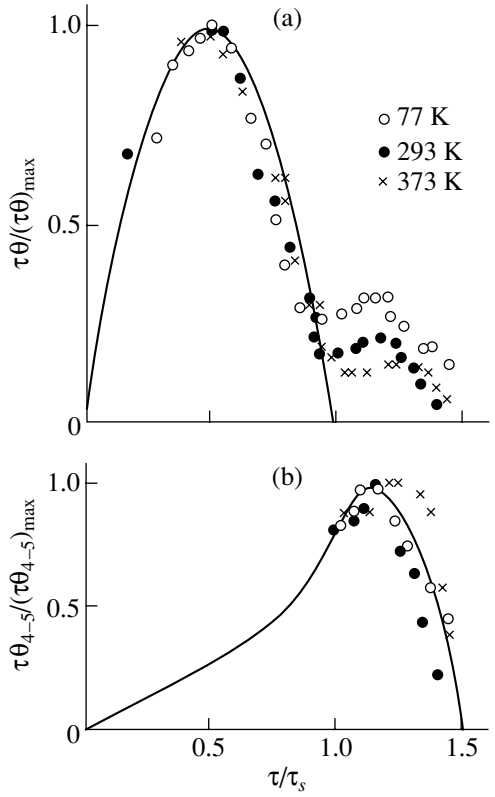

Fig. 4. Products (a) $\tau\theta(\tau)$ and (b) $\tau\theta_{4-5}(\tau)$ at the fourth and fifth stages of strain hardening for copper [6] as functions of stress at different temperatures in reduced coordinates.

3. MODELS OF STRAIN HARDENING AT THE FOURTH AND FIFTH STAGES

Most of the models proposed for explaining the emergence of the fourth and fifth strain-hardening stages are based on the assumption that the new stages of this process appear due to a change in the parameters

of the dislocation cell structure formed at the preceding (second and third) stages under large strains. For example, the emergence of the fourth stage is attributed in [2] to the formation of additional obstacles (so-called debris) to the motion of dislocations in the walls of dislocations cells. In [23, 25], this effect is associated with an increase in the density of dislocations in the walls due to their redistribution from the bulk to the cell boundaries and due to thinning of the dislocation cell walls under large strains [25]. In [24], the emergence of additional strain hardening at the end of the third stage is explained by the emergence of long-range stresses inside the cells due to misorientation of the lattice between neighboring cells, whereas in [27], this effect is attributed to the resulting emergence of a network of disclination dipoles that additionally strengthen the crystal.

The following question arises: is the formation of a dislocation cell structure a necessary condition for the emergence of the fourth and fifth stages of strain hardening? It is well known that, for example, the cell structure is manifested weakly in Al–Mg solid solutions at 3–5 at. % Mg, but the fourth hardening stage is observed in these materials [2, 13]. In Ge crystals [30], a dislocation network (rather than dislocation cell) structure is formed at the fourth stage; nevertheless, the fifth stage is observed. These facts indicate that the strain hardening of a crystal is not associated directly with the dislocation distribution in it but is determined by the local interaction of dislocations and the evolution of their density under deformation. The nonuniform nature of the dislocation distribution affects only the quantitative parameters of strain hardening.

For example, in accordance with the two-phase model of the dislocation cell structure, the flow stress is given by [31]

$$\tau = f\tau_w + (1 - f)\tau_c, \tag{10}$$

where f is the relative volume occupied by the cell walls in the crystal and $\tau_{w,c} = \alpha\mu b\rho_{w,c}^{1/2}$ and $\rho_{w,c}$ are the flow stresses and dislocation densities in the walls and in the bulk of the cells, respectively. Since $\rho_c \ll \rho_w$, we have $\tau \approx f\tau_w$; i.e., the formation of the cell structure causes only a decrease in the effective constant of interaction between dislocations ($f\alpha < \alpha$), the relative volume ($f \approx 0.2$–0.3) remaining unchanged at the second and third stages [21] by virtue of the similitude principle which holds for dislocation cell structures [22].

Whether or not this principle holds at the fourth and fifth stages, when there is no dislocation cell structure and a strongly disoriented (fragmented) dislocation structure dominates [7–15], has been unclear until recently. This problem has been a subject of discussions [25]. The experimental proof of the validity of the similitude principle in the case of fragmented structures has been obtained recently in [14, 15]. According to the results obtained in [15, 32], the volume fraction $f \approx 0.05$–0.1 of the boundaries of fragments in which dislocations are concentrated remains unchanged at the fourth and fifth stages. The deformation only enhances the lattice misorientation due to an accumulation of dislocations of like sign in the boundaries of the fragments. In contrast to the walls of dislocations cells formed as a result of interaction between statistically random dislocations, fragment boundaries form the so-called geometrically essential dislocations (GEDs) [14, 15]. Their emergence is associated with accommodation processes [33], whose intensity increases with an increase in the plastic strain of the crystal.

The evolution of dislocation density in the fragment walls apparently determines the strain hardening at the fourth and fifth stages by analogy with the evolution of dislocation density in the walls of dislocation cells, which determined the strain hardening at the second and third stages [21]. Experiments show [11, 13–15] that the boundaries with a high dislocation density in which GEDs are concentrated start to be formed at the third strain-hardening stage. Upon an increase in the degree of strain, the separation between the boundaries decreases and becomes comparable to the distance between the walls of dislocation cells at the beginning of the fourth stage.

4. GEOMETRICALLY ESSENTIAL DISLOCATIONS AND ASSOCIATED STRAIN HARDENING

The existence of a dislocation cell structure at the second and third stages of the strain-hardening curves and a fragmented dislocation structure at the fourth and fifth stages indicates that a two-phase state is formed in the crystal in the course of plastic deformation. Consequently, the total density of dislocations in the crystal under the assumption of a small dislocation density in the bulk of the cells and fragments should be described by the following expression:

$$\rho(\gamma) = f_1\rho_1(\gamma) + f_2\rho_2(\gamma), \tag{11}$$

where ρ_1 and ρ_2 are the densities of dislocations in the walls of the cells and fragments, respectively, and f_1 and f_2 are the volume fractions of cell and fragment walls in the crystal. In accordance with the similitude principle for dislocation structures, these quantities remain unchanged during deformation. For the flow stress, we have

$$\tau(\gamma) = \alpha\mu b[f_1\rho_1(\gamma) + f_2\rho_2(\gamma)]^{1/2}. \tag{12}$$

The evolution of the dislocation density in the cell walls, in accordance with Eq. (3), is described by the following expression [19]:

$$\rho_1(\gamma) = \left(\frac{k_f}{k_a}\right)^2\left(1 - \exp\left(1 - \frac{1}{2}k_a\gamma\right)\right)^2. \tag{13a}$$

As regards the evolution of the dislocation density in the fragment walls, we assume that it is described by an

equation of type (3) with the GED annihilation coefficient βk_a and with the coefficient δk_f of GED multiplication at forest dislocations, where $\beta < 1$ and $\delta < 1$ are certain phenomenological coefficients. As a result of dislocation density evolution in the fragment walls, we obtain the following expression, which is similar to Eq. (13a):

$$\rho_2(\gamma) = \left(\frac{\delta k_f}{\beta k_a}\right)^2\left(1 - \exp\left(1 - \frac{1}{2}\beta k_a\gamma\right)\right)^2. \quad (13b)$$

Substituting expressions (13a) and (13b) into Eq. (12), we arrive at the dependence of the flow stress on strain at the second–fifth stages:

$$\tau(\gamma) = \tau_s\left[\left(1 - \exp\left(-\frac{1}{2}k_a\gamma\right)\right)^2 + \frac{f_2\delta^2}{f_1\beta^2}\left(1 - \exp\left(-\frac{1}{2}\beta k_a\right)\right)^2\right]^{1/2}. \quad (14a)$$

Putting $\gamma \longrightarrow \infty$ in this expression, we obtain the following relationship between the steady stresses at the third and fifth stages:

$$\tau_5 = c_1\tau_s, \quad c_1 = (1 + c)^{1/2}, \quad c = \frac{f_2\delta^2}{f_1\beta^2}. \quad (14b)$$

According to the results presented in Fig. 4a, we have the quantity $c_1 = 1.5$ and, hence, $c = 1.25$ for polycrystalline copper. Curve *1* in Fig. 5 depicts the $\tau(\gamma)$ dependence for $c_1 = 1.5$ and $\beta = 0.1$. Curve *2* in this figure illustrates this dependence for $f_2 = 0$, i.e., in the absence of GEDs. Since $k_a \approx 5$ for copper at room temperature [21], it can be seen from Fig. 5 that the onset of the fourth and fifth strain-hardening stages takes place at strains $\gamma > 1$ and $\gamma > 10$, respectively.

Differentiating Eq. (14a) with respect to γ, we obtain the following dependence of the strain-hardening coefficient $\theta = d\tau/d\gamma$ on strain at the second–fifth stages on the strain-hardening curve:

$$\theta(\Gamma) = \theta_2\frac{(1 - \exp(-\Gamma/2))\exp(-\Gamma/2) + (f_2\delta^2/f_1\beta)(1 - \exp(-\beta\Gamma/2))\exp(-\beta\Gamma/2)}{[(1 - \exp(-\Gamma/2))^2 + (f_2\delta^2/f_1\beta^2)(1 - \exp(-\beta\Gamma))^2]^{1/2}}, \quad (15)$$

where $\theta_2 = (1/2)\alpha f_1^{1/2} bk_f$; for brevity, we have introduced the notation $\Gamma = k_a\gamma$. Curve *2* in Fig. 6a demonstrates the dependence of the strain-hardening coefficient $\theta(\gamma)$ (15) on the flow stress $\tau(\gamma)$ (14a). The straight line *1* in this figure shows the dependence $\theta(\tau)$ plotted according to Eq. (6), i.e., in the absence of GEDs. It can be seen that the emergence of these dislocations is responsible for the plateau in the $\theta(\tau)$ curve for large stresses ($\tau > \tau_s$). Using Eq. (15), we obtain the following estimate for the strain-hardening coefficient at the fourth stage for $k_a\gamma = 10$ ($\tau/\tau_s = 1.1$):

$$\theta_4 = c_3\theta_2,$$
$$c_3 = \frac{f_2\delta^2}{f_1\beta^2}\frac{0.24\beta}{[1 + 0.16 f_2\delta^2/f_1\beta^2]^{1/2}} \approx 0.03. \quad (16)$$

The calculated value of c_3 is of the same order of magnitude as the experimental values of $c_3 = 0.05$–0.1 [1–6]. As regards the empirical relationship (1b) between θ_4 and τ_s, it follows from relationships (16) and $\tau_s = 2\theta_2/k_a$ that coefficient c_2 in Eq. (1b) is equal to $c_3k_a/2 \approx 0.1$; i.e., it has a correct value but depends on temperature.

Curve *2* in Fig. 6b shows the dependence of the product

$$\theta(\Gamma)\tau(\Gamma) = \theta_2\tau_s[(1 - \exp(-\Gamma/2))\exp(-\Gamma/2) + (f_2\delta^2/f_1\beta)(1 - \exp(-\beta\Gamma/2))\exp(-\beta\Gamma/2)] \quad (17)$$

on $\tau(\gamma)$ in the dimensionless $\theta\tau/(\theta\tau)_{max}$–$\tau/\tau_s$ coordinates. It can be seen that the presence of the fragmented structure leads to the emergence of an additional peak in the $\theta\tau$–τ curves for large plastic strains (under stresses $\tau > \tau_s$). This can be seen especially clearly if we subtract dependence *1* in Fig. 6b, which demonstrates the purely parabolic variation of the product $\theta\tau$ at the second and third stages of strain hardening of the crystal in accordance with formula (7), from the total dependence *2* in the same figure. The result of this subtraction is depicted by the dashed line in Fig. 6b and by the solid line in Fig. 4b. It can be seen that the theoretical dependence is in good agreement with the experimental data.

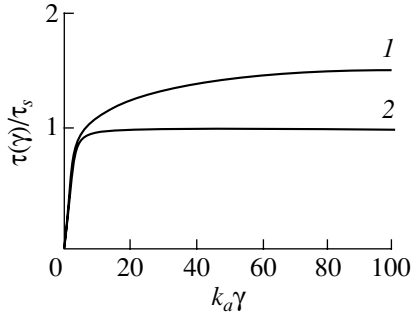

Fig. 5. Strain-hardening curves for the crystal according to Eq. (14a) in the (*1*) presence and (*2*) absence of the fourth and fifth strain-hardening stages.

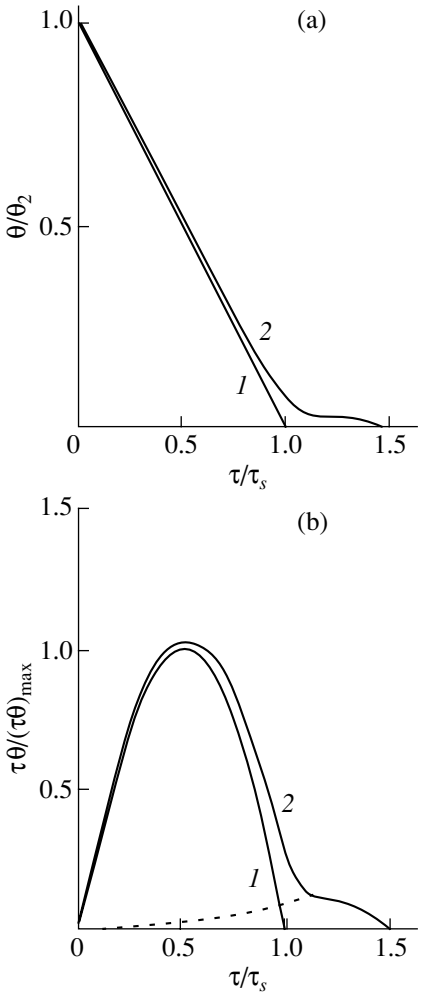

Fig. 6. Dependences of (a) the strain-hardening coefficient θ given by Eqs. (15), (16), and (14a) and (b) the product $\theta\tau$ on the stress τ at parameters $\beta = 0.1$ and $c_1 = 1.5$.

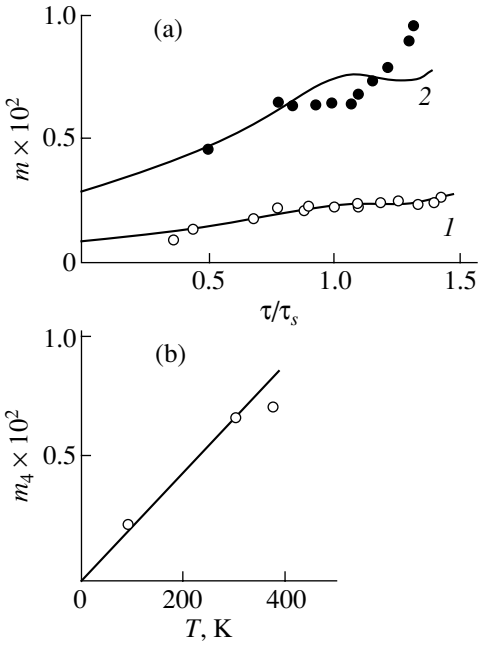

Fig. 7. (a) Dependences of the strain-rate sensitivity coefficient m of flow stress on the stress τ in copper [6] at temperatures of (*1*) 77 and (*2*) 293 K. The curves are calculated on the basis of formulas (19a) and (14a). (b) Temperature dependence of the strain-rate coefficient for copper [6] at the fourth strain-hardening stage.

Concluding this section, we give the numerical estimate of coefficient δ obtained by using formula (14b). Since $f_2 \approx 0.05$ [15] and $f_1 \approx 0.25$ [21], we have $\delta = 0.22$ for $c_1 = 1.5$ and $\beta = 0.1$. Thus, the coefficients of multiplication and annihilation of GEDs are approximately an order of magnitude smaller than the corresponding coefficients for statically random dislocations. This is apparently due to the fact that in contrast to the latter dislocations, GEDs are predominantly dislocations of the same sign, which might affect their multiplication and annihilation.

5. FLOW STRESS RATE-SENSITIVITY COEFFICIENT

Another way of verifying the proposed approach to analyzing the strain hardening of crystals under high plastic strains is to compare the theoretical and experimental dependences of the rate sensitivity coefficient $m = (\partial \ln\tau/\partial \ln\dot\gamma)_T$ of the flow stress on these stresses. Figure 7a shows the experimental dependences of coefficient m for polycrystalline copper at temperatures of 77 and 293 K [6]. It can be seen that at stresses corresponding to the third strain-hardening stage (first stage of dynamic recovery), the coefficient increases smoothly with an increase in the stress τ. At the fourth stage, it remains approximately unchanged, while at the fifth stage (second dynamic recovery stage), it starts increasing again.

The dependence of the flow stress on the strain rate may be due to the following two reasons. The first is associated with the rate and temperature sensitivity of the constant of interaction between dislocations in the case of their crossing:

$$\alpha(T, \dot\gamma) = \alpha_0 + \frac{H_0 - kT\ln(\dot\gamma_0/\dot\gamma)}{\xi\mu b^3}, \qquad (18)$$

where α_0 is the temperature-independent constant of interaction between dislocations; H_0 is the total height of the potential barrier in the case of crossing of dislocations, which is overcome due to thermal fluctuations; $\dot\gamma_0$ is the preexponential factor; and ξ is a numerical coefficient of the order of unity. The second cause of the temperature and rate sensitivity of flow stresses is associated with annihilation of screw dislocations through

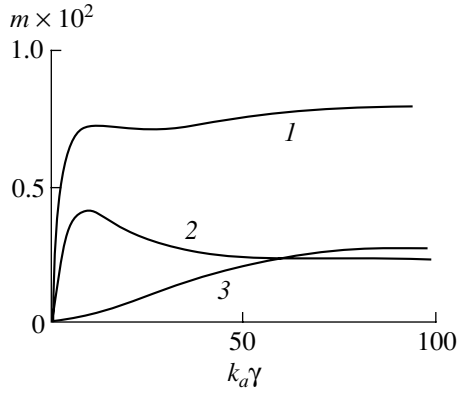

Fig. 8. Dependences of the strain-rate sensitivity coefficient m of flow stress on the strain γ according to formula (19a) at the (*1*) second–fifth, (*2*) second and third, and (*3*) fourth and fifth stages of strain hardening.

cross slip, namely, with the rate and temperature dependence of the dislocation annihilation coefficient (4).

Taking into account these circumstances and expressions (13) and differentiating Eq. (12) with respect to $\dot{\gamma}$, we obtain the following dependence of the strain-rate sensitivity of the flow stress on the degree of strain at the second–fifth stages in the strain-hardening curve of the crystal:

$$m(\Gamma) = m_0 + \left[\left(\frac{1-(3/2)\exp(-\Gamma/2)}{1-\exp(-\Gamma/2)}\right)\frac{f_1\rho_1}{\rho} + \left(\frac{1-(1+(1/2)\beta)\exp(-\beta\Gamma/2)}{1-\exp(-\beta\Gamma/2)}\right)\frac{f_2\rho_2}{\rho}\right]m_a, \quad (19a)$$

$$m_0 = \left(\frac{\partial \ln\alpha}{\partial \ln\dot{\gamma}}\right)_T = \frac{kT}{\alpha\xi\mu b^3}, \qquad m_a = -\left(\frac{\partial \ln k_a}{\partial \ln\dot{\gamma}}\right) = \frac{kT}{A}. \quad (19b)$$

Curve *1* in Fig. 8 shows the theoretical dependence of coefficient m on the degree of strain for $m_0 = 3 \times 10^{-3}$ and $m_a = 5 \times 10^{-3}$. The general nature of this dependence is in accordance with the results presented in [34] on the strain dependence of coefficients m for polycrystalline aluminum at various temperatures at the second–fifth stages of strain hardening. Curves *2* and *3* in Fig. 8 illustrate the contribution of the second–third and fourth–fifth strain-hardening stages, respectively, to the total coefficient m.

The solid curves in Fig. 7a show the dependence of m on the flow stress for two experimental temperatures in accordance with Eq. (14a) and (19a). At 77 K, $m_0 = 10^{-3}$ and $m_a = 1.8 \times 10^{-3}$ (curve *1*), while at 293 K, $m_0 = 3 \times 10^{-3}$ and $m_a = 5 \times 10^{-3}$ (curve *2*). It can be seen that these curves are in satisfactory agreement with the experimental results obtained in [6] for copper (and in [35] for aluminum). This is also confirmed by the approximately linear temperature dependence of the strain-rate coefficient m_4 at the fourth strain-hardening stage, which follows from formulas (19) (Fig. 7b).

CONCLUSION

Thus, the above analysis of the strain hardening of crystals under large plastic strains shows that, as in the case of the first three stages, the strain hardening at the fourth and fifth stages is determined by the contact interaction of dislocations and the evolution of their density in the course of deformation.

REFERENCES

1. J. Gil Sevillano and E. Aernoudt, Prog. Mater. Sci. **25**, 69 (1980).
2. A. D. Rollet, U. F. Kocks, and R. D. Doherty, in *Proceedings of the Symposium on Formability and Metallurgical Structure*, Ed. by A. K. Sachdev and J. D. Embury (Metallurgical Society, Warredale, 1987), p. 211.
3. E. Aernoudt, J. Gil Sevillano, and P. van Houtte, *Constitutive Relations and Their Physical Basis*, Ed. by S. Andersen, J. Bild-Sorensen, and N. Hansen (Roskild, Denmark, 1988), p. 1.
4. M. E. Kassner, Metall. Trans. A **20**, 2001 (1989).
5. H. Siethoff and W. Schroter, Z. Metallkd. **75**, 475 (1984).
6. M. Zehetbauer and V. Seumer, Acta Metall. Mater. **41**, 577 (1993).
7. G. Langford and M. Coehn, Trans. Am. Soc. Met. **62**, 623 (1969).
8. A. S. Malin and M. Hatherly, Met. Sci. **13**, 463 (1979).
9. V. V. Rybin, *Severe Plastic Deformations and Fracture of Metals* (Metallurgiya, Moscow, 1986).
10. D. A. Huges and W. D. Nix, Mater. Sci. Eng. A **122**, 153 (1989).
11. N. A. Koneva and É. V. Kozlov, Izv. Vyssh. Uchebn. Zaved., Fiz. **33**, 89 (1990).
12. P. Guyot and G. M. Raynaudt, Acta Metall. Mater. **39**, 317 (1991).
13. D. A. Hughes, Acta Metall. Mater. **41**, 1421 (1993).
14. N. Hansen and D. A. Hughes, Phys. Status Solidi A **149**, 155 (1995).
15. D. A. Hughes and N. Hansen, Acta Metall. Mater. **48**, 2958 (1999).
16. U. F. Kocks, J. Eng. Mater. Technol. **H98**, 76 (1976).
17. H. Mecking and U. F. Kocks, Acta Metall. **29**, 1865 (1981).
18. Y. Estrin and H. Mecking, Acta Metall. **32**, 57 (1984).
19. G. A. Malygin, Fiz. Tverd. Tela (Leningrad) **29**, 2067 (1987) [Sov. Phys. Solid State **29**, 1189 (1987)].
20. G. A. Malygin, Phys. Status Solidi A **119**, 423 (1990).
21. G. A. Malygin, Usp. Fiz. Nauk **169**, 979 (1999).
22. D. Kuhlmann-Wilsdorf and N. Hansen, Metall. Trans. A **20**, 2393 (1989).
23. P. Haazen, J. Phys. (Paris) **50**, 2445 (1989).

24. A. S. Argon and P. Haazen, Acta Metall. **41**, 3289 (1993).
25. Y. Estrin, L. S. Toth, A. Molinari, and Y. Brechet, Acta Mater. **46**, 5509 (1998).
26. M. Zehetbauer, Acta Metall. Mater. **41**, 589 (1993).
27. M. Seefeld and P. Klimanek, Modell. Simul. Mater. Sci. Eng. **6**, 349 (1998).
28. A. Seeger, R. Berner, and H. Wolf, Z. Phys. **155**, 247 (1959).
29. G. A. Malygin, Fiz. Tverd. Tela (St. Petersburg) **37**, 3 (1995) [Phys. Solid State **37**, 1 (1995)].
30. H. G. Brion and P. Haazen, Philos. Mag. A **51**, 879 (1985).
31. H. Mughrabi, Acta Metall. **31**, 1367 (1983).
32. M. Muller, M. Zehetbauer, A. Borbely, and T. Ungar, Z. Metallkd. **86**, 827 (1995).
33. M. F. Ashby, Philos. Mag. **21**, 399 (1970).
34. H. P. Stuwe and P. Les, Acta Mater. **46**, 6375 (1998).
35. P. Les, M. Zehetbauer, E. F. Rauch, and I. Kopacz, Scr. Mater. **41**, 523 (1999).

Translated by N. Wadhwa

Physics of the Solid State, Vol. 43, No. 10, 2001, pp. 1917–1922. Translated from Fizika Tverdogo Tela, Vol. 43, No. 10, 2001, pp. 1839–1844.

DEFECTS, DISLOCATIONS, AND PHYSICS OF STRENGTH

The Hardening and Loss of Strength of Thin Surface Layers of LiF Monocrystals and Zirconium Ceramics under Conditions of Cyclic Nanoindenting

Yu. I. Golovin, V. I. Ivolgin, V. V. Korenkov, and B. J. Farber*

Tambov State University, Tambov, 392622 Russia
e-mail: golovin@tsu.tmb.ru
** Zircoa Corp., Cleveland, Ohio, USA*
e-mail: bfarber@zircoa.com
Received March 15, 2001

Abstract—Low-cycle surface fatigue is still relatively poorly investigated, especially in the case of accumulation of surface fractures during nanocontact interactions between solids. A new technique of modeling fatigue during a short nanocontact interaction based on repeated dynamic nanoindenting is proposed. The results of investigation of model LiF crystals and industrial ZrO_2 ceramics show that, at a small number of cycles N of about 20, the material is hardened under the indenter. As N increases, the hardening is replaced by a loss of strength reflected in the formation and growth of microcracks. *© 2001 MAIK "Nauka/Interperiodica".*

The most widely spread type of loading of structures, devices, and machines during their operation is cyclic loading (either alternating or more complex), under which fatigue phenomena develop. According to some estimates [1], more than 80% of all failures are caused by fatigue. They are typical of aerospace and rocket machinery, all kinds of engines, transport devices, etc. The exclusive importance of the diagnostics of fatigue fractures promoted the development of numerous diverse contact (such as the visualization of microcracks with luminescent solids) or contactless (ultrasonic and γ-defectoscopic; magnetic and electromagnetic) techniques of determining fatigue cracks. At the same time, the problem of the nature of fatigue fractures, which is still unclear, stimulated intense laboratory studies of high-cycle, low-cycle, fretting, impact, thermal, surface, corrosion, and other types of fatigue [2, 3]. Recently, substantial progress was reached in understanding the physical nature of fatigue: a mechanism of the formation and development of fatigue cracks was proposed, defects in a crystal lattice were shown to play a decisive role in the hardening and destruction of metals, and the important role played by oxidation processes was noticed. On the other hand, the sphere of the so-called low-cycle fatigue, related to the operation of a material under substantial plastic deformations when submicrocracks appear after several tens or hundreds of cycles of loading [4], remains poorly studied.

Until recently, laboratory fatigue tests of materials were carried out chiefly with macroscopic bulk specimens according to a conventional technique of uniaxial tension–compression or bending. As early as in the beginning of the XXth century, the exclusive role played by the surface in the nucleation and development of fatigue cracks was discovered [5] (by some estimates, up to 75% of fatigue fractures nucleate on the surface of a structural material). Moreover, the development of modern technologies requires a new scale of sizes as regards the surface fatigue when a contact spot from a nanometer to tens of micrometers undergoes short cyclic loading. A typical example of this kind is the working element (a ball made of a wear-resistant material such as ZrO_2 ceramics) in a ball mill used for obtaining fine-disperse powders. The surface of such a ceramic ball periodically repeatedly contacts for a short time (of tens or hundreds of microseconds) with the treated material and neighbor balls. The fatigue surface fracture of one of the balls causes an avalanche-like destruction of the remaining balls, because ZrO_2 powder is the strongest abrasive compound. The macroscopic fatigue tests of such materials [6] are scarcely applicable to prediction of its working capacity under actual conditions, because, with a decrease in the size of the loaded zone by many orders of magnitude, a number of new factors affecting the properties of the material appear [7]. A high localization of the load results in stronger hardening of the material in the zone of deformation, so that, even in mild materials, the stresses can approach the theoretical ultimate strength (about 0.1 of Young's modulus) [8].

One can approach the actual conditions of short nanocontact interactions during milling, grinding, dry friction, fretting, etc., including the effects of periodic alternate loading, by repeatedly dynamically nanoin-

1063-7834/01/4310-1917$21.00

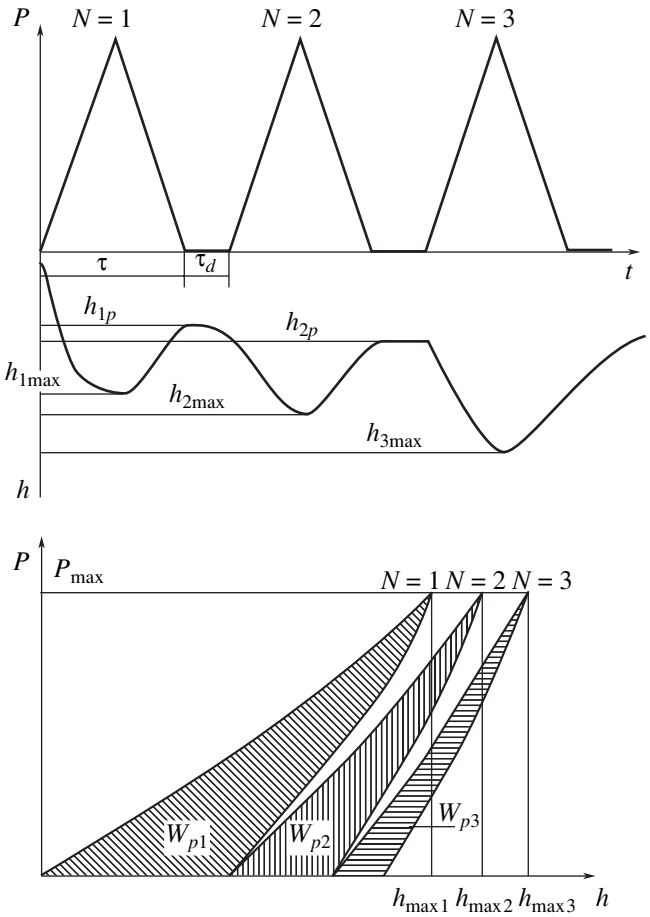

Fig. 1. A scheme of the cyclic loading and the kinetics of the formation of an indentation for the symmetrical triangular load used in the experiment.

denting the same surface spot. A nanoindenter with high spatial (~0.1 nm) and time (to 0.33 μs) resolutions provides a high degree of control of the conditions of contact dynamic loading and deforming, which is especially valuable in modeling actual nanocontact interactions. In contrast to macroscopic techniques, in which the interactions of bodies are averaged over a large number of contact points, dynamic indenting enables one to study the dynamics of elementary processes at the level of a short nanocontact. Similarly, cyclic loading of the same indentation allows one to model an elementary act of a low-cycle fatigue, while wide variations in the amplitude, duration, duty factor, and the number of pulses of applied loads of various forms allow one to investigate the time and rate characteristics of the appearance and accumulation of fatigue cracks in thin subsurface layers of a material.

To approve the applicability of the technique of nanoindenting to the investigation of low-cycle fatigue, we used an experimental device developed in the nanoindenting laboratory of the Tambov State University. The details of construction and operation of its prototype are outlined in [8]. An electrodynamic drive controlled by a computer allowed us to create loads from 10 μN to 250 mN with a duration from 20 ms to 50 s. In this work, the loading pulse had a symmetric triangular shape with a duration τ of 0.02, 0.04, 0.1, and 0.2 s at an amplitude of 100, 125, 150, 200, and 250 mN. The cycling of loading was either continuous or had a delay between cycles of 5 or 10 ms (Fig. 1). Depending on the hardness of the specimen, the depth of penetration of the indenter Δh was measured at a limit of 10 μm with a resolution Δh of 10 nm or 1 μm (Δh = 1 nm). In order to ensure loading of the same surface spot during the whole experiment, along with cyclic loading with the drive, the indentation was constantly additionally loaded at a 5% level of the maximum load used in the experiment. The main parameters of the experiment, namely, the depth of penetration of the indenter h and the load P as functions of time, were stored on a computer, and the resulting $P(h)$ dependence was shown in a display in real time. As the subject of investigations, we used nominally pure LiF monocrystals (as the model material for indentometry) and a bulk specimen of ZrO_2 ceramics alloyed with MgO for obtaining a partially stabilized zirconia (PSZ) structure.

Figure 2 shows typical dependences of the load on the depth of penetration of an indenter in the studied materials after the first ten cycles of loading–off-loading at τ = 0.2 s for (a) LiF and (b) ZrO_2. As a factor of the mechanical losses during the macroscopic fatigue tests, people conventionally use the ratio of the work W_p (Fig. 1) spent on plastic deformation to the total work W_{tot} spent by the drive: $\Psi = W_p/W_{tot}$. As follows from Fig. 2, the part of the energy of plastic deformation in the work spent by the drive, which is determined by the area of the loop formed by the curves of loading and off-loading [9], is large only in the first cycle of loading. Already in the next cycle, it does not exceed several percents of the energy of plastic deformation in the first cycle. By the fourth or fifth cycle, the character of the deformation of a material under the indenter becomes practically macroscopically elastic. As follows from our results (Fig. 3), at various times of the loading–off-loading cycle both on LiF and ZrO_2, Ψ quickly decreases by the fourth or fifth cycle and reaches a constant value that does not change for hundreds or, sometimes, many thousands of cycles. One can expect this state to change only when fatigue fracture begins, i.e., when microcracks nucleate in the contact zone between the indenter and material [10, 11].

Despite the common tendencies in behavior of ionic crystals and ceramics, which can be qualified as the hardening of subsurface layers under the effect of a local load, there are certain quantitative differences. One such difference is a strong rate dependence of the low-cycle fatigue of LiF. For example, at τ = 0.02 s and P_{max} = 200 mN, the first signs of fatigue fracture appear

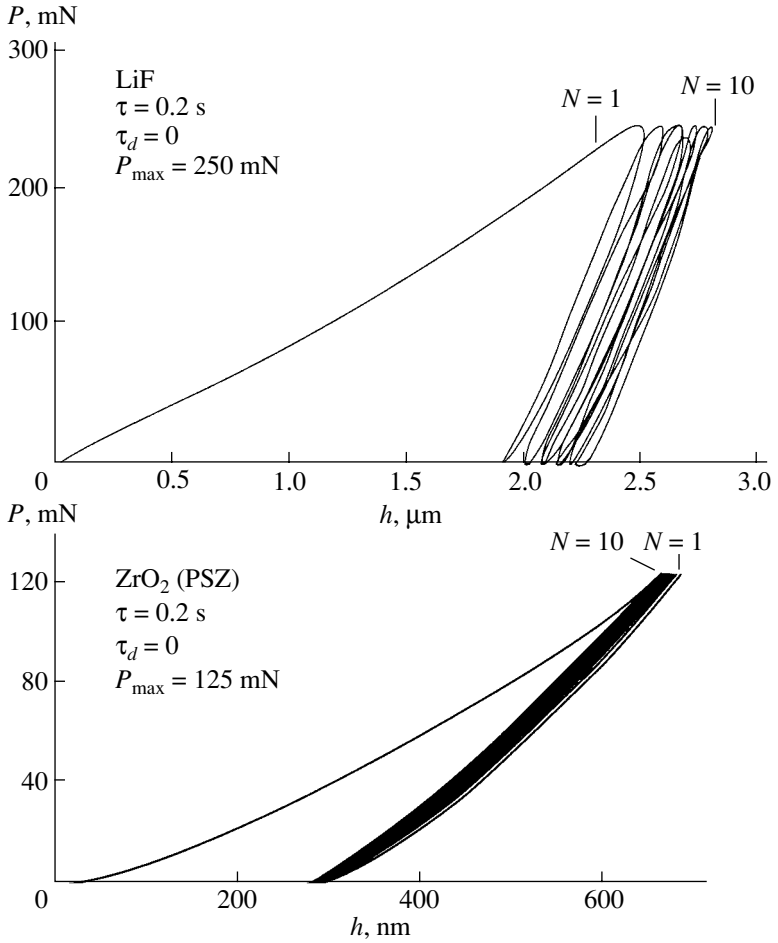

Fig. 2. Typical dependences of the load on the penetration depth of an indenter under cyclic loading (N = 10) for (a) LiF and (b) ZrO_2. The duration of a cycle τ = 0.2 s and the maximum load on the indenter P_{max}, mN: (a) 250 and (b) 125.

within the first 50 to 100 cycles (Fig. 4a), which is not noticed at τ = 0.2 s. The indication is a sharp increase in the vibration of the indenter, which results in the corresponding widening of the hysteresis loop and increase in W_p and, accordingly, in Ψ (because the energy of elastic deformation W_e remains practically constant after the first four or five cycles). This stage can be considered the loss of strength that leads to the appearance of fatigue cracks. Upon further increase in N, ψ fluctuates around a value which is several or, sometimes, ten times as large as those typical of $5 \le N \le 10$ (Fig. 4b). The depths of both the maximum unrecovered (h_{max}) and plastically recovered (h_p) indentations in LiF increase with an increase in N, but their ratio $\eta = h_p/h_{max}$, which characterizes the elastic recovery [12], remains practically unchanged (Fig. 5). At the same P_{max} and N values, but with τ = 0.1 s, the signs of fatigue fracture of LiF are much weaker (Fig. 4b, curve *2*) and, at τ = 0.2 s, are not noticed up to $N = 10^3$.

In ZrO_2 ceramics, the fatigue fracture manifests itself in a similar increase in the vibrations of the indenter (Fig. 6a) but at a substantially larger number of cycles (N ~ 150–200) and $\tau \ge 0.2$ s (Fig. 6b). This fact indirectly confirms the conclusion from [13] that the cracks that appear during statistical hardness tests in PSZ ceramics are much longer than those formed dur-

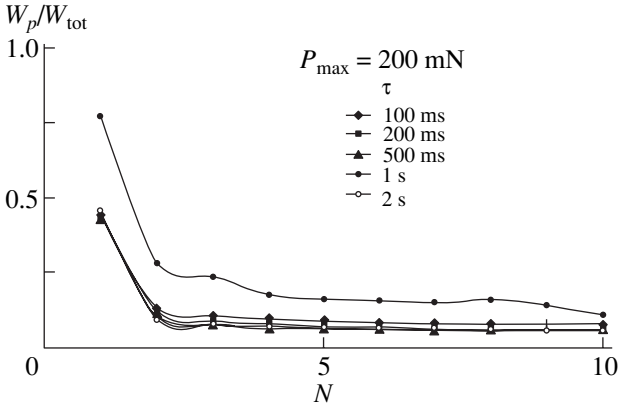

Fig. 3. The factor of mechanical losses $W_p/(W_p + W_e)$ under cyclic loading ($N \le 10$) in materials with different hardness, dynamic strength, and wear resistance: (*1*) LiF and (*2*) ZrO_2.

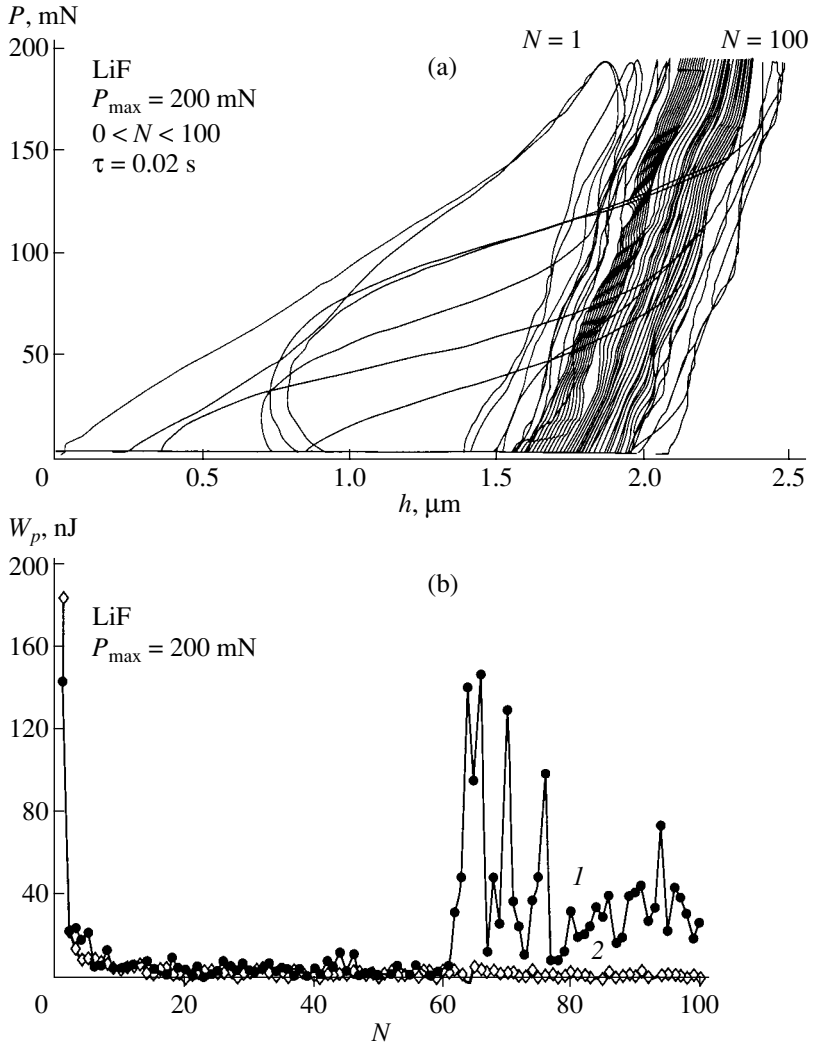

Fig. 4. The loss of strength of LiF monocrystals during cyclic loading at $N \leq 100$ manifested itself (a) in the widening of hysteresis loops and (b) in the change in energy spent on plastic deformation under the same conditions: (*1*) τ = 20 ms and P_{max} = 200 mN; (*2*) τ = 100 ms and P_{max} = 200 mN.

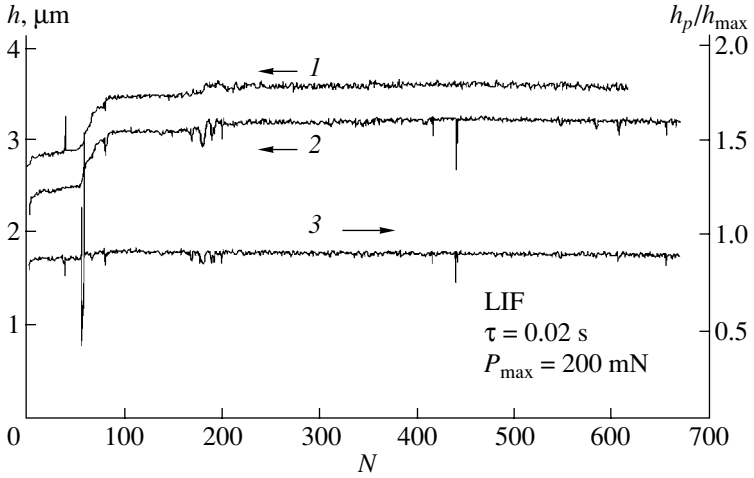

Fig. 5. The kinetics of the change in the penetration depth of an indenter during cyclic tests of LiF at τ = 20 ms and P_{max} = 200 mN: (*1*) the h_{max} depth of an unrecovered indentation in a cycle; (*2*) the h_p depth of a recovered indentation in a cycle; and (*3*) the degree of elastic recovery of the depth of an indentation η.

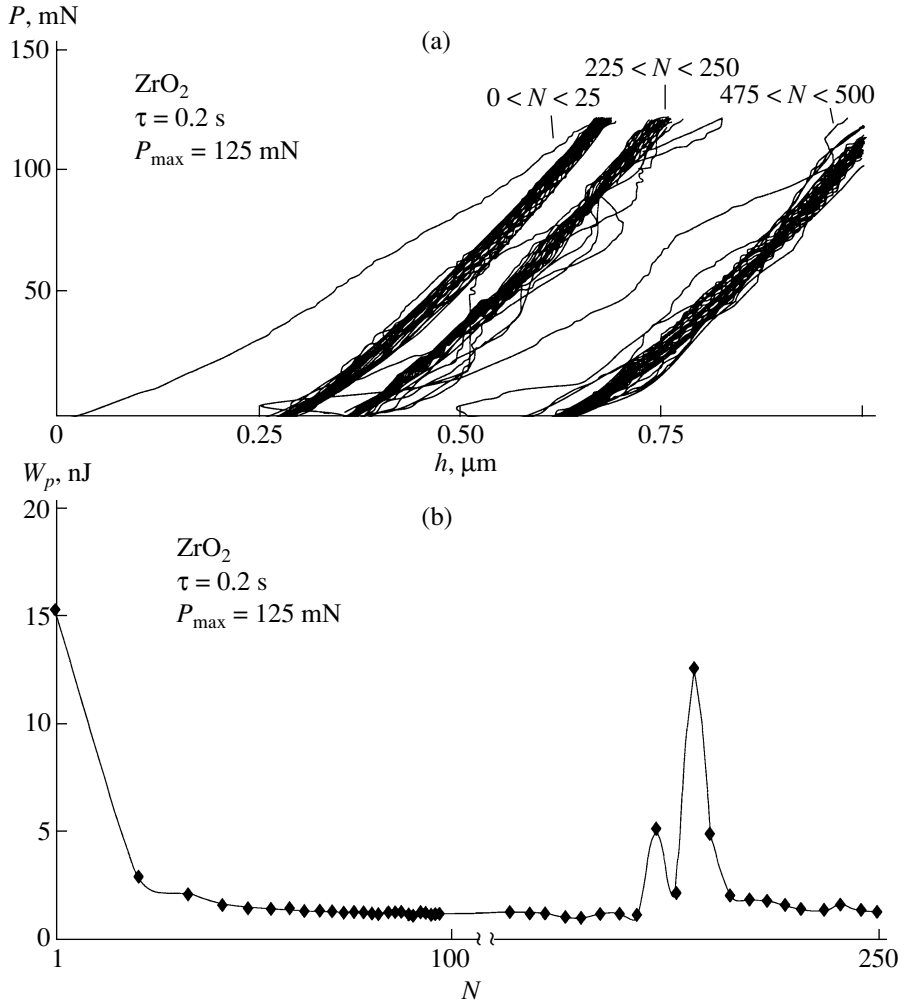

Fig. 6. The fatigue loss of strength of ZrO_2 ceramics at $\tau = 0.2$ s and $P_{max} = 125$ mN manifested itself (a) in the widening of the hysteresis loops and (b) in the change in energy spent on plastic deformation.

ing dynamic tests, which means that the fracture strength of PSZ increases with an increase in the rate of loading. The recovered and unrecovered maximal depths of an indentation very rapidly increase after the beginning of fatigue fracture and do not relax to the original values for all 800 cycles of loading. Furthermore, the reproducibility of the results is much worse in the case of ceramics: only in two of the ten tests carried out under the same conditions could we notice the signs of fatigue fracture, while in LiF they were observed at a 100% probability.

Thus, the first experiments showed that the technique of dynamic indenting is, in principle, applicable to low-cycle fatigue tests of thin subsurface layers of materials with various structure, hardness, and impact strength. Similarly to macrotests, the material is hardened in the first cycles of loading and then looses its strength under the concurrent formation of cracks. The fatigue fracture is manifested in a sharp increase in the vibrations of an indenter at the nucleation of a microcrack and its subsequent growth, which results in a sharp increase in the irreversible losses of energy in the cycle. Moreover, the appearance of a fatigue crack in the subsurface layer causes a very rapid change both in the unrecovered maximum (h_{max}) and plastically recovered (h_p) depths of an indentation, although their ratio $\eta = h_p/h_{max}$ is not affected by the fatigue fracture, which means that the elastic recovery of the indentation depth weakly depends on the number of cycles of loading, as well as on the generation and growth of fatigue microcracks.

ACKNOWLEDGMENTS

This work was financially supported by the Russian Foundation for Basic Research, project no. 01-02-16573, and the Ministry of Education of the Russian Federation, project no. E00-34-123.

REFERENCES

1. St. Kocan'da, *Fatigue Failure of Metals* (Wydawnictwa Naukowo-Techniczne, Warsaw, 1972; Metallurgiya, Moscow, 1976), translated from Polish.
2. J. Collins, *Failure of Materials in Mechanical Design* (Wiley, New York, 1981; Mir, Moscow, 1984).
3. R. B. Waterhouse, *Fretting Fatigue* (Applied Science Publ., Barking, 1981).
4. S. Suresh, *Fatigue of Materials* (Cambridge Univ. Press, Cambridge, 1998).
5. V. S. Ivanova and V. F. Terent'ev, *Nature of Metal Fatigue* (Metallurgiya, Moscow, 1975).
6. M. Fiset, G. Huard, M. Grenier, *et al.*, Wear **217**, 271 (1998).
7. Yu. I. Golovin and A. I. Tyurin, Materialovedenie, No. 1, 14 (2001); Materialovedenie, No. 2, 10 (2001).
8. Yu. I. Golovin, V. I. Ivolgin, V. V. Korenkov, and A. I. Tyurin, Zh. Tekh. Fiz. **70** (5), 82 (2000) [Tech. Phys. **45**, 609 (2000)].
9. M. Sakai, Acta Metall. Mater. **41** (6), 1751 (1993).
10. M. Z. Huq and J. P. Celis, Wear **225**, 53 (1999).
11. M. D. Kriese, D. A. Boismier, N. R. Moody, and W. W. Gerberich, Eng. Fract. Mech. **61**, 1 (1998).
12. A. E. Giannakopoulos and S. Suresh, Scr. Mater. **40** (10), 1191 (1999).
13. R. J. Anton and G. Subhash, Wear **239**, 27 (2000).

Translated by Yu. Novakovskaya

Physics of the Solid State, Vol. 43, No. 10, 2001, pp. 1923–1926. Translated from Fizika Tverdogo Tela, Vol. 43, No. 10, 2001, pp. 1845–1848.

MAGNETISM AND FERROELECTRICITY

Skin Effect under the Conditions of Ferromagnetic and Spin-Wave Resonance

R. N. Nosov and D. I. Sementsov

Ul'yanovsk State University, Ul'yanovsk, 432700 Russia

e-mail: sements@quant.univ.simbirsk.su

Received November 13, 2000

Abstract—An expression for the electromagnetic field penetration depth in a metallic magnetic layer is derived taking into account the complexity of the high-frequency permeability under the conditions of ferromagnetic and spin-wave resonance. The frequency dependences of the skin depth and its dependences on the magnitude and type of spin pinning are determined from a numerical analysis of the solutions of the motion equation for magnetization. Some features of the dependences associated with the nature of the spin-wave spectrum are revealed. © *2001 MAIK "Nauka/Interperiodica".*

1. If the mean free path of conduction electrons in a nonferromagnetic metal is much smaller than the penetration depth δ_0 of the electromagnetic field in a sample, the normal skin effect takes place and the skin depth is determined by the relationship $\delta_0 = c/\sqrt{2\pi\sigma\omega}$, where c is the speed of light in free space, ω is the field frequency, and σ is the conductivity of the metal [1]. The skin depth for a ferromagnetic metal is defined as $\delta = \delta_0/\sqrt{\mu}$, where the permeability μ of the sample is a function of frequency that takes the magnetic characteristics, geometry, and orientation of the sample with respect to the microwave field into account [2]. However, at the ferromagnetic resonance frequency in the absence of dissipative processes in the spin system, we obtain $\mu \longrightarrow \infty$ and $\delta = 0$, which is not observed in reality. The inclusion of dissipation makes the quantity $\mu = \mu' - i\mu''$ and the quantity δ complex-valued. In this case, the quantity δ loses its simple physical meaning and the magnetic field penetration depth in the metal is determined not by its real component δ but by the quantity $\delta_1 = \delta_0/\mathrm{Re}\sqrt{\mu}$. In the present work, we analyze the frequency dependence of the penetration depth $\delta_1(\omega)$ for the microwave field in a layer of a ferromagnetic metal of thickness $\mathbf{h}(t)$ under resonance conditions when the microwave field $\mathbf{h}(t)$ is perpendicular to the magnetizing field $\mathbf{H}$ oriented along the normal to the layer surface.

2. Directing the Z axis along the normal and placing the origin at the center of the layer, we can write the distribution of the microwave field in the layer by assuming that the amplitude of the wave incident on the layer is equal to h_0 [1]:

$$\mathbf{h}(z) = \mathbf{h}_0\exp[(L-z)/\delta] = \mathbf{h}_0\exp\left[(L-z)\left(\frac{1}{\delta_1}-\frac{i}{\delta_2}\right)\right], \quad (1)$$

where

$$\delta_1 = \frac{\delta_0}{\sqrt{|\mu|}\cos\varphi}, \quad \delta_2 = \frac{\delta_0}{\sqrt{|\mu|}\sin\varphi},$$

$$|\mu| = \sqrt{\mu'^2 + \mu''^2}, \quad \varphi = \frac{1}{2}\arctan(\mu''/\mu').$$

It can be seen from Eq. (1) that the actual depth of penetration of the microwave field in the layer is defined by δ_1. In order to determine this quantity, we should determine the value of μ, which involves solving of the equation of motion for magnetization $\mathbf{M}$. Taking into account the attenuation in the spin system, we write this equation with a relaxation term in the Hilbert form [3]:

$$\dot{\mathbf{M}} = \gamma[\mathbf{M}\mathbf{H}^{\mathrm{eff}}] + \frac{\xi}{M}[\mathbf{M}\dot{\mathbf{M}}], \quad (2)$$

where γ is the magnetomechanical ratio, ξ is the dimensionless parameter of attenuation, and the effective magnetic field is given by

$$\mathbf{H}^{\mathrm{eff}} = \mathbf{H}_0 + \mathbf{h}(t) + \alpha\nabla^2\mathbf{M} + \beta\mathbf{n}[\mathbf{n}\mathbf{M}] - 4\pi\hat{N}\mathbf{M}. \quad (3)$$

Here, the magnetizing field $\mathbf{H}_0$ and the unit vector $\mathbf{n}$ of the easy magnetization axis are oriented along the normal; α and β are the exchange interaction and uniaxial anisotropy constants, respectively; and $\hat{N}$ is the tensor of the demagnetizing coefficients.

Introducing small deviations of magnetization $\mathbf{m}(r, t)$ from the equilibrium magnetization $\mathbf{M}_0$ into Eq. (2), linearizing this equation, and taking into account the axial symmetry of the problem, we obtain the following equation for the circular components $m^{\pm} = m_x \pm i m_y$ [4]:

$$\frac{d^2m^{\pm}}{dz^2} \pm \nu^2 m^{\pm} = -\frac{1}{\alpha}h^{\pm}(z). \quad (4)$$

1063-7834/01/4310-1923$21.00

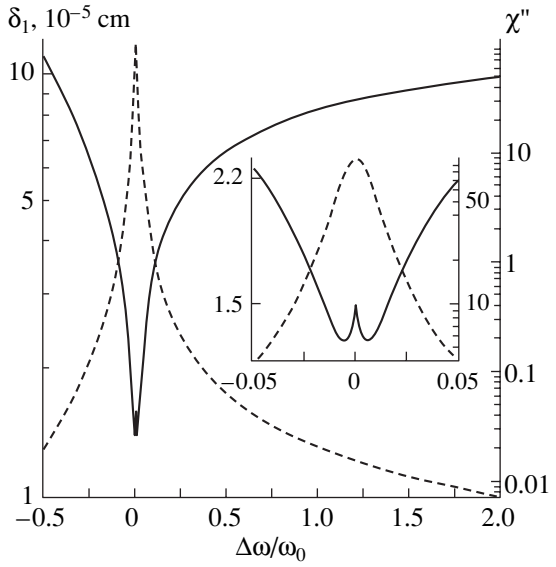

Fig. 1. Frequency dependences of the skin depth δ_1 (solid line) and the imaginary susceptibility component χ'' (dashed line) in the absence of surface pinning of spins.

We will carry out the subsequent analysis for the component $m^+ \equiv m$ responsible for natural oscillations of the spin system. The solution to Eq. (4) should be sought with the general boundary conditions

$$\left(d_i m \pm \frac{dm}{dz}\right)_{z = \pm L} = 0, \tag{5}$$

where d_i are the parameters of spin pinning at the surfaces of the layer.

It is difficult to find an analytic solution to Eq. (4) with a nonuniform distribution of the microwave field over the layer thickness which is defined by Eq. (1). For this reason, we will find an approximate solution corresponding to a uniform field distribution in the layer, which is valid, strictly speaking, only at $L \ll \delta$. In this case, $m(z)$ does not depend on δ. Averaging $m(z)$ over the layer thickness, we obtain

$$\langle m \rangle = \frac{1}{2L}\int_{-L}^{L} m(z)dz = (\chi' - i\chi'')h, \tag{6}$$

where the real and imaginary components of the high-frequency magnetic susceptibility of the layer are defined as

$$\begin{aligned}
\chi' &= \frac{q_1^2 + q_2^2}{\alpha\Delta^2}[(p_1q_1 + p_2q_2)((\nu_1^2 - \nu_2^2)^2 - 4\nu_1^2\nu_2^2) \\
&\quad - 4\nu_1\nu_2(\nu_1^2 - \nu_2^2)(p_2q_1 - p_1q_2) - \Delta(\nu_1^2 - \nu_2^2)], \\
\chi'' &= \frac{q_1^2 + q_2^2}{\alpha\Delta^2}[(p_1q_2 - p_2q_1)((\nu_1^2 - \nu_2^2)^2 - 4\nu_1^2\nu_2^2) \\
&\quad - 4\nu_1\nu_2(\nu_1^2 - \nu_2^2)(p_1q_1 + p_2q_2) + 2\Delta\nu_1\nu_2].
\end{aligned} \tag{7}$$

In these expressions, we changed over to the dimensionless parameters $\nu \equiv \nu L$, $d_i \equiv d_i L$, and $\alpha = \dfrac{\alpha}{L^2}$ and introduced the following notation:

$$p_1 + ip_2 = \tan\nu + \frac{(d_1 + d_2)\nu}{2d_1d_2},$$

$$q_1 + iq_2 = \frac{(d_1 + d_2)\cot 2\nu}{d_1d_2} - \frac{\nu}{d_1d_2} + \frac{1}{\nu},$$

$$\nu^2 = \frac{(1 - i\xi)\omega - \omega_0}{\alpha\gamma M_0},$$

$$\Delta = (q_1^2 + q_2^2)(\nu_1^2 - \nu_2^2)^2, \quad \nu = \nu_1 - i\nu_2.$$

The complex microwave susceptibility in the general form describes the entire excitation spectrum of the spin system in a thin layer. Considering that $\mu = 1 + 4\pi\chi$, we see that the real and imaginary components of the permeability appearing in Eq. (1) satisfy the equations $\mu' = 1 + 4\pi\chi'$ and $\mu'' = 4\pi\chi''$.

3. We will describe below the results of a numerical analysis carried out on the basis of relationships (1) and (7). The curves presented in the figures are plotted on the semilogarithmic scale and are the frequency dependences of two quantities on the pinning parameter: the depth δ_1 of penetration of the microwave field into the sample and the imaginary component χ'' of the high-frequency susceptibility, which determines the spectrum of the spin-wave resonance (SWR) in the film. Here, the frequency dependence is the dependence of the above quantities on the normalized detuning $\Delta\omega/\omega_0$ from the frequency of the uniform (ferromagnetic) resonance. The dependence of the pinning parameters is shown at a fixed frequency detuning. For our calculations, we chose the parameters of a magnetic permalloy film, namely, $\sigma = 10^{17}$ s^{-1}, $\xi = 10^{-2}$, $M_0 = 10^3$ G, and $\omega_0 = 10$ GHz.

Figure 1 shows the frequency dependences of the quantities δ_1 and χ'' for $d_1 = d_2 = 0$ in the absence of pinning on both surfaces of the film. It is well known that the absence of pinning leads to vanishing of the spin-wave resonance spectrum and to the excitation of only a homogeneous mode at the ferromagnetic resonance frequency. The $\delta_1(\omega)$ dependence in this figure indicates that the electromagnetic field penetration depth in the sample, as expected, decreases abruptly under ferromagnetic resonance conditions. However, an analysis shows that the skin depth in the immediate vicinity of the resonance frequency increases insignificantly and attains a local maximum at the point corresponding to the peak of χ'', which can be clearly seen in the inset to Fig. 1. The existence of this local maximum is due to the fact that the quantity δ_1 depends not only on $|\mu|$ but also on the phase φ. Since the inequality $|\mu'| \ll \mu''$ holds

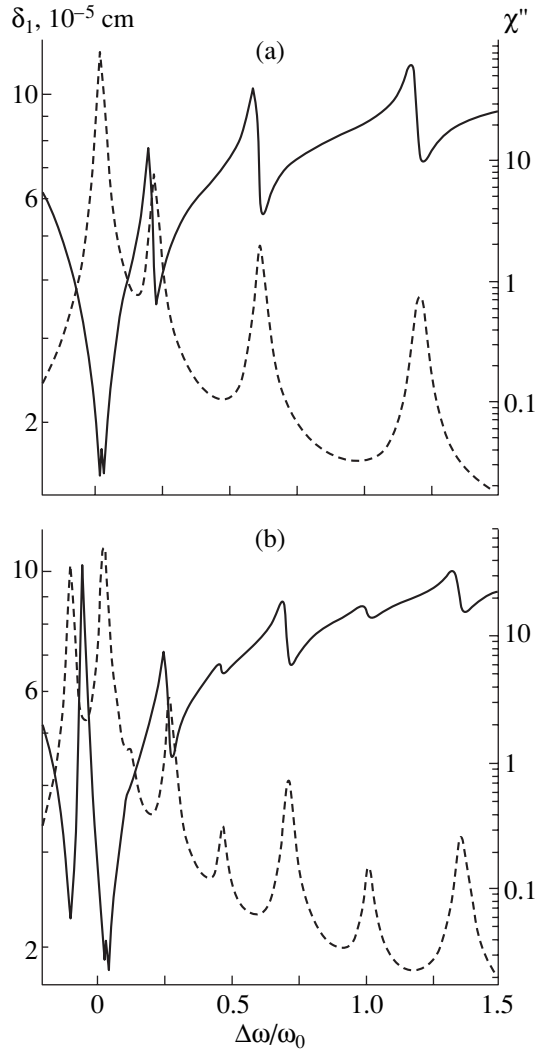

Fig. 2. Frequency dependences of the skin depth δ_1 (solid line) and the imaginary susceptibility component χ'' (dashed line) for (a) symmetric ($d_1 = d_2 \longrightarrow \infty$) and (b) asymmetric ($d_1 \longrightarrow \infty$ and $d_2 = -3$) pinning of surface spins.

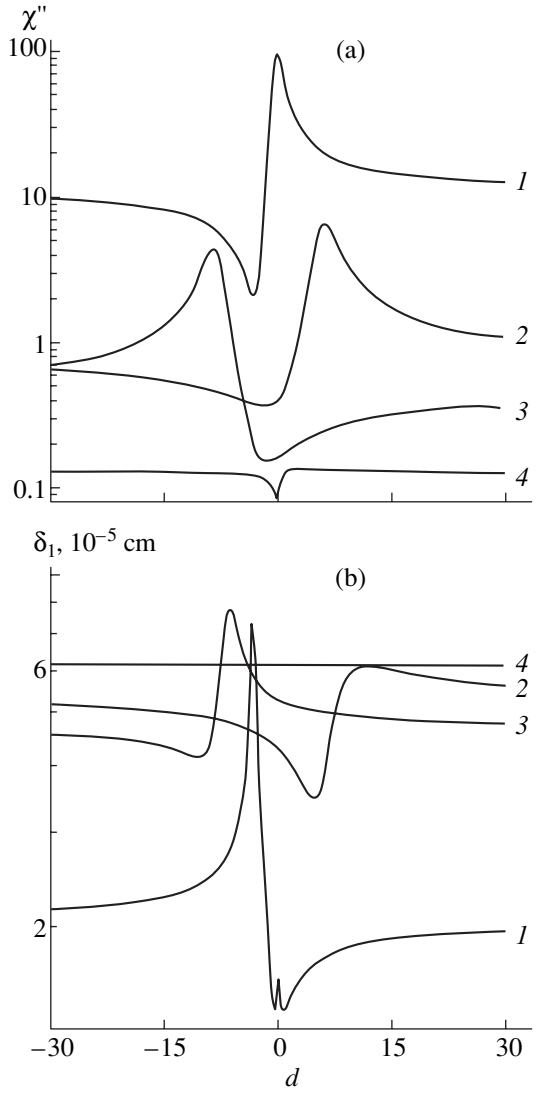

Fig. 3. Dependences of (a) the imaginary susceptibility component and (b) the skin depth on the type and degree of surface pinning at the frequency detuning $\Delta\omega/\omega_0 =$ (*1*) 0, (*2*) 0.17, (*3*) 0.28, and (*4*) 0.4.

in the vicinity of the resonance frequency, for $\omega \cong \omega_0$, we have

$$\delta_1 \cong \delta_0\sqrt{\frac{2}{\mu''}}\left(1 - \frac{|\mu'|}{2\mu''}\right) = \frac{\delta_0}{\sqrt{2\pi\chi''}}\left(1 - \frac{|1 + 4\pi\chi''|}{8\pi\chi''}\right). \quad (8)$$

On account of the characteristic dependence $\chi'(\omega)$ passing through zero for $\omega = \omega_0$, relationship (8) leads to the existence of a local maximum at $\omega \approx \omega_0$ so that $\delta_1(\omega_0) \cong \delta_0\sqrt{2/\mu_0''} = \delta_0/\sqrt{2\pi\chi_0''}$, where $\mu_0'' = \mu''(\omega_0)$ and $\chi_0'' = \chi''(\omega_0)$.

Figure 2 shows similar dependences for two types of pinning: symmetric pinning (Fig. 2a), when $d_1 = d_2 \longrightarrow \infty$ (the spins are completely pinned on both surfaces), and asymmetric pinning (Fig. 2b), when $d_1 \longrightarrow \infty$ and $d_2 = -3$ (incomplete pinning on one of the surfaces). The existence of surface pinning of spins leads to the emergence of resonance peaks corresponding to spin-wave modes in the spectrum of magnetization oscillations. In the case of symmetric pinning, the spectrum contains odd-order modes in addition to the homogeneous mode, whereas in the case of asymmetric pinning, the SWR spectrum also contains even modes whose intensity is much lower than the intensity of odd modes. The emergence of an anisotropy of the "easy plane" type on one of the surfaces of the layer, i.e., the negative value of the pinning parameter d_2, leads to the emergence of a resonance peak corresponding to the surface mode (Fig. 2b) at a frequency $\omega < \omega_0$. In this case, analysis of the frequency dependences of the quantities δ_1 and χ'' indicates that the peaks in the $\chi''(\omega)$

dependence do not correspond exactly to the minima of the function $\delta_1(\omega)$ but are slightly displaced relative to one another due to the dependence of the skin depth δ_1 on the phase of the quantity μ. It is also worth noting that having attained its minimum at $\omega \approx \omega_0$, the microwave field penetration depth δ_1 increases nonmonotonically with frequency. This increase is mainly determined by the frequency dependence of the quantity $(\omega\chi'')^{-1/2}$.

An analysis of these dependences also shows that at a fixed frequency, both χ'' and δ_1 are functions of surface pinning. These dependences are significant in the vicinity of the parameters d_i corresponding to the resonance conditions for one of the modes of the SWR spectrum. By way of an example, Fig. 3 shows several characteristic dependences of the quantities χ'' (Fig. 3a) and δ_1 (Fig. 3b) on parameter d in the case of symmetric pinning ($d_1 = d_2 = d$) for several frequency detuning parameters $\Delta\omega/\omega_0 = 0$, 0.17, 0.28, and 0.4 (curves *1–4*). All the curves correspond to the spectral region in which bulk modes are excited. The characteristic spike in curves *1* is observed in the range of values d close to zero, where the homogeneous mode is excited. The dependence $\delta_1(d)$ for this mode at $d = 0$ has a local maximum determined by relationships (8). Curves *2* and *3* have a characteristic spike corresponding to the first spin-wave mode of the spectrum for two types of surface anisotropy, which are determined by the sign of parameter d. Curves *4* correspond to the frequency lying between adjacent odd modes ($n = 1, 3$) and matching none of the peaks of the $\chi''(\omega)$ spectrum at any parameter d. For this reason, the corresponding $\chi''(d)$ curve displays only a low spike in the range of $d \approx 0$, which is completely flattened in the $\delta(d)$ dependence. Thus, the shape of the curves considered above substantially depends on the choice of the frequency for which they are plotted.

The above analysis shows that the depth of penetration of the high-frequency field in a ferromagnetic metal in the frequency range in which the spin-wave resonance spectrum is excited is determined by the magnitude and the phase of the complex susceptibility of the sample, which considerably depends on the type of surface pinning of spins.

REFERENCES

1. L. D. Landau and E. M. Lifshitz, *Course of Theoretical Physics*, Vol. 8: *Electrodynamics of Continuous Media* (Nauka, Moscow, 1982; Pergamon, New York, 1984).
2. A. I. Akhiezer, V. G. Bar'yakhtar, and S. V. Peletminskii, *Spin Waves* (Nauka, Moscow, 1967; North-Holland, Amsterdam, 1968).
3. A. G. Gurevich and G. A. Melkov, *Magnetic Oscillations and Waves* (Nauka, Moscow, 1994).
4. R. N. Nosov and D. I. Sementsov, Fiz. Tverd. Tela (St. Petersburg) **42** (8), 1430 (2000) [Phys. Solid State **42**, 1471 (2000)].

Translated by N. Wadhwa

Physics of the Solid State, Vol. 43, No. 10, 2001, pp. 1927–1933. Translated from Fizika Tverdogo Tela, Vol. 43, No. 10, 2001, pp. 1849–1854.

MAGNETISM AND FERROELECTRICITY

Drift Motion of Domain Boundaries in Garnet Ferrites in an Acoustic Wave Field

V. S. Gerasimchuk and A. A. Shitov

Donbass State Architectural and Construction Academy, Makeevka, Donetsk oblast, 86123 Ukraine

e-mail: vsg@donace.dn.ua

Received January 12, 2001

Abstract—The drift motion of a 180° domain boundary in garnet ferrites with two nonequivalent sublattices is studied in an elastic stress field induced by an acoustic wave propagating in the domain boundary plane. The dependences of the drift velocity on the amplitude and polarization of the acoustic wave are obtained, and the drift motion conditions for a strip domain structure are determined. © *2001 MAIK "Nauka/Interperiodica".*

1. INTRODUCTION

Considerable interest in the dynamics of domain boundaries in magnetic-ordered crystals has been motivated by their possible use as magnetic recording media. This explains the large number of works dealing with the interaction of external magnetic fields and domain boundaries. The domain structure of magnets, apart from magnetic fields, is efficiently affected by an acoustic wave field. In particular, Vlasko-Vlasov and Tikhomirov [1, 2] experimentally investigated the interaction of ultrasonic waves with Bloch lines and 180° domain boundaries in yttrium iron garnets. These authors examined forced linear oscillations of Bloch lines and domain boundaries and revealed interesting phenomena of oriented motion, continuous generation, and changes in the density of Bloch lines and domain boundaries. The influence of acoustic waves on the dynamics of domain boundaries in different-type magnets was theoretically analyzed in [3–6]. The theory of domain boundary drift in ferromagnets was developed by Gorobets and Denisov [3, 4] on the basis of approximate Slonchevskiĭ equations. The effect of acoustic waves on domain boundaries in two-sublattice systems (a weak ferromagnet and an anisotropic ferrimagnet) was investigated in our earlier works [5, 6] within the approach based on analyzing the nonlinear equations of motion for sublattice magnetization vectors. All theoretical calculations in [3–6] were performed for the simplest case when the acoustic wave propagates normally to the domain boundary plane.

In this work, the nonlinear motion of a 180° domain boundary in garnet ferrites in a field of acoustic waves traveling parallel to the domain boundary plane (which corresponds to the geometry of experiments described in [1, 2]) was theoretically investigated within the Lagrangian formalism.

2. THEORETICAL TREATMENT

2.1. The nonlinear macroscopic dynamics of garnet ferrites with two nonequivalent sublattices in an acoustic wave field is described on the basis of the Lagrangian density L represented in terms of the unit antiferromagnetic vector $\mathbf{l}$ ($\mathbf{l}^2 = 1$) [7, 8]:

$$L(\mathbf{l}) = M_0^2\left\{\frac{\alpha}{2c^2}\dot{\mathbf{l}}^2 - \frac{\alpha}{2}(\nabla\mathbf{l})^2 - \frac{\beta_1}{2}l_x^2 - \frac{\beta_2}{2}l_y^2 - \gamma u_{ik}l_i l_k + \frac{\nu}{gM_0}\frac{l_z\dot{l}_x - l_x\dot{l}_z}{1+l_y}\right\}. \quad (1)$$

Here, dots indicate the time derivatives; M_0 is the magnitude of the sublattice magnetization vector; $c = gM_0(\alpha\delta)^{1/2}/2$ is the characteristic velocity, which coincides with the minimum phase velocity of spin waves; δ and α are the constants of the uniform and nonuniform exchange interactions, respectively; g is the gyromagnetic ratio; β_1 and β_2 are the effective anisotropy constants; u_{ik} is the elastic strain tensor; γ is the magnetoelastic constant; and $\nu = |M_1 - M_2|/M_{1,2}$ is the parameter characterizing the conditions of validity of the dynamic model for garnet ferrites [7]. By ignoring the sublattice noncollinearity ($\delta \longrightarrow \infty$), we assume that the studied ferrimagnet at a distance from the compensation point exhibits nearly ferromagnetic (FM) properties. In the vicinity of the compensation point, the magnitudes of the sublattice magnetization vectors $\mathbf{M}_1$ and $\mathbf{M}_2$ differ insignificantly ($\nu \longrightarrow 0$) and the dynamic properties of the ferrimagnet are similar to those of the antiferromagnetic (AFM) crystal. The term describing the energy of the elastic subsystem is not included in relationship (1), because, hereafter, we treat the acoustic wave as a specified external field and disregard the

inverse effect of the magnetic subsystem on the elastic subsystem.

Making allowance for the fact that the magnitude of the **I** vector is constant, we change over to the angular variables θ and φ, that is,

$$l_z = il_x = \sin\theta\exp(i\varphi), \quad l_y = \cos\theta. \tag{2}$$

The Lagrangian density in terms of the angular variables has the following form:

$$\begin{aligned} L\{\theta,\varphi\} = M_0^2\Bigg\{&\frac{\alpha}{2c^2}(\dot\theta^2+\dot\varphi^2\sin^2\theta) \\ &-\frac{\alpha}{2}[(\nabla\theta)^2+(\nabla\varphi)^2\sin^2\theta]-\frac{\beta_1}{2}\sin^2\theta\sin^2\varphi \\ &-\frac{\beta^2}{2}\cos^2\theta-\gamma[\sin2\theta(u_{zy}\cos\varphi+u_{yx}\sin\varphi) \\ &+u_{yy}\cos^2\theta+\sin^2\theta(u_{zz}\cos^2\varphi+u_{xz}\sin2\varphi+u_{xx}\sin^2\varphi)] \\ &+\frac{\nu}{gM_0}\dot\varphi(1-\cos\theta)\Bigg\}. \end{aligned} \tag{3}$$

The dynamic retardation of domain boundaries due to dissipative processes is accounted for in the dissipative function

$$F = \frac{\lambda M_0}{2g}\dot{\mathbf{l}}^2 = \frac{\lambda M_0}{2g}(\dot\theta^2+\dot\varphi^2\sin^2\theta), \tag{4}$$

where λ is the Hilbert damping constant.

The equations of motion in terms of the angular variables θ and φ with inclusion of the relaxation terms take the form

$$\begin{aligned} &\alpha\left(\Delta\theta-\frac{1}{c^2}\ddot\theta\right)+\sin\theta\cos\theta\left[\alpha\left(\frac{1}{c^2}\dot\varphi^2-(\nabla\varphi)^2\right)\right. \\ &\left.-\beta_1\sin^2\varphi+\beta_2\right]+\frac{\nu}{gM_0}\dot\varphi\sin\theta-\gamma[\sin2\theta \\ &\times(u_{zz}\cos^2\varphi+u_{xz}\sin2\varphi+u_{xx}\sin^2\varphi-u_{yy}) \\ &+2\cos2\theta(u_{zy}\cos\varphi+u_{yx}\sin\varphi)] = \frac{\lambda}{gM_0}\dot\theta, \end{aligned} \tag{5}$$

$$\begin{aligned} &\alpha\nabla[\sin^2\theta(\nabla\varphi)]-\frac{\alpha}{c^2}\frac{d}{dt}(\dot\varphi\sin^2\theta) \\ &-\beta_1\sin^2\theta\sin\varphi\cos\varphi-\frac{\nu}{gM_0}\dot\theta\sin\theta \\ &+\gamma[\sin^2\theta(u_{zz}\sin2\varphi-2u_{xz}\cos2\varphi-u_{xx}\sin2\varphi) \\ &+\sin2\theta(u_{zy}\sin\varphi-u_{yx}\cos\varphi)] = \frac{\lambda}{gM_0}\dot\varphi\sin^2\theta. \end{aligned} \tag{6}$$

Under the condition $0 < \beta_1 < \beta_2$, the domain boundary is stable when the **I** vector rotates in the *XZ* plane and the magnetization distribution is inhomogeneous along the *Y* axis [8]. For this boundary, the condition $\theta = \theta_0 = \pi/2$ is met and the angular variable $\varphi = \varphi_0(y)$ satisfies the equation

$$\alpha\varphi_0'' - \beta_1\sin\varphi_0\cos\varphi_0 = 0, \tag{7}$$

where the primes denote the derivative with respect to the *y* variable. The solution of Eq. (7) with the boundary conditions $\varphi_0(-\infty) = 0$ and $\varphi_0(+\infty) = \pi$ for a static 180° domain boundary has the form

$$\begin{aligned} \varphi_0' &= \frac{1}{y_0}R\sin\varphi_0 = \frac{1}{y_0}R\rho\cosh^{-1}\frac{y}{y_0}, \\ \cos\varphi_0(y) &= -R\tanh\frac{y}{y_0}, \end{aligned} \tag{8}$$

where $y_0 = \sqrt{\alpha/\beta_1}$ is the thickness of the domain boundary, $R = \pm1$ is the topological charge of the domain boundary, and $\rho = \pm1$ is the parameter describing the sense of rotation of the **I** vector in the domain boundary. As is known, 180° domain boundaries that separate domains with opposite magnetization directions in a strip domain structure possess opposite topological charges *R*. In the domain boundaries, the **I** vector can rotate from $-R$ to $+R$ (or in the opposite direction) toward either the positive or negative direction of the *Z* axis, depending on the *R* parameter. Consequently, the adjacent domain boundaries in the strip domain structure with the **I** vector rotating in the *XZ* plane are characterized by the value of $l_z(y = \pm\infty) = \mp R$ and one of the two values of $l_x(y = 0) = \pm\rho$. In the presence of an external field and a certain combination of signs of the topological charges *R* and the parameters ρ for the adjacent domain boundaries, the strip domain structure as a whole can execute a translational motion in a weak ferromagnet [5]. Now, we demonstrate that a similar effect occurs in an anisotropic ferrimagnet when the acoustic wave propagates parallel to the domain boundary plane.

Let us solve the set of equations (5) and (6). For this purpose, we fall back on a version of the perturbation theory for solitons [5, 9–11]. Note that, in the case when the acoustic wave propagates parallel to the domain boundary plane ($k_x \neq 0$, $k_z \neq 0$, and $k_y = 0$), the local position of the domain boundary center depends on both the time and transverse coordinates $Y(\mathbf{r}_\perp, t)$. Hence, unlike the calculations performed in [5, 9–11], we introduce the collective variable $Y(\mathbf{r}_\perp, t)$ as a coordinate of the domain boundary center, where $\mathbf{r} = (x, z)$. Under the assumption that the acoustic wave amplitude is sufficiently small, we will seek the solution to the set

of equations (5) and (6) in the form of expansions as follows:

$$\theta(\mathbf{r}, t) = \pi/2 + \theta_1(\xi, \mathbf{r}_\perp, t) + \theta_2(\xi, \mathbf{r}_\perp, t) + \ldots,$$
$$\varphi(\mathbf{r}, t) = \varphi_0(\xi) + \varphi_1(\xi, \mathbf{r}_\perp, t) + \varphi_2(\xi, \mathbf{r}_\perp, t) + \ldots, \quad (9)$$

where $\xi = y - Y(\mathbf{r}_\perp, t)$ and the subscripts $n = 1, 2, \ldots$ indicate the order of smallness in the acoustic wave amplitude. The function $\varphi_0(\xi)$ describes the unperturbed domain boundary and obeys relationships (8). The functions θ_n and φ_n ($n = 1, 2, \ldots$) characterize the distortion of the domain boundary due to excitation of spin waves. The drift velocity of the domain boundary is defined as the instantaneous velocity $V(\mathbf{r}_\perp, t) = \dot{Y}(\mathbf{r}_\perp, t)$ averaged over the oscillation period: $V_{dr} = \overline{V(\mathbf{r}_\perp, t)}$, where the vinculum indicates averaging over the period of the acoustic wave.

Now, we consider a monochromatic acoustic wave propagating parallel to the domain boundary plane at a frequency ω: $\mathbf{u}(\mathbf{r}_\perp, t) = \mathbf{u}_0 \exp(i\mathbf{k}_\perp\mathbf{r}_\perp, -i\omega t)$, where $\mathbf{k}_\perp\mathbf{r}_\perp = k_x x + k_z z$. By representing the collective variable as the series $Y = Y_1 + Y_2 + \ldots$, we obtain the following system of equations to the first order in the acoustic wave amplitude:

$$\left(\hat{L} + \frac{1}{\omega_1^2}\frac{\partial}{\partial t^2} + \frac{\omega_r}{\omega_r^2}\frac{\partial}{\partial t}\right)\varphi_1(\xi, \mathbf{r}_\perp, t)$$
$$+ \frac{\omega_\nu}{\omega_1^2}\frac{\partial}{\partial t}\theta_1(\xi, \mathbf{r}_\perp, t) = \frac{R\sin\varphi_0(\xi)}{y_0\omega_1^2}$$
$$\times\left(\frac{\partial^2 Y_1}{\partial t^2} + \omega_r\frac{\partial Y_1}{\partial t} - \omega_1^2 y_0^2\Delta_\perp Y_1\right) + \frac{i\gamma}{\beta_1} \quad (10)$$
$$\times \exp[i(\mathbf{k}_\perp\mathbf{r}_\perp - \omega t)][(k_z u_{0z} - k_x u_{0x})\sin 2\varphi_0(\xi)$$
$$- (k_z u_{0x} + k_x u_{0z})\cos 2\varphi_0(\xi)],$$

$$\left(\hat{L} + \sigma + \frac{1}{\omega_1^2}\frac{\partial^2}{\partial t^2} + \frac{\omega_r}{\omega_r^2}\frac{\partial}{\partial t}\right)\theta_1(\xi, \mathbf{r}_\perp, t)$$
$$-\frac{\omega_\nu}{\omega_1^2}\frac{\partial}{\partial t}\varphi_1(\xi, \mathbf{r}_\perp, t) = -\frac{R\omega_\nu}{y_0\omega_1^2}\frac{\partial Y_1}{\partial t}\sin\varphi_0(\xi) \quad (11)$$
$$+ \frac{i\gamma u_{0y}}{\beta_1}\exp[i(\mathbf{k}_\perp\mathbf{r}_\perp - \omega t)]$$
$$\times[(k_z\cos\varphi_0(\xi) + k_x\sin\varphi_0(\xi))],$$

where $\Delta_\perp = \partial^2/\partial x^2 + \partial^2/\partial z^2$, $\sigma = (\beta_2 - \beta_1)/\beta_1$, $\omega_1 = c/y_0$ is the activation frequency of the lower branch of bulk spin waves, $\omega_r = \lambda\delta g M_0/4$ is the characteristic relaxation frequency, $\mathbf{k}_\perp$ is the wave vector of the acoustic wave, $k_\perp = |\mathbf{k}_\perp| = \omega/s$, and s is the acoustic wave velocity.

The operator $\hat{L} = -y_0^2\frac{d^2}{d\xi^2} + 1 - \frac{2}{\cosh^2(\xi/y_0)}$ has the known wave functions $f_0(\xi) = \frac{1}{\sqrt{2y_0}}\cosh^{-1}\frac{\xi}{y_0}$ and $f_p(\xi) = \frac{1}{b_p\sqrt{L}}\left(\tanh\frac{\xi}{y_0} - ipy_0\right)\exp(ip\xi)$ (where L is the crystal length) and the eigenvalues $\lambda_0 = 0$ and $\lambda_p = b_p^2 = 1 + p^2 y_0^2$.

The solution to the system of the first-order equations (10) and (11) is sought in the form of an expansion in the complete set of eigenfunctions of the $\hat{L}$ operator. As a result, we obtain

$$\varphi_1(\xi, t) = \mathrm{Re}\left\{\frac{i\gamma}{2\beta_1}[-b_1\sqrt{L}f_{p=0}(\xi)\right.$$
$$+ R\rho(k_x u_{0x} - k_z u_{0z})D_1(\xi)$$
$$\left.- (k_x u_{0z} + k_z u_{0x})D_2(\xi)]\exp(i\mathbf{k}_\perp\mathbf{r}_\perp - i\omega t)\right\},$$
$$\theta_1(\xi, t) = \mathrm{Re}\left\{\left[-b_1\sqrt{L}f_{p=0}(\xi) + \frac{\sqrt{2y_0}f_0(\xi)}{\sigma - q}\right.\right. \quad (12)$$
$$\times\left(\frac{i\gamma\rho}{\beta_1}k_x u_{0y} - \frac{R\rho\omega_\nu V_1}{\omega_1^2 y_0}\right) + \frac{\omega\nu\gamma R\rho}{2\beta_1\omega_0}(k_x u_{0x} - k_z u_{0z})D(\xi)$$
$$\left.\left. + (k_x u_{0z} + k_z u_{0x})D_4(\xi)\right]\exp(i\mathbf{k}_\perp\mathbf{r}_\perp - i\omega t)\right\}.$$

Here, we used the following designations:

$$b_1 = \frac{2i\omega\nu}{\omega_0}\frac{Rk_z u_{0y}}{(1-q)(1-q+\sigma) - (\omega\nu/\omega_0)^2},$$
$$b_2 = \frac{i\gamma}{\beta_1}\frac{R(1-q)k_z u_{0y}}{(1-q)(1-q+\sigma) - (\omega\nu/\omega_0)^2},$$
$$D_1(\xi) = \int_{-\infty}^{+\infty} A_1(p)B_1(p)d(py_0),$$
$$D_2(\xi) = \int_{-\infty}^{+\infty} A_2(p)B_1(p)d(py_0),$$
$$D_3(\xi) = \int_{-\infty}^{+\infty} A_1(p)B_2(p)d(py_0),$$
$$D_4(\xi) = \int_{-\infty}^{+\infty} A_2(p)B_2(p)d(py_0),$$

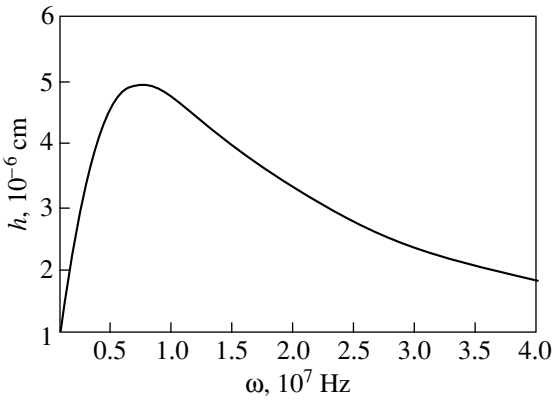

Fig. 1. Dependence of the displacement magnitude h on the acoustic field frequency ω for $Y_3Fe_5O_{12}$.

$$A_1(p) = \frac{\tanh(\xi/y_0)\cos(p\xi) + py_0\sin(p\xi)}{\cosh(\pi py_0/2)},$$

$$A_2(p) = \frac{\tanh(\xi/y_0)\sin(p\xi) - py_0\cos(p\xi)}{\sinh(\pi py_0/2)},$$

$$B_1(p) = \frac{\lambda_p - q + \sigma}{(\lambda_p - q)(\lambda_p - q + \sigma) - (\omega\nu/\omega_0)^2},$$

$$B_2(p) = \frac{B_1(p)}{\lambda_p - q + \sigma},$$

$$q = q_1 + iq_2, \quad q_1 = \left(\frac{\omega}{\omega_1}\right)^2,$$

$$q_2 = \left(\frac{\omega\omega_r}{\omega_1^2}\right), \quad \omega_0 = \beta_1 g M_0.$$

As follows from solution (12), the acoustic wave traveling in the domain boundary plane excites localized and nonlocalized spin waves. It should be noted that these excitations are produced by both transverse and longitudinal acoustic oscillations. In the case when the acoustic wave propagates normally to the domain boundary plane, spin waves are excited only by transverse components of the acoustic wave [6]. From the condition of vanishing of the Goldstone mode [5] for the system of equations (10) and (11), we obtain the equation for the domain boundary velocity, that is,

$$R\rho\left(\frac{\partial^2 Y_1}{\partial t^2} + \left(\omega_r - \frac{i\omega_\nu\omega\nu}{(\sigma - q)\omega_0}\right)\frac{\partial Y_1}{\partial t} - \omega_1^2 y_0^2 \Delta_\perp Y_1\right) = \frac{y_0\omega_1^2\omega\nu\gamma\rho}{(\sigma - q)\omega_0\beta_1} k_x u_{0y}\exp(i\mathbf{k}_\perp\mathbf{r}_\perp - i\omega t). \quad (13)$$

The solution of this equation has the form

$$Y_1 = \frac{y_0\omega_1^2\omega\nu\gamma}{(\sigma - q)\omega_0\beta_1} \times \frac{Rk_x u_{0y}}{\left(\frac{\omega_1 y_0\omega}{s}\right)^2 - i\omega\left(\omega_r - \frac{i\omega_\nu\omega\nu}{(\sigma - q)\omega_0}\right) - \omega^2} \times \exp(i\mathbf{k}_\perp\mathbf{r}_\perp - i\omega t). \quad (14)$$

Relationship (14) allows us to determine the domain boundary velocity in the linear approximation of the acoustic wave amplitude: $V_1 = -i\omega Y_1$. It follows from relationship (14) that $V(\mathbf{r}_\perp, t) \sim \nu$. Therefore, domain boundary oscillations are not excited in a garnet ferrite whose dynamic properties are similar to the properties of the antiferromagnetic crystal ($\nu \longrightarrow 0$). A similar situation—a lack of any drift motion of domain boundaries within the linear approximation—is also observed when the acoustic wave propagates normally to the domain boundary plane in weak ferromagnets [5]. In ferrite materials characterized by the parameter $\nu \neq 0$, the acoustic wave induces an oscillatory motion of domain boundaries. In particular, the mean magnitude of the domain boundary displacement at the frequency $\omega \sim 10^6$ s^{-1} in yttrium garnet ferrite (at $n \approx 5 \times 10^{-3}$) is of the order of 10^{-6} cm. This magnitude is in agreement with the experimental displacements of domain boundaries observed in [1]. The frequency dependence of the displacement magnitude h is depicted in Fig. 1. It is worth noting that the domain boundary oscillations in the given geometry are induced by the longitudinal component of the acoustic field. In the case when the acoustic wave propagates normally to the domain boundary plane, the oscillations in ferrite materials are excited only by the transverse components of the acoustic wave [6].

2.2. The equation for the function $\varphi_2(\xi, \mathbf{r}_\perp, t)$ in the second approximation can be written in the following form:

$$\hat{L}\varphi_2(\xi, \mathbf{r}_\perp, t) = \left(\frac{\partial^2 Y_2}{\partial t^2} + \omega_r\frac{\partial Y_2}{\partial t} - \omega_1^2 y_0^2\Delta_\perp Y_2\right)\frac{R\sin\varphi_0}{\omega_1^2 y_0} - 2y_0\theta_1(\xi, \mathbf{r}_\perp, t)\theta_1'(\xi, \mathbf{r}_\perp, t)R\sin\varphi_0 + \frac{2}{\omega_1^2}\left(\frac{\partial Y_1}{\partial t}\right)\varphi_1'(\xi, \mathbf{r}_\perp, t) + \left[\Delta_\perp Y_1 - \left(\frac{1}{c}\frac{\partial Y_1}{\partial t}\right)^2\right] \times \frac{\sin 2\varphi_0}{2} + \varphi_1^2(\xi, \mathbf{r}_\perp, t)\sin 2\varphi_0 + \frac{\omega_{nu}}{\omega_1^2}\theta_1'(\xi, \mathbf{r}_\perp, t) + \frac{\varphi_1'(\xi, \mathbf{r}_\perp, t)}{\omega_1^2}\left(\frac{\partial^2 Y_1}{\partial t^2} + \omega_r\frac{\partial Y_1}{\partial t} - \omega_1^2 y_0^2\Delta_\perp Y_1\right) \quad (15)$$

$$+\frac{2i\gamma}{\beta_1}\exp(i\mathbf{k}_\perp\mathbf{r}_\perp - i\omega t)\Big[((k_z u_{0z} - k_x u_{0x})\cos 2\varphi_0 + (k_z u_{0x} + k_x u_{0z})\sin 2\varphi_0)\varphi_1(\xi, \mathbf{r}_\perp, t) + (k_x u_{0y}\cos\varphi_0 - k_z u_{0y}\sin\varphi_0)\frac{\theta_1(\xi, \mathbf{r}_\perp, t)}{2}\Big].$$

Within the second approximation, the equation for the function $\theta_2(\xi, \mathbf{r}_\perp, t)$ does not involve $Y_2(\mathbf{r}_\perp, t)$ in an explicit form. Hence, this equation will not concern us in our subsequent analysis. The solution to Eq. (15) can be sought as an eigenfunction expansion of the $\hat{L}$ operator. Here, we do not present the complete solution of the equations in the second approximation, because our interest is only in the drift motion of domain boundaries. In order to determine the domain boundary velocity $V_2(t)$, it is sufficient to deduce the expression for the $d_0^{(2)}$ coefficient in the expansion

$$\varphi_2(\xi, \mathbf{r}_\perp, t) = \mathrm{Re}\Big\{\sum_p [d_p^{(2)} f_p(\xi) + d_0^{(2)} f_0(\xi)] \times \exp[i(\mathbf{k}_\perp\mathbf{r}_\perp - \omega t)]\Big\} \quad (16)$$

and to set it equal to zero. As a result, with allowance made for the solutions of the first-order equations, we obtain the following equation for the collective coordinate, which describes the dynamics of domain boundaries within the perturbation theory in the second order:

$$R\rho\left(\frac{\partial^2 Y_2}{\partial t^2} + \omega_r\frac{\partial Y_2}{\partial t} - \omega_1^2 y_0^2\Delta_\perp Y_2\right) = N + N_1\exp(2i\omega t) + N_2\exp(-2i\omega t). \quad (17)$$

Here,

$$N = \omega_1^2 y_0\sqrt{2y_0}\,\mathrm{Re}\int_{-\infty}^{\infty} d\xi f_0(\xi)\Big\{\frac{\theta_1^*\theta_1'}{2}\sin\varphi_0 - \varphi_1^*\varphi_1\frac{\sin 2\varphi}{4y_0} - \frac{(\varphi_1^*)'}{4\omega_1^2 y_0}\left(\frac{\partial^2 Y_1}{\partial t^2} + (\omega_r + 2i\omega)\frac{\partial Y_1}{\partial t} - \omega_1^2 y_0^2\Delta_\perp Y_1\right)$$

$$-\frac{\nu}{2\omega_0 y_0}\left(\frac{\partial Y_1}{\partial t}\right)(\theta_1^*)' - \frac{i\gamma}{2\beta_1 y_0}\Big[(k_z u_{0z} - k_x u_{0x})\varphi_1^* \quad (18)$$

$$\times\cos 2\varphi_0 + (k_z u_{0x} + k_x u_{0z})\varphi_1^*\sin 2\varphi_0 - \frac{k_z u_{0y}}{2}\theta_1^*\sin\varphi_0 + \frac{k_x u_{0y}}{2}\theta_1^*\cos\varphi_0\Big]\exp(i\mathbf{k}_\perp\mathbf{r}_\perp - i\omega t)\Big\},$$

where asterisks indicate the complex conjugations. The expressions for coefficients N_1 and N_2 are similar to relationship (18). These coefficients are not given in an explicit form, because, after subsequent averaging of the solution to Eq. (17), the terms with N_1 and N_2 become zero. By integrating Eq. (17) and averaging the obtained solution over the period of the acoustic wave, we can determine the drift velocity of the domain boundary $V_{\mathrm{dr}} = \bar{V}_2 = \overline{\frac{\partial Y_2}{\partial t}}$; that is,

$$V_{\mathrm{dr}} = R\rho\mu_1(\omega)(k_x u_{0y})(k_z u_{0y}) + R\rho\mu_2(\omega)[(k_x u_{0x})(k_z u_{0x}) - (k_x u_{0z})(k_z u_{0z}) - (k_z u_{0x})(k_z u_{0z}) + (k_x u_{0x})(k_x u_{0z})] + \rho\mu_3(\omega)(k_z u_{0y})[(k_x u_{0z}) + (k_z u_{0x})] + \rho\mu_4(\omega)(k_x u_{0y})[(k_x u_{0x}) - (k_z u_{0z})], \quad (19)$$

where $\mu_i(\omega)$ stands for the nonlinear mobilities of domain boundaries, which depend on the parameters of the magnet and the acoustic wave under investigation. In the general form, expressions for $\mu_i(\omega)$ are cumbersome. For this reason, it is expedient to consider the extreme cases. Before proceeding to the dependence of the drift velocity on the nonlinear mobility $\mu_i(\omega)$, we dwell on the following circumstance. As was noted above, the adjacent domain boundaries possess opposite topological charges R. Therefore, the drift of a strip domain structure formed by these boundaries can occur only when the ρ parameters for the adjacent domain boundaries differ from each other. In other words, the **I** vectors in the adjacent domain boundaries should have opposite orientations, whereas the sense of their rotation should be the same. In this case, the products $R\rho$ for the adjacent domain boundaries are of the same sign and the domain boundaries move in the same direction; i.e., the domain structure executes a motion.

Let us now analyze the frequency dependence of the nonlinear mobility $\nu \longrightarrow 0$ in a number of special cases. We consider a ferrimagnet in the vicinity of the compensation point, i.e., in the antiferromagnetic limit ($\mu_3(\omega)$). In this case, the mobilities $\mu_3(\omega)$ and $\mu_4(\omega)$ are proportional to ν and are equal to zero and the main contribution to the drift velocity is made by the nonlinear mobility $\mu_1(\omega)$ defined by the expression

$$\mu_1^{\mathrm{AFM}}(\omega) = -\mu_0\frac{q_2^2}{[(1+\sigma-q_1)^2 + q_2^2][(\sigma-q_1)^2 + q_2^2]}, \quad (20)$$

where $\mu_0 = \dfrac{\pi y_0 g\gamma^2 M_0}{4\beta_1\lambda}$. In the long-wave approximation, which is of considerable experimental interest and

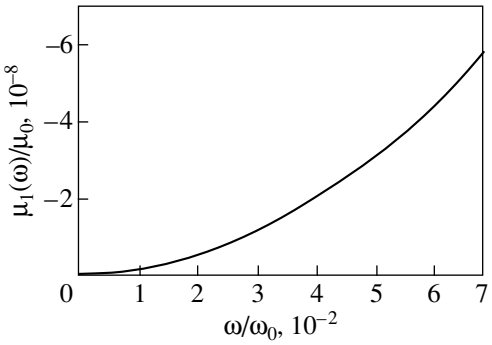

Fig. 2. Frequency dependence of the nonlinear mobility $\mu_1(\omega)$ in the long-wave approximation for $Y_3Fe_5O_{12}$.

corresponds to the frequency range $\omega = sk_\perp \ll 10^{10}$ s^{-1}, relationship (20) reduces to the following form:

$$\mu_1^{\mathrm{AFM}}(\omega) = -\mu_0 \frac{q_2^2}{(1+\sigma)^2\sigma^2}. \tag{21}$$

The drift velocity of domain boundaries can be estimated from the numerical parameters that characterize the garnet ferrite near the compensation point. For example, the numerical parameters for $Gd_3Fe_5O_{12}$ are as follows [12]: $y_0 \sim 10^{-4}$ cm, $M_0 = 4.5$ Oe, $\beta_1 \approx 603.3$, $\sigma \sim 1$, $g = 1.76 \times 10^7$ (s Oe)$^{-1}$, $\lambda \approx 5 \times 10^{-2}$, and $\gamma M_0^2 \sim 7.3 \times 10^6$ erg/cm^3. For a characteristic velocity of sound $s \sim 10^5$ cm/s and a limiting value of the strain tensor $ku_0 \sim 10^5$, the drift velocity of domain boundaries can be as high as 10^{-5} cm/s. In the short-wave approximation ($\omega \gg 10^{11}$ s^{-1}),

$$\mu_1^{\mathrm{AFM}}(\omega) = -\mu_0 \frac{q_2^2}{q_1^4}. \tag{22}$$

The second mobility $\mu_2^{\mathrm{AFM}}(\omega)$ in expression (19) at an arbitrary frequency has the form

$$\mu_2^{\mathrm{AFM}}(\omega) = \frac{\mu_0}{8}\int_{-\infty}^{\infty} B_1(p)d(py_0)\int_{-\infty}^{\infty} B_1^*(n) \times \frac{(p+n)^2y_0^2(p-n)^2y_0^2}{\sinh(\pi(p+n)y_0/2)\sinh(\pi(p-n)y_0/2)}d(ny_0) \approx \frac{\eta\mu_0}{(1-q_1)^2+q_2^2},$$

where the numerical parameter η is approximately equal to 5×10^{-15}.

Now, we consider the garnet ferrite in the ferromagnetic limit ($\delta \longrightarrow \infty$). In the long-wave approximation, the nonlinear mobility $\mu_1^{\mathrm{FM}}(\omega)$ is given by

$$\mu_1^{\mathrm{FM}}(\omega) = -\mu_0 \frac{\omega^2\nu^2}{\sigma(\sigma+1)\omega_0^2}. \tag{23}$$

In the short-wave approximation, we have

$$\mu_1^{\mathrm{FM}}(\omega) = -\mu_0 \frac{\sigma(\omega\nu/\omega_0)^4}{(1+\sigma-(\omega\nu/\omega_0)^2-q_2^2)^2(\sigma^2+q_2^2)}. \tag{24}$$

In the ferromagnetic limit, the drift velocity associated with the nonlinear mobility $\mu_1^{\mathrm{FM}}(\omega)$ within the long-wave approximation, for example, for $Eu_3Fe_5O_{12}$, is equal to 10^{-6} cm/s. This estimate was obtained using the following parameters for $Eu_3Fe_5O_{12}$ [12]: $y_0 \approx 3.7 \times 10^{-6}$ cm, $\beta_1 \approx 8.5$, $\sigma \sim 1$, $\lambda \approx 0.04$, $M_0 = 93.3$ Oe, $\gamma M_0^2 \approx 4.1 \times 10^6$ erg/cm^3, $g = 1.76 \times 10^7$ (s Oe)$^{-1}$, and $w_0 \approx 1.4 \times 10^{10}$ s^{-1}. The nonlinear mobilities $\mu_2^{\mathrm{FM}}(\omega)$ and $\mu_3^{\mathrm{FM}}(\omega)$ in the ferromagnetic limit at arbitrary frequencies are defined by the relationships

$$\mu_2^{\mathrm{FM}}(\omega) = \mu_0\eta \frac{(1+\sigma)^2+(\omega\nu/\omega_0)^2+q_2^2}{(1+\sigma+q_2^2-(\omega\nu/\omega_0)^2)^2+q_2^2(\sigma+2)^2},$$

$$\mu_3^{\mathrm{FM}}(\omega) = \frac{q_2(\omega\nu/\omega_0)(\sigma+2)}{(1+\sigma-q_2^2-(\omega\nu/\omega_0)^2)^2+q_2^2(\sigma+2)^2}.$$

The nonlinear mobility $\mu_4^{\mathrm{FM}}(\omega)$ within the long-wave approximation is represented as

$$\mu_4^{\mathrm{FM}}(\omega) = -\frac{1}{4}\frac{\sigma(\sigma^2+\sigma+2)(\omega\nu/\omega_0)^2\omega\omega_1^2\omega_\nu y_0^2}{(\sigma+1)\sigma^2s^2[(\omega_\nu\omega\nu/\omega_0)^2+(\sigma\omega\omega_1^2y_0^2/s^2)^2]}.$$

In the short-wave approximation, $\mu_4^{\mathrm{FM}}(\omega)$ is defined by the expression

$$\mu_4^{\mathrm{FM}}(\omega) = -\frac{1}{2}\frac{(\omega\nu/\omega_0)^3q_2}{[(1+\sigma-q_2^2-(\omega\nu/\omega_0)^2)^2+q_2^2(\sigma+2)^2][\sigma+q_2^2]}.$$

Vlasko-Vlasov and Tikhomirov [1] experimentally studied the $Y_3Fe_5O_{12}$ garnet ferrite. For this compound, the drift velocity of domain boundaries at $\nu = 5 \times 10^{-3}$ can be estimated from relationships (17) and (18) with the following parameters [12]: $y_0 \approx 10^{-5}$ cm, $\beta_1 \approx 0.6$, $\sigma \sim 1$, $\lambda \approx 10^{-4}$, $M_0 = 140$ Oe, $\gamma M_0^2 \approx 3.5 \times 10^6$ erg/cm^3, $g = 1.76 \times 10^7$ (s Oe)$^{-1}$, and $\omega_0 \approx 1.5 \times 10^9$ s^{-1}. Within the long-wave approximation, the nonlinear mobility $\mu_1(\omega)$ is determined by an expression similar to relationship (23) and the drift velocity for $Y_3Fe_5O_{12}$ is equal

to 10^{-4} cm/s. The frequency dependence of the nonlinear mobility $\mu_1(\omega)$ in the long-wave approximation is plotted in Fig. 2. In the short-wave approximation, we obtain

$$\mu_1(\omega) = -\mu_0\left(\frac{\omega_0\omega_\nu^3}{\nu\omega^4}\right).$$

Now, we analyze the dependence of the drift velocity on the polarization of the acoustic wave under the assumption that the frequency ω and the components of vector **k** in expressions (19)–(24) are related through the sound dispersion law: $\omega = sk$ ($k = |\mathbf{k}|$), where the velocity of sound s is different for longitudinal and transverse waves.

Since the acoustic wave propagates in the domain boundary plane, i.e., in the (XZ) plane, we assume that $\mathbf{k} = (k_x, 0, k_z) = k(\cos\varphi_s, 0, \sin\varphi_s)$. In this case, the possible polarizations of the acoustic wave are as follows.

(1) A transverse wave with the displacement vector perpendicular to the domain boundary plane. For this wave, $\mathbf{u} = u_0(0, 1, 0)$ and the drift velocity at a specified sound frequency can be written in the form

$$V_{dr} = \frac{R\rho}{2}\mu_1(\omega)(k_t u_0)^2 \sin 2\varphi_s, \qquad (25)$$

where $k_t = \omega/s_t$ and s_t is the velocity of transverse sound.

(2) A transverse wave with the displacement vector lying in the domain boundary plane for which $\mathbf{u} = u_0(-\sin\varphi_s, 0, \cos\varphi_s)$. According to relationship (19), the drift velocity is represented as

$$V_{dr} = -\frac{R\rho}{2}\mu_2(\omega)(k_t u_0)^2 \sin 4\varphi_s. \qquad (26)$$

(3) A longitudinal wave with $\mathbf{u} = u_0(\cos\varphi_s, 0, \sin\varphi_s)$. For this wave, the drift velocity is determined by the formula

$$V_{dr} = \frac{R\rho}{2}\mu_2(\omega)(k_l u_0)^2 \sin 4\varphi_s. \qquad (27)$$

Here, $k_l = \omega/s_l$ and s_l is the velocity of longitudinal sound.

It follows from relationships (25)–(27) that, in the case when the acoustic wave propagates parallel to the domain boundary plane, the domain boundary can drift in both longitudinal and transverse acoustic waves. If the acoustic wave travels perpendicularly to the domain boundary plane, as was shown earlier in [6], the drift occurs only at the transverse polarization of the acoustic wave. Since the drift velocity in formulas (25)–(27) is proportional to the product $R\rho$, these expressions describe not only the drift of a single domain boundary but also the drift of the strip domain structure as a whole.

REFERENCES

1. V. K. Vlasko-Vlasov and O. A. Tikhomirov, Fiz. Tverd. Tela (Leningrad) **32** (6), 1678 (1990) [Sov. Phys. Solid State **32**, 978 (1990)].
2. V. K. Vlasko-Vlasov and O. A. Tikhomirov, Fiz. Tverd. Tela (Leningrad) **33** (12), 3498 (1991) [Sov. Phys. Solid State **33**, 1964 (1991)].
3. Yu. I. Gorobets and S. I. Denisov, Ukr. Fiz. Zh. **35** (2), 271 (1990).
4. S. I. Denisov, Fiz. Tverd. Tela (Leningrad) **31** (11), 270 (1989) [Sov. Phys. Solid State **31**, 1992 (1989)].
5. V. S. Gerasimchuk and A. L. Sukstanskiĭ, Zh. Éksp. Teor. Fiz. **106** (4), 1146 (1994) [JETP **79**, 622 (1994)].
6. V. S. Gerasimchuk and A. A. Shitov, J. Phys.: Condens. Matter **12** (13), 3119 (2000).
7. B. A. Ivanov and A. L. Sukstanskiĭ, Zh. Éksp. Teor. Fiz. **84** (1), 370 (1983) [Sov. Phys. JETP **57**, 214 (1983)].
8. V. G. Bar'yakhtar, B. A. Ivanov, and A. L. Sukstanskiĭ, Zh. Éksp. Teor. Fiz. **78** (4), 1509 (1980) [Sov. Phys. JETP **51**, 757 (1980)].
9. V. S. Gerasimchuk and A. L. Sukstanskii, J. Magn. Magn. Mater. **146**, 232 (1995).
10. V. G. Bar'yakhtar, Yu. I. Gorobets, and S. I. Denisov, Zh. Éksp. Teor. Fiz. **98** (4), 1345 (1990) [Sov. Phys. JETP **71**, 751 (1990)].
11. V. S. Gerasimchuk and A. L. Sukstanskiĭ, Zh. Éksp. Teor. Fiz. **103** (1), 151 (1993) [JETP **76**, 82 (1993)].
12. S. Krupička, *Physik der Ferrite und der verwandten magnetischen Oxide* (Academia, Praha, 1973; Mir, Moscow, 1976).

Translated by O. Borovik-Romanova

Physics of the Solid State, Vol. 43, No. 10, 2001, pp. 1934–1940. Translated from Fizika Tverdogo Tela, Vol. 43, No. 10, 2001, pp. 1855–1863.

MAGNETISM AND FERROELECTRICITY

A Magnetic Resonance Study of $La_{1-x}Sr_xMnO_3$ Manganites

N. A. Viglin*, S. V. Naumov*, and Ya. M. Mukovskiĭ**

** Institute of Metal Physics, Ural Division, Russian Academy of Sciences, ul. S. Kovalevskoĭ 18, Yekaterinburg, 620219 Russia*

*** Moscow Institute of Steel and Alloys, Leninskiĭ pr. 4, Moscow, 117936 Russia*

e-mail: viglin@imp.uran.ru

Received February 13, 2001

Abstract—Single crystals of $La_{0.9}Sr_{0.1}MnO_3$ and $La_{0.8}Sr_{0.2}MnO_3$ manganites are examined using magnetic resonance in the temperature range 80–370 K. It is found that magnetostatic oscillations arise near the Curie temperature. The possible reasons for the appearance of additional lines in the ferromagnetic resonance (FMR) spectrum are considered, and the anisotropy field and the type of crystalline magnetic anisotropy in the $La_{0.8}Sr_{0.2}MnO_3$ compound are determined. It is shown that the crystalline magnetic anisotropy in the $La_{0.9}Sr_{0.1}MnO_3$ compound exhibits specific features associated with its type of crystal structure. © *2001 MAIK "Nauka/Interperiodica".*

1. INTRODUCTION

Lanthanum manganites have attracted the particular attention of researchers owing to the unusual effects revealed in these compounds. The considerable interest expressed in the study of manganite materials is a result of its offering ambiguous interpretation of the observed phenomena. In a number of publications, the unique magnetic and electrical properties of lanthanum manganites, in particular, the giant magnetoresistance effect, have been treated as a consequence of the so-called phase-separated state, when the spatially separated ferromagnetic and antiferromagnetic regions coexist in a material [1]. For example, this interpretation of the magnetic and electrical properties of manganite compounds was proposed by Wollan and Koehler [2], who carried out the low-temperature neutron diffraction investigation of the $La_{0.82}Ca_{0.18}MnO_3$ crystal and obtained neutron diffraction patterns in which a set of peaks corresponded to the antiferromagnetic and ferromagnetic ordering.

It is clear that a crystal becomes inhomogeneous when regions with magnetic and electrical properties differing from those of the crystal matrix are formed in the bulk of the crystal. In turn, this leads to an inhomogeneous magnetization of the sample in external constant and alternating magnetic fields. These magnetic inhomogeneities in manganites can be revealed by the ferromagnetic resonance (FMR) method, which is very sensitive to inhomogeneous magnetization of the studied samples. In this case, the FMR spectra contain distorted lines of uniform ferromagnetic resonance and additional lines.

As a rule, lanthanum manganites with a giant magnetoresistance can be obtained from the $LaMnO_3$ antiferromagnet with the Néel temperature $T_N = 141$ K [1]. This compound has an orthorhombic structure with the lattice parameters $a \approx 5.74$, $b \approx 7.66$, and $c \approx 5.53$ Å [3]. The substitution of Sr for approximately 18% La in a $LaMnO_3$ crystal leads to a structural transition from the orthorhombic to rhombohedral structure [1]. Furthermore, the $La_{1-x}Sr_xMnO_3$ compound undergoes several structural phase transitions with a change in the temperature [4]. In the $La_{0.8}Sr_{0.2}MnO_3$ crystal, the structural transition occurs at a temperature of the order of 100 K [1, 4]. In the $La_{0.9}Sr_{0.1}MnO_3$ manganite, two structural transitions are observed at approximately 100 and 300 K [5]. The magnetic structure of the $La_{1-x}Sr_xMnO_3$ compound also undergoes a transformation from the antiferromagnetic state at $x = 0$ to the ferromagnetic state with $T_C \approx 160$ K at $x = 0.1$ and $T_C \approx 300$ K at $x = 0.2$ [4].

The stoichiometric compound $LaMnO_3$ contains La^{3+} and Mn^{3+} ions. For Mn^{3+} ions ($3d^4$; spin $S = 2$; the ground state is the orbital doublet), the electron paramagnetic resonance (EPR) signal has a rather large linewidth ($\Delta H \sim 2.5$ kOe) [6]. In addition to the Mn^{3+} ions, lanthanum manganites doped with bivalent ions substituting for trivalent lanthanum contain Mn^{4+} ions. These ions can also be formed in the case of La^{3+} defects and the oxygen nonstoichiometry. In an octahedral crystal field, Mn^{4+} ions ($3d^3$, spin $S = 3/2$) reside in the ground state, which corresponds to the A_2 orbital singlet. As a consequence, the spin-lattice relaxation of the magnetic moments of these ions is weak and the EPR line is relatively narrow. However, when constructing a model of the paramagnetic centers responsible for the EPR signal in manganese perovskites, the strong exchange interaction between mixed-valence ions (Mn^{3+} and Mn^{4+}) in doped compounds should also be taken into account. These pairs of ions are traditionally described in terms

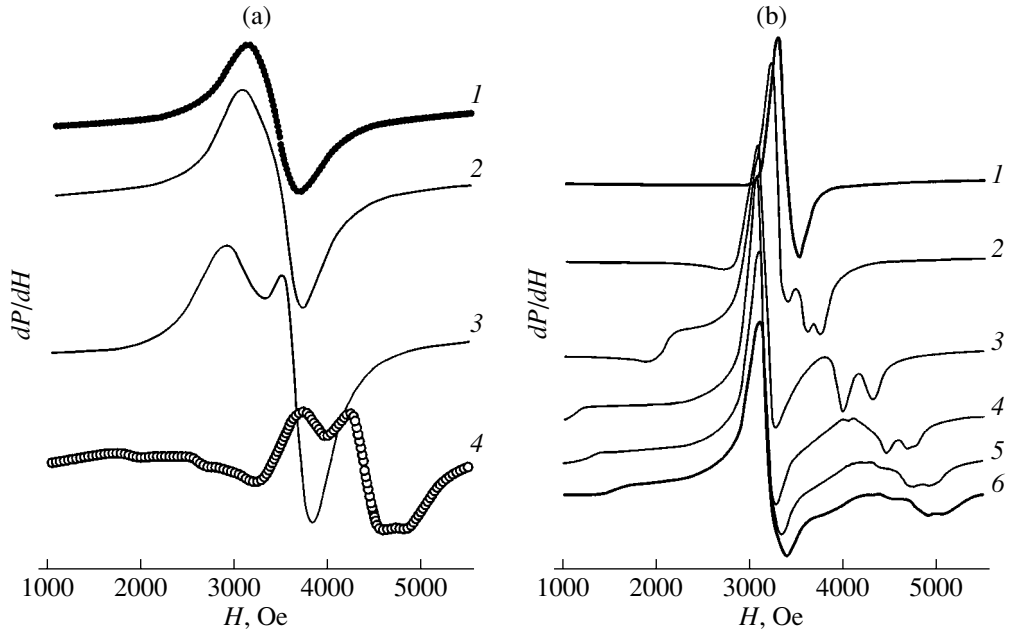

Fig. 1. Magnetic resonance spectra dP/dH of (a) $La_{0.9}Sr_{0.1}MnO_3$ and (b) $La_{0.8}Sr_{0.2}MnO_3$ at different temperatures: (a) (*1*) 180, (*2*) 170, (*3*) 160, and (*4*) 140 and (b) (*1*) 320, (*2*) 310, (*3*) 300, (*4*) 290, (*5*) 280, and (*6*) 270 K.

of the double exchange coupling model. Within this model, electron transfer between the nearest-neighbor Mn^{3+} and Mn^{4+} ions occurs through a Mn–O–Mn chain [7]. Therefore, the system under consideration consists of three components: the Mn^{4+} ion (s), the Mn^{3+} ion (σ), and (3) the lattice (L). In this system, the components are bound to each other through channels of relaxation. The relaxation rates can be designated as R_{sL}, $R_{\sigma L}$, $R_{\sigma s}$, and $R_{s\sigma}$. In the case when the rate R_{sL} of spin-lattice relaxation of Mn^{3+} ions is considerably less than the rate $R_{\delta s}$ (or $R_{s\sigma}$) of cross-relaxation between Mn^{4+} and Mn^{3+} ions and the direct spin-lattice relaxation of Mn^{4+} ions can be ignored (R_{sL}, $R_{\sigma L} \ll R_{\sigma s}$, $R_{s\sigma}$), there arises a "bottleneck" situation [7].

2. EXPERIMENTAL TECHNIQUE

The magnetic resonance measurements were performed on an ERS-231 standard spectrometer operating in the X band ($\nu \approx 9.4$ GHz). The spectrometer was equipped with a nitrogen-flow cryostat, which made it possible to change the temperature of samples in the range from 80 to 400 K. We studied samples of $La_{0.9}Sr_{0.1}MnO_3$ and $La_{0.8}Sr_{0.2}MnO_3$ monophase single crystals with Curie temperatures of the order of 150 and 300 K, respectively. It should be noted that the evolution of the magnetic resonance spectra is observed at higher temperatures. Specifically, the magnetic resonance spectra of $La_{0.9}Sr_{0.1}MnO_3$ samples (with the Curie temperature $T_C = 152$ K [5]) change starting from 170 K (Fig. 1). For $La_{0.8}Sr_{0.2}MnO_3$ samples ($T_C = 302$ K [8]), the spectra begin to change at 320 K. The reason for this difference will be discussed below.

In order to perform correct magnetic resonance measurements in the ferromagnetic range, we prepared spherical samples. The spherical shape of the samples prevented distortion in the FMR lines, which has usually been observed in samples of an arbitrary shape due to the shape anisotropy. For this purpose, cubes with an edge size of about 1 mm were produced from $La_{0.9}Sr_{0.1}MnO_3$ and $La_{0.8}Sr_{0.2}MnO_3$ single crystals with the use of diamond polishing pastes. Then, spheres were fabricated from the cubes through spinning. The spheres were polished using abrasive pastes with a sequentially decreasing grain size. The final polishing was performed on an abrasive with a grain size of less than 1 μm. The crystal axes in the samples were determined by x-ray diffraction analysis, after which the samples were cemented to a quartz fiber through the use of a special device in such a way that the c axis was directed along the fiber. In the experiments, the sample was rotated about the quartz fiber. The external magnetic field was aligned with the plane formed by the b and a axes.

3. RESULTS AND DISCUSSION

The magnetic resonance spectra dP/dH of the $La_{0.9}Sr_{0.1}MnO_3$ and $La_{0.8}Sr_{0.2}MnO_3$ spherical samples with a diameter of 0.7 mm are displayed in Figs. 1a and 1b, respectively. It can be seen that a decrease in the temperature leads to splitting of the magnetic resonance line into several components. The resonance fields of these signals change with a decrease in the temperature. The temperature at which the magnetic resonance spectra begin to change is slightly higher

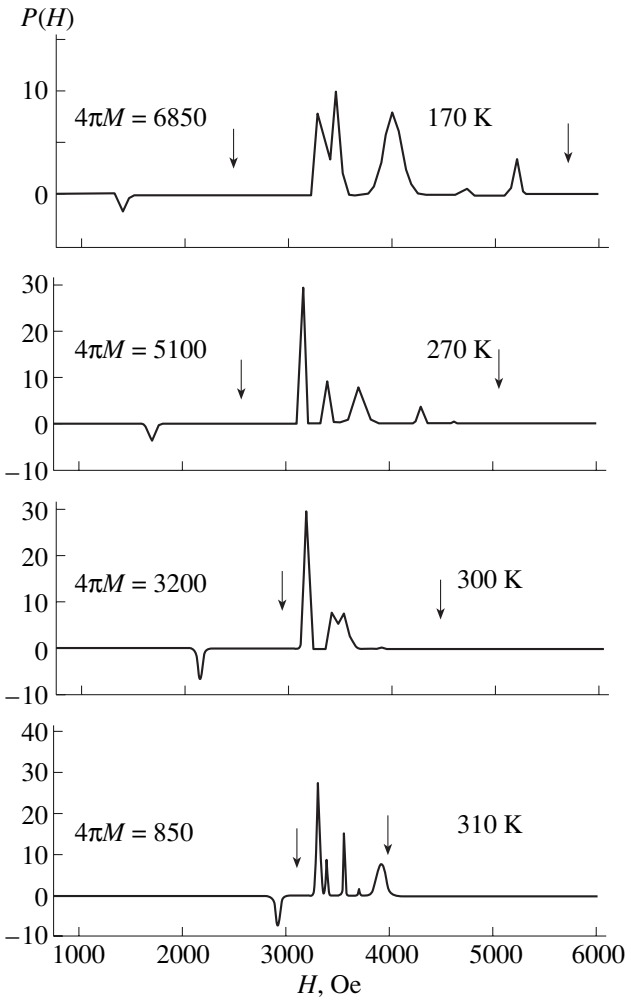

Fig. 2. Magnetic resonance spectra $P(H)$ of $La_{0.8}Sr_{0.2}MnO_3$ in the form of a sum of Gaussian functions with linewidths decreased by a factor of 10. The relative intensities of lines and the magnetic field scale are unchanged.

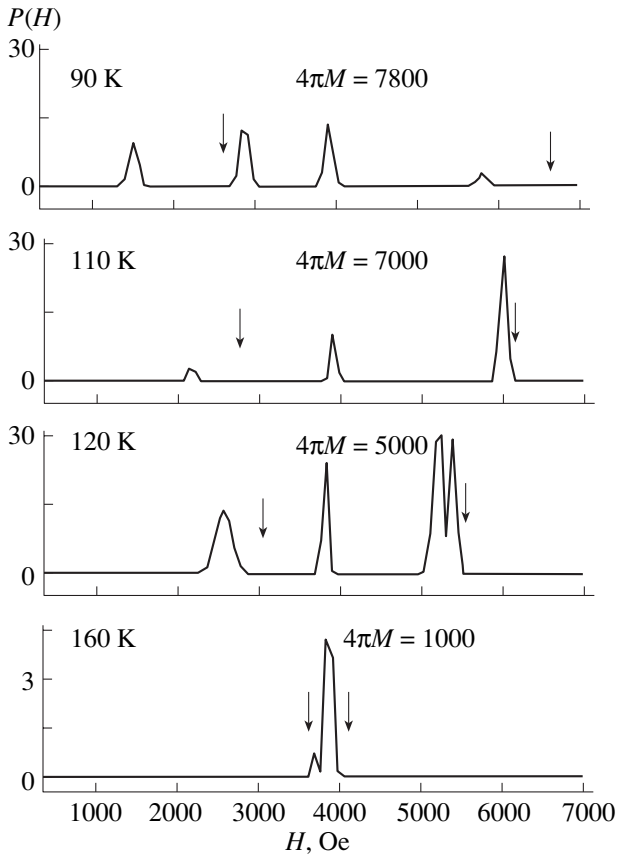

Fig. 3. Magnetic resonance spectra $P(H)$ of $La_{0.9}Sr_{0.1}MnO_3$ in the form of a sum of Gaussian functions with linewidths decreased by a factor of 10. The relative intensities of lines and the magnetic field scale are unchanged.

than the T_C point. The magnetic resonance spectra $P(H)$ of the $La_{0.8}Sr_{0.2}MnO_3$ and $La_{0.9}Sr_{0.1}MnO_3$ samples at different temperatures are depicted in Figs. 2 and 3, respectively. For clarity, all the peaks are represented by the Gaussian lines; the resonance fields are shown in actual scale, the relative intensities of signals are unchanged, and the linewidths are decreased by a factor of 10 in order to prevent the overlapping of lines. As is seen, all the additional peaks for the $La_{0.8}Sr_{0.2}MnO_3$ compound are located in the magnetostatic wave range, which is determined by the relationship $H_r - 2\pi M_0/3 < H < H_r + 4\pi M_0/3$ [9], where H_r is the resonant field of ferromagnetic resonance, H is the external magnetic field, and M_0 is the saturation magnetization. The magnetizations were calculated from the following expression for the antiresonance field [9]:

$$H_{AR} = \sqrt{H_r^2 + (2\pi M_0)^2} - 2\pi M_0. \qquad (1)$$

It is seen from Fig. 2 that, for the $La_{0.8}Sr_{0.2}MnO_3$ crystal, one of the lines in the low-field range has the opposite phase and can be interpreted as the antiresonance signal. The magnetizations calculated from expression (1) are in satisfactory agreement with those obtained in [8]. Therefore, it can be assumed that the magnetostatic oscillations manifest themselves in the magnetic resonance spectrum of the $La_{0.8}Sr_{0.2}MnO_3$ compound, which can involve the antiresonance signal in addition to the FMR signal.

The range of magnetostatic oscillations in the $La_{0.9}Sr_{0.1}MnO_3$ compound was estimated using the magnetization data taken from [10]. This range is indicated by the vertical arrows in Fig. 3. It can be seen that all the additional lines, except the line located at the lowest fields, fall in the magnetostatic wave range. The low-field signal outside the magnetostatic wave range is not an antiresonance signal, because its resonance field does not obey relationship (1) and the phase of this signal is identical to that of the other signals. For this reason, the nature of this signal remains unclear. All the other additional lines in the magnetic resonance spectra of the $La_{0.9}Sr_{0.1}MnO_3$ and $La_{0.8}Sr_{0.2}MnO_3$ samples can be attributed to magnetostatic oscillations.

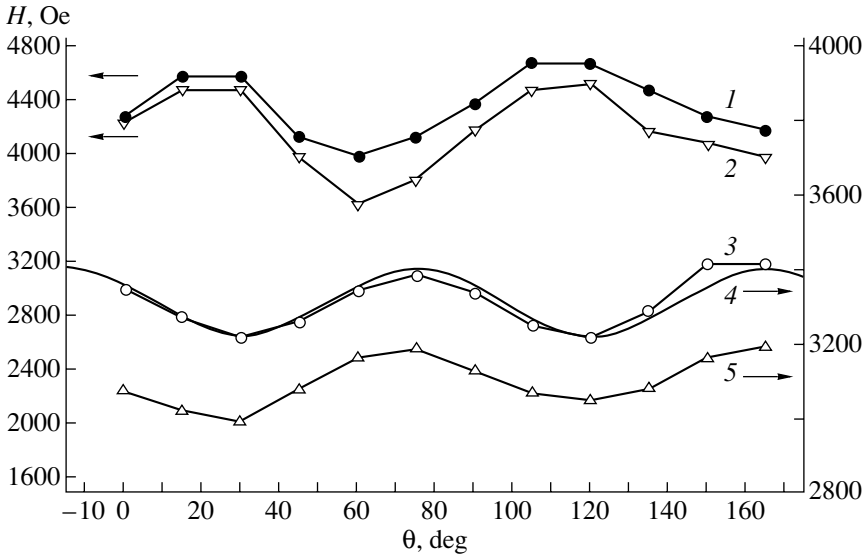

Fig. 4. Angular dependences of (*1*, *2*, *5*) the resonance fields of the additional lines and (*3*) the FMR field for $La_{0.8}Sr_{0.2}MnO_3$ at 270 K. (*4*) Angular dependence of the resonance field for a cubic crystal in an external magnetic field lying in the cube face plane according to the calculation from formula (2).

In uniform external static and microwave magnetic fields, magnetostatic oscillations in a spherical sample can be caused by the following factors [9]: (1) the deviation of the sample shape from spherical, the cleavages and roughness of the sample surface, the field distortion caused by the sample holder, and mechanical stresses; (2) crystalline anisotropy; and (3) magnetic or electric inhomogeneity of the crystal.

The factors associated with shape imperfection and mechanical stress, to some extent, occur in all cases; however, their effect can be reduced to a minimum through careful performance of the experiment. The magnetic or electric inhomogeneity in the bulk of the crystal and the crystalline anisotropy remain the most probable factors. Owing to the crystalline magnetic anisotropy, oscillations of different types (which are independent in the isotropic sample) become coupled. As will be shown below, the anisotropy in our samples is small and, hence, this factor is improbable [9].

The structural transitions in lanthanum manganites, depending on the degree of their doping with Sr ions, could be responsible for the magnetic inhomogeneity in the crystal due to nonuniform doping. However, these inhomogeneities were not revealed by the x-ray powder diffraction analysis. The structural inhomogeneity at the temperatures of structural transitions can give rise to magnetic inhomogeneity. However, these transitions for our samples occur in the temperature ranges below and above the temperature at which the magnetostatic oscillations arise (170 K for $x = 0.1$ and 320 K for $x = 0.2$). Consequently, these inhomogeneities do not cause magnetostatic oscillations.

For the $La_{1-x}Sr_xMnO_3$ compounds, the electrical conductivity and its type (semiconductor or metallic) strongly depend on the temperature and the degree of doping [4]. As a result of nonzero electrical conductivity, the amplitude and phase of the microwave magnetic field in the sample become dependent on the coordinate. In turn, this leads to inhomogeneous magnetization of the sample and can be responsible for the additional broadening of the FMR line and the excitation of spin waves [9]. The inhomogeneous broadening of the FMR line becomes dependent on the ratio between the sample size d and the depth δ of field penetration into the sample. The contribution to the linewidth is maximum when the parameters d and δ are of the same order of magnitude and decreases at $d \ll \delta$ or $d \gg \delta$ [11]. The skin depth can be estimated using the data on electrical conductivity taken from [4] for the $La_{1-x}Sr_xMnO_3$ compounds at $x = 0.1$ and 0.2 according to the expression $\delta(\rho/\mu_0\omega)^{0.5}$ (where ρ is the resistivity, $\mu_0 = 4\pi \times 10^7$ V s/A m, and $\omega = 2\pi \times 9 \times 10^9$ Hz) [6]. The resistivity of the sample with $x = 0.1$ at 170 K is estimated as $\rho \approx 20\ \Omega$ cm; hence, we obtain $\delta \approx 1.7$ mm, which is larger (even though of the same order of magnitude) than the size of the sample with diameter $d = 0.7$ mm. The resistivity of the sample with $x = 0.2$ at 300 K ($\rho \approx 5 \times 10^{-4}\ \Omega$ cm) is substantially less, and, correspondingly, the skin depth ($\delta \approx 0.008$ mm) is appreciably smaller than the sample size. Therefore, the contribution to the linewidth of the FMR signal at temperatures near T_C for spherical samples 0.7 mm in diameter at $x = 0.1$ should be larger than that at $x = 0.2$.

Thus, the electrical conductivity of the materials under investigation results in the inhomogeneous magnetization of spherical samples in the microwave magnetic field and can bring about the excitation of magnetostatic oscillations. At the same time, the inhomogeneous magnetization and the excitation of

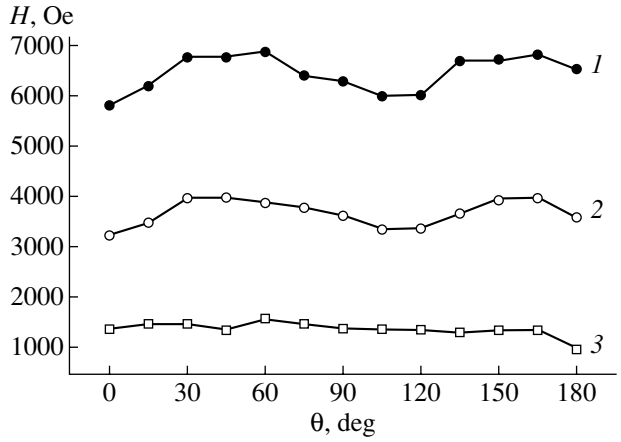

Fig. 5. Angular dependences of (*1*, *3*) the resonance fields of the additional lines and (*2*) the FMR field for $La_{0.9}Sr_{0.1}MnO_3$ at 80 K.

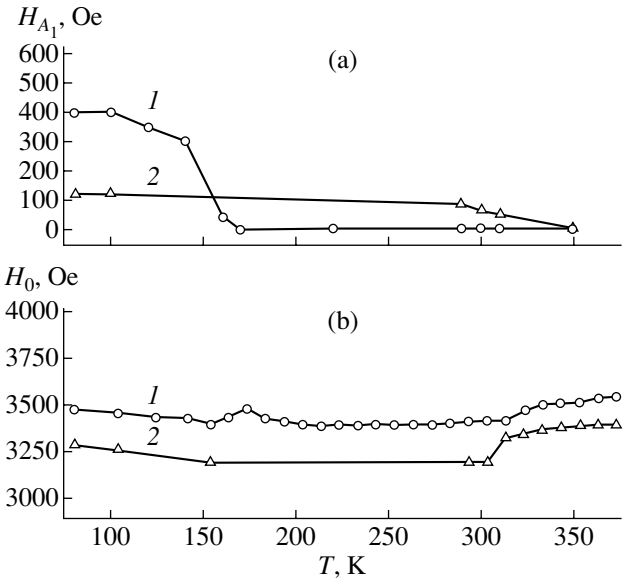

Fig. 6. Temperature dependences of (a) the anisotropy and (b) FMR fields for (*1*) $La_{0.9}Sr_{0.1}MnO_3$ and (*2*) $La_{0.8}Sr_{0.2}MnO_3$ samples.

magnetostatic waves can be associated with the occurrence of randomly arranged regions (magnetic polarons), whose magnetization differs from that of the matrix. It seems likely that both factors take place. This can be judged from the angular dependence of the resonance fields assigned to the additional lines (Figs. 4, 5). The resonance field anisotropy for different additional lines can either coincide with the FMR anisotropy or differ from it considerably. As is known, in the presence of the crystalline magnetic anisotropy, the dependences of the resonance fields of the FMR signals and the lines attributed to magnetostatic oscillations on the angle between the magnetic field direction and the crystallographic axes are identical [9]. It can be assumed that the inhomogeneous magnetization due to the electrical conductivity and the microwave field penetration (decreasing with an increase in the depth) into the sample retains a spherical symmetry about a constant magnetic field. Apparently, the anisotropy of magnetostatic oscillations excited by inhomogeneities of this type is identical in character to that associated with the crystalline magnetic anisotropy. The inhomogeneous magnetization caused by randomly arranged regions, with the magnetization differing from that of the crystal matrix, leads to the excitation of magnetostatic waves whose anisotropy does not coincide with the crystalline magnetic anisotropy of the matrix. In general, the same effect can stem from the domain structure and the twinning observed in lanthanum manganite crystals [12]. However, the appearance of a number of additional lines at temperatures higher than the Curie point suggests that their nature can be associated with magnetic polarons, which are formed at temperatures somewhat higher than the T_C point.

Let us consider the crystalline magnetic anisotropy of the resonance field in the studied samples. First and foremost, we should note that the $La_{0.9}Sr_{0.1}MnO_3$ and $La_{0.8}Sr_{0.2}MnO_3$ samples in the temperature range from 100 to 340 K have different crystal structures: the crystal containing 10% Sr has an orthorhombic structure and the crystal with 20% Sr has a rhombohedral structure [12]. It is known that the rhombohedral lattice in which the angle between the axes is equal to 60° (in the $La_{0.8}Sr_{0.2}MnO_3$ crystal, the angle between the rhombohedral lattice axes is close to 60°) is characterized by cubic close packing [13]. Therefore, the crystal lattice of this sample, to a good approximation, can be treated as a cubic lattice. (The temperature of the structural transition in this compound is below 100 K.) Figure 4 shows the angular dependence of the resonance field for the $La_{0.8}Sr_{0.2}MnO_3$ crystal at 270 K in a magnetic field aligned with the plane passing through the *a* and *b* axes. It can be seen from Fig. 4 that the crystalline magnetic anisotropy of the studied crystal has a period of 90° and is qualitatively similar to the anisotropy of the cubic crystal in the case when the external magnetic field is aligned with the plane of the cube face. The FMR and anisotropy fields can be calculated according to the expression for the FMR frequency in a cubic crystal [9], that is,

$$\frac{w}{\gamma} = \sqrt{[H + H_{A_1}(1 + \cos^2 2\theta)]} \times \sqrt{[H + H_{A_1}(2 - 4\sin^2 2\theta)]}, \quad (2)$$

where ω is the resonance frequency, γ is the gyromagnetic ratio of an electron, H is the external magnetic field, H_{A_1} is the anisotropy field, and θ is the angle between the direction of the magnetic field aligned with the plane of the cubic crystal face and the crystal edge. In order to estimate the anisotropy field H_{A_1}, the depen-

dences of the resonance magnetic field on the frequency, the anisotropy field, and the θ angle (solid line in Fig. 4) were calculated from this formula. Then, the calculated and experimental dependences were compared and the fields H_{A_1} and $H_r = \omega/\breve{a}$ were determined as the fitting parameters. The temperature dependence thus obtained, $H_{A_1}(T)$, is plotted in Fig. 6a. The temperature dependence of the FMR field with due regard for the anisotropy below the T_C temperature is displayed in Fig. 6b.

A different situation is observed for the $La_{0.9}Sr_{0.1}MnO_3$ sample, because this crystal has an orthorhombic structure. In this case, the angles between the *a* and *b* axes are close to 90° but the *b* axis is longer than the two other axes (*a* and *c*), which are approximately equal to each other. Apparently, the crystalline magnetic anisotropy in this crystal upon its rotation in the (001) plane exhibits extrema not only at 90° intervals but also at intermediate angles. As is seen from Fig. 5, the minima of the resonance field are observed at approximately 110° intervals. In an orthorhombic crystal with the lattice parameters $a = 5.59$, $b = 7.72$, and $c = 5.54$ Å [5], this angle is formed at the intersection of the (120) and $(\hat{1}20)$ planes. It is evident that, in this case, the calculation according to formula (2) is incorrect; however, the anisotropy field H_{A_1} can be roughly estimated. As follows from formula (2) at $H_{A_1} \ll H_r$, the anisotropy field is estimated as $H_{A_1} \approx (H_r^{\max} - H_r^{\min})/1.5$. The estimates obtained are shown in Fig. 6.

Figure 7 displays the temperature dependence of the EPR linewidth ΔH for the $La_{0.9}Sr_{0.1}MnO_3$ sample in a magnetic field aligned along the *b* axis. It is worth noting that, for both the EPR linewidth and the resonance field, a small anisotropy (of the order of 50 Oe), which decreases with an increase in the temperature, is observed in the *ab* plane of the crystal. A similar anisotropic behavior of the EPR linewidth was observed earlier in [6] for a crystal with 5% Sr. Moreover, as the temperature increased, the EPR linewidth ceased to increase at the same temperature at which the relative anisotropy in this crystal began to decrease. In the $La_{0.9}Sr_{0.1}MnO_3$ sample, as was shown in [5], the unit cell volume increases linearly with an increase in the temperature from 170 to 300 K, whereas the structure remains orthorhombic. The structural transition is observed above 300 K, which is accompanied by a considerable change in the lattice parameters. It can be seen from Fig. 7 that the EPR linewidth ΔH linearly increases in the temperature range from 170 to 300 K. Above 300 K, the linewidth remains constant (ΔH = 830 Oe). The resonance field in the temperature range 170–300 K does not change and corresponds to the factor $g = 1.997$. At temperatures higher than 300 K, the *g* factor slightly decreases and becomes equal to 1.896.

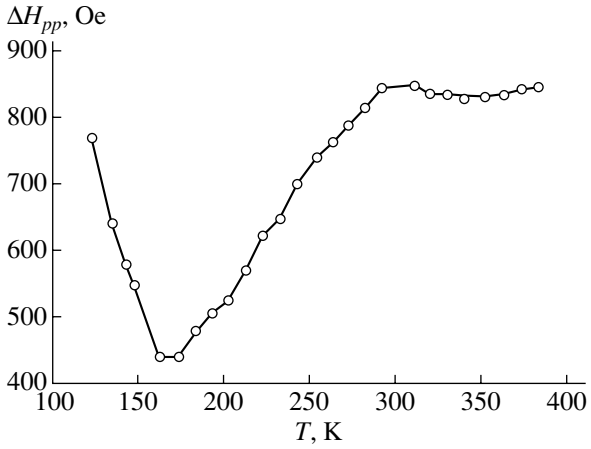

Fig. 7. Temperature dependence of the EPR linewidth for $La_{0.9}Sr_{0.1}MnO_3$.

The anisotropy of the linewidth ΔH in the paramagnetic range can be explained in terms of the contribution of the Dzyaloshinski–Moriya antisymmetric interaction between heterovalent manganese ions [6]. A linear increase in the EPR linewidth ΔH with an increase in the temperature from 170 to 300 K and cessation of this increase at 300 K can be due to the bottleneck situation in the $La_{0.9}Sr_{0.1}MnO_3$ compound. This situation arises if the spin-lattice relaxation rates R_{sL} and $R_{\sigma L}$ of Mn^{4+} and Mn^{3+} ions are considerably less than the cross-relaxation rates $R_{\sigma s}$ and $R_{s\sigma}$. In this case, as the temperature increases, the linewidth increases and reaches saturation when the temperature-dependent spin-lattice relaxation rate becomes approximately equal to the cross-relaxation rate, which is weakly dependent on temperature, i.e., when $R_{\sigma L} \approx R_{s\sigma}$. Most likely, this situation takes place. The EPR linewidth for the $La_{0.8}Sr_{0.2}MnO_3$ sample increases linearly with an increase in the temperature to 400 K. The line itself has a distorted shape, which is characteristic of conducting materials due to the contribution from the dispersion signal to the absorption signal (Fig. 1b).

4. CONCLUSION

Thus, it was demonstrated that the inhomogeneous magnetization arises in lanthanum manganites doped with Sr ions (from 10 to 20%). In particular, this leads to the appearance of additional lines in the FMR spectra. Most likely, the additional lines are associated with the excitation of magnetostatic oscillations. It can also be assumed that magnetic polarons make a certain contribution to the magnetic inhomogeneity of the samples, because a number of additional lines appear at temperatures above the Curie point. In this case, the anisotropy of resonance fields of these lines considerably differs from that of the FMR field.

The magnetic anisotropy in the $La_{0.8}Sr_{0.2}MnO_3$ sample is similar to cubic anisotropy with a low anisotropy

field $H_{A_1} \approx 100$ Oe, which is approximately constant in the temperature range from 80 to 300 K. The angular dependence of the resonance field H_r for the $La_{0.9}Sr_{0.1}MnO_3$ sample exhibits minima at 110° intervals rather than at the expected 90° intervals, which correspond to the directions of the crystal axes. It seems likely that this character of the anisotropy is associated with the specific location of the {120} planes in the orthorhombic $La_{0.9}Sr_{0.1}MnO_3$ crystal.

ACKNOWLEDGMENTS

This work was supported by the International Association of Assistance for the promotion of co-operation with scientists from the New Independent States of the former Soviet Union (project no. 30253) and the Ministry of Science and Technology of the Russian Federation (project no. 5, agreement no. 2.4.99).

REFERENCES

1. É. L. Nagaev, Usp. Fiz. Nauk **166** (8), 833 (1996) [Phys. Usp. **39**, 781 (1996)].
2. E. O. Wollan and W. C. Koehler, Phys. Rev. **100**, 545 (1955).
3. W. E. Pickett and D. J. Singh, Phys. Rev. B **53** (3), 1146 (1996).
4. A. A. Mukhin, V. Yu. Ivanov, V. D. Travkin, *et al.*, Pis'ma Zh. Éksp. Teor. Fiz. **68** (4), 331 (1998) [JETP Lett. **68**, 356 (1998)].
5. V. S. Gaviko, V. E. Arkhipov, A. V. Korolev, *et al.*, Fiz. Tverd. Tela (St. Petersburg) **41** (6), 1064 (1999) [Phys. Solid State **41**, 969 (1999)].
6. V. A. Ivanshin, J. Deisenhofer, H.-A. Krug von Nidda, *et al.*, Phys. Rev. B **61**, 6213 (2000).
7. A. Shengelaya, Guo-meng Zhao, H. Keller, and K. A. Müller, Phys. Rev. Lett. **77**, 5296 (1996); A. Shengelaya, Guo-meng Zhao, H. Keller, *et al.*, Phys. Rev. B **61**, 5888 (2000).
8. S. E. Lofland, S. M. Bhagat, K. Ghosh, *et al.*, Phys. Rev. B **56**, 13705 (1997).
9. A. G. Gurevich and G. A. Melkov, *Magnetic Oscillations and Waves* (Nauka, Moscow, 1994).
10. A. V. Korolyov, V. Ye. Arhipov, V. S. Gaviko, *et al.*, J. Magn. Magn. Mater. **213**, 63 (2000).
11. N. A. Viglin, A. A. Samokhvalov, N. M. Chebotaev, and B. A. Gizhevskiĭ, Fiz. Tverd. Tela (Leningrad) **30**, 1814 (1988) [Sov. Phys. Solid State **30**, 1042 (1988)].
12. F. Moussa, M. Hennion, J. Rodríguez-Carvajal, and H. Moadden, Phys. Rev. B **54**, 15149 (1996).
13. B. F. Ormont, *Introduction to Physical Chemistry and Crystal Chemistry of Semiconductors* (Vysshaya Shkola, Moscow, 1968).

Translated by O. Borovik-Romanova

Physics of the Solid State, Vol. 43, No. 10, 2001, pp. 1941–1947. Translated from Fizika Tverdogo Tela, Vol. 43, No. 10, 2001, pp. 1864–1870.

MAGNETISM AND FERROELECTRICITY

Growth of Nanosized MnAs/Si(111) Magnetoelectronic Heterostructures and Their Magnetooptical Study

A. G. Banshchikov*, A. V. Kimel'*, R. V. Pisarev*, A. A. Rzhevskiĭ*, N. S. Sokolov*, A. Keen, Th. Rasing**, Ahsan M. Nazmul***, and M. Tanaka*****

**Ioffe Physicotechnical Institute, Russian Academy of Sciences, ul. Politekhnicheskaya 26, St. Petersburg, 194021 Russia*
e-mail: rzhev@pop.ioffe.rssi.ru
***Research Institute for Materials, University of Nijmegen, 6525 ED Nijmegen, The Netherlands*
****The University of Tokyo, Bunkyo-ku, Tokyo 113-8654, Japan*
Received March 20, 2001

Abstract—Thin (6–12 nm) epitaxial MnAs films were MBE-grown on Si(111) substrates under different technological conditions. The films feature essentially different surface morphology. This manifests itself in the formation, on the silicon surface, of hexagonal-shaped crystallites, whose dimensions vary depending on the growth conditions. The volume and surface magnetic properties of the films were studied using the magnetooptical Kerr effect and optical second harmonic generation. The Kerr effect was found to scale linearly with the effective thickness of the magnetic layer. The thickness of the magnetically disordered transition layer formed near the interface with the substrate was estimated. The surface and volume hysteresis properties of the films were found to be different. A contribution to the second-harmonic intensity was observed which is an odd function of magnetization. This effect originates from the interference of the magnetic and nonmagnetic contributions to the nonlinear polarization. © *2001 MAIK "Nauka/Interperiodica".*

1. INTRODUCTION

Hybrid heterostructures produced by growing ferromagnetic films on the surface of semiconductors have recently become a subject of considerable interest. Such materials are expected to form the basis of a new generation of magnetoelectronic devices combining semiconducting and magnetic properties [1, 2].

Due to the clearly pronounced ferromagnetic properties of the manganese arsenide, MnAs films grown on semiconducting substrates of GaAs or Si are presently considered to be a most promising material for magnetoelectronic applications [3]. The investigation of thin MnAs films is attracting intense interest. This is associated with the possibility of realization of new, spin-dependent transport and magnetooptical phenomena near the magnet–semiconductor interface. At the same time, despite the noticeable progress in the growth technology of thin MnAs epitaxial films on semiconductors attained in recent years [4–6], the influence of technological conditions on the processes that occur in the initial stage of magnetic-layer formation and determine the structural and magnetic quality of films near the interface with the substrate remains unclear.

This paper reports on the process of growth, surface morphology, structural perfection, and magnetic properties of thin (6–12 nm) MnAs/Si(111) epitaxial films. The growth process, structural quality, and surface morphology of the films were studied using RHEED, x-ray diffraction, and atomic-force microscopy. The magnetic properties of films were measured using the magnetooptical Kerr effect (MOKE). Because the MOKE develops within a region with a thickness of the order of the light penetration depth, this technique permits one to probe the magnetic properties of films in the bulk of a material. However, despite the high sensitivity of this method, the information obtained is of an integrated character and the spatial resolution it provides is not adequate for investigation of the magnetic state directly near the surface or the interface with the substrate. At the same time, it is known that the method based on the measurement of the intensity of the second harmonic generation (SHG) is sensitive to the presence of surfaces or interfaces [7]. SHG arises in centrosymmetric media, because the space-inversion symmetry is broken at an interface, and it permits one to probe interface-adjoining regions of the order of a few atomic layers thick. In order to investigate the magnetic properties of films near an interface, this work made use, in addition to the traditional magnetooptical MOKE, the SHG in an external magnetic field. The magnetically induced SHG has recently been successfully employed in investigating boundary properties of comparatively thick (40–70 nm) MnAs films on Si(111) [8].

2. GROWTH, STRUCTURE, AND MORPHOLOGY OF MnAs/Si(111) SAMPLES

The MnAs films were grown on Si(111) substrates in an ultrahigh-vacuum chamber (ULVAC MBC-508) by molecular beam epitaxy. We used Si(111) substrates with a misorientation of about 1.5°. To obtain an atom-

Parameters of MnAs/Si(111) heterostructures

Samples	Substrate temperature, °C	As_4/Mn flux ratio	Average film thickness, nm	Crystallite height, nm	Ratio of transverse dimensions to height for crystallites
A	350	1.2	6	7	(–)
B	350	2.0	12	100	1.7 : 1
C	350	5.4	12	20	1 : 1
D	400	1.2	10	50	6 : 1
E	450	1.2	6	30	5 : 1
G	350	2.0	12	100	2 : 1
H	450	2.0	12	100	6 : 1

ically clean silicon surface, the substrates were chemically treated, after which they were placed in a growth chamber and annealed at 900°C under an As_4 beam for a few minutes. The growth started when the Mn beam was admitted into the chamber. To study the effect of growth conditions on the magnetic-layer perfection, the films were prepared at various substrate temperatures and various intensities of the As_4 and Mn beams. The average film thickness was derived from the amount of material deposited on the substrate. The parameters of the films used in the study are listed in the table. The film quality was monitored *in situ* using RHEED with 20-keV electrons. RHEED images showed that a uniform smooth MnAs layer with a (2×2) superstructure formed only in sample A. The other samples exhibited island-type growth of the MnAs layer.

The surface morphology of the samples obtained was investigated with a Digital Instruments atomic-force microscope. The samples featured essentially different morphology. Figure 1 displays the surface topography of three different samples. In sample A (Fig. 1a), the deposited material is distributed uniformly over the substrate surface to form a practically smooth surface with nonuniformities on the scale of a few nanometers. The silicon surface of samples D and B (Figs. 1b, 1c) reveals crystallite growth. The shape of the crystallites, as projected on the substrate plane, is a hexagon, which is characteristic of the 6/*mmm* hexagonal structure of MnAs. The crystallites vary markedly in size depending on the actual growth conditions. The table contains data on the height and transverse dimensions of the crystallites in various samples.

The structural perfection of the films prepared was studied using x-ray diffraction in $\vartheta - 2\vartheta$ geometry. The diffraction measurements showed the growth to be epitaxial. In addition to strong silicon peaks, the x-ray diffraction patterns show distinct peaks due to the (0001)-, (0002)-, and (0004)-type planes of the MnAs hexagonal structure (Fig. 2). The growth plane is the (0001) face.

3. MAGNETOOPTICAL STUDY

The MOKE and SHG studies were conducted in reflected light according to the technique described in [8]. The SHG measurements were performed in meridional geometry; the MOKE studies, in meridional and polar geometries [9]. We used a femtosecond Ti–sapphire laser ($\lambda = 0.8$ μm) with a pulse duration of 100 fs and repetition frequency of 82 MHz and a CW helium–neon laser ($\lambda = 0.633$ μm). The rotation of the plane of light polarization in the MOKE studies was measured with a sensitivity of 10″. Because MnAs has a comparatively low Curie temperature ($T_C = 318$ K [10]), the average power incident on a sample was limited to 15 mW in order to prevent possible sample heating. Investigation of the azimuthal dependences of the MOKE and SHG was made possible through providing for possible rotation of the samples within the azimuthal angle range $0° < \theta < 360°$. A magnetic field H of up to ±1.5 kOe was applied to the samples.

Figure 3 shows field dependences of the meridional MOKE measured on films A and B at a wavelength $\lambda = 0.633$ μm incident on a sample at an angle $\varphi = 15°$. The hysteresis loops are symmetrical and have a shape typical of ferromagnetic samples. The azimuthal dependences of the meridional MOKE do not exhibit substantial anisotropy. The MOKE field dependences measured in polar geometry in the magnetic-field range from –1.5 to +1.5 kOe, showing an absence of saturation, with the polar effect in various films being about an order of magnitude smaller than the meridional effect. This implies the presence of a hard magnetization axis perpendicular to the surface.

Figures 4a and 4b plot the meridional MOKE and the coercive field versus the average film thickness. As follows from Fig. 4a, the MOKE increases with increasing average thickness of the films. The experimental points can be fitted to a linear dependence. A comparison of the measurements shown in Fig. 4b and the data listed in the table and displayed in Fig. 2 reveals that the coercive fields are the highest in the films with larger crystallites.

Figure 5 presents azimuthal dependences of the SHG intensity in film G measured in meridional geom-

etry at $\lambda = 0.8$ μm with light incident at $\varphi = 15°$. The measurements were carried out for four combinations of the entrance–exit polarizations of the linearly polarized light, namely, PP, PS, SP, and SS. The azimuthal dependences of the second-harmonic intensity for the PP and SP polarization combinations can be presented in the form

$$I(2\omega, \theta) = (a\cos 3\theta + b\cos\theta + c)^2, \quad (1a)$$

and for the PS and SS combinations, they can be presented as

$$I(2\omega, \theta) = (a\sin 3\theta + b\sin\theta + c)^2, \quad (1b)$$

where *a*, *b*, and *c* are fitting coefficients. The SHG azimuthal dependences measured on other samples are qualitatively similar. Samples C and G exhibited a noticeable, while small, change in the SHG intensity under magnetization reversal for the PS and SS polarization combinations. The magnetic contrast of the SHG in samples C and G measured for the PS combination of polarizations was 3–5%, which is substantially less than that observed in thicker films studied earlier [8]. In the other samples, the magnetic contrast did not exceed 2%. Figures 6a and 6b present field dependences of the magnetically induced SHG and meridional MOKE measured at one of the maxima in the azimuthal dependences obtained for the C and G samples. The hysteresis loops obtained for the SHG are seen to be more narrow than those obtained for the MOKE. This point was also mentioned in [8].

4. DISCUSSION OF RESULTS

The studies of the field dependences of the meridional and polar MOKE indicate that the films exhibit easy-plane anisotropy. At the same time, the dependences of the magnitude of the MOKE (Fig. 4a) and of the coercive field (Fig. 4b) on the average thickness suggest that these films differ in their volume magnetic properties.

The dependence of the magnitude of the MOKE on the average thickness (Fig. 4a) can be accounted for by assuming the effective thickness of the magnetic layer in different films to be different and to depend on the thickness of the transition layer. This layer forms in the initial stage of growth in close vicinity to the interface and has neither a structural nor magnetic order. The existence of a transition layer in the structures under study is indicated by the fact that the straight line in Fig. 4a crosses the horizontal axis not at the origin but near the point of 2 nm. To check this assumption, the data of Fig. 4a were replotted into coordinates where the ordinate was the magnitude of the MOKE and the abscissa was the parameter ξ determining the effective thickness of the magnetic layer. The parameter ξ was derived from x-ray measurements as the ratio of the total intensity of the diffraction peaks from the (0001)-, (0002)-, and (0004)-type planes in the MnAs hexagonal structure to that of the peaks due to the (111) and (222) planes of the silicon substrate. The results, displayed in Fig. 7, show the experimental points to fall on a straight line passing through the origin. This result supports the conjecture of the existence of a transition layer about 2 nm thick in the structures under study.

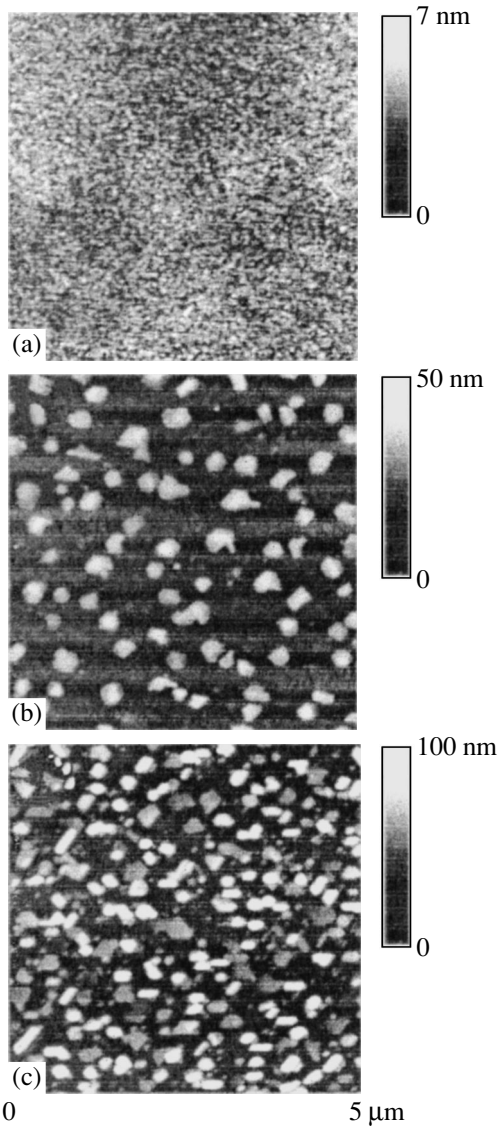

Fig. 1. Surface topography of the structures under study obtained by atomic-force microscopy; (a) film A, (b) film D, and (c) film B.

In the limit of small thickness, the dependence of the magnitude of the MOKE on the film thickness at small incidence angles can be written as [11]

$$\pm\phi_k + i\varepsilon_k = (2\omega/c)[N_s/(1 - N_s^2)]Q\varphi h, \quad (2)$$

where ϕ is the rotation of the polarization plane; ε is the ellipticity; Q is the magnetooptical parameter of the medium, which is proportional to the magnetization;

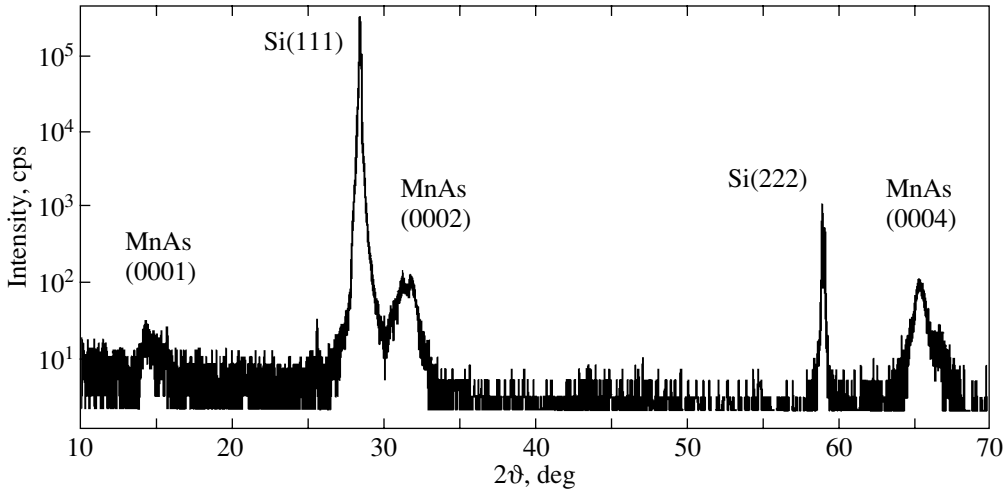

Fig. 2. X-ray diffraction pattern of film D.

N_s is the refractive index of the substrate; and φ is the angle of incidence of light on the sample. As follows from Eq. (2), the magnitude of the Kerr effect is proportional to the thickness and does not depend on the film refractive index. Thus, the linear growth in Fig. 7 reflects a general characteristic feature of the MOKE in thin magnetic films.

The broad spread of coercive fields observed in the experiment (Fig. 4b) can be explained if one assumes that the MnAs crystallites are so small as to make the domain formation in them energetically unfavorable. In this case, sample magnetization reversal can proceed through the hard process of uniform rotation of the magnetization. Because the samples were shown to have easy-plane anisotropy and the magnetic crystallographic anisotropy energy in the hexagonal plane of a film can be neglected, the coercive fields can be due to the shape anisotropy of the crystallites.

To establish the nature of the anisotropy and of the sources of the magnetically induced SHG, we consider the possible mechanisms of SHG in the structures under study. The expression for the double-frequency nonlinear polarization induced by the electric field **E** of

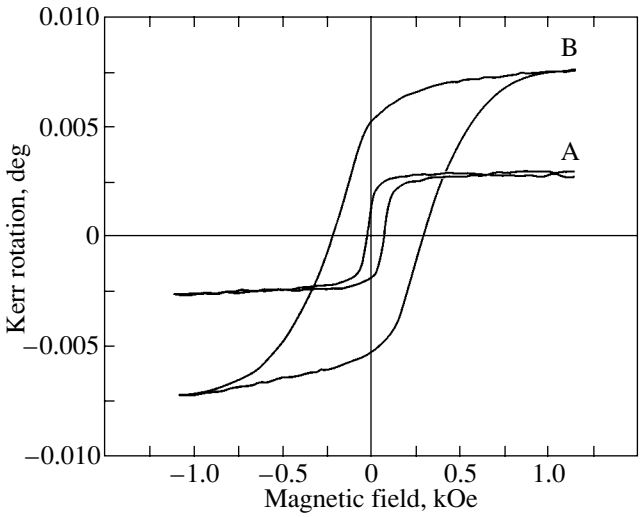

Fig. 3. Field dependences of the meridional MOKE measured at λ = 0.63 μm for φ = 15° in films A and B.

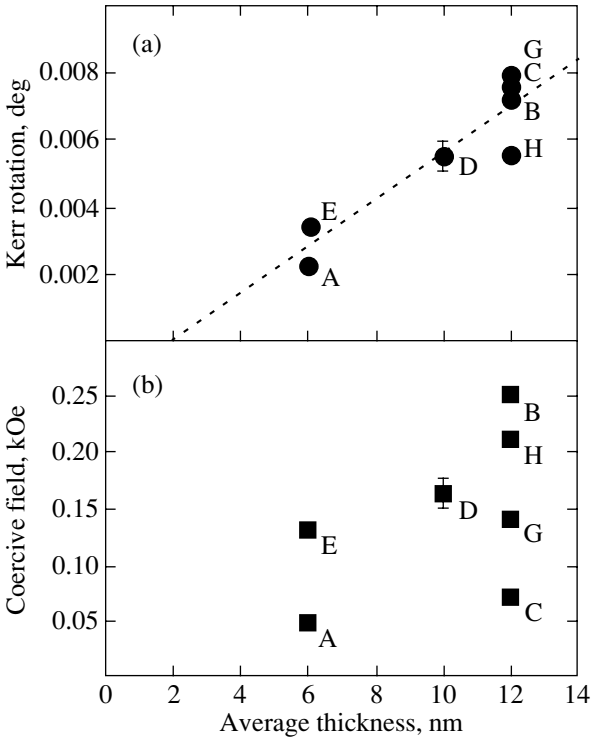

Fig. 4. (a) MOKE and (b) coercive field versus average film thickness measured at λ = 0.63 μm for φ = 15°.

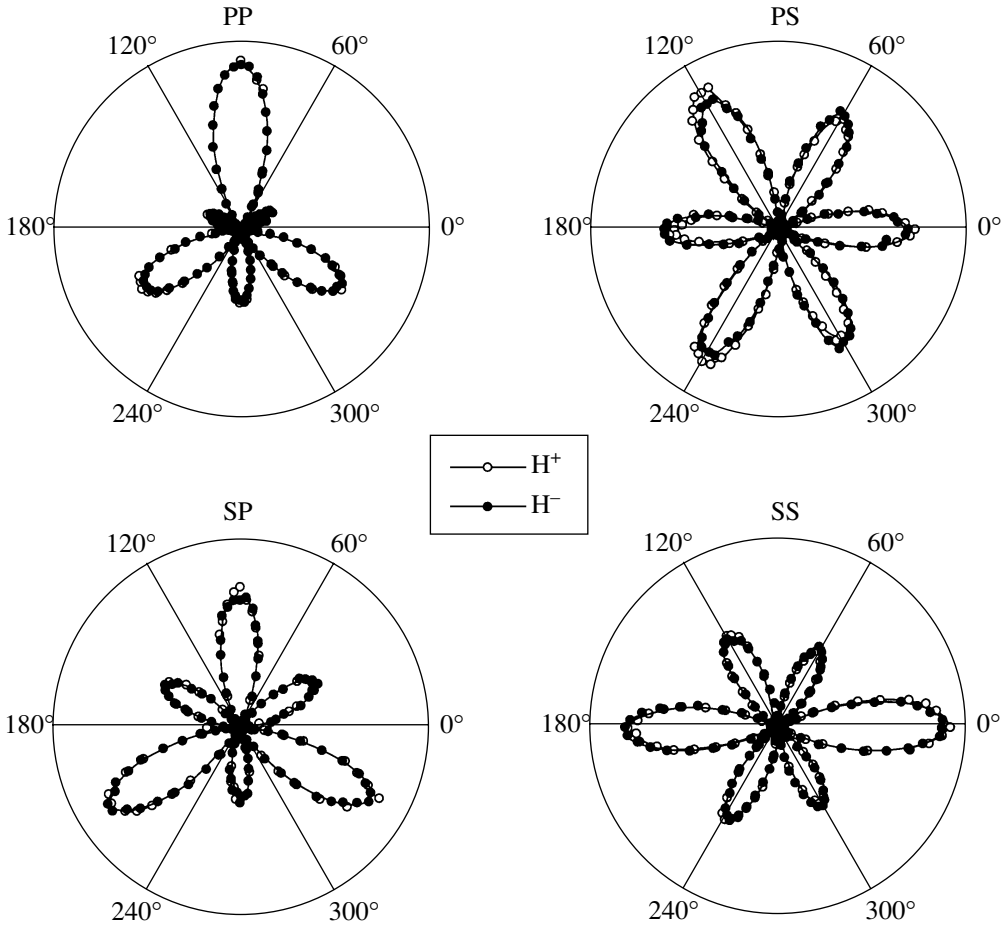

Fig. 5. SHG azimuthal dependences measured in film G for different entrance–exit light polarization combinations at $\lambda = 0.8$ μm for $\varphi = 15°$.

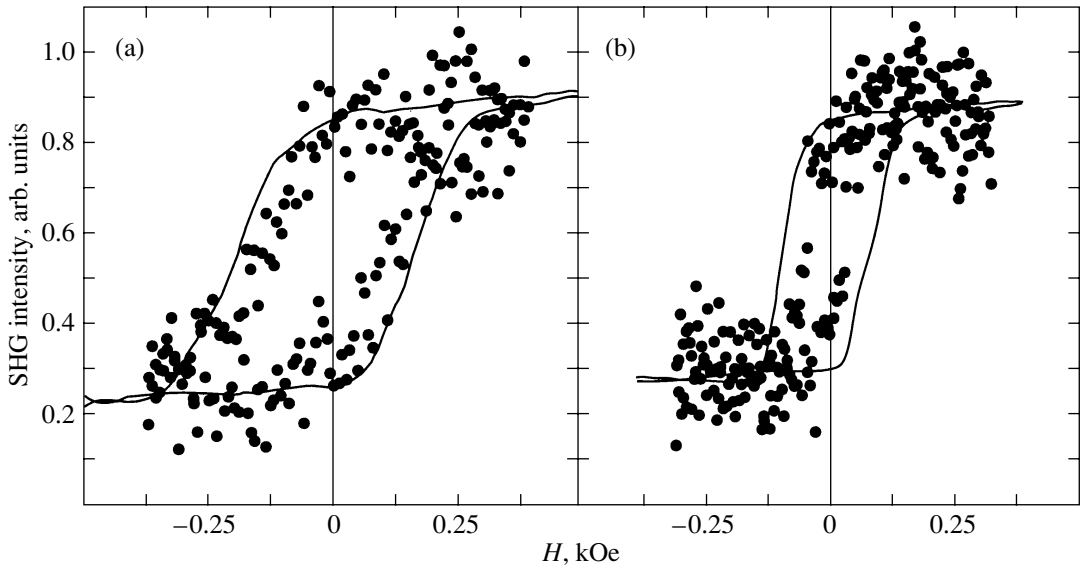

Fig. 6. Field dependences of the magnetically induced optical second-harmonic intensity (points) and of the magnetooptical MOKE (solid lines) measured on films (a) G and (b) C at $\lambda = 0.8$ μm for $\varphi = 15°$.

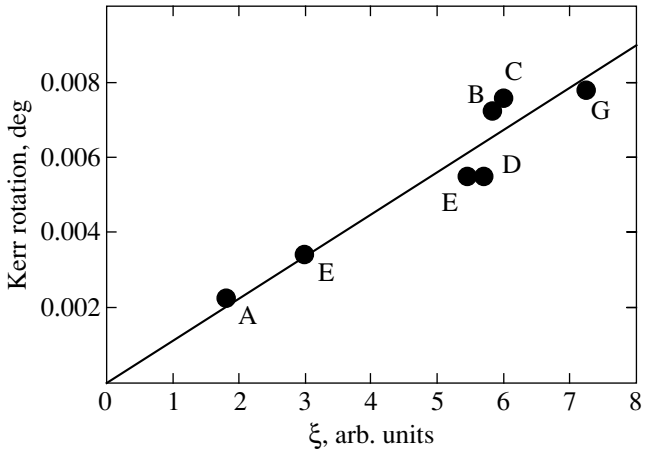

Fig. 7. Dependence of the MOKE on the ξ parameter determining the effective thickness of the film magnetic layer.

the light wave in a medium with magnetization **M** can be written as

$$P_i(2\omega) = \alpha_{ijk}E_jE_k + \beta_{ijkl}E_jE_kM_l + \gamma_{ijkl}E_j\nabla_kE_l, \quad (3)$$

where the first and second terms relate to the nonmagnetic and the magnetically induced contribution to the SHG, respectively. The tensors $\hat{\alpha}$ and $\hat{\beta}$ have nonzero components only in noncentrosymmetric media [12]. Because MnAs and Si have centrosymmetric crystal structures belonging to the 6/*mmm* and *m*3*m* symmetry groups, respectively, SHG in the volume of these materials is forbidden in the electric dipole approximation. However, SHG can appear at the air/MnAs and MnAs/Si interfaces, where the space-inversion symmetry is broken. One has also to include the contribution to the nonlinear polarization from the film and substrate volume, which can be produced from the quadrupole mechanism described by the third term in Eq. (3). In Si, this mechanism can provide a noticeable contribution to the nonlinear polarization comparable to the surface contribution [13].

A symmetry analysis of the $\hat{\alpha}$, $\hat{\beta}$, and $\hat{\gamma}$ tensors for the 6/*mmm* group shows that the contribution to the nonlinear polarization from the surface, the thin MnAs layer near the interface, and the bulk of the film should be isotropic. This contribution is represented in Eqs. (1) by the constant term *c*. The presence of terms proportional to cos3θ and sin3θ in Eqs. (1) implies that the system has a threefold axis. The silicon symmetry group contains a threefold axis. This means that the anisotropic term proportional to cos3θ and sin3θ is due to the substrate. This contribution originates through the electric-dipole mechanism in the region adjoining the interface and from electric quadrupole transitions in regions with thicknesses of the order of the light penetration depth. As shown in [14], in semiconductors of silicon structure the electric-dipole and electric-quadrupole mechanisms have the same symmetry. In addition to terms proportional to cos3θ and sin3θ, Eqs. (1) also contain terms proportional to cos3θ and sin3θ. Model calculations show that these terms in Eqs. (1) are due to the silicon substrates being slightly misoriented (by ~1.5°) from the (111) plane. Thus, because SHG sources do not produce an anisotropic, magnetically induced contribution, the slight change in the SHG intensity observed under magnetization reversal is caused by interference of the magnetically induced isotropic contribution arising at the interfaces and the anisotropic nonmagnetic contribution produced by the substrate. The narrowing of the hysteresis loops of the magnetically induced SHG compared to those of the MOKE (Fig. 6) indicates that the remagnetization is induced at the surface and is subsequently transfered into the bulk of the film.

5. CONCLUSIONS

Thus, we have studied the effect of growth technology on the magnetic and magnetooptical properties of thin (6–12 nm) MnAs/Si(111) epitaxial heterostructures. The magnetooptical Kerr effect and optical second harmonic generation were employed to investigate the dependence of the magnetic characteristics on the magnetic-layer thickness and surface morphology. The magnitude of the MOKE was observed to increase in proportion to the magnetic-layer thickness. The thickness of the transition layer forming near the magnet–semiconductor interface was determined to be about 2 nm. A technique based on x-ray diffraction has been proposed which takes into account the effect of the transition layer on the magnetooptical properties of films. The hysteresis characteristics of the magnetooptical Kerr effect and of the magnetically induced SHG were found to be different, which implies a difference between the volume and the interface magnetic properties of films. It was shown that the difference between the volume hysteresis properties of films can be caused by the shape anisotropy of the crystallites. The character of the anisotropy in the SHG azimuthal dependences was studied, and the sources of the nonlinear optical signal were analyzed. It was shown that there is a contribution to the SHG intensity that is an odd function of magnetization and originates from interference in the magnetically induced isotropic contribution produced by the film and the anisotropic nonmagnetic contribution due to the substrate.

ACKNOWLEDGMENTS

This work was supported by the Russian Foundation for Basic Research, Japanese project JSPS, INTAS, and the NWO Dutch–Russian Cooperation Program.

REFERENCES

1. G. A. Prinz, Science **282**, 1660 (1998).
2. H. Ohno, Science **281**, 951 (1998).
3. *Magnetic Films & Surfaces: Digest of the 15th International Conference, Kyoto, 1997.*
4. F. Schippan, A. Trempert, L. Däweritz, *et al.*, J. Cryst. Growth **201/202**, 674 (1999).
5. M. Kästner, F. Schippan, P. Schützebdübe, *et al.*, J. Vac. Sci. Technol. B **18**, 2052 (2000).
6. K. Akeura, M. Tanaka, T. Nishinaga, and J. De Boeck, J. Appl. Phys. **79**, 4957 (1996).
7. *Nonlinear Optics of Metals*, Ed. by K. H. Bennemann (Oxford Univ. Press, Oxford, 1998).
8. A. G. Banshchikov, A. V. Kimel', V. V. Pavlov, *et al.*, Fiz. Tverd. Tela (St. Petersburg) **42**, 115 (2000) [Phys. Solid State **42**, 909 (2000)].
9. G. S. Krinchik, *Physics of Magnetic Phenomena* (Mosk. Gos. Univ., Moscow, 1985).
10. *Handbook of Physical Quantities*, Ed. by I. S. Grigoriev and E. Z. Meilikhov (Énergoizdat, Moscow, 1991; CRC Press, Boca Raton, 1997).
11. E. R. Moog, S. D. Bader, and J. Zak, Appl. Phys. Lett. **56**, 2687 (1990).
12. R. R. Birss, *Symmetry and Magnetism* (North-Holland, Amsterdam, 1966).
13. H. W. K. Tom, T. F. Heinz, and Y. R. Shen, Phys. Rev. Lett. **51**, 1983 (1983).
14. J. E. Sipe, D. J. Moss, and H. M. van Driel, Phys. Rev. B **35**, 1129 (1987).

Translated by G. Skrebtsov

Physics of the Solid State, Vol. 43, No. 10, 2001, pp. 1948–1951. Translated from Fizika Tverdogo Tela, Vol. 43, No. 10, 2001, pp. 1871–1874.

MAGNETISM AND FERROELECTRICITY

Nonlinear Dielectric Susceptibility of Dipole Impurities Dissolved in the Lattice of Quantum Paraelectrics

S. A. Prosandeev

Rostov State University, pr. Stachki 194, Rostov-on-Don, 344090 Russia

Received November 23, 2000; in final form, February 26, 2001

Abstract—A general relation is derived for calculating the nonlinear dielectric susceptibility of a system placed in an external ac magnetic field, which consists of tunneling and interacting dipole impurities described by the Hamiltonian of the transverse Ising model and a lattice of ions whose dynamics is specified in the soft-mode model with the possible ferroelectric phase transition suppressed by zero-point quantum oscillations. It is shown that the relaxation peaks in the dielectric response can be enhanced several times through relaxator interaction with the soft mode. A general expression is obtained to describe the deviation from the Arrhenius law in this case. The results of this work can be employed for interpretation of recent experiments that revealed a strong effect of isovalent impurities at extremely low concentrations on the macroscopic properties of incipient ferroelectrics. © *2001 MAIK "Nauka/Interperiodica".*

Although the $KTaO_3$ and $SrTiO_3$ incipient ferroelectrics exhibit a great permittivity at low temperatures, they do not undergo a ferroelectric phase transition down to the lowest temperatures studied because of its suppression by zero-point quantum oscillations of ions [1]. Recent experiments showed that isotopic substitution of oxygen ions in $SrTiO_3$ gives rise to a phase transition [2]. The phase transition can also be stimulated by small additions, for instance, of 0.7% Ca [3–5]. In all these cases, however, the dispersion of the permittivity is small and the system behaves close to the way in which a soft-mode system with a modified Curie temperature behaves. It should be pointed out that the temperature behavior of the dielectric susceptibility in the vicinity of the phase transition deviates from the Curie–Weiss law due to the zero-point quantum oscillations. This deviation was described in [6, 7]. The situation becomes particularly complex in the cases where dipole impurities are in comparatively deep potential wells, which gives rise to noticeable dispersion. Studies of the dielectric response in $KTaO_3$:Li solid solutions revealed that, already at very low Li concentrations (of the order of one percent), the dielectric function exhibits a giant dispersion and the magnitude of the relaxation response at the peak exceeds the dielectric susceptibility of the host lattice many times [8, 9]. These data show that dipole impurities in incipient ferroelectrics affect the susceptibility of the host lattice by increasing it. In turn, the host lattice acts on the impurities, enhancing the dispersion of their dielectric response.

It was shown [10, 11] that the coupling of the ferroelectric soft mode with relaxators enhances the interaction between impurities. While this point is important for correct description of the dielectric susceptibility of the systems under consideration, one should not disregard the change in the properties of the host lattice itself due to its interaction with dipole impurities. The purpose of this work was to consider both contributions to the resultant dielectric susceptibility and to demonstrate that the first contribution is essential only at relatively high impurity concentrations, whereas at low concentrations, the renormalization of the host-lattice properties is more significant. Moreover, in this work, the dependence of the dielectric susceptibility on the amplitude and frequency of the external field was studied in considerable detail. It was shown that, because of the high permittivity of incipient ferroelectrics, the field dependence of the total dielectric response is complicated by the nonlinear contribution due to the impurities. This makes determination of the parameters of the Ginzburg–Devonshire expansion of the thermodynamic potentials in weak fields impossible.

Mode mixing was also considered earlier as applied to KDP [12, 13] and ideal $PbTiO_3$ and $KNbO_3$ [14], which the above authors believe to feature a mixed order–disorder and soft-mode character of the phase transition. The Slater model of the dielectric response was modified in [15] for the case where the relaxation polarizability exists in parallel to the ionic polarizability. The study performed in this work substantially enhances these approaches by taking into account quantum effects in the lattice dynamics, tunneling, impurity interaction, dispersion, and polarization (both static and induced by an external field). The final relations can be used for treatment of the available data on the solid solutions of incipient ferroelectrics. Interestingly, the susceptibility exhibits a similar behavior in relaxors, a broader class of substances. In these substances, however, random fields play the role of ion quantum oscillations that suppress the phase transition.

1063-7834/01/4310-1948$21.00

We write the equation for the dipole density matrix ρ_d in the relaxation time approximation:

$$d\rho_d/dt = [H_d\rho_d]/i\hbar - (\rho_d - \bar{\rho}_d)/\tau, \quad (1)$$

where $[AB] = AB - BA$ and

$$\bar{\rho}_d = \exp(-H_d/k_BT)/\mathrm{Sp}(\exp(-H_d/k_BT)) \quad (2)$$

is the Boltzmann-averaged density matrix. The dipole Hamiltonian is written in terms of the transverse Ising model [16]:

$$H_d = -\Omega\sum_i s_i^x - 2\mu E\sum_i s_i^z - \lambda P_h\sum_i s_i^z - \sum_{i<j} J_{ij}s_i^z s_j^z, \quad (3)$$

where P_h is the host-lattice polarization, Ω is the tunneling integral, μ is the impurity dipole moment, E is the external electric field, λ is the coupling constant of the polarization and the dipole moment, J_{ij} is the dipole moment interaction constant, and s_i^z is the quasi-spin operator. Substituting (3) in Eq. (1) and performing the Fourier transform, we obtain

$$\xi\rho_d = -\Omega[s^x\rho_d] - u[s^z\rho_d], \quad (4)$$

where

$$\xi = i\hbar\nu - \hbar\omega, \quad u = 2\mu E + \lambda P_h + J_0\langle s^z\rangle. \quad (5)$$

Here, $\nu = 1/\tau$. The procedure of density matrix averaging is explained in some detail in the Appendix.

These averages can be used to write the dipole polarization in the form

$$P_d = 2\mu n_d\mathrm{Sp}(\sigma^z\rho_d) = \mu n_d(\rho_{d11} - \rho_{d22}). \quad (6)$$

Substituting the relations derived in the Appendix yields

$$P_d = 2\mu n_d f(u), \quad (7)$$

where

$$f(u) = \frac{i\hbar\nu u}{4(i\hbar\nu - \hbar\omega)e_+}\tanh\frac{e_+}{k_BT}. \quad (8)$$

It is seen that the dependence on external fields enters only into the quantity $u = (2\mu E + \lambda P_h + J_0\langle s^s\rangle)$. Hence, the derivative with respect to the field needed to derive the susceptibility can be found in the following general form:

$$\chi_d = \varepsilon_0^{-1}dP_d/dE = \varepsilon_0^{-1}2\mu n_d F(2\mu + \lambda P_h' + J_0\langle s^z\rangle') = 2\mu n_d(2\mu + \lambda dP_h/dE + J_0\varepsilon_0\chi_d/2\mu n_d)F/\varepsilon_0, \quad (9)$$

where $F = f'(u)$ and $u = 2\mu E + \lambda P_h + J_0\langle s^z\rangle$. Calculation of the derivatives yields

$$F = f'(u) = [16(1 + i\omega\tau)e_+^2]^{-1} \times \{(\Omega^2/e_+)\tanh(e_+/k_BT) + (u^2/k_BT)\cosh^2(e_+/k_BT)\}. \quad (10)$$

The first contribution has the character of the susceptibility derived empirically by Barrett for quantum paraelectrics [17]. The second contribution has the form of the well-known Langevin function.

The dipole impurity susceptibility can now be found from Eq. (9), that is,

$$\chi_d = 2\mu n_d F\varepsilon_0^{-1}(2\mu + \lambda dP_h/dE)/(1 - J_0F). \quad (11)$$

To calculate the host-lattice susceptibility, we consider the corresponding contribution to the free energy:

$$F_h = \alpha p^2/2 + \beta\rho^4/4 + \gamma p^6/6 - \lambda n_d\langle s^z\rangle p - (E + e)p, \quad (12)$$

where e is the random field produced by the impurities and p is the local polarization needed to calculate the macroscopic polarization according to the expression

$$P_h = \int_{-\infty}^{\infty} p(e)f(e)de. \quad (13)$$

Here, $f(e)$ is the random-field distribution function. The equilibrium condition for the system requires that

$$\alpha p + \beta p^3 - \lambda\langle s^z\rangle - (E + e) = 0. \quad (14)$$

Taking the derivative with respect to E gives

$$\chi_h = (1 + \lambda\varepsilon_0\chi_d/2\mu)/\varepsilon_0 A(T, p), \quad (15)$$

where $A[(T, p(e)] = \alpha + 3\beta p^2 + 5\gamma p^4$. Equations (11) and (15) yield

$$\chi_d(p) = \frac{1}{\varepsilon_0}\frac{2\mu n_d F(\lambda + 2A(T, p)\mu)}{\varepsilon_0 A(T, p) - J_0A(T, p)F - \lambda^2 n_d F},$$
$$\chi_h(p) = \frac{1}{\varepsilon_0}\frac{1 - J_0F + 2\lambda\mu n_d F}{\varepsilon_0 A(T, p) - J_0A(T, p)F - \lambda^2 n_d F}. \quad (16)$$

These expressions should be averaged over the random field e. We finally obtain the following relation for the resultant susceptibility:

$$\chi = \frac{1}{\varepsilon_0}\int_{-\infty}^{\infty} de\, f(e)\frac{1 + 4\lambda\mu n_d F^* + 4\mu^2 n_d A(T, p)F^*}{A(T, p) - \lambda^2 n_d F^*}, \quad (17)$$

where $F^* = F/(1 - J_0F)$.

The above expression for the nonlinear dielectric susceptibility of the solid solutions of incipient ferroelectrics makes it possible to solve the problem of determining its dependence on the field, temperature, frequency and amplitude of the external field, polarization, tunneling integral, and impurity interaction energy. We readily see that, as the coupling constant of dipoles with the soft mode increases, the denominator in the expression decreases, which can result in a manifold enhancement of relaxation peaks in the dielectric response.

Let us now consider some particular cases.

(1) $u = 0$ (linear susceptibility in the paraphase):

$$e_+ = \sqrt{(\Omega)^2 + u^2}/2 = \Omega/2, \quad (18)$$

$$F = f'(0) = [2\omega(1 + \omega\tau)]^{-1}\tanh(\Omega/2k_BT). \quad (19)$$

It is seen that, in this case, the temperature dependence of the susceptibility reproduces the quantum relation of Barrett [17].

(2) $E \neq o$, $\Omega = 0$:

$$F = f'(u) = [4(1 + \omega\tau)k_BT]^{-1}\cosh^{-2}(u/2k_BT). \quad (20)$$

The susceptibility obtained in this case coincides with the one derived from the Langevin function describing the polarization of ordering dipoles. Note that, because of the strong field dependence of F and the smallness of A in quantum paraelectrics, the behavior of the nonlinear susceptibility in the weak-field domain (up to the fields which correspond to complete ordering of dipole impurities) cannot be described by the function derived from the Ginzburg–Devonshire expansion within the field range usually covered in an experiment. This accounts for the field dependence of the parameters of the Ginzburg–Devonshire potential expansion for the solid solutions of incipient ferroelectrics, which was observed in [18].

The data obtained permit us to find the deviation from the Arrhenius law:

$$\tau^* = \tau/[1 - (J_0g + \lambda^2 n_d g/A)], \quad (21)$$

where $g = (1 + i\omega\tau)F$ is a frequency-independent quantity; at high temperatures, $\tau = \tau_0\exp(U/k_BT)$. As is seen from this relation, the divergence of the relaxation time can be due to direct and indirect interactions between impurities. The latter interaction is greatly enhanced at small A, i.e., at a large host-lattice susceptibility. This relation can account for the apparent freezing-out of dipoles at a certain temperature, which is made evident by applying the Vogel–Fulcher empirical expression to treatment of the experimental data. In actual fact, the deviation from the standard Arrhenius formula can be due both to the soft mode being coupled to the impurity dipoles and to the dipole freezing-out. In order to isolate the first contribution, it would be desirable to derive an expression containing experimentally measurable quantities. To derive such a relation, we made the following simplifications:

$$\begin{aligned}\tau &= \theta_0 e^{\frac{U}{k_BT}}\frac{4 + r\chi_\infty(4 + r\chi)}{4 + t\chi_\infty(4 + r\chi_\infty)} \\ &\approx \theta_0 e^{\frac{U}{k_BT}}\frac{4 + r\chi}{4 + r\chi_\infty} \approx \theta_0 e^{\frac{U}{k_BT}}\frac{\chi}{\chi_\infty},\end{aligned} \quad (22)$$

where $r = \lambda\varepsilon_0/\mu \equiv \gamma/3$ and $\chi_\infty = A^{-1}(T)$. This dependence of the relaxation time on the permittivity was obtained in [19]. In our case, however, χ_∞ is a function of temperature; moreover, we can refine this relation by making use of the first estimate in formula (22). The expression thus derived permits one to isolate the contribution due to soft-mode coupling to the dipole moments of impurities from an experimental dependence of the relaxation time. The findings indicating that the deviation from the Arrhenius law follows this theory are reported in [20].

In addition to enhancing the dielectric susceptibility due to the dipole coupling to the soft mode, dipole impurities also bring about the suppression of high susceptibilities at the peak, which are associated with random fields. Our consideration is specific in that the soft mode acted upon by random fields becomes harder. According to experiments, the random field effect is particularly strong at the susceptibility peak, where the mean square polarization is highest. As a result, the susceptibility peak shifts toward higher temperatures, while the susceptibility decreases near the phase transition point.

The relations obtained here can be readily generalized to the case of scatter in the relaxation times, potential barrier heights, and dipole moments of single dipoles and clusters. In this case, the susceptibility could become enhanced through the interaction of large clusters with relatively small, single dipoles. While being present in larger numbers, the latter play, in the final expressions, the same role as the soft mode and the clusters act as dipoles in our model. In disordered crystals, polar regions can also play the part of a soft mode. These issues are, however, beyond the scope of this study and will be covered in a separate communication.

APPENDIX

Equation (4) can be recast in the matrix form as

$$\begin{pmatrix} \xi\rho_{d11} + \Omega\dfrac{\rho_{d21} - \rho_{d12}}{2} & (\xi + u)\rho_{d12} + \Omega\dfrac{\rho_{d22} - \rho_{d11}}{2} \\ (\xi - u)\rho_{d21} - \Omega\dfrac{\rho_{d22} - \rho_{d11}}{2} & \xi\rho_{d22} - \Omega\dfrac{\rho_{d21} - \rho_{d12}}{2} \end{pmatrix} = i\hbar\nu\begin{pmatrix} \bar{\rho}_{d11} & \bar{\rho}_{d12} \\ \bar{\rho}_{d21} & \bar{\rho}_{d22} \end{pmatrix}. \quad (23)$$

We now write out the sum and the difference between the first and second diagonal elements (and between the first and second nondiagonal elements) as follows:

$$\begin{aligned}
\xi(\rho_{d11}-\rho_{d22})+\Omega(\rho_{d21}-\rho_{d12}) &= i\hbar\nu(\bar\rho_{d11}-\bar\rho_{d22}),\\
\xi(\rho_{d11}+\rho_{d22}) &= i\hbar\nu(\bar\rho_{d11}+\bar\rho_{d22}),\\
\xi(\rho_{d21}-\rho_{d12})-u(\rho_{d21}+\rho_{d12})+\Omega(\rho_{d11}-\rho_{d22}) &= i\hbar\nu(\bar\rho_{d21}-\bar\rho_{d12}),\\
\xi(\rho_{d21}+\rho_{d12})-u(\rho_{d21}-\rho_{d12}) &= i\hbar\nu(\bar\rho_{d21}+\bar\rho_{d12}).
\end{aligned} \tag{24}$$

These equations yield

$$\begin{aligned}
\rho_{d11}-\rho_{d22} = &-\frac{i\hbar\nu u\Omega}{\xi(\xi^2-u^2-\Omega^2)}(\bar\rho_{d21}+\bar\rho_{d12})\\
&-\frac{i\hbar\nu\Omega}{\xi^2-u^2-\Omega^2}(\bar\rho_{d21}-\bar\rho_{d12})\\
&+\frac{i\hbar\nu(\xi^2-u^2)}{\xi(\xi^2-u^{P2}-\Omega^2)}(\bar\rho_{d21}-\bar\rho_{d12}).
\end{aligned} \tag{25}$$

The mean $\bar\rho_d$ can be determined using the eigenvalues of the Hamiltonian $H_{d0} = -\Omega s^x + us^z$, that is,

$$e_\pm = \pm 2^{-1}\sqrt{\Omega^2+u^2}. \tag{26}$$

Here, $e_\pm$ are the upper (larger) and lower (smaller) eigenvalues, respectively. Now, we can recast the averaged density matrix in the form

$$\bar\rho_d = \exp(-H_d/k_BT)/2\cosh(e_+/k_BT). \tag{27}$$

To find the density matrix, we use the following expression:

$$\begin{aligned}
&\rho_{dij}\\
&= \frac{\langle i|+\rangle\exp(-e_+/k_BT)\langle+|j\rangle+\langle i|-\rangle\exp(e_+/k_BT)\langle-|j\rangle}{2\cosh(e_+/k_BT)},
\end{aligned} \tag{28}$$

where $|+\rangle$ denotes the state with energy e_+; $|-\rangle$, the state with energy e_-.

The projections of the eigenvectors on localized states can be found from the equations

$$\begin{aligned}
(-u/2-e_\pm)\langle\pm|1\rangle-(\Omega/2)\langle\pm|2\rangle &= 0,\\
-(\Omega/2)\langle\pm|1\rangle+(u/2-e_\pm)\langle\pm|2\rangle &= 0.
\end{aligned} \tag{29}$$

The second equation yields

$$\langle\pm|2\rangle = -[\Omega/(-u+2e_\pm)]\langle\pm|1\rangle. \tag{30}$$

Using the normalization condition $|\langle\pm|1\rangle|^2+|\langle\pm|2\rangle|^2=1$ and Eq. (30), we come to

$$\begin{aligned}
|\langle\pm|1\rangle|^2 &= (-u+2e_\pm)/4e_\pm,\\
|\langle\pm|2\rangle|^2 &= (u+2e_\pm)/4e_\pm,\\
\langle1|\pm\rangle\langle\pm|2\rangle^2 &= -\Omega/4e_\pm.
\end{aligned} \tag{31}$$

It follows from Eq. (28) that

$$\begin{aligned}
\bar\rho_{d11} &= 1/2+(u/4e_+)\tanh(e_+/k_BT),\\
\bar\rho_{d22} &= 1/2-(u/4e_+)\tanh(e_+/k_BT),\\
\bar\rho_{d12} &= \bar\rho_{d21} = (\Omega/4e_+)\tanh(e_+/k_BT).
\end{aligned} \tag{32}$$

These relations describe the temperature dependence of the density matrix averaged over the Boltzmann distribution for the complex case of dipoles coupled with the soft mode, which is considered here.

REFERENCES

1. K. A. Müller and H. Burkard, Phys. Rev. B **19**, 3593 (1979).
2. R. Wang and M. Itoh, Phys. Rev. B **62**, R731 (2000).
3. J. G. Bednorz and K. A. Müller, Phys. Rev. Lett. **52**, 2289 (1984).
4. J. Dec, W. Kleemann, U. Bianchi, and J. G. Bednorz, Europhys. Lett. **29**, 31 (1995).
5. W. Kleemann, J. Dec, Y. G. Wang, *et al.*, J. Phys. Chem. Solids **61**, 167 (2000).
6. A. B. Réchester, Zh. Éksp. Teor. Fiz. **60**, 782 (1971) [Sov. Phys. JETP **33**, 423 (1971)].
7. D. E. Khmel'nitskiĭ and V. L. Shneerson, Fiz. Tverd. Tela (Leningrad) **13**, 832 (1971) [Sov. Phys. Solid State **13**, 687 (1971)].
8. U. T. Hochli, K. Knorr, and A. Loidl, Adv. Phys. **39**, 405 (1990).
9. V. Trepakov, V. Vikhnin, M. Savinov, *et al.*, Ferroelectrics **235**, 59 (1999).
10. B. E. Vugmeister and M. D. Glinchuk, Rev. Mod. Phys. **62**, 993 (1990).
11. V. S. Vikhnin, Fiz. Tverd. Tela (Leningrad) **26**, 906 (1984) [Sov. Phys. Solid State **26**, 552 (1984)].
12. V. G. Vaks, *Introduction to the Microscopic Theory of Ferroelectrics* (Nauka, Moscow, 1973).
13. A. Bussmann-Holder and K. H. Michel, Phys. Rev. Lett. **80**, 2173 (1998).
14. Y. Girshberg and Y. Yacoby, J. Phys.: Condens. Matter **11**, 9807 (1999).
15. A. V. Turik, Izv. Akad. Nauk SSSR, Ser. Fiz. **57**, 35 (1993).
16. R. Blinc and B. Zeks, *Soft Modes in Ferroelectrics and Antiferroelectrics* (North-Holland, Amsterdam, 1974; Mir, Moscow, 1975).
17. J. H. Barrett, Phys. Rev. **86**, 118 (1952).
18. G. V. Belokopytov, Ferroelectrics **168**, 69 (1998).
19. G. I. Skanavi, *Physics of Dielectrics* (GITTL, Leningrad, 1949).
20. S. A. Prosandeev, V. A. Trepakov, M. E. Savinov, and S. E. Kapphan, J. Phys.: Condens. Matter **13**, 719 (2001).

Translated by G. Skrebtsov

Physics of the Solid State, Vol. 43, No. 10, 2001, pp. 1952–1957. Translated from Fizika Tverdogo Tela, Vol. 43, No. 10, 2001, pp. 1875–1879.

MAGNETISM AND FERROELECTRICITY

Temperature Behavior of the Order Parameter in $Pb_5Ge_3O_{11}$

V. A. Vazhenin, V. B. Guseva, V. Ya. Shur, E. V. Nikolaeva, and M. Yu. Artemov

Research Institute of Physics and Applied Mathematics, Ural State University, pr. Lenina 51, Yekaterinburg, 620083 Russia
e-mail: vladimir.vazhenin@usu.ru

Received March 15, 2001

Abstract—The temperature dependence of the spontaneous polarization in the $Pb_5Ge_3O_{11}$ lead germanate (PGO) is experimentally investigated using optical, magnetic resonance, and conventional electrical measurements. The deviations from the temperature dependence typical of second-order phase transitions at temperatures below 420 K are explained in terms of incomplete polarization switching and polarization induced by a residual depolarization field. The low-temperature anomalies are interpreted without consideration of additional structural transformations. The internal bias field is determined from the experimental temperature dependence of the perfect polarization of PGO single crystals in an electric field. *© 2001 MAIK "Nauka/Interperiodica".*

1. INTRODUCTION

Lead germanate $Pb_5Ge_3O_{11}$ (PGO) at 450 K undergoes a second-order ferroelectric phase transition accompanied by a change in symmetry from $P6(C_{3h}^1)$ at 473 K to $P3(C_3^1)$ at room temperature [1, 2]. Iwasaki *et al.* [3] revealed a nonlinear temperature dependence of the spontaneous polarization squared and showed that this dependence can be closely approximated by two straight lines. These findings gave impetus to the search for other temperature anomalies. Specific features were also revealed in the temperature dependences of many parameters for ferroelectric [4–7] and paraelectric [8–10] phases. The observed anomalies (at ~250 [7], ~420 [3–6], ~500 [6, 10], and ~580 K [8–10]) were interpreted as a manifestation of additional structural transformations [3–11]. In particular, Babushkin [11] proposed a hypothetical sequence of structural transitions in PGO crystals [the praphase with the space group $P62m(D_{3h}^3)$] characterized by three order parameters, two of which could be transformed as an axial vector. In the present work, an attempt was made to explain the temperature dependences of the spontaneous polarization $P_s(T)$ (which were obtained in optical, electrical, and magnetic resonance measurements of PGO compounds) without resorting to the concept of additional structural transformations.

2. EXPERIMENTAL TECHNIQUE

In order to obtain independent experimental data on the temperature behavior of the spontaneous polarization $P_s(T)$ in PGO compounds, we measured the parameters of the EPR spectra of Gd^{3+} and Mn^{2+} impurity trigonal centers and the optical activities, which are related to the averaged spontaneous polarization by known formulas.

The experiments were performed with PGO single crystals grown in air (or a nitrogen atmosphere) by the Czochralski method from the melt of stoichiometric composition. The samples were prepared in the form of plates (0.5–1 cm^2) cut normally to the polar axis. Magnetic resonance measurements were made using 1-mm-thick samples doped with 0.005–0.01 mol % Gd_2O_3 or Mn_2O_3. The optical and electrical measurements were carried out with the use of undoped PGO samples 8 and 3 mm thick, respectively. No noticeable effect of the doping on the temperature dependence of the spontaneous polarization was observed.

The EPR spectra were recorded on a spectrometer operating in the 3-cm band. The temperature of samples was changed by blowing them with liquid-nitrogen vapor or hot air. For this purpose, the sample was placed at the center of a quartz tube located in a microwave resonant cavity. The tube had double walls, between which the air was evacuated.

The axial fine-structure parameter b_{20} and the trigonal symmetry parameter b_{43} were determined from the EPR spectra. The latter parameter for an arbitrary orientation of the magnetic field is proportional to the domain splitting (the spacing between the lines attributed to identical transitions in Gd^{3+} centers located in domains of opposite polarizations) [12]. In order to avoid the errors associated with overlapping of EPR signals from different domains, the EPR measurements at temperatures close to the ferroelectric transition point were performed using a sample with deposited electrodes. This made it possible to suppress the EPR signals from domains of a particular type by polarizing the sample prior to each measurement. Earlier [12], we proved that the b_{20} parameter obeys the equation $b_{20}(P_s, T) = b_{20}(T) + \Delta b_{20}(P_s)$. The values of $\Delta b_{20}(P_s)$

1063-7834/01/4310-1952$21.00

were determined as the difference between the measured parameters $b_{20}(P_s, T)$ and the $b_{20}(T)$ values obtained by extrapolating the temperature dependence measured in the paraphase to the ferroelectric phase.

The specific optical rotatory power ρ was measured by the modulation method (λ = 632.5 nm). A 3-mm-thick PGO plate served as the modulator of optical rotation. The modulation frequency was 10–100 Hz. The absolute accuracy in measurements was equal to ±0.5′. The relative error was less than 10^{-3}.

The spontaneous polarization was also determined by the conventional method using the switched charge obtained from the dielectric hysteresis loop. The measurements were performed at frequencies of 10–100 Hz with the use of transparent electrodes based on indium and tin oxides. The spontaneous polarization at room temperature was equal to 4.8 ± 0.2 μC/cm^2.

The temperature dependences of all the optical and magnetic resonance parameters (Δb_{20} for Gd^{3+} and Mn^{2+} trigonal centers, ρ^2, and b_{43}^2) normalized to the corresponding values at room temperature turned out to be qualitatively similar to each other (Fig. 1). A similar temperature dependence of ρ^2 was obtained in [13].

The relationship between the above characteristics and the spontaneous polarization P_s can be determined from symmetry analysis. According to this analysis, the expansions of the b_{43} and ρ parameters in powers of P_s can contain only the terms with odd powers, whereas the expansion of the Δb_{20} parameter involves only the terms with even powers. As a rule, good agreement with experimental data can be achieved with allowance made only for the first terms of the series [14]. Taking into account the differences in the nature of the interrelation between the aforementioned parameters and the spontaneous polarization P_s [14], the observed similarity in the temperature behavior of ρ^2, b_{43}^2, and Δb_{20} (Fig. 1) indicates that terms with powers higher than two in the corresponding expansions in terms of P_s are sufficiently small. Therefore, it can be inferred that the temperature dependences of ρ^2, b_{43}^2, and Δb_{20} are proportional to the temperature dependence of the spontaneous polarization squared $P_s^2(T)$ with a high degree of accuracy.

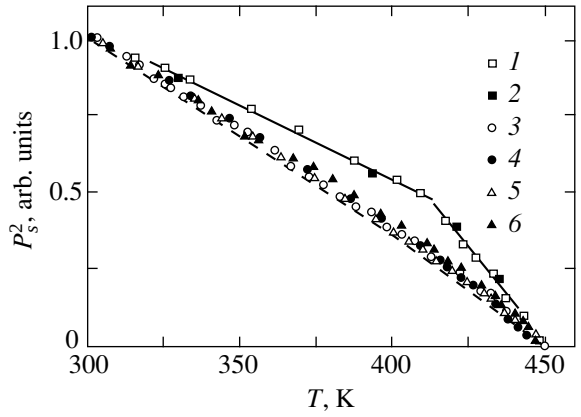

Fig. 1. Temperature dependences of the square of spontaneous polarization determined by different methods: (*1*) electrical measurements in this work, (*2*) electrical measurements performed by Iwasaki *et al.* [3], (*3*) data on the b_{43} parameter for Gd^{3+} centers, (*4*) data on the Δb_{20} parameter for Gd^{3+} centers, (*5*) data on the Δb_{20} parameter for Mn^{2+} centers, and (*6*) optical activity. All the data are normalized to the corresponding parameters at $T = 300$ K. The solid line shows the approximation proposed in [3]. The dashed line represents the approximation according to formula (2) over a wide range of temperatures.

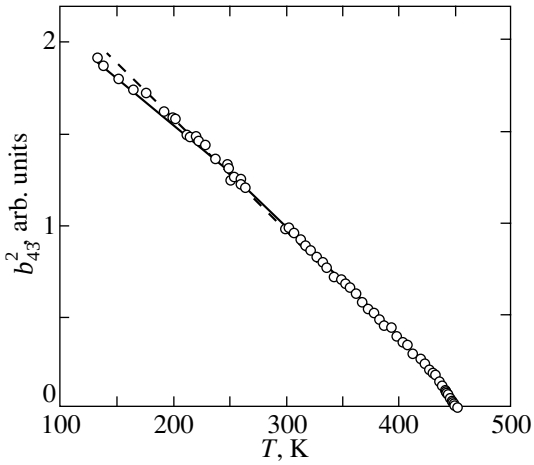

Fig. 2. Temperature dependence of b_{43}^2. The solid line shows the approximation according to formula (2), and the dashed line represents the approximation without regard for nonlinearity.

3. THE TEMPERATURE ANOMALY AT 250 K

Bush and Venevtsev [7] revealed a specific feature in the dielectric characteristics of PGO crystals at $T \approx 250$ K. Babushkin [11] assumed that this feature is associated with the structural transformation. In order to verify experimentally the occurrence of this transformation, we measured the temperature dependence of the domain splitting squared over a wide range of temperatures (Fig. 2). It should be noted that, in the case when the experimental points are approximated by straight-line segments (as was proposed in [11]), the inflection point in the dependence $P_s^2(T) \sim b_{43}^2(T)$ is also observed near 250 K.

According to the sequence of structural transitions proposed in [11], the symmetry of PGO crystals should change from $P3$ (C_3^1) at room temperature to $P31m$ (C_{3V}^2) upon cooling to temperatures below 250 K. However, this assertion cannot be verified by the EPR

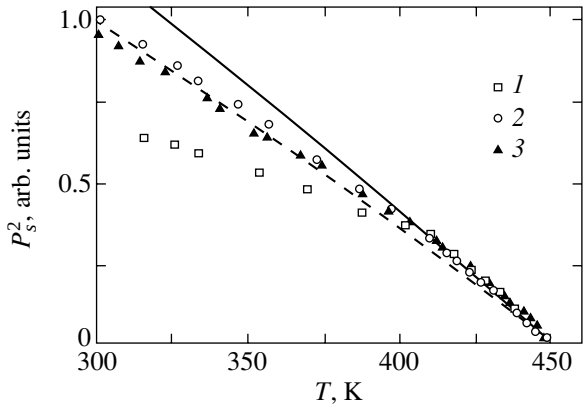

Fig. 3. Temperature dependences of the square of the spontaneous polarization determined from (*1*) the electrical measurements, (*2*) the b_{43} parameters for Gd^{3+} centers, and (*3*) the optical activity. The data are normalized to the corresponding parameters at 420 K. The dashed line shows the approximation of the dependence $b_{43}^2(T)$ according to formula (2) over a wide range of temperatures. The solid line is obtained by scaling the dashed line.

method for the studied samples, because the Gd^{3+} impurity ions in these space groups have the same symmetry. This is confirmed by the fact that, at 220 K, there exists a disagreement between the locations of extrema in the azimuthal angular dependences of the domain splitting in the EPR spectra and the width of the Gd^{3+} EPR signals at $\theta = 85°$ ($5/2 \longleftrightarrow 7/2$, θ is the polar angle of the magnetic induction B, $z \parallel C_3$), which was clearly observed at $T = 300$ K [15].

The nonlinear behavior of the spontaneous polarization squared P_s^2 over a wide range of temperatures can be explained by assuming that there is a considerable contribution of the term proportional to P^6 in the expansion of the thermodynamic potential:

$$\Phi = \Phi_0 + \alpha P^2/2 + \beta P^4/4 + \gamma P^6/6. \qquad (1)$$

As a result, we obtain the following relationship:

$$P_s^2 = -\frac{1}{\beta}\left[\alpha_0(T - T_C) + \frac{\gamma\alpha_0^2}{\beta^2}(T - T_C)^2\right]. \qquad (2)$$

It can be seen from Fig. 2 that, in general, relationship (2) closely approximates the experimental dependence $P_s^2(T) \sim b_{43}^2(T)$ (the root-mean-square deviation is approximately equal to 0.001), except for a small portion near $T = 420$ K (Fig. 1).

The dependence $P_s^2(T) \sim b_{43}^2$ can be described over a wide range of temperatures with the same accuracy (the root-mean-square deviation is ~0.001) under the assumption that the β coefficient depends on temperature or that the α quantity substantially depends on the term involving $(T - T_C)^2$. At the same time, the assumptions that the term proportional to P^6 makes a significant contribution to potential (1), the β quantity depends on the temperature, and the dependence $\alpha(T)$ has a nonlinear behavior does not lead to a noticeable improvement in the approximation of the results obtained in the optical and magnetic resonance investigations in the vicinity of 420 K and, especially, the results of the electrical measurements (Fig. 1).

4. THE TEMPERATURE ANOMALY AT 420 K

As is clearly seen from Fig. 1, the temperature dependences of the spontaneous polarization determined from traditional measurements (in this work and by Iwasaki *et al.* [3]) of the field dependences of the switched charge (the change in the surface charge determined from the hysteresis loop) differ significantly from those obtained in optical and magnetic resonance measurements and can be closely approximated by straight-line segments [3].

Since the absolute values of the polarization cannot be directly determined from the optical and magnetic resonance measurements, a comparison of these data with the results of the electrical measurements can be made only after their normalization. However, after the normalization of all the experimental data to the corresponding values at room temperature (Figs. 1, 2), the temperature dependences $P_s^2(T)$ and $b_{43}^2(T)$ exhibit a dissimilar behavior, which has not found a reasonable explanation (see Section 3). For this reason, we proposed another normalization to the values measured at 420 K (Fig. 3) by assuming that it is in this range of temperatures (420–450 K) that the behavior of $P_s^2(T)$ is most adequately described by all the methods used and that the quantities ρ^2, b_{43}^2, and P_s^2 in relative units are identical in magnitude. The data shown by the solid line in Fig. 3 were obtained by multiplying the values of $b_{43}^2(T)$ (the dashed line in Fig. 3) into a constant in order to achieve the best description of the experimental data on ρ^2, b_{43}^2, and P_s^2 in the temperature range 420–450 K.

The observed deviation of the results obtained in the electrical measurements from the hypothetical dependence $P_s^2(T)$ (displayed by the solid line in Fig. 3) can be caused by an incomplete polarization switching in the surface layer due to residual depolarization fields [16, 17] (this switching occurs in parallel with the incomplete switching in the bulk of the material).

The dielectric layer (gap) on the surface of ferroelectrics [18] prevents complete compensation for depolarization fields through external screening (the redistribution of charges at electrodes). The residual depolarization field E_{rd} is determined by the ratio

between the thickness of the dielectric gap L and the sample thickness d [16, 19]:

$$E_{rd} = (2L/d)(P_s/\varepsilon_L\varepsilon_0), \quad (3)$$

where ε_L is the permittivity of the dielectric gap.

The residual depolarization field can be compensated for only by the processes that occur through mechanisms of bulk screening: (1) the redistribution of space charge carriers, (2) the reorientation of defect dipoles, and (3) the injection of carriers from electrodes through the dielectric gap [16]. The ratios of the contributions from the particular mechanisms for various ferroelectrics differ considerably and depend on the temperature. Earlier [20], we experimentally demonstrated for PGO crystals that, even after bulk screening, there exists a field capable of changing the polarization direction in a surface layer approximately 100 μm thick. In the case when the bulk screening occurs through the redistribution of charge carriers (the dominant mechanism of screening in PGO compounds), the layer thickness is governed by the screening length. This should lead to surface polarization switching, viz., the formation and growth of tapered domains of a submicron cross section [21]. These vestigial domains play a crucial role in the course of polarization switching in the opposite direction, because they bring about the formation of new domains and facilitate the formation of steps in moving domain walls [16].

As the temperature decreases, the contribution from the incomplete switching in the surface layer increases at the expense of an increase in the residual depolarization field $E_{rd}(T) \sim (T_C - T)^{1/2}$ (under the assumption that the change in the dielectric gap thickness is disregarded). It is also evident that, at temperatures near T_C, the sizes of vestigial domains are small at a relatively high conductivity and the contribution from this effect can be ignored.

It is seen from Fig. 3 that, as the temperature decreases, the spontaneous polarization determined from the optical and magnetic resonance measurements decreases compared to the hypothetical polarization $P_s^2(T)$ (solid line). In order to explain this difference, let us consider the data reported in the monograph by Fridkin [18]. In this work, it was shown that, after screening of the residual depolarization field E_{rd} (3) due to the redistribution of charge carriers, the electric field coinciding in sign with the depolarization field is retained in the bulk of the ferroelectric and the lower the temperature, the stronger the electric field. This field induces a polarization that partially compensates for the spontaneous polarization P_s. The resultant mean polarization, which is measured using the optical and EPR methods, can be evaluated from the expression

$$P = P_s\frac{2}{\sqrt{3}}\cos\frac{1}{3}\left(\arccos\left\{\frac{-E/2\beta}{|\alpha/3\beta|^{3/2}}\right\}\right), \quad (4)$$

which is one of the roots of the equation

$$(4\pi/C)(T - T_C)P + \beta P^3 - E = 0, \quad (5)$$

where $(4\pi/C)(T - T_C) = \alpha$. This root is real at temperatures far away from the ferroelectric transition point and in weak electric fields compared to the depolarization field. It is evident that the field E in expression (4) should be close in order of magnitude to the internal bias field. According to the measurements performed in [19], the latter field for PGO crystals at room temperature is equal to 1–1.5 kV/cm. The estimation made for these fields according to formula (4) with the parameters obtained in Section 6 for the thermodynamic potential (1) leads only to an insignificant decrease in P_s (≈0.1%) and leaves the results of the optical and magnetic resonance measurements unexplained (Fig. 3). In the case of electrical measurements, this mechanism should be more efficient because of the longer time of internal screening [19].

Therefore, the decrease in the spontaneous polarization P_s (determined from the electrical measurements) observed with a decrease in the temperature can be qualitatively explained by the joint action of the aforementioned mechanisms. The elucidation of the mechanisms responsible for the different behavior of the spontaneous polarization $P_s^2(T)$ obtained from optical and EPR measurements calls for further investigation into the temperature dependence $P_s(T)$ for the same samples but with the use of different experimental techniques.

5. HIGH-TEMPERATURE ANOMALIES

Rumyantsev *et al.* [5] observed a small jump in the temperature dependence of the b_{20} parameter for Gd^{3+} trigonal centers in PGO crystals at $T \sim 640$ K. This jump can be associated with the specific features that manifest themselves in temperature anomalies of the lattice parameter, dc conductivity, permittivity (at ~570 K) [7], birefringence, optical axis orientation (~660 K) [8], and exoelectron emission [9]. In the present work, this feature was analyzed using the electron paramagnetic resonance of Mn^{2+} impurity ions, because the b_{20} parameter for these ions is one order of magnitude larger [22] than that for Gd^{3+} centers [11].

Careful measurements of the location of the Mn^{2+} EPR lines ($B \parallel C_3$) at temperatures up to 660 K revealed a nearly linear variation (without any features) in the b_{20} parameter in the paraelectric phase. These measurements also demonstrated that, at $T > 550$ K, the high-field wings of all the hyperfine components of the $1/2 \longleftrightarrow 3/2$ transition are identically broadened, whereas the lines of other transitions (at $B \parallel C_3$ and $B \perp C_3$) remain symmetric. It was found that the observed broadening of the spectral lines increases with an increase in the temperature.

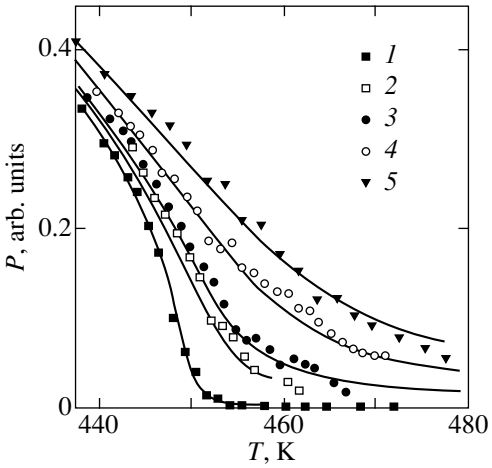

Fig. 4. Temperature dependences of the polarization for PGO crystals in different electric fields *E*: (*1*) 0, (*2*) 2.5, (*3*) 4, (*4*) 10, and (*5*) 17.5 kV/cm. Solid lines show the approximations according to relationship (5).

A detailed examination of the evolution of the EPR spectra for Gd^{3+} trigonal centers revealed an asymmetric broadening of the Gd^{3+} EPR signals at temperatures above 600 K ($B \parallel C_3$), except for the signals corresponding to the $1/2 \longleftrightarrow -1/2$ transition.

Analysis of the possible reasons for the broadening of the EPR signals allowed us to draw the inference that the observed effect is associated with an uncontrollable temperature gradient across the sample. This is confirmed by the fact that the character of the broadening depends on the sample shape and that the broadening of the Mn^{2+} EPR lines is observed only in the case of the transition ($1/2 \longleftrightarrow 3/2$) for which the value of $\partial B_{res}/\partial T$ is maximum.

Thus, the uncontrollable temperature gradient can be responsible for the distortion of the spectral line shape and, hence, can lead to the error in determining the location of the resonance lines. Most likely, it is because of this uncontrollable temperature gradient that the authors of [5] made the inference that there is an additional feature in the temperature dependence of the location of the Gd^{3+} EPR lines for PGO crystals at temperatures above the T_C point.

6. POLARIZATION OF PGO CRYSTALS IN AN ELECTRIC FIELD

In order to make certain that the ferroelectric transition in PGO crystals is the second-order phase transition, we determined the temperature dependences of the polarization in different electric fields (Fig. 4). For this purpose, we measured the differences in the locations of resonance lines attributed to the $1/2 \longleftrightarrow 3/2$ transition in Gd^{3+} centers (at $\theta = 63°$ and $\varphi = 0°$), which form the domain doublet in the ferroelectric phase. The dependences for different electric fields were obtained using different samples, because they experienced a noticeable degradation in subsequent cycles of measurements.

The electric field applied to the sample induces a considerable polarization at temperatures above the ferroelectric transition point [23]. It is worth noting that, in the absence of an external electric field, an appreciable polarization tail is also observed in the paraelectric phase.

The solid lines in Fig. 4 represent the results of the approximation of the experimental points measured at temperatures above 420 K. This approximation was performed according to relationship (5) (which is characteristic of second-order phase transitions) with the parameters $C = 6600$ K and $\beta = 0.94 \times 10^{-9}$ (esu/cm^2)$^{-2}$. Since the absolute values of the polarization cannot be directly determined from optical and magnetic resonance measurements, these parameters were calculated from the value of $P_s(295\ \text{K}) = 4.8\ \mu\text{C/cm}^2$ [3].

The polarization tail observed in the paraelectric phase in the absence of an external electric field (Fig. 4, curve *1*) can be attributed to the internal bias field with a strength of 0.18 kV/cm. With allowance made for the temperature difference, this value is in reasonable agreement with the results obtained in [19].

ACKNOWLEDGMENTS

We are grateful to E.L. Rumyantsev and A.E. Nikiforov for their participation in discussions of the results and A.V. Kukushkin for supplying the experimental data.

This work was supported in part by the American Foundation for Civilian Research and Development for the promotion of cooperation with scientists from the New Independent States of the former Soviet Union, grant no. REC-005.

REFERENCES

1. Y. J. Iwata, J. Phys. Soc. Jpn. **43**, 961 (1977).
2. M. I. Kay, R. E. Newnham, and R. W. Wolfe, Ferroelectrics **9**, 1 (1975).
3. H. Iwasaki, S. Mjyazawa, H. Koizumi, *et al.*, J. Appl. Phys. **43**, 4907 (1972).
4. V. N. Gavrilov, A. G. Zakhar'yants, É. V. Zolotoyabko, *et al.*, Fiz. Tverd. Tela (Leningrad) **25**, 10 (1983) [Sov. Phys. Solid State **25**, 4 (1983)].
5. E. L. Rumyantsev, V. A. Vazhenin, and M. S. Gol'dshteĭn, Fiz. Tverd. Tela (Leningrad) **21** (8), 2522 (1979) [Sov. Phys. Solid State **21**, 1457 (1979)].
6. V. V. Dem'yanov and V. D. Sal'nikov, Fiz. Tverd. Tela (Leningrad) **16** (12), 3626 (1974) [Sov. Phys. Solid State **16**, 2353 (1974)].
7. A. A. Bush and Yu. N. Venevtsev, Izv. Akad. Nauk SSSR, Neorg. Mater. **17** (2), 302 (1981).
8. M. Malinovski, A. Pietraszko, and M. Polomska, Phys. Status Solidi A **41**, K55 (1977).

9. K. H. Germann, W. Mueller-Lierheim, H. H. Otto, and T. Suski, Phys. Status Solidi A **35**, K165 (1976).
10. G. I. Rozenman and E. I. Boĭkova, Kristallografiya **23**, 644 (1978) [Sov. Phys. Crystallogr. **23**, 359 (1978)].
11. A. N. Babushkin, Author's Abstract of Candidate's Dissertation (Ural State Univ., Sverdlovsk, 1986).
12. V. A. Vazhenin, Yu. A. Sherstkov, and K. M. Zolotareva, Fiz. Tverd. Tela (Leningrad) **17** (8), 2485 (1975) [Sov. Phys. Solid State **17**, 1655 (1975)].
13. O. G. Vlokh, *Spatial Dispersion Phenomena in Parametric Crystal Optics* (Vishcha Shkola, Lvov, 1984).
14. A. E. Nikiforov, A. I. Krotkiĭ, V. A. Vazhenin, and Yu. M. Kartashev, Fiz. Tverd. Tela (Leningrad) **21** (10), 2900 (1979) [Sov. Phys. Solid State **21**, 1672 (1979)].
15. V. A. Vazhenin and K. M. Starichenko, *Quantum Chemistry and Radiospectroscopy of Solids*, Preprint, Inst. Khimii UNTs Akad. Nauk SSSR (Inst. of Chemistry, Ural Research Center, USSR Academy of Science, Sverdlovsk, 1984), p. 23.
16. V. Ya. Shur, in *Ferroelectricity and Related Phenomena*, Vol. 10: *Ferroelectric Thin Films: Synthesis and Basic Properties*, Ed. by C. A. Paz de Araujo, J. F. Scott, and G. W. Taylor (Gordon and Breach, Amsterdam, 1996), Chap. 6, pp. 153–192.
17. V. Ya. Shur and E. L. Rumyantsev, Ferroelectrics **191**, 319 (1997).
18. V. M. Fridkin, *Photoferroelectrics* (Nauka, Moscow, 1976; Springer-Verlag, Berlin, 1979).
19. V. Ya. Shur, Yu. L. Popov, and N. V. Korovina, Fiz. Tverd. Tela (Leningrad) **26** (3), 781 (1984) [Sov. Phys. Solid State **26**, 471 (1984)].
20. V. Ya. Shur, A. L. Gruverman, N. V. Korovina, *et al.*, Fiz. Tverd. Tela (Leningrad) **30** (1), 299 (1988) [Sov. Phys. Solid State **30**, 172 (1988)].
21. V. Janovec, Czech. J. Phys. **9** (4), 468 (1959).
22. V. A. Vazhenin, A. D. Gorlov, and A. P. Potapov, Fiz. Tverd. Tela (Leningrad) **28** (7), 2043 (1986) [Sov. Phys. Solid State **28**, 1142 (1986)].
23. A. E. Devonshire, Philos. Mag., Suppl. **3** (10), 85 (1954).

Translated by O. Borovik-Romanova

Physics of the Solid State, Vol. 43, No. 10, 2001, pp. 1958–1961. Translated from Fizika Tverdogo Tela, Vol. 43, No. 10, 2001, pp. 1880–1883.

MAGNETISM AND FERROELECTRICITY

Behavior of a Lead Scandium Tantalate Ferroelectric in an AC Electric Field

L. S. Kamzina and N. N. Kraĭnik

Ioffe Physicotechnical Institute, Russian Academy of Sciences, Politekhnicheskaya ul. 26, St. Petersburg, 194021 Russia

Received March 16, 2001

Abstract—The behavior of an incompletely ordered lead scandium tantalate ferroelectric (the degree of ordering $s = 0.8$) in the region of the spontaneous ferroelectric transition is studied in ac electric fields by dielectric and optical methods. Dielectric nonlinearity of two types is observed. In fields above 2 kV/cm, the nonlinearity is caused by induced polarization effects and macrohysteresis behavior, whereas in weak fields, it is most probably associated with the dynamics of domain walls and/or phase boundaries. *© 2001 MAIK "Nauka/Interperiodica".*

1. INTRODUCTION

$PbB'_{1/2}B''_{1/2}O_3$-type compounds, which, in addition to typical relaxor behavior, exhibit a spontaneous transition between the ferroelectric and relaxor states in the absence of an electric field at temperatures below the maximum of the permittivity, occupy a particular place among the large number of disordered perovskite ferroelectrics. The degree of diffuseness of the phase transition between the ferroelectric and paraelectric phases depends on the degree of ordering s of the B' and B'' ions in the octahedral lattice sites. Among these compounds are certain compositions of the PLZT ceramics [1, 2], as well as single crystals and the ceramics of lead scandium tantalate $PbSc_{1/2}Ta_{1/2}O_3$ (PST) [3] and lead scandium niobate $PbSc_{1/2}Nb_{1/2}O_3$ (PSN) [4]. The degree of ordering of the B' and B'' ions (s) in the latter two compounds can be varied by properly varying the temperature regime of single-crystal growth or by thermally treating already grown samples. Materials with a long-range order ($s \sim 1$) undergo a first-order ferroelectric phase transition, have no intermediate relaxor phase, and, hence, are devoid of all the main features characteristic of relaxor compounds. As the degree of ordering s decreases, the temperature range within which the relaxor state can exist broadens and the materials exhibit typical relaxor features; however, the spontaneous phase transition persists even in disordered materials. Chu *et al.* [5] showed that the relaxor state in partially ordered PST ceramics exists within a temperature range ~150°C wide and extends up to 170°C. In our earlier work [6], we found that a pure paraelectric phase exists only above 400°C. This suggests the possible use of such materials to relate the conventional ferroelectric to the relaxor behavior in the same compound without application of external action, as well as to follow the relation between them in dc and ac electric fields.

The existence of a spontaneous first-order ferroelectric transition in PST crystals was also confirmed by a number of dielectric and optical measurements. For instance, a sharp drop in the permittivity was observed at a temperature T_d in a sample cooled below the temperature of the maximum of ε [1], the dielectric parameters were found to be frequency-independent within a temperature range immediately below T_d [5], and an anomaly in the heat of the transition and double dielectric hysteresis loops were observed above the spontaneous transition temperature T_d [3, 7]. Small-angle light scattering (SAS) measurements performed on stoichiometric PST crystals differing in degree of ion ordering revealed an anomalously narrow peak at T_d, indicating the percolation nature of the spontaneous transition [8].

It should be pointed out that these unusual properties are characteristic only of the stoichiometric PST and PSN compositions. An attempt was made to study the effect of lead vacancies on the occurrence of a spontaneous ferroelectric transition in PST ceramics [4]. It was shown that the disorder in the arrangement of Sc^{3+} and Ta^{5+} ions does not in itself inhibit spontaneous ferroelectric transitions in disordered compounds and that only a specific number of lead vacancies is capable of suppressing a spontaneous transition and stimulating a purely relaxor behavior.

The effect of a dc electric field on the character of the spontaneous phase transition and the relaxor behavior in such compounds has recently become the subject of many studies. This interest stems from the fact that the electric field exerts different influences on these states and affects the homogeneity and stability of the ferroelectric state. It was shown that the temperature of the spontaneous ferroelectric transition T_d increases linearly with an increase in the field amplitude in almost ordered PST and PSN samples. This dependence deviates slightly from a straight line for disor-

dered samples [5, 9, 10]. A dc electric field narrows the temperature range of existence of the relaxor phase.

However, in order to fully understand the dynamics of the polar regions and the nature of the relaxor behavior, as well as the mechanisms responsible for the dielectric nonlinearity and its relation to the crystal structure, it is necessary to perform experiments in ac electric fields of various frequencies and amplitudes. The available data relate primarily to the effect of the ac field amplitude in extreme cases, namely, in weakly disordered compounds with a clearly pronounced phase transition [11] or in strongly disordered substances lacking long-range order [1]. The behavior of lead magnium niobate (PMN), a typical relaxor, in ac fields [12–14], as well as of conventional ferroelectrics with a normal domain structure has been studied fairly well. Polarization switching in ferroelectrics with a distinct phase transition occurs in rather strong fields, and the dielectric hysteresis is not induced until the amplitude of the ac field has exceeded the coercive field. The permittivity of a relaxor compound exhibits a strong dependence on the ac field amplitude already in weak electric fields, which is primarily connected with the interface dynamics of the polar regions [15].

The dielectric nonlinearity of substances occupying an intermediate position between normal ferroelectrics and relaxors has practically not been studied, excepting the work by Tan and Viehland [1], who investigated the changes in the dielectric nonlinearity in PLZT ceramics, which are associated with changes in the La content.

This paper reports on the effect the amplitude of an ac electric field exerts on the dielectric response of stoichiometric disordered PST crystals near the temperature of the spontaneous ferroelectric transition and in the intermediate phase. This study was aimed at establishing which polarization switching mechanism is dominant and how it is connected with changes in the nature of the relaxing elements.

2. EXPERIMENTAL TECHNIQUE AND SAMPLES

The permittivity and $\tan\delta$ of PST crystals (the degree of ordering $s = 0.8$, $T_d = 24°C$, and $T_{max\varepsilon} = 28°C$) were measured along the ⟨100⟩ crystallographic direction at a frequency of 1 kHz under heating from 0 to 70°C at a rate of 1 K/min. The amplitude of the ac measuring field was varied from 1 to 600 V/cm. The optical transmission and small-angle light scattering were studied at 50 Hz in the same temperature range in ac electric fields of up to 4 kV/cm.

3. EXPERIMENTAL RESULTS AND DISCUSSION

Figure 1 presents temperature dependences of the permittivity (curves *1–3*) and the loss tangent (curves *1'*, *3'*) for a stoichiometric PST crystal at various measuring field amplitudes. It is seen that, as the amplitude of

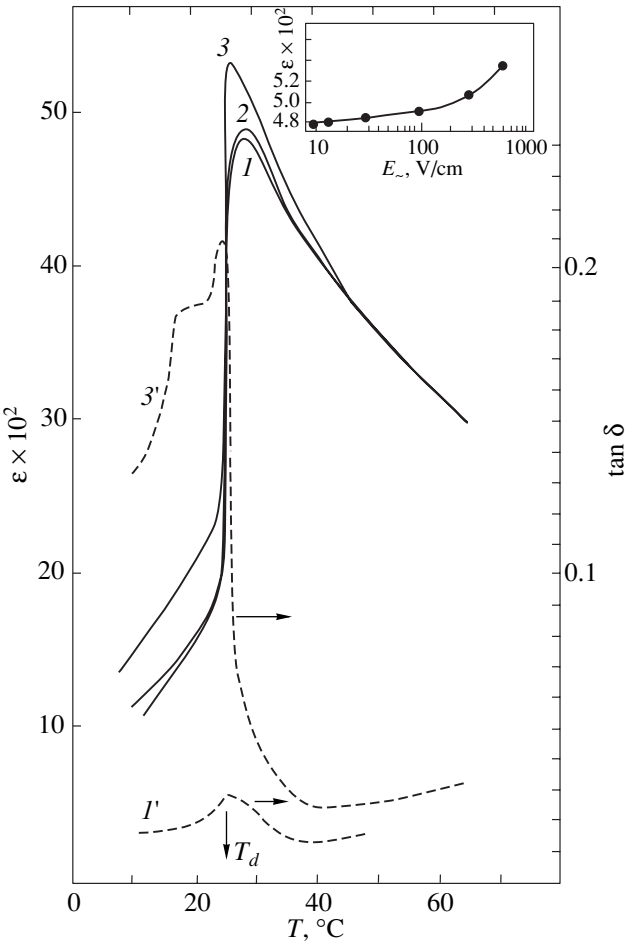

Fig. 1. Temperature dependences of (*1–3*) the permittivity ε and (*1'*, *3'*) the loss tangent ($\tan\delta$) for a PST crystal ($s = 0.8$) at different amplitudes of the ac measuring field E (V/cm): (*1*, *1'*) 1, (*2*) 125, and (*3*, *3'*) 600. The ac field frequency is 1 kHz. The inset shows the dependence of the maximum ε on the ac field amplitude.

the measuring field increases to 600 V/cm, T_{max} slightly shifts toward lower temperatures (by ~2°C) and ε at the maximum increases (inset in Fig. 1). In fields below 100 V/cm, the maximum value of ε remains practically constant; only in stronger fields, ε_{max} depends nonlinearly on the ac field amplitude. At 600 V/cm, the maximum value of ε varies by ~10%. Near the point of the spontaneous phase transition T_d, the temperature dependences of ε coincide within the field range covered (curves *1–3*). The nonlinearity observed in the PST crystal under study is substantially smaller than that in the classical relaxor PMN [14]. In our crystal, the degree of ordering *s* is 80% and, hence, only 20% of the sample volume remains disordered; this is what accounts for the substantially smaller nonlinearity. An increase in the ac field amplitude results in a shift of the temperature of the maximum of ε toward lower temperatures but leaves the position of the spontaneous ferroelectric transition point unchanged within the experi-

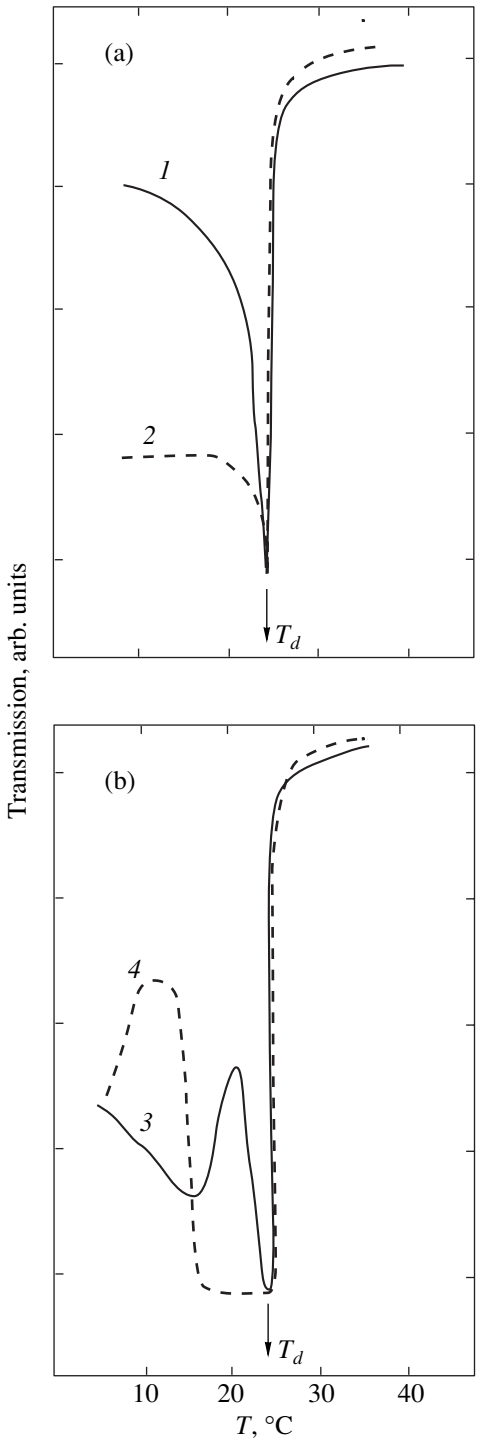

Fig. 2. Dependences of the optical transmission on temperature for a PST crystal at different amplitudes of the ac measuring field E (kV/cm): (a) (*1*) 0 and (*2*) 1; (b) (*3*) 2 and (*4*) 4. The ac field frequency is 50 Hz.

mental accuracy. This is confirmed by the temperature dependences of $\tan\delta$ (curves *1'*, *3'* in Fig. 1). The maximum of $\tan\delta$ lies at the transition point T_d and does not depend on the measuring field amplitude within the field range covered.

As is seen from Fig. 1, the temperatures of the spontaneous phase transition and the maximum of ε in the PST crystal are fairly close to one another; we may recall also that the more ordered the ions are, the smaller this temperature interval is. Moreover, the anomaly in ε at the spontaneous phase transition is not very distinct, with only a sharp drop of ε being seen as the sample is cooled. Therefore, dielectric measurements alone are insufficient for reliably describing the effect of an ac electric field on the pattern and position of these anomalies.

As was shown in our earlier studies [8, 9], the spontaneous phase transition in these crystals is of a percolation nature; hence, the average cluster size of the new phase at the percolation threshold tends to the size of the sample, this transition brings about the formation of a large-scale nonuniform structure, and the phase transition is accompanied by the appearance of anomalously narrow SAS peaks and, as a consequence, by a minimum in the optical transmission.

Figures 2a and 2b display temperature dependences of the optical transmission at a frequency of 50 Hz for the PST crystal on which the dielectric measurements were made. We readily see that the minimum in the optical transmission lies at T_d and that this temperature does not depend on the electric field within the range $0 < E < 2$ kV/cm (curves *1*, *2* in Fig. 2a). As the ac field increases above 2 kV/cm, the minimum transmission that indicates the formation of a large-scale structure extends over an ever broader temperature range. At $E = 4$ kV/cm, it becomes observable below T_d and extends over a temperature range ~8°C wide (curves *3*, *4* in Fig. 2b).

Let us discuss the results obtained. To establish the mechanism responsible for the observed nonlinearity in strong and weak fields, we consider the dielectric hysteresis loops for ceramic PST samples presented in [3]. At temperatures $T < T_d$, a disordered ceramic PST exhibits a conventional hysteresis loop with a small coercive force (~4 kV/cm). As the temperature of the spontaneous ferroelectric transition is approached, the coercive force decreases. At temperatures slightly above T_d, stoichiometric disordered PST samples in the intermediate relaxor phase exhibit distinct double dielectric hysteresis loops. These loops confirm the onset of a first-order phase transition. Similar loops are observed in our PST crystals as well. As follows from [3], in weak fields of up to 1 kV/cm, the dependence $P(E)$ in the relaxor state at $T > T_d$ is practically linear and, hence, the nonlinearity observed in the dielectric response in fields of up to 1 kV/cm (see inset in Fig. 1) is most probably connected with the dynamics of the domain and interface states rather than with the hysteresis behavior, which is induced by the electric field.

The nonlinearity changes its pattern with increasing the ac field. At temperatures slightly below T_d, a field of 2 kV/cm (curve *3* in Fig. 2b) is high enough to induce macroscopic polarization and formation of a macro-

domain structure within a narrow temperature range (~2°C); this is what is responsible for the minimum transmission. Increasing the field to 4 kV/cm (curve *4* in Fig. 2b) broadens the temperature range of existence of the field-induced macrodomain structure and macroscopic polarization to 8°C.

4. CONCLUSION

Thus, our dielectric and optical studies of stoichiometric disordered PST single crystals clearly indicate two different types of dielectric nonlinearity in these crystals. One of them is observed in fields of up to 2 kV/cm and is related, most probably, to the dynamics of domain walls and/or phase boundaries; the other, to field-induced polarization effects and macrohysteresis behavior. The behavior of domain processes near T_d in ac fields calls for further investigation.

ACKNOWLEDGMENT

This work was supported by the Russian Foundation for Basic Research, project no. 01-02-17801.

REFERENCES

1. Q. Tan and D. Viehland, Phys. Rev. B **53** (21), 14103 (1996).
2. O. Bidault, N. Manguy, and B. Dkhil, Ferroelectrics **240** (1–4), 191 (2000).
3. F. Chu, N. Setter, and A. K. Tagantsev, J. Appl. Phys. **74** (8), 5129 (1993).
4. F. Chu, I. M. Reaney, and N. Setter, J. Appl. Phys. **77** (4), 1671 (1995).
5. F. Chu, C. R. Fox, and N. Setter, J. Am. Ceram. Soc. **81** (6), 1577 (1998).
6. L. S. Kamzina, N. N. Kraĭnik, L. M. Sapozhnikova, *et al.*, Pis'ma Zh. Tekh. Fiz. **14** (19), 1760 (1988) [Sov. Tech. Phys. Lett. **14**, 764 (1988)].
7. F. Chu, I. M. Reaney, and N. Setter, J. Appl. Phys. **78** (7), 1947 (1995).
8. L. S. Kamzina and A. L. Korzhenevskiĭ, Pis'ma Zh. Éksp. Teor. Fiz. **50** (3), 146 (1989) [JETP Lett. **50**, 163 (1989)].
9. L. S. Kamzina and N. N. Kraĭnik, Fiz. Tverd. Tela (St. Petersburg) **42** (1), 136 (2000) [Phys. Solid State **42**, 142 (2000)].
10. L. S. Kamzina and N. N. Kraĭnik, Fiz. Tverd. Tela (St. Petersburg) **42** (9), 1664 (2000) [Phys. Solid State **42**, 1712 (2000)].
11. S. Li, W. Cao, and L. E. Cross, J. Appl. Phys. **69**, 7219 (1991).
12. A. K. Tagantsev and A. E. Glazounov, Phys. Rev. B **57** (1), 18 (1998).
13. A. E. Glazounov, A. K. Tagantsev, and A. J. Bell, Phys. Rev. B **53** (17), 11281 (1996).
14. D. Vieland, M. Wittig, and L. E. Cross, Philos. Mag. A **64**, 835 (1991).
15. A. E. Glazounov, A. K. Tagantsev, and A. J. Bell, Ferroelectrics **184**, 217 (1996).

Translated by G. Skrebtsov

Physics of the Solid State, Vol. 43, No. 10, 2001, pp. 1962–1967. Translated from Fizika Tverdogo Tela, Vol. 43, No. 10, 2001, pp. 1884–1889.

LATTICE DYNAMICS AND PHASE TRANSITIONS

Second-Order Terms in the Phonon–Phason Dynamic Matrix of an Icosahedral Quasicrystal

S. B. Rochal

Rostov State University, pr. Stachki 194, Rostov-on-Don, 344090 Russia

e-mail: rochal@phys.runnet.ru

Received January 11, 2001

Abstract—They fourth-order terms (in the wave vector components) of the phonon–phason dynamic matrix are obtained for an icosahedral quasicrystal. In this order, the dynamic matrix has nine independent coefficients: three phonon–phonon, three phason–phonon, and three phason–phason coefficients. The number of independent coefficients in the phonon block of the constructed dynamic matrix is greater by unity than that for an isotropic medium. The corresponding features of acoustic phonon dispersion in the *i*-AlPdMn alloy considered. It is shown that when the fourth-order terms are taken into account, the intensity of diffuse scattering in the vicinity of Bragg reflections decreases in accordance with the law $\alpha/(q^2 + \beta q^4)$, where q is the distance to a reflection in the reciprocal space and coefficients α and β depend on the direction of vector **q**. © *2001 MAIK "Nauka/Interperiodica".*

1. INTRODUCTION

The quasicrystals discovered in 1984 [1] possess additional Goldstone degrees of freedom [2] which are absent in the crystal state. In contrast to conventional modulated crystal phases which also possess phason degrees of freedom, phason deformations in quasicrystals are associated with discrete displacements of atoms or jumps. In the long-wavelength limit, the energy of phason modes, like the energy of acoustic modes, tends to zero [2]. The phason mode in quasicrystals corresponds to correlated atomic jumps or diffusion [3, 4] rather than to continuous atomic displacements. Phason degrees of freedom in quasicrystals at room temperature are frozen. The activation of the phason degrees of freedom upon heating modifies the physical properties of quasicrystals. In the quasicrystalline alloy AlPdMn, an elevation of temperature from 700 to 1100 K increases the heat capacity at constant volume by a factor exceeding 1.5 [5]. According to the well-known theorems from crystal physics, the presence of the fivefold axis leads to isotropy of the fourth-rank tensor with respect to the rotation about this axis; consequently, the existence of the icosahedral symmetry leads to complete isotropy of any tensor of rank four. For this reason, the form of the elastic moduli of an icosahedral quasicrystal is the same as in the isotropic case. However, the high-frequency investigation of natural vibrations [6] indicates that there is a difference in the effective shear moduli measured in an AlPdMn single crystal along the two- and fivefold axes. The splitting becomes clearly distinguishable at temperatures above 700°C. This effect can be interpreted as the result of the dynamic interaction between the phonon and phason degrees of freedom in the framework of the model proposed in [7].

The central object in various problems associated with the phonon–phason dynamic elasticity of quasicrystals is the phonon–phason dynamic matrix (DM) $C_{ij}(\mathbf{q})$, where $i, j = 1, 2, \ldots, 6$ and **q** is the three-component wave vector. As an example of the first publications in which the DM was obtained for an icosahedral quasicrystals, we can consider [3]. The physical meaning of the C_{ij} matrix is quite simple and is similar to that of the (3×3) DM of acoustic phonons in an ordinary crystal. The six-component vector $U_i(\mathbf{q})$ has three components describing the amplitudes of usual (phonon) waves with the wave vector **q** and three components characterizing the amplitudes of phason waves, whereas the six-component vector $C_{ij}U_j$ is equal to the amplitude of the elastic restoring force. Its first three components correspond to ordinary and the second three to generalized phason forces. Accordingly, the scalar quantity $1/2C_{ij}U_i(\mathbf{q})U_j(-\mathbf{q}) = E(\mathbf{q})$ is equal to the volume density of the phonon–phason elastic energy in the reciprocal space. Only the first elements of the DM of an icosahedral crystal, which are quadratic in the wave vector components and significant at small magnitudes of vector **q**, have been calculated to date. Hence, the solution of the elastodynamic problems is possible only in the long-wavelength limit corresponding to the simplest quadratic dependence of the energy of phonon and phason excitations on the wave vector. For example, we note that even the DM of a periodic 1D linear atomic chain corresponds to a more complex dispersion: $2\lambda/M(1 - \cos qa)$, where a is the period, M is the mass of the atoms, and λ is the elastic constant [8]. The present work is aimed at constructing higher-order terms of the DM, which make it possible to account for the next power in the dependence of the energy of phonon–phason modes on the wave vector.

1063-7834/01/4310-1962$21.00 © 2001 MAIK "Nauka/Interperiodica"

2. GROUP-THEORETIC ANALYSIS

In the expression for the elastic energy of a quasicrystal, the model of a continuous medium with icosahedral symmetry is traditionally used. The energy is written as the sum of differential invariants of spatial first derivatives of the fields of phonon and phason displacements [2]. The Fourier transformation of this expression is practically reduced to formal substitutions:

$$\partial_i w_j(\mathbf{R}) \longrightarrow q_i w_j(\mathbf{q}),$$
$$E_{ij}(\mathbf{R}) \longrightarrow 1/2(q_j u_i(\mathbf{q}) + q_i u_j(\mathbf{q})),$$

where u_i and w_j are two components of the six-dimensional vector $\mathbf{U}$ and symbol $\partial_i w_j$ indicates the derivative of the ith component of the phason field $\mathbf{w}$ with respect to the ith component of the radius vector. The quantities $\partial_i w_j$ and E_{ij} are the tensor components of phason and ordinary deformations. Vector $\mathbf{U}(\mathbf{R})$ characterizes the field of generalized displacements in the direct space, and vector $\mathbf{U}(\mathbf{q})$ characterizes the amplitudes of these displacements in the reciprocal space. Retaining the definition of the five elastic coefficients of the icosahedral quasicrystal and using the system of coordinates [9], quadratic in the wave vector components, we can write the elastic energy density in the reciprocal space in the form

$$E = \lambda I_1 + \mu I_2 + K_1 I_3 + K_2 I_4 + K_3 I_5, \tag{1}$$

where invariants I_j can be expressed in the following form:

$$I_1 = 1/2(\mathbf{uq})^2, \quad I_2 = 1/2\{(\mathbf{uq})^2 + |\mathbf{u}|^2|\mathbf{q}|^2\},$$
$$I_3 = 1/2|\mathbf{w}|^2|\mathbf{q}|^2,$$
$$I_4 = 1/2\{-(|\mathbf{w}|^2|\mathbf{q}|^2)/3 + 4[q_1q_2w_1w_2 + \tau q_3^2 w_1^2 - 1/\tau q_2^2 w_1^2 + \text{cyclic permutation}]\}; \tag{2}$$
$$I_5 = \{q_1^2 u_1 w_1 + 1/\tau q_1^2 u_2 w_2 - \tau q_1^2 u_3 w_3 + 2/\tau q_1 q_2 u_1 w_1 - 2\tau q_1 q_2 u_2 w_1 + \text{cyclic permutation}\}.$$

The components of the DM, quadratic in the wave vectors, can be obtained as the second derivatives of energy (1) with respect to generalized amplitudes:

$$C_{ij} = \frac{\partial^2 E}{\partial U_i \partial U_j}. \tag{3}$$

The blocks of this matrix coincide with the matrices presented in [9], but after the renotation and modern redefinition of the elastic moduli [10] (see matrices (17)–(19) in the Appendix), or with the results obtained in [10] after the correction of two misprints in the phonon–phason block. It should be noted that the construction of the next terms in the powers of the wave vector components in the model of a continuous medium within the traditional approach is equivalent to the construction of the elastic energy quadratic in the higher-order spatial derivatives of the field $\mathbf{U}(\mathbf{R})$.

It would be much simpler to directly construct the invariant terms of the Fourier transform of the elastic energy instead of constructing detailed differential invariants. In fact, all the linearly independent invariants quadratic in the field components $\mathbf{U}(\mathbf{q})$ and containing the fourth power of the components of the wave vector $\mathbf{q}$ are required. It should be borne in mind that the wave vector components and the components of field $\mathbf{u}$ are transformed in accordance with the ordinary (first) vector representation of group I_h, while the components of field $\mathbf{w}$ are transformed in accordance with the second vector representation of the same group. Taking advantage of the fact that both vector representations become equivalent when group I_h is limited by group T_h, the problem can be solved consistently. We will first construct the invariants of group T_h. As generators of this group, we can choose the following symmetry elements: C_2^x, C_2^y, C_3^{xyz}, C_2^{xy}, and I. The matrices corresponding to these generators in the vector representation are given below:

$$m(C_2^x) = \begin{pmatrix} 1 & 0 & 0 \\ 0 & -1 & 0 \\ 0 & 0 & -1 \end{pmatrix}, \quad m(C_2^y) = \begin{pmatrix} -1 & 0 & 0 \\ 0 & 1 & 0 \\ 0 & 0 & -1 \end{pmatrix},$$
$$m(C_3^{xyz}) = \begin{pmatrix} 0 & 0 & 1 \\ 1 & 0 & 0 \\ 0 & 1 & 0 \end{pmatrix}, \quad m(C_2^{xy}) = \begin{pmatrix} 0 & 1 & 0 \\ 1 & 0 & 0 \\ 0 & 0 & -1 \end{pmatrix},$$
$$m(I) = \begin{pmatrix} -1 & 0 & 0 \\ 0 & -1 & 0 \\ 0 & 0 & -1 \end{pmatrix}.$$

In all, there exist nine fourth-degree invariants constructed from the components of the wave vector and the components of another vector $\mathbf{v}$:

$$J_1 = q_1^4 v_1^2 + q_2^4 v_2^2 + q_3^4 v_3^2,$$
$$J_2 = q_1^4 v_2^2 + q_2^4 v_3^2 + q_3^4 v_1^2,$$
$$J_3 = q_1^4 v_3^2 + q_2^4 v_1^2 + q_3^4 v_2^2, \tag{4}$$
$$J_4 = q_1^3 q_2 v_1 v_2 + q_2^3 q_3 v_2 v_3 + q_3^3 q_1 v_3 v_1,$$
$$J_5 = q_1^3 q_3 v_1 v_3 + q_2^3 q_1 v_2 v_1 + q_3^3 q_2 v_3 v_2,$$
$$J_6 = q_1^2 q_2^2 v_1^2 + q_2^2 q_3^2 v_2^2 + q_3^2 q_1^2 v_3^2,$$
$$J_7 = q_1^2 q_2^2 v_2^2 + q_2^2 q_3^2 v_3^2 + q_3^2 q_1^2 v_1^2,$$
$$J_8 = q_1^2 q_2^2 v_3^2 + q_2^2 q_3^2 v_1^2 + q_3^2 q_1^2 v_2^2,$$
$$J_9 = q_1^3 q_2 q_3 v_2 v_3 + q_2^3 q_3 q_1 v_3 v_1 + q_3^3 q_1 q_2 v_1 v_2.$$

Upon rotation about the fivefold axis lying along direction $\langle 1, \tau, 0\rangle$, where $\tau = (\sqrt{5} + 1)/2$, vector **q** is transformed with the help of the matrix

$$\frac{1}{2}\begin{pmatrix} 1/\tau & \tau & -1 \\ -\tau & 1 & 1/\tau \\ 1 & 1/\tau & \tau \end{pmatrix}. \quad (5)$$

Vector **u** is transformed similarly, while vector **w** is transformed under the action of the matrix

$$\frac{1}{2}\begin{pmatrix} -\tau & -1/\tau & -1 \\ 1/\tau & 1 & -\tau \\ 1 & -\tau & -1/\tau \end{pmatrix}. \quad (6)$$

Carrying out averaging of invariants (4) over group I_h and taking vector **u** for **v**, we obtain three linearly independent phonon–phonon invariants:

$$\begin{aligned} T_1 &= I_1|\mathbf{q}|^2, \\ T_2 &= I_2|\mathbf{q}|^2, \\ T_3 &= 1/\tau J_2 - \tau J_3 + 8/\tau J_4 - 8\tau J_5 \\ &\quad + 6/\tau J_6 - 6\tau J_7 + 4J_8 + 16J_9. \end{aligned} \quad (7)$$

Thus, the phonon component of the correction to the elastic energy can be written in the form $\Delta E^{\text{phonon}} = \lambda' T_1 + \mu' T_2 + \xi_\parallel T_3$. The terms corresponding to the first and second invariants can be easily obtained by multiplying block (17) in the Appendix by $|\mathbf{q}|^2$ and carrying out the substitution of λ' for λ and μ' for μ. The correction to the phonon–phonon block, which corresponds to T_3, is given in the Appendix in the form of matrix (20).

Taking vector **w** for the quantity **v** and averaging invariants (4) over group I_h, we obtain three linearly independent phason–phason invariants:

$$\begin{aligned} T_4 &= I_3|\mathbf{q}|^2, \\ T_5 &= I_4|\mathbf{q}|^2, \\ T_6 &= 2J_1 - 1/\tau J_2 + \tau J_3 - 4\tau J_4 \\ &\quad + 4/\tau J_5 + 6J_8 - 12J_9. \end{aligned} \quad (8)$$

Finally, the phason component of the correction to the elastic energy can be represented in the form $\Delta E^{\text{phason}} = K_1' T_4 + K_2' T_5 + \xi_\perp T_6$. The terms corresponding to the fourth and fifth invariants can be easily obtained by multiplying block (19) by $|\mathbf{q}|^2$ and substituting K_1' for K_1 and K_2' for K_2. The correction to the phason–phason block, which corresponds to T_6, is given in the Appendix in the form of matrix (21).

Three phonon–phason invariants can be represented in the form of linear combinations of 12 terms, each of which is invariant relative to the action of group T_h:

$$\begin{aligned} S_1 &= q_1^4 u_1 w_1 + q_2^4 u_2 w_2 + q_3^4 u_3 w_3, \\ S_2 &= q_1^4 u_2 w_2 + q_2^4 u_3 w_3 + q_3^4 u_1 w_1, \\ S_3 &= q_1^4 u_3 w_3 + q_2^4 u_1 w_1 + q_3^4 u_2 w_2, \\ S_4 &= q_1^3 q_2 u_1 w_2 + q_2^3 q_3 u_2 w_3 + q_3^3 q_1 u_3 w_1, \\ S_5 &= q_1^3 q_2 u_2 w_1 + q_2^3 q_3 u_3 w_2 + q_3^3 q_1 u_1 w_3, \\ S_6 &= q_1^3 q_2 u_1 w_3 + q_2^3 q_1 u_2 w_1 + q_3^3 q_2 u_3 w_2, \\ S_7 &= q_1^3 q_3 u_3 w_1 + q_2^3 q_1 u_1 w_2 + q_3^3 q_2 u_2 w_1, \\ S_8 &= q_1^2 q_2^2 u_1 w_1 + q_2^2 q_3^2 u_2 w_2 + q_3^2 q_1^2 u_3 w_3, \\ S_9 &= q_1^2 q_2^2 u_2 w_2 + q_2^2 q_3^2 u_3 w_3 + q_3^2 q_1^2 u_1 w_1, \\ S_{10} &= q_1^2 q_2^2 u_3 w_3 + q_2^2 q_3^2 u_1 w_1 + q_3^2 q_1^2 u_2 w_2, \\ S_{11} &= q_1^2 q_2 q_3 u_2 w_3 + q_2^2 q_3 q_1 u_3 w_1 + q_3^2 q_1 q_2 u_1 w_2, \\ S_{12} &= q_1^2 q_2 q_3 u_3 w_2 + q_2^2 q_3 q_1 u_1 w_3 + q_3^2 q_1 q_2 u_2 w_1. \end{aligned} \quad (9)$$

Ultimately, we have

$$\begin{aligned} T_7 &= I_5|\mathbf{q}|^2 = S_1 + 1/\tau S_2 - \tau S_3 + 2/\tau S_4 - 2\tau S_5 \\ &\quad - 2\tau S_6 + 2/\tau S_7 - 1/\tau S_8 + \tau S_9 - S_{10} + 2/\tau S_{11} - 2\tau S_{12}, \\ T_8 &= 5S_1 + (3\tau - 2)S_2 + (1 - 3\tau)S_3 + (12\tau - 8)S_4 \\ &\quad - 4\tau S_5 + (4 - 12\tau)S_6 + (4\tau - 4)S_7 - 6\tau S_8 \\ &\quad + (6\tau - 6)S_9 - 6S_{10} - 12S_{11} - 12S_{12}, \\ T_9 &= (3\tau - 2)S_1 + (9 - 3\tau)S_2 - 3S_3 + 12S_4 \\ &\quad - 8S_5 + 0S_6 + (16 - 12\tau)S_7 + (6\tau - 6)S_8 \\ &\quad - 6S_9 - 6\tau S_{10} + (12 - 12\tau)S_{11} - 24S_{12}. \end{aligned} \quad (10)$$

The phonon–phason component of the correction to the elastic energy can be written as $\Delta E^{\text{inter}} = K_3' T_7 + K_4 T_8 + K_5 T_9$. The terms corresponding to T_8 and T_9 can be obtained by differentiating these invariants with respect to the corresponding generalized amplitudes according to formula (3).

3. DISCUSSION

By way of an example, we consider the dispersion of acoustic phonons in the *i*-AlCuLi alloy, which was measured in [11] at room temperature. The downward deviation of the dispersion dependence $\omega(q)$ from a straight line becomes noticeable even for wave vectors of the order of 0.2 A^{-1}. The difference between the

Table 1. Eigenvalues of matrix (20) for different directions of the wave vector **q** and polarization **u**

$\mathbf{q} = \langle 1, \tau, 0\rangle$		$\mathbf{q} = \langle \tau^2, 1, 0\rangle$		$\mathbf{q} = \langle 1, 0, 0\rangle$	
$\mathbf{u} = \langle 1, \tau, 0\rangle$,	$\delta_{ef} = -6\xi_{\parallel}$	$\mathbf{u} = \langle \tau^2, 1, 0\rangle$,	$\delta_{ef} = 10/9\xi_{\parallel}$	$\mathbf{u} = \langle 1, 0, 0\rangle$,	$\delta_{ef} = 0$
$\mathbf{u} = \langle -\tau, 1, 0\rangle$,	$\delta_{ef} = 2\xi_{\parallel}$	$\mathbf{u} = \langle 1, -\tau^2, 0\rangle$,	$\delta_{ef} = -14/9\xi_{\parallel}$	$\mathbf{u} = \langle 0, 1, 0\rangle$,	$\delta_{ef} = 2/\tau$
$\mathbf{u} = \langle 0, 0, 1\rangle$,	$\delta_{ef} = 2\xi_{\parallel}$	$\mathbf{u} = \langle 0, 0, 1\rangle$,	$\delta_{ef} = -14/9\xi_{\parallel}$	$\mathbf{u} = \langle 0, 0, 1\rangle$,	$\delta_{ef} = -2\tau$

velocities of acoustic phonons propagating in different symmetric directions becomes significant for wave vectors of the order of 0.4 A^{-1}. This effect can be attributed to the contribution of invariant T_3, as a result of which the elastic symmetry of the problem becomes exactly icosahedral. Obviously, invariants I_1, I_2, T_1, and T_2 are isotropic. If we consider that the phason degrees of freedom are frozen (which corresponds to room temperature) and disregard various mechanisms of phonon attenuation, the dispersion relations for transverse and longitudinal acoustic waves can be determined by solving the traditional system of equations

$$c_{ij}(\mathbf{q})u_j = \rho\omega^2 u_i, \tag{11}$$

where $c_{ij}(\mathbf{q})$ is the phonon block of the constructed DM and ρ is the mass density of the quasicrystal. If the wave vector of phonons lies along a five-, three-, or twofold axis (these directions are usually investigated in experiments), the dispersion relations for longitudinal and transverse phonons have the following form:

$$\rho\omega^2 = (\lambda + 2\mu)\mathbf{q}^2 + (\lambda' + 2\mu')\mathbf{q}^4 + \delta_{ef}\mathbf{q}^4, \tag{12}$$

$$\rho\omega^2 = \mu\mathbf{q}^2 + \mu'\mathbf{q}^4 + \delta_{ef}\mathbf{q}^4. \tag{13}$$

Comparison with the experimental data for *i*-AlCuLi [11] shows that the quantities $\lambda' + 2\mu'$ and μ' are negative. The quantities δ_{ef} given in Table 1 are determined by the eigenvalues of matrix (17), which depend on the directions of the wave vector **q** and polarization **u**. Naturally, the eigenvalues coincide for all equivalent directions.

The data presented in Table 1 indicate that, unlike the transverse waves propagating along the twofold axis, the waves propagating along the five-and threefold axes remain doubly degenerate even when the fourth-degree terms are taken into account. Unfortunately, reliable quantitative estimates of the quantities λ', μ', and $\xi_{\parallel}$ cannot be obtained from the experimental measurements made in [11]. Using the constructed DM, we can also consider the case of thermally activated phasons and obtain the dispersion relations for interacting phonon–phason excitations by analogy with [7], as was done in the long-wavelength limit.

The second interesting field in which the obtained results can be applied are theoretical and experimental investigations of diffuse scattering in quasicrystals. In contrast to crystals, the shape of equal-intensity line contours around Bragg reflections for quasicrystals is anisotropic and the main contribution to diffuse scattering comes from spatial fluctuations of phason degrees of freedom [12]. Analysis of the intensity profile around Bragg reflections is the main method presently used for determining the phason elastic constants for quasicrystals. Without considering the theoretical substantiation, we point out that in the recent publications by de Boissieu *et al.* [12–14], the intensity of diffuse scattering near the reflection corresponding to the reciprocal space vector **Q** at a finite distance **q** from the reflection is approximated by an expression of the type

$$I(\mathbf{Q}^{\parallel} + \mathbf{q}) = \sum_{i,j=1}^{3} \alpha_Q [c_{ij}(\mathbf{q})^{\parallel}]^{-1} Q_i^{\parallel} Q_j^{\parallel} + \sum_{i,j=1}^{3} \beta_Q [c_{ij}(\mathbf{q})^{\perp}]^{-1} Q_i^{\perp} Q_j^{\perp}, \tag{14}$$

where α_Q and β_Q are the proportionality factors determined by the reflection index, the Debye–Waller factor, the crystal temperature, the freezing temperature for the phason degrees of freedom, and some other factors. Vectors $\mathbf{Q}^{\parallel}$ and $\mathbf{Q}^{\perp}$ are the so-called parallel and perpendicular components of the six-dimensional reciprocal-space vector **Q**, respectively. Matrices $c_{ij}(\mathbf{q})^{\parallel}$ and $c_{ij}(\mathbf{q})^{\perp}$ are the phonon and phason blocks of the DM, respectively. Since the DM components themselves are proportional to pair products of the wave vector components, the intensity defined by formula (14) decreases in direct proportion to the squared distance to the Bragg reflection in the reciprocal space. At the same time, the experimentally observed decrease in the intensity $I(q)$ of diffuse scattering deviates from the $1/q^2$ law [15]. (See also reference [23] in [10] on the necessity of the inclusion of higher-order terms in the DM.) Since it is these fluctuations of the phason degrees of freedom that make a predominant contribution to the diffuse scattering intensity, it is expedient to take into account the second-order terms in the phason block.

The intensity of diffuse scattering is usually measured in a plane perpendicular to the twofold axis of an icosahedral quasicrystal (for definiteness, we assume that this is the (0, 0, 1) plane). This plane involves six symmetric directions: two twofold, two threefold, and two fivefold axes. For these directions, we can avoid the procedure of matrix inversion if we use the following well-known relation from linear algebra:

$$\sum_{i,j=1}^{3} (M_{ij})^{-1} Q_i Q_j = \sum_{l=1}^{3} (\mathbf{e}^l \mathbf{Q})^2 / n_l, \tag{15}$$

Table 2. Data required for calculating the phason component of the diffuse scattering intensity

$\mathbf{q}_0$	$\langle\rangle^\perp$	K	K'	N
	$\langle\tau, -1, 0\rangle/N$	$K_1 - 4/3K_2$	$2\xi_\perp + K_1' - 4/3K_2'$	$\sqrt{\tau+2}$
$q\langle 1, \tau, 0\rangle/N$	$\langle 0, 0, 1\rangle$	$K_1 + 2/3K_2$	$2\xi_\perp + K_1' + 2/3K_2'$	
	$\langle 1, \tau, 0\rangle/N$	$K_1 + 2/3K_2$	$2\xi_\perp + K_1' + 2/3K_2'$	$\sqrt{\tau+2}$
	$\langle\tau, 1, 0\rangle/N$	$K_1 - 4/3K_2$	$2\xi_\perp + K_1' - 4/3K_2'$	$\sqrt{\tau+2}$
$q\langle -1, \tau, 0\rangle/N$	$\langle 0, 0, 1\rangle$	$K_1 + 2/3K_2$	$2\xi_\perp + K_1' + 2/3K_2'$	
	$\langle 1, -\tau, 0\rangle/N$	$K_1 + 2/3K_2$	$2\xi_\perp + K_1' + 2/3K_2'$	$\sqrt{\tau+2}$
	$\langle 1, \tau^2, 0\rangle/N$	$K_1 + 4/3K_2$	$1\frac{5}{9}\xi_\perp + K_1' + 4/3K_2'$	$\sqrt{3\tau+3}$
$q\langle \tau^2, 1, 0\rangle/N$	$\langle 0, 0, 1\rangle$	$K_1 - 2/3K_2$	$3\frac{7}{9}\xi_\perp + K_1' - 2/3K_2'$	
	$\langle -\tau^2, 1, 0\rangle/N$	$K_1 - 2/3K_2$	$3\frac{7}{9}\xi_\perp + K_1' - 2/3K_2'$	$\sqrt{3\tau+3}$
	$\langle -1, \tau^2, 0\rangle/N$	$K_1 + 4/3K_2$	$1\frac{5}{9}\xi_\perp + K_1' + 4/3K_2'$	$\sqrt{3\tau+3}$
$q\langle -\tau^2, 1, 0\rangle/N$	$\langle 0, 0, 1\rangle$	$K_1 - 2/3K_2$	$3\frac{7}{9}\xi_\perp + K_1' - 2/3K_2'$	
	$\langle \tau^2, 1, 0\rangle/N$	$K_1 - 2/3K_2$	$3\frac{7}{9}\xi_\perp + K_1' - 2/3K_2'$	$\sqrt{3\tau+3}$
	$\langle 1, 0, 0\rangle$	$K_1 - 1/3K_2$	$4\xi_\perp + K_1' - 1/3K_2'$	
$q\langle 1, 0, 0\rangle$	$\langle 0, 1, 0\rangle$	$K_1 + (\tau - 1/3)K_2$	$2(1-\tau)\xi_\perp + K_1' + (\tau - 1/3)K_2'$	
	$\langle 0, 0, 1\rangle$	$K_1 + (2/3 - \tau)K_2$	$2\tau\xi_\perp + K_1' + (2/3 - \tau)K_2'$	
	$\langle 0, 1, 0\rangle$	$K_1 - 1/3K_2$	$4\xi_\perp + K_1' - 1/3K_2'$	
$q\langle 0, 1, 0\rangle$	$\langle 0, 0, 1\rangle$	$K_1 + (\tau - 1/3)K_2$	$2(1-\tau)\xi_\perp + K_1' + (\tau - 1/3)K_2'$	
	$\langle 1, 0, 0\rangle$	$K_1 + (2/3 - \tau)K_2$	$2\tau\xi_\perp + K_1' + (2/3 - \tau)K_2'$	

Note: The first column contains the symmetry direction of the wave vector. The second column contains the normalized vector $\langle\rangle^\perp$ of phason polarization. The next two columns contain expressions for the effective constants K and K'. The last column contains the normalization factor.

where $\mathbf{e}^l$ and n_l are normalized eigenvectors and eigenvalues of matrix M_{ij}, respectively, and $(M_{ij})^{-1}$ is a matrix reciprocal to M_{ij}. One of the normalized eigenvectors of the matrix, $c_{ij}(\mathbf{q})^\parallel$, is a unit vector parallel to vector $\mathbf{q}$. The corresponding eigenvalue is $\lambda + 2\mu$. Two other unit eigenvectors are perpendicular to the wave vector, while the corresponding eigenvalues are equal to each other and to μ. Knowledge of the eigenvalues and eigenvectors of the block $c_{ij}(\mathbf{q})^\perp$ makes it possible to transform the phason contribution to the diffuse scattering intensity into the form

$$I_{\text{phason}}(\mathbf{Q}^\parallel + \mathbf{q}) = \sum_{i=1}^{3} \frac{\beta_Q \left| \langle\rangle_i^\perp \mathbf{Q}^\perp \right|^2}{(K_i q^2 + K_i' q^4)}. \qquad (16)$$

The data required for practical applications of this formula are given in Table 2.

APPENDIX

The part of the symmetric dynamic matrix $\begin{pmatrix} C^{\parallel} & C^{\parallel\perp} \\ C^{\perp\parallel} & C^{\perp} \end{pmatrix}$, which is quadratic in the wave vector components, can be presented in the form of three blocks:
the phonon–phonon block

$$c^{\parallel} = \begin{pmatrix} \mu|q|^2 + (\lambda+\mu)q_1^2 & (\lambda+\mu)q_1q_2 & (\lambda+\mu)q_1q_3 \\ (\lambda+\mu)q_1q_2 & \mu|q|^2 + (\lambda+\mu)q_2^2 & (\lambda+\mu)q_2q_3 \\ (\lambda+\mu)q_1q_3 & (\lambda+\mu)q_2q_3 & \mu|q|^2 + (\lambda+\mu)q_3^2 \end{pmatrix}, \quad (17)$$

the phonon–phason block

$$c^{\parallel\perp} = K_3 \begin{pmatrix} q_1^2 - \tau q_2^2 + 1/\tau q_3^2 & 2\tau^{-1}q_1q_2 & -2\tau q_1q_3 \\ -2\tau q_1q_2 & q_2^2 - \tau q_3^2 + \tau^{-1}q_1^2 & 2\tau^{-1}q_2q_3 \\ 2\tau^{-1}q_1q_3 & -2\tau q_2q_3 & q_3^2 - \tau q_1^2 + \tau^{-1}q_2^2 \end{pmatrix}, \quad (18)$$

and the phason–phason block

$$c^{\perp} = \begin{pmatrix} A_1 & 2K_2q_1q_2 & 2K_2q_1q_3 \\ 2K_2q_1q_2 & A_2 & 2K_2q_3 \\ K_2q_1q_3 & 2K_2q_2q_3 & A_3 \end{pmatrix}, \quad (19)$$

where $A_i = K_1q^2 - K_2(q^2/3 + \tau^{-1}q_{i+1}^2 - \tau q_{i+2}^2)$. The nontrivial fourth-degree correction to the phonon–phonon block has the form

$$\xi_{\parallel} \begin{pmatrix} A_1 & B_1 & B_3 \\ B_1 & A_2 & B_2 \\ B_3 & B_2 & A_3 \end{pmatrix}, \quad (20)$$

where $A_i = \frac{2}{\tau}q_{i+2}^4 + \frac{12}{\tau}q_i^2q_{i+1}^2 - 2\tau q_{i+1}^4 + 8q_{i+1}^2q_{i+2}^2 - 12\tau q_i^2q_{i+1}^2$ and $B_i = \frac{8}{\tau}q_i^3q_{i+1} - 8\tau q_{i+1}^3q_i + 16q_iq_{i+1}q_{i+2}^2$. The nontrivial fourth-degree correction to the phason–phason block has the form

$$\xi_{\perp} \begin{pmatrix} A_1 & B_1 & B_3 \\ B_1 & A_2 & B_2 \\ B_3 & B_2 & A_3 \end{pmatrix}, \quad (21)$$

where $A_i = 4q_i^4 + 2\tau q_{i+1}^4 - \frac{2}{\tau}q_{i+2}^4 + 12q_{i+1}^2q_{i+2}^2$ and $B_i = \frac{4}{\tau}q_iq_{i+1}^3 - 4\tau q_i^3q_{i+1} - 12q_iq_{i+1}q_{i+2}^2$.

ACKNOWLEDGMENTS

This work was supported by the Russian Foundation for Basic Research.

REFERENCES

1. D. Shechtman, I. Blech, D. Chatias, and J. W. Cahn, Phys. Rev. Lett. **53** (20), 1951 (1984).
2. P. Bak, Phys. Rev. Lett. **54** (14), 1517 (1985).
3. T. C. Lubensky, in *Introduction to Quasicrystals*, Ed. by M. V. Jaric (Academic, Boston, 1988), p. 200.
4. G. Coddens, S. Lyonnard, B. Hennion, and Y. Calvayrac, Phys. Rev. Lett. **83** (16), 3226 (1999).
5. K. Edagava and K. Kajiaama, in *Contributed Talk at the 7th International Conference on Quasicrystals, Stuttgart, 1999.*
6. M. Feuerbacher, M. Weller, and K. Urban, in *Proceedings of the 6th International Conference on Quasicrystals, Tokyo, 1997.*
7. S. B. Rochal and V. Lorman, Phys. Rev. B **52** (2), 874 (2000).
8. J. P. Elliott and P. G. Dawber, *Symmetry in Physics* (Macmillan, London, 1981; Mir, Moscow, 1983), Vol. 2.
9. M. V. Jaric and D. R. Nelson, Phys. Rev. B **37** (9), 4458 (1988).
10. M. J. Capitan, Y. Calvayrac, A. Quivy, *et al.*, Phys. Rev. B **60** (9), 6398 (1999).
11. M. Windisch, J. Hafner, M. Krajci, and M. Mihalkovic, Phys. Rev. B **49** (13), 8701 (1994).
12. M. de Boissieu, M. Boudard, B. Hennion, *et al.*, Phys. Rev. Lett. **75** (1), 89 (1995).
13. M. Boudard, M. de Boissieu, A. Letoublon, *et al.*, Europhys. Lett. **33** (3), 199 (1996).
14. M. de Boissieu, Poster contribution at APERIODIC 2000, Nijmengen, Holland, 2000.
15. R. Bellisent and N. Schramchenko, private communication.

Translated N. Wadhwa

Physics of the Solid State, Vol. 43, No. 10, 2001, pp. 1968–1971. Translated from Fizika Tverdogo Tela, Vol. 43, No. 10, 2001, pp. 1890–1893.

LATTICE DYNAMICS AND PHASE TRANSITIONS

Structural Phase Transitions in $CdTiO_3$

Yu. V. Kabirov, B. S. Kul'buzhev, and M. F. Kupriyanov

Rostov State University, Rostov-on-Don, 344090 Russia

e-mail: kupri@phys.runnet.ru

Received November 30, 2000

Abstract—The reconstructive phase transition from the ilmenite-like $CdTiO_3$ modification to the perovskite modification is investigated thoroughly. It is revealed that the reconstructive transition is determined by size effects, results in the formation of the closest packing of the ilmenite $CdTiO_3$ structure, and is irreversible with a decrease in temperature. The perovskite $CdTiO_3$ modification undergoes displacive structural phase transitions at temperatures of 110, 220, and 380°C. The first displacive phase transition is isostructural, whereas the second and third transitions are associated with rotations of oxygen octahedra. © *2001 MAIK "Nauka/Interperiodica".*

1. INTRODUCTION

Among the well-known displacive structural phase transitions observed in oxygen octahedral structures (perovskites, pyrochlores, potassium–tungsten bronzes, ilmenites, etc.), which are usually accompanied by considerable changes in dielectric, mechanical, optical, and other physical properties [1], reconstructive phase transitions have long been attracting the particular attention of physicists [2]. However, only a few examples of reconstructive phase transitions in complex oxides have been reported to date. Among these are the following transitions: (1) the cubic–hexagonal phase transition in $BaTiO_3$ [3], (2) the pyrochlore–perovskite phase transitions in $PbTiO_3$ thin films and ZTS-type solid solutions [4], (3) the phase transition in strontium bismuth tantalate (SBT) from the fluorite-type structure to the Aurivillius layered structure during the preparation of SBT in the form of thin films [5], and (4) the ilmenite–perovskite phase transition in $CdTiO_3$ [6].

The main objective of the present work was to investigate the reconstructive phase transition from the ilmenite-like $CdTiO_3$ modification to the perovskite modification. Moreover, it was revealed earlier in [7] that the perovskite $CdTiO_3$ modification undergoes displacive high-temperature phase transitions similar to those observed in $CaTiO_3$ [8]. In this respect, it was of interest to examine structural transformations of the perovskite $CdTiO_3$ modification over a wide range of temperatures. This analysis was also performed in our work.

2. EXPERIMENTAL TECHNIQUE

The formation of the ilmenite-like $CdTiO_3$ modification from titanium and cadmium oxides and the reconstructive ilmenite–perovskite phase transition were characterized by *in situ* x-ray diffraction analysis using a DRON-3M diffractometer (CoK_α radiation, Fe filter), which was equipped with a special temperature attachment. The temperature in the x-ray diffraction chamber was maintained to within 0.5 K with the use of a VRT-2 instrument. The x-ray diffraction patterns were recorded in the Bragg–Brentano geometry by scanning a detector (one degree per minute) in the 2Θ angle range $35° < 2\Theta < 47°$, which includes the characteristic diffraction peaks of the initial components (CdO and TiO_2) used in synthesizing $CdTiO_3$ and the characteristic peaks of the resulting ilmenite-like and perovskite $CdTiO_3$ modifications.

The stoichiometric mixture of CdO (chemically pure) and TiO_2 (analytical grade) in the rutile phase was prepared by grinding these oxides in an alcohol for 2 h. The samples thus obtained were checked for stoichiometry against x-ray spectroscopic analysis with an EDAX-DX-95 instrument. The mean size of CdO and TiO_2 crystallites was of the order of 0.5 μm. The concentrations of the initial and resulting crystalline phases at different temperatures in the range from 20 to 1042°C were determined from the integral-intensity ratios of the corresponding diffraction reflections.

In addition to our earlier observations [9], the behavior of the electrical conductivity of the perovskite $CdTiO_3$ single crystal was examined with an E7-8 bridge in the temperature range from 20 to 300°C.

3. RESULTS AND DISCUSSION

The temperature dependence of the concentration ratio of CdO and TiO_2 in the ilmenite-like and perovskite modifications of $CdTiO_3$ revealed that the first portions of the ilmenite-like $CdTiO_3$ phase are formed at temperatures of 600–650°C. The maximum content of this phase (80%) is observed at a temperature of 850°C. At 900°C, apart from the initial components (20%) and the ilmenite-like $CdTiO_3$ phase, there appears the perovskite $CdTiO_3$ phase, which indicates the onset of the

reconstructive ilmenite–perovskite phase transition. This transition proceeds rather rapidly and ceases at 1000°C. As follows from the diffraction patterns, the perovskite $CdTiO_3$ phase at these temperatures does not exhibit a cubic structure (perovskite has a monoclinic unit cell).

The investigation of the reconstructive phase transition from the ilmenite-like $CdTiO_3$ modification to the perovskite modification revealed the following features. After the formation of the ilmenite-like $CdTiO_3$ modification, the parameters A_H and C_H of the hexagonal cell increase with an increase in the temperature to 850°C (Fig. 1). However, at higher temperatures ($850 < T < 950$°C), when the ilmenite-like modification transforms into the perovskite modification, the unit cell parameters A_H and C_H decrease significantly. This behavior of A_H and C_H with an increase in the temperature can be explained as follows.

The ilmenite-type $CdTiO_3$ structure has a hexagonal closest packing of oxygen-containing layers between which cadmium and titanium ions and holes in oxygen octahedra alternate along the Z axis [10]. The mean distance between these layers is defined as $h = C_H/6$ [11]. The ilmenite-like $CdTiO_3$ modification at room temperature ($A_H = 5.240$ Å and $C_H = 14.838$ Å) is characterized by $h = 2.473$ Å, which considerably exceeds the h distance in structures similar to α-Al_2O_3 and in many ilmenites ($MgTiO_3$, $FeTiO_3$, $MnTiO_3$, and $LiNbO_3$). This suggests that the ilmenite-like $CdTiO_3$ modification at room temperature has a rather loose structure along the Z axis. Crystal structures with a cubic closest packing (for example, the perovskite-type structure) can be described by the hexagonal unit cell with the following parameters: $\mathbf{C}_H = \mathbf{a}_p + \mathbf{b}_p + \mathbf{c}_p$, $\mathbf{A}_H = \mathbf{c}_p - \mathbf{b}_p$, and $\mathbf{B}_H = \mathbf{b}_p - \mathbf{a}_p$ (where $\mathbf{a}_p$, $\mathbf{b}_p$, and $\mathbf{c}_p$ are the parameters of the perovskite unit cell). In this setting, $h = C_H/3$.

Now, we introduce the quantity $k = (h - h_0)/h_0$, where h_0 is the distance between layers in the closest packing of an idealized structure consisting of bivalent oxygen ions ($R_0 = 1.36$ Å) and h is calculated from the C_H parameters of the corresponding compounds.

Figure 2 depicts the (k, R_i) diagram for corundum-, ilmenite-, and perovskite-type structures. Here, R_i stands for the mean radii of the ions located between the oxygen-containing layers of the closest packings. For perovskite structures, these are ions of the B sort (Ti, Sn, Zr, and Hf). In these structures, ions of the A sort occupy layers of the cubic closest packing. In corundum-type structures with simple oxides, ions of the same sort (Al, Fe, Cr, and V) are located between layers of the hexagonal packing, whereas in ilmenite-type structures, ions of different sorts are arranged along the Z_H axis. For the compounds presented in Fig. 2, we used the mean radii of the corresponding ions [12]. Perovskite-type structures are indicated by the letter p. The $BaTiO_3$-H notation signifies the hexagonal barium titanate modification in which, unlike

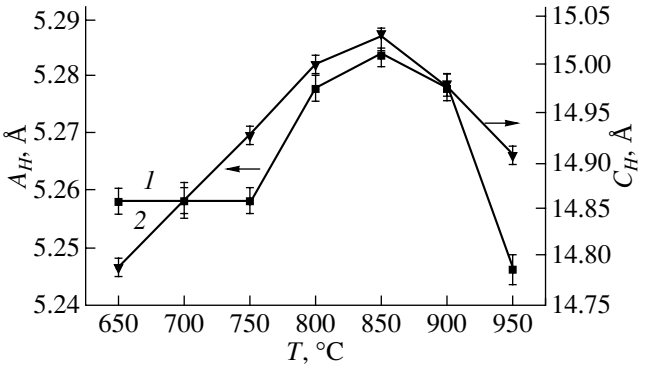

Fig. 1. Temperature dependences of the parameters (*1*) A_H and (*2*) C_H of a hexagonal cell of the ilmenite-like $CdTiO_3$ modification.

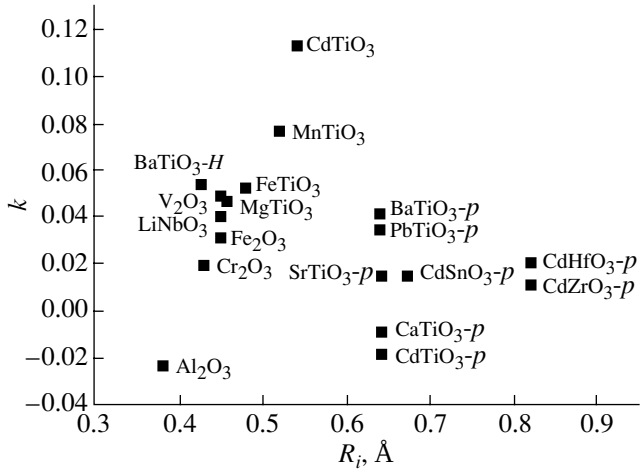

Fig. 2. Dependences of the k ratios on the effective ionic radii of the cations located between the oxygen-containing layers of the closest packings.

ilmenite-type structures, barium and oxygen ions occupy layers of the closest packing.

Under normal conditions, the perovskite $CdTiO_3$ phase ($a_p = c_p = 3.790$ Å, $b_p = 3.803$ Å, $\beta_p = 91.10°$) has a looser structure as compared to the ilmenite-like phase ($A_H = 5.240$ Å and $C_H = 14.838$ Å). The packing coefficients of these phases are equal to 0.67 and 0.625, respectively. As can be seen from Fig. 2, an increase in the mean ionic radius brings about an increase in the h distance, especially, in ilmenite structures. It was found that $h = 2R_i + 1.41$ (Å).

From the crystal chemical standpoint, the reconstructive phase transition from the ilmenite to perovskite $CdTiO_3$ modification occurs through the incorporation of cadmium ions (located in interlayer positions) into layers of the closest packing. This rearrangement of cadmium ions leads to a decrease in the unit cell parameters A_H and C_H and a change in the packing of the $CdTiO_3$ structure from the hexagonal to the cubic type. In this case, the sixfold coordination of the nearest

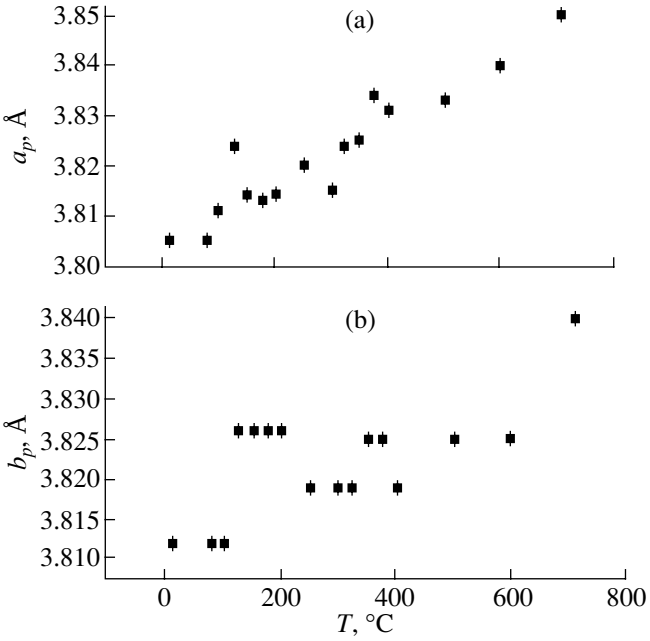

Fig. 3. Temperature dependences of the unit cell parameters (a) $a_p = c_p$ and (b) b_p of the perovskite $CdTiO_3$ modification.

environment of cadmium atoms changes over to the 12-fold coordination and the *h* distance decreases considerably (for the perovskite $CdTiO_3$ structure, h = 2.194 Å), which indicates the formation of the $CdTiO_3$ structure with a closer packing. The results obtained suggest that, under external pressure, the formation of the ilmenite-like $CdTiO_3$ phase in the course of its synthesis can be limited. On the other hand, the synthesis of $Cd_{1-x}A_xTiO_3$ solid solutions, in which the *A*-type ions (for example, Mg, Mn, and others) have a smaller radius compared to cadmium ions, provides a means for stabilizing the ilmenite-like $CdTiO_3$ phase up to higher temperatures. This can be used for designing new high-temperature ferroelectric materials similar to $LiNbO_3$ in their physical properties.

X-ray diffraction investigation of the phase transition from the ilmenite-like $CdTiO_3$ modification to the perovskite modification demonstrated that the transition with an increase in temperature is attended by a substantial decrease in the angular half-widths of diffraction reflections associated with the ilmenite-like phase. Specifically, the angular half-widths of the (110) and (104) reflections decrease from 0.65° to 0.25° in the temperature range $650 < T < 950$°C. This can be explained by an increase in the coherent scattering regions and a decrease in the structural inhomogeneities (microstrains) to a certain limit in the course of crystallization. Further increase in the coherent scattering regions and the development of a block structure of $CdTiO_3$ at temperatures above 950°C result in the reconstructive phase transition from the ilmenite-like $CdTiO_3$ modification to the perovskite modification. Therefore, the size effect (growth of the crystalline phase) is the most probable physical cause of this transition.

The temperature dependences of the unit cell parameters of the perovskite $CdTiO_3$ modification are displayed in Fig. 3. The accuracy in determination of these parameters is equal to 0.003 Å. As can be seen from Fig. 3, the unit cell parameters exhibit a nonmonotonic behavior with an increase in temperature. For example, an increase in the temperature to $T_1 = 110$°C brings about a substantial increase in the parameters $a_p = c_p$ and b_p (by 0.013 and 0.011 Å, respectively) and a change in the unit cell volume ($\Delta V = +0.0019$ Å^3). Yakubovskiĭ *et al.* [13] proved that the perovskite $CdTiO_3$ modification at a temperature of 110°C is characterized by a shift of the IR absorption edge, which was interpreted as a manifestation of the second-order phase transition. An increase in temperature in the range from 220 to 240°C leads to a decrease in the parameter b_p and an increase in $a_p(c_p)$. In our earlier work [9], we noted that the birefringence curve $\Delta n(T)$ for the perovskite $CdTiO_3$ modification exhibits a small kink at a temperature $T_2 = 220$°C. Moreover, the measurements of the electrical conductivity *G* of the perovskite $CdTiO_3$ single crystal (Fig. 4), which were per-

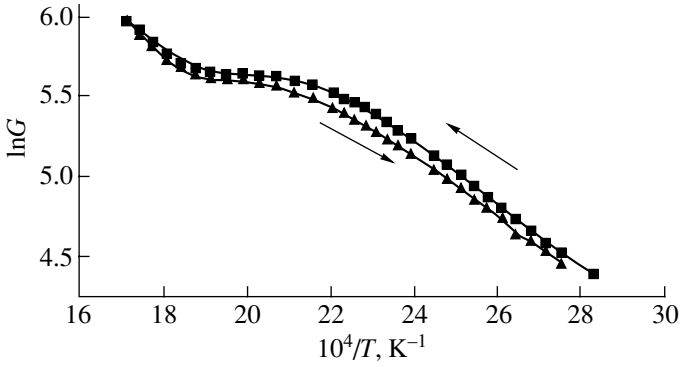

Fig. 4. Dependence $\ln G(10^4/T)$ for a single crystal of the perovskite $CdTiO_3$ modification.

formed in the present work, also revealed a nonlinear logarithmic dependence of G on the reciprocal of the temperature at T_2. The activation energy E_a of charge carriers was estimated at the following values: 0.751 eV (in the temperature range 20–180°C), 0.079 eV (180–270°C), and 0.776 eV (270–320°C) (Fig. 4). As the temperature increases to T_3 = 380°C, the unit cell parameters a_p and b_p increase by 0.012 and 0.005 Å, respectively. At higher temperatures (up to 710°C), the unit cell parameters exhibit a monotonic behavior.

The temperature dependences of the intensities of superstructure reflections for the $CdTiO_3$ crystal indicate that the (047), (285), and (481) reflections are retained up to a temperature of 1042°C, whereas the (081), (267), and (465) reflections disappear at approximately 400°C. This suggests that only antiparallel displacements of cadmium atoms can occur in the high-temperature range (up to 1042°C). A decrease in the temperature is accompanied by displacements of oxygen atoms (starting with 400°C), then (below 200°C) by oxygen octahedron rotations (similar to those described in [14]) about the fourfold axes of the cubic praphase, and by an increase in the displacement of cadmium atoms. As a rule, these distortions are associated with the condensation of the M_3 and R_{25} modes. At 110°C, the $CdTiO_3$ crystal undergoes an isostructural phase transition attended by insignificant octahedron distortions.

4. CONCLUSION

The (k, R_i) diagram (Fig. 2) can readily be extended to other oxygen octahedral compounds. This makes it possible to analyze the structural stability of these compounds at different k ratios and ionic radii. The results obtained in this work suggest that the reconstructive phase transitions due to size effects can occur at higher pressures (for example, the ilmenite–perovskite phase transitions in $MnTiO_3$ and other ilmenites), during preparation of thin films based on the perovskite $CdTiO_3$ modification (the perovskite–ilmenite phase transitions), and upon quenching of $CdTiO_3$ samples from high temperatures (the perovskite–ilmenite phase transitions).

ACKNOWLEDGMENTS

We are grateful to L.A. Reznichenko for assistance in performaning part of the experiment.

REFERENCES

1. F. Jona and G. Shirane, *Ferroelectric Crystals* (Pergamon, Oxford, 1962; Mir, Moscow, 1981).
2. M. D. Burger, Kristallografiya **16** (6), 1084 (1971) [Sov. Phys. Crystallogr. **16**, 959 (1971)].
3. R. M. Gleister and H. F. Kay, Proc. Phys. Soc. London **76** (491), 763 (1960).
4. F. N. Martin, Phys. Chem. Glasses **6** (4), 143 (1976).
5. J. F. Scott, Ferroelectrics Review **1**, 129 (1998).
6. M. L. Sholokhovich, O. P. Kramarov, B. F. Proskuryakov, and E. I. Éknadiosyants, Kristallografiya **13**, 1102 (1968) [Sov. Phys. Crystallogr. **13**, 967 (1968)].
7. V. M. Lebedev, Yu. N. Venevtsev, and G. S. Zhdanov, Kristallografiya **15** (2), 377 (1970) [Sov. Phys. Crystallogr. **15**, 318 (1970)].
8. X. Liu and R. C. Liebermann, Phys. Chem. Miner. **20**, 171 (1993).
9. Yu. V. Kabirov, M. F. Kupriyanov, Ya. Dets, and P. Wawzala, Fiz. Tverd. Tela (St. Petersburg) **42** (7), 1291 (2000) [Phys. Solid State **42**, 1329 (2000)].
10. H. D. Megaw, Acta Crystallogr. **7**, 187 (1954).
11. A. R. Verma and P. Krishna, *Polymorphism and Polytypism in Crystals* (Wiley, New York, 1966; Mir, Moscow, 1969).
12. G. B. Bokii, *Crystal Chemistry* (Mosk. Gos. Univ., Moscow, 1960).
13. M. A. Yakubovskiĭ, V. I. Zametin, and L. N. Rabkin, Izv. Vyssh. Uchebn. Zaved., Fiz. **1**, 150 (1978).
14. K. S. Aleksandrov, A. T. Anistratov, B. V. Beznosikov, and N. V. Fedoseeva, *Phase Transitions in Crystals of ABX_3 Haloid Compounds* (Nauka, Novosibirsk, 1981).

Translated by O. Borovik-Romanova

Physics of the Solid State, Vol. 43, No. 10, 2001, pp. 1972–1978. Translated from Fizika Tverdogo Tela, Vol. 43, No. 10, 2001, pp. 1894–1900.

LOW-DIMENSIONAL SYSTEMS AND SURFACE PHYSICS

Electron-Stimulated Desorption of Europium Atoms from an Oxidized Tungsten Surface

V. N. Ageev, Yu. A. Kuznetsov, and N. D. Potekhina

Ioffe Physicotechnical Institute, Russian Academy of Sciences, Politekhnicheskaya ul. 26, St. Petersburg, 194021 Russia

Received February 22, 2001

Abstract—The yield of europium atoms in electron-stimulated desorption from Eu layers adsorbed on the surface of oxidized tungsten was studied with a surface-ionization detector as a function of the incident-electron energy, surface coverage by europium, and degree of tungsten oxidation. The yield of Eu atoms measured as a function of electron energy exhibits a distinct resonant character with peaks at electron energies corresponding to europium and tungsten core-level ionization energies. The peaks associated with the europium ionization reach a maximum intensity at europium coverages less than 0.1 and decrease subsequently to zero with increasing coverage, while the peaks due to tungsten ionization pass through the maximum intensity at a monolayer europium coverage. The coverage corresponding to the maximum europium atom yield grows with increasing tungsten oxidation. The results obtained are accounted for by the formation of the europium and tungsten core excitons. In the first case, the particles desorb in the reverse motion toward the surface of the oxidized tungsten; in the second, they desorb as a result of repulsion between the tungsten core exciton and the EuO molecule. © *2001 MAIK "Nauka/Interperiodica".*

1. INTRODUCTION

Bombardment of a solid by electrons is widely employed in the analysis of the geometric structure and composition of a solid's surface. Under certain conditions, however, this process can substantially modify the original state of the surface, quite often in an unpredictable way. The most significant of the surface-modifying processes under electron bombardment is electron-stimulated desorption (ESD), which occurs when the potential energy of electronic excitation transforms directly into the kinetic energy of desorbing particles [1].

Unfortunately, the present ESD models are not capable of unambiguously predicting the behavior of the surface of a solid under bombardment by electrons. The limited nature of the ESD models proposed thus far is due primarily to the lack of experimental data on the fluxes of desorbing neutrals due to the difficulties involved in their detection.

We have succeeded in detecting ESD of alkali metal neutrals using a surface-ionization detector [2] and in measuring their cross sections and energy distributions when ejected from layers adsorbed on the surface of oxidized tungsten [3, 4] and molybdenum [5]. The results of the measurements were interpreted in terms of a model in which desorption of alkali-metal atoms occurs because of the overlap of the valence shells of the alkali-metal atoms and of the negative oxygen ions after core-vacancy Auger decay in oxygen and relaxation of its charge. It was found that the atomic repulsion forces depend on the valence-shell structure of the interacting particles. This stresses the importance of understanding the extent to which the valence shell configuration of adsorbed particles affects the yield and the energy distribution of desorbing neutrals.

This stimulated a series of our studies into the ESD of rare-earth metal (REM) neutrals from layers adsorbed on the surface of transition-metal oxides. On the one hand, the REMs enjoy broad application in electronics, electrical engineering, oil processing and car industry, in space technology, and in the production of permanent magnets and structural and HTSC ceramics [6]. On the other hand, the number of 4*f* electrons varies smoothly along the REM series, thus making it possible to study the effect of this factor on the ESD characteristics. We revealed a resonant character of the yield of europium atoms (as a function of the incident electron energy) from a layer adsorbed on a tungsten surface covered by an oxygen monolayer [7], this character of the ESD yield of neutrals having been established for the first time. This publication describes further experiments performed to explain the mechanism of this phenomenon.

2. EXPERIMENTAL

The experimental setup and the measurement techniques used were described earlier in considerable detail [8]. The measurements were conducted in a bakeable stainless-steel chamber at a base pressure below 5×10^{-10} Torr. The ESD yield of europium atoms was measured with a surface-ionization detector, which had a textured tungsten ribbon heated to $T = 2000$ K. The Eu ionization efficiency was $\sim 10^{-3}$ ion/atom. The target was a textured tungsten ribbon with a preferential (100) orientation measuring $70 \times 2 \times 0.01$ mm. The target was

cleaned of carbon by heating it in an oxygen environment at a pressure of 1×10^{-6} Torr and a temperature $T = 1800$ K for 3 h. The target cleanness was checked in a separate setup using Auger electron spectroscopy, measurements of the work function, and thermal desorption spectroscopy. The oxygen monolayer on the target surface was prepared by exposure to oxygen at a pressure of 1×10^{-6} Torr and a target temperature $T = 1600$ K for 300 s. The oxygen coverage obtained in this procedure was slightly in excess of one monolayer [9]. The oxide film on the surface of the target was obtained by exposing it to oxygen at a pressure of 1×10^{-6} Torr and a target temperature $T = 1100$ K for 300 s.

The electron emitter was a polycrystalline tungsten filament 0.15 mm in diameter drawn parallel to the target. The electron energy scale was corrected for the contact potential difference between the emitter and the target after oxygen adsorption [10]. This difference was 1 eV; the external potential difference was thus reduced by 1 eV. The change in the contact potential difference caused by the europium adsorption was disregarded for the reason outlined below. The incident electron current density did not exceed 10^{-5} A/cm^2 at an electron energy of 100 eV, and, therefore, irradiation of the target by electrons did not noticeably heat it.

The europium was deposited on the oxidized target surface at $T = 300$ K from a directly heated evaporator made of a tantalum tube, into which metallic europium was placed. The tube, 3 mm in diameter, had several holes arranged along it to ensure uniform europium deposition on the target. The purity of the europium flow was monitored with a quadrupole mass spectrometer. The deposited europium concentration was determined using thermal desorption spectroscopy, as well as checked by measuring the europium surface ionization current from the target as heated to $T = 1800$ K. The europium concentration corresponding to a monolayer coverage was established using thermal desorption and Auger electron spectroscopy [11]. The formation of a monolayer of deposited europium was indicated by the Eu neutrals reaching a maximum ESD yield. The europium monolayer on a tungsten surface coated by an oxygen monolayer corresponded to a europium concentration of 7.5×10^{14} atoms/cm^2, and that on a tungsten surface coated by a thick oxide film was 1×10^{15} atoms/cm^2.

3. RESULTS

Figure 1 plots the yield of Eu atoms from a tungsten surface coated by an oxygen monolayer, which was measured as a function of incident electron energy E_e at a target temperature $T = 300$ K for various europium coverages. The Eu atom yield is seen to depend in a fairly complicated manner both on the electron energy E_e and on the surface coverage by europium Θ. At low coverages (curve *1* in Fig. 1), the threshold of the Eu appearance is independent of the europium coverage despite the fact that the target work function decreases practically linearly with increasing coverage. It can be assumed that the europium adsorption gives rise not only to a decrease in the work function but also simultaneously to an increase in the europium core-level energies caused by chemical shifts. These two effects apparently cancel as the europium coverage changes. Accordingly, the Eu atom appearance threshold does not depend on coverage and is close to 24 eV, which is the ionization energy of the europium 5*p* level [12].

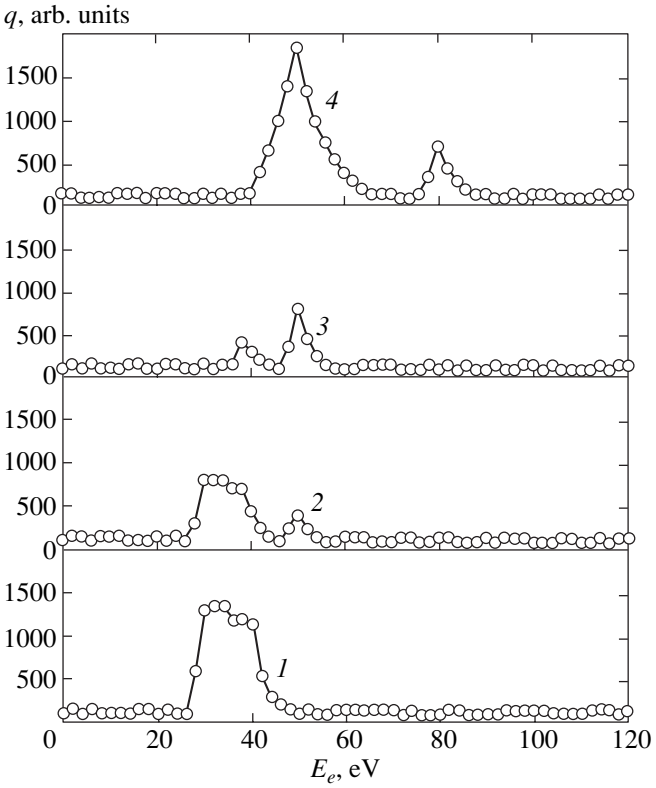

Fig. 1. ESD yield q of europium atoms from a tungsten surface covered by an oxygen monolayer plotted versus the incident electron energy E_e for various europium coverages Θ = (*1*) 0.07, (*2*) 0.18, (*3*) 0.35, and (*4*) 0.70.

The Eu atom ESD grows strongly above the threshold with increasing electron energy and passes through a maximum in the vicinity of $E_e = 32$ eV. One more feature is observed on the falling side of this peak near 38 eV. As the europium coverage increases, the intensity of the 32 and 38 eV features decreases without any change in their shape and one more peak appears at an electron energy of 50 eV (curve *2* in Fig. 1). The peak at $E_e \sim 32$ eV disappears at a europium coverage $\Theta > 0.35$, apparently simultaneously with the feature at 38 eV, while a small peak at $E_e \sim 37$ eV remains (curve *3* in Fig. 1). The intensity of the peak at $E_e \sim 50$ eV increases with increasing Θ, and an additional peak forms at $E_e \sim 80$ eV (curve *4* in Fig. 1). Thus, the intensities of the peaks at 32 and 38 eV decrease with increasing Θ for $\Theta > 0.1$, whereas those of the 50 and 80 eV peaks increase.

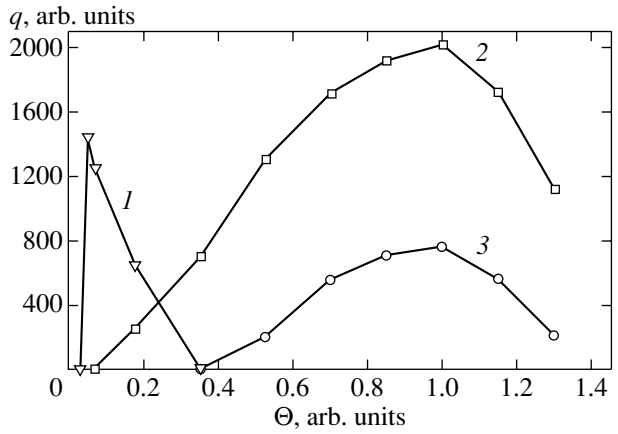

Fig. 2. Yield q of europium atoms from a tungsten surface covered by an oxygen monolayer plotted versus europium coverage Θ for various incident electron energies E_e = (*1*) 32, (*2*) 50, and (*3*) 80 eV.

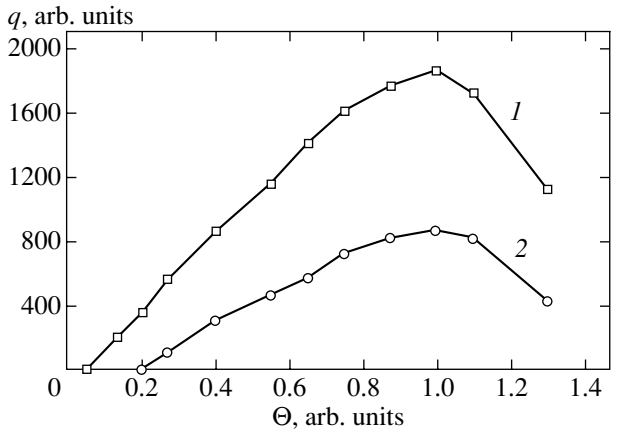

Fig. 3. Yield q of europium atoms from a tungsten surface covered by an oxide film plotted versus europium coverage Θ for various incident electron energies E_e = (*1*) 50 and (*2*) 80 eV.

The intensities of the Eu ESD peaks at 32, 50, and 80 eV measured as a function of europium coverage of a tungsten surface coated by an oxygen monolayer are shown graphically in Fig. 2. The peaks form at europium coverages of 0.05, 0.07, and 0.35, respectively. The 32 and 38 eV peaks pass through a maximum at very low coverages (less than 0.1) and fall off nearly linearly to zero already at a coverage $\Theta \sim 0.35$. In their place, a maximum peaking at about 37 eV remains. The intensities of the peaks at 50 and 80 eV grow nearly linearly with increasing europium coverage and pass through a maximum at a coverage identified as monolayers.

The 32 and 38 eV peaks disappear when the substrate is heated by a few tens of degrees. They reappear, however, after the substrate has cooled down to room temperature. The intensities of the peaks at 37, 50, and 80 eV depend only weakly on temperature up to $T \sim 500$ K.

Oxidation of the substrate up to the formation of several oxide layers on the surface changes the dependence of the Eu ESD atom yield on the incident electron energy and on the surface coverage by europium. Figure 3 presents the dependences of the 50 and 80 eV peak intensities on the europium coverage of a tungsten surface coated by an oxide film. It is seen that, at low coverages, the Eu yield grows linearly with increasing coverage for both peaks and passes through a maximum, as in the case of tungsten coated by an oxygen monolayer. The maximum is reached, however, at coverages about 30% higher than in the case of substrates with a monolayer oxygen coating. The peak at $E_e \sim 50$ eV forms at the same coverage as on a substrate with a monolayer oxygen coverage, and the peak at ~80 eV is seen clearly already at $\Theta \sim 0.25$, i.e., at a coverage smaller than in the case of a substrate coated with an oxygen monolayer. Therefore, a substrate with an oxide film exhibits Eu atom yield peaks at 32, 38, 50, and 80 eV simultaneously (Fig. 4).

We have observed the Eu ESD atom yield to depend on the sequence of barium and europium coadsorption on a tungsten surface coated by an oxygen monolayer. Preadsorption of barium up to a 0.05 coverage virtually does not affect the Eu atom yield. If, however, the same amount of barium is deposited after europium, Eu neutrals are observed to desorb already at a coverage of about 0.03.

4. DISCUSSION OF RESULTS

Europium adsorbed on oxidized tungsten lowers the work function and, hence, resides on the surface in the form of positive ions [13]. Therefore, neutralization of the Eu^+ ions under electronic excitation of the adsorption bond is an important stage in the ESD of Eu atoms. To make discussion of electronic transitions bringing about the ESD of Eu atoms more revealing, Fig. 5 displays a diagram of electronic transitions in the W–O–Eu system, which is not corrected for chemical shifts.

The ESD appearance threshold of Eu atoms is very close to that of the alkali metal atoms from layers adsorbed on oxidized surfaces of tungsten [4] and molybdenum [5], which is associated with the ionization energy of the oxygen 2*s* level [3]. The dependence of the Eu atom yield on the incident electron energy differs qualitatively, however, from that for the alkali metal atoms, whose yield passes through a flat maximum with increasing electron energy in the 100–150 eV region. For the Eu atoms, this dependence consists of sharp peaks, i.e., has a resonant character, and the peak positions correlate with the core-level ionization energies of europium and tungsten [12].

The main alkali-metal neutral ESD excitation channel [3] that is associated with the vacancy formation at the oxygen 2*s* level, which is subsequently filled by the electron from the oxygen 2*p* level (and the Auger electron neutralizes the adsorbed alkali-metal ion), appar-

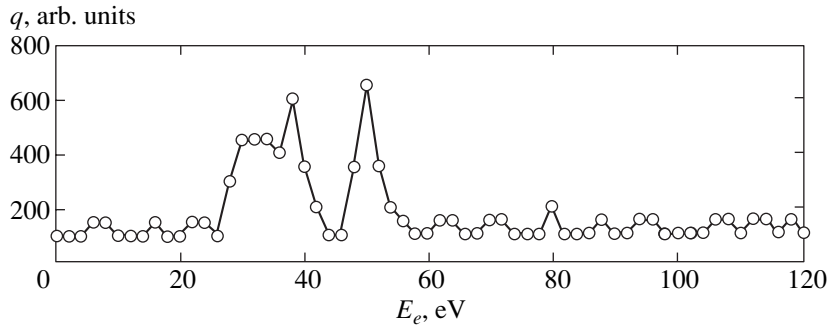

Fig. 4. ESD yield q of europium atoms from a tungsten surface covered by an oxide film plotted versus incident electron energy E_e for europium coverage $\Theta = 0.25$.

ently does not operate in the case of the Eu atom ESD. In this channel, the repulsion of the alkali metal atom results from its valence shell overlapping with that of the negative oxygen ion, which recovers its charge by trapping the substrate electrons. Because of the existence of two electrons in the 6*s* valence shell of the europium atoms, the radius of the positive europium ion is not affected substantially after its neutralization and, hence, its repulsion from the negative oxygen ion does not occur. This excitation channel is also not operative in the case of the neutral ESD of barium, which has two electrons in the outer shell [4].

The ESD appearance threshold of Eu atoms can be associated with the ionization of the europium 5*p* level having an ionization energy of 24 eV [12] and with the subsequent transfer of the excited electron to the quasi-bound state formed by the 5*d*6*s* band, which dissociates through resonant Auger decay [14]. The width of this band (~12.7 eV) is sufficiently close to that of the Eu neutral ESD peak associated with the excitation of the europium 5*p* level. Indeed, the giant 5*p*–5*s* resonance is well known to exist in photoemissions from europium. This resonance is assigned to the very high density of empty states near the Fermi level and to the weak *s*–*d* valence-band hybridization [15]. The forming Eu^{+2} ion starts to move toward the surface driven by the image forces, which appear because of the increase in its charge and as a result of the reduced repulsion between the outer shells of the europium ion and the substrate atoms [16]. After neutralization, the Eu atoms are reflected from the surface and pass through the adsorbed europium film. The decrease in the Eu atom yield associated with the ionization of the europium 5*p* level with increasing Eu coverage is accounted for by the resonant reionization of the atoms when they pass through the adsorbed europium ion film. This explanation is in agreement with experiments [17] and calculations [18] made for the scattering of 1.2-keV Li^+ ions from an Al(100) surface partially coated by alkali metals. The Li^+ neutralization probability does not have a threshold due to the alkali-metal coverage and increases approximately linearly with increasing coverage. However, the above-mentioned results were obtained for Li^+ ions of 1.2 keV energy, while the kinetic energy of Eu ESD atoms estimated from the data available for the alkali-metal and barium atoms [4] should not exceed a few tenths of an electronvolt. Because the Li^+ charge exchange probability grows nearly linearly with decreasing kinetic energy [19], there is nothing strange in that the yield of very slow Eu atoms reaches its maximum at coverages below 0.1. As the europium coverage increases, the ESD probability of neutrals becomes very low. Earlier, we observed ESD of atoms associated with the reverse motion of particles at the substrate in the case of cesium [20] and barium [21] atoms escaping from layers adsorbed on a tungsten surface covered by an oxygen monolayer, as well as for lithium atoms leaving a layer adsorbed on a molybdenum surface with an oxygen monolayer [22]. No ESD of neutrals was observed to occur in the overwhelming majority of adsorption systems after adsorbate core-level ionization. This ESD channel of neutrals is apparently very specific, and its efficiency depends on the probability of neutralization of the ions reflecting from the surface and on the probability of neutral particles passing through adsorbed films.

Note the very sharp temperature dependence of the intensity of the Eu atom yield peaks at 32 and 38 eV, which disappear already after the substrate has been

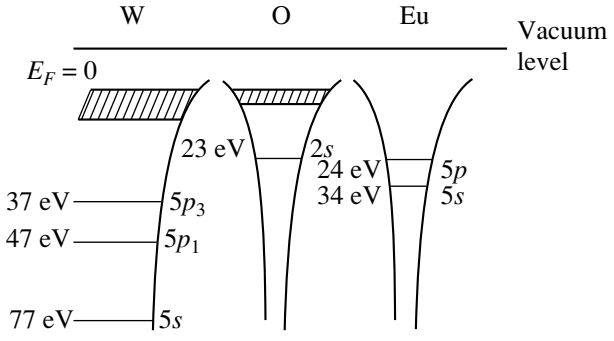

Fig. 5. Electron energy level diagram for the W–O–Eu adsorption system (schematic).

heated a few tens of degrees above room temperature. ESD of barium atoms was observed only after the oxidized tungsten was cooled below room temperature [21].

The ionization probability of adsorbed europium by electrons should not depend on the substrate temperature, and the neutralization of the Eu^{+2} ions increases with increasing temperature because of the increased density of the conduction electrons. Since the Eu atom ESD yield that is associated with the europium core-level ionization decreases with increasing substrate temperature, the probability of the europium atoms passing through the adsorbed europium layer decreases with increasing temperature because of the increased amplitude of vibrations in the adsorbed layer. Another possible explanation of the temperature dependence of the Eu atom ESD yield involves the reversible rearrangement of the oxidized W(100) surface [23]. The rearrangement may change the angular distribution of the Eu neutrals escaping in the ESD, and, because the Eu neutral flux is measured in our experiments within a narrow solid angle, the signal of the desorbing Eu atoms should, accordingly, decrease with increasing temperature.

The reason for the existence of the concentration threshold in the ESD appearance of Eu atoms remains unclear. This threshold is, however, not associated with surface defects, which would not be involved in the Eu atom ESD in any case. Indeed, preliminary adsorption of a 0.05 barium monolayer does not change the concentration threshold of the Eu atom escape, while adsorption of the same amount of barium carried out after the adsorption of europium reduces the ESD appearance threshold of Eu atoms down to 0.03 monolayers.

The resonance peaks of the Eu atom ESD yield observed at electron energies of 37, 50, and 80 eV correlate with the ionization energies of the $5p_{3/2}$, $5p_{1/2}$, and 5*s* tungsten core levels, which are 37, 47, and 77 eV, respectively [12]. The peak at 37 eV overlaps with that at 38 eV, which was assigned to the ionization of the europium 5*s* level. However, the 37 eV peak remains under europium deposition up to $\Theta > 0.35$ and substrate heating up to $T > 330$ K, whereas the 38 eV peak disappears under these conditions. Therefore, the peak at 37 eV was assigned to the ionization of the tungsten $5p_{3/2}$ level.

The resonances in the europium atom ESD yield occurring at the tungsten core-level ionization energies (Fig. 5) can be accounted for if one assumes that, at these energies, the surface emits EuO molecules, which cannot be discriminated from the Eu atoms using a surface-ionization detector. The ESD of EuO molecules results from the breaking of the W–O bond, a process favored by the core-exciton formation. However, the temperature dependence of the surface ionization current of desorbing particles correlates fairly well with that of the Eu atoms. Let us analyze the possibility of such a correlation for the surface ionization current of the Eu atoms and EuO molecules.

Let a flux of *MX* molecules of density ν hit the surface and *M*, M^+, *MX*, *X*, and X_2 particles desorb from the surface with the flux densities ν_i. Note that $\nu_{M^+} = \alpha\nu_M$, where α is the degree of surface ionization. We denote the surface concentration of the corresponding particles by N_M, N_{M^+}, N_X, N_{MX}, and N_{X_2}.

In a steady state, one can write the balance equations for the *M* and *MX* particles as

$$\nu = \nu_{MX} + \nu_M(1 + \alpha), \tag{1}$$

$$\nu = \nu_{MX} + K_{MX}N_{MX} - K^{\text{ass}}N_M N_X \tag{2}$$

and two more equations for the X and X_2 particles, which we do not need here. Here, K_{MX} and K^{ass} are the rate constants of the surface dissociation and association reactions, $\nu_i = C_i N_i$, and C_i is the desorption rate constant for the *i*th particle, which depends on temperature according to the Arrhenius law $C_i = C_i^0 \exp(-l_i/kT)$, where l_i is the heat of desorption.

Equations (1) and (2) yield the following expression for the flux of the M^+ ions desorbing from the surface:

$$\nu_{M^+} = \alpha\nu_M = \frac{\alpha\nu}{(1 + \alpha)(1 + C_{MX}/K_{MX}) + \chi^{\nu_X}}, \tag{3}$$

where

$$\chi^{\nu_X} = \frac{K^{\text{ass}}C_{MX}}{C_X C_M K_{MX}} < \chi^{\nu} \tag{4}$$

is an analog of the equilibrium constant but takes into account the desorption of the reacting particles. As follows from Eq. (3), the ionization coefficient of the flux ν ($\beta = \nu_{M^+}/\nu$) for molecules coincides with that for the atomic flux $\beta_0 = \alpha/(1 + \alpha)$ if the inequalities

$$C_{MX}/K_{MX} \ll 1, \quad \chi^{\nu_X} \ll 1 \tag{5}$$

are met.

We estimate these quantities for the EuO molecule residing on tungsten at a temperature $T = 2000$ K. Recalling that the dissociation energies of the *MX* molecule on the surface (D_S) and in the gas phase (D) are related through

$$D_S = D + l_{MX} - l_M - l_X, \tag{6}$$

we obtain

$$\frac{C_{MX}}{K_{MX}} = \frac{C_{MX}^0}{K_{MX}^0}\exp\left(\frac{D - l_M - l_X}{kT}\right). \tag{7}$$

For europium on tungsten, we have $l_{\text{Eu}} = 3.0$ [11] or 4.4 eV [24], $l_{\text{O–W}} = 7.8$ eV (the β_2 phase existing at high T) [25], and D(EuO) = 5.8 eV [26]. For the argument of the exponential in Eq. (7), we obtain

$\Delta = -D + l_{Eu} + l_O = 5.0$ or 6.4 eV, depending on the heat of europium desorption from tungsten assumed. The ratio of the prefactors in Eq. (7) can be estimated from that of the partition functions of the complexes activated for desorption and dissociation. For the case of labile adsorption, it reduces to the ratio of the vibrational partition functions $f(\omega_i) \approx kT/\hbar\omega_i$ for three vibrational modes of the activated complexes with frequencies ω_i, because one of the vibrational modes in the direction of the reaction, characterized by ω^{des} or ω^{dis}, for the desorption and dissociation, respectively, is translational motion:

$$\frac{C_{MX}}{K_{MX}} \approx \frac{\omega^{dis}}{\omega^{des}}\left(\frac{\omega_3^{dis}}{\omega_3^{des}}\right)^2, \quad (8)$$

where ω^{des} is the vibration frequency of the whole complex activated for desorption relative to the surface, ω^{dis} is the stretch vibration frequency in the complex for dissociation, and ω_3^{des} and ω_3^{dis} correspond to rocking and bending of each complex, respectively. In a complex which is more loose for dissociation, the vibrational frequencies are lower than ω_i^{des} and, therefore, the ratio (8) is less than unity. However, if a vibration with ω_3^{des} becomes rotational, ratio (8) can increase by an order of magnitude. This issue is analyzed in more detail in [27]. As a result, estimation for the $MX \equiv$ EuO molecule on tungsten yields

$$C_{MX}/K_{MX} < 10\exp(-\Delta/kT). \quad (9)$$

Irrespective of the value of Δ accepted (5.0 or 6.4 eV), ratio (9) in Eq. (3) for EuO is negligible.

To estimate χ^ν in Eq. (4), we accept that C_M^0 and $C_X^0 \approx 10^{13}$ s^{-1} and that the association rate constant K^{ass} for M and X is estimated from the number of collisions in two-dimensional motion, $K^{ass} = (4/3)\gamma R_{MX}(2\pi kT/\mu)^{1/2}$ [28], where μ is the reduced mass and R_{MX} is the interatomic separation in the MX molecule. For EuO, we have $\mu = 15.4$ amu, $R_{MX} \sim 2.5$ Å [29], and

$$K^{ass} \approx \gamma\ 8.6 \times 10^{-3}\ \text{cm}^{-3}\ \text{s}. \quad (10)$$

Substituting Eqs. (6), (9), and (10) in Eq. (4) yields

$$\chi^\nu < 10^{-28}\gamma\exp(D/kT) = 0.5 \times 10^{-13}\gamma\nu. \quad (11)$$

In our work, the fluxes ν of neutrals in europium ESD are much lower than 10^{13} cm^{-2} s^{-1}; therefore, the quantity χ^ν in Eq. (3) is likewise small, and, hence, $\beta(\text{EuO}) \approx \beta(\text{Eu})$. This shows that EuO molecules can desorb in the ESD of europium adsorbed on oxidized tungsten. Thus, the detector based on surface ionization does not discriminate the EuO molecules from the Eu atoms.

Adsorbed ions Eu^+ can become neutralized in the course of tungsten core-vacancy filling by oxygen Auger electrons. However, this process does not give rise to the ESD of Eu neutrals for the same reason as in the case of the oxygen 2*s* vacancy decay, because the radius of the europium atom does not increase substantially after the Eu^+ neutralization. The most probable ESD channel under excitation of the tungsten 5*s* and 5*p* levels remains desorption of the EuO molecules.

The higher ESD yield of Eu atoms at 50 eV (tungsten 5*p*) than at 80 eV (tungsten 5*s*), seen in Fig. 2, is most probably associated with the higher excitation probability of the 5*p* state to which transitions from the 6*s* and 5*d* levels are allowed, whereas the 5*s* level can relax only to the 6*p* state.

The dependence of the Eu atom ESD yield for E_e = 50 and 80 eV on Θ, which exhibits a maximum, can be probably accounted for by the growth of the EuO reionization at large Θ due to of the increasing density of empty states in the surface band.

5. CONCLUSIONS

Thus, our study of europium ESD from the surface of oxidized tungsten has revealed, for the first time, a purely resonant character of the dependence of the yield of Eu neutrals on the incident electron energy. The Eu atom yield was found to be connected with the excitation of the 5*p* and 5*s* core levels of europium (the 32 and 38 eV peaks) and 5*p* and 5*s* of tungsten (the 50 and 80 eV peaks). The resonant character of the dependence of the yield on the electron energy is accounted for (as is the photoelectron spectra of europium reported in [15]) by the quasi-atomic, local nature of the excited state (of the exciton type) in the core-vacancy field. It was shown that excitation of the tungsten 5*p* and 5*s* levels results in desorption of the EuO molecules, whose ionization coefficient on tungsten at T = 2000 K coincides with that of the Eu atoms on tungsten. Although the main features of europium ESD from the surface of oxidized tungsten have been interpreted in this paper, some aspects of this phenomenon still remain unclear (for instance, the nature of the concentration thresholds of the ESD appearance).

ACKNOWLEDGMENTS

We are indebted to S.Yu. Davydov for fruitful discussions.

This study was supported by the Russian State Program "Surface Atomic Structures" (project no. 4.5.99) and, partially, by the Russian Foundation for Basic Research, project no. 99-02-17972.

REFERENCES

1. V. N. Ageev, Prog. Surf. Sci. **47** (1–2), 55 (1994).
2. V. N. Ageev, Yu. A. Kuznetsov, and B. V. Yakshinskiĭ, Fiz. Tverd. Tela (Leningrad) **24** (2), 349 (1982) [Sov. Phys. Solid State **24**, 199 (1982)].
3. V. N. Ageev, Yu. A. Kuznetsov, and N. D. Potekhina, Fiz. Tverd. Tela (St. Petersburg) **38** (2), 609 (1996) [Phys. Solid State **38**, 335 (1996)].

4. V. N. Ageev, Yu. A. Kuznetsov, and N. D. Potekhina, Surf. Sci. **367**, 113 (1996).
5. V. N. Ageev and Yu. A. Kuznetsov, Phys. Low-Dimens. Struct., Nos. 1/2, 113 (1999).
6. G. V. Tsyganova, N. Yu. Pasechnik, and N. N. Smirnova, Vysokochist. Veshchestva, No. 2, 43 (1991).
7. V. N. Ageev and Yu. A. Kuznetsov, Pis'ma Zh. Tekh. Fiz. **26** (13), 86 (2000) [Tech. Phys. Lett. **26**, 579 (2000)].
8. V. N. Ageev, O. P. Burmistrova, and Yu. A. Kuznetsov, Fiz. Tverd. Tela (Leningrad) **29** (6), 1140 (1987) [Sov. Phys. Solid State **29**, 1000 (1987)].
9. V. N. Ageev and N. I. Ionov, Fiz. Tverd. Tela (Leningrad) **11**, 3200 (1969) [Sov. Phys. Solid State **11**, 2593 (1970)].
10. M. L. Knotek, Springer Ser. Chem. Phys. **24**, 139 (1983).
11. V. N. Ageev and A. Yu. Afanas'eva, Fiz. Tverd. Tela (St. Petersburg) **43** (4), 739 (2001) [Phys. Solid State **43**, 772 (2001)].
12. *Practical Surface Analysis by Auger and X-ray Photoelectron Spectroscopy*, Ed. by D. Briggs and M. Seah (Wiley, New York, 1983; Mir, Moscow, 1987).
13. S. Yu. Davydov, Pis'ma Zh. Tekh. Fiz. **27** (7), 68 (2001) [Tech. Phys. Lett. **27**, 295 (2001)].
14. S. Haffner, G. G. Olson, and D. W. Lynch, Phys. Rev. B **60** (24), 16346 (1999).
15. G. Rossi, Y. Y. Yeh, I. Lindau, and J. Nogami, Surf. Sci. **152/153**, 743 (1985).
16. P. R. Antoniewicz, Phys. Rev. B **21** (9), 3811 (1980).
17. C. B. Weare and J. A. Yarmo, Surf. Sci. **348**, 369 (1996).
18. D. G. Goryunov, A. G. Borisov, G. E. Makhmetov, *et al.*, Surf. Sci. **401**, 206 (1998).
19. A. G. Borisov and J. P. Gauyacq, Surf. Sci. **445**, 430 (2000).
20. V. N. Ageev, Yu. A. Kuznetsov, and N. D. Potekhina, Fiz. Tverd. Tela (St. Petersburg) **35** (1), 156 (1993) [Phys. Solid State **35**, 82 (1993)].
21. V. N. Ageev, Yu. A. Kuznetsov, and N. D. Potekhina, Fiz. Tverd. Tela (St. Petersburg) **36** (5), 1444 (1994) [Phys. Solid State **36**, 790 (1994)].
22. V. N. Ageev and Yu. A. Kuznetsov, Fiz. Tverd. Tela (St. Petersburg) **42** (4), 759 (2000) [Phys. Solid State **42**, 780 (2000)].
23. H. M. Kramer and E. Bauer, Surf. Sci. **92**, 53 (1980).
24. M. V. Loginov and M. A. Mittsev, Fiz. Tverd. Tela (Leningrad) **22** (6), 1701 (1980) [Sov. Phys. Solid State **22**, 992 (1980)].
25. V. N. Ageev and N. I. Ionov, Zh. Tekh. Fiz. **39** (8), 1523 (1969) [Sov. Phys. Tech. Phys. **14**, 1142 (1969)].
26. S. Smoes, P. Coppens, C. Berman, and J. Drowart, Trans. Faraday Soc. **65**, 682 (1969).
27. N. D. Potekhina, Zh. Tekh. Fiz. **40** (3), 620 (1970) [Sov. Phys. Tech. Phys. **15**, 469 (1970)].
28. E. Rideal, *Consepts in Catalysis* (Academic, London, 1968; Mir, Moscow, 1971).
29. M. C. Day, Jr. and J. Selbin, *Theoretical Inorganic Chemistry* (Reinhold, New York, 1969; Khimiya, Moscow, 1976), p.122.

Translated by G. Skrebtsov

Physics of the Solid State, Vol. 43, No. 10, 2001, pp. 1979–1981. Translated from Fizika Tverdogo Tela, Vol. 43, No. 10, 2001, pp. 1901–1903.

LOW-DIMENSIONAL SYSTEMS AND SURFACE PHYSICS

Sensor Studies of the Initial Stages of the Cadmium Telluride Film Formation through Vapor Deposition

A. P. Belyaev, V. P. Rubets, and S. A. Kukushkin*

St. Petersburg Technological Institute (Technical University), Moskovskiĭ pr. 26, St. Petersburg, 198013 Russia

**Institute of Problems in Machine Science, Russian Academy of Sciences, Vasil'evskiĭ Ostrov, Bol'shoĭ pr. 61, St. Petersburg, 199178 Russia*

e-mail: Belyaev@TU.SPB.RU

Received February 27, 2001

Abstract—The results of sensor and electron-microscopic studies of the initial stages of cadmium telluride film formation through vapor deposition on a substrate at room temperature and on a substrate cooled by liquid nitrogen (highly nonequilibrium conditions) are reported. A piezoelectric quartz resonator is used as a sensor. The kinetic curves of the sensor analytical signal and photomicrographs are presented. A jumplike character of the nucleation process and a quasi-periodical growth mechanism for island films are disclosed. A sequence of new-phase island ensembles is formed in an analogous way. These islands increase the substrate surface coverage in a quasi-discrete manner. The experimental results are shown to agree with current theory of the first-order phase transitions and models of layer formation in highly nonequilibrium conditions. © *2001 MAIK "Nauka/Interperiodica".*

1. INTRODUCTION

Sensor methods of analysis of a great variety of objects [1] have gained acceptance in recent decades. In this connection, it seems to be considerably promising to try to use these methods for studying the formation mechanisms of films, the surface properties of which often play a decisive role [2, 3]. The present work is a realization of studies of such type on cadmium telluride films by means of a piezoelectric quartz sensor.

2. SAMPLES AND EXPERIMENTAL TECHNIQUES

The processes of formation of cadmium telluride films, synthesized through vapor deposition on a substrate at room temperature and on a substrate cooled to 120 K (highly nonequilibrium conditions, HNC), were studied. Cadmium telluride films several tenths of a micrometer in thickness were used as substrates. Film substrates with an area $S = 0.28$ cm^2 were deposited on the surface of silver electrodes applied to crystalline quartz. The latter served simultaneously as the basis of a piezoelectric quartz resonator. The film crystalline structure had a strongly smeared texture.

The samples studied were synthesized by open evaporation [4] of CdTe powder at a temperature of 720 K. Their thicknesses were controlled by means of an MII-4 microinterferometer. Electron-microscopic studies were carried out using a PÉM-100 microscope.

Investigations of the film formation processes were performed by means of a piezoelectric quartz sensor with a characteristic constant $A = 1670$ kHz/mm. The sensor was connected to a standard KIT-1 device (layer-thickness quartz meter), which was preliminary calibrated with cadmium telluride films. A calibration curve was plotted using continuous films and was then extrapolated to the region of small thicknesses. The reactor influence upon the sensor temperature was evaluated in a special experiment, in which the reactor, heated to the synthesis temperature, was brought into contact with the substrate (without a powder sublimated in the synthesis process). All investigations were carried out in vacuum (~10^{-3} Pa).

3. EXPERIMENTAL RESULTS

The processes of formation of cadmium telluride films were explored on the basis of sensor and electron-microscopic measurements. The main results of the investigations are represented in Figs. 1 and 2.

Figure 1 demonstrates kinetic curves for the shift of quartz sensor resonance frequency Δf in the course of the film synthesis process. Curves *1* and *2* correspond to samples synthesized on room-temperature substrates, and curve *3* corresponds to a sample prepared under HNC. The measurement conditions for curves *1* and *3* and curve *2* differed in the method of film-substrate preparation employed. Curves *1* and *3* were obtained in the course of synthesis on a freshly prepared film-substrate, which was preliminary kept in a vacuum for several hours. Curve *2* describes the synthesis on the film obtained in the process of measurement of curve *1*. The time interval between the measurements of curves *1* and *2* was approximately several tens of seconds.

1063-7834/01/4310-1979$21.00

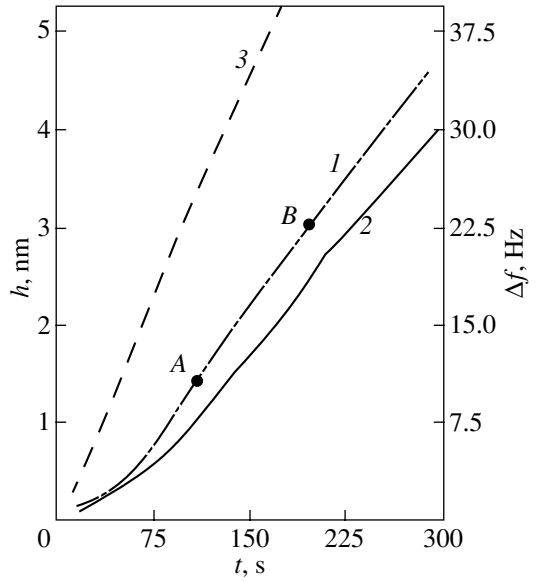

Fig. 1. Kinetic curves for the CdTe film synthesis on substrates at temperatures of (*1*, *2*) 300 and (*3*) 120 K. The curves were obtained by means of a piezoelectric resonant sensor. Curves *1* and *3* correspond to synthesis on a freshly prepared film substrate, and curve *2* corresponds to synthesis on a film formed in the process represented by curve *1*.

The kinetic curves measured at room temperature are independent of the film-substrate preparation conditions and correspond to an oscillatory stepwise function damping in its amplitude and tending asymptotically to a linear function. The frequency and amplitude of oscillations increase with the evaporator temperature. The kinetic curves measured under the HNC correspond to a monotonically increasing function.

Figure 2 presents photomicrographs of the film surface that correspond to the instants of the strongest change in Δf (points *A* and *B* in Fig. 1) during film synthesis on a substrate at room temperature. It follows from Fig. 2 that these instants correspond to island films with a surface coverage of ~ 0.16 (at instant *A*) and ~ 0.27 (at instant *B*).

4. DISCUSSION OF RESULTS

In the present work, the shift in the resonance frequency of the piezoelectric resonator Δf is used as a main analytical signal. This frequency shift was due to the formation of a layer at the surface of the piezoelectric sensor. The operation of such a sensor is based on the fact that the resonance frequency f of a piezoelectric crystal depends upon its effective thickness h [5]:

$$f = v/(2h), \quad (1)$$

where v is the sound velocity in the crystal.

As is clear from Eq. (1), this dependence is simply the condition for creation of standing waves inside a crystal having a thickness h. Thus, it is obvious that h is, in fact, an effective thickness, because it should allow for not only the geometrical crystal thickness but also the condition of its surfaces reflecting acoustic waves.

In our experiments, films were formed on one of the quartz crystal surfaces. The properties of the film, such as its material, thickness, type (island or continuous film), surface morphology, and elastic characteristics, contributed to the effective crystal thickness and, thus, caused a resonance frequency shift Δf. Therefore, the curves in Fig. 1 not only demonstrate the frequency change Δf in the course of the synthesis of cadmium telluride films but also reflect the changes in their acoustic properties.

Films of the II–VI compounds obtained through vapor deposition are formed by normal layer-by-layer

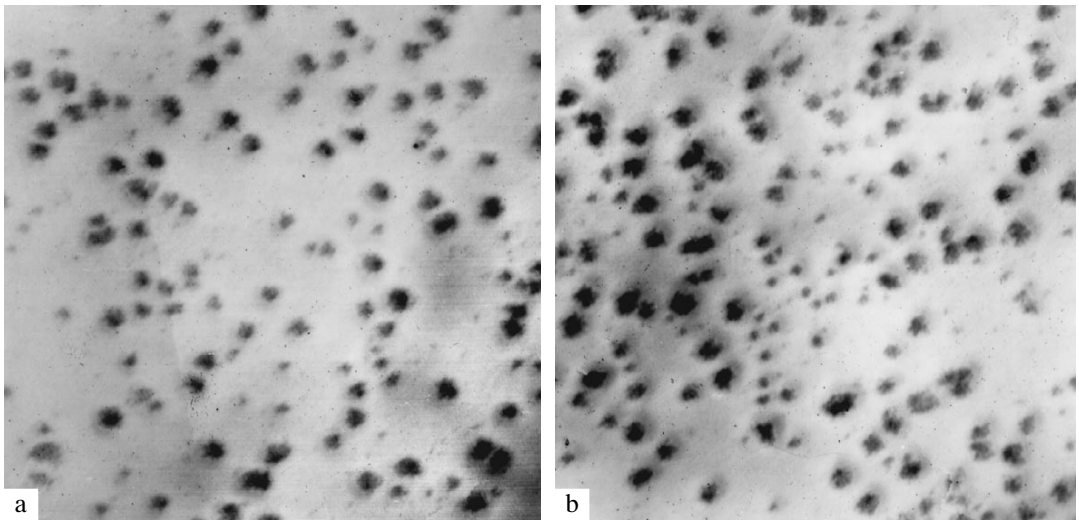

Fig. 2. Electron photomicrographs of an island film at the growth stages corresponding to points (a) *A* and (b) *B* on curve *1* in Fig. 1 (×80 000).

growth [6]. This is indicated in images of the surface obtained by means of an electron microscope at the initial stages of film growth (Fig. 2). Three-dimensional islands several tens of nanometers in diameter, which are formed on the substrate, are clearly visible in the photomicrographs. As is evident from these photographs, a higher coverage of the surface n_i corresponds to later instants of the abrupt change in Δf. At the first point, we have $n_A \approx 0.16$, while at the second, $n_B \approx 0.27$. Since analogous photographs made at intermediate instants demonstrate practically constant coverage of the substrate surface by islands, it is natural to associate the abrupt changes in the analytical signal with the changes in the coverage.

This assumption agrees with calculations of the real (V_i) and effective (V_i') volumes of the island film at different stages of its growth. The real volume is calculated using the formula

$$V_i = \frac{2}{3}\pi \bar{R}_i^3 N_i S. \quad (2)$$

Here, the islands are supposed to have a semispherical form. Their mean radius $\bar{R}_i$ and their density of filling of the substrate surface N_i are determined on the basis of electron-microscope studies.

The effective volume V_i' is calculated using the formula

$$V_i' = \Delta h_i S, \quad (3)$$

in which Δh_i are determined from the sensor measurements of Δf by using the $\Delta h = f(\Delta f)$ calibration curve.

For the states shown on curve 1 (Fig.1) by points A and B for a film of area $S = 0.28$ cm^2, calculations give $V_A = 3.40 \times 10^{-8}$ cm^3, $V_A' = 4.03 \times 10^{-8}$ cm^3, $V_B = 5.94 \times 10^{-8}$ cm^3, and $V_B' = 8.54 \times 10^{-8}$ cm^3.

From the closeness of the V_i and V_i' values and the above discussion, one can conclude that the abrupt changes in the analytical signal Δf on the kinetic curve are, indeed, associated with the abrupt creation of new-phase islands on the sensor surface.

This conclusion correlates with current theory of first-order vapor–solid phase transitions on a solid surface [7]. At the first stage of the transition, a layer of adatoms is formed on the surface, which corresponds to a monotonic increase in Δf on the kinetic curve. Then, when the critical concentration is achieved, an ensemble of three-dimensional nuclei of the solid phase is formed from the two-dimensional adatom vapor. This is accompanied by a stepwise change in the elastic properties of the substance on the substrate surface, and an abrupt increase in the analytical signal Δf is observed on the kinetic curve, because this signal, as has been indicated above, is determined, in particular, by the acoustic characteristics of the substance.

Because of the formation of the new phase, the adatom concentration at the substrate is lowered and the formation of nuclei is stopped. However, the vapor is supplied continuously by the source. As a consequence, the adatom concentration on the substrate starts to grow again, which corresponds to the next region of the Δf monotonic growth on the kinetic curve. At the instant the concentration reaches its critical value, nuclei start to arise again, which is accompanied by an abrupt change in the elastic properties and gives rise to a new jump in Δf on the kinetic curve. However, since the relative contribution of new islands to the volume of the growing island film is lower in this case, jumps in the analytical signal on the kinetic curve have a lower amplitude. It is obvious that the described process will be repeated further on until the coalescence of separate islands of the new phase results in the formation of a continuous film.

In conclusion, we make a remark with reference to the vapor condensation in highly nonequilibrium conditions. It is well known [8–10] that, in this case, nuclei of the new phase are formed mainly in the vapor phase and, as a consequence, the processes described above should not occur on the substrate surface. This is why the kinetic curves for these processes are almost monotonic.

ACKNOWLEDGMENTS

This work was supported by the Russian Foundation for Basic Research, project nos. 99-03-32676 and 99-03-32768.

REFERENCES

1. *Devices for Nondestructive Control of Materials and Productions*, Ed. by V. V. Klyuev (Mashinostroenie, Moscow, 1976).
2. A. P. Belyaev, V. P. Rubets, and M. Yu. Nuzhdin, Fiz. Tekh. Poluprovodn. (St. Petersburg) **34** (10), 1208 (2000) [Semiconductors **34**, 1157 (2000)].
3. S. A. Kukushkin and V. V. Slezov, *Disperse Systems on Solid Surfaces (Evolutional Approach): Mechanisms of Thin Film Formation* (Nauka, St. Petersburg, 1996).
4. I. P. Kalinkin, V. B. Aleskovskiĭ, and A. V. Simashkevich, *Epitaxial Films of II–VI Compounds* (Leningr. Gos. Univ., Leningrad, 1978).
5. V. V. Malov, *Piezoresonant Transducers* (Énergoatomizdat, Moscow, 1989).
6. A. P. Belyaev, V. P. Rubets, M. Yu. Nuzhdin, and I. P. Kalinkin, Fiz. Tverd. Tela (St. Petersburg) **43** (4), 745 (2001) [Phys. Solid State **43**, 778 (2001)].
7. S. A. Kukushkin and A. V. Osipov, Usp. Fiz. Nauk **168** (10), 1083 (1998) [Phys. Usp. **41**, 983 (1998)].
8. A. P. Belyaev, V. P. Rubets, and I. P. Kalinkin, Neorg. Mater. **34** (3), 281 (1998).
9. A. P. Belyaev, V. P. Rubets, and I. P. Kalinkin, Fiz. Tverd. Tela (St. Petersburg) **39** (2), 382 (1997) [Phys. Solid State **39**, 333 (1997)].
10. A. P. Belyaev, V. P. Rubets, and I. P. Kalinkin, Zh. Tekh. Fiz. **71** (4), 133 (2001) [Tech. Phys. **46**, 495 (2001)].

Translated by A. Sonin

Physics of the Solid State, Vol. 43, No. 10, 2001, pp. 1982–1988. Translated from Fizika Tverdogo Tela, Vol. 43, No. 10, 2001, pp. 1904–1910.

FULLERENES AND ATOMIC CLUSTERS

Theoretical Study of the Toroidal Forms of Carbon and Related Endohedral Complexes with Lithium

A. A. Kuzubov[1, 2], P. V. Avramov[2], S. G. Ovchinnikov[1, 2], S. A. Varganov[2], and F. N. Tomilin[2, 3]*

[1]*Krasnoyarsk State Technical University, Krasnoyarsk, Russia;*

[2]*Kirensky Institute of Physics, Siberian Division, Russian Academy of Sciences, Akademgorodok, Krasnoyarsk, 660036 Russia*

[3]*Institute of Chemistry and Chemical Technology, Siberian Division, Russian Academy of Sciences, Krasnoyarsk, Russia*

**e-mail: felix@iph.krasn.ru*

In final form received April 3, 2001

Abstract—The atomic and electron structures of toroidal carbon molecules (C_{240} and two C_{120} isomers) and related endohedral complexes with lithium ($Li_2@C_n$ and $Li_4@C_n$) were theoretically studied using both nonempirical (3–21*G* basis set) and semiempirical (MNDO) calculation schemes. For the metal-containing compounds, the behavior of lithium atoms embedded into internal cavities of the carbon framework was studied using methods of molecular dynamics. It is demonstrated that the structure of electron levels of metal-containing carbon complexes exhibits an embedded state in the forbidden band, which appears due to the presence of electrons accepted from metal atoms. The position of this embedded state and the bandgap width depend both on the initial carbon structure and on the amount of metal atoms incorporated. © *2001 MAIK "Nauka/Interperiodica".*

1. INTRODUCTION

To date, a large number of cluster compounds representing allotropic forms of carbon have been discovered. Exhibiting a large variety of structures and possessing unusual properties, these objects have drawn special attention of researchers. One of the families of carbon clusters represents toroidal forms of carbon. Molecules of this type, experimentally observed for the first time in 1992 [1], appear as closed surfaces composed of various carbon polygons, including pentagons, hexagons, and heptagons (Fig. 1). The presence of pentagons provides for a positive curvature of the surface, while heptagons account for a negative curvature. According to experimental data, toroidal carbon molecules may contain various numbers of atoms (from 80 to several thousands) and exhibit rather complicated shapes (Fig. 2).

Since 1992, a number of papers have been published devoted to theoretical investigation of toroidal carbon molecules. Itoh and Ihara [2–4] and Johnson [5] studied the dependence of the energies and electron structures of clusters on the amount of atoms and the geometric parameters of these objects (symmetry, internal and external diameters, etc.). In [6], Itoh and Ihara thoroughly studied C_{240} isomers (in that investigation, cluster geometries were optimized by the molecular dynamics method and the electron structures were calculated by the Hückel method). Dunlap [7] and Menner [8] studied the atomic and electron structures of still greater toroidal molecules: Dunlap described carbon tori containing 240, 540, and 576 atoms and obtained bandgap widths of 1, 0.04, and 0.02 eV, respectively; Menner studied a C_{1960} molecule, for which he obtained a bandgap width of 0.05 eV. Both researchers employed empirical potentials for the molecular geometry optimization and used the tight binding model for the electron structure calculations. In the general case, the distinctions between the electron structures of toroidal molecules were explained in terms of differences in atomic structures.

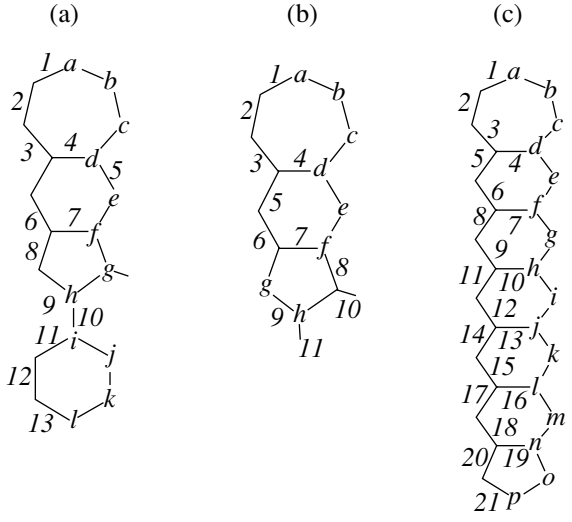

Fig. 1. Segments of toroidal carbon molecules: (a) C_{120} (long); (b) C_{120} (short); (c) C_{240}. Inequivalent atoms are indicated by letters and the bonds between these atoms are enumerated.

Of much greater interest are the derivatives of toroidal carbon molecules, in particular, metal-containing complexes. No data on such objects have been reported so far, although investigation of the geometry of toroidal molecules containing metal atoms in cavities, the electron structure of such complexes, and the behavior of incorporated metal atoms is a very interesting task.

We have theoretically studied the toroidal forms of carbon and related electron-doped derivatives (endohedral complexes with lithium) using the methods of quantum chemistry and molecular dynamics, aiming at establishing regularities in the spatial and electron structures of these molecules.

2. OBJECTS AND METHODS OF INVESTIGATION

We have theoretically studied the toroidal molecules containing 120 and 240 carbon atoms (Figs. 1, 2). In the case of C_{120}, we studied two isomers differing in values of their internal and external diameters and in arrangement of pentagons and heptagons. The structures of C_{120} (with elongated segments) and C_{240} compounds were proposed in [2, 3]. In addition to this C_{120} isomer denoted C_{120} (long), we have also studied another C_{120} isomer referred to hereinafter as "short." The coordinates of inequivalent atoms in the C_{120} (short) isomer are given in Table 1.

In addition to the toroidal carbon structures, we studied the related metal-containing complexes with lithium (Figs. 2d, 2f), in particular, compounds containing two and four alkali metal atoms inside the carbon clusters. In this study, the main attention was paid to determining the positions of metal atoms, the behavior of these atoms at a given temperature (300 K in this model calculation), and the influence of embedded metal atoms upon the electron structure of the toroidal carbon framework.

The calculations were performed using semiempirical (MNDO) and nonempirical (3–21*G* basis set) calculation schemes. The latter method was applied only to C_{120} isomers and used to assess the applicability of various calculation schemes to the clusters studied. The calculations of toroidal molecules were performed with symmetry limitations: C_5 for C_{120} (long) and C_{240}; D_{5d} for C_{120} (short). No such limitations were posed on the metal-containing complexes, which allowed all possible coordinations of the metal atoms to be determined. To check for the fact that a given system occurred in a local energy minimum, we calculated the vibrational spectra of compounds. The absence of complex modes was indicative of the occurrence of a local minimum. Containing large numbers of atoms, the systems under consideration may possess several local minima. For determining the global minimum of energy, we considered various initial positions of atoms which led, in the course of optimization, to atomic configurations corresponding to various local minima. An analysis of these results allowed the global minimum of energy to be determined, which was additionally verified by comparison with molecular dynamics data. All structures were calculated in both singlet and triplet states using a GAMESS program [9].

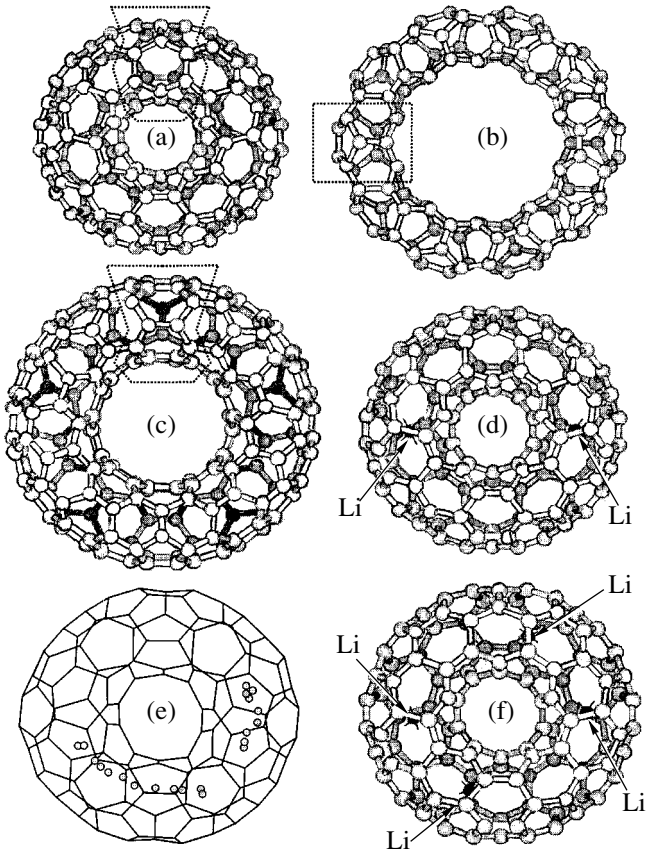

Fig. 2. Schematic diagrams showing the structures of toroidal carbon molecules and related complexes with lithium: (a) C_{120} (long); (b) C_{120} (short); (c) C_{240}; (d) $Li_2@C_{120}$ (long); (e) trajectories of the lithium atom in the course of molecular modeling of the $Li_2@C_{120}$ (long) complex; (f) $Li_4@C_{120}$ (long) complex. Dashed contours in (a)–(c) frame molecular segments depicted in Fig. 1.

Table 1. The coordinates of inequivalent atoms (Å) in the C_{120} (short) isomer calculated using the MNDO method for a molecule with the *D*5*d* symmetry

x	*y*	*z*
0.0000	4.6992	1.2477
0.0000	6.0552	1.6057
0.7582	7.1114	0.2071
0.6784	5.1688	1.4971
1.5186	6.4116	–1.2346
1.2622	6.7170	1.1064
1.2650	4.1822	0.7031

Table 2. Interatomic distances (Å) between inequivalent atoms in various toroidal carbon molecules

Bond number	C_{120} (long)		C_{120} (short)		C_{240}
	MNDO	3–21*G*	MNDO	3–21*G*	
1	1.477	1.474	1.471	1.454	1.433
2	1.378	1.333	1.417	1.364	1.413
3	1.485	1.472	1.513	1.507	1.469
4	1.386	1.341	1.357	1.312	1.371
5	1.466	1.447	1.523	1.531	1.448
6	1.420	1.385	1.457	1.425	1.489
7	1.479	1.464	1.516	1.539	1.423
8	1.477	1.461	1.461	1.415	1.427
9	1.477	1.458	1.510	1.520	1.450
10	1.411	1.374	1.434	1.405	1.388
11	1.495	1.490	1.402	1.346	1.478
12	1.466	1.447			1.483
13	1.485	1.472			1.498
14					1.431
15					1.456
16					1.483
17					1.470
18					1.407
19					1.494
20					1.468
21					1.482
22					1.395

Table 3. Energies (per atom) and bandgap widths of various toroidal carbon molecules and related complexes with lithium atoms

Object	$\Delta E_{HO–LU}$, eV	$-E$/atom, eV
C_{120} (long), MNDO	6.454	127.18
C_{120}, 3–21*G*	7.809	1024.34
C_{120} (long), 3–21*G* (opt. MNDO)	7.138	1024.31
$Li_2@C_{120}$ (long)	1.611	125.19
$Li_4@C_{120}$ (long)	2.114	123.27
C_{120} (short) MNDO	5.828	126.62
C_{120} (short), 3–21*G*	7.181	1023.85
C_{120} (short), 3–21*G* (opt. MNDO)	6.201	1023.81
$Li_2@C_{120}$ (short)	2.686	124.57
$Li_4@C_{120}$ (short)	4.634	122.58
C_{240}	4.422	127.27
$Li_2@C_{240}$	4.304	126.29
$Li_4@C_{240}$	3.603	125.31

The behavior of lithium atoms in metal-containing complexes was studied using the method of molecular dynamics. Requiring no empirical intermolecular and interatomic potentials, this method is widely employed at present for investigation of the dynamic properties of molecular systems [10]. In this study, the behavior of lithium atoms in complexes with carbon was simulated by a demonstrative version of the HyperChem 5.02 program capable of performing calculations with the aid of semiempirical (MNDO, PM3) potentials.

3. CALCULATIONS OF TOROIDAL MOLECULES

Before studying various carbon clusters and related complexes, it is necessary to consider differences in the spatial and electron structures of these molecules as determined from various methods (semiempirical and nonempirical). For buckminsterfullerene, the most accurate values of bond lengths were obtained using semiempirical methods (PM3, MNDO) [11]. A nonempirical calculation using a 3–21*G* basis set leads to a double bond length 0.04 Å shorter than that given by the semiempirical methods (the same difference is observed for C_{60}). The length of a bond with the bond order (determined according to [9]) about unity was virtually the same (Table 2, Fig. 1).

Changes in the electron structure were not less significant. The electron levels determined from semiempirical calculations were much closer to each other than those obtained from nonempirical methods (Fig. 3). Despite this shift, the structure of levels in the valence band region remained qualitatively unchanged. Nevertheless, the shift led to a certain difference in estimates of the bandgap width (Table 3) obtained from semiempirical and nonempirical methods (e.g., the difference was 1.35 eV for both C_{120} isomers).

A comparative analysis of data for the C_{120} isomers (Table 3) showed that the C_{120} (short) molecule is energetically less favorable (by 66.8 and 58 eV according to estimates obtained using the MNDO method and the nonempirical calculation employing 3–21*G* basis set, respectively). We explain this discrepancy in terms of small diameter of the internal cavity in this isomer leading to higher bond stresses in the cluster. As a result, the bond lengths in the polygons of C_{120} (short) have proved to be smaller than those in the corresponding polygons of C_{120} (long). Despite this difference, the proportional bond ratios in the like cycles of both isomers were very close.

Each pentagon or heptagon in C_{240} molecules, in contrast to those in C_{120} isomers, is surrounded by hexagons; this circumstance significantly changed the bond lengths in some polygons (Table 2, Fig. 1). However, certain features typical of the interatomic distances in C_{120} are also retained in C_{240}. In particular, the shortest bonds are those shared by heptagons and hexagons (bonds *4* in all structures) and those originating from the vertices of pentagons (bonds *10* in C_{120} and *22* in C_{240}).

4. ENDOHEDRAL COMPLEXES WITH LITHIUM

Upon optimization of the molecular geometry of the carbon complexes containing two lithium atoms, the incorporated metal atoms resided at the opposite ends of the internal cavity of the carbon clusters. Embedded in the C_{120} (long) molecule, lithium atoms are spaced by 7.79 Å and coordinated against bonds *5* of the carbon molecule (Figs. 1, 2d). In the C_{120} (short) isomer, the distance between embedded metal atoms is 10.9 Å and these atoms are located in the cavity near bonds *11*. In the $Li_2@C_{240}$ complex, lithium atoms spaced 10.5 Å apart are located near bonds *22*. It must be noted that, in all cases, lithium atoms occur at virtually equal distances from walls of the internal cavity.

In the complexes containing four lithium atoms, the incorporated particles were differently coordinated in the two C_{120} isomers. In the $Li_4@C_{120}$ (long) complex, alkali metal atoms exhibited coupling: atoms in the couple are spaced 4.48 Å apart and the distance between two couples is 6.44 Å (Fig. 2f). The $Li_4@C_{120}$ (short) complex adopted a configuration with maximum possible distances between alkali metal atoms: 8 Å between nearest neighbors and 11.6 Å between opposite atoms. In the $Li_4@C_{240}$ molecule, lithium atoms are also distributed in the internal cavity so as to be maximum spaced (with the distances 7.5 and 10.39 Å between nearest neighbors and opposite atoms, respectively).

The results of our calculations showed that the introduction of alkali metal (i.e., electron donor) atoms into carbon clusters leads to distortion of the framework structure. This is manifested by increasing bond lengths in the carbon cluster at the metal coordination sites. Because of the large size of carbon clusters studied, changes in carbon–carbon bond lengths become less pronounced with increasing distance from lithium atoms. The increase in the carbon–carbon bond lengths in the metal-containing clusters in comparison with that in the metal-free initial toroidal molecules is evidence of an antibonding character of the vacant states occupied by the electrons accepted from embedded metal atoms.

The process of complex formation with alkali metal atoms leads to a change in electron structure of the toroidal carbon molecules. In contrast to the pure carbon tori, where the lowest energy states are singlets, a minimum energy in the complexes of C_{120} with two or four lithium atoms [except for $Li_4@C_{120}$ (short)] is attained in the triplet states. An energy difference between triplet and singlet states for $Li_2@C_{120}$ (long), $Li_4@C_{120}$ (long), $Li_2@C_{120}$ (short), and $Li_4@C_{120}$ (long) amounts to 1.26, 0.05, 0.06, and 0.34 eV, respectively. In order to establish a reason for this behavior, it is necessary to consider the vacant levels of C_{120} isomers. The lowest vacant state (see Figs. 4a, 4b) is level *A*, which is followed by a doubly degenerate level E_1; in the complexes containing two metal atoms, these levels exhibit inversion. Two electrons introduced with lithium atoms fill the vacant electron states of the carbon framework,

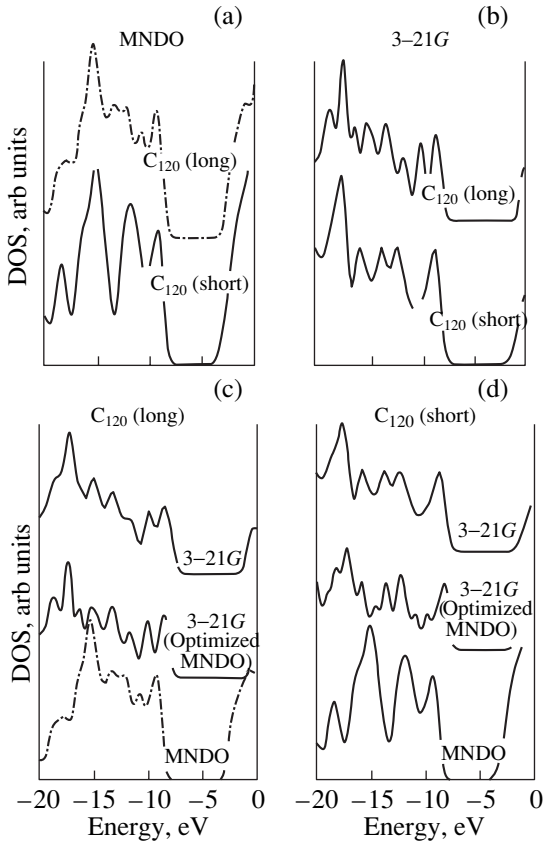

Fig. 3. Densities of states in toroidal carbon cluster structures calculated from various methods: (a) C_{120} (long) and C_{120} (short), MNDO; (b) C_{120} (long) and C_{120} (short), 3–21*G*; (c) C_{120} (long), MNDO, 3–21*G* optimized by MNDO, and 3–21*G*; (d) C_{120} (short), MNDO, 3–21*G* optimized by MNDO, and 3–21*G*.

occupying first the two orbitals corresponding to a lowest vacant state of the E_1 level. According to the Hund rule, this leads to the appearance of a triplet. The inversion of levels also takes place in $Li_4@C_{120}$ (short), where the embedded state (similar to that described above) is represented by two levels accommodating four electrons (accepted from alkali metal atoms) which form a singlet. No such alteration in the arrangement of levels takes place in the $Li_4@C_{120}$ (long) complex, where two (of the four) electrons occupy level *A* and two other electrons occupy the two levels previously forming the degenerate E_1 level, thus yielding a ground triplet state.

Calculations performed for the metal-containing C_{240} complexes showed that singlet states are energetically more favorable than triplet states (the gain being 0.38 and 0.1 eV in $Li_2@C_{240}$ and $Li_4@C_{240}$, respectively). In this case, sequential filling of singly degenerate levels *A* is preferred (Fig. 4c).

In all metal-containing complexes studied, the set of levels filled by electrons accepted from incorporated lithium atoms (embedded state) is situated ~1–4 eV

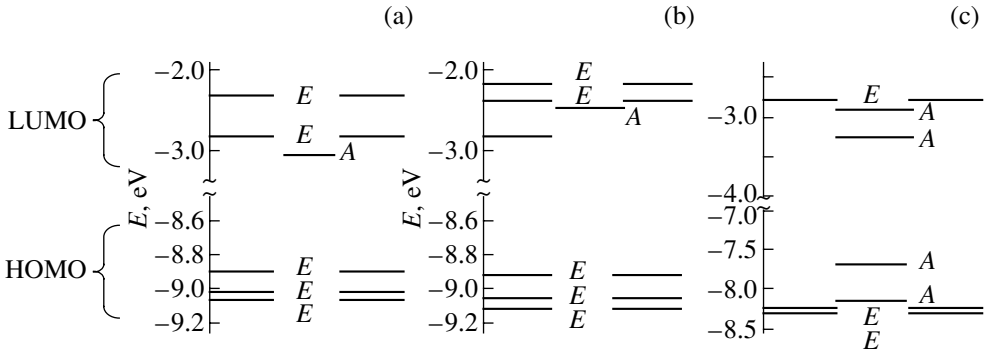

Fig. 4. Electron energy level structure in the valence band of toroidal carbon molecules: (a) C_{120} (short); (b) C_{120} (long); (c) C_{240}.

above the other filled levels. Thus, the passage of electrons from metal atoms to the carbon framework of the complex leads to formation of the embedded state (Fig. 5). A similar process was observed in the metal complexes of C_{60} fullerenes [1]. The shift of electron levels under the action of positively charged lithium atoms is less pronounced in the toroidal carbon molecules than in C_{60}, which is related to the greater dimensions of the former clusters. However, we may suggest that the same factor accounts for the inversion of energy levels leading to the triplet state formation in the case of toroidal molecules. This is confirmed by the results of calculation of the isoelectron C_{120}^{-2} ion, where no such inversion of levels takes place.

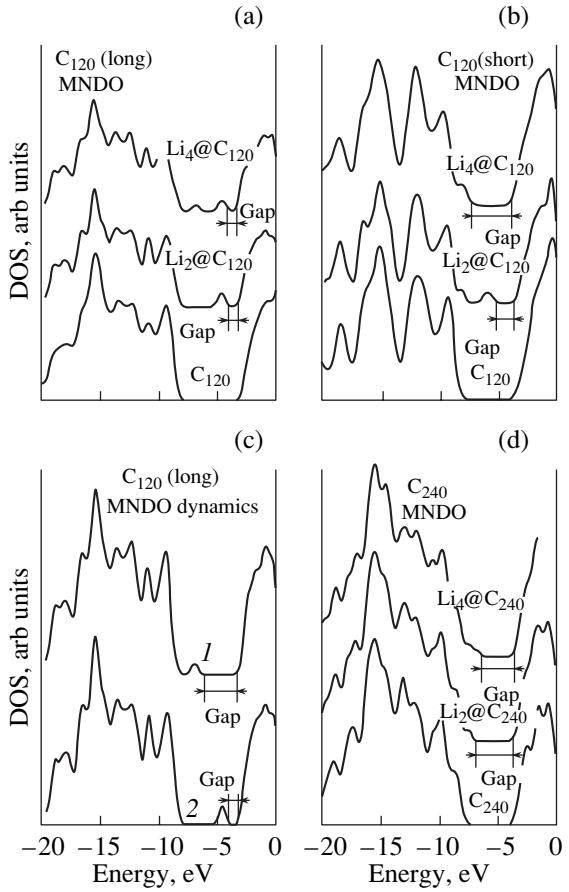

Fig. 5. Densities of states in metal-containing complexes $Li_n@C_m$ calculated from the MNDO method: (a) C_{120} (long), $Li_2@C_{120}$ (long), and $Li_4@C_{120}$ (long); (b) C_{120} (short), $Li_2@C_{120}$ (short), and $Li_4@C_{120}$ (short); (c) $Li_2@C_{120}$ (long) simulated by molecular dynamics method for lithium atoms spaced at (*1*) R_{min} = 2.95 Å and (*2*) R_{max} = 7.75 Å; (d) C_{240}, $Li_2@C_{240}$, and $Li_4@C_{240}$.

As can be seen from Figs. 5a, 5b, and 5d, the embedded level positions depend on the amount of incorporated metal atoms. As the number of such atoms increases, the embedded state in C_{240} complexes (Fig. 5d) shifts toward vacant levels. This displacement leads to a decrease in the bandgap width (Table 3). The metal-containing complexes based on C_{120} (short) exhibit an opposite pattern (Fig. 5b, Table 3), whereby the embedded state is situated closer to the vacant levels in $Li_2@C_{120}$ (short) than in the complex with four metal atoms. In the complexes based on C_{120} (long) with either two or four lithium atoms (Fig. 5a, Table 3), the embedded state shifts so as to completely shorten the forbidden band (1.8 eV). Thus, we may conclude that the appearance of the embedded state in the electron structure is a general property of all lithium-intercalated toroidal carbon compounds.

5. MOLECULAR DYNAMICS OF METAL-CONTAINING COMPLEXES OF TOROIDAL CARBON MOLECULES WITH LITHIUM

We have employed the molecular dynamics method to study the behavior of the incorporated alkali metal atoms inside a carbon cluster framework. The calculations were performed for both singlet and triplet states of the complexes containing two or four lithium atoms.

In C_{120} (short) isomers with any number of incorporated atoms and any multiplicity of the ground sate, the guest atoms performed small oscillations in a potential well at an energy minimum determined in the course of

the geometry optimization. The oscillating atoms did not leave the space bounded by *d–e–f* hexagon (Figs. 1, 2). This behavior is explained by the small internal diameter of this carbon cluster. In addition, a toroidal molecule of this type contains adjacent cavities with a diameter of ~2.8 Å connected by 2.2-Å windows. These windows play the role of barriers keeping lithium atoms within strictly confined regions inside the carbon molecule.

A significantly different pattern is observed for the guest metal atoms incorporated into the C_{120} (long) isomer. Since this isomer structure is characterized by a considerably greater internal diameter (~4 Å) as compared to that in C_{120} (short) and the inner surface is free of nodes (as well as that in C_{120} (short)), the incorporated metal atoms can move freely over the whole cavity of the carbon core. Nevertheless, the inner surface still has potential minima of two types. The first (global) minimum is situated in the vicinity of bond *5* (Figs. 1, 2d). The second minimum (with a higher energy) is at the center of a *d–e–f* hexagon (Fig. 1). Simulations of the behavior of lithium atoms in $Li_2@C_{120}$ and $Li_4@C_{120}$ complexes in the triplet state showed guest atoms passing from one minimum to another. These transitions were only performed between neighboring minima and did not significantly affect the positions of incorporated atoms. The same behavior was typical of lithium atoms in simulations of $Li_4@C_{120}$ complexes in the singlet state.

However, an essentially different pattern was observed for $Li_2@C_{120}$ complexes in the singlet state. Here, the incorporated alkali metal atoms, also passing from one minimum to another, shifted toward each other to form a pair spaced ~3 Å apart. After that, atoms of the couple jointly performed transitions between adjacent minima, thus migrating over the internal cavity. The Li– Li distance in the couple exhibited oscillations, but the maximum spacing between atoms never exceeded 6.3 Å. This behavior, as well as the resulting appearance of a nonzero orbital angular momentum of ions in the molecule at elevated temperatures, are explained by a change in the total orbital angular momentum of electrons. Indeed, the total angular moment of the system, representing a sum of the electron orbital angular momentum, nuclear angular momentum, and spin, has to be conserved. An increase in the temperature leads to changes in the effective internuclear distances and, hence, modifies the electron wavefunction of the system so that $\psi(r, R_0) \neq \psi(r, R_T)$, because the set of nuclear coordinates entering as parameters into this wavefunction also changes with the temperature ($\{R_0\} \neq \{R_T\}$). Therefore, the whole system (remaining in the state of the same multiplicity) must compensate for a change in the electron orbital angular momentum. This is achieved by changing the ion orbital angular momentum, as manifested by the motion of lithium atoms in the singlet state. The nonzero value of the spin component leads to a change in the proportion between the electron and ion orbital angular momenta and in the onset temperature for the motion of atoms inside the cavity. This circumstance explains the absence of motions of the incorporated Li atoms in $Li_2@C_{120}$ complexes in the triplet state. A similar effect is observed upon changing the number of incorporated atoms in the same carbon framework.

Thus, the $Li_2@C_{120}$ complexes in the singlet state exhibit various atomic configurations with different electron structures depending on the temperature. Figure 5c shows two such structures, corresponding to the maximum and minimum distances between lithium atoms. The temperature-induced variations in the electron spectra must be accompanied by superposition of the electron structures corresponding to different configurations, so that some of the related spectral features must be smeared. This refers, in particular, to the embedded state. As the lithium atoms are removed from one another, the embedded state shifts toward vacant orbitals; on the contrary, a decrease in the spacing between metal atoms drives the embedded state away from the vacant levels. The difference between the positions of the embedded state reaches ~2 eV.

It should be noted, however, that a multiplet character of the system cannot be revealed without allowance for the correlation effects. Therefore, interpretations of the temperature dependence of the experimental photoelectron spectra allow us to judge the spin state of the carbon complexes studied.

The complexes of toroidal carbon C_{240} with different (two or four) numbers of lithium atoms exhibited no significant motions of incorporated metal atoms in either the singlet or triplet state. This can be explained by the presence of deep potential minima (absent in C_{120} tori of smaller diameter) on the inner surface of the carbon framework.

6. CONCLUSIONS

Toroidal carbon molecules possess significantly different atomic and electron structures. Factors such as the number of atoms in the cluster, symmetry, dimensions (internal and external diameters), and order of cycles connected in a segment affect both the structure of electron energy levels and the bandgap width.

The introduction of alkali metal atoms into internal cavities of the toroidal carbon molecules leads to analogous changes in the atomic and electron structures of all objects studied. The presence of lithium atoms increased the interatomic distances in the carbon framework of the complex as compared to those in the initial structure. The electron structure exhibited an embedded state in the forbidden band. The position energy of this state depends on a number of factors (amount of incorporated atoms, structure of the initial carbon molecule, multiplicity, etc.). On the whole, the effect of incorporated metal atoms reduces to the decrease in the bandgap width related to the appearance of the embedded state. The molecular dynamics data indicate that, under certain conditions (sufficiently large size of the internal cavity, the absence of barriers

or minima on the inner surface, or singlet ground state), the experimental spectra would exhibit smearing of the peak corresponding to the embedded levels, which is related to the mobility of metal ions in cavities of the carbon tori.

Files with film of the molecular dynamics are accessible on the server of the Kirensky Institute of Physics (Kirensky.iph.krasn.ru). The authors are ready to provide these data on request via e-mail (felix@iph.krasn.ru).

ACKNOWLEDGMENTS

All calculations were performed at the Collective User Center "Quantum-Chemical Calculations of Nanoclusters" of the Krasnoyarsk Scientific-Educational High-Tech Center supported by the Federal Targeted Program "State Support for the Integration of Higher Education and Fundamental Science" (project no. 69). The authors gratefully acknowledge support from the Federal Programs "High-Temperature Superconductors" (project no. 99019) and "Fullerenes and Atomic Clusters" and from the NATO Scientific Affairs Division (project PST.CLG 974818).

REFERENCES

1. B. M. Terrones, Philos. Trans. R. Soc. London, Ser. A **354**, 2025 (1992).
2. S. Itoh and S. Ihara, Phys. Rev. B **47**, 1703 (1993).
3. S. Itoh and S. Ihara, Phys. Rev. B **47**, 12908 (1993).
4. S. Itoh and S. Ihara, Phys. Rev. B **48**, 8323 (1993).
5. J. K. Johnson, Phys. Rev. B **50**, 17575 (1994).
6. S. Itoh and S. Ihara, Phys. Rev. B **49**, 13970 (1994).
7. B. I. Dunlap, Phys. Rev. B **46**, 1933 (1992).
8. V. Menner, Phys. Rev. B **57**, 14886 (1998).
9. M. W. Schmidt, K. K. Baldridge, J. A. Boatz, *et al.*, J. Comput. Chem. **14**, 1347 (1993).
10. R. Car and M. Parinello, Phys. Rev. Lett. **55** (22), 2471 (1985).
11. S. A. Varganov, P. V. Avramov, and S. G. Ovchinnikov, Fiz. Tverd. Tela (St. Petersburg) **42** (2), 378 (2000) [Phys. Solid State **42**, 388 (2000)].

Translated by P. Pozdeev

Physics of the Solid State, Vol. 43, No. 10, 2001, pp. 1989–1994. Translated from Fizika Tverdogo Tela, Vol. 43, No. 10, 2001, pp. 1911–1915.

FULLERENES AND ATOMIC CLUSTERS

Analysis of the Parameters of a Smeared Orientational Transition at 250–260 K in C_{60} Crystals

G. A. Malygin

Ioffe Physicotechnical Institute, Russian Academy of Sciences, Politekhnicheskaya ul. 26, St. Petersburg, 194021 Russia
e-mail: malygin.ga@pop.ioffe.rssi.ru

Received January 29, 2001

Abstract—The orientational structural transformation in C_{60} crystals at temperatures of 250–260 K is investigated within the theory of smeared first-order phase transitions. The parameters of this transformation are analyzed using the experimental temperature dependences of the heat capacity and the inelastic (ferroelastic) strain rate in the phase transition range. The elementary volume of the transformation (11–83 nm^3) in a correlated motion of C_{60} molecules and the spontaneous shear strain of the lattice (2.4×10^{-2}) upon its transformation from the simple cubic to the face-centered cubic structure are determined. © *2001 MAIK "Nauka/Interperiodica".*

1. INTRODUCTION

Crystals C_{60} at temperatures below 250–260 K undergo an orientational transition from the face-centered cubic to the primitive cubic structure [1, 2]. The occurrence of the structural transformation in C_{60} crystals in this temperature range is confirmed by characteristic peaklike anomalies in the temperature dependences of the heat capacity [1], internal friction [3, 4], and mechanical properties [5–7]. Calorimetric studies [8, 9] have revealed that C_{60} crystals exhibit an endothermal effect at temperatures of 250–260 K.

As a rule, orientational transformations (second-order phase transitions) in crystalline materials are characterized by asymmetric (λ-shaped) peaks in the temperature dependences of their properties. However, many compounds, including C_{60} crystals [6, 9], exhibit symmetric (Λ-shaped) peaks, as well as peaks of intermediate shapes. For example, bell-shaped peaks in the temperature dependences of crystal properties are typical of smeared first-order phase transitions [10]. Similar peaks are observed upon orientational and structural transitions in dielectrics [11], ferroelectrics and ferroelastics (for example, in the high-temperature superconducting ceramics $YBa_2Cu_3O_{6+\delta}$ [10, 13]) [12], and metal alloys with the so-called shape memory effect [10]. The available data allow one to make the inference that the orientational structural transition in C_{60} at temperatures of 250–260 K is the first-order phase transition [3, 14]. This transformation is accompanied by the thermal effect [8, 9] and a sufficiently large (of the order of 1%) change in the crystal volume [14, 15].

There exist two opinions concerning the origin of smeared phase transitions. According to the first point of view [16, 17], the smearing of phase transitions is determined by the influence of composition fluctuations or structural defects in a crystal on the critical temperature of the phase transformation. As a consequence, the critical temperature fluctuates about the mean phase-transition temperature according to a random (for example, Gaussian) distribution law [17]. The second (not too formal) view holds that the smearing of phase transitions is caused by a cooperative correlated motion of particles (atoms and molecules) in the course of the phase transition in the crystal. The cooperative character of their motion (reorientation) is associated with the existence and the motion of interphase (twin) boundaries, which are characteristic of first-order phase transitions. The interaction of interphase boundaries with structural defects in the crystal brings about a decrease in the mobility of the boundaries. In turn, this necessitates further supercooling of the crystal, which leads to an increase in the temperature range of the transformation. In this case, the phase transition range depends on the concentration of structural defects and external (mechanical, electric, or magnetic) fields applied to the crystal (and interphase boundaries). As a result, the critical temperature of the phase transition can either slightly increase or decrease. These concepts underlay the phenomenological theory of smeared phase transitions which has been developed in my recent works [10, 18]. This theory makes it possible to describe quantitatively Λ-shaped peaks in the temperature dependences of the crystal properties in the temperature range of the phase transition and to analyze its basic parameters.

In this work, the structural transformation in C_{60} crystals at temperatures of 250–260 K is investigated within the framework of the phenomenological theory of smeared phase transitions. The parameters of this transformation are analyzed using the temperature dependences of the mechanical [6] and calorimetric [9] properties of these crystals in the phase transition range 250–260 K. This analysis is performed in Section 4. The basic relationships used in the theory of smeared phase transitions are given in Sections 2 and 3.

1063-7834/01/4310-1989$21.00

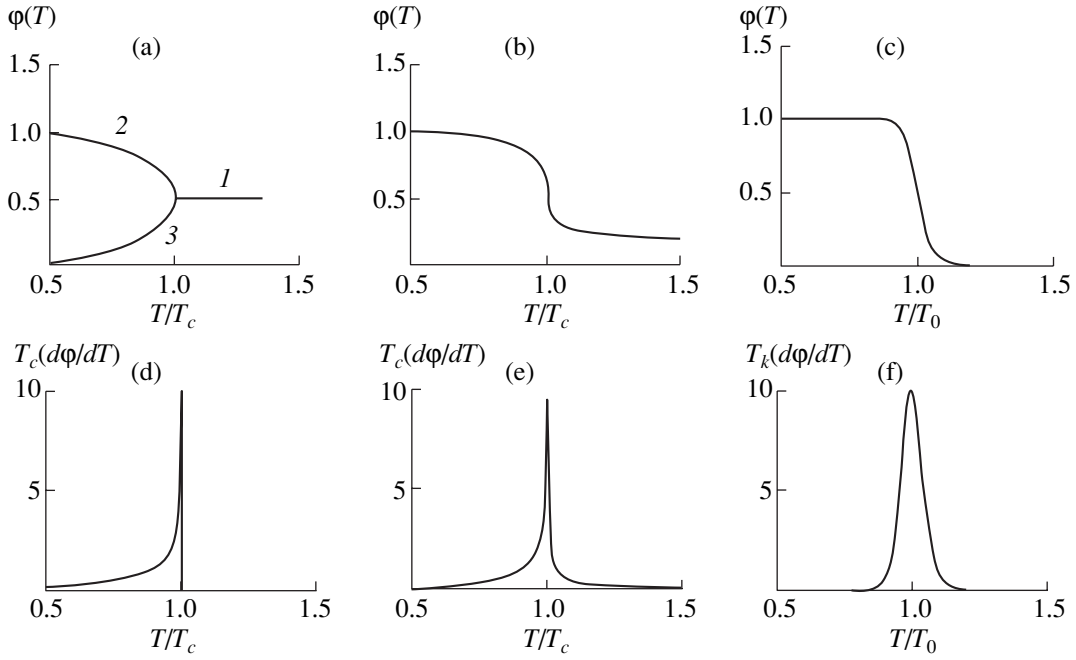

Fig. 1. Temperature dependences of (a–c) the relative volume φ of the low-temperature phase and (d–f) the derivative $d\varphi/dT$ upon (a, d) second-order, (c, f) first-order, and (b, e) intermediate-order (between first- and second-order) phase transitions.

2. SMEARED PHASE TRANSITIONS

In the framework of the thermodynamic approach, the evolution in the phase state of a system of particles (atoms and molecules) is governed by the change in the free energy $\Delta F = \Delta U - T\Delta S$, where ΔU is the change in the internal energy, ΔS is the change in the entropy, and T is the temperature of the system. The change in the internal energy involves two components, namely, the change in the self-energy of particles and the change in the energy of interaction between particles in different states. In the self-consistent field model [19], the relationship for the free energy of transition has the following form [10, 18]:

$$\Delta F(\varphi, T) = \Delta U_{12}\varphi + U_0\varphi(1-\varphi) + kT[\varphi\ln\varphi + (1-\varphi)\ln(1-\varphi)], \quad (1)$$

where φ is the relative number of particles in a new phase state and k is the Boltzmann constant. In the right-hand side of expression (1), the first term describes the change in the energy of particles, the second term represents the energy of interaction between particles in different states, and the third term characterizes the change in the entropy upon phase transition. The parameters ΔU_{12} and U_0 specify the quantitative scale of the corresponding terms in expression (1).

In the case of purely orientational transitions (second-order transitions), the self-energy of particles remains unchanged ($\Delta U_{12} = 0$). The orientational ordering of the particles is caused by the interparticle interaction, and their disordering is associated with the entropy term. The equilibrium state is determined by the conditions

$$\frac{\partial\Delta F}{\partial\varphi} = 0, \quad \frac{\partial^2\Delta F}{\partial\varphi^2} \geq 0. \quad (2)$$

As a result, the temperature dependence of the number of orientationally ordered particles can be written in the implicit form

$$\frac{T}{T_c} = \frac{2(2\varphi-1)}{\ln\left(\frac{\varphi}{1-\varphi}\right)}, \quad T_c = \frac{U_0}{2k}. \quad (3)$$

This dependence is depicted in Fig. 1a. At temperatures above the critical point T_c, owing to the thermal motion, the numbers of particles with different orientations are equal to each other (φ = 1/2). This means that particles are orientationally disordered (straight line *1*). At temperatures below the critical point, the interaction between particles is strong enough to provide orientational ordering. It can be seen that a decrease in the temperature brings about an increase in the number of orientationally ordered particles (curve *2*) and a decrease in the number of disordered particles (curve *3*).

Let us now consider the case when the term that describes the change in the self-energy of particles upon a phase transition is dominant in relationship (1); i.e., $|\Delta U_{12}| \gg U_0$, which corresponds to a first-order

phase transition. In this case, according to the first condition in relationships (2), we have [10, 20]

$$\varphi(T) = \left[1 + \exp\left(\frac{\Delta U_{12}}{kT}\right)\right]^{-1}. \quad (4)$$

The change in the energy of particles upon a phase transition is defined by $\Delta U_{12} = \omega\Delta u$, where ω is the elementary volume of the transformation and Δu is the change in the particle energy per unit volume of the crystal, that is,

$$\Delta u = q\frac{T - T_0}{T_0} - \xi_{ik}\tau_{ik} - \delta_0 P. \quad (5)$$

Here, q is the transition heat, ξ_{ik} stands for the spontaneous shear strains of the lattice upon its transformation into a form with a lower symmetry, $\delta_0 = \Delta V/V$ is the relative change in the crystal volume upon this transformation, τ_{ik} is the mechanical stress applied to the crystal, P is the applied hydrostatic pressure, and T_0 is the critical (characteristic) temperature of the transformation in the absence of external fields and defects.

As follows from formulas (4) and (5), the temperature dependence of φ in the absence of external actions has the form

$$\varphi(T) = \left[1 + \exp\left(B\frac{T - T_0}{T}\right)\right]^{-1}, \quad B = \frac{\omega q}{kT_0}. \quad (6)$$

Figure 1c shows the dependence plotted according to this equation at the parameter $B = 40$. It can be seen that the behavior and features of this dependence differ from those of the dependence for a purely orientational transition (Fig. 1a). Relationship (6) describes the transition of a given system of particles from one ordered state to another ordered state (for example, the transformation of the lattice from one type to another), which differs from the second-order phase transition when the disordered state at the critical temperature transforms into the ordered state.

Unlike the purely orientational transition, the critical temperature of the first-order phase transition cannot be exactly determined (Fig. 1c), because this transition is smeared; i.e., it occurs in the temperature range [10]

$$\Delta T = \frac{4T_0}{B} = 4\frac{kT_0^2}{\omega q}, \quad (7)$$

which depends on the elementary transformation volume ω and the transformation heat q. In this case, the role of the critical (exactly determined) temperature is played by the characteristic temperature T_0, at which, according to formula (6), $\varphi = 1/2$. In the presence of external fields (forces), the characteristic temperature that corresponds to the conditions $\Delta u = 0$ and $\varphi = 1/2$, according to expression (5), can be represented in the form

$$T_k = T_0 + \frac{T_0}{q}(\varepsilon_{ik}\tau_{ik} + \delta_0 P). \quad (8)$$

It is evident that formula (8) is the generalized Clausius–Clapeyron relationship for first-order phase transitions.

From expressions (4), (5), and (8), it follows that the high-temperature phase is predominant in the crystal at $\Delta u > 0$ ($T > T_k$) and the low-temperature phase dominates at $\Delta u < 0$ ($T < T_k$). Therefore, relationships (4) and (6) describe the phase equilibrium in the crystal. It should be noted that the condition of thermodynamic stability for this equilibrium [the second condition in relationships (2)] is not met for the phase states described by expressions (4) and (6). Instead, the phases are in mechanical (kinetic) equilibrium due to the interaction of interphase boundaries with structural defects in the crystal [10, 20].

It is clear that transitions of intermediate types should be observed between the first-order and second-order phase transitions. Making allowance for both the first and second terms in relationship (1), we obtain the following temperature dependence of the relative fraction of the low-temperature phase (in the implicit form):

$$\frac{T}{T_c} = \frac{B(T_k/T_c) + 2(2\varphi - 1)}{B + \ln\left(\frac{\varphi}{1 - \varphi}\right)}. \quad (9)$$

This equation is transformed into expression (3) at $B = 0$ and into formulas (4) and (6) at $T_c = 0$. Figure 1b displays the temperature dependence plotted according to formula (9) at $B = 2$ and $T_k/T_c = 1.05$. It is seen from this figure that the dependence $\varphi(T)$ exhibits a high-temperature "tail" at $T > T_c$ as compared to the curve $\varphi(T)$ for a purely orientational transition (Fig. 1a).

3. EFFECT OF PHASE TRANSITIONS ON THE PROPERTIES OF CRYSTALS

In experimental investigations, the properties of crystals are frequently described using differential characteristics, for example, the heat capacity $c = dQ/dT$ [1, 8, 9] and the plastic strain rate $\dot{\varepsilon} = d\varepsilon/dt$ [6], where Q is the thermal energy of the crystal, ε is the inelastic strain of the crystal, and t is the time. As a rule, phase transitions strongly affect these characteristics which manifests itself in the appearance of specific peaks in the corresponding curves.

For example, in the case of a first-order phase transition attended by the heat release or heat absorption $\Delta Q(T) = q\varphi(T)$, the change in the heat capacity of the crystal and the heat release (or heat absorption) rate are determined, respectively, by the formulas

$$\Delta c(T) = q\frac{d\varphi}{dT}, \quad \frac{d\Delta Q}{dt} = q\dot{T}\frac{d\varphi}{dT}, \quad (10)$$

where $\dot{T} = \text{const}$ is the rate of change in the temperature. Similarly, when the phase transition occurs, for example, under conditions of the uniaxial stress $\sigma = \tau/m$, the inelastic (pseudoelastic) strain $\varepsilon(T)$ of the crystal (due

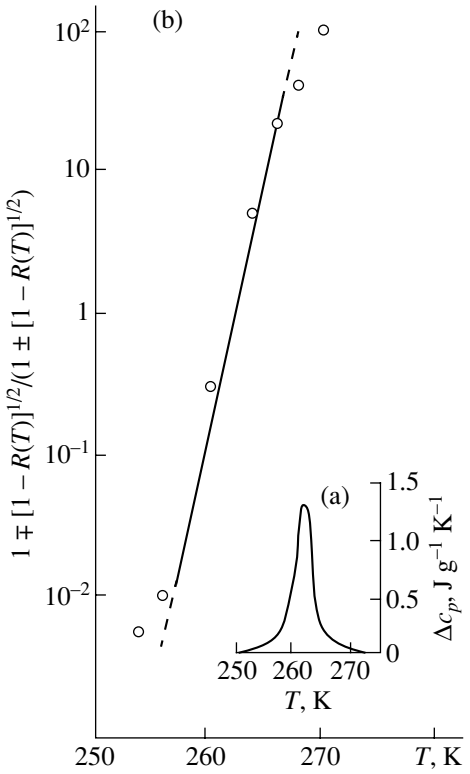

Fig. 2. Temperature dependences of the heat capacity Δc_p for C_{60} crystals (a) according to the data taken from [6] and (b) in the coordinates specified by expression (13b).

to the emergence of the strains $\xi_{ik} = \xi$ upon orientational transformation of the lattice) is determined by the formula $\varepsilon(T) = \varepsilon_m \varphi(T)$, where $\varepsilon_m = m\xi$ and m is an orientational factor dependent on the orientation of interphase boundaries with respect to the tension (or compression) axis of the crystal. Consequently, the rate of change in the inelastic strain with temperature and the rate of change in the inelastic strain with time at T = const are defined, respectively, as

$$\frac{d\varepsilon}{dT} = \varepsilon_m \frac{d\varphi}{dT}, \quad \dot{\varepsilon}(T) = \varepsilon_m \dot{T} \frac{d\varphi}{dT}. \tag{11}$$

Therefore, the character of the temperature dependences $\Delta c(T)$ and $\dot{\varepsilon}(T)$ is determined by the derivative $d\varphi/dT$. The calculation of this derivative in the general case of relationship (1) under the condition $\partial \Delta F/\partial \varphi = 0$ leads to the following expression:

$$\frac{d\varphi}{dT} = -\frac{\left(B + \ln\frac{\varphi}{1-\varphi}\right)^2 \varphi(1-\varphi)}{BT_k + T_c\left[2(2\varphi - 1) - 4\varphi(1-\varphi)\left(B + \ln\frac{\varphi}{1-\varphi}\right)\right]}. \tag{12a}$$

Hence, it follows that the derivative $d\varphi/dT$ for the second-order phase transition (i.e., at $B = 0$) takes the form

$$\frac{d\varphi}{dT} = -\frac{\left(\ln\frac{\varphi}{1-\varphi}\right)^2 \varphi(1-\varphi)}{T_c\left[2(2\varphi - 1) - 4\varphi(1-\varphi)\ln\frac{\varphi}{1-\varphi}\right]}. \tag{12b}$$

For the first-order phase transition ($T_c = 0$), we obtain

$$\frac{d\varphi}{dT} = -\frac{B}{T_k}\left(1 + B^{-1}\ln\frac{\varphi}{1-\varphi}\right)^2 \varphi(1-\varphi) \approx -\frac{B}{T_k}\varphi(1-\varphi). \tag{12c}$$

The approximate expression in formula (12c) holds under the condition $\ln\frac{\varphi}{1-\varphi} \gg B$.

Figures 1d–1f display the temperature dependences of the derivative $d\varphi/dT$, which are plotted according to formulas (12) and correspond to the curves $\varphi(T)$ in Figs. 1a–1c, respectively. It is evident that, unlike the second-order transitions characterized by a λ-shaped peak (Fig. 1d), the first-order transitions should manifest themselves in a diffuse Λ-shaped peak in the temperature dependences of the crystal properties in the phase transition range (Fig. 1f).

4. PARAMETERS OF THE SMEARED PHASE TRANSITION IN C_{60} CRYSTALS AT TEMPERATURES OF 250–260 K

Shpeĭzman *et al.* [6, 9] observed Λ-shaped peaks in the calorimetric curves of C_{60} crystals in the temperature range near 250 K. Figure 2a shows a similar peak obtained in the study of the heat release and heat capacity for a relatively large C_{60} crystal [6]. According to relationships (6) and (12c), the temperature dependence of the heat capacity due to the phase transition can be represented as

$$\Delta c_p(T) = \Delta c_m \frac{4\exp(B(T - T_0)/T_0)}{[1 + \exp(B(T - T_0)/T_0)]^2}, \quad \Delta c_m = \frac{qB}{4T_0}, \tag{13a}$$

where Δc_m is the maximum heat capacity at $T = T_0$.

By designating $R(T) = \Delta c_p(T)/\Delta c_m$, this dependence can be rewritten as

$$\ln\frac{1 \mp [1 - R(T)]^{1/2}}{1 \pm [1 - R(T)]^{1/2}} = B\frac{T - T_k}{T_0}, \tag{13b}$$

where the upper and lower signs before the square root sign refer to the ascending and descending portions of the Λ-shaped peak, respectively. Figure 2b depicts the experimental dependence $\Delta c_p(T)$ (Fig. 2a) in the coor-

dinates specified by relationship (13b). As can be seen, the $\Delta c_p(T)$ dependence in these coordinates is represented by a straight line, except for the lowest and highest portions of the curve [$R(T) \ll 1$ and $\varphi(T) \ll 1$], in which the approximate expression (12c) becomes invalid. According to relationship (13b), the slope of the straight line depends on the B parameter defined by formula (6). In the case under consideration, at $T_0 = 262$ K, we have $B = 224$. After substituting these parameters into relationship (7), we found that the phase transition is smeared in the temperature range $\Delta T = 4.7$ K.

It follows from the data presented in Fig. 2a that the maximum heat capacity Δc_m is equal to 1.29 J g^{-1} K^{-1} and, hence, according to formula (13a), the transition heat q_0 is approximately equal to 6 J g^{-1}. This estimate is in agreement with the data available in the literature [1, 9]. In the case when the density of C_{60} crystals is 1.62 g cm^{-3} [5], we obtain $q = 9.7$ J cm^{-3}. Consequently, the elementary volume ω of the transformation is determined from relationship (6) as follows: $\omega = (kT_0/q)B = 83 \times 10^{-21}$ cm^3 (i.e., $\omega = 83$ nm^3). When the lattice parameter a for C_{60} is equal to 1.41 nm, the number of molecules involved in the elementary act of correlated transformation is estimated as $n = \omega/a^3 \approx 27$. These estimates agree with the results of neutron investigations of the orientational transition in C_{60} [2, 21], according to which the elementary volume of the transformation is equal to 64 nm^3 and the smearing of the phase transition is observed in the temperature range $\Delta T \approx 5$ K.

Figure 3a depicts the dependence of the strain rate for the C_{60} crystal in the temperature range of the orientational transition upon a stepwise change in the temperature at a mean rate $\dot{T} \approx 1$ K min^{-1} and at an applied compressive stress of 6.7 MPa [6]. It is seen that the $\dot{\varepsilon}(T)$ dependence has a Λ-shaped form. At $T_0 = 252$ K, the strain rate reaches a maximum value of 6.4×10^{-6} s^{-1}. The temperature dependence of the strain rate in the phase transition range is described by an expression similar to relationship (13a), that is,

$$\dot{\varepsilon}(T) = \dot{\varepsilon}_{\max}\frac{4\exp(B(T-T_k)/T_0)}{[1+\exp(B(T-T_k)/T_0)]^2}, \qquad \dot{\varepsilon}_{\max} = \frac{\varepsilon_m B}{4T_0}\dot{T}, \tag{14a}$$

where, according to formula (8),

$$T_k = T_0 + \frac{T_0}{q}\varepsilon_m\sigma. \tag{14b}$$

Figure 3b shows the temperature dependence of the strain rate in the coordinates specified by relationship (13b), where $R(T) = \dot{\varepsilon}(T)/\dot{\varepsilon}_{\max}$. It can be seen that, in these coordinates, the experimental points fit a straight line whose slope corresponds to the parameter $B = 32$. In this case, the smearing of the phase transition is observed in the temperature range $\Delta T = 31.5$ K. The elementary volume of the transformation at $q = 9.7$ J cm^{-3} is equal to 11.5 nm^3, and, hence, the number n of molecules involved in the act of correlated transformation is four.

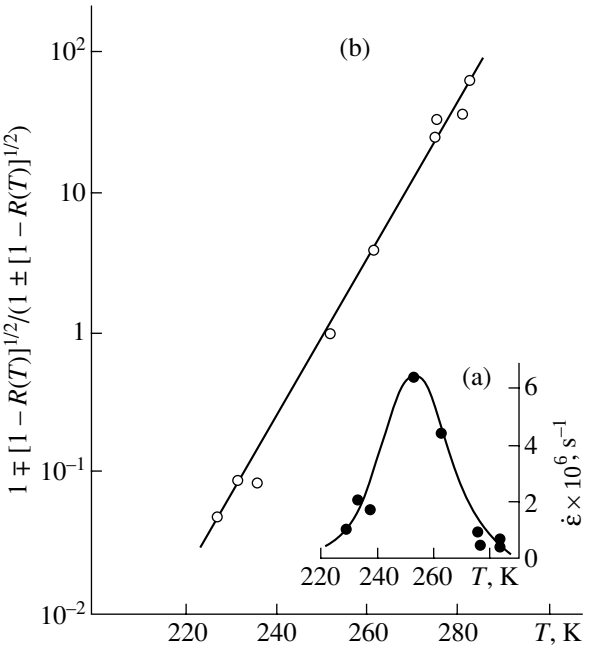

Fig. 3. Temperature dependences of the inelastic strain rate $\dot{\varepsilon}$ for C_{60} crystals (a) according to the data taken from [6] and (b) in the coordinates specified by expression (13b).

From relationship (14a), we found that $\varepsilon_m = 1.2 \times 10^{-2}$. Consequently, the spontaneous shear strain ξ of the lattice upon its transformation from the face-centered cubic to the primitive cubic structure is equal to 2.4×10^{-2} at $m = 0.5$. This value is of the same order of magnitude as the lattice dilatation upon this transformation: $\delta_0 = \Delta V/V \approx 10^{-2}$ [14, 15]. Relationship (14b) allows one to estimate the shift in the characteristic temperature under the compressive stress $\sigma = 6.7$ MPa. According to the estimates, this shift is small (of the order of 2 K).

5. CONCLUSION

Thus, the theory of smeared first-order phase transitions makes it possible to evaluate quantitatively the parameters of the orientational structural transformation in C_{60} crystals at temperatures of 250–260 K and to elucidate the influence of this transformation on the crystal properties.

ACKNOWLEDGMENTS

I am grateful to B.I. Smirnov, V.V. Shpeĭzman, and V.M. Egorov for their participation in discussions of the results.

This work was supported by the Russian Scientific and Technical Program "Fullerenes and Atomic Clusters," project no. 98065 "Cluster."

REFERENCES

1. P. A. Heiney, J. E. Fisher, A. R. McGhie, *et al.*, Phys. Rev. Lett. **66** (22), 2911 (1991).
2. B. Sundquist, Adv. Phys. **48** (1), 1 (1999).
3. S. Hoen, N. G. Chorpa, X.-D. Xiang, *et al.*, Phys. Rev. B **46** (19), 12737 (1992).
4. N. P. Kobelev, A. P. Moravskiĭ, Ya. M. Soĭfer, *et al.*, Fiz. Tverd. Tela (St. Petersburg) **36** (9), 2732 (1994) [Phys. Solid State **36**, 1491 (1994)].
5. V. V. Shpeĭzman, N. N. Peschanskaya, V. M. Egorov, *et al.*, Fiz. Tverd. Tela (St. Petersburg) **41** (6), 1115 (1999) [Phys. Solid State **41**, 1017 (1999)].
6. V. V. Shpeĭzman, N. N. Peschanskaya, V. M. Egorov, *et al.*, Fiz. Tverd. Tela (St. Petersburg) **42** (9), 1721 (2000) [Phys. Solid State **42**, 1771 (2000)].
7. V. D. Natsik, S. V. Lubenets, and L. S. Fomenko, Fiz. Nizk. Temp. **22** (3), 337 (1996) [Low Temp. Phys. **22**, 264 (1996)].
8. G. A. Samara, J. E. Schirber, B. Morosin, *et al.*, Phys. Rev. Lett. **67** (22), 3136 (1991).
9. V. M. Egorov, R. K. Nikolaev, B. I. Smirnov, and V. V. Shpeĭzman, Fiz. Tverd. Tela (St. Petersburg) **41** (3), 550 (1999) [Phys. Solid State **41**, 494 (1999)].
10. G. A. Malygin, Usp. Fiz. Nauk **171** (2), 187 (2001).
11. A. N. Tsotsorin, S. A. Gridnev, S. P. Rogova, and A. G. Luchaninov, Izv. Akad. Nauk, Ser. Fiz. **62** (8), 1579 (1998).
12. G. A. Malygin, Fiz. Tverd. Tela (St. Petersburg) **35** (11), 2993 (1993) [Phys. Solid State **35**, 1470 (1993)].
13. S. A. Gridnev and O. N. Ivanov, Sverkhprovodimost: Fiz., Khim., Tekh. **5** (7), 1143 (1992).
14. P. A. Heiney, G. B. Vaughan, J. E. Fischer, *et al.*, Phys. Rev. B **45** (8), 4544 (1992).
15. W. I. David, R. M. Ibberson, and T. Matsuo, Proc. R. Soc. London, Ser. A **442** (1914), 129 (1993).
16. V. V. Kirillov and V. A. Isupov, Ferroelectrics **5** (1), 3 (1971).
17. R. L. Moreira and R. P. Lobo, J. Phys. Soc. Jpn. **61** (6), 1992 (1992).
18. G. A. Malygin, Fiz. Tverd. Tela (St. Petersburg) **36** (5), 1489 (1994) [Phys. Solid State **36**, 815 (1994)].
19. M. Fisher, *The Nature of Critical Points* (Univ. of Colorado Press, Boulder, 1965; Mir, Moscow, 1968).
20. G. A. Malygin, Zh. Tekh. Fiz. **66** (11), 112 (1996) [Tech. Phys. **41**, 1145 (1996)].
21. L. Pintschovius, S. L. Chaplo, G. Roth, and G. Heger, Phys. Rev. Lett. **75** (15), 2843 (1995).

Translated by O. Borovik-Romanova

Physics of the Solid State, Vol. 43, No. 10, 2001, pp. 1995–1998. Translated from Fizika Tverdogo Tela, Vol. 43, No. 10, 2001, pp. 1916–1919.

FULLERENES AND ATOMIC CLUSTERS

Relationships for Total Energies of C_n Fullerenes and Their Derivatives Containing Nitrogen and Boron Atoms in the Polyhedral Carbon Cage

I. V. Stankevich* and R. Seto**

** Nesmeyanov Institute of Organoelement Compounds, Russian Academy of Sciences, ul. Vavilova 28, Moscow, 117813 Russia*

*** Moscow State University, Vorob'evy gory, Moscow, 119899 Russia*

e-mail: stan@ineos.ac.ru

Received March 5, 2001

Abstract—The relationships characterizing the ground-state total energies of polyhedral carbon clusters and their derivatives containing boron and nitrogen atoms in the polyhedral cage are derived. These relationships do not depend on computational details and can be used for testing *ab initio* and semiempirical methods. The field of application of the inequalities obtained is illustrated by several examples. © *2001 MAIK "Nauka/Interperiodica".*

1. INTRODUCTION

Investigation into the chemical structure and physicochemical properties of heterofullerenes and heteronanotubulenes with different distributions of nitrogen and boron atoms in the polyhedral cage has been stimulated by many factors, such as the discovery of polyhedral carbon clusters (fullerenes), experimental studies demonstrating the possibility of replacing particular carbon atoms of fullerenes by boron and nitrogen atoms [1–3], the existence of Ti_8C_{12} and similar clusters [4–6], and recent synthesis of boron nitrides with a tubular structure [7].

To date, numerous theoretical works dealing with quantum-chemical calculations of similar systems have been published (see, for example, [8–16] and references therein).

Among the chemical compounds containing boron and nitrogen atoms, many structures are isoelectronic and isostructural to their carbon analogs. Analysis of recent calculations has revealed that the substitution of B–N bonds for particular C–C bonds in hydrocarbon molecules or carbon clusters leads, in many cases, to a considerable decrease in the total energy. For example, according to the MNDO calculations, the total energies for benzene and borazine molecules (see Fig. 1, systems 1*a* and 1*b*, respectively) differ by 44 eV, whereas these energies for C_{60} and $C_{58}BN$ clusters differ by 34 eV [11]. Other examples are available in [8, 14].

In the present work, the difference between the ground-state total energies for isostructural and isoelectronic polyhedral carbon clusters C_n and their B,N-derivatives was demonstrated by the example of particular polyhedral molecules of the $(BN)_xC_{n-2x}$ compounds. It was shown that the observed difference has a general character and does not depend on the calculation procedure (undeniably, this procedure needs to be substantiated theoretically).

The main purpose of this work was to demonstrate that the following relationships characterizing the ground-state energies of fullerenes are valid for a rather wide class of $(BN)_xC_{n-2x}$ ($n - 2x \geq 0$) clusters:

$$E((BN)_xC_{n-2x}) + \Delta E < E(C_n). \qquad (1)$$

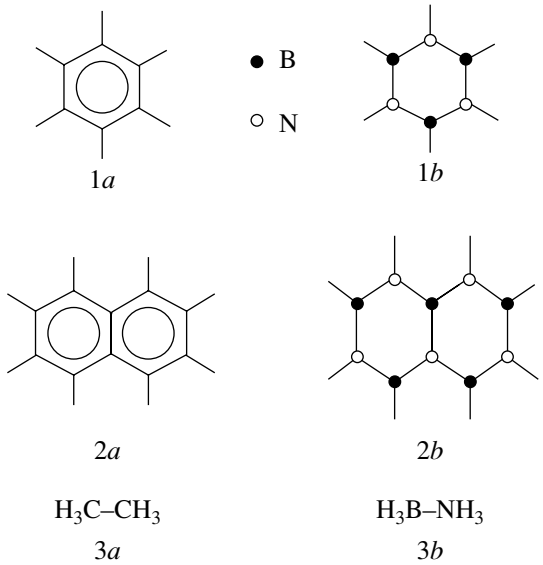

Fig. 1. A scheme illustrating the transition from the carbon skeleton to the skeleton containing the B–N bonds by the example of three pairs of molecules.

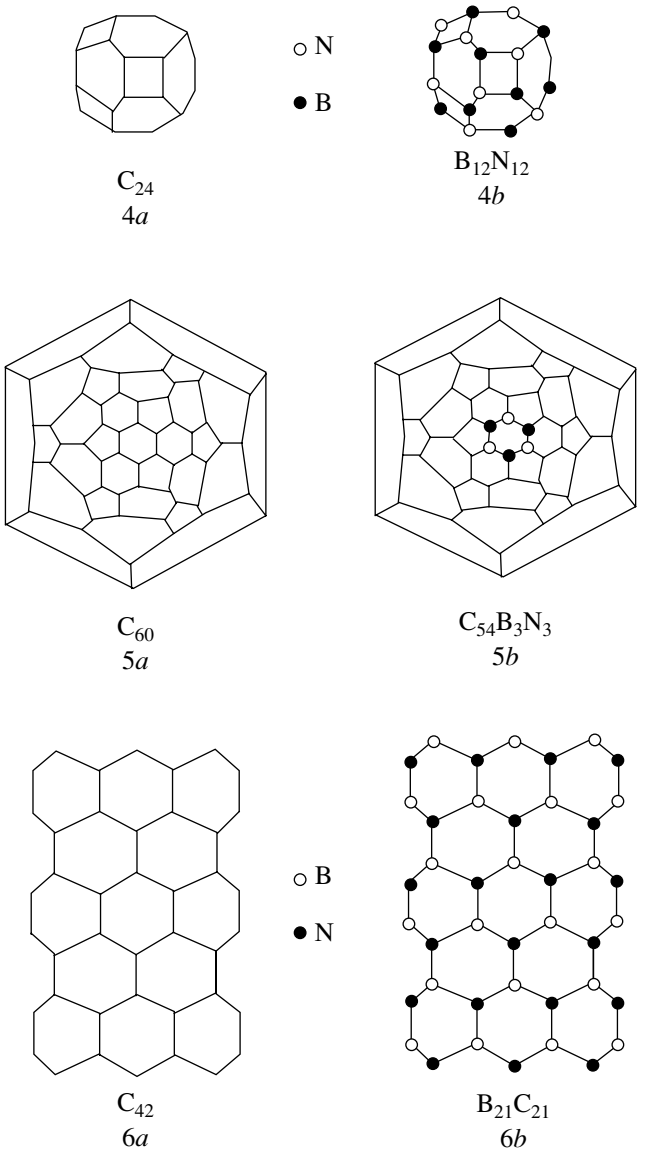

Fig. 2. (4*a*–6*a*) Three carbon clusters and (4*b*–6*b*) their B,N-derivatives. Cluster 6*a* can be considered a fragment of the graphite layer or a fragment of the single-layer tubulene.

Here, $E(Q)$ is the ground-state energy of the cluster Q and

$$\Delta E = \sum_{\mu=1}^{n}\sum_{\mu<\nu}\frac{\pm 1}{|\mathbf{R}_\mu - \mathbf{R}_\nu|},$$

where $\mathbf{R}_\mu$ and $\mathbf{R}_\nu$ are the coordinates of the μth and ν th nuclei, respectively, and the subscripts μ and ν refer only to B and N atoms. In the case when the μ and ν subscripts refer to atoms of different types, the corresponding term in the expression for ΔE is positive. If the μ and ν subscripts indicate atoms of the same type, this term is negative.

2. THEORETICAL BACKGROUND

Let us consider a molecular system consisting of n atoms in terms of the n-dimensional vector $\mathbf{Z} = (Z_1, Z_2, \ldots, Z_n)$ with the components Z_μ, where Z_μ is the nuclear charge of the μth atom ($\mu = 1, \ldots, n$). In these notations, for example, the hydrogen molecule H_2 is described by the vector $\mathbf{Z} = (1, 1)$, whereas the methane molecule CH_4 is represented by the vector $\mathbf{Z} = (6, 1, 1, 1, 1)$. The carbon cluster C_n is described by the n-dimensional vector $\mathbf{Z} = (6, 6, \ldots, 6)$.

The spinless nonrelativistic Hamiltonian of the molecular system in the Born–Oppenheimer approximation in atomic units (au) can be written as

$$H(\mathbf{Z}) = -\frac{1}{2}\sum_{i=1}^{m}\Delta_i - \sum_{i=1}^{m}\sum_{\mu=1}^{n}\frac{Z_\mu}{|\mathbf{r}_i - \mathbf{R}_\mu|} + \frac{1}{2}\sum_{i\neq j}\frac{1}{|\mathbf{r}_i - \mathbf{r}_j|} + \frac{1}{2}\sum_{\mu\neq\nu}\frac{Z_\mu Z_\nu}{|\mathbf{R}_\mu - \mathbf{R}_\nu|}.$$

Here, m is the number of electrons; $\mathbf{r}_i$ and $\mathbf{R}_\mu$ are the coordinates of the ith electron and the μth nucleus, respectively; and Δ_i is the Laplace operator in the $\mathbf{r}_i$ coordinates.

We assume that the $\mathbf{Z}$ vector can be represented in the form

$$\mathbf{Z} = \alpha_1\mathbf{Z}^{(1)} + \alpha_2\mathbf{Z}^{(2)}, \quad \alpha_1 + \alpha_2 = 1,$$
$$0 < \alpha_1, \quad \alpha_2 < 1,$$

where $\mathbf{Z}^{(1)}$ and $\mathbf{Z}^{(2)}$ are the n-dimensional vectors with integral nonnegative components. Then, the Hamiltonian can be rewritten in the following form [17]:

$$H(\mathbf{Z}) = \alpha_1 H(\mathbf{Z}^{(1)}) + \alpha_2 H(\mathbf{Z}^{(2)}) + \alpha_1\alpha_2\sum_{\mu=1}^{n}\sum_{\mu<\nu}\frac{(\mathbf{Z}_\mu^{(1)} - \mathbf{Z}_\mu^{(2)})(\mathbf{Z}_\nu^{(2)} - \mathbf{Z}_\nu^{(1)})}{|\mathbf{R}_\mu - \mathbf{R}_\nu|}.$$

By using the normalized trial function Ψ, which contains $\{\mathbf{R}_\mu\}$ as parameters, and denoting the ground-state energies as $\{E(\mathbf{Z}^{(1)}), E(\mathbf{Z}^{(2)}), E(\mathbf{Z})\}$ of the Hamiltonians $\{H(\mathbf{Z}^{(1)}), H(\mathbf{Z}^{(2)}), H(\mathbf{Z})\}$, respectively, we obtain the mean value of the Hamiltonian $H(\mathbf{Z})$ in the form

$$\langle\Psi|H(\mathbf{Z})|\Psi\rangle = \alpha_1\langle\Psi|H(\mathbf{Z}^{(1)})|\Psi\rangle + \alpha_2\langle\Psi|H(\mathbf{Z}^{(2)})|\Psi\rangle + \alpha_1\alpha_2\sum_{\mu=1}^{n}\sum_{\mu<\nu}\frac{(\mathbf{Z}_\mu^{(1)} - \mathbf{Z}_\mu^{(2)})(\mathbf{Z}_\nu^{(2)} - \mathbf{Z}_\nu^{(1)})}{|\mathbf{R}_\mu - \mathbf{R}_\nu|},$$

where

$$E(\mathbf{Z}^{(1)}) \le \langle\Psi|H(\mathbf{Z}^{(1)})|\Psi\rangle, \quad E(\mathbf{Z}^{(2)}) \le \langle\Psi|H(\mathbf{Z}^{(2)})|\Psi\rangle$$

and

$$E(\mathbf{Z}) = \min(\langle\Psi|H(\mathbf{Z})|\Psi\rangle),$$

Consequently,

$$\alpha_1 E(\mathbf{Z}^{(1)}) + \alpha_2 E(\mathbf{Z}^{(2)}) + \alpha_1\alpha_2 \sum_{\mu=1}^{n}\sum_{\mu<\nu} \frac{(\mathbf{Z}_\mu^{(1)} - \mathbf{Z}_\mu^{(2)})(\mathbf{Z}_\nu^{(2)} - \mathbf{Z}_\nu^{(1)})}{|\mathbf{R}_\mu - \mathbf{R}_\nu|} < E(\mathbf{Z}). \quad (2)$$

Note that this inequality is the modification of a similar relationship derived by Mezey (see, for example, [18, 19]).

3. RESULTS AND DISCUSSION

Relationship (2) makes it possible to estimate, from below, the ground-state energy of a C_n polyhedral cluster consisting of n atoms. As was noted above, this carbon cluster can be described by the n-dimensional vector $\mathbf{Z} = (6, 6, \ldots, 6)$. Let us assume that any two atoms of this cluster, for example, carbon atoms with numbers 1 and 2, are symmetrically equivalent to each other. Now, we formally replace the first and second carbon atoms in the C_n cluster by the B and N atoms, respectively, leaving the geometry of the cluster unchanged. In this case, the $(BN)C_{n-2}$ system is described by the vector $\mathbf{Z}^{(1)} = (5, 7, 6, \ldots, 6)$. Similarly, we replace the first and second atoms in the C_n cluster by the N and B atoms, respectively. As a result, we also obtain the heteroatomic cluster $(BN)C_{n-2}$. This cluster has the same energy as the former cluster but is described by the vector $\mathbf{Z}^{(2)} = (7, 5, \ldots, 6)$. The vector $\mathbf{Z}$ can be represented as the sum

$$\mathbf{Z} = \frac{1}{2}\mathbf{Z}^{(1)} + \frac{1}{2}\mathbf{Z}^{(2)}.$$

Then, relationship (2) can be rewritten as

$$\frac{1}{2}E(\mathbf{Z}^{(1)}) + \frac{1}{2}E(\mathbf{Z}^{(2)}) + \frac{1}{|R_1 - R_2|} \le E(\mathbf{Z}),$$

where $E(\mathbf{Z}^{(1)}) = E(\mathbf{Z}^{(2)})$. Hence, we obtain

$$E((BN)C_{n-2}) + \frac{1}{|R_1 - R_2|} \le E(C_N).$$

In the general case, we assume that x pairs of the (C, C) atoms (x is the number of pairs) in the C_n cluster (for example, the cluster atoms involved in the C–C bonds) are replaced by the B–N/N–B pairs and the modified cluster $(BN)_nC_{n-2x}$ remains invariant upon rearrangement of the B and N atoms in all these pairs. In this case, the $\mathbf{Z}$ vector of the C_n cluster can be represented as $\mathbf{Z} = 0.5\mathbf{Z}^{(1)} + 0.5\mathbf{Z}^{(2)}$, where the vectors $\mathbf{Z}^{(1)}$ and $\mathbf{Z}^{(2)}$ refer to the $(BN)_xC_{n-2x}$ cluster and differ from each other only in the sequence of components that correspond to the $\{B \longrightarrow N, N \longrightarrow B\}$ rearrangement. Note that, upon rearrangement, the total energy of this heteroatomic cluster remains invariant. Several pairs of polyhedral molecular systems that meet these conditions are shown in Fig. 2.

Now, we analyze the expression

$$\alpha_1\alpha_2 \sum_{\mu=1}^{n}\sum_{\mu<\nu} \frac{(\mathbf{Z}_\mu^{(1)} - \mathbf{Z}_\mu^{(2)})(\mathbf{Z}_\nu^{(2)} - \mathbf{Z}_\nu^{(1)})}{|\mathbf{R}_\mu - \mathbf{R}_\nu|}.$$

In this formula, the summands are nonzero only when the μth components of the $\mathbf{Z}^{(1)}$ and $\mathbf{Z}^{(2)}$ vectors, as well as the νth components of the $\mathbf{Z}^{(1)}$ and $\mathbf{Z}^{(2)}$ vectors, correspond to atoms of different types. In addition, if the μth and νth components of either of the two vectors $\mathbf{Z}^{(1)}$ and $\mathbf{Z}^{(2)}$ correspond to atoms of the same type, these summands are negative. In the case when the μth and νth components of either of the two vectors $\mathbf{Z}^{(1)}$ and $\mathbf{Z}^{(2)}$ refer to atoms of different types, the summands are positive. Consequently, the (B, B) and (N, N) pairs make the negative contributions to the energy difference ΔE, the contributions made by the (B, N) pairs to ΔE are positive, and the contributions from the (B, C), (N, C), and (C, C) pairs are equal to zero. Since $\alpha_1 = \alpha_2 = 0.5$, $Z_N = 7$, and $Z_B = 5$, formula (2) for the ground-state energies of the $(BN)_nC_{n-2x}$ and C_n clusters is readily transformed into relationship (1). Note that inequality (1) has an electrostatic nature. The value of ΔE coincides (up to a sign) with the energy of point charges $\pm e$ on the B and N atoms. For crystals such as graphite and hexagonal boron nitride, inequality (1) can be rewritten for the mean total energies. The calculation of the specific energy ΔE_i for these systems is reduced to an estimation of the Madelung constant. Figures 1 and 2 illustrate the field of application of inequality (1).

It should be noted that the sign of ΔE is determined primarily by the first coordination spheres of the B and N atoms. If the B–B and N–N bonds are absent in the $(BN)_xC_{n-2x}$ cluster, ΔE will be positive.

Let us now consider the two following examples.

(1) Figure 2 depicts the Schlegel diagram for the (I_h)-C_{60} fullerene (5*a*). According to our calculations with the Hartree–Fock method in the 6-31G basis set, the bond lengths in the six-membered ring of the 5*a* fullerene alternate and are equal to 1.452 and 1.375 Å, respectively. Now, we replace the particular carbon atoms in one of the hexagons of the 5*a* cluster by the B and N atoms in such a way as to obtain the $(BN)_3C_{54}$ (5*b*) cluster.

Then, it immediately follows from formula (1) that the ground-state energies of these clusters [C_{60} and $(BN)_3C_{54}$] should satisfy the inequality $E(C_{60}) - E((BN)_3C_{54}) > 1.52$ au.

(2) It is assumed that the structure of the 4*a* cluster (Fig. 2) is described by a semiregular truncated octahedron for which the length of each edge is equal to L. We replace all carbon atoms in the 4*a* fullerene by the B or N atoms in such a way as to obtain the $B_{12}N_{12}$ cluster (4*b* in Fig. 2). Simple calculations show that $\Delta E \sim 18.144L^{-1}$. The value of ΔE at $L = 1.54$ Å is equal to 6.23 au. It follows from formula (1) that the ground-state energies at this geometry of the clusters obey the inequality $E(C_{24}) - E(B_{12}N_{12}) > 6.23$ au.

4. CONCLUSION

Thus, it was demonstrated that inequality (1) has a general character. This formula makes it possible to estimate the difference between the total energies of carbon clusters and their B,N-derivatives without having to employ complex calculations. The relationships obtained in this work can also be used for tubulenes and their B,N-derivatives. Formula (1) does not depend on the computational details of the quantum-chemical method. Therefore, inequality (1) can be used for checking the quality of *ab initio* and semiempirical calculations of molecular systems.

ACKNOWLEDGMENTS

We are grateful to L.A. Chernozatonskiĭ, A.L. Chistyakov, and N.P. Gambaryan for their valuable discussions of the results.

This work was supported by the Russian Foundation for Basic Research and the Russian Scientific and Technical Program "Topical Directions in the Physics of Condensed Matter," Subprogram "Fullerenes and Atomic Clusters."

REFERENCES

1. H. W. Kroto, J. R. Heath, S. C. O'Brien, *et al.*, Nature (London) **318**, 162 (1985).
2. W. Krätshmer, L. D. Lamb, K. Fostiropoulos, and D. R. Huffman, Nature (London) **347**, 354 (1990).
3. V. I. Sokolov and I. V. Stankevich, Usp. Khim. **62** (6), 455 (1993).
4. T. Guo, C. Jin, and R. E. Smalley, J. Phys. Chem. **95**, 4948 (1991).
5. T. Guo, K. Kerns, and A. Gastleman, Science **255**, 1411 (1992).
6. M. S. Dresselhaus, G. Dresselhaus, and P. Eklund, *Science of Fullerene and Nanotubes* (Academic, San Diego, 1996).
7. T. Oku, T. Hirano, M. Kuno, *et al.*, Mater. Sci. Eng. B **B74**, 206 (2000).
8. I. V. Stankevich, A. L. Chistyakov, E. G. Gal'pern, and N. P. Gambaryan, Zh. Strukt. Khim. **36** (6), 986 (1995).
9. L. Lou, T. Guo, P. Nordlander, and R. E. Smalley, J. Chem. Phys. **99**, 5301 (1993).
10. P. J. Hay, J. Phys. Chem. **97**, 3081 (1992).
11. X. Xia, D. A. Jelski, J. R. Bowser, and T. F. George, J. Am. Chem. Soc. **114**, 6493 (1992).
12. I. V. Stankevich, A. L. Chistyakov, and E. G. Gal'pern, Izv. Akad. Nauk, Ser. Khim., No. 10, 1712 (1993).
13. I. Silaghi-Dimitsescu, I. Haiduc, and D. B. Sowerby, Inorg. Chem. **32**, 3755 (1993).
14. M. E. Zandler, E. C. Behram, M. B. Arrasmith, *et al.*, J. Mol. Struct.: THEOCHEM **362**, 215 (1996).
15. E. G. Gal'pern, V. V. Pinyaskin, I. V. Stankevich, and L. A. Chernozatonskii, J. Phys. Chem. B **101** (5), 705 (1997).
16. I. V. Stankevich and L. A. Chernozatonskiĭ, Fiz. Tverd. Tela (St. Petersburg) **41**, 1515 (1999) [Phys. Solid State **41**, 1386 (1999)].
17. E. E. Daza and J. L. Villaveces, J. Chem. Inf. Comput. Sci. **34**, 309 (1994).
18. P. F. Mezey, Int. J. Quantum Chem., Symp. **15**, 279 (1981).
19. P. F. Mezey, Int. J. Quantum Chem. **29**, 85 (1986).

Translated by N. Korovin